Transactions of the ASME®

Journal of Engineering for Gas Turbines and Power

Published Quarterly by The American Society of Mechanical Engineers

VOLUME 122 • NUMBER 1 • JANUARY 2000

Transactions of the ASME, Journal of Engineering for Gas Turbines and Power (ISSN 0742-4795) is published quarterly (Jan., April, July, Oct.) for $215.00 per year by The American Society of Mechanical Engineers, Three Park Avenue, New York, NY 10016. Periodicals postage paid at New York, NY and additional mailing offices. POSTMASTER: Send address changes to Transactions of the ASME, Journal of Engineering for Gas Turbines and Power, c/o THE AMERICAN SOCIETY OF MECHANICAL ENGINEERS, 22 Law Drive, Box 2300, Fairfield, NJ 07007-2300.
CHANGES OF ADDRESS must be received at Society headquarters seven weeks before they are to be effective. Please send old label and new address.
PRICES: To members, $40.00, annually: to nonmembers, $215.00. Add $40.00 for postage to countries outside the United States and Canada.
STATEMENT from By-Laws. The Society shall not be responsible for statements or opinions advanced in papers or . . . printed in its publications (B7.1, par. 3).

INDEXED by Applied Mechanics Reviews and Engineering Information, Inc. Canadian Goods & Services Tax Registration #126148048

TECHNICAL PAPERS

This journal is printed on acid-free paper, which exceeds the ANSI Z39.48-1992 specification for permanence of paper and library materials. ♾™
♻ 85% recycled content, including 10% post-consumer fibers.

Internal Combustion Engines

Power

J. H. Horlock

J. B. Young

Whittle Laboratory,
Cambridge University,
Madingley Road,
Cambridge, CB3 0DY,
United Kingdom

G. Manfrida

Dipartimento di Energetica "Sergio Stecco,"
Università di Firenze,
Via S. Marta 3,
50139 Firenza,
Italy

Exergy Analysis of Modern Fossil-Fuel Power Plants

The definition of open cycle rational efficiency is unequivocally based on the ratio of the actual shaft work output from a power plant to the maximum work that could be obtained in a reversible process between prescribed inlet and outlet states. However, different constraints may be applied to such an ideal reversible process, and the maximum work obtainable will then vary, as will the value of the rational efficiency. Attention has been drawn to this issue before in the literature and it is discussed further here. In particular, the consequences of defining the outlet state for the ideal process are critical. A further complication occurs when water or steam is injected into a gas turbine plant. Three definitions of rational efficiency are discussed here and some illustrative calculations presented. There are small but significant differences between the values of the three derived efficiencies.

1 Introduction

The use of availability (and/or exergy) in the analysis of power plant performance is well established. Several text books give details of the thermodynamic approach used; those by Kotas (1985), Szargut et al. (1988), and Moran (1989) are totally concerned with availability and exergy, but other more general text books (e.g., Obert (1960); Haywood (1980); Gyftopoulos and Beretta (1991); Bejan et al. (1996)) also include relevant chapters.

The concept of power plant rational efficiency was introduced to provide a criterion of performance relating the actual shaft work output from a power plant to the work output that would be achievable under some specified ideal operating condition (e.g., Szargut and Petela (1965)). The plant rational efficiency was therefore to be distinguished from the plant overall efficiency, commonly used in industry, which is based on the calorific value (or heating potential) of the fuel.

In practice, however, the specification of a suitable ideal process from which to calculate the ideal shaft work is not as straightforward as might be supposed. This was first emphasised by Stodola (1924) and well illustrated subsequently by Obert (1960), who considered three examples of an ideal reaction of carbon with air entering separately at standard pressure and temperature (p_0, T_0), but with products discharging at three different conditions: (a) separately at (p_0, T_0), (b) mixed at (p_0, T_0), and (c) separately at pressures corresponding to the partial pressures of the constituents within the atmosphere. In discussing his examples, Obert showed that the ideal work is little different for the three cases (a), (b), and (c).

These examples are illustrated diagrammatically in Fig. 1 for the combustion of a hydrocarbon fuel with an air supply in excess of stoichiometric requirements. Also shown is a "reference" case (d), similar to (a), but with reactants (fuel, oxygen, and nitrogen) entering separately at pressure (p_0, T_0) and products leaving individually at pressure (p_0, T_0). Here we shall consider cases (b), (c), and (d) in detail but in reverse order. In each of these three cases it is assumed that H_2O leaves in the vapour state. For case (c) this poses no problem as the products leave in the atmospheric equilibrium state (assuming the relative humidity is less than unity). But cases (b) and (d) require consideration of hypothetical or fictitious states (see Kotas and the discussion below in Section 4).

For case (d) the ideal work is the change in Gibbs free energy of the fuel $[-\Delta G_0]_{WV}$ in a reaction to the vapour state (an alternative approach by Bejan et al. (1996) postulates water leaving in the compressed liquid equilibrium state so the change in Gibbs free energy is then $[-\Delta G_0]_{WL}$, which is different from $[-\Delta G_0]_{WV}$. Moran called the ideal work for case (c) "the chemical availability of the fuel at p_0 and T_0," and showed that it is little different from $[-\Delta G_0]_{WV}$ for many fuels. This case (c) may be regarded as a classical definition of rational efficiency, but as Moran pointed out, rational efficiencies are, for simplicity, often calculated on the basis of case (d) (see Haywood (1980), (1991)).

Case (b), in which the ideal work output is reduced below that of case (c) by an amount equal to the mixing loss associated with further discharge to the atmosphere, is an alternative which is examined in more detail in this paper. Recently developed fossil-fuel power plants (in particular the combined cycle gas turbine plant, CCGT) employ quite low gas exhaust temperatures (less than 100°C) thus reducing the loss of thermal exergy in the exhaust stack. In such cases the loss of exergy associated with a failure to expand the products to atmospheric partial pressures (virtually impossible in practice) becomes comparable with the loss of thermal exergy. Gyftopoulos and Beretta (1991) drew attention to the practice of keeping the exhaust gas temperature above the dewpoint (to avoid corrosion effects) and suggested that the assumed discharge state for an ideal process might allow for such practice, presumably by assuming an exit temperature equal to the dewpoint temperature. This would then lead to ignoring a specified amount of thermal exergy loss as well as mixing loss in the ideal process. However, we have not developed that approach here.

To summarise, in this paper we consider,

1. the impact of recent developments in power plant technology on the different rational efficiencies which can be found in the literature
2. the particular problem, related to the practice of water or steam injection, which leads to the discharge of wetter exhaust gases and an effect on rational efficiency
3. the relation between the irreversibility in combustion and the loss of exergy due to mixing in the exhaust

Finally, full exergy calculations are given for three modern power plants with the rational efficiencies calculated according to three definitions based on cases (b), (c), and (d).

Contributed by the Advanced Energy Systems Division of The American Society of Mechanical Engineers for publication in the ASME Journal of Engineering for Gas Turbines and Power.

Manuscript received by the Advanced Energy Systems Division August 28, 1998; final revision received by the ASME Headquarters July 5, 1999. Technical Editor: M. J. Moran.

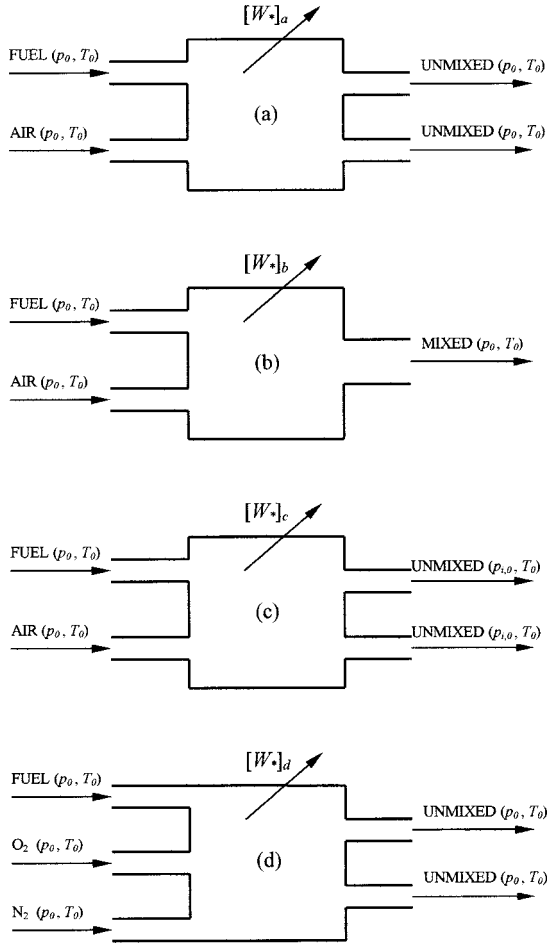

Fig. 1 Definitions of four ideal processes

2 The General Statement of Rational Efficiency

As indicated in the introduction, the use of availability and exergy leading to the definition of rational efficiency is well covered in the literature and is therefore only briefly outlined here.

With reference to an open-circuit steady-flow power plant supplied with fuel and atmospheric air, the general definition of rational efficiency η is,

$$\eta = \frac{W}{W_*}, \tag{1}$$

where W is the net shaft work output from the actual plant, and W_* the maximum work obtainable from an ideal (fully reversible) plant operating between inlet and outlet states which need to be prescribed. (The subscript * refers throughout to ideal processes.)

W for the actual plant is directly measurable, but W_* depends on how the inlet and outlet states are specified. Nevertheless, if the only heat transfer is with an environment at temperature T_0, it is always correct to write,

$$W_* = B_{\mathrm{IN}} - B_{\mathrm{OUT}}, \tag{2}$$

where $B = H - T_0 S$ is the steady-flow availability function and the subscripts imply summation over all reactant streams at inlet and all product streams at outlet.

The exergy E is often used in preference to the availability function in order to provide a direct measure of the maximum work potential relative to a datum state B_{DAT},

$$E = B - B_{\mathrm{DAT}}. \tag{3}$$

The exact definition of the datum state (see for example Kotas (1985); Szargut et al. (1988)) is not essential, so long as a fixed definition is used and since the main concern is usually with differences in exergy. Thus, equation (2) may be written

$$W_* = B_{\mathrm{IN}} - B_{\mathrm{OUT}} = E_{\mathrm{IN}} - E_{\mathrm{OUT}}. \tag{4}$$

It is often convenient, but by no means necessary, to set $E_{\mathrm{OUT}} = 0$ by definition (i.e., that $B_{\mathrm{DAT}} = B_{\mathrm{OUT}}$), thus implying that no further work can be extracted from the exhaust leaving the ideal process. Here, however, we shall follow the usual practice of taking the datum state as that of a standard environmental atmosphere (subscript 0), at pressure p_0 and temperature T_0 but with concentrations of the constituent gases (and their partial pressures) as defined by Kotas. Thus, we define $B_{\mathrm{DAT}} = B_0$ and $E_0 = 0$, but we do not necessarily take $E_{\mathrm{OUT}} = E_0$.

An alternative expression for W_* can be obtained by application of the steady-flow exergy equation to the real plant. Thus,

$$W_* = E_{\mathrm{IN}} - E_{\mathrm{OUT}} = W + \sum (I_{CR} + I_Q) + I_{\mathrm{QEX}} + I_{\mathrm{MEX}}, \tag{5}$$

where I_{CR}, I_Q, I_{QEX} and I_{MEX} all represent lost work due to irreversibility. For a particular component (compressor, combustion chamber, turbine, etc.) I_{CR} is the lost work due to internal

Nomenclature

B, E, G, H, I, S = all denote values per mole of fuel supplied.
B = steady-flow availability function
e = exergy of H_2O per mole
E = exergy
G = Gibbs function
H = enthalpy
I = irreversibility (lost work)
I_{CR} = component irreversibility (internal entropy creation)
I_Q = component irreversibility (external heat transfer)
I_C = combustion irreversibility ($I_C = I_{CT} + I_{CP} + \Delta$)
I_{QEX} = exhaust thermal irreversibility
I_{MEX} = exhaust mixing irreversibility
n = number of moles
p = pressure
p_0 = standard pressure (1 bar)
p_i = partial pressure
S = entropy
T = temperature
T_0 = standard temperature (25°C)
W = work output from real plant
W_* = work output from ideal plant
$[WED]$ = work of extraction and delivery
α, β, γ = correction terms on efficiency defined in text
x = mole fraction
η = rational efficiency
μ = chemical potential
ν = stoichiometric coefficient

Subscripts

a, b, c, d = referring to ideal processes
DAT = datum state
FUEL = fuel
0 = standard atmospheric condition
i = species i
IN = inlet to plant
OUT = outlet from plant
SAT = saturated
STACK = exhaust gas
WL = water (liquid)
WV = water vapour
* = ideal process

irreversibility and I_Q is the lost work due to heat transfer with the environment (zero for most components). I_{CR} and I_Q are summed over all components. For convenience, the lost work associated with discharging the hot exhaust gases directly to atmosphere is split into the following two terms:

— the "thermal" irreversibility I_{QEX} is the work which could be obtained by reversible cooling of the hot exhaust gases to temperature T_0.
— the "mixing" irreversibility I_{MEX} is the work which could be obtained by bringing the now cooled gases into chemical equilibrium with the environment via a reversible process

Expressions for the component lost work terms are given in the literature (Moran (1982); Kotas (1985)) but the particular irreversibilities I_C (the lost work in the combustion chamber), and I_{MEX} are discussed in detail later in this paper.

Combining equations (1), (4), and (5) gives a general expression for η in terms of the lost work,

$$\eta = 1 - \frac{\sum (I_{CR} + I_Q) + I_{QEX} + I_{MEX}}{E_{IN} - E_{OUT}}. \quad (6)$$

3 Three Definitions of Rational Efficiency

Referring now to Fig. 1, the three cases (b), (c), and (d) are considered in reverse order. Complete combustion is assumed in each case as excess air is always supplied in gas turbine combustion chambers and there is no reactive exergy left in the exhaust.

3.1 Case (d). The simplest prescription for W_* and η is based on case (d) (see Fig. 1(d)), the approximate approach frequently used, as indicated by Moran:

$$[W_*]_d = [-\Delta G_0]_{WV} \quad (7)$$

$$\eta_d = \frac{W}{[W_*]_d} = \frac{W}{[-\Delta G_0]_{WV}}. \quad (8)$$

$[\Delta G_0]_{WV}$ is the change in Gibbs function (products minus reactants) for a stoichiometric reaction where all chemical species enter and leave separately and individually at standard pressure p_0 and temperature T_0, and water leaves as a vapour. Thus,

$$[\Delta G_0]_{WV} = \sum_{\text{prods}} \nu_i \mu_i(T_0, p_0) - \sum_{\text{reacts}} \nu_i \mu_i(T_0, p_0), \quad (9)$$

where ν_i is the stoichiometric coefficient, and μ_i is the chemical potential of species i. Note that although $[-\Delta G_0]_{WV}$ is defined in terms of a stoichiometric oxygen-fuel mixture, $[W_*]_d$ is actually unaffected by the presence of excess oxygen and nitrogen so long as these enter and leave the plant at the same pressure and temperature.

3.2 Case (c). A "classical" definition of rational efficiency is that based on Obert's case (c), see Fig. 1(c). It is conceptually possible to obtain extra work by expanding each species reversibly and isothermally from p_0 to $p_{i,0}$, the partial pressure at which it exists in the standard atmosphere, but this is offset by the corresponding requirement to compress the oxygen and nitrogen entering the plant from their standard atmospheric partial pressures to p_0. Thus for case (c),

$$[W_*]_c = E_{IN} - E_{OUT} = E_{IN} = [-\Delta G_0]_{WV} + [WED], \quad (10)$$

where, assuming all species behave as semi-perfect gases, the term $[WED]$ (the work of extraction and delivery) is given by,

$$[WED] = RT_0 \sum_{\text{prods}} \nu_i \ln\left(\frac{p_0}{p_{i,0}}\right) - RT_0 \sum_{\text{air}} \nu_i \ln\left(\frac{p_0}{p_{i,0}}\right)$$

$$= RT_0 \sum_{\text{prods}} n_i \ln\left(\frac{p_0}{p_{i,0}}\right) - RT_0 \sum_{\text{air}} n_i \ln\left(\frac{p_0}{p_{i,0}}\right). \quad (11)$$

The use of the term $[WED]$ should be explained. It may be thought of as the difference between what Haywood calls the work of extraction of air from the environment (to storage at (p_0, T_0)) and the work of delivery of products to the environment (from storage at (p_0, T_0)). Some authors refer to it as the chemical exergy component of the products less that of the air used in combustion.

Since air is supplied from the standard atmosphere in that datum state (i.e., with zero exergy), E_{IN} is simply the exergy of the fuel E_{FUEL}, so that,

$$[W_*]_c = E_{FUEL} = [-\Delta G_0]_{WV} + [WED]. \quad (12)$$

E_{FUEL} is also called the fuel chemical availability by Moran, the availability of the fuel by Gyftopoulos and Beretta, and the chemical exergy of the fuel by Kotas and by Bejan et al. The rational efficiency is now,

$$\eta_c = \frac{W}{[W_*]_c} = \frac{W}{E_{FUEL}}. \quad (13)$$

As for $[W_*]_d$, $[W_*]_c$ is unaltered by the presence of excess air, because the extra work obtained by expanding the excess gases with the other exhaust products is exactly cancelled by the extra work of compression at inlet—the pressure ratios $(p_0/p_{i,0})$ being the same in both cases. $[W_*]_c$ has been tabulated by Moran (1989) for various fuels.

3.3 Case (b). The third definition for rational efficiency follows from Obert's case (b). At inlet, fuel and "mixed" air enter with each stream at pressure p_0 and temperature T_0, but the exhaust products leave in a fully mixed state at atmospheric temperature T_0 and "total" pressure p_0. (In the ideal process there has been no irreversible mixing in reaching this state.)

The reversible work associated with this process is still given by Eq. (2), but the subscript OUT now refers to the exhaust condition in the stack after cooling to T_0 (but before expanding each constituent to its standard atmospheric partial pressure). The subscript STACK is used to denote this exhaust state (i.e., at "mixed" pressure p_0 and temperature T_0) and, hence, for the new ideal process, $E_{OUT} = E_{STACK}$. Note, however, that availability values are still measured above the datum of the environmental state ($B_0 = B_{DAT}$, $E_0 = 0$), so that $E_{STACK} - E_0 = E_{STACK}$.

The reversible work and rational efficiency are now,

$$[W_*]_b = E_{IN} - E_{STACK} \quad (14)$$

$$\eta_b = \frac{W}{[W_*]_b} = \frac{W}{E_{IN} - E_{STACK}}. \quad (15)$$

$[W_*]_b$ now depends on the species concentrations in the exhaust (the same for the real and the ideal process). Furthermore, the exergy E_{STACK} is equal to the lost work that would be associated with the discharge from the state STACK to the environmental state. This lost work of delivery (which is not included in $[W_*]_b$) is given by,

$$I_{MEX} = RT_0 \sum_{\text{prods}} n_i \ln\left(\frac{p_{i,STACK}}{p_{i,0}}\right), \quad (16)$$

where $p_{i,STACK}$ and $p_{i,0}$ are the partial pressures of species in the exhaust gas and the standard atmosphere, respectively.

The ideal work is now related to the real work through the equation,

$$[W_*]_b = W + \sum (I_{CR} + I_Q) + I_{QEX}, \quad (17)$$

and the rational efficiency may be written as

$$\eta_b = 1 - \frac{\Sigma\,(I_{CR} + I_Q) + I_{\mathrm{QEX}}}{E_{\mathrm{IN}} - E_{\mathrm{STACK}}} = 1 - \frac{\Sigma\,(I_{CR} + I_Q) + I_{\mathrm{QEX}}}{E_{\mathrm{FUEL}} - I_{\mathrm{MEX}}}. \tag{18}$$

4 H_2O in the Exhaust Gas

The determination of I_{MEX} (and the evaluation of the rational efficiency for plants with water injection), requires the determination of the exergy of H_2O in various states.

Figure 2 shows various states of H_2O, all at temperature T_0. State A is liquid water at pressure p_0 (i.e., pressurised above the saturation pressure $p_{\mathrm{SAT}}(T_0)$), states B and C are saturated liquid and vapour, respectively, and state 0 is the state of the H_2O in the standard atmosphere. The partial pressure of the water vapour in state 0 is $p_{WV,0}$ and is related to a specified relative humidity, $RH = (p_{WV,0}/p_{\mathrm{SAT}})$, (Kotas (1985)).

The enthalpy and entropy of liquid water are virtually independent of pressure, and, hence, the molar exergy of states A and B are almost equal, $e_A \cong e_B$. Also, $e_B = e_C$ and, by definition, $e_0 = 0$. Hence, assuming water vapour behaves as a semi-perfect gas, $(e_A - e_0) \cong (e_C - e_0) = -RT_0 \ln (RH)$.

In a real power plant, the H_2O in the exhaust gas is usually in vapour form because the stack temperature is deliberately chosen to be higher than the dewpoint temperature. On the other hand, the atmospheric temperature T_0 is normally below the dewpoint temperature. The true equilibrium state of the H_2O in the exhaust from the ideal plant exhausting at temperature T_0 is therefore a mixture of water vapour at partial pressure p_{SAT} and condensed liquid water at pressure p_0.

In evaluating the contribution of water to the term I_{MEX} it is convenient to consider a fictitious metastable vapour state MN lying on the isothermal T_0, but at a pressure $p_{WV,\mathrm{STACK}}$ rather than the saturation pressure p_{SAT}. The exergy of this state MN is $e_{MN} \cong RT_0 \ln (p_{WV,\mathrm{STACK}}/p_{WV,0})$, i.e., not the same as that of states B and C $(e_C = RT_0 \ln (p_{\mathrm{SAT}}/p_{WV,0}))$.

Similarly, in evaluating the exergy change in case (d) and E_{FUEL} in case (b), there is the option of choosing the equilibrium (liquid) state at (p_0, T_0), or another fictitious metastable state MH for the water (vapour) at exit from the ideal process shown in Fig. 1(*d*). Moran defines the chemical exergy of a hydrocarbon fuel using case (c) of Fig. 1, but using a value of $[-\Delta G_0]_{WV}$ determined from the vapour state MH leaving in case (d). He points out, however, that if the water leaves case (d) in the liquid state A there will be a change in this value to $[-\Delta G_0]_{WL}$ (a correction of $(e_{MH} - e_A) \cong RT_0 \ln (p_0/p_{\mathrm{SAT}})$) as in the (modified) case (d) considered by Bejan et al.

Parallel problems to these arise when choosing the higher or lower calorific value $[-\Delta H_0]$ as the basis for plant overall efficiency, but there the differences between the two values is of substantial significance because of the high enthalpy of vaporisation of water. The difference in exergy between the states MH and A is much smaller as indicated in the last paragraph.

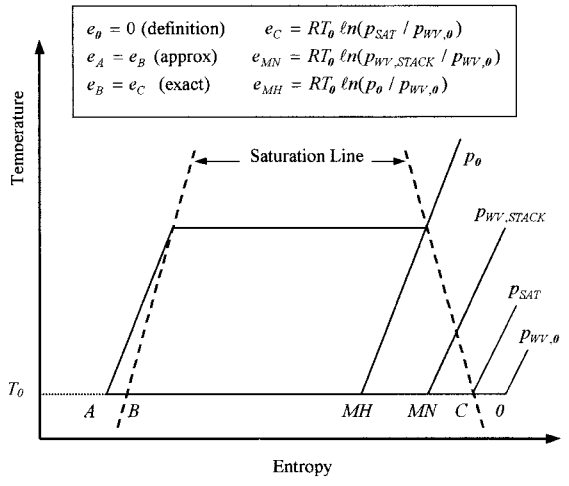

Fig. 2 Schematic (*T-s*) diagram for H_2O showing the molar exergy of various states

5 Power Plants With Water Injection

Problems also arise for water present in the exhaust which is injected into the plant rather than coming from the oxidation of hydrogen in the fuel. In particular, gas turbines with water injection represent a technology which is gaining popularity due to the associated increase in power output and cycle efficiency. Typical examples are the STIG and RWI plants, see Macchi et al. (1995).

In terms of the fluid streams crossing the control surfaces enclosing the real and ideal plants, the only differences lie in the addition of extra streams of liquid water at inlet and a corresponding increase in the water content of the exhaust gas.

The water supplied at inlet (for all three ideal processes) has exergy corresponding to state A in Fig. 2, i.e., $n_W e_A \cong n_W RT_0 \ln (p_{\mathrm{SAT}}/p_{WV,0})$, where n_W is the number of moles of water supplied externally per mole of fuel. For the classical ideal process (c), the water exergy at outlet is zero. For the ideal process (d) (if based on the exit vapour state MH), the extra H_2O at outlet has exergy $n_W e_{MH}$. For the ideal process (b), the extra H_2O at outlet (if based on the exit vapour state MN) has exergy $n_W e_{MN}$. It should be noted, however, that for the process (b) the partial pressure of water vapour in the exhaust $(p_{WV,\mathrm{STACK}})$ increases with increasing water injection and this alters the value of e_{MN}.

The values of ideal work for the three processes are, therefore,

$$[W_*]_d = E_{\mathrm{IN}} - E_{\mathrm{OUT}} = E_{\mathrm{FUEL}} - [WED] + n_W e_A - n_W e_{MH} \tag{19}$$

$$[W_*]_c = E_{\mathrm{IN}} - E_{\mathrm{OUT}} = E_{\mathrm{FUEL}} + n_W e_A \tag{20}$$

$$[W_*]_b = E_{\mathrm{IN}} - E_{\mathrm{OUT}} = E_{\mathrm{FUEL}} + n_W e_A + I_{\mathrm{MEX}}, \tag{21}$$

where I_{MEX} includes the contribution due to the increased water vapour content at state STACK, which now contributes $(n_C + n_W) RT_0 \ln (p_{WV,\mathrm{STACK}}/p_{WV,0})$, n_C being the number of moles of H_2O produced in combustion per mole of fuel supplied. Corresponding rational efficiencies can be calculated by substitution in Eqs. (8), (13), and (15).

6 Relationships Between Irreversibilities

For open cycles, an interesting relationship may be established between (*WED*), the irreversibility I_{MEX} involved in the discharge of the exhaust gases at T_0, and part of the irreversibility in combustion. (Note that this relationship, as derived below, is not applicable to cycles with water injection.)

The lost work I_C in an adiabatic combustion process with air and fuel entering the chamber individually at (p_1, T_1) and products leaving at (p_2, T_2), is given by,

$$I_C = T_0(S_2 - S_1) = T_0[\Delta S_0]_{WV} + T_0 \sum_{\mathrm{prods}} n_i \left[\phi_i(T_2) - R \ln \left(\frac{p_{i,2}}{p_0} \right) \right] - T_0 \sum_{\mathrm{air}} n_i \left[\phi_i(T_1) - R \ln \left(\frac{p_{i,1}}{p_0} \right) \right], \tag{22}$$

where $\phi_i(T) = \int (c_p/T)dT$ and $T_0[\Delta S_0]_{WV} = [\Delta H_0]_{WV} - [\Delta G_0]_{WV}$. $[\Delta H_0]_{WV}$ and $[\Delta S_0]_{WV}$ refer, like $[\Delta G_0]_{WV}$, to the change in enthalpy and entropy in a combustion process with all reactant and product species individually supplied and exhausted at (p_0, T_0). Equation (22) can also be written,

$$I_C = I_{CT} + I_{CP} + \Delta, \tag{23}$$

where,

$$I_{CT} = T_0[\Delta S_0]_{WV} + T_0 \sum_{\text{prods}} n_i \phi_i(T_2) - T_0 \sum_{\text{air}} n_i \phi_i(T_1)$$

$$I_{CP} = RT_0 \sum_{\text{air}} n_i \ln\left(\frac{p_1}{p_0}\right) - RT_0 \sum_{\text{prods}} n_i \ln\left(\frac{p_2}{p_0}\right)$$

$$\Delta = RT_0 \sum_{\text{air}} n_i \ln\left(\frac{p_{i,1}}{p_1}\right) - RT_0 \sum_{\text{prods}} n_i \ln\left(\frac{p_{i,2}}{p_2}\right).$$

In terms of the mole fractions, the expression for Δ becomes,

$$\Delta = RT_0 \sum_{\text{air}} n_i \ln(x_i) - RT_0 \sum_{\text{prods}} n_i \ln(x_i), \qquad (24)$$

where $x_i = (p_i/p)$ is the mole fraction of species i. Similarly, Eqs. (16) and (11) for I_{MEX} and $[WED]$ can be written,

$$I_{\text{MEX}} = RT_0 \sum_{\text{prods}} n_i \ln\left(\frac{p_{i,\text{STACK}}}{p_0}\right) + RT_0 \sum_{\text{prods}} n_i \ln\left(\frac{p_0}{p_{i,0}}\right)$$

$$= RT_0 \sum_{\text{prods}} n_i \ln(x_i) + RT_0 \sum_{\text{prods}} n_i \ln\left(\frac{p_0}{p_{i,0}}\right) \qquad (16a)$$

$$[WED] = RT_0 \sum_{\text{prods}} n_i \ln\left(\frac{p_0}{p_{i,0}}\right) + RT_0 \sum_{\text{air}} n_i \ln(x_i). \qquad (11a)$$

It therefore follows that,

$$[WED] = I_{\text{MEX}} + \Delta, \qquad (25)$$

and the irreversibility in the combustion process may be written,

$$I_C = I_{CT} + I_{CP} + [WED] - I_{\text{MEX}}. \qquad (23a)$$

The full statement of exergy flux corresponding to case (c) is then, from Eqs. (5), (12), and (23*a*),

$$[W_*]_c = E_{\text{FUEL}} = [-\Delta G_0]_{WV} + [WED] = W + \Sigma(I_{\text{CR}} + I_Q) + \{[WED] - I_{\text{MEX}}\} + I_{\text{QEX}} + I_{\text{MEX}},$$

where ΣI_{CR} now includes, for the combustion process, $I_C = I_{CT} + I_{CP}$ (but not Δ). Using this modified definition of ΣI_{CR} results in the identity,

$$[-\Delta G_0]_{WV} = W + \Sigma(I_{CR} + I_Q) + I_{\text{QEX}}, \qquad (26)$$

so that the exact expression for η_d can be written,

$$\eta_d = 1 - \frac{\Sigma(I_{CR} + I_Q) + I_{\text{QEX}}}{[-\Delta G_0]_{WV}}. \qquad (27)$$

This is the approach frequently followed in exergy analyses of real power plants (e.g., Haywood (1991); Horlock (1992)), with the irreversibilities being determined from local (total) pressures and mean specific heats.

7 Relationships Between Rational Efficiencies

Since all three terms in Eq. (25) are relatively small in comparison with $[-\Delta G_0]_{WV}$, it is possible to derive approximate relations between the three efficiencies η_d, η_c, and η_b. Writing,

$$\alpha = \frac{I_{\text{MEX}}}{[-\Delta G_0]_{WV}}, \quad \beta = \frac{[WED]}{[-\Delta G_0]_{WV}},$$

$$\gamma = \frac{[WED] - I_{\text{MEX}}}{[-\Delta G_0]_{WV}} = \frac{\Delta}{[-\Delta G_0]_{WV}} = \beta - \alpha,$$

the three rational efficiencies may be related as follows,

$$\eta_d = \eta_c(1 + \beta) \qquad (28)$$

$$\eta_b = \frac{\eta_d}{1 + \beta - \alpha} = \eta_c \frac{1 + \beta}{1 + \gamma} \cong \eta_c(1 + \alpha). \qquad (29)$$

Some magnitudes for α, β, and γ, together with the differences between the three efficiencies are presented in the following section.

8 Calculations for Some Gas Turbine Cycles

Calculations of the three efficiencies have been undertaken for some modern gas turbine cycles using an established computer code (Carcasci and Faccini (1996)) modified to include exergy balances.

8.1 The General Electric LM2500 STIG Plant. The GE LM2500 STIG plant has a facility for injecting steam into the HP and LP turbines. The design features include two-stage compression with overall pressure ratio $18 \cdot 7$, combustion temperature 1500 K and turbine cooling air abstraction 9 percent of the air mass flowrate at engine inlet. For no steam injection, the three efficiencies and dimensionless irreversibilities α, β, and γ are as follows:

$$\eta_c = 0 \cdot 352 \quad \eta_d = 0 \cdot 369 \quad \eta_b = 0 \cdot 361$$

$$\alpha = 0 \cdot 0247 \quad \beta = 0 \cdot 0441 \quad \gamma = 0 \cdot 0195.$$

For 8 percent steam injection, the efficiencies are as follows:

$$\eta_c = 0 \cdot 399 \quad \eta_d = 0 \cdot 423 \quad \eta_b = 0 \cdot 420.$$

Two exergy loss histograms, nondimensionalised with reference to the fuel exergy, are shown in Fig. 3. The notation is self-

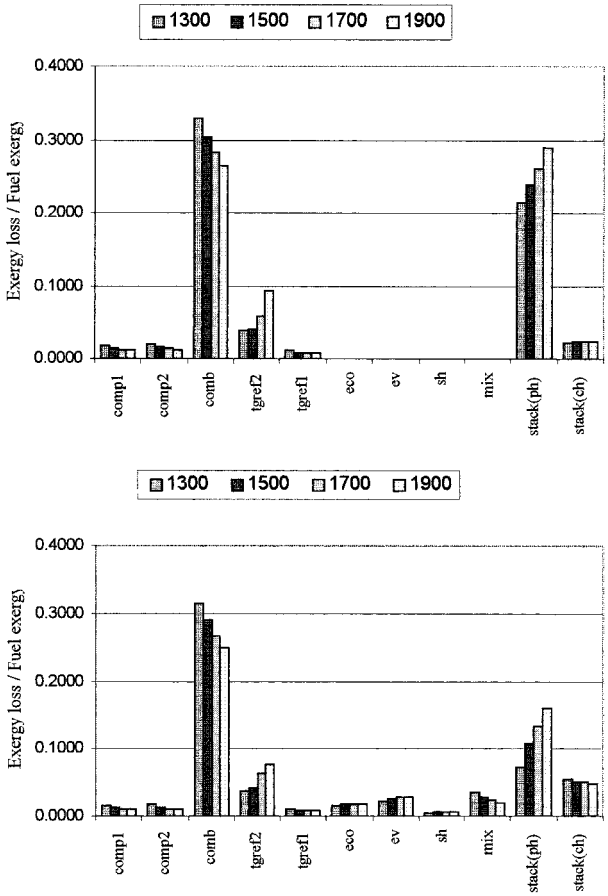

Fig. 3 Exergy losses for LM2500 STIG plant with (*a*) 0 percent and (*b*) 8 percent steam injection

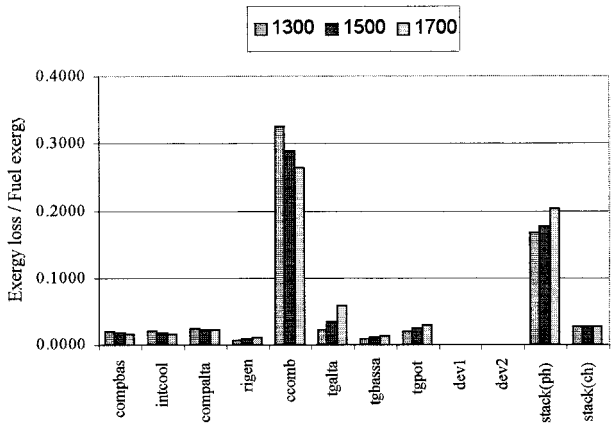

Fig. 4 Exergy losses for the WR21 recuperative plant

explanatory with the exception of the terms stack(ph) and stack(ch) which refer, respectively, to the thermal and mixing irreversibilities of the exhaust, I_{QEX} and I_{MEX}. The diagrams include a sensitivity analysis showing the effect of increasing the combustion temperature from 1300 to 1900 K. Steam injection produces a major performance improvement but the irreversibility connected with the release to the environment of a humid air stream is significant, with I_{MEX} increasing from 2 percent for no steam injection to 5 percent for 8 percent steam injection.

8.2 The Westinghouse/Rolls-Royce WR21. The Westinghouse/Rolls-Royce WR21 is a recuperative gas turbine for marine application. The design features include two-stage inter-cooled compression with overall pressure ratio $12 \cdot 8$, heat exchanger effectiveness $0 \cdot 93$, combustion temperature 1500 K and cooling air abstraction 14 percent of air mass flowrate at engine inlet. The calculated efficiencies and values of α, β, and γ are as follows:

$$\eta_c = 0 \cdot 371 \quad \eta_d = 0 \cdot 389 \quad \eta_b = 0 \cdot 381$$

$$\alpha = 0 \cdot 0267 \quad \beta = 0 \cdot 0482 \quad \gamma = 0 \cdot 0215.$$

The exergy loss histogram is shown in Fig. 4, including a sensitivity analysis showing the effect of increasing the combustion temperature from 1300 to 1700 K. In comparison to the LM2500 of Fig. 3(a), the thermal stack exergy loss I_{QEX} is considerably reduced (15–20 percent, compared with 22–27 percent for the LM2500). This is a consequence of the lower exhaust gas temperature in the recuperated cycle. It should also be noted that α, β, and γ, although small, are still comparable with some of the other component exergy losses.

8.3 The ABB GT24 Combined-Cycle Plant. The ABB GT24 is a gas turbine with two-stage combustion designed for combined cycle operation. The design features include three-stage compression with overall pressure ratio $30 \cdot 3$, combustion temperature 1508 K (main and reheat combustors), and total turbine cooling air abstraction 21 percent of air mass flowrate at engine inlet. The three efficiencies and values of α, β, and γ are as follows:

$$\eta_c = 0 \cdot 543 \quad \eta_d = 0 \cdot 567 \quad \eta_b = 0 \cdot 557$$

$$\alpha = 0 \cdot 0263 \quad \beta = 0 \cdot 0441 \quad \gamma = 0 \cdot 0178.$$

The exergy loss histogram is shown in Fig. 5. There are a large number of individual losses in this complex plant but it is particularly interesting to note the magnitude of the lost work in the combustion process. Splitting the combustion into two stages leads to a combustion irreversibility of $18 \cdot 76 + 8 \cdot 76 = 27 \cdot 55$ percent, which is significantly below the $29 \cdot 5$ percent of the LM2500 with no steam injection and a similar firing temperature of 1500 K.

It is also interesting to note that, although for both the LM2500 and WR21 the mixing exergy loss term in the exhaust I_{MEX} is substantially less than the thermal exergy loss term I_{QEX}, the reverse is true for the GT24, due to the low exhaust temperature ($\sim$100°C) of this combined cycle plant. Attention is thus drawn to the point made by Gyftopoulos and Beretta (and referred to earlier) that a rational efficiency could be defined which ignored both these quantities in an ideal process.

9 Discussion and Conclusions

For closed cycles, thermodynamic efficiency is defined as the ratio of the net work output to the heat supplied. It may then be compared to the efficiency of a reversible engine operating between the same temperature levels. However, for open cycles rational efficiency should be used, defined as the ratio of the actual net work output to the reversible work output obtainable in an ideal process between certain inlet and outlet states. Three such ideal processes are discussed in this paper, and three expressions for rational efficiency then follow.

It is useful, in discussing the merits of using any one of these, to consider the probable uses in practice, namely:

1 assessing the performance of a particular type of plant (e.g., a gas turbine) with changes in design parameters, such as com-

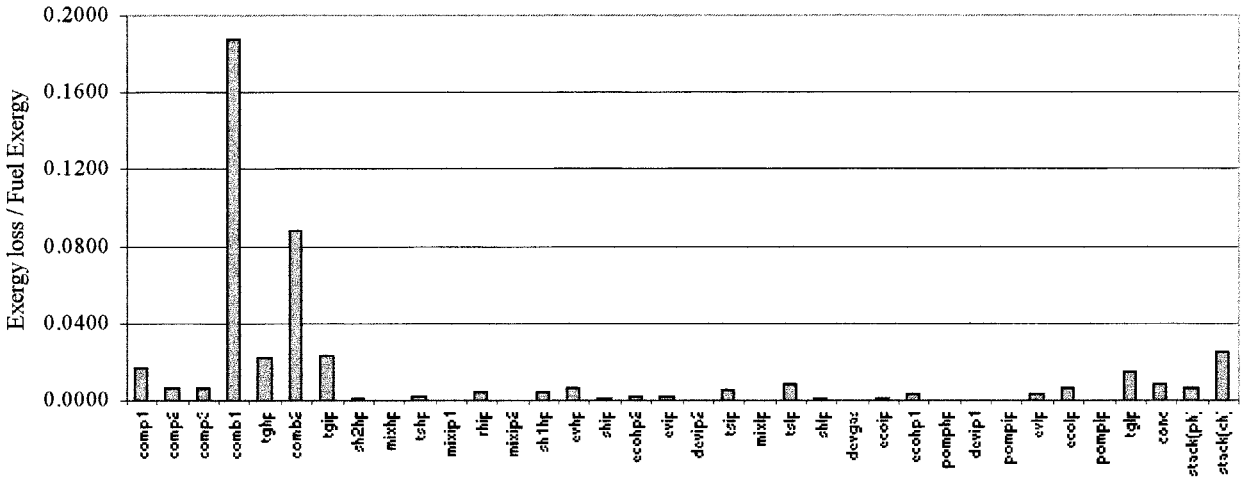

Fig. 5 Exergy losses for the GT24 combined cycle plant

bustion temperature (and hence air/fuel ratio), given the environmental conditions

2 assessing the comparative performance of different types of plant in utilizing the energy (or exergy) of a fuel, given the environmental conditions

It can be argued that η_b is the most realistic criterion for both purposes. The fact that the I_{MEX} contribution to exergy destruction is directly subtracted from the denominator, and not accounted within the irreversibility balance for consistency, does not mean that this type of irreversibility mechanism does not exist, only that in practice it is virtually unavoidable.

More generally, it has to be said that the three efficiencies differ little, although η_d and η_b are always greater than η_c. Use of η_c has a limitation in its practical application, as it implies that work is recoverable from the (cooled) exhaust gases, whereas this is not feasible in practice. Use of η_d involves an invalid definition of the ideal process, since its defined outlet state is entirely different from that of the real process. Nevertheless, the use of η_d along the lines explained in section 6, in which $[WED]$, Δ and I_{MEX} are all ignored, is a useful quick way of assessing efficiency and the location of major losses without serious approximation.

Relevant aspects also relate to the consideration of newly proposed cycles, often involving water or steam injection and/or a very low stack temperature. In these cases, even if the results in terms of the three definitions of rational efficiency are comparable, new sources of exergy destruction arise (e.g., discharge of very wet streams of combustion gases to the environment). Further, the traditional thermal exergy destruction (due to release of hot stack gases) can be of the same size or even lower than that connected with chemical mixing with the reference environment.

References

Bejan, A., Tsatsaronis, G., and Moran, A., 1996, *Thermal Design and Optimization*, Wiley, New York.

Bettagli, N., and Manfrida, G., 1995, "Power Generation Using Liquid Hydrogen Fuel: A Possible Power Plant Scheme," *Hypothesis 1*, Int. Conf., Gaeta, Italy.

Carcasci, C., and Facchini, B., 1996, "A Numerical Method for Power Plant Simulation," ASME *J. Energy Resource Tech.*, Vol. 118, pp. 36–43.

Gyftopoulos, E. P., and Beretta, G. P., 1991, "Thermodynamics, Foundations and Applications," MacMillan, New York.

Haywood, R. W., 1980, *Equilibrium Thermodynamics*, Wiley, New York.

Haywood, R. W., 1991, *Analysis of Engineering Cycles*, Pergamon, New York.

Horlock, J. H., 1992, *Combined Power Plants*, Pergamon, New York.

Kotas, T. J., 1985, *The Exergy Method of Thermal Power Analysis*, Butterworth,

Macchi, E., Consonni, S., Lozza, G., and Chiesa, P., 1995, "An Assessment of the Thermodynamic Performance of Mixed Gas-Steam Cycles, Parts A and B," ASME JOURNAL OF ENGINEERING GAS TURBINES AND POWER, Vol. 117, pp. 489–508.

Moran, M. J., 1989, *Availability Analysis: A Guide to Efficient Energy Use*, ASME Press, New York.

Obert, E. F., 1960, *Concepts of Thermodynamics*, McGraw-Hill, New York.

Stecco, S. S., and Manfrida, G., 1988, "Exergy Analysis of a Reactive Hydrogen-Oxygen Steam Cycle for Peak-Load Power Generation," Proceedings, 23rd Intersociety Energy Conversion Engineering Conf., ASME Paper 88-93-54.

Stodola, A., 1924, *Steam and Gas Turbines*, Springer, Berlin.

Szargut, J., Morris, D. R., Stewart, F. R., 1988, *Exergy Analysis of Thermal, Chemical and Metallurgical Processes*, Hemisphere, PA.

Szargut, J., and Petela, R., 1965, *Egzergia* (in Polish), Naukowa-Technicze, Warsaw.

G. Woetting

B. Caspers

E. Gugel

CFI GmbH & Co. KG,
Oeslauer Strasse 35,
96472 Roedental, Germany

R. Westerheide
FhG-IWM,
79108 Freiburg, Germany

High-Temperature Properties of SiC-Si3N4 Particle Composites

Due to promising results in literature, SiC-Si_3N_4 particle composites in the range 0–100 percent SiC were evaluated. Focusing on high-temperature properties, mainly Y_2O_3 was used as sintering additive. Consolidation occurred primarily by hot-pressing, sintering tests were performed for comparison. Besides short-term properties like strength, toughness etc., long-term properties like creep and oxidation behavior were determined. Results as a function of SiC-content and microstructure were discussed with respect to materials' performance at high temperatures and possibilities of their production on a technical scale.

Introduction

Silicon carbide (SiC) as well as silicon nitride (Si_3N_4 resp. SN) are already seen for a long time as candidates for long-term high-temperature applications under severe conditions, e.g., in gas turbines. However, there are still no satisfying solutions available on a technical scale and at reasonable costs. SiC suffers from its inherent low thermal shock resistance, SN by property degradations due to oxidation and creep, though a lot of progress was made during the last years (Woetting, 1995; Klemm, 1995). This comprises extensive knowledge about the effect of type and amount of sintering additives, the purity of raw materials as well as processing conditions on developing microstructure and resulting properties.

Especially for liquid-phase sintered SN these items control the amount, characteristic and constitution of the remaining grain-boundary phase which determines long-term high-temperature properties to a high extent (Woetting, 1997). Long-term stability would result with very small amounts of a highly pure Si-O-N or a completely absent grain-boundary phase, however, such materials cannot be sintered and lose in strength and toughness. Thus, microstructure and properties approach those of solid-state sintered SiC (Tanaka, 1989).

Recently, however, a promising new concept was published (Niihara, 1991), disclosing an improvement of mechanical as well as thermo-mechanical properties of sintered (hot-pressed) SN by incorporating nano-sized SiC-particles. This initiated intensive work worldwide to clarify whether these improvements are due to an intrinsic "nanocomposite effect" or to further microstructural changes (Hermann, 1995; Westerheide, 1997).

Another point of interest was to analyze if these effects are associated with a certain amount and particle size of SiC. Initial work was done with amorphous SiC-SN-powders, obtained by polymer pyrolysis with the drawback of technological difficulties in manufacturing of components as well as with respect to costs.

Thus, the aim of the present work was to investigate if the reported effects can also be realized with technical crystalline powders of reasonable purity. With this respect, the whole compositional range from 0–100 percent was screened with a concentration on the SN-rich side. As long-term high-temperature properties were in the focus of interest, only Y_2O_3 was used as sintering additive. For comparison, one composition containing simultaneously *Y* and Al as grain-boundary constituents was introduced. To reveal the effect of the SiC-SN-ratio, compositions were densified primarily by hot-pressing. Besides this, however, all compositions were also sintered and characterized in comparison with the hot-pressed ones in order to demonstrate the possibility to manufacture also complex components economically.

Experimental Procedure

In order to evaluate the whole range of SiC-SN-composites, the compositions listed in Table 1 were prepared. Basic powders were SN-BAYSINID ST (BAYER AG/H. C. Starck), SiC-UF25 (H. C. Starck), and Y_2O_3-Grade C (H. C. Starck). Focusing on high-temperature properties, mainly Y_2O_3 was used as sintering additive. To demonstrate the undesirable effect of the simultaneous presence of Al in the liquid phase of the densified material, one composition of this kind was enclosed.

In order to establish a comparable chemical composition of the liquid phase in the different materials, SN-powder was preoxidized in some cases. The molar ratio of the added Y_2O_3 to SiO_2, introduced by the oxygen content of the base powders, was directed to be 0.5–1.0. This should result in the crystallization of the very oxidation-resistant phases Y_2SiO_5 and $Y_2Si_2O_7$ in the grain-boundary phase of all compositions.

Base powders were co-milled in SN-lined planetary mill pots with SN-balls in *n*-propanol to avoid contamination by milling debris and hydrolysis. The resulting slurry was dried, sieved and hot-pressed with graphite dies. In order to reach complete densification for the different compositions, hot-pressing conditions had to be adjusted and resulted in temperatures between 1800–1850°C. Thus, the different compositions reveal differences in their thermal history. However, they are all dense (less than 1 percent porosity) and the composition of their grain-boundary phase is quite similar, with the exception of composition 100SC-AY which also contains Al.

Hot-pressed discs of 150 mm diameter were ground on both sides and cut to prepare samples for the determination of mechanical, thermo-mechanical and thermo-chemical properties as well as for the microstructural characterization. Testing conditions are outlined together with the results in the following. For comparison, some sintering trials were performed to get information on the ability to produce such materials on a technical scale by sintering and on the properties achievable by this route.

Results and Discussion

Table 2 summarizes all results obtained with the hot-pressed materials. Description and discussion for the different properties occurs in the following after introduction of the resulting microstructures.

Contributed by the International Gas Turbine Institute (IGTI) of THE AMERICAN SOCIETY OF MECHANICAL ENGINEERS for publication in the ASME JOURNAL OF ENGINEERING FOR GAS TURBINES AND POWER. Paper presented at the International Gas Turbine and Aeroengine Congress and Exhibition, Stockholm, Sweden, June 2–5, 1998; ASME Paper 98-GT-465.

Manuscript received by IGTI March 25, 1998; final revision received by the ASME Headquarters October 20, 1999. Associate Technical Editor: R. Kielb.

Table 1 SiC-SN compositions evaluated

Code	Composition (SiC + SN = 100) SiC %	SN %	Additive
100SC-AY	100	0	Y_2O_3 + AlN
100SC-Y	100	0	Y_2O_3
75SC-Y	75	25	Y_2O_3
30SC-Y	30	70	Y_2O_3
20SC-Y	20	80	Y_2O_3
5SC-Y	5	95	Y_2O_3
100SN-Y	0	100	Y_2O_3

Microstructure of the Hot-Pressed SiC-SN Composites. Figure 1 is a collection of SEM-prints of the different materials after plasma-etching. Figure 1(*a*) shows the microstructure of 100SC-Y to consist mainly of globular grains. Grain size is small and seems to depend mainly on the particle size of the base powder. Black regions to be seen should not be residual porosity, but grains broken out during preparation of the polished microsection. 100SC-YA has a very similar microstructure concerning grain size and shape with some more visible grain-boundary phase (not shown).

Figure 1(*b*) represents material 75SC-Y characterized by few dispersed, rod-like β-SN-grains within the SiC-matrix. Preferably, the SN-grains are etched away by the plasma method, individual SiC-grains as well as the residual grain-boundary phase were not contrasted.

With material 30SC-Y (Fig. 1(*c*)) matrix is built up by SN with inter and intragranular dispersed SiC particles. Thus, SiC-particles, probably below a certain size, get incorporated into the growing SN-grains. In comparison with 20SC-Y (Fig. 1(*d*)), 5SC-Y (Fig. 1(*e*)) and especially the SiC-free material 100SN-Y (Fig. 1(*f*)) it becomes obvious, that with increasing content SiC acts as a grain-growth inhibitor. With decreasing SiC-content the common microstructure of SN becomes dominating, characterized by the presence of elongated interlocked β-SN-grains and the continuous grain-boundary phase.

The mentioned location of SiC-particles in as well as between SN-grains is additionally shown in Fig. 2 for 5SC-Y by means of TEM. It seems that the maximum size of SiC to become incorporated into SN-grains is about 20 nm. Bigger particles remain in the grain-boundaries and triple points, respectively. Basically, these microstructures are very similar to those of Niihara's materials (Pan, 1996).

Table 2 Properties of hot-pressed SiC/SN-composites

Code	ρ-HP [g/cm³]	σ-RT [MPa]	σ-1400°C [MPa]	Young's Modulus RFM [1] RT [GPa]	RFM [1] 1300°C [GPa]	CT [2] 1400°C [GPa]	K_{Ic} VHI [MPa.√m]	K_{Ic} SENPB [MPa.√m]	HV 10 [GPa]	Oxidation 1400°C 100 h [mg/cm²]	Creep 1400°C/100MPa dε / dt [1/h]	ε [%]	Mineral Phases (X-ray)
100 SC-AY	3.25	744 ± 93	144 ± 5	412	311	-	3.5	-	25.7	3.77	1.10^{-4}	Fracture	SiC, n.d.
100 SC-Y	3.31	791 ± 57	572 ± 46	428	402	297	3.5	3.3	20.3	0.43	2.10^{-6}	0.07	SiC, Trace Y_2SiO_5
75 SC-Y	3.32	652 ± 92	422 ± 23	362	334	288	4.1	3.9	20.7	0.38	3.10^{-5}	0.58	17 β-SN, SiC, N-Ap.* vw
30 SC-Y	3.31	747 ± 62	584 ± 39	336	311	278	5.3	4.1	16.9	0.30	2.10^{-5}	0.48	43 β-SN, SiC, N-Ap. vw
20 SC-Y	3.31	764 ± 27	524 ± 21	324	304	273	5.2	5.2	16.5	0.35	9.10^{-6}	0.23	65 β-SN, SiC, N-Ap. vw
5 SC-Y	3.31	815 ± 60	523 ± 18	315	297	279	5.2	6.4	15.4	0.31	6.10^{-6}	0.20	76 β-SN, SiC, N-Ap. vw
100 SN-Y	3.31	841 ± 32	538 ± 34	316	298	302	7.0	7.3	14.8	0.13	3.10^{-5}	0.45	82 β-SN, - , N-Ap. vw

[1] Resonant Frequency Method
[2] Creep Test
* N-Apatite $Y_5(SiO_4)_3N$

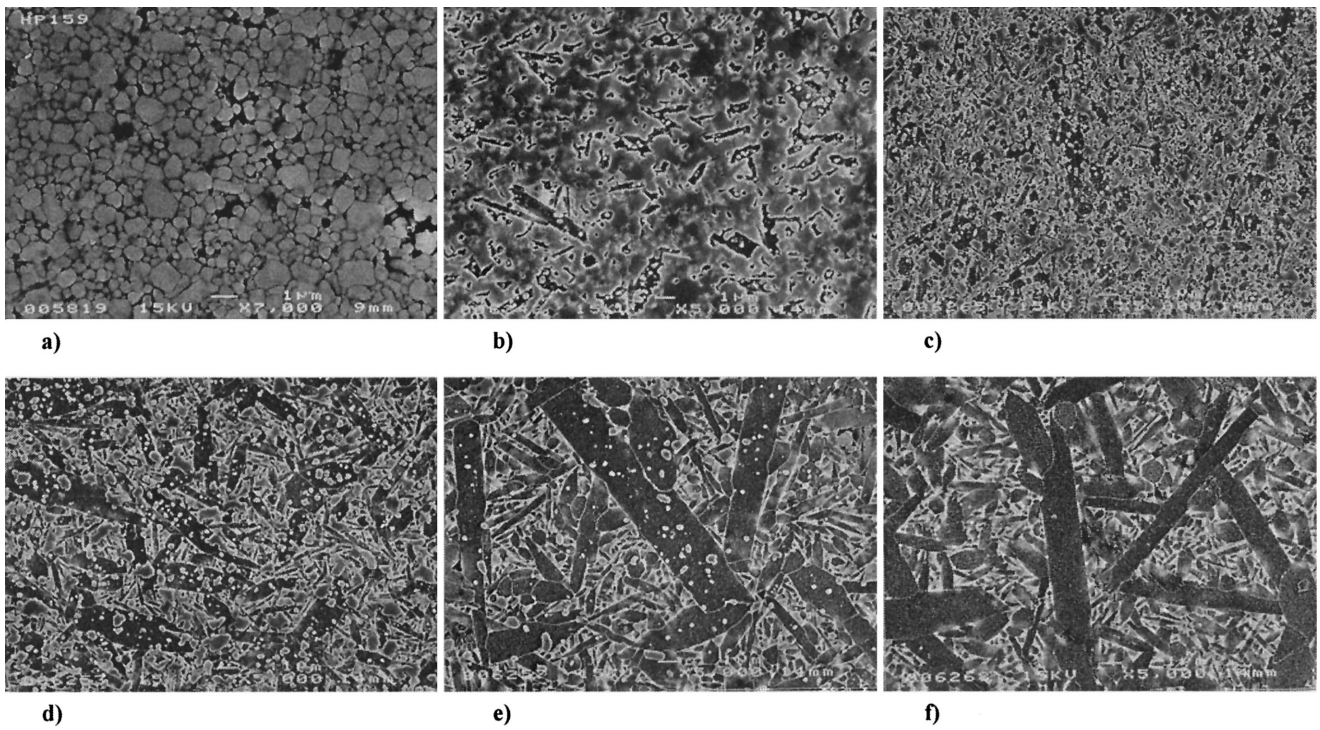

Fig. 1 Microstructure of SiC-SN materials (SEM, etched; Code: see Table 1); (*a*) 100SC, (*b*) 75SC, (*c*) 30SC, (*d*) 20SC, (*e*) 5SC and (*f*) 100SN.

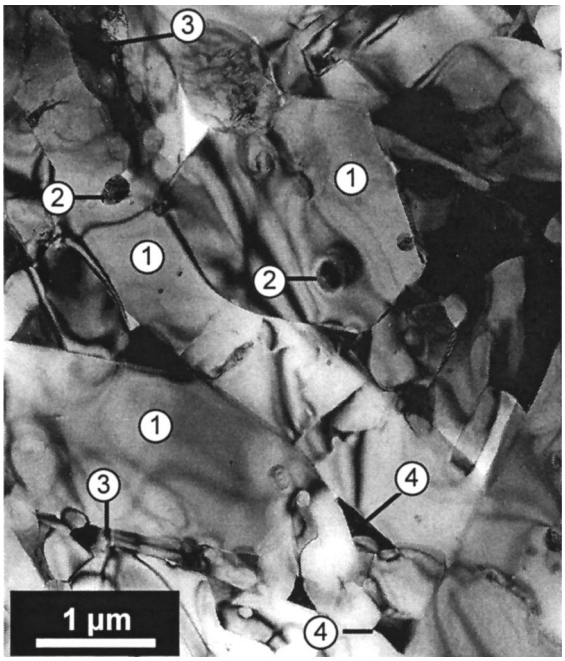

Fig. 2 TEM investigation of the SiC/Si_3N_4 composite with 5 percent SiC; 1: Si_3N_4; 2: SiC intracrystalline; 3: SiC intercrystalline; 4: secondary phase.

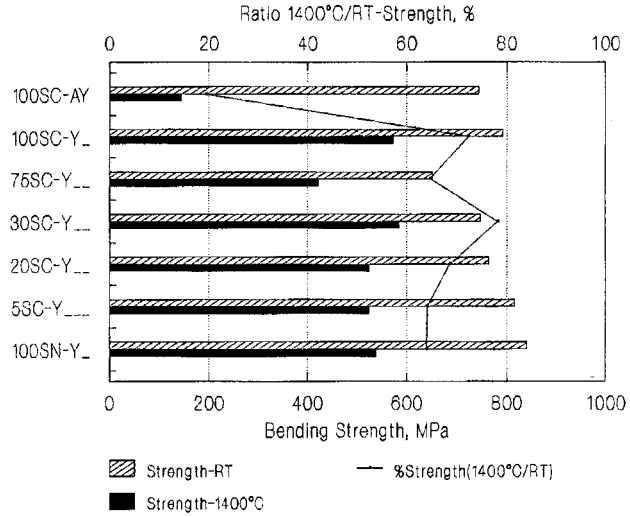

Fig. 3 Bending strength at room-temperature and 1400°C in air of hot-pressed SiC-SN-materials

Results of X-ray analysis given in Table 2 show that materials consist of β-SN and SiC according to about their original ratios. The grain-boundary phase of the "as hot-pressed" samples contains some traces of crystalline N-apatite $Y_5(SiO_4)_3N$ instead of the Y-silicates anticipated. This seems to be due to the strong reducing conditions within the graphite moulds leading to some oxygen and silica loss, respectively, shifting the overall composition to the more Y_2O_3 and N-rich corner of the phase system.

Mechanical Properties at Room-Temperature and at 1400°C. This property set comprises 4-point-bending at room temperature as well as at 1400°C in air (40/20 mm), fracture toughness evaluation by means of Vickers hardness indentations and analysis of crack length (VHI) as well as by SENPB with a natural crack obtained by the bridging method (VAMAS, 1997), Vickers hardness (10 kp/HV10) and the dynamic Young's modulus as a function of temperature, determined by the resonant frequency method up to about 1300°C in air as well as analyzed by the creep tests at 1400°C in air.

In Fig. 3 mean values of the bending strength at room temperature as well as at 1400°C are plotted, together with the calculated ratio of the 1400°C strength to the room-temperature strength in percent. It can be seen that most variants show a room-temperature strength of about 750–800 MPa, the lower value of the 75SC-Y seems not to be a material characteristic, but results of processing problems. The strength level is surprisingly high for the pure, liquid-phase sintered SiC-variants but not the optimum to be reached for pure SN, probably due to the relatively extensive grain-growth which took place already (see Fig. 1(*f*)). However, no influence of the SiC-content on the room-temperature strength is seen, as reported by Niihara.

The strength at 1400°C is of the order of 500–600 MPa, again with the exception of 75SC-Y with just about 400 MPa and the 100SC-AY variant. Besides these latter results, the mentioned 1400°C-strength level qualifies all other Y_2O_3-doped materials as suitable for applications at high temperatures. This can also be seen from the calculated ratio of the 1400°C-strength to the room-temperature strength (in percent), which varies between 65 and 75 percent for these materials. On the other hand, this ratio drops for the comparative material 100SC-AY to about 20 percent, demonstrating the dramatic negative effect of the simultaneous presence of Al besides *Y* in the grain-boundary phase. This also points out the necessity for highly pure base-powders for this group of materials to be used at high temperatures.

Figure 4 represents the fracture toughness values determined by two different methods as well as the hardnesss values of the SiC-SN variants. Though there are some inconsistencies with individual values, a clear trend reveals for the fracture toughness to increase with decreasing SiC-content. This can be related with the microstructure of these materials as the SN-rich grades show the characteristic elongated SN-grains leading to high fracture toughness values by an "in-situ" toughening. The dependency on the SiC-content is more or less linear and does not show a maximum with SiC contents of 5–30 percent, as described by Niihara.

Also the hardness shows a clear dependency on the SiC-content following possibly the rule of mixture of the harder SiC and the less harder SN-phases. Surprisingly, for the 100SC-AY variant, an extremely high hardness was analyzed, succeeding the 100SC-Y variant by more than 25 percent. This, however, is not of importance for the high-temperature behavior.

The Young's moduli of the different compositions as a function of temperature are plotted in Fig. 5 for the absolute values (Fig. 5(*a*)) as well as for their relative changes with respect to the room-temperature value (Fig. 5(*b*)). As can be seen from Fig. 5(*a*), there are distinguished differences between the different compositions with respect to the absolute values at room-temperature,

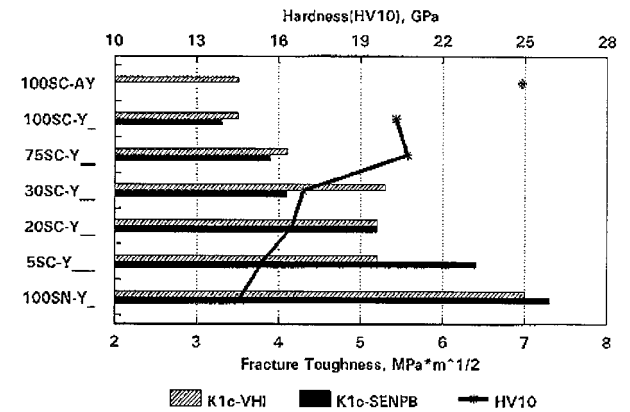

Fig. 4 Fracture toughness and hardness of hot-pressed SiC-SN-materials

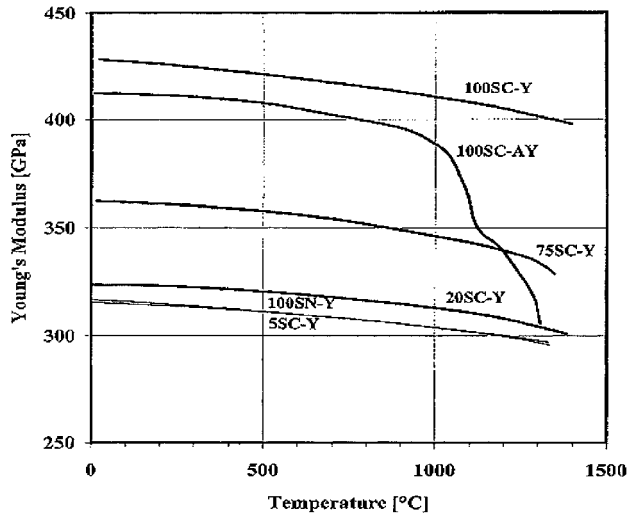

a)

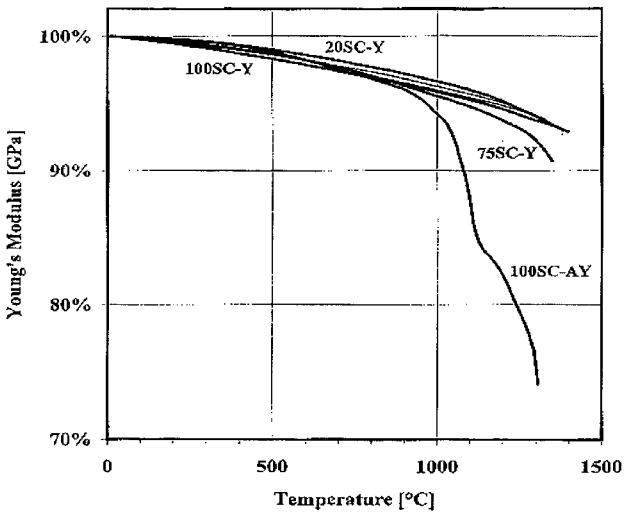

b)

Fig. 5 Young's moduli of the hot-pressed SiC-SN-materials as a function of temperature (*a*) absolute values and (*b*) relative changes

following more or less the rule of mixture of high-modulus SiC and lower modulus SN.

Temperature dependences of Young's moduli show relatively small changes for all compositions containing only Y_2O_3 as sintering additive up to temperatures of about 1350°C, determined by the resonant frequency method (RFM). A second set of Young's moduli was calculated from the strain of the samples during the creep test at 1400°C, based on a special displacement measurement (Table 2). All in all, these values are in accordance with the RFM-results and confirm the high-temperature stability of the Y_2O_3-doped materials.

In opposite, composition 100SC-AY containing simultaneously *Y* and Al reveals a marked drop at temperatures above 1000°C, indicating a softening of the grain-boundary phase. This different behavior is best seen by the plot of the relative values in Fig. 5(*b*). Whereas all *Y*-doped compositions prove to be very stable up to temperatures of about 1350°C with a retention of about 95 percent of the room-temperature value, composition 100SC-AY is not qualified for applications at temperatures above 1000°C. The reason for this is only the effect of Al, being considered in the selection of base powders and sintering additives for materials to be applied at high temperatures.

Long-Term High-Temperature Properties. With this respect, creep and oxidation behavior at 1400°C for at least 100 h

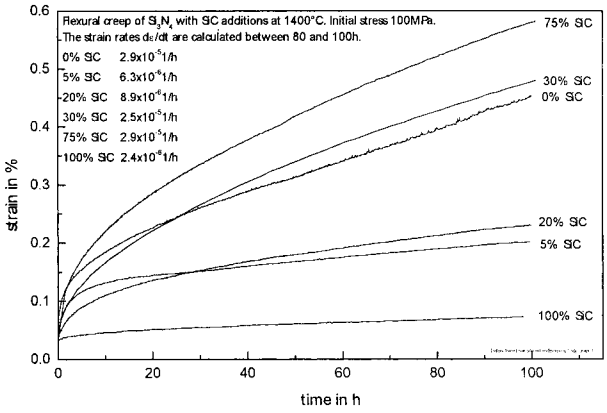

Fig. 6 Flexural creep of hot-pressed SiC-SN-materials

was determined. The first was analyzed in 4-point-bending, 40/20 mm fixture and 100 MPa initial stress in air, in order to get basic information on the deformation behavior at high temperatures. For detailed investigations, creep has to be determined in tensile mode because of the well-known difficulties with shifting of the neutral axis in flexure. The oxidation behaviour was investigated by using a muffle furnace with samples placed on SSiC-rods.

Strain as a function of time for the different compositions is plotted in Fig. 6. As can be seen, there is a positive effect of small amounts of SiC (5–20 percent), resulting in materials with an improved creep resistance in comparison with 100SN-Y. 30SC-Y is as resistant as 100SN-Y, while still increasing SiC-contents lead to increased creep. This might be associated with the markedly higher contents of Fe, Al and Ca of the SiC-powder UF25 in comparison with the SN-powder BAYSINID. Surprisingly, 100SC-Y does not follow this trend, but shows the highest creep resistance of all Y-doped samples. This cannot be explained till now.

Again, 100SC-AY deforms most at high temperatures (not shown), indicating once more the strongly negative effect of the presence of Al in the grain-boundary on high-temperature properties. With the testing conditions applied, creep rate is in the order of 10^{-4} 1/h and the sample fractured after about 10 h. With creep rates in the order of 10^{-6} 1/h, compositions containing only *Y* and SiC-contents up to about 20 percent qualify for applications at high temperatures.

A more negative effect of rising SiC-additions to SN-base material results for the oxidation behavior, as represented in Fig. 7. Lowest weight gain is found for 100SN-Y while for *Y*-doped

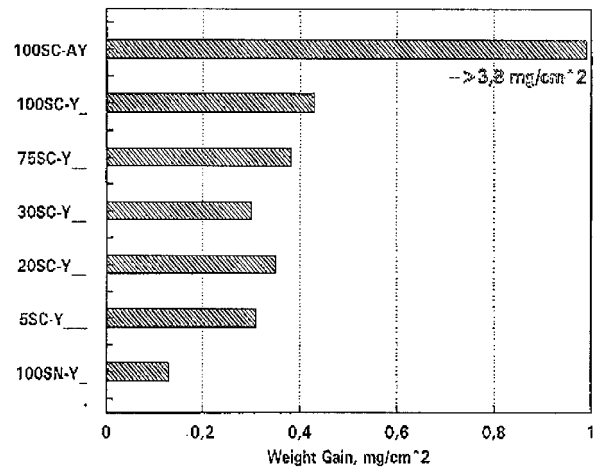

Fig. 7 Oxidation of hot-pressed SiC-SN-materials (1400°C, 100 h, air)

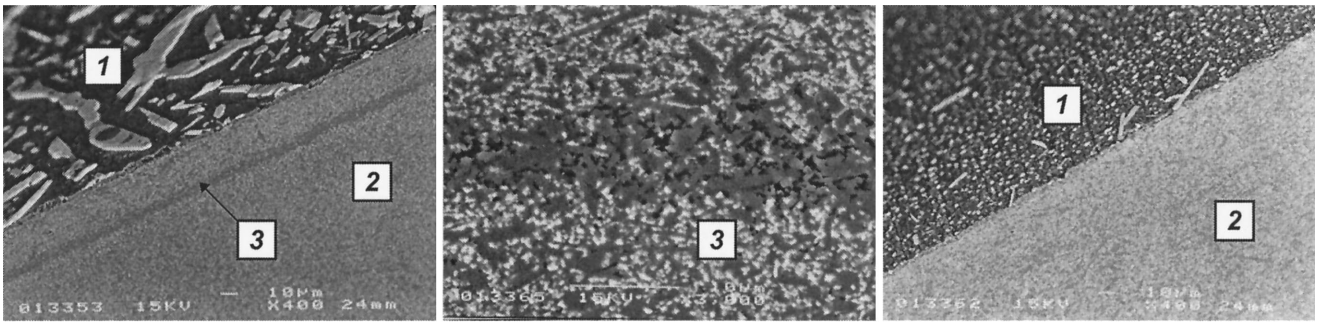

a) *400x* b) *3000x* c) *400x*

Fig. 8 SEM-analysis of materials' degradation by oxidation at 1400°C; (*a*) and (*b*) 100SN with formation of secondary pore zone; (*c*) 5SC/95SN without this effect (1: oxidized surface; 2: cross section through sample; 3: secondary porosity).

compositions containing SiC, the weight gain rises on a double or threefold level of the 100SN-Y material. However, this is still a relatively low level. A dramatic increase results from the simultaneous presence of Al and *Y* in 100SC-AY, indicating that Al also favors oxidation.

The extent of materials degradation by oxidation is represented by SEM-analysis of oxidized samples (Fig. 8). As can be seen, in contrast to the results of weight gain, strongest degradation occurs in 100SN-Y with the formation of secondary pores (Figs. 8(*a*, *b*)). Probably, the low weigth gain is due to some vaporization of grain-boundary phase. With increasing SiC-content, the formation of secondary pores and bulk degradation is suppressed, obviously because a more dense and stable oxidation layer forms (Fig. 8(*c*)). This is interpreted as a very positive effect of SiC-additions, improving long-term high-temperature stability and has also been found recently by another research group (Klemm, 1997).

Sintering Experiments. With all compositions described above, sintering trials were performed by the so-called two-step gas-pressure sintering technique. This technique comprises a first sintering step under relatively low gas-pressure to a densification stage where no more open porosity is present in the samples. In a second step, gas-pressure is increased to 10 MPa, supporting densification by the action of this isostatic pressure on the samples. Composition of the gas has to be established in order to avoid reaction with constituents of the samples. All *Y*-doped compositions could be densified by this technique to comparable densities as with hot-pressing at 1850–1900°C. 100SC-AY already reached complete densification at 50°C lower temperature.

Properties and their dependences on SiC-content were very similar to the hot-pressed grades. Strength at room-temperature as well as at 1400°C was about 10 percent lower, obviously due to residual microporosity. This also influenced the oxidation resistance. Thus, various variants still show attractive properties, especially with respect to their long-term high-temperature behavior. Succeeding in densification of these composites by sintering opens up manufacturing of more geometrically complex components in an economical way.

Conclusions

With the used raw-materials and processing technique, composites were obtained with microstructures meeting the requirements for the so-called "nano-composite concept", i.e., the presence of the inter as well as intragranular SiC-particles. All compositions show attractive properties at room-temperature. Whereas room-temperature strength does not hardly show any dependence of the SiC-content, KIc, hardness as well as Young's modulus, follow more or less the rule of mixture of the SiC/SN-ratio. No "nano-composite effect" was found over the whole compositional range.

Properties at high temperatures are mainly effected by the sintering additives used besides the SiC-content. The presence of *Y* and Al in the grain-boundary phase results in a dramatic material degradation at temperatures above 1000°C. Only *Y*-doped materials show attractive properties up to about 1400°C, characterized by about 70 percent of the room-temperature strength at 1400°C (air), more than 90 percent of the room-temperature Young's modulus at 1300°C (air), creep rates in the order of 10^{-5}–10^{-6} 1/h at 1400°C, 100 MPa (air) and oxidation weight gain of 0.2–0.4 mg/cm^2 at 1400°C after 100 h.

Creep is reduced for compositions containing 5–20 percent SiC in comparison with 100SN-Y, revealing a compositional dependency on the SiC-content. Tough oxidation weight gain increases with rising SiC-content, degradation of the bulk material by the formation of secondary porosity is reduced. Thus, the presence of up to about 20 percent SiC provides an improvement of the long-term high-temperature stability of such composites.

Of importance is the proof that all the SiC-SN composites investigated can be sintered to high densities with only diminishing loss in properties in comparison with the hot-pressed grades. Thus, also components with a more complex geometry can be produced in an economic way.

Acknowledgments

We gratefully acknowledge support of this work by German ministry BMBF under project No. 03M2116 and project management by FA Juelich/NMT.

References

Herrmann, M., Rupp, E., Schubert, Ch., and Rendtel, A., 1998, "Preparation and Properties of Si_3N_4/SiC Nanocomposite Materials," to be published in *J. Am. Ceram. Soc.*

Klemm, H., Herrmann, M., and Schubert, Chr., Hermel, W., 1996, "Problems and Prospects of Silicion Nitride Materials for Applications at Temperatures above 1400°C," Proceedings, 3rd Europ. Workshop on High Temperature Materials, ESA-WPP-104, pp. 32–39.

Klemm, H., Herrmann, M., and Schubert, Chr., 1997, "High Temperature Oxidation of Silicon Nitride Based Ceramic Materials," presented at 6th Int. Conf. on Ceramic Materials and Components for Engines, Arita, Japan, 1997.

Niihara, K., 1991, "New Design Concept of Structural Ceramics—Ceramic Nanocomposites," *J. Ceram. Soc. Jpn.*, Vol. 99, pp. 974–982.

Pan, X., Mayer, J., Ruehle, M., and Niihara, K., 1996, "Silicon Nitride Based Ceramic Nanocomposites," *J. Am. Ceram. Soc.*, Vol. 79, pp. 585–590.

Tanaka, I., and Pezotti, G. et al., 1989, "Hot-Isostatic Press Sintering and Properties of Silicon Nitride Without Additives," *J. Am. Ceram. Soc.*, Vol. 72, pp. 1656–1660.

VAMAS Round Robin on Fracture Toughness Measurement of Ceramic Matrix Composites, Final Report 32, Sept. 1997, Japan Fine Ceramic Center, Nagoya, ISSN 1016-2186.

Westerheide, R., Woetting, G., Schmitz, H. W., and Foitzik, A., 1997, "Economical Realization of the SiC/Si_3N_4-Nanocomposite Concept," to be published in "Silicates Industriel", Belgium.

Woetting, G., Frassek, L., and Gugel, E., 1996, "New Developments on Silicon Nitride-Based Ceramics for High Temperature Applications," Proceedings, 3rd Europ. Workshop on High Temperature Materials, ESA-WPP-104, pp. 40–45.

Woetting, G., and Gugel, E., 1997, "Influence of Grain-Boundary Phase Amount on Properties of Dense Si_3N_4," cfi/Ber. DKG, Vol. 74, pp. 239–244.

High Temperature Oxidation and Corrosion of Silicon-Based Non-Oxide Ceramics

H. Klemm

M. Herrmann

C. Schubert

Fraunhofer IKTS Dresden,
Winterbergstrasse 28,
Dresden, FRG D-01277

The present study is focussed on the oxidation behavior of nonoxide silicon-based ceramics. Various Si_3N_4 and SiC ceramics were examined after long term oxidation tests (up to 5000 h) at 1500°C in ambient air. The damage mechanisms were discussed on the basis of a comprehensive chemical and microstructural analysis of the materials after the oxidation tests. The diffusion of oxygen into the material and its further reaction in the bulk of the material were found to be the most critical factors during long term oxidation treatment at elevated temperatures. However, the resulting damage in the microstructure of the materials can be significantly reduced by purposeful microstructural engineering. Using Si_3N_4/SiC and Si_3N_4/$MoSi_2$ composite materials provides the possibility to improve the high temperature stability.

Introduction

Nonoxide silicon-based ceramics such as Si_3N_4 and SiC are promising candidates for use as structural components in advanced heat engines at temperatures between 1300 and 1500°C. Recently developed materials exhibit remarkably high mechanical properties at elevated temperatures [1–4]; however, their actual application is still limited by their insufficient long term reliability under severe thermal, environmental and mechanical loading conditions. The major limitations determining the long term reliability of silicon nitride and silicon carbide materials is the evolution of damage caused by creep or subcritical crack growth during service at elevated temperatures. In ambient air these damage mechanisms are additionally influenced by the interaction of the material with the oxidative environment. The accumulation of these damages will ultimately dictate the performance and lifetime of the material and must be consequently predictable before the structural component can be confidently applied. For that reason a key aim in developing silicon-based nonoxide ceramic materials for long term applications at high temperatures is the comprehensive understanding of these processes, especially focussing on the correlations between microstructural features (e.g., composition and condition of the grain boundary phase) and lifetime determining processes. A schematic survey of the failure mechanisms occurring during long term exposure of silicon nitride materials under severe thermal, environmental and mechanical loading conditions is given in Fig. 1.

Whereas the time-to-failure behavior at lower stresses is determined predominantly by microstructural changes as a consequence of creep deformation, the failure at higher stresses is mainly caused by subcritical crack growth (SCG) from pre-existing flaws. After a longer exposure at elevated temperatures (>100 h) these damage mechanisms are furthermore influenced by oxidation processes (newly formed oxidation damages) with the consequence of an additional degradation of the lifetime performance of the material [5–8].

The effect of the oxidative corrosion on the long term mechanical behavior of silicon-based nonoxide materials at elevated temperatures has been the objective of several studies. At lower temperatures and in the first stage the oxidation process can initially be of some benefit by the healing of pre-existing surface flaws, thereby reducing the critical defect size [9–12]. Other authors have demonstrated that the oxidation process can increase the creep resistance and the time to failure [13–15]. The most probable explanation of these effects is the diffusion of the creep cavitation enhancing impurities to the edge of the specimen. After long term exposure at temperatures of 1400°C and higher, however, these beneficial effects were ousted by the results of oxidation processes. Besides the upper oxidation surface layer being formed, various microstructural changes in the bulk of the materials to a depth of more than 1 mm were observed after long term oxidation treatment at temperatures between 1400 and 1500°C. For example, the composition of the grain boundary can change due to penetration of oxygen into the material. The result of these processes is usually a deterioration of the crack growth resistance, in particular of the threshold of crack growth [5]. Other authors [6, 7] reported that, as a result of the segregation of the sintering additive cations from the grain boundary phase into the surface oxide scale, a degraded layer containing numerous micropores was formed just beneath the oxidation layer during high temperature treatment at 1400°C. A degradation in strength was observed as a consequence of these damages. Under stress loading conditions these micropores can also promote crack opening processes with the result of a shorter time to failure of the material. Such an oxidation enhanced crack propagation was described by Wereszczak [16], who tested a HIP'ed silicon nitride with 6 percent Y_2O_3 as the sintering aid in dynamic fatigue in ambient air and inert (argon or nitrogen) environments. On the fracture surface of the specimen tested in air he observed a characteristic stress-oxidation damage zone, which weakened the material. On the contrary, there was no such damage in inert environments.

For that reason a key objective in developing nonoxide silicon-based ceramic materials for long term applications at high temperatures is the comprehensive understanding of oxidation processes.

The present study is focussed on the oxidation behavior of three Si_3N_4 materials, one SiC material and two Si_3N_4 composites (Si_3N_4/SiC and Si_3N_4/$MoSi_2$). Based on a comprehensive chemical and microstructural analysis of the materials after more than 1000 h oxidation at 1500°C, an interpretation of the different oxidation mechanisms obtained is suggested. Finally, the potential of the materials is discussed in terms of time-to-failure behavior at elevated temperatures.

Experimental Procedure

The studies were conducted on an S SiC (B, C) (SSiC), a HIP'ed Si_3N_4 without sintering additives (HIPSN), two hot pressed Si_3N_4 materials with Y_2O_3 (SNY) and Y_2O_3/Al_2O_3 (SNY/Al) and the Si_3N_4 composites Si_3N_4/SiC (SNC) and Si_3N_4/$MoSi_2$ (SNMo) with Y_2O_3 as a sintering additive (hot pressed). The materials exhibited

Contributed by the International Gas Turbine Institute (IGTI) of THE AMERICAN SOCIETY OF MECHANICAL ENGINEERS for publication in the ASME JOURNAL OF ENGINEERING FOR GAS TURBINES AND POWER. Paper presented at the International Gas Turbine and Aeroengine Congress and Exhibition, Stockholm, Sweden, June 2–5, 1998; ASME Paper 98-GT-480.

Manuscript received by IGTI March 25, 1998; final revision received by the ASME Headquarters October 20, 1999. Associate Technical Editor: R. Kielb.

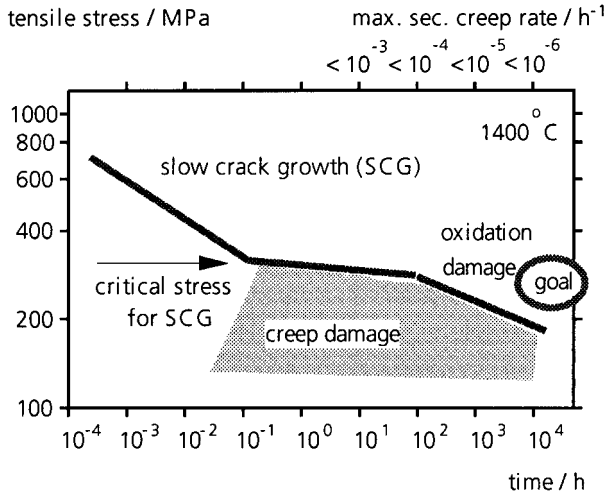

Fig. 1 Failure mechanisms of Si_3N_4 materials during long term mechanical testing at elevated temperatures in air (SCG: slow crack growth)

the typical microstructure as known from literature: HIPSN mainly globular grains with a average grain size of 0.3 μm; SSiC 8 μm; SNY, SNC, SN Mo and SNY/Al with elongated grains with 0.25 μm and 0.3 μm (SNY/Al) in the shortest dimension. The phase composition of the materials was determined by X-ray diffractometry using CuKα radiation. XRD showed the presence of β-Si_3N_4 or SiC with a small amount of α-Si_3N_4 ($<$5 percent) and SiC and $MoSi_2$ in the composite. A large part of the grain boundary phase was found to be crystallized with Y-apatite structure in the Si_3N_4 materials SNY, SNC, SN Mo, and SNY/Al.

The oxidation resistance of the materials was studied using bending bars with dimensions of approximately 3 mm $\times$ 4 mm $\times$ 50 mm in a high temperature furnace at 1500°C in air with periodical measurement of the weight gain up to 5000 h. After oxidation, the phase composition of the oxidation surface layer and the bulk below the oxidation layer was investigated by XRD. To assess the damage caused by the oxidation after 1000 h, the oxidized specimens were also tested in bending and compared with the strength of the as-hot-pressed samples. Information about the microstructural alterations was obtained by observing polished and etched (CF_4-plasma) surface sections in the SEM.

Results and Discussion

Mechanical Properties. Selected mechanical properties of the materials investigated are summarized in Table 1. The differences in the mechanical properties of these materials was mainly the result of the amount and composition of the grain boundary phase. Materials both with a high refractory grain boundary phase (SiO_2 in HIPSN) and without (SSiC) exhibit superior high temperature creep resistance; however, the level of their room temperature properties was found to be quite poor in comparison to the materials with a weaker grain boundary phase with better mechanical properties at ambient temperatures and a degradated creep resistance [17]. The creep data of the materials in this study were calculated using the deflection in the inner span of the four-point bending cell between 90 and 100 h. Note that the creep tests were conducted in bending (the nonlinearity of the elastic stress distribution in the beam and the difference of the materials under tension and compression were neglected).

Oxidation Resistance. The oxidation behavior of all materials investigated approximately obeyed a parabolic mechanism. However, the weight gain was found to vary between the materials observed. During oxidation a protective oxide layer was formed on the surface of the nonoxide materials. Caused by the different grain boundary chemistry, the composition of the oxidation layer was different, which consequently led to changes in softening point and viscosity and finally to different diffusion coefficients of oxygen into the materials. The HIP'ed Si_3N_4 and the SiC material were found to be the most stable materials. The HIPSN material exhibited the lowest weight gain because a quite clean protective layer of pure SiO_2 with the lowest diffusion coefficient of oxygen was formed. In the case of SSiC, the parabolic oxidation rate increased after 1000 h, and the weight gain was found to be about twice that of the HIP'ed Si_3N_4. Possible explanations for this behavior are the presence of boron in the SiO_2 glass (B was used as a sintering aid in this material) or an accelerated formation of cracks caused by a greater degree of crystallization of crystobalite during cooling. The results of the oxidation tests performed on these two materials at 1500°C for 2500 h are summarized in Fig. 2 as the weight gain as a function of the square root of time.

The oxidation rate constants, calculated from the slope of the Δm versus $\sqrt{t}$ plot of the data between 1000 and 2500 h, exhibit the following values:

HIPSN: $K_{ox} = 5.2 \times 10^{-8}$ mg^{2}cm^{-4}s^{-1};
SSiC: $K_{ox} = 3.1 \times 10^{-7}$ mg^{2}cm^{-4}s^{-1}.

XRD of the oxidation layer showed the presence of crystallized SiO_2 (cristobalite) in both materials. Only β-Si_3N_4 or SiC were detected in the bulk below the oxidation layer.

A similar oxidation behavior of the two "additive-free" materials was confirmed by observing polished and etched cross sections of the Si_3N_4 material after 2500 h (Fig. 3(*a*) and the SSiC material (Fig. 3(*b*)) after 1000 h of oxidation treatment at 1500°C. The microstructural development during oxidation was found to be similar in both materials. A dense oxidation layer consisting of glassy silica was observed. The cracks found in this oxidation layer are the consequence of the crystallization of cristobalite in combination with volume shrinkage during cooling, as mentioned above. Below the oxidation layer, no differences in the microstructure and chemical composition in comparison to the one in the as-sintered condition were observed.

In summary of these results, it can be concluded that the oxidation process of the additive-free materials was mainly controlled by oxygen diffusion through the upper oxidation scale. The oxidation of the materials was found to occur at the interface between the oxidation surface and the bulk of the materials.

Figure 4 shows the oxidation behavior of the materials with yttria and yttria/alumina as the sintering additive at 1500°C. In both materials, especially in the case of the alumina-containing material, the oxidation in terms of weight gain was found to be higher than in the additive-free materials. This behavior was the consequence of increased oxygen diffusion into the material caused by the chemistry of the surface layer formed during the oxidation process (lower eutectic and viscosity due to the yttria and the yttria/alumina present). This behavior was confirmed by the oxidation rates of the two materials:

SNY: $K_{ox} = 1.1 \times 10^{-7}$ mg^{2}cm^{-4}s^{-1};
SNY/Al: $K_{ox} = 1.1 \times 10^{-5}$ mg^{2}cm^{-4}s^{-1}.

The oxidation kinetics were found to be nearly parabolic as well; however, a decreasing oxidation rate was observed, espe-

Table 1 Mechanical properties of the materials investigated; σ_{RT} and σ_{14}: four-point bending strength at room temperature and 1400°C, K_{Ic}: SENB t = 0.15 mm, $\dot{\epsilon}$: 200 MPa, 1400°C

material	ρ/g/cm^3	σ_{RT}/MPa	σ_{14}/MPa	K_{Ic}/MPa$\sqrt{m}$	$\dot{\epsilon}/h^{-1}$
HIPSN	3.20	510	500	3.0	8.0×10^{-6}
SSiC	3.18	430	430	2.8	1.5×10^{-6}
SNY/Al	3.30	950	720	8.5	6.0×10^{-5}
SNY	3.29	1180	730	8.2	1.5×10^{-5}
SNC	3.29	820	750	7.4	1.8×10^{-5}
SN Mo	3.47	930	730	8.2	1.8×10^{-5}

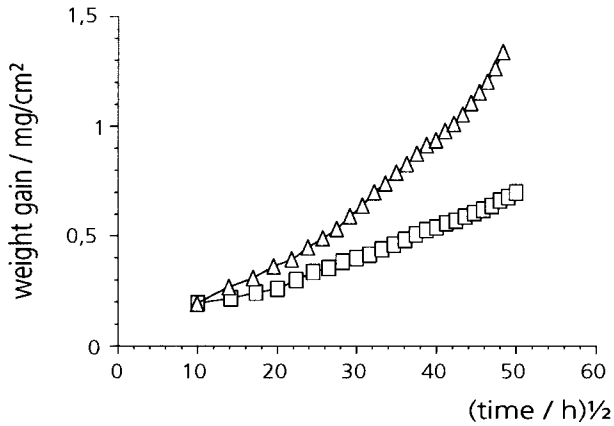

Fig. 2 Oxidation behavior of the SSiC and the Si_3N_4 materials without additives at 1500°C, illustrated as the weight gain as a function of the square root of time (□ HIPSN, △ SSiC, 2500 h)

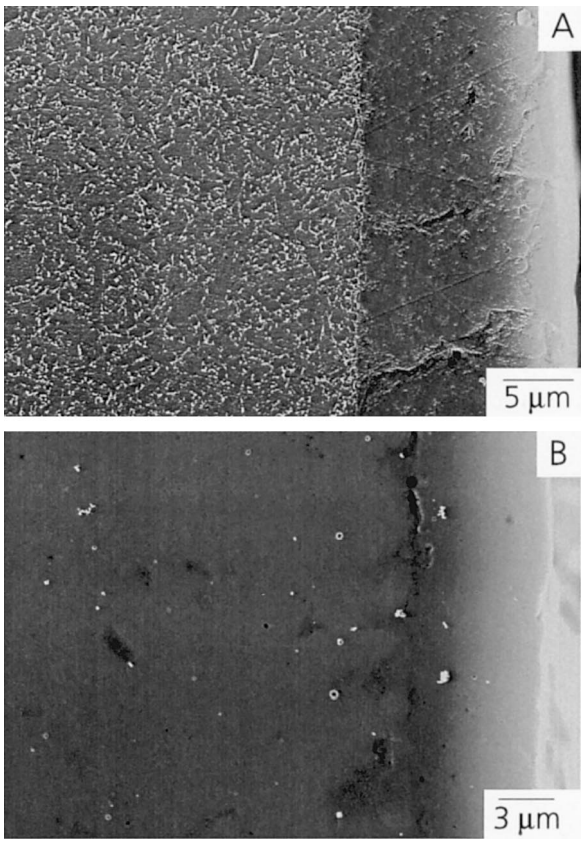

Fig. 3 SEM images of polished cross sections of the Si^3N_4 material (*A*) after 2500 h, and the SSiC material (*B*) after 1000 h of oxidation treatment at 1500°C

cially in the case of the SNY/Al material. This behavior is thought to be due to evaporation processes during the oxidation of the Si_3N_4 material, as reported recently [18].

The upper oxidation layer of these materials consisted of crystalline $Y_2Si_2O_7$ and cristobalite in a glassy layer consisting mainly of SiO_2. Some crystalline Si_2ON_2, in addition to Si_3N_4 and $Y_2Si_2O_7$, was detected by XRD in the bulk of the material just beneath the oxidation layer.

More information about the oxidation of the SNY and SNY/Al materials was obtained by SEM studies of the surface region of the oxidized specimens. The microstructure of these materials was found to be changed considerably. Figure 5 shows the microstructure of the SNY/Al material after 1000 h (*a*) and SNY after 2500 h (*b*) oxidation at 1500°C. In both materials the polished cross

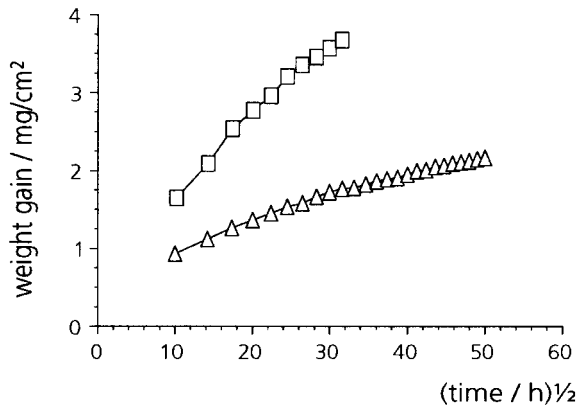

Fig. 4 Oxidation behavior of the Si_3N_4 materials with Y_2O_3 and Y_2O_3/Al_2O_3 as sintering additives at 1500°C, illustrated as the weight gain as a function of the square root of time (□ SNY/Al 1000 h, △ SNY 2500 h)

section of the surface region exhibited a considerably damaged microstructure with cracks, pores, and grain boundary phase regions extending to the middle of the specimen, similar to various Si_3N_4 materials described in the literature [5–7]. The effect of the oxidation treatment can be seen particularly in the case of the Al_2O_3-containing material.

The presence of Al_2O_3 results in an additional change in the chemistry of the protective oxidation layer. Due to the lower eutectic and viscosity of the oxidation layer, the oxygen diffusion was found to be the highest of all the materials investigated. In contrast to the additive-free materials, in which the diffusion of the oxygen proceeded only to the interface between the surface oxi-

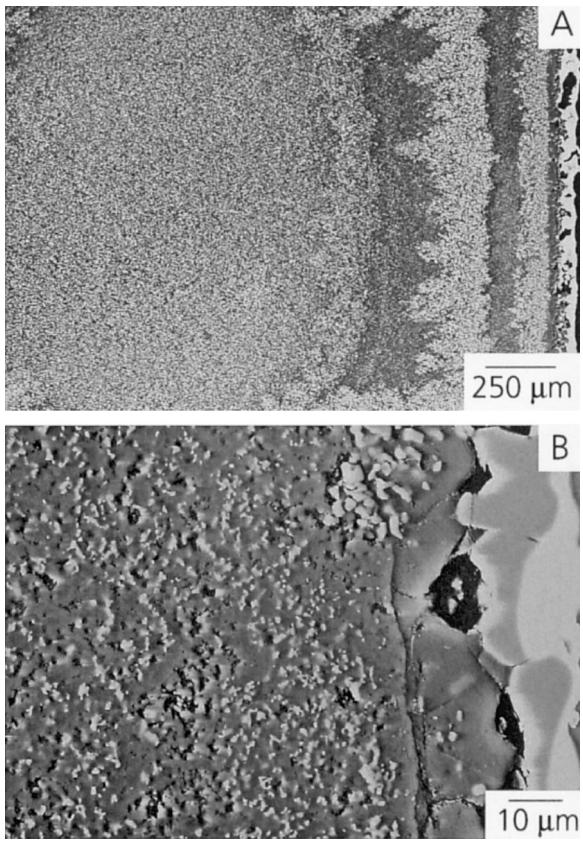

Fig. 5 Microstructural damage in the surface region of the Si_3N_4 materials with Y_2O_3/Al_2O_3, 1000 h (*a*) and Y_2O_3, 2500 h (*b*) as sintering additives after oxidation at 1500°C

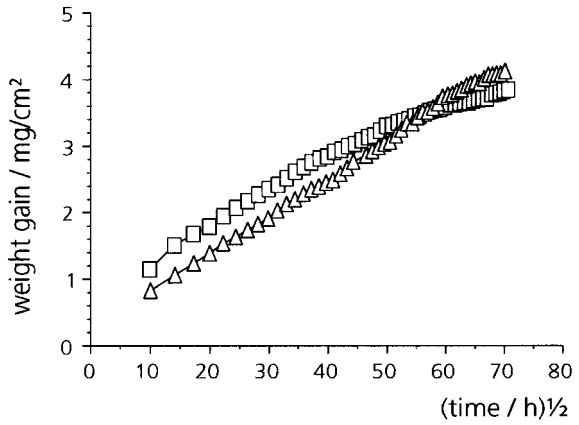

Fig. 6 Oxidation behavior of the Si_3N_4 composites at 1500°C (□ Si_3N_4/SiC, △ $Si_3N_4/MoSi_2$, 5000 h)

dation layer and the bulk, some oxygen diffusion into the bulk of the materials with Y_2O_3 and Y_2O_3/Al_2O_3 was observed.

The oxidation process in these materials occurs predominantly in the glassy phase of (1) the oxidation layer and (2) the grain boundaries and triple junctions between the silicon nitride grains. It is supposed that the oxidation occurring in the upper oxidation scale was controlled by the dissolution of Si_3N_4 into the glassy phase of the oxidation layer. If the rate of the dissolution of Si_3N_4 into the glass was smaller than necessary to react completely with the oxygen diffusing through the upper oxidation layer, the residual oxygen could propagate into the bulk of the Si_3N_4, as observed in the Y_2O_3- and especially in the Y_2O_3/Al_2O_3-containing material used in this study.

This residual oxygen was responsible for the microstructural alterations and damages observed in the yttria-containing materials. As a consequence of the oxidation in the grain boundaries of the bulk beneath the upper oxidation layer, an increased SiO_2 activity in the grain boundary phase was observed. The accumulation of SiO_2 in the surface scale of the material results in the known damage mechanisms, e.g., increased evaporation processes in the upper surface scale of the Si_3N_4 as proposed in a former report [18] or the segregation of the grain boundary cations (Y^{3+}/Al^{3+}) to the surface during high temperature oxidation observed particularly in the Al_2O_3-containing material. As already reported by Clarke [19], the SiO_2-rich layer at the surface of the material creates a chemical gradient and a driving force for the grain boundary phase cations to diffuse into this silica-rich glass in the surface of the material.

All these processes observed during oxidation in the SNY and SNY/Al materials finally led to the damaged microstructure shown in Fig. 5(*a*) and (*b*). The consequence of this damaged microstructure was a significantly reduced room temperature bending strength after oxidation at 1500°C, which was found to be about three times lower than in the as-hot-pressed condition.

Improved Oxidation Resistance in Si_3N_4-Based Composites. As shown above, the diffusion of oxygen into the bulk material and the resulting oxidation processes were found to be the main factors leading to alterations of the microstructure and consequently to the degradation of the mechanical properties of the Si_3N_4 materials with sintering additives.

In former studies Si_3N_4/SiC and $Si_3N_4/MoSi_2$ composite materials were found to obey a less severe oxidation mechanism in comparison to the monolithic Si_3N_4 material, with the consequence of an improved microstructural and mechanical stability after high temperature oxidation [18, 20–22]. Figure 6 shows the oxidation behavior up to 5000 h at 1500°C in air of two Si_3N_4 composites with SiC and $MoSi_2$. The oxidation rate constants exhibit these values:

SNC: $K_{ox} = 8.4 \times 10^{-7}$ mg^{2}cm^{-4}s^{-1};
SNMo: $K_{ox} = 9.7 \times 10^{-7}$ mg^{2}cm^{-4}s^{-1}.

In spite of the higher oxidation in terms of the weight gain in comparison to a monolithic Si_3N_4 material with the same composition (Fig. 4), the residual strength of the composite materials was found to be considerably less degradated after oxidation. Figure 7 shows the results of the bending tests of the three materials performed after 1000 h oxidation at 1400, 1450 and 1500°C. The "pest" oxidation observed in $MoSi_2$ materials at lower temperatures was not found. This was the consequence of the rapid formation of a dense oxidation layer consisting mainly of silica at temperatures ≥1400°C preventing the diffusion of a large amount of oxygen into the material.

While a reduction of the residual strength after 1000 h oxidation at 1500°C to a level of about 450 MPa was observed in the case of the Si_3N_4 material, the composite materials exhibited a considerably higher residual strength (650–700 MPa).

These results should be attributed to the microstructural development of the composite materials during the oxidation treatment, namely a significantly lower amount of damages than in the Si_3N_4 material, although the oxidation processes also occurred in the bulk composites. As shown in Fig. 8 and Fig. 9, no cracks, pores or accumulations of glassy phase were found in the microstructures of the oxidized Si_3N_4/SiC and $Si_3N_4/MoSi_2$ composite specimens.

This behavior was the consequence of different processes in the surface region of the materials, resulting in a changed oxidation mechanism in the composites. The important feature of the composite materials was the increased formation of Si_2ON_2 instead of SiO_2, producing an additional layer between the oxidation surface and the bulk of the silicon nitride composite materials. The formation of crystalline Si_2ON_2 in the composite materials was detected by XRD. Additionally, the Si_2ON_2 crystallites were found by their typical partial-fiber twin-like appearance in polished and plasma etched sections in the SEM images in Fig. 8(*b*) and Fig. 9(*b*) [9, 10]. The damage processes described above did not occur, with the result of a considerably less degraded microstructure of the composite materials after long term oxidation treatment at elevated temperatures.

The significantly reduced defect size in the composite material gives an idea as to the potential in terms of their stability and time-to-failure behavior at elevated temperatures.

The results of time-to-failure tests at 1400°C are summarized in Fig. 10. The additive-free materials (e.g., SSiC) exhibited superior high temperature stability; however, because of their brittleness the mechanical level which these materials were able to survive was found to be quite low in comparison to the Si_3N_4 materials with additives. The influence of oxidation was found to be less severe because of the simple diffusion-controlled oxidation mechanism. The oxygen penetrated through the protective layer of amorphous

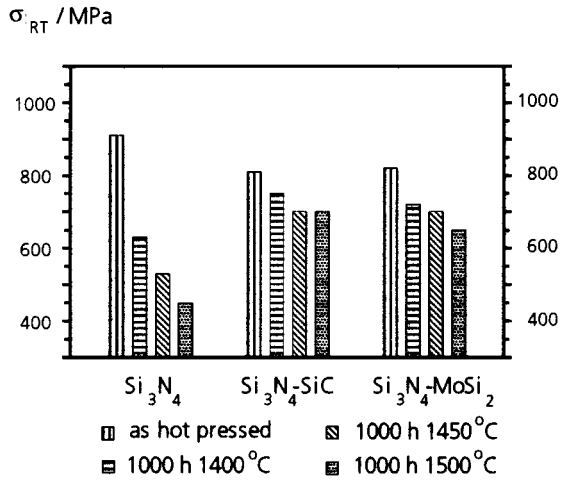

Fig. 7 Comparison of the bending strength of the Si_3N_4 materials as hot pressed and after 1000 h oxidation treatment at 1400, 1450, and 1500°C

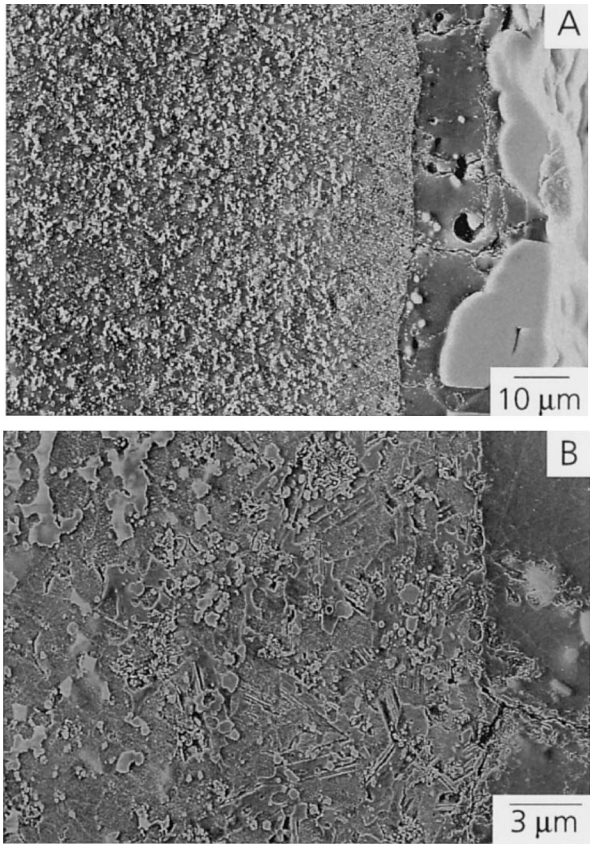

Fig. 8 (*a*) Surface region of a polished and etched cross section and (*b*) Si_2ON_2 interlayer in the bulk of the SNC material after 2500 h of oxidation at 1500°C

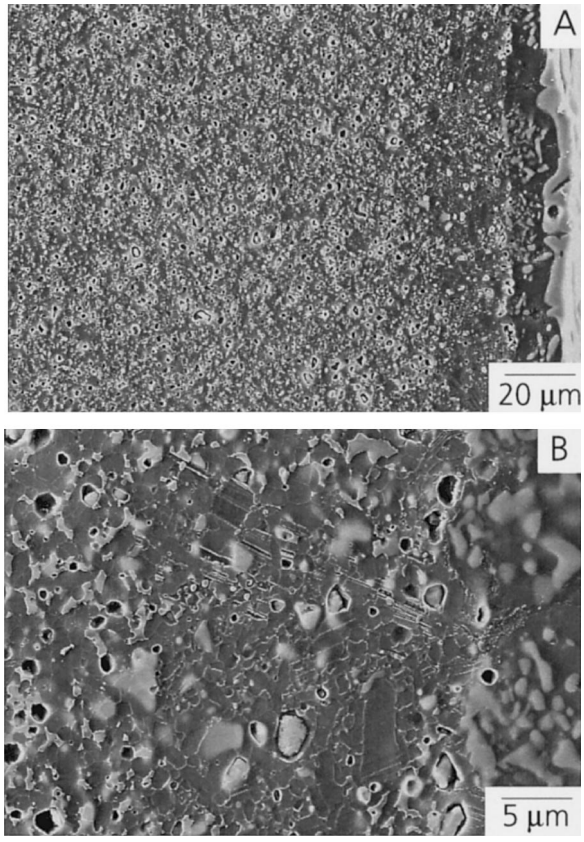

Fig. 9 (*a*) Surface region of a polished and etched cross section and (*b*) Si_2ON_2 interlayer in the bulk of the Si_3N_4-$MoSi_2$ composite material after 2500 h of oxidation at 1500°C in air

and crystalline SiO_2 and reacted at the interface between this oxidation layer and the bulk of the material without any changes in the microstructure and chemical composition of the bulk material.

The stress level in the lifetime tests of the additive-containing Si_3N_4 materials was found to be higher. This was the consequence of the interaction of an elongated microstructure developed during sintering with the grain boundary phase. The normally degradating effects of the weaker grain boundary phase (amount, softening point, viscosity) observed in creep and SCG at elevated temperatures [17] were less serious due to a highly crystallized grain boundary phase.

While the Si_3N_4 materials exhibited nearly the same behavior at higher stresses after short time, the monolithic Si_3N_4 material was observed to be considerably more damaged after long term testing in comparison to the Si_3N_4 composites (all materials with nearly the same base material composition, Y_2O_3 as sintering additive). The increased SiO_2 activity in the upper region of the bulk material was responsible for the degraded microstructure (cracks, pores, grain boundary phase inhomogeneities) which consequently led to a reduced SCG resistance of the monolithic Si_3N_4 material. As a consequence of the altered oxidation mechanism in the Si_3N_4 composite materials, with the formation of Si_2ON_2 instead of SiO_2, the microstructural degradation during oxidation was found to be considerably reduced.

Conclusion

The influence of oxidation on high temperature stability and time-to-failure behavior of silicon-based nonoxide ceramics was studied. The materials without sintering aids exhibited the highest stability in terms of oxidation. The influence of oxidation was found to be less severe on the lifetime behavior because of the simple diffusion-controlled oxidation mechanism. However, the mechanical level at which these materials were able to survive was found to be quite low in comparison to the Si_3N_4 materials with additives.

In the case of the additive-containing materials, the diffusion of oxygen into the materials was found to be increased because of the

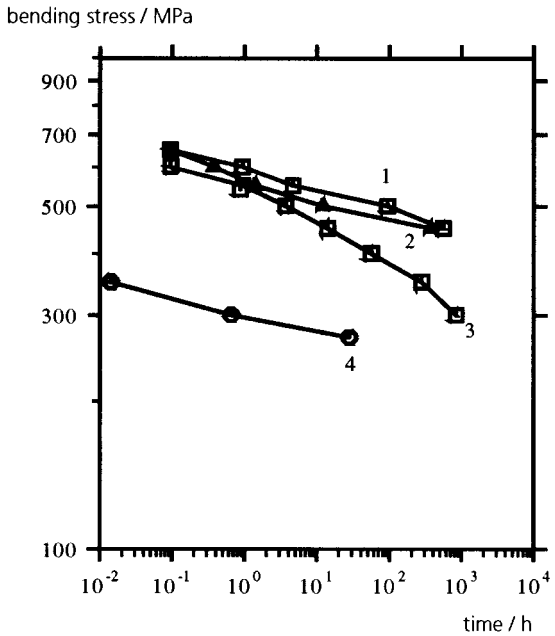

Fig. 10 Comparison of time-to-failure behavior of silicon-based nonoxide materials at 1400°C in bending; 1 SNMo, 2 SNC, 3 SNY, 4 SSiC

weaker properties (softening point, viscosity) of the protective oxidation layer. As a consequence of the higher amount of oxygen diffusion, oxidation processes with an increased formation of SiO_2 took place in the upper region of the bulk material, which were responsible for the microstructural degradation of the materials during oxidation and the resulting degraded behavior in time to failure at elevated temperatures.

In the case of the composite Si_3N_4 materials, the oxidation mechanism was found to be different. The microstructural degradation was found to be considerably reduced because of the formation of Si_2ON_2 instead of SiO_2 during oxidation, which consequently led to a significantly reduced defect size in these composite materials after oxidation. The higher oxidation stability of the Si_3N_4/SiC and the Si_3N_4/$MoSi_2$ composite materials was found to be the main reason of the improved behavior in time to failure at elevated temperatures.

Acknowledgments

This study was supported by the Deutsche Forschungsgemeinschaft (DFG) under contract number He 1958/3-5.

References

1 Pezzotti, G., 1993, "Si_3N_4/SiC-Platelet Composite Without Sintering Aids: A Candidate for Gas Turbine Engines," *J. Am. Ceram. Soc.*, Vol. 76, No. 5, pp. 1313–1320.

2 Menon, M. N., et al., 1994, "Creep and Stress Rupture Behavior of an Advanced Silicon Nitride," *J. Am. Ceram. Soc.*, Vol. 77, No. 5, pp. 1217–1241.

3 Watanabe, K., et al., 1991, "Development of Silicon Nitride Radial Turbine Rotors," Proceedings, 4th Int. Symp. Ceram. Mater. & Engines, R. Carlson, T. Johanson, and T. Kahlman, eds., Elsevier London, pp. 1009–1016.

4 Gasdaska, C. J., 1994, "Tensile Creep in an in Situ Reinforced Silicon Nitride," *J. Am. Ceram. Soc.*, Vol. 77, No. 9, pp. 2408–2418.

5 Tressler, R. E., 1990, "Environmental Effects on Long Term Reliability of SiC and Si_3N_4-Ceramics," in *Ceram. Trans.*, Vol. 10, R. E. Tressler, ed., pp. 99–124.

6 Van der Biest, O., Weber, C., and Garguet, L. A., 1989, "Role of Oxidation on Creep and High-Temperature Failure of Silicon Nitride," Proceedings, 3th Int. Symp. Ceram. Mater. & Components for Engines, V. Tennery, ed., Columbus, OH.

7 Nishimura, N., Masuo, E., and Takita, K., 1991, "Effect of Microstructural Degradation on the Strength of Silicon Nitride after High-Temperature Exposure," Proceedings, 4th Int. Symp. Ceram. Mater. & Components for Engines, R. Carlson, T. Johansson, and T. Kahlman, eds., Elsevier London, pp. 1139–1146.

8 Wereszczak, A. A., Ferber, M. K., Kirkland, T. P., More, K. L., Foley, M. R., and Yeckley, R. L., 1995, "Evolution of Stress Failure Resulting from High-Temperature Stress-Corrosion Cracking in a Hot Isostatically Pressed Silicon Nitride," *J. Am. Ceram. Soc.*, Vol. 78, No. 8, pp. 2129–2140.

9 Van der Biest, O., and Weber, C., 1990, "Effects of Oxidation on Long-Term Failure of Silicon Nitride," *Ceram. Trans.*, Vol. 10, R. E. Tressler, ed., pp. 125–139.

10 Kim, H. E., and Moorhead, A. J., 1990, "Effects of Gaseous Corrosion on the Strength of SiC and Si_3N_4," *Ceram. Trans.*, Vol. 10. R. E. Tressler, ed., pp. 81–92.

11 Clarke, D. R., Lange, F. F., and Schnittgrund, G. D., 1982, "Strengthening of a Silicon Nitride by Post Fabrication Heat Treatment," *J. Am. Ceram. Soc.*, Vol. 65, pp. C51–52.

12 Choi, S. R., Tikare, V., and Pawlik, R., 1991, "Crack Healing in Silicon Nitride Due to Oxidation," Proceedings, *Ceram. Eng. Sci. Proc.*, Vol. 12, pp. 190–202.

13 Wereszczak, A. A., Kirkland, T. P., and Ferber, M., 1995, "Differences in Creep Performance of a HIPed Silicon Nitride in Ambient Air and Inert Environments," Proceedings, 19th Annual Cocoa Beach Conf. & Exp., January 8–12, 1995.

14 Lewis, M. H., Heath, C. H., Winder, M. S., and Lumby, R. J., 1984, "High Temperature Creep and Fracture of β-Si_3N_4 Ceramic Alloys," in *Deformation in Ceramics Materials II*, R. E. Tressler and R. C. Bradt, eds., Plenum N.Y., pp. 605–612.

15 Lange, F. F., Davis, G. I., and Graham, H. C., 1977, "Compressive Creep and Oxidation Resistance of an Si_3N_4-Material Fabricated in the System Si_3N_4-Si_2N_2O-$Y_2Si_2O_7$," *J. Am. Ceram. Soc.*, Vol. 60, pp. 249–252.

16 Wereszczak, A. A., Breder, K., and Ferber, M. K., 1993, "Role of Oxidation in the Time-Dependent Failure Behavior of Hot Isostatically Pressed Silicon Nitride at 1370°C," *J. Am. Ceram. Soc.*, Vol. 76, No. 11, pp. 2929–2922.

17 Klemm, H., and Pezzotti, G., 1994, "Fracture Toughness and Time-Dependent Strength Behavior of Low-Doped Silicon Nitrides for Applications at 1400°C," *J. Am. Ceram. Soc.*, Vol. 77, pp. 553–561.

18 Klemm, H., Herrmann, M., and Schubert, C., 1997, "Silicon Nitride Materials with an Improved High Temperature Oxidation Resistance," *Ceram. Eng. & Sci. Proc.*, Vol. 18, No. 3, pp. 615–623.

19 Clarke, D. R., 1983, "Thermodynamic Mechanism for Cation Diffusion Through an Intergranular Phase: Application to Environmental Reactions with Nitrogen Ceramics," in *Progress in Nitrogen Ceramics*, NATO ASI Series, Series E: Applied Sciences, No. 65, F. L. Riley, ed., Martinus Nijhoff, The Hague, Netherlands, pp. 421–426.

20 Klemm, H., Tangermann, K., Schubert, C., and Hermel, W., 1996, "Influence of Molybdenum Silicide Additions on High-Temperature Oxidation Resistance of Silicon Nitride Materials," *J. Am. Ceram. Soc.*, Vol. 79, No. 9, pp. 2429–2435.

21 Klemm, H., Herrmann, M., and Schubert, C., 1995, "Problems and Prospects of Silicon Nitride Materials for Applications at Temperatures Above 1400°C," *High Temp.–High Press*, Vol. 27/28, pp. 449–456.

22 Herrmann, M., Klemm, H., Schubert, C., and Hermel, W., 1997, "Long-Term Behavior of SiC/Si_3N_4-Nanocomposites at 1400–1500°C," *Key Engineering Mater.*, pp. 132–136; 1977–1980.

System Identification of Jet Engines

N. Sugiyama
sugiyama@nal.go.jp
National Aerospace Laboratory,
7-44-1 Jindaiji Higashi, Chofu,
Tokyo 182-8522,
Japan

System identification plays an important role in advanced control systems for jet engines, in which controls are performed adaptively using data from the actual engine and the identified engine. An identification technique for jet engine using the Constant Gain Extended Kalman Filter (CGEKF) is described. The filter is constructed for a two-spool turbofan engine. The CGEKF filter developed here can recognize parameter change in engine components and estimate unmeasurable variables over whole flight conditions. These capabilities are useful for an advanced Full Authority Digital Electric Control (FADEC). Effects of measurement noise and bias, effects of operating point and unpredicted performance change are discussed. Some experimental results using the actual engine are shown to evaluate the effectiveness of CGEKF filter.

Introduction

High performance of modern jet engines has been attained by steady efforts focused on technological improvements of individual engine components and materials. It is considered that the improvement is close to limitations and higher performance is difficult without innovative new technologies. However, there is a possibility to improve performance by a control. Current engines are operating with sufficient safety margins, such as temperature and surge margin, considering engine to engine variations, deterioration, sensor and actuator error, distortion, etc. If important engine variables can be identified precisely, the control can reduce these margins and improve performance by using the latent capabilities of the engine. System identification plays a very important role in such controls, and will become a very important part of future FADEC, a Full Authority Digital Electric Control, of jet engines.

A concept of advanced FADEC for future engines is shown in Fig. 1. It will include a schedule control and a multivariable robust control at a more advanced level than that of conventional FADECs. Also included will be a performance seeking control, a redundant control and a condition monitoring for higher efficiency, reliability, safety, maintainability, etc. Moreover, it will be a part of the flight/propulsion integrated control, exchanging information with the flight control system. All of these controls may require an internal model-engine and the construction of an adaptive control system, in which controls are performed adaptively, depending on the operating condition, referring data from the actual engine, the internal model engine and the flight control system. For example, a performance-seeking control can be realized by reliable estimations of surge margin, turbine inlet temperature, thrust, efficiency, etc. An engine condition monitoring system can be realized by estimations of engine component deviation parameters. All of these estimation data will be supplied from an internal model-engine constructed by an on-line system identification technique, as shown in Fig. 1.

Many works on system identification of jet engines have been done. The major objectives of these works are (i) diagnostics of engine condition (Kerr, 1991; Urban, 1992; Doel, 1992), (ii) improvement of propulsion/flight performance (Luppold, 1989; Espana, 1993; Adibhatla, 1993; Orme, 1994), and (iii) improvement of the reliability of control system (Merrill, 1988; Volponi, 1994). Most of these techniques are based on linear theories and not applicable to a nonlinear system directly. Usually, linear identification systems are designed at selected operating points; then identification at a specific operating point is performed interpolating those. This piecewise technique was widely used because the computational burden was low. However, due to current remarkable progress of micro-processor or DSP boards in speed, cost, weight, power consumption, etc., it become possible that a nonlinear system model is applied directly to identification process, instead of a piecewise linear model.

A system identification technique for jet engines using the Constant Gain Extended Kalman Filter (CGEKF) has been designed for a two-spool turbofan engine and evaluated by nonlinear dynamic simulation test and actual engine running test. It has been concluded that the CGEKF is a promising candidate for system identification in future FADEC.

Constant Gain Extended Kalman Filter (CGEKF)

A nonlinear dynamical system is expressed as follows:

$$\dot{\mathbf{x}} = \mathbf{f}(\mathbf{x}, \mathbf{u}) + \mathbf{G}\mathbf{v}$$

$$\mathbf{y}_m = \mathbf{g}_m(\mathbf{x}, \mathbf{u}) + \mathbf{w}$$

$$\mathbf{y}_u = \mathbf{g}_u(\mathbf{x}, \mathbf{u}) \tag{1}$$

where, $\mathbf{x}$: state vector, $\mathbf{u}$: control vector, $\mathbf{y}_m$: measurable output vector, $\mathbf{y}_u$: unmeasurable output vector, $\mathbf{v}$: system noise vector, $\mathbf{w}$: measurement noise vector, and $\mathbf{G}$: system noise transfer matrix. By linearizing Eq. (1) at a specific operating point, a linearized engine model is derived as follows:

$$\dot{\mathbf{x}} = \mathbf{A}\mathbf{x} + \mathbf{B}\mathbf{u} + \mathbf{G}\mathbf{v}$$

$$\mathbf{y}_m = \mathbf{C}\mathbf{x} + \mathbf{D}\mathbf{u} + \mathbf{w}$$

$$\mathbf{y}_u = \mathbf{C}_u\mathbf{x} + \mathbf{D}_u\mathbf{u} \tag{2}$$

where, ($\mathbf{A}$, $\mathbf{B}$, $\mathbf{C}$, $\mathbf{D}$, $\mathbf{C}_u$, $\mathbf{D}_u$): system matrices. Assuming noise covariance matrices:

$$E(\mathbf{v}\mathbf{v}') = \mathbf{Q}, \quad E(\mathbf{w}\mathbf{w}') = \mathbf{R},$$

$$E(\mathbf{v}) = \mathbf{0}, \quad E(\mathbf{w}) = \mathbf{0} \tag{3}$$

maximum likelihood estimates of state, measurable and unmeasurable output vector, $\hat{\mathbf{x}}$, $\hat{\mathbf{y}}_m$ and $\hat{\mathbf{y}}_u$, are given by,

$$\dot{\hat{\mathbf{x}}} = \mathbf{A}\hat{\mathbf{x}} + \mathbf{B}\mathbf{u} + \mathbf{K}(\mathbf{y}_m - \mathbf{C}\hat{\mathbf{x}} - \mathbf{D}\mathbf{u})$$

Contributed by the International Gas Turbine Institute (IGTI) of The American Society of Mechanical Engineers for publication in the ASME Journal of Engineering for Gas Turbines and Power. Paper presented at the International Gas Turbine and Aeroengine Congress and Exhibition, Stockholm, Sweden, June 2–5, 1998; ASME Paper 98-GT-99.

Manuscript received by IGTI March 2, 1998; final revision received by the ASME Headquarters October 20, 1999. Associate Technical Editor: R. Kielb.

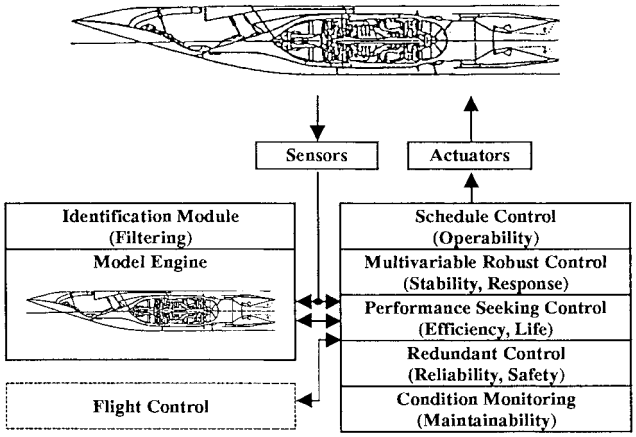

Fig. 1 Concept of advanced FADEC

$$\hat{\mathbf{y}}_m = \mathbf{C}\hat{\mathbf{x}} + \mathbf{D}\mathbf{u}$$

$$\hat{\mathbf{y}}_u = \mathbf{C}_u\hat{\mathbf{x}} + \mathbf{D}_u\mathbf{u} \tag{4}$$

where,

$$\mathbf{K} = \mathbf{P}\mathbf{C}'\mathbf{R}^{-1} \tag{5}$$

K is the linear Kalman filter gain matrix. **P** is the steady-state solution of the Riccati differential equation associated to the covariance matrix of the estimates and can be calculated from

$$\mathbf{A}\mathbf{P} + \mathbf{P}\mathbf{A}' + \mathbf{G}\mathbf{Q}\mathbf{G}' - \mathbf{P}\mathbf{C}'\mathbf{R}^{-1}\mathbf{C}\mathbf{P} = \mathbf{0}. \tag{6}$$

Extending this method to nonlinear system, maximum likelihood estimates, $\hat{\mathbf{x}}$, $\hat{\mathbf{y}}_m$ and $\hat{\mathbf{y}}_u$, are given by

$$\dot{\hat{\mathbf{x}}} = \mathbf{f}(\hat{\mathbf{x}}, \mathbf{u}) + \mathbf{K}(\hat{\mathbf{x}}, \mathbf{u})(\mathbf{y}_m - \mathbf{g}_m(\hat{\mathbf{x}}, \mathbf{u}))$$

$$\hat{\mathbf{y}}_m = \mathbf{g}_m(\hat{\mathbf{x}}, \mathbf{u})$$

$$\hat{\mathbf{y}}_u = \mathbf{g}_u(\hat{\mathbf{x}}, \mathbf{u}). \tag{7}$$

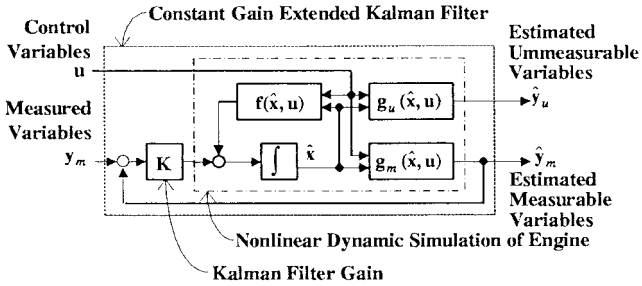

Fig. 2 Concept of CGEKF

At a specific operating point, $\mathbf{K}(\hat{\mathbf{x}}, \mathbf{u})$ is obtained by Eq. (5). $\mathbf{K}(\hat{\mathbf{x}}, \mathbf{u})$ is a nonlinear function of the operating point and must be evaluated repeatedly when the operating point is moving. This is called the Extended Kalman Filter (EKF) and requires a great deal of computer power. To overcome the substantial computational burden imposed by the EKF, Safonov and Athan suggested the use of Constant Gain Extended Kalman Filter (CGEKF), in which filter gain, **K**, is a constant matrix designed at a representative operating point. They also showed the conditions under which a class of nonlinear observers is nondivergent (Safonov, 1978; Misawa, 1989). This provides a basis for design of practical, nondivergent CGEKF estimators. It should be noted that the differentiation of equation in the linearization process might unfavorably affect the guaranteed robustness properties of CGEKF.

The CGEKF is diagrammed as shown in Fig. 2. It is almost a nonlinear dynamic simulation of system, except for the so-called innovation process, $\mathbf{K}(\mathbf{y}_m - \hat{\mathbf{y}}_m)$, the Kalman filter gain multiplied by a difference between measured variables and estimated variables. CGEKF for advanced control must run in real time or faster than real time and can be realized using currently available microprocessors or DSP boards with significant computational capability.

CGEKF for Turbo Fan Engine

A two-spool turbofan engine is considered here (refer to Fig. 3). Engine component performance data and some overall perfor-

Nomenclature

A, **B**, **C**, **D** = engine system matrices
$E(\cdot)$ = Expected value of $(\cdot)$
f$(\cdot)$, **g**$(\cdot)$ = function of $(\cdot)$
G = system noise transfer matrix
K = Kalman filter gain matrix
P, **Q**, **R** = covariance matrix of estimate, system noise and measurement noise
u = control vector
v = system noise vector
w = measurement noise vector
x = state vector
y = output vector

Superscript

$(\cdot)^{-1}$ = matrix inverse
$(\cdot)'$ = matrix transpose
$\dot{}$ = derivative
$\hat{}$ = estimate

Subscript

c, e = engine component deviation, engine
m, u = measurable, unmeasurable
b = bias

Engine Variables

A = nozzle area deviation parameter
F = thrust
G = flow deviation parameter
h = enthalpy
M = flight Mach number
m = stored mass
N, N_h, N_l = rotational speed
P, p = total and static pressure
S_{fc} = thrust specific fuel consumption
S_m = surge margin
T, t = total and static temperature
u = stored energy
W = air or gas flow rate
W_f = fuel flow rate
ξ = variable stator angle
η = efficiency deviation parameter

Subscripts (refer to Fig. 3 and Fig. 4)

h, l = high- and low-pressure rotor
fh, *ft*, *hc*, *ht*, *lt*, *mn*, *bn* = engine component name
0, 2, 21, 3, 4, 41, 5, 3*b*, 5*b* = engine station number

Acronyms

BAV = bleed air valve
CGEKF = constant gain extended Kalman filter
DSP = digital signal processing
EKF = extended Kalman filter
ECDP = engine component deviation parameter
FADEC = full authority digital electric control of jet engine
VSV = variable stator vane

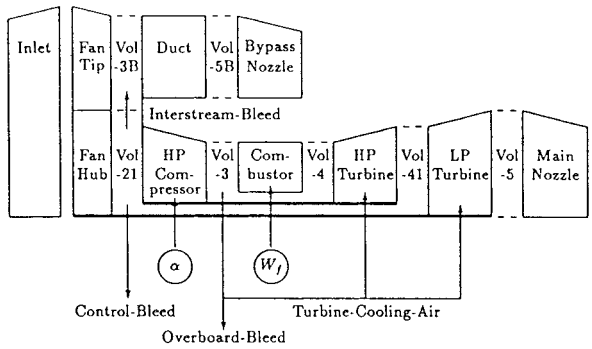

Fig. 3 Configuration of two spool turbofan engine

mance data, including dynamic performance, are available for this engine. The schematic model in Fig. 3 can be diagrammed as shown in Fig. 4, replacing the engine components with the computational modules developed by the author (Sugiyama, 1990). This diagram is a nonlinear simulation block diagram. In Fig. 4, computational modules for compressor (COMP), turbine (TURB), nozzle (NOZL), combustor (COMB), duct (DUCT), inlet (INLET), rotor (ROTOR), and volume (VOL) are used. Among these modules, the rotor and volume are dynamic modules and the rest are static modules.

Engine state vector, $\mathbf{x}_e$, is defined as follows:

$$\mathbf{x}_e = (N_l,\ N_h,\ m_{21},\ u_{21},\ m_3,\ u_3,\ m_4,\ u_4,\ m_{41},\ u_{41},\ m_5,\ u_5,\ m_{3b},\ u_{3b},\ m_{5b},\ u_{5b})', \quad (8)$$

where N_l: low-pressure rotor speed, N_h: high-pressure rotor speed, m_{21}: stored mass at volume-21, u_{21}: stored energy at volume-21, and so on. Since inter-component volumes are not so big in usual jet engines, its dynamics do not contribute significantly to dynamic behavior of jet engine in the frequency range under 10 Hz (Seldner, 1972). Hence, volume dynamics can be neglected. Then, engine state vector, $\mathbf{x}_e$, becomes

$$\mathbf{x}_e = (N_l,\ N_h)'. \quad (9)$$

Engine component deviation parameter (ECDP) vector, $\mathbf{x}_c$, is defined as follows:

$$\mathbf{x}_c = (G_{fh},\ \eta_{fh},\ G_{ft},\ \eta_{ft},\ G_{hc},\ \eta_{hc},\ G_{ht},\ \eta_{ht},\ G_{lt},\ \eta_{lt},\ A_{mn},\ A_{bn})', \quad (10)$$

where G_{fh}: flow deviation parameter of fan-hub, η_{fh}: efficiency deviation parameter of fan-hub, and so on. A_{mn} and A_{bn}: area deviation parameters of main and bypass-nozzle, respectively. Since $\mathbf{x}_c$ is artificial state vector which can be estimated by the Kalman filter, state equation,

$$\dot{\mathbf{x}}_c = \mathbf{0} \quad (11)$$

must be added to the engine state equation in Eq. (1). This means that $\mathbf{x}_c$ is changed when a difference between measured value and estimated value exists, as shown in Eq. (7). If an engine component performance is changed gradually or suddenly, it causes a difference between measurement and estimation; then the CGEKF changes $\mathbf{x}_c$ until the difference goes to zero. Total state vector, $\mathbf{x}$, becomes $\mathbf{x} = (\mathbf{x}_e,\ \mathbf{x}_c)'$.

Control vector, $\mathbf{u}$, is defined as follows:

$$\mathbf{u} = (W_f,\ \xi,\ M,\ p_0,\ t_0)' \quad (12)$$

where W_f: fuel flow rate, ξ: variable stator vane (VSV) angle, M: flight Mach number, p_0: ambient pressure, t_0: ambient temperature. Since M, p_0, and t_0 are independent variables, they are treated as control variables.

Measurable vector, $\mathbf{y}_m$, is selected as follows:

$$\mathbf{y}_m = (N_l,\ N_h,\ P_{21},\ T_{21},\ P_3,\ T_3,\ P_4,\ P_{41},\ T_{41},\ P_5,\ T_5,\ P_{3b},\ T_{3b})', \quad (13)$$

where P_{21}: total pressure at volume-21, T_{21}: total temperature at volume-21, and so on.

Unmeasurable vector, $\mathbf{y}_u$, is selected as follows:

$$\mathbf{y}_u = (F,\ T_4,\ W_{mn},\ W_{bn},\ S_{fc},\ S_m)', \quad (14)$$

where F: net thrust, T_4: turbine inlet total temperature, W_{mn}: air flow rate of main-nozzle, W_{bn}: air flow rate of bypass-nozzle, S_{fc}: thrust specific fuel consumption, S_m: surge margin of compressor.

Dimensions of state, control and output vector are summarized as follows:

Normal state: $\mathbf{x}_e = 2$

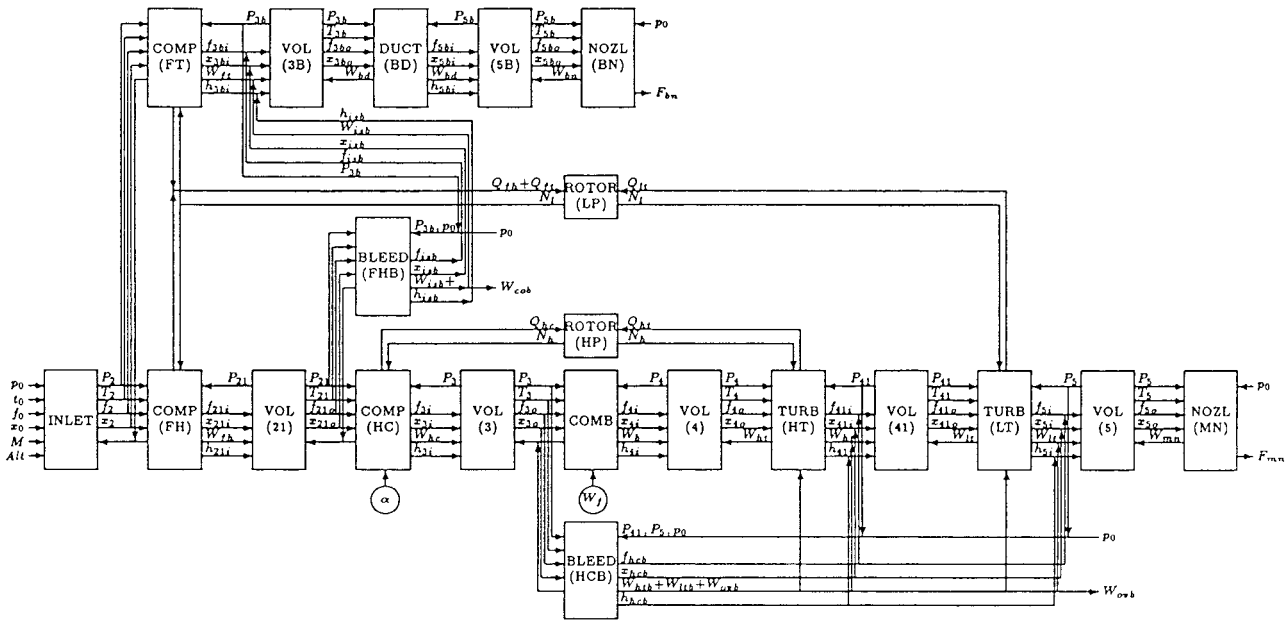

Fig. 4 Simulation block diagram of two-spool turbofan engine

Artificial state: $\mathbf{x}_c = 12$

Control: $\mathbf{u} = 5$

Measurable output: $\mathbf{y}_m = 13$

Unmeasurable output: $\mathbf{y}_u = 6$

A necessary condition for the existence of the Kalman filter is the observability of model. In the jet engine model described above, necessary condition for the observability (Espana, 1993) is

$$(\text{dimension of } \mathbf{x}_c) \leq (\text{dimension of } \mathbf{y}_m). \tag{15}$$

This condition is fulfilled with one extra measurement.

Assigning state, control and output variables as above, the Kalman filter gain at a specific operating point is obtained by the following procedures:

1 Compute system matrices, **A**, **B**, **C**, **D**, $\mathbf{C}_u$, and $\mathbf{D}_u$, in Eq. (2), which is a linearized form of Eq. (1). Some existing simulation software include this capability, but great care must be paid to utilize those because a linearization is very sensitive to the method applied (Sugiyama, 1994).
2 Define scaling values of state, control and output variables, and normalize system matrices, **A**, **B**, **C**, **D**, $\mathbf{C}_u$, and $\mathbf{D}_u$, in order to maintain numerical robustness.
3 Assume noise covariance matrices, G, Q and R, in Eq. (2) and (3). **R** is a stochastic characteristic of measurement signal and may be known, but **R** and **Q** are not defined clearly. They can be treated as free design parameters to tune the Kalman filter.
4 check the observability of (**A**, **C**) and compute Kalman filter gain, **K**, by Eq. (5).

Then, CGEKF is mechanized using this gain matrix, **K**. As mentioned above, CGEKF is almost a nonlinear simulation of jet engine, except for the innovation process.

A detailed nonlinear dynamic simulation of jet engine as shown in Fig. 4 can run in real-time, or a frame time of simulation becomes less than 1 msec, if a computer power is more than 100 Mflops.[1] This computer power is easily available from current micro-processors.

[1] Computational speed of current micro processors are over 100 Mflops and enough for realization of CGEKF. They are also good in size, weight, power consumption, and cost. Frame time for a two-spool turbofan engine, modeled as shown in Fig. 4, was approximately 0.2 msec on a DEC's Alpha Station computer which uses Alpha21164 300 MHz CPU and has approximately 600 Mflops. This frame time means the CGEKF can run 5 times faster than real time.

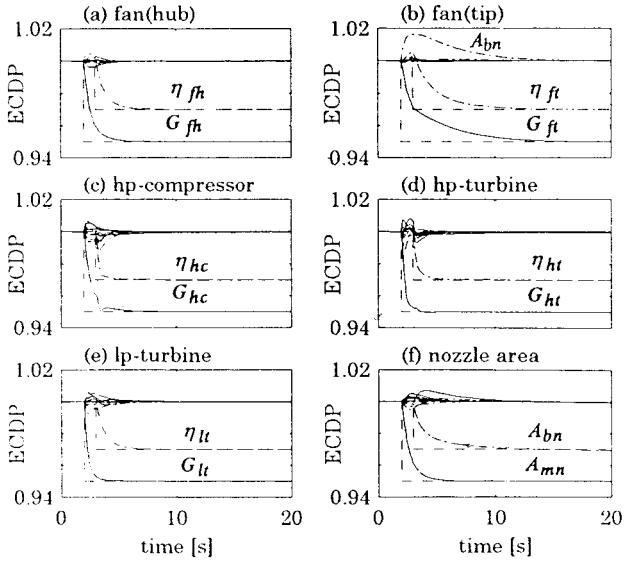

Fig. 5 Estimation of engine component deviation parameter change

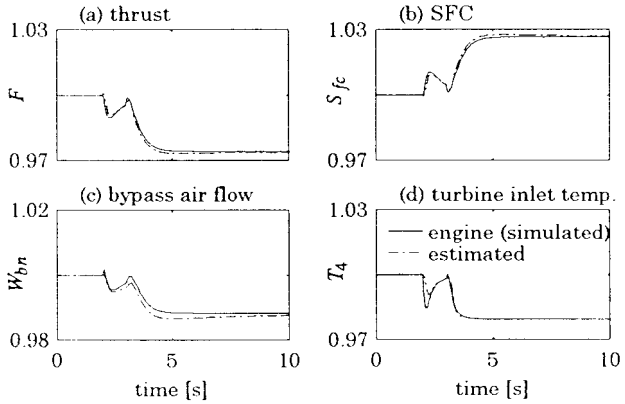

Fig. 6 Estimation of unmeasurable variables

Nonlinear Simulation Results

Estimation of Engine Component Deviation Parameters (ECDP). The Kalman filter gain matrix, **K**, was designed at a ground maximum thrust condition. When flow and efficiency parameter changes are implanted in gas path components of the engine, the CGEKF can recognize the ECDP change as shown in Fig. 5. For the fan (hub) component, flow parameter, G_{fh}, dropped 5 percent at $t = 2$ s, and the efficiency parameter, η_{fh}, dropped 3 percent at $t = 3$ s, intentionally as shown in Fig. 5(*a*). Two ECDPs correspond to G_{fh} and η_{fh} are changed apparently, but other ECDPs are slightly changed in transient, but go to zero rapidly. The ECDP estimation is successfully completed in 5 s. Similar parameter changes are implanted in the fan (tip) (Fig. 5(*b*)), high-pressure compressor (Fig. 5(*c*)), high-pressure turbine (Fig. 5(*d*)), and low-pressure turbine (Fig. 5(*e*)). The main nozzle area parameter, A_{mn}, dropped 5 percent at $t = 2$ s, and the bypass nozzle area parameter, A_{bn}, dropped 3 percent at $t = 3$ s as shown in Fig. 5(*f*). Single or simultaneous ECDP changes can be evaluated in CGEKF.

Estimation of Unmeasurable Variable. Figure 6 shows estimation of unmeasurable variables, (a) thrust, F, (b) specific fuel consumption, S_{fc}, (c) bypass air flow rate, W_{bn}, and (d) turbine inlet temperature, T_4, along with engine values computed in the nonlinear dynamic simulation. In the simulation, ECDP changes are implanted in the hc-compressor as shown in Fig. 5(*c*), i.e., the flow deviation parameter, G_{hc}, dropped 5 percent at $t = 2$ s, and the efficiency deviation parameter, η_{hc}, dropped 3 percent at $t =$

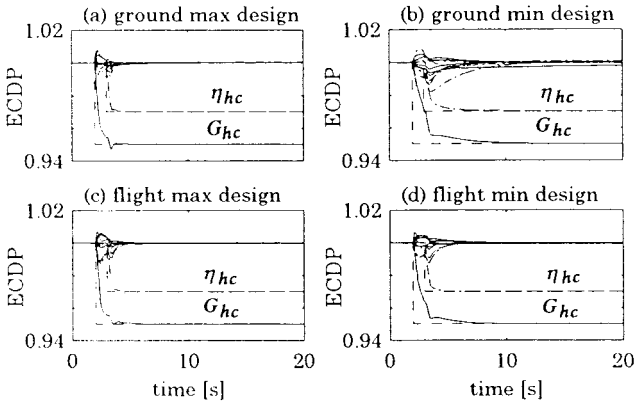

Fig. 7 Effect of operating point

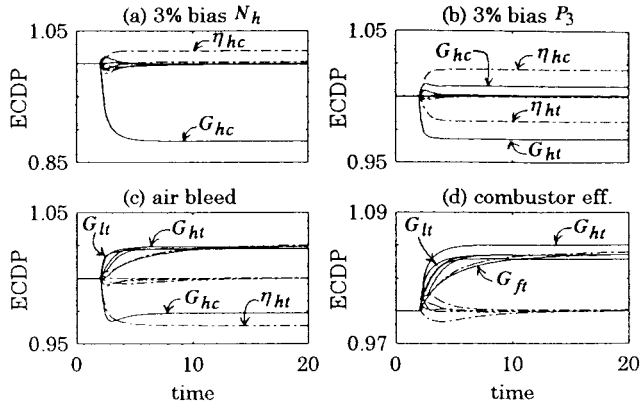

Fig. 8 Effect of measurement bias and unpredicted system change

3 s. Estimation errors are observed in transient, but disappeared rapidly. The reliable estimation of unmeasurable variables is a key factor for advanced adaptive control of jet engines.

Effect of Operating Point. The CGEKF uses a single gain matrix, **K**, for the full flight envelope. Figure 7 shows comparison of CGEKF, using four kinds of **K**, designed at (a) the ground maximum thrust point, (b) the ground idle point, (c) the flight maximum thrust point, and (d) the flight idle point. Here the ground means sea-level static condition and the flight means flight in Mach = 0.8 at the altitude = 10,000 m (32,800 ft). When parameter change is implanted in the hc-compressor as in Fig. 5(*c*), CGEKF's estimates at ground maximum condition is shown in Fig. 7. It is obvious that estimations are similar for four CGEKFs designed at the different operating points. This fact is checked at several operating points and confirms the validity of utilizing the CGEKF in jet engine application. Actually, the gain matrix, **K**, designed at ground maximum is preferable in view of scaling problem, because most of variables at ground maximum are close to maximum values, and also actual data are available.

Effect of Matrices, G, Q, and R, and Measurement Noise. Three matrices, **G**, **Q**, and **R**, in Eq. (2) and (3) are defined by characteristics of system noise and measurement noise in nature. But they can be treated as free design parameters of CGEKF, since they are not defined clearly in an actual engine/sensor system. These matrices affect response time and noise sensitivity of CGEKF. For simplicity, each of **G**, **Q**, and **R** is set as a unit matrix multiplied by a scalar constant. The response time of estimation is defined by eigen values of $(\mathbf{A} - \mathbf{KC})$ in Eq. (4). Increasing **G** and **Q**, and decreasing **R** result in faster response, but more sensitive to noise. They should be defined by compromise.

Effect of Measurement Bias. The Kalman filter is very critical to measurement error, such as bias and drift. When measurement biases exist, the second equation in Eq. (2) is rewritten as

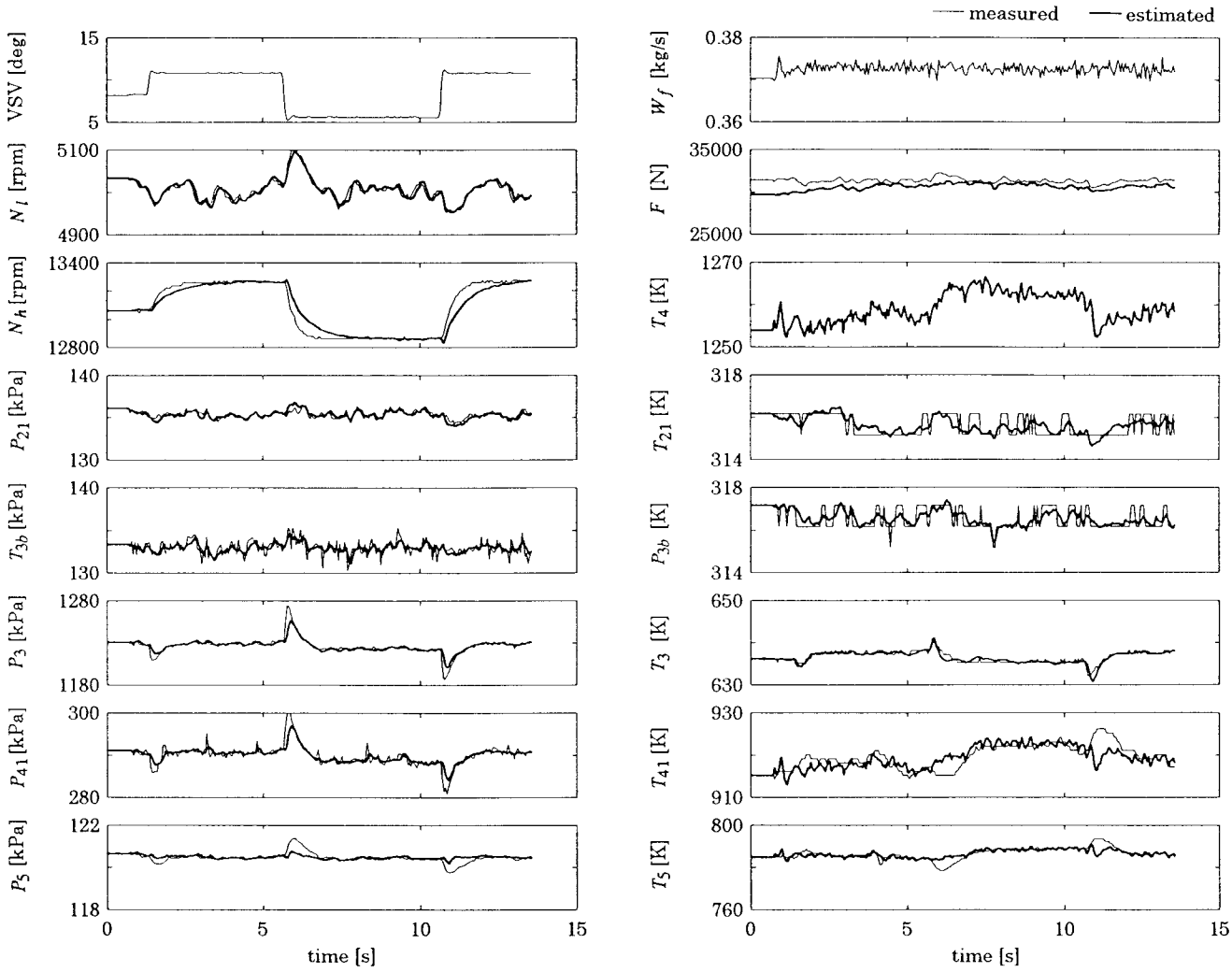

Fig. 9 Measured variables and estimated variables respond to VSV change

$$(\mathbf{y}_m + \mathbf{y}_b) = \mathbf{C}\mathbf{x} + \mathbf{D}(\mathbf{u} + \mathbf{u}_b) + \mathbf{w}, \tag{16}$$

where, $\mathbf{y}_b$ and $\mathbf{u}_b$ is measurement biases in output variables and control variables, respectively. Then, if $\mathbf{C}$ is invertible,

$$\mathbf{y}_m = \mathbf{C}(\mathbf{x} + \mathbf{C}^{-1}(\mathbf{D}\mathbf{u}_b - \mathbf{y}_b)) + \mathbf{D}\mathbf{u} + \mathbf{w} \tag{17}$$

This means that measurement biases are equivalent to ECDP change, $\mathbf{C}^{-1}(\mathbf{D}\mathbf{u}_b - \mathbf{y}_b)$. In other words, measurement biases cannot be distinguished from component parameter changes.

Figure 8(*a*) shows estimates of ECDP when measurement of the high-pressure rotor speed, N_h, is biased +3 percent at $t = 2$ s. Measurement bias causes incorrect estimates as the high pressure compressor's performance changes. When the compressor delivery pressure, P_3, is biased +3 percent at $t = 2$ s, ECDPs of many components move simultaneously as shown in Fig. 8(*b*), by which we cannot derive a meaningful result. But changes of ECDPs for components close to P_3, i.e., G_{ht}, η_{ht}, G_{hc}, and η_{hc}, are relatively large.

Effect of Unpredicted System Change. In this turbofan engine case, 12 ECDPs are selected. There may be many other ECDPs which affect performance of engine. If an unmodeled system change occurs, CGEKF cannot work. In Fig. 8(*c*), 5 percent of compressor air flow is extracted at the exit of hp-compressor, which is not assumed in designing CGEKF; then many ECDPs are changed simultaneously and we cannot derive a meaningful result. In Fig. 8(*d*), the combustion efficiency is decreased 5 percent which is also not assumed in designing CGEKF; then many ECDPs are changed simultaneously and we cannot derive a meaningful result again. But changes of the flow and the nozzle area deviation parameters are relatively large, and changes of the efficiency deviation parameters are small.

Simultaneous change of many ECDPs as shown in Fig. 8 can be considered as sensor failure or unpredicted system change, since the possibility of those may be higher than that of simultaneous characteristic changes of many engine components.

Results of Engine Test

The effectiveness of the CGEKF was evaluated for an actual two spool turbofan engine, whose configuration is shown in Fig. 3. To realize component performance changes in the actual engine, the controller of variable stator vane (VSV) of compressor and bleed air valve (BAV) at the final stage of the hp-compressor are redesigned to control these independently. The CGEKF used here is designed including VSV as a control variable and excluding the effect of BAV. The change of VSV may result in a hp-compressor performance change if the CGEKF ignores VSV input, but the change of BAV may be considered the unpredicted system change mentioned above (refer to Fig. 8(*c*)).

Effect of VSV Change. Figure 9 shows engine variable responses to VSV angle change. Measured variables are in thin lines and estimated variables of CGEKF in thick lines. Fuel flow is kept constant at a middle power condition and VSV is changed ±2.5 degrees around nominal value. Bigger VSV angle is the closed side of VSV and means smaller air flow rate for a specific rotational speed. When VSV angle changes, high pressure rotor speed changes its level, and pressures and temperatures downstream of hp-compressor change abruptly in transient, but converge to slightly different levels. Obviously estimated values of CGEKF are good estimates of actual values.

Using these measured values, CGEKF estimated all ECDPs as shown in Fig. 10. The flow deviation parameter of hp-compressor, G_{hc}, is estimated to be changed ±7 percent, but other deviation parameters are not changed noticeably. This coincides with the hp-compressor characteristics, that is, when VSV is closed 2.5 degrees, the air flow is decreased approximately 7 percent and the efficiency is not changed at this operating point. Thus the CGEKF successfully recognized the performance deviation of hp-compressor.

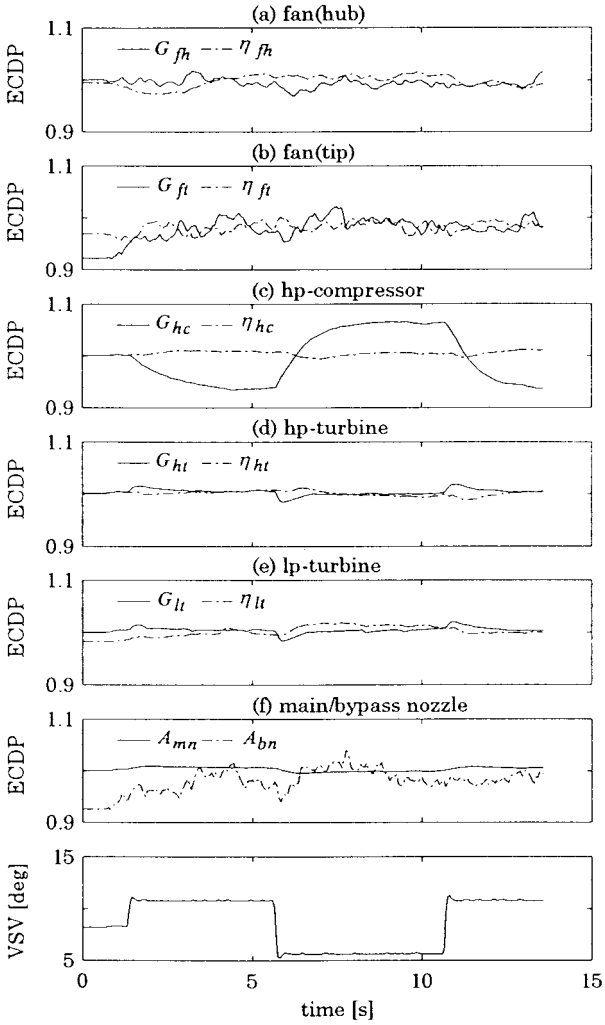

Fig. 10 ECDP estimation respond to VSV change

Effect of BAV Change. Figure 11 shows all ECDP's responses to BAV change, along with the compressor delivery pressure, P_3, to indicate the instance of BAV opening. The amount of bleed air is approximately 3 percent. When BAV is opened, pressures downstream of the hp-compressor decrease suddenly and temperatures increase. ECDPs of several components change simultaneously as analyzed in Fig. 8(*c*), and the CGEKF cannot determine the true reason. This is a example of the unpredicted system change.

Remarks

Sensor Failure. Accurate measurement is essential for the success of system identification. But reliability of measurement system is lower than that of engine. It is necessary for a reliable identification to include a capability to reject the effect of sensor noise, bias, drift, and failure. Figure 12 shows an example of such system. For simplicity, we assume (i) the system has four sensors, and (ii) three sensors are enough for the design of CGEKF, or observability. Then, five CGEKFs can be constructed as shown in Fig. 12. CGEKF-0 uses four sensor signals, y_1, y_2, y_3, and y_4. CGEKF-1 uses three sensors except y_1, CGEKF-2 uses three sensors except y_2, and so on. Normally, CGEKF-0 is working.

First, range and rate of each sensor signal is checked. If a failure of sensor-*i* is detected, CGEKF-0 is switched to CGEKF-*i*, which does not use sensor-*i*. Next, sensor signals are fed to five CGEKFs. If a difference between estimates of sensor-*j*($\hat{y}_j$) generated by CGEKF-0 and CGEKF-*j* is greater than a specified value, the

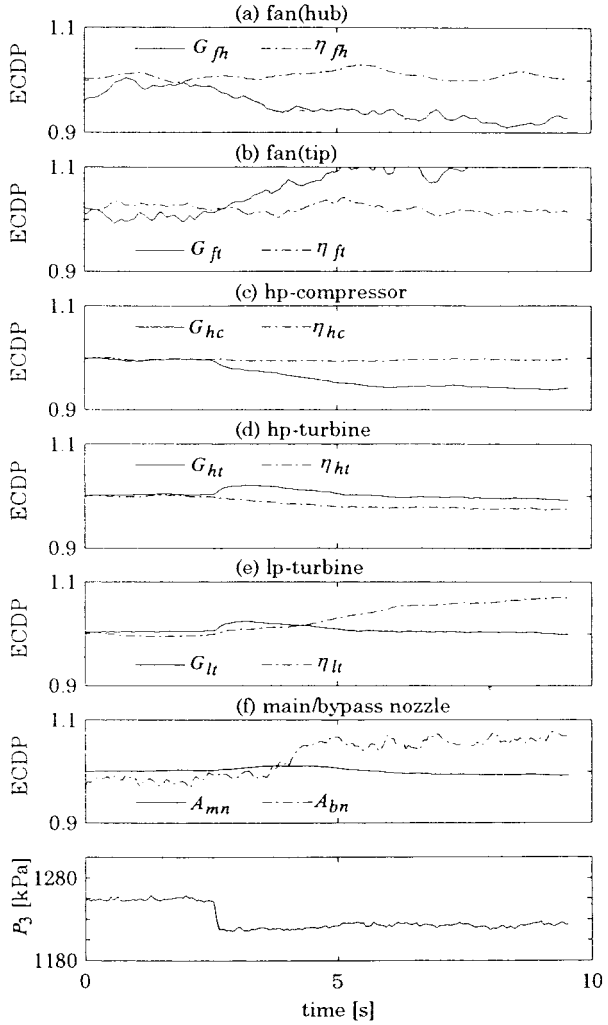

Fig. 11 ECDP estimation respond to BAV open

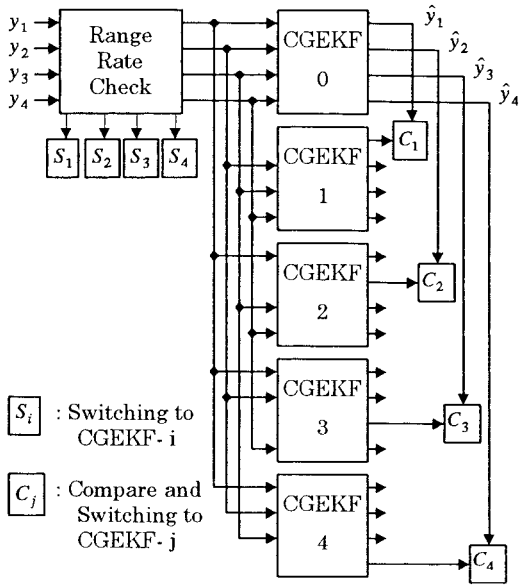

Fig. 12 Sensor failure accommodation

sensor-j(y_j) is considered to be failed. So the identification system can recognize sensor-j's failure and switch the filter to CGEKF-j. Thus the identification system can survive from one sensor failure by switching the filter. CGEKF is almost a nonlinear dynamic simulation and requires computational power. So, the design of CGEKFs in Fig. 12 must be restricted only to accommodation of important sensors, considering a computer power.

In the turbofan engine case, at least 12 variables must be measured to construct CGEKF, as described in Eq. (15). Since the abovementioned CGEKF was designed by 13 measurements, one measurement can be omitted. Figure 13(*a*) shows measured response (thin line) and estimated response (thick line) of thrust, F, by CGEKF designed by 13 measurements (CGEKF-0). Figure 13(*b*) shows measured and estimated response of compressor delivery pressure, P_3, by CGEKF designed by 12 measurements without P_3 (CGEKF-1). Figure 13(*c*) shows measured and estimated response of compressor delivery temperature, T_3, by CGEKF designed by 12 measurements without T_3 (CGEKF-2). The estimation precision of P_3 and T_3 without sensors are approximately 5 percent. If one of these sensors is failed, the difference in estimated value by CGEKF-0, -1 and -2 becomes large, and then, the identification system can suggest sensor failure and switch to a healthy CGEKF.

Reduction of Measurement. Normal number of sensors for a turbofan engine control is less than 10. To realize CGEKF identification system by using these normal sensors, one method is to omit some ECDPs. Estimatable ECDPs are defined by sensor locations, or by checking observability of combination of sensing variables, $\mathbf{y}_m$, and ECDPs, $\mathbf{x}_c$. If an omitted ECDP is changed, CGEKF identification cannot work correctly since it is an unpredicted system change. Another method is to use combined performance deviation parameters and decrease number of EDCPs. For example, a combined flow and efficiency characteristics of lp-turbine and nozzle are possible, and thus, number of ECDPs can be decreased. In this case, the CGEKF cannot discriminate performance changes in lp-turbine and nozzle.

Position Error. A sensor can measure only a local value, which is not equivalent to the value represented in the nonlinear dynamic engine model. Since temperatures and pressures in an engine are spatially distributed, measured values depend on the sensor positions. This is called position error. Measured values must be corrected to the values represented in the engine model, in

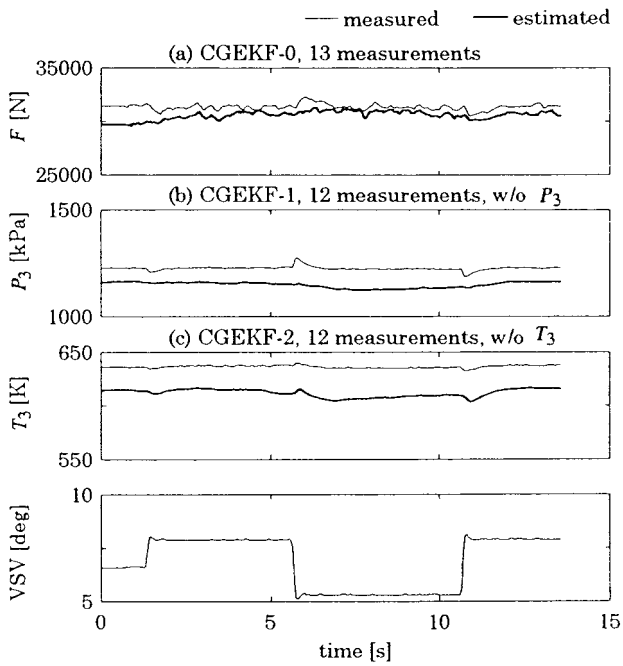

Fig. 13 Estimation of non-measured variables

which averaged values are used in general. Simple relations between local value and averaged value are useful for this correction. Without this correction, the CGEKF identification cannot work correctly since it becomes measurement bias.

Numerical Robustness. The nonlinear dynamic simulation as shown in Fig. 4, on which the CGEKF identification method is based, is not numerically robust as a piecewise linear model method. For example, abrupt big change in control variable occasionally moves the operating point into the area where component characteristics are not defined, and causes numerical instability. The nonlinear engine model must be carefully coded, not to move into such area, and to recover quickly if it happens. Small integration step size is effective for numerical robustness in general, though it cause difficulty in real-time operation.

Conclusions

The system identification technique using the constant gain extended Kalman filter was developed. The effectiveness of the filter was evaluated for a two-spool turbofan engine. It can recognize parameter changes of engine component and estimate unmeasurable variables over full flight envelope. This capability is useful for an advanced FADEC. High quality measurement, i.e., low noise, drift and bias, is important for reliable identification. The method developed will become a important part of a future jet engine control, in which a robust multivariable control, a performance seeking control, a condition monitoring are implemented.

Acknowledgment

This work was supported in part by the Hyper/Supersonic Transport Propulsion System Program of AIST, MITI. The author thanks R. Yanagi, S. Sekine and S. Enomoto of the National Aerospace Laboratory for their support in the preparation of actual engine data.

References

Adibhatla, S., and Johnson, K. L., 1993, "Evaluation of a Nonlinear PSC Algorithm on a Variable Cycle Engine," AIAA 93-2077.

Adibhatla, S., and Gastineau, Z., 1994, "Tracking Filter Selection and Control Mode Selection for Model Based Control," AIAA 94-3204.

Doel, D. L., 1992, "TEMPER—A Gas-Path Analysis Tool for Commercial Jet Engines," ASME Paper 92-GT-315.

Espana, M. D., 1993, "On the Estimation Algorithm for Adaptive Performance Optimization of Turbofan Engines," AIAA 93-1823.

Kerr, L. J., Nemec, T. S., and Gallops, G. W., 1991, "Real-Time Estimation of Gas Turbine Engine Damage Using a Control Based Kalman Filter Algorithm," ASME Paper 91-GT-216.

Luppold, R. H., Roman, J. R., Gallops, G. W., and Kerr, L. J., 1989, "Estimating In-Flight Engine Performance Variations Using Kalman Filter Concepts," AIAA 89-2584.

Merrill, W. C., DeLaat, J. C., and Bruton, W. M., 1988, "Advanced Detection, Isolation, and Accommodation of Sensor Failures—Real-Time Evaluation," *Journal of Guidance*, Vol. 11, No. 6, pp. 517–526.

Misawa, E. A., and Hedrick, J. K., 1989, "Nonlinear Observers—A State-of-the-Art Survey," ASME *Journal of Dynamic Systems, Measurement, and Control*, Vol. 111, pp. 344–352.

Orme, J. S., and Conners, T. R., 1994, "Supersonic Flight Test Results of a Performance Seeking Control Algorithm on a NASA F-15 Aircraft," AIAA 94-3210.

Safonov, M. G., and Athans, M., 1978, "Robustness and Computational Aspects of Nonlinear Stochastic Estimators and Regulators," *IEEE Transactions on Automatic Control*, Vol. AC-23, No. 4, pp. 717–725.

Seldner, K., Mihaloew, J. R., and Blaha, R. J., 1972, "Generalized Simulation Technique for Turbojet Engine System Analysis," NASA TN D-6610.

Sugiyama, N., 1990, "Generalized High Speed Simulation of Gas Turbine Engines," ASME Paper 90-GT-270.

Sugiyama, N., 1994, "Derivation of System Matrices From Nonlinear Dynamic Simulation of Jet Engines," *Journal of Guidance, Control, and Dynamics*, Vol. 17, No. 6, pp. 1320–1326.

Sugiyama, N., 1996, "On-Line System Identification of Jet Engine," AIAA 96-2590.

Urban, L. A., and Volponi, A. J., 1992, "Mathematical Methods of Relative Engine Performance Diagnostics," SAE 922048.

Volponi, A. J., 1994, "Sensor Error Compensation in Engine Performance Diagnostics," ASME Paper 94-GT-58.

Best Paper Award Cycle Innovations Technical Committee

Internal Reforming Solid Oxide Fuel Cell-Gas Turbine Combined Cycles (IRSOFC-GT): Part A—Cell Model and Cycle Thermodynamic Analysis

A. F. Massardo
Mem. ASME

F. Lubelli

Dipartimento di Macchine Sistemi Energetici e Trasporti
Universita di Genova,
Via Montallegro 1,
16145 Genova,
Italia

The aim of this work is to investigate the performance of internal reforming solid oxide fuel cell (IRSOFC) and gas turbine (GT) combined cycles. To study complex systems involving IRSOFC a mathematical model has been developed that simulates the fuel cell steady-state operation. The model, tested with data available in literature, has been used for a complete IRSOFC parametric analysis taking into account the influence of cell operative pressure, cell and stream temperatures, fuel-oxidant flow rates and composition, etc. The analysis of IRSOFC-GT combined cycles has been carried out by using the ThermoEconomic Modular Program TEMP (Agazzani and Massardo, 1997). The code has been modified to allow IRSOFC, external reformer and flue gas condenser performance to be taken into account. Using as test case the IRSOFC-GT combined plant proposed by Harvey and Richter (1994) the capability of the modified TEMP code has been demonstrated. The thermodynamic analysis of a number of IRSOFC-GT combined cycles is presented and discussed, taking into account the influence of several technological constraints. The results are presented for both atmospheric and pressurised IRSOFC.

Introduction

The fuel cell power generation system is expected to be one of the future promising power generation methods, which can provide efficient energy conversion rates, flexible fuel utilization and site selection with very low pollutant emissions.

In fuel cell the conversion energy is a direct electrochemical kinetic process and it is not subject to the limitations of the Carnot cycle. Moreover, the exergy losses associated with the fuel oxidation process are small compared to conventional combustion. The electrochemical oxidation of the fuel is accompanied by a release of heat energy and an electron flow. For the electrochemical reactions to proceed the temperature of the reactants must raise to a threshold depending upon the type of electrolyte used. The environmental preservation would be attained by higher efficiency values from the carbon dioxide production point of view, while NO_x emissions are greatly reduced when compared to conventional power plant emissions (Hirschenhofer et al., 1994).

High temperature fuel cell, as the MCFC (molten carbonate fuel cell) or SOFC (solid oxide fuel cell) are still in the development stage. However, they have much potential to achieve high efficiency for electricity production and they have already demonstrated their performance with several tens of kW stacks and units. Particularly SOFC is supposed to be suitable for both large power plants and small cogeneration unit (Drenckhahn and Lezuo, 1996).

There have been several proposals for integrated cycles involving SOFC, the most investigated configuration is the utilization of a SOFC as a topping unit, thanks to the very high SOFC operative temperature (≅1300 K), for an existing or future conventional power plant (Wilson and Korakianitis, 1997; Korakianitis et al., 1997; Pilidis and Ulizar, 1997). In this field of particular interest there are the systems using SOFCs and gas turbines (GT) (Stephenson and Ritchey, 1997; Bevc et al., 1996; Fry et al., 1997).

In this paper atmospheric and pressurized SOFCs associated with GT systems have been analysed. The first step to be able to study complex cycles involving SOFC is to obtain thermodynamic data for SOFC in operation. Therefore, a mathematical model has been developed that simulates the steady-state operation of a SOFC, with or without internal reforming (IR).

The model has been tested utilizing available data published in literature, and has been used as a module of the ThermoEconomic Modular Program (TEMP) software (Agazzani and Massardo, 1997), to carry out SOFC-GT combined cycle thermodynamic and thermoeconomic analyses. The thermodynamic analysis is described in this part, while the thermoeconomic analysis will be presented in the second part of this work (Massardo, 1998).

The internal reforming SOFC mathematical model, the results of the complete IRSOFC parametric analysis, and the assessment of the modified TEMP software, based on the Harvey-Richter (1994) plant data are presented. Finally, the thermodynamic analysis of a number of original IRSOFC-GT combined cycles are presented and discussed in depth.

IRSOFC Model

As already stated the first step to be able to study complex systems involving IRSOFC is to obtain thermodynamic data for cell operation, that is a cell model is necessary to carry out cell performance analysis. Several models have been presented in literature for SOFC or IRSOFC (Bessette, 1994; Costamagna, 1997; Harvey and Richter, 1994).

In this work a model has been developed taking into account the

Contributed by the International Gas Turbine Institute (IGTI) of The American Society of Mechanical Engineers for publication in the ASME Journal of Engineering for Gas Turbines and Power. Paper presented at the International Gas Turbine and Aeroengine Congress and Exhibition, Stockholm, Sweden, June 2–5, 1998; ASME Paper 98-GT-577.

Manuscript received by IGTI March 31, 1998; final revision received by the ASME Headquarters October 20, 1999. Associate Technical Editor: R. Kielb.

following aspects: the model must be robust and reliable; the cell performance must be evaluated with a direct mathematical approach (not utilizing performance curves or correlations) to allow the model to be useful for a wide range of IRSOFCs; and the model must be easy to be integrated in the thermoeconomic tool used for complex cycles analysis (TEMP code).

For the development of the model the following main assumptions have been used: adiabatic cell; equilibrium reforming and shifting reactions; cathode exit stream temperature equal to anode exit stream temperature; H_2 ion transportation responsible for electrical flow; cathode stream composed of O_2 and N_2; and anode stream composed of CH_4, CO, CO_2, H_2, H_2O. The current density (A/m^2) and the fuel utilization coefficient have been considered as input values.

The reactions considered inside the cell have been:

$$\begin{aligned} &\overset{x}{CH_4} + H_2O \leftrightarrow CO + 3H_2 && \text{reforming} \\ &\overset{y}{CO} + H_2O \leftrightarrow CO_2 + H_2 && \text{shifting} \\ &\overset{z}{H_2} + \tfrac{1}{2}O_2 \rightarrow H_2O && \text{electrochemical} \end{aligned} \tag{1}$$

Reforming and shifting reactions have been considered at equilibrium and, as a function of temperature, they have been represented by

$$K_{p\ \text{reforming}} = \frac{p_{H_2}^3 \cdot p_{CO}}{p_{CH_4} \cdot p_{H_2O}} \quad K_{p\ \text{shifting}} = \frac{p_{CO_2} \cdot p_{H_2}}{p_{CO} \cdot p_{H_2O}}, \tag{2}$$

where the equilibrium constants K_{pref} and K_{pshif} have been directly correlated to the temperature:

$$\log K_p = AT^4 + BT^3 + CT^2 + DT + E, \tag{3}$$

where the constant values are (Bossel, 1992):

	Reforming	Shifting
A	$-2.6312 \cdot 10^{-11}$	$5.47 \cdot 10^{-12}$
B	$1.2406 \cdot 10^{-7}$	$-2.574 \cdot 10^{-8}$
C	$-2.2523 \cdot 10^{-4}$	$4.6374 \cdot 10^{-5}$
D	$1.95027 \cdot 10^{-1}$	$-3.91500 \cdot 10^{-2}$
E	-66.139488	13.209723

From the knowledge of the fuel utilization coefficient the hydrogen and oxygen moles have been evaluated. To evaluate the CH_4 and CO moles the equilibrium constant equation has been utilized (where chemical symbols represent the number of moles):

$$CH_4^e = CH_4^i - x$$

$$CO^e = CO^i + -y$$

$$CO_2^e = CO_2^i + y$$

$$H_2^e = H_2^i + 3x + y - z$$

$$H_2O^e = H_2O^i - x - y + z \tag{4}$$

At the exit of the anode the total number of moles is the sum of the terms of the right hand side of the Eq. (4), and the equilibrium conditions have been written as

$$K_{p\ \text{reforming}} = \frac{\left(\frac{CO^i + x - y}{NM^i + 2x}\right) \cdot \left(\frac{H_2^i + 3x + y - z}{NM^i + 2x}\right) \cdot p_{\text{cell}}^2}{\left(\frac{CH_4^i - x}{NM^i + 2x}\right) \cdot \left(\frac{H_2O^i - x - y + z}{NM^i + 2x}\right)} \tag{5}$$

$$K_{p\ \text{shifting}} = \frac{\left(\frac{H_2^i + 3x + y - z}{NM^i + 2x}\right) \cdot \left(\frac{CO_2^i + y}{NM^i + 2x}\right)}{\left(\frac{CO^i + x - y}{NM^i + 2x}\right) \cdot \left(\frac{H_2O^i - x - y + z}{NM^i 2x}\right)}, \tag{6}$$

where the unknowns are x and y (z is known from the fuel utilization coefficient value). The system (Eqs. 5 and 6) has been solved using a classical Newton-Raphson method.

The cell electrical power has been calculated as the product of cell current intensity by cell electrodes voltage. Since when one mole of H_2 reacts in one second the corresponding current generated is 96439 A, the current intensity is easy to be evaluated. The voltage evaluation has been carried out based on the knowledge of the cell open circuit potential (ideal Nerst potential):

$$E = U_g + \frac{RT}{nF} \ln \frac{p_{H_2} (p_{O_2})^{1/2}}{p_{H_2O}}. \tag{7}$$

The Nerst potential is reduced when the electrical cell circuit is closed due to the following irreversibilities:

1 ohmic resistance of the cell elements
2 polarization of the electrodes

Ohmic resistances have been evaluated using the Ohm equation ($R = \rho L/A$), where, as suggested by Bessette (1994)

$$\begin{aligned} \rho &= 0.008114 e^{(600/T)} && \text{(air electrode)} \\ \rho &= 0.00294 e^{(10350/T)} && \text{(electrolyte)} \\ \rho &= 0.00298 e^{(-1392/T)} && \text{(fuel electrode)} \end{aligned}.$$

The electrode polarisation effect has been evaluated using (Achenbach, 1994)

$$\frac{1}{R_c} = K_c \cdot \frac{4F}{RT} \left(\frac{p_{O_2}}{p^o}\right)^m e^{-(E_{\text{activation cathode}}/RT)} \tag{8}$$

$$\frac{1}{R_A} = K_a \cdot \frac{2F}{RT} \cdot \left(\frac{p_{H_2}}{p^o}\right)^m e^{-(E_{\text{activation anode}}/RT)}, \tag{9}$$

where $E_{\text{anode act}} = 110$ kJ/mole, $E_{\text{cathode act}} = 160$ kJ/mole, p^o reference pressure, $K_c = 1.49\ 10^{10}$, $K_a = 2.13\ 10^8$ (A/m^2), and $m = 0.25$.

Nomenclature

E, U_g = Nerst and Gibbs potential, respectively
F = Faraday constant
h = enthalpy
K_p = equilibrium constant
I, V = current, voltage respectively
m = mass flow rate
n = electron number
NM = number of moles
P = power
p, Δp = pressure, pressure drop respectively
R = gas constant
T = temperature
x, y, z = CH_4, CO, H_2 reactant moles respectively
β, η = pressure ratio, efficiency respectively
ρ = electrical resistivity

Superscripts

i, o = inlet, outlet respectively

Subscripts

a, c = anode, cathode respectively
act = activation
f, air = fuel, air respectively
ST = standard cell

Table 1 IRSOFC performance comparison

Reference	$V_{ref.}$	V_{IRSOFC}	$\Delta V / V$ (%)	$\Delta T / T$ (%)
Achenbach ,1994	0.682	0.693	1.6	1.1
Hirano et al. ,1992	0.715	0.753	5.3	2.5
Hirano et al. ,1992	0.606	0.563	7.0	4.9
Costamagna ,1997	0.71	0.68	4.2	2.2
Costamagna ,1997	0.85	0.782	8.0	not av.
Harvey-Richter, 1994	0.60	0.64	6.6	not av.

All the described chemical and electrical calculations need the knowledge of the cell temperature. Unfortunately, at the beginning of the analysis, this datum is not available. To solve this problem two different ways based on cell energy conservation equation have been used. In the first option a tentative cell temperature has been assumed and the cell characteristics evaluated. Then the enthalpy variation inside the cell has been calculated and a new cell temperature obtained. The process is iterated until the satisfaction of a prescribed tolerance or a maximum iteration number. In the second approach the temperature has been directly obtained satisfying the conservation equation. The solution—cell temperature value—has been obtained using a bisection method.

Several IRSOFC investigations have demonstrated that the second approach has been more effective because it is more stable, and accurate (it does not utilize average concentration values for the cell energy balance). More details of the model have been reported in Lubelli (1998).

Table 1 shows the results obtained using the model described for a number of SOFCs.

Unfortunately, often the data available in literature are not complete. Therefore, where necessary they have been assumed using authors' experience. Nevertheless, the results of the present model agree well with the reference data. The model can thus be considered as a reliable basis for developing IRSOFC studies.

IRSOFC Parametric Analysis

The cell model has been used to carry out a complete IRSOFC parametric analysis; all the results refer to a "STANDARD CELL" defined as follows: operative cell pressure: 101300 Pa; anode inlet temperature: 1173 K; cathode inlet temperature: 873 K; fuel composition: 67 percent H_2, 22 percent CO, 11 percent H_2O; oxidant stream–air; fuel to oxidant ratio 0.04; and O_2 utilisation factor 22 percent.

The effect of the following parameters have been analyzed:

1 Operative pressure: the effect of this parameter is shown in Fig. 1, where the cell voltage is plotted versus operative pressure (current density being the parameter). Cell voltage increase has been correlated with the modification of the equilibrium of the shifting and reforming reactions and also to the partial pressure changes. Figure 1 also demonstrates that the voltage increase is not directly proportional to operative pressure.

Figure 2 shows the modification of the cell power ratio (P/P_{ST}) versus current density (operative pressure being the parameter). The influence of operative pressure is evident, and it is higher when large cell current densities are selected.

2 Anode and cathode inlet temperature: the temperature effect on cell power is presented in Fig. 3. The increase of both anode and cathode inlet temperature shows a positive influence on ohmic and polarization losses. Due to the low fuel to air ratio value and to the cathode higher temperature variation the effect of cathode data is quite apparent.

3 Anodic and cathodic flow rates: Figure 4 shows the influ-

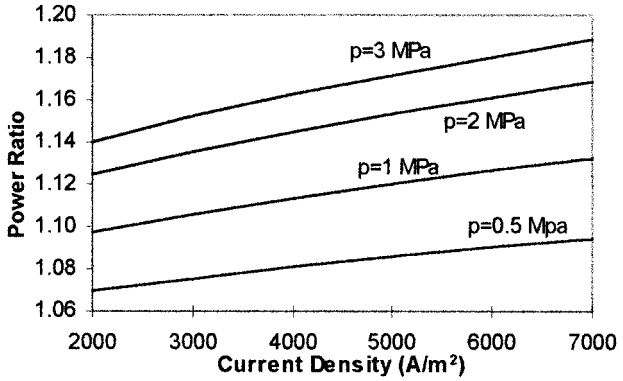

Fig. 2 Operative pressure influence on IRSOFC power ratio (P/P_{ST}) versus current density

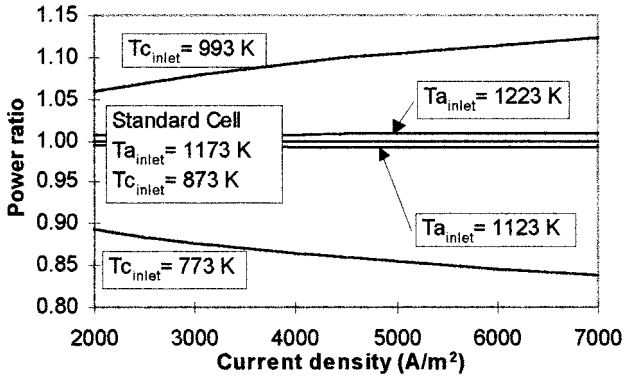

Fig. 3 Cathode and anode inlet temperature influence on IRSOFC power ratio (P/P_{ST}) versus current density

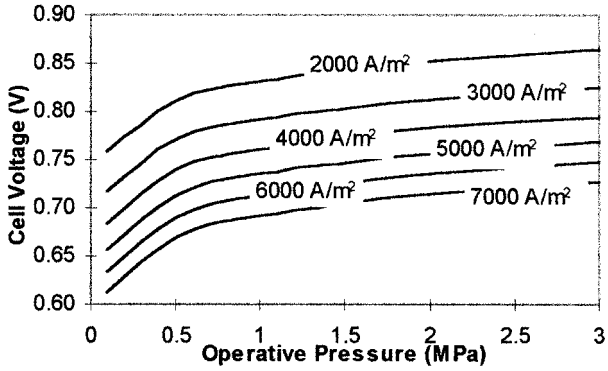

Fig. 1 Cell current density influence on IRSOFC voltage versus operative pressure

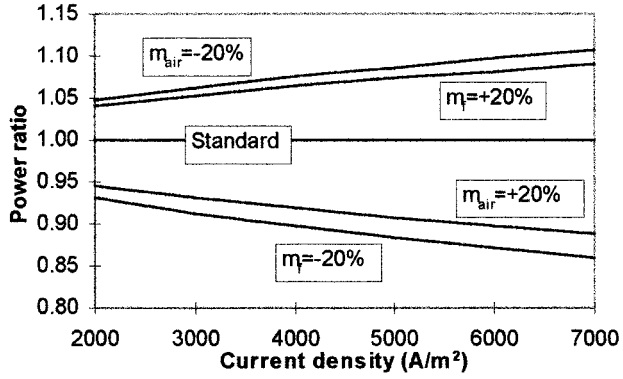

Fig. 4 Fuel and oxidant influence on IRSOFC power ratio (P/P_{ST}) versus current density

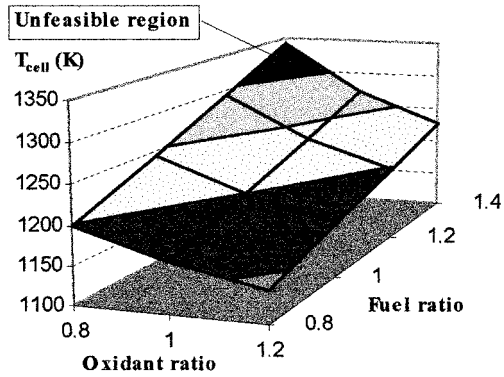

Fig. 5(*a*) IRSOFC temperature versus oxidant and fuel flow ratios

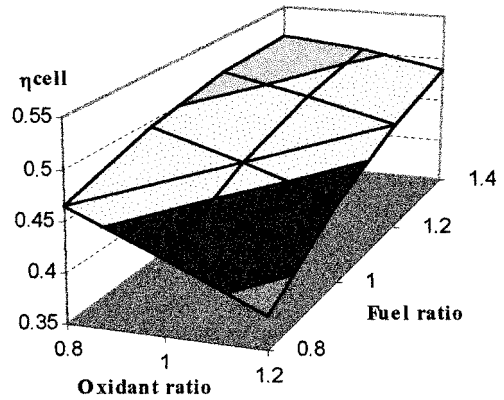

Fig. 5(*b*) IRSOFC efficiency versus oxidant and fuel flow ratios

ence of the fuel and oxidant flow rates modification (+/−20 percent) on the cell power. The flow rates influence the cell operative temperature, and consequently the cell performance characteristics. Moreover, when a high current density value has been selected the influence of flow rates variation is more clear.

Finally an analysis has been carried out varying both flow rates at a fixed current density (3000 A/m^2). Cell temperature and efficiency are presented in Fig. 5(*a*) and 5(*b*) respectively. The need to operate with high fuel/air ratio (high efficiency condition) is evident. However, attention must be used to avoid high cell temperature values (maximum $T_{cell} < 1300$ K).

Indeed oxidant flow rate must also be controlled to operate with O_2 utilization coefficient in the range suggested in the literature (Kaneko et al., 1991). All the data shown have been obtained with the O_2 utilization coefficient well inside this range.

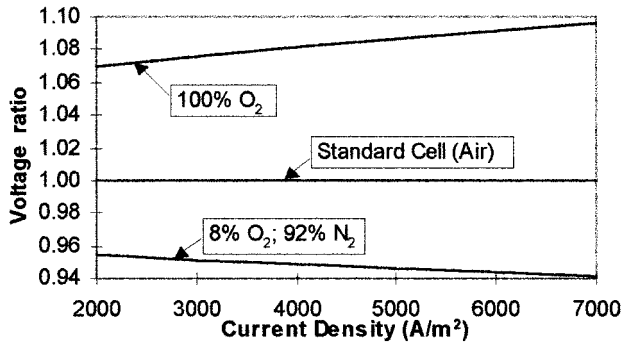

Fig. 6 Oxidant chemical composition influence on IRSOFC voltage ratio (V/V_{ST}) versus current density

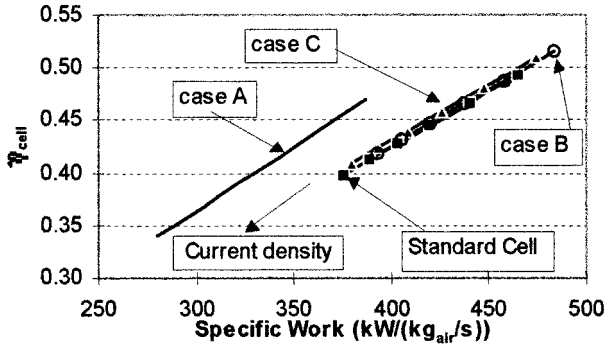

Fig. 7 Fuel composition influence on IRSOFC specific work versus current density (O_2 utilization factor is constant)

4 Fuel and oxidant composition: the influence of two different oxidant compositions is shown in Fig. 6. The composition of the first oxidant is 100 percent O_2, while the composition of the second one is 8 percent O_2 and 92 percent N_2. Cell voltage modification is mainly correlated to the presence of the oxygen partial pressure in the Nerst equation. Obviously, the use of pure oxygen must be carefully considered from an economical point of view.

Figure 7 shows cell efficiency versus specific work for four different fuel compositions (Standard: 67 percent H_2, 22 percent CO, 11 percent H_2O; A: 17.1 percent CH_4, 2.94 percent CO, 4.36 percent CO_2, 26.26 percent H_2, 49.34 percent H_2O; B: 97 percent H_2, 3 percent H_2O; C: 80 percent H_2, 20 percent CO_2); assuming fixed O_2 utilization factor ($\cong$ 22 percent), while the current density is considered as a parameter (from 2000 to 7000 A/m^2).

The internal reforming influence is evident for case A, where CH_4 is present at the fuel cell inlet; while the results for the other

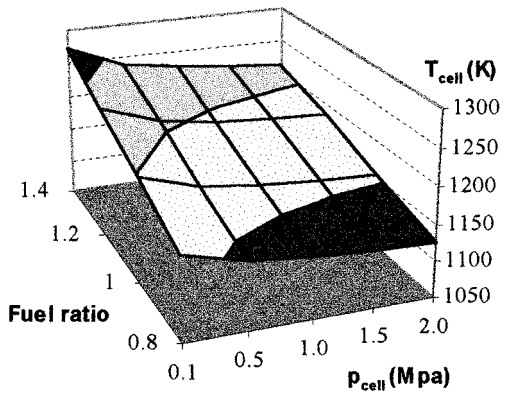

Fig. 8(*a*) IRSOFC temperature versus fuel flow ratio and operative pressure

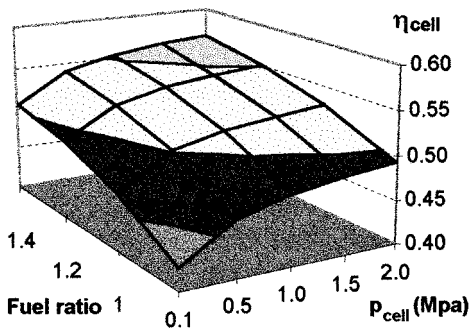

Fig. 8(*b*) IRSOFC efficiency versus fuel flow ratio and operative pressure

fuel compositions are quite similar. For all the cases the current density increase reduces both efficiency and specific work.

Finally the simultaneous influence of two parameters has been considered. As an example Fig. 8 shows cell temperature and efficiency vs operative cell pressure and fuel flow rate. The effects of both variables are evident. It is possible to note that when the variables are not set at standard conditions (*ST*) they allow high efficiency values with feasible cell temperatures ($T_{cell} < 1300$ K) to be obtained.

Cells that operate at high fuel flow rate show high efficiency and high cell temperature values, sometimes higher than the cell temperature limit (when cells operate at atmospheric pressure). On the contrary the temperature of cells working at high pressure and low fuel flow rate are well inside the feasible field, but unfortunately the reduced T_{cell} values get the cell irreversibilities to increase and the beneficial effect of high operating pressure vanishes (low cell efficiency).

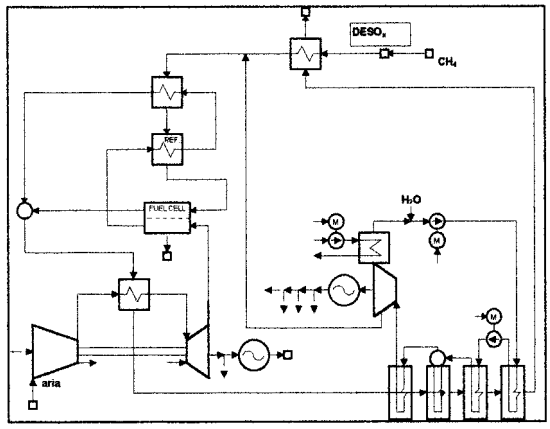

Fig. 10 FCGT2 plant lay-out

SOFC and GT Integration Analysis

The SOFC mathematical model previously described has been integrated in the code TEMP, a modular simulator tool for the thermoeconomic analysis of advanced thermal energy systems developed by the authors. The targets of the tool are thermodynamic and exergy analysis and thermoeconomic analysis including environomic and optimization (Agazzani et al., 1998). The capability of the original modular simulator tool has been demonstrated for gas, steam, and complex combined plants (Agazzani and Massardo, 1997).

In this work the IRSOFC module already described, an external reformer module and a flue-gas-condenser module have been developed and included in the TEMP software as described by Lubelli (1998).

To verify the capability of the modified TEMP code the plant proposed by Harvey and Richter (1994) has been used as a test-case.

The results obtained using TEMP agree very well the data published by the cited Authors, the difference in the efficiency is less than 0.8 percent. However, a deep analysis of the component performance showed some differences. Particularly the SOFC voltage computed using the TEMP cell model is higher than the corresponding reference datum (see Table 1); as a consequence the SOFC exit stream is colder and the gas turbine power is reduced. Due to the increase of SOFC's power the total power is practically the same. The difference in the SOFC performance evaluation should be due to the different cell models utilized by Harvey and Richter and by the authors. However, another aspect must be taken into account: the detailed geometrical and electrical data of Harvey–Richter's fuel cell, required by the present model, have been not completely available, and some assumptions have been made by the authors. However, modifying some SOFC's data (i.e., electrical resistance, electrolyte thickness, etc.) the results obtained using TEMP have been found coincident with the Harvey-Richter's data not only for the whole plant, but also for any component (Lubelli, 1998). Therefore, the modified TEMP code can be considered a reliable tool for SOFC-GT combined cycle analysis.

Several high efficiency ($\cong 0.65$) proposals have been presented in literature for atmospheric SOFC and GT integration. A number of new plant lay-out have been analyzed by the authors and have been reported in Lubelli (1998), in this paper the best two are presented. Figure 9 shows the scheme of the plant FCGT1, and Fig. 10 of the plant FCGT2. Both plants generate electrical power by SOFC, GT and steam turbine.

In the first case the inlet cathode stream (air at about atmospheric pressure) has the same temperature of the expander outlet section; the outlet cathode stream, at about 1300 K, has been utilized to heat the air at the compressor outlet, and this stream at the heat exchanger outlet has been utilized to burn the residual fuels existing in the anodic stream at the SOFC exit (also external fuel (CH_4) injection in the combustion chamber can be used).

The combustion chamber outlet temperature has been about 1200 K, and this hot stream has been utilized to reform the preheated CH_4 fuel used in the SOFC and also to produce steam through a heat recovery steam generator. Part of the steam has

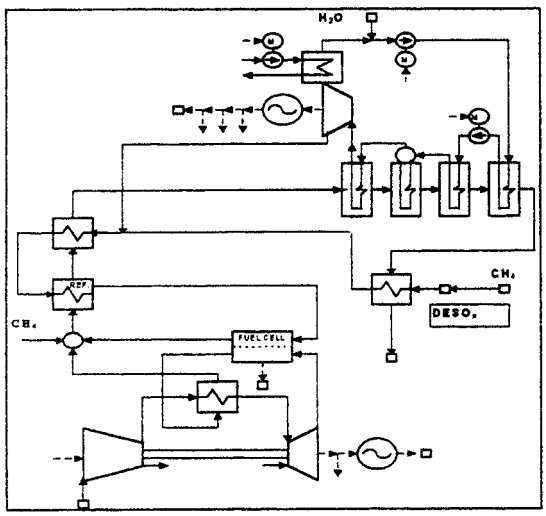

Fig. 9 FCGT1 plant lay-out

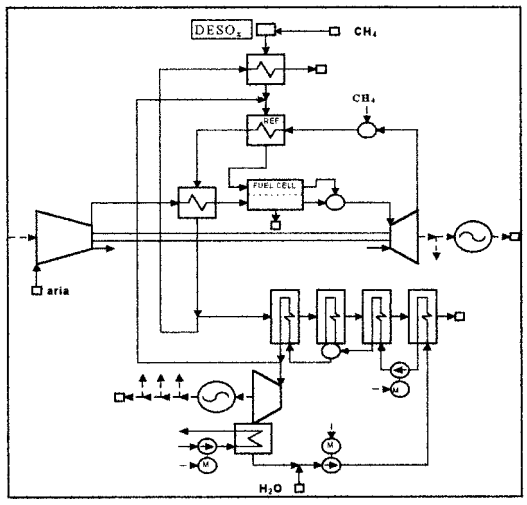

Fig. 11 FCGT3 plant lay-out

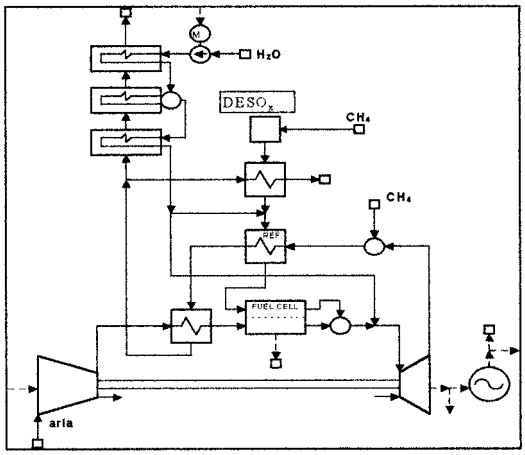

Fig. 12 FCGT4 plant lay-out

Table 2 IRSOFC-GT plant fixed data

Compressor polytropic efficiency	0.86
Turbine polytropic efficiency	0.88
Mechanical efficiency	0.997
Fuel pressure at system inlet	3 MPa
Fuel temperature at system inlet	289 K
Electrical generator efficiency	0.985
Fuel Cell Power Condit. efficiency	0.95
Air inlet temperature	288 K
Air inlet Pressure	101300 Pa
Pre-heater pressure drop ($\Delta p/p$)	0 03
Pre-reformer pressure drop ($\Delta p/p$)	0.03
Fuel Cell pressure drop	0.00−0.05
Steam generator: - superheater ($\Delta p/p$)	gas side 0.01, water side 0.08
Steam generator:- evaporator ($\Delta p/p$)	gas side 0.01, water side 0.01
Steam generator:- economizer ($\Delta p/p$)	gas side 0.01, water side 0.10
Approach point temperature	30 K
Combustion Chamber Pressure drop	0.03
SOFC Current Density (A/m^2)	3000

been utilized in the reformer, and part has been expanded in a steam turbine. The critical aspects of this lay-out are mainly the maximum temperature of the heat exchangers and of the SOFC.

In the FCGT2 plant the SOFC stream at the cathode exit has been directly utilized to preheat and reform the fuel, and its temperature has increased through the CO and H_2 combustion at the SOFC anode outlet section. In this case no external CH_4 injection has been considered.

The hot stream at the combustion chamber outlet has been utilized first to heat the air working in the gas turbine expander and then to generate steam in a heat recovery steam generator. The steam required for the external reformer has been bled from the steam turbine.

A number of proposals have been presented in literature for integration between GT and pressurized SOFC. Usually SOFCs have been used in gas systems downstream the compressor before the combustion chamber or directly takes the place of it. These systems have been showed efficiencies greater than 70 percent.

Several plant lay-out have been analyzed by the authors, and the results have been completely reported by Lubelli (1998). In this paper two solutions are discussed in depth: FCGT3 (Fig. 11) and FCGT4 (Fig. 12). In these schemes the compressor is utilized to pressurize SOFC module. The compressed air is preheated before entering the cell cathode; at the cell exit the anode and cathode streams have been mixed and the residual H_2 and CO have been burned in a combustion chamber. In this way the stream temperature increases up to a maximum value before the expander inlet. The stream at the expander exit has been then reheated burning a small fuel flow rate to obtain a temperature that allows the reforming of the SOFC fuel to be obtained using the correct steam to fuel ratio to avoid carbon deposition. The stream at the reformer exit has been utilized to generate steam.

Part of this steam has been used in the reformer and part has been expanded to generate electrical power. The steam has been expanded in a steam turbine until the condenser pressure (case FCGT3), or it has been injected in the gas turbine and expanded in this component until the atmospheric pressure (case FCGT4). The first plant (FCGT3) is more complex because the steam turbine and the condenser are used.

IRSOFC-GT Power System Analysis

The data used in this study is shown in Table 2, moreover several technological constraints have been considered: heat exchanger maximum temperature (1223 K); maximum gas turbine inlet temperature (1573 K with cooling, 1153 K without cooling); SOFC maximum temperature (1300 K); minimum anode inlet fuel temperature (1123 K) (Hirano et al., 1992); minimum steam to carbon ratio (2.0) (Macchi and Campanari, 1997); minimum steam turbine quality (0.86); maximum steam turbine inlet temperature (823 K); and maximum oxygen utilization factor (0.52). These constraints are very important because they allow the thermodynamic analysis to be carried out for plants where only available technology is used (obviously IRSOFC module is considered under development). In this way some technological problems shown in previous works presented in literature (see as an example the very high temperature level for the blower in the plant proposed by Harvey and Richter, 1994), can be eliminated.

On the other hand it is worth noting that the four lay-out presented utilize a very simple steam recovery generator (single pressure). The authors carried out also a number of analyses by using complex steam bottoming cycles (three pressure levels with re-heat), ORC systems (Organic Rankine Cycle, Agazzani et al., 1996) and NH_3-H_2O systems (Galeazzo, 1996). The results showed that the use of complex steam plants, are not very useful (Lubelli, 1998). However, more studies are required to improve the results obtained for IRSOFC-NH_3-H_2O combined cycles as already done by Lobachyov and Richter (1997) for MCFC-NH_3-H_2O combined cycles. Moreover, the use of nonconventional NH_3 bottoming systems is not justified, particularly if the reliability, durability, environmental impact, and costs of such a system are taken into account.

The results of the investigation carried out for the FCGT1 system are shown in Fig. 13; the results have been obtained with a constant current density value (3000 A/m^2) and with the external reformer at equilibrium condition. It is possible to note that, to verify the cell maximum temperature constraint, the compressor pressure ratio must be greater than 15 if the fuel to air ratio is equal to 3.5 percent, while, if this ratio is 3.0 percent, the pressure ratio must be greater than 8. The effect of fuel to air ratio has been quite evident: when it has been reduced the efficiency has been reduced itself from 0.69−0.71 to 0.65−0.67. Also the effect of the com-

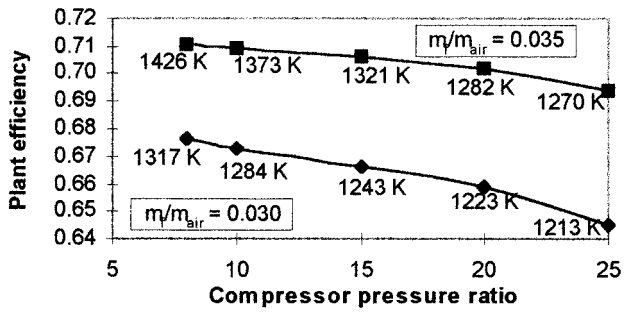

Fig. 13 Fuel to air ratio influence on FCGT1 plant efficiency versus compressor pressure ratio (current density 3000 A/m^2)

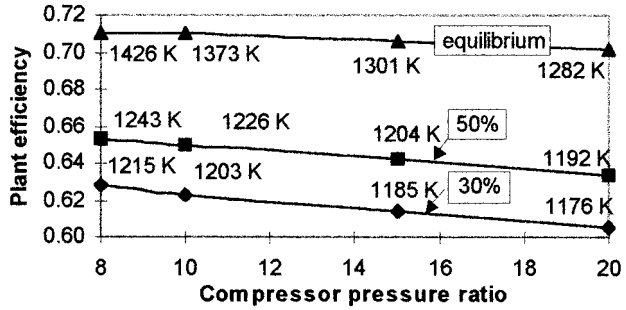

Fig. 14 External reformer operative condition influence on FCGT1 efficiency versus pressure ratio (m_f/m_{air} = 3.5 percent)

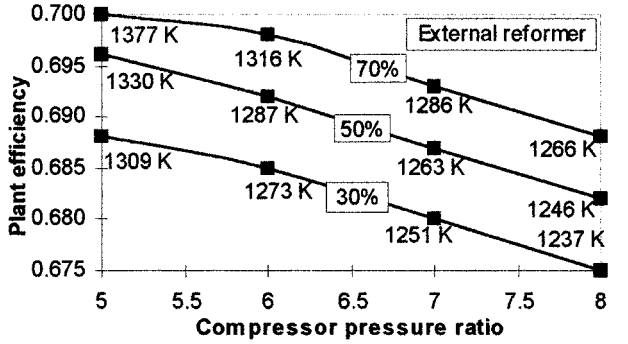

Fig. 16 External reformer operative conditions influence on FCGT2 efficiency versus pressure ratio (m_f/m_{air} = 3.5 percent)

pressor pressure ratio has been evident: if pressure ratio is high the cathode stream temperature is low and the effect on cell temperature is evident too. When pressure ratio has been equal to 25 the cell exit stream temperature has been about 1270 K for m_f/m_{air} = 3.5 percent and about 1213 K for m_f/m_{air} = 3.0 percent.

Taking into account the plant lay out (Fig. 9) the maximum temperature in the heat exchanger downstream the compressor has been higher than the fixed constraint. In fact, with external reforming at equilibrium all the results obtained whit m_f/m_{air} = 3.5 percent do not verify this constraint, while for m_f/m_{air} = 3.0 percent the results have been acceptable only if the compressor pressure ratio has been greater than 19.5. All the results should be acceptable if the use of a ceramic heat exchanger is considered as already discussed by Agazzani et al. (1999). Another way to obtain results that verify the heat exchanger temperature constraint is the modification of the external reforming reaction equilibrium. Figure 14 shows the results obtained for different external reformer condition (m_f/m_{air} = 3.5 percent); in this case when the reforming percentage is lower than 50 percent the results verify all the constraints. Unfortunately, the plant efficiency greatly decreases.

SOFC-GT lay out FCGT2 has been proposed to eliminate the negative influence of the heat exchanger temperature constraint. In this case the SOFC temperature and the heat exchanger temperature have been not directly correlated. Figure 15 shows plant efficiency versus pressure ratio (external reforming percentage is the parameter).

The results have been obtained with m_f/m_{air} equal to 3 percent, and all the system constraints have been verified. The maximum efficiency has been obtained for external reforming at equilibrium and for low compressor pressure ratio, where the maximum cell temperature values have been observed.

When the fuel to air ratio has been increased to 3.5 percent the results shown in Fig. 16 have been obtained. In this case the equilibrium reforming condition does not allow the cell temperature constraint to be verified. Therefore, the results are shown only for reduced reforming percentage (30, 50, and 70 percent). The influence of this parameter on the efficiency drop is about 1.5 percent. For reforming at 50 percent and 70 percent a limit on the pressure ratio must be considered (pressure ratio greater than 5.5 for 50 percent reforming, and greater than 6 for 70 percent). However, the efficiency level is very interesting: when the pressure ratio is 6.2 and reforming percentage 70 percent, the efficiency of the SOFC-GT combined plant is 69.8 percent.

Another interesting result is shown in Fig. 17 where the plant efficiency is plotted versus plant specific work (kW/kg_{air}/s). In this figure pressure ratio and cell temperature are also included. All the data refer to m_f/m_{air} = 3.5 percent and reforming percentage equal to 50 percent. The figure shows also the results obtained for the FCGT1 lay out. It is necessary to point out that the results shown for the FCGT1 system are always not feasible because the constraint on the maximum heat exchanger temperature has been not verified. For the second system FCGT2 the results are feasible if the pressure ratio is greater than 5.5 (SOFC temperature about 1300 K). As already discussed the efficiency is near 70 percent, and the specific work is very high (1210 kW/kg/s) about three times the specific work of conventional combined gas-steam plants.

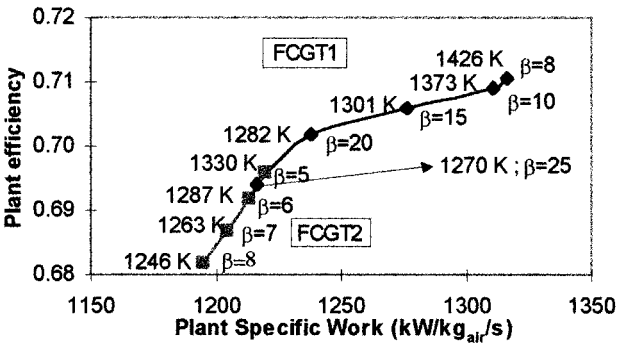

Fig. 17 FCGT1 and FCGT2 efficiencie versus specific work (Δp_c = 0)

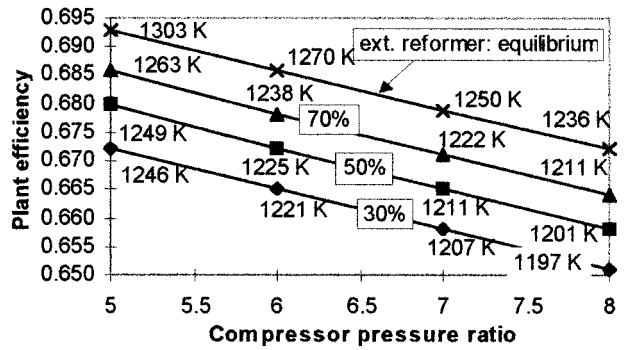

Fig. 15 External reformer operative conditions influence on FCGT2 efficiency versus pressure ratio (m_f/m_{air} = 3.0 percent)

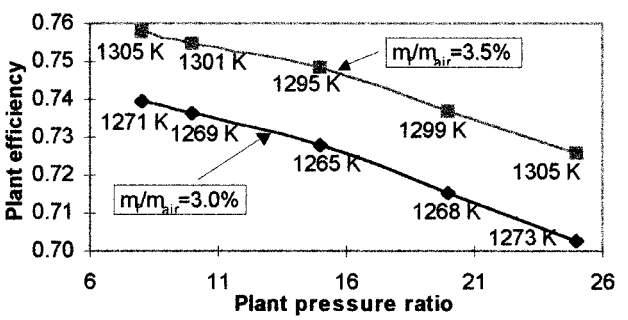

Fig. 18 Fuel to air ratio influence on FCGT3 plant efficiency versus system pressure ratio (ext. ref. at equilibrium)

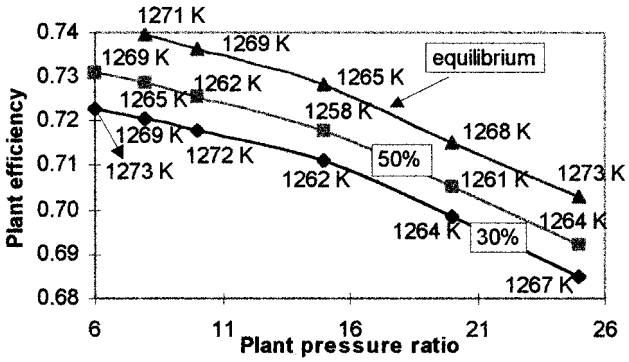

Fig. 19 External reformer operative conditions influence on FCGT3 efficiency versus system pressure ratio (m_f/m_{air} = 3.0 percent)

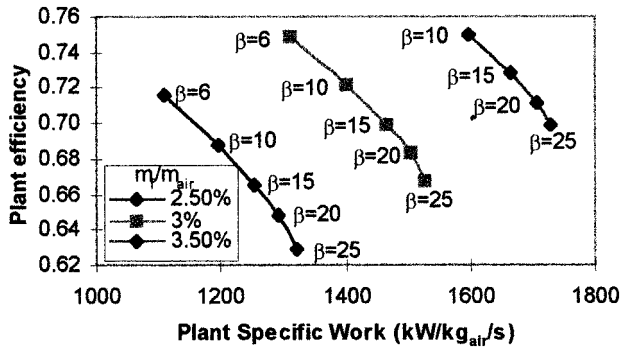

Fig. 21 Fuel to air ratio influence on FCGT4 plant efficiency versus specific work (Δp_c = 0%)

The results obtained analyzing the system FCGT3 are shown in Fig. 18 where the efficiency has been plotted versus pressure ratio (m_f/m_{air} is the parameter and the external reforming is considered at equilibrium). Both cases show very high efficiency values, particularly when the pressure ratio is low (<8), and verify the cell temperature constraint.

Pressure ratio lower than 8 are not possible because the air at the compressor exit is too cold and a large quantity of heat is necessary to heat the air to the temperature required for SOFC operation. Thus, the heat has been not sufficient to generate the steam for correct external reformer operation (T_{cell} is practically constant). In Fig. 19 the influence of the external reformer operating conditions (m_f/m_{air} = 3 percent) is presented. From reforming equilibrium to reforming at 50 percent the efficiency drops of about 1 percent, and similar reduction is evident for reforming from 50 percent to 30 percent. The influence of pressure ratio has been again confirmed. For external reforming at 50 percent and 30 percent it has been possible to operate at lower pressure ratio values than at reforming equilibrium condition (pressure ratios between 6 and 8 are now possible). The cell and maximum heat exchanger temperature constraints have been always verified. In the case analyzed the feasible (all the constraints are verified) best efficiency value (75.8 percent) has been obtained for pressure ratio equal to 8, m_f/m_{air} = 3.5 percent (if m_f/m_{air} = 3 percent the best efficiency is 74 percent).

The last plant considered is a modified version of FCGT3, in fact in FCGT4 the steam turbine is not present and the steam not used in the external reformer is injected in the gas turbine expander. Figure 20 shows the efficiency vs pressure ratio (m_f/m_{air} ratio is the parameter). If m_f/m_{air} = 3.5 percent the cell temperature has been a maximum value for pressure ratio equal to 10, while for low pressure ratio values the results are not feasible. Reducing m_f/m_{air} (3 percent, 2.5 percent) the minimum feasible pressure ratio is equal to 6 and all the SOFC temperature values verify the constraint (1300 K). If the pressure ratio has been lower than 6 steam generation problems have been found as already discussed for the previous plant. The best efficiency value is 75 percent for m_f/m_{air} = 3.5 percent at pressure ratio equal to 10 (T_{cell} = 1307 K) and 74.9 percent for m_f/m_{air} = 3 percent at pressure ratio equal to 6 (T_{cell} = 1281 K).

The efficiency versus specific work is plotted in Fig. 21; in this case the effect of m_f/m_{air} is evident, particularly for the specific work values. If m_f/m_{air} = 3.5 percent very high specific work has been obtained (1600–1700 kW/kg/s), but also for m_f/m_{air} = 3 percent the specific work is in the range 1300 to 1500 kW/kg/s (three to four times the specific work of conventional combined gas-steam plants).

To conclude the thermodynamic investigation the influence of current density (A/m^2) is shown in Fig. 22. It is necessary to remember that all the data previously presented have been obtained for current density of 3000 A/m^2 (see also Fig. 2). If the current density is greater than this value the plant efficiency is reduced, while cell temperature is increased; nevertheless, in this condition the cell surface (cell volume) necessary to complete the electrochemical reaction is low. The opposite is evident if the current density is lower than the standard value: the plant efficiency increases, the SOFC temperature decreases and the cell surface (and cell volume) raises (Lubelli, 1998). However, it is possible to observe that the current density influence on the com-

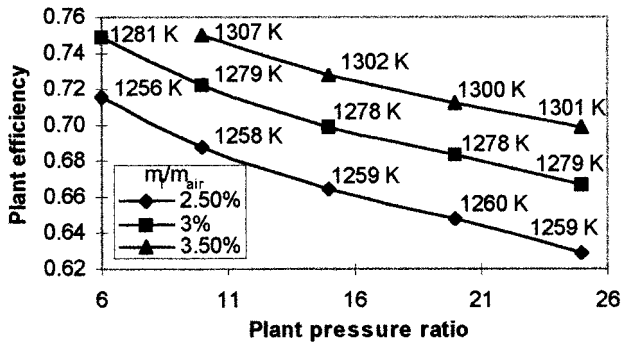

Fig. 20 Fuel to air ratio influence on FCGT4 plant efficiency versus system pressure ratio (ext. ref. at equilibrium)

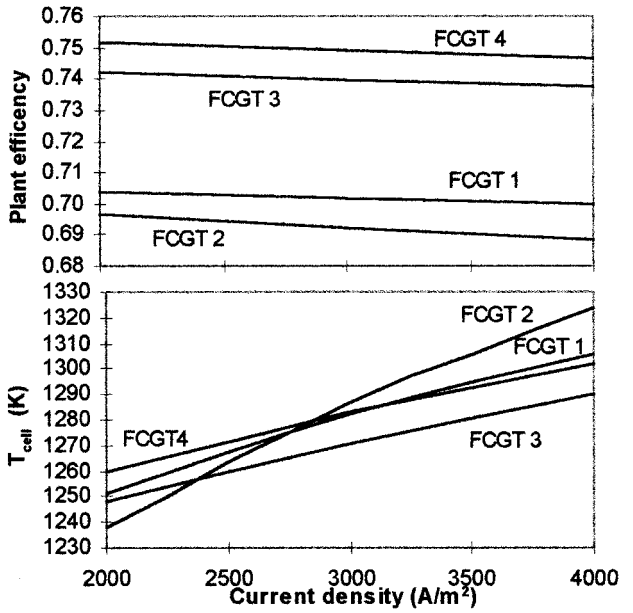

Fig. 22 IRSOFC temperature and combined IRSOFC-GT plant efficiency versus cell current density (ρ_{ST} = 3000 A/m^2)

Table 3 IRSOFC, GT, and steam turbine power (%)

PLANT	GT	IR-SOFC	ST
FCGT1	10.94	84.23	4.83
FCGT2	12.14	82.35	5.51
FCGT3	39.87	59.33	0.80
FCGT4	37.00	63.00	0.00

bined IRSOFC-GT systems is not high ($\Delta\eta = 0.5$ percent), while the effect on cell temperature is evident, particularly for FCGT2 configuration. If the current density is assumed equal to 2000 A/m^2 all the systems show low cell temperature values ($<$1300 K). Unfortunately, always the FCGT1 lay out does not verify the heat exchanger maximum temperature constraint.

Finally, an example of the distribution of the power generated by IRSOFC, GT and steam turbine is presented in Table 3. When atmospheric IRSOFC are used (FCGT1 and FCGT2 plants) the power is generated mainly by fuel cell (82–84 percent), while GT generates about 11–12 percent of the whole power and steam turbine contribution is reduced (4–6 percent). When pressurized IRSOFCs are used (FCGT3 and FCGT4 plants), it is important to note that in this case the compressor aim is to pressurize not only the GT (combustion chamber and expander) but also the fuel cell. In this way the compressor power must be allocated part to GT and part to IRSOFC (if 100 units of power are generated by GT and IRSOFC—40 percent and 60 percent respectively—about 16 units are needed for the compressor).

Conclusions

In this paper the assessment of the performance of an internal reforming solid oxide fuel cell (IRSOFC) based on a mathematical model developed here has been described. Also the assessment of the thermodynamic performance of a number of IRSOFC plus gas turbine (GT) combined cycle for a range of cycle parameters has been presented.

The main conclusions of this work are as follows:

- the IRSOFC model developed is reliable and its results agree well with the data available in literature (see Table 1)
- fuel cell technology can be well integrated with gas turbine and steam cycle technology to yield functional high efficiency power generation schemes (Figs. 9–12)
- the proposed cycles are significantly simpler than other systems presented in the literature (complex or exotic bottoming cycles have been not used)
- the proposed combined cycle configurations and the use of several constraints allow technological problems shown in previous works presented in literature to be eliminated
- the proposed system efficiencies are considerably higher (65–70 percent atmospheric cells; 74–76 percent pressurized cells) than the 58 percent efficiency achieved by the most advanced today's combined cycle plant—see Fig. 13–20
- the proposed system specific work is considerably higher than that obtained for classical gas-steam combined plants (Fig. 17, 21)
- power is generated mainly in the IRSOFC section (about 80–85 percent) when atmospheric cells are used; GT generates about 40 percent of the whole plant power when pressurized cells are used, and in this case attention must be used for the correct allocation of the compressor power (Table 3)
- CO_2 and NO_x emissions are particularly reduced, due to the very high efficiency level (CO_2) and the particular electrochemical energy conversion inside the fuel cell (NO_x); when a combustion chamber is included in the lay-out care must be used for NO_x control

It has been demonstrated that SOFC-GT cycles could be very attractive, although reliability and durability compatible with conventional power plants, and lower cost, essential to market entry, have to be still proved.

In the second part of this work (Massardo, 2000) the thermoeconomic aspects of the proposed systems will be addressed using SOFC cost and/or costing equations developed by the author and the exergy-thermoeconomic section of the code TEMP.

Acknowledgments

The authors wish to thank the Ministero Italiano dell' Universita e della Ricerce Scientifica e Tecnologica (MURST Cofinanziamento 1999) for the support of the present work.

References

Achehnbach, E., 1994, "Three-Dimensional and Time-Dependent Simulation of a Planar SOFC Stack," *J. of Power Sources*, Vol. 49.

Agazzani, A., Massardo, A., and Korakianitis, T., 1999, "An Assessment of the Performance of Closed Cycles With and Without Heat Rejection at Cryogenic Temperatures," ASME JOURNAL OF ENGINEERING FOR GAS TURBINES AND POWER, Vol. 121, pp. 458–465.

Agazzani, A., Frangopoulos, C., and Massardo, A. F., 1998, "Environmental Influence on the Thermoeconomic Optimisation of a Combined Plant with No_x Abatement," ASME JOURNAL OF ENGINEERING FOR GAS TURBINES AND POWER, Vol. 120, pp. 557–565.

Agazzani, A., and Massardo, A. F., 1997, "A Tool for Thermoeconomic Analysis and Optimisation of Gas, Steam and Combined Plants," ASME JOURNAL OF ENGINEERING FOR GAS TURBINES AND POWER, Vol. 119, No. 4, pp. 885–892.

Bessette, N. F., 1994, "Modeling and Simulation for Solid Oxide Fuel Cell Power System," PhD thesis, Georgia Institute of Technology, Atlanta, GA.

Bevc, F. P., Lundberg, W. L., and Bachovchin, D. M., 1996, "Solid Oxide Fuel Cell Combined Cycles," ASME Paper 96-GT-447.

Bossel, U. G., 1992, Final Report on SOFC Data Facts and Figures, Swiss Federal Office of Energy, Berne, CH.

Campanari, S., and Macchi, E., 1997, "Cicli Integrati con Celle a Combustibile ad Ossidi Solidi e Cicli Combinati Gas Vapore," S. Stecco Conference, Milan, June.

Costamagna, P., 1997, "Aspetti fluodinamici e di trasporto in reattori monolitici elettrochimici. Simulazione delle celle a combustibile ad ossidi solidi," Ph.D. thesis, University of Genoa.

Drenckhahn, W., and Lezuo, A., 1996, "Fuel Cells for Decentralized Cogeneration Plants," Power Gen Europe, Budapest.

Fry, M. R., Waston, H., and Hatchman, J. C., 1997, "Design of a Prototype Fuel Cell/Composite Cycle Power Station," Proceedings, Instn. Mech. Engrs., Vol. 211, Part. A, p. 171.

Harvey, S. P., and Richter, H. J., 1994, "Gas Turbine Cycles With Solid Oxide Fuel Cells. Part I and Part II," *ASME Journal of Energy Resources Technology*, Vol. 116, pp. 305–318.

Hirano, A., Suzuki, M., and Ippommatsu, M., 1992, "Evaluation of a New Solid Oxide Fuel Cell System by Non-Isothermal Modeling," *Journal of Electrochemical Society*, Vol. 139.

Hirschenhofer, J. H., Stauffer, D. B., and Engleman, R. R., 1994, *Fuel Cells Handbook*, (*Revision 3*), DOE/METC-94/1006, Morgantown, WV.

Korakianitis, T., Grantstrom, J., Wassingbo, P., and Massardo, A., 1997, "Parametric Performance of Combined Power Plants With Various Power-Efficiency Enhancements," ASME Paper 97-GT-286.

Lobachyov, K. V., and Richter, H. J., 1997, "Addition of Highly Efficient Bottoming Cycles for the Nth Generation MCFC Power Plant," *ASME Journal of Energy Resources Technology*, Vol. 119, pp. 103–108.

Lubelli, F., 1998, "Modellizzazione di celle a combustibile ad ossidi solidi ed integrazione con impianti per la conversione di energia," Master thesis, University of Genoa.

Massardo, A., 2000, "Internal Reforming Solid Oxide Fuel Cell Gas Turbine Combined Cycle (IRSOFC-GT): Part B—Exergy and Thermoeconomic Analyses," submitted for publication in ASME Transactions.

Pilidis, P., and Ulizar, I., 1996, "Design of a Semiclosed Cycle Gas Turbine with Carbon Dioxide-Argon as Working Fluid," ASME Paper 97-GT-125.

Stephenson, D., and Ritchey, I., 1997, "Parametric Study of Fuel Cell Gas Turbine Combined Cycle Performance," ASME Paper 97-GT-340.

Wilson, D. G., and Korakianitis, T., 1997, *The Design of High Efficiency Turbomachinery and Gas Turbines*, Prentice-Hall, Englewood Cliffs, NJ.

Vaporization Cooling for Gas Turbines, the Return-Flow Cascade

J. L. Kerrebrock
Massachusetts Institute of Technology,
31-268 MIT 77 Massachusetts Avenue,
Cambridge, MA 02139

D. B. Stickler
Aerodyne Research Inc.,
Billerica, MA 01821

A new paradigm for gas turbine design is treated, in which major elements of the hot section flow path are cooled by vaporization of a suitable two-phase coolant. This enables the blades to be maintained at nearly uniform temperature without detailed knowledge of the heat flux to the blades, and makes operation feasible at higher combustion temperatures using a wider range of materials than is possible in conventional gas turbines with air cooling. The new enabling technology for such cooling is the return-flow cascade, which extends to the rotating blades the heat flux capability and self-regulation usually associated with heat-pipe technology. In this paper the potential characteristics of gas turbines that use vaporization cooling are outlined briefly, but the principal emphasis is on the concept of the return-flow cascade. The concept is described and its characteristics are outlined. Experimental results are presented that confirm its conceptual validity and demonstrate its capability for blade cooling at heat fluxes representative of those required for high pressure ratio high temperature gas turbines.

1.0 Introduction

In the conventional conception of the gas turbine, the materials of the working parts of the engine including the compressor, turbine and combustion chamber operate hot. In the earliest engines they operated at the local gas' stagnation temperature; this set a rather low limit on the turbine inlet temperature and resulted in correspondingly low power per unit of airflow, and low efficiencies. Most modern engines use air cooling to maintain the metal temperatures in the combustor and turbine substantially below the gas temperatures. The compression ratios are limited by the temperature of the compressor outlet air which in most cases is the coolant for the turbine. Under the constraints of currently available cooling technology the high coolant temperature also limits the firing temperatures to values well below those corresponding to stoichiometric combustion of hydrocarbon fuels. Since the compression ratio and turbine inlet temperature are linked for maximum power, increasing the compression ratio to improve thermal efficiency results in higher cooling air temperatures as well as a reduction in the amount of air available for cooling, exacerbating the cooling problem. Thus, the efficiencies and power densities attained, though very impressive, are significantly below those that are potentially achievable with turbine inlet temperatures corresponding to stoichiometric combustion, and correspondingly high compression ratios. Furthermore, there are substantial thermodynamic penalties associated with the bleed of compressor discharge air for cooling, penalties considerably in excess of those dictated by the heat exchange to the cooling system. The technologies required for solution of these problems and the cost and fabrication difficulty of the high temperature superalloy turbine materials have caused high performance gas turbines to be expensive.

A new approach to gas turbine design is proposed here, in which the gas path is cooled by a flowing liquid or by evaporation of a fluid, providing such uniform and effective cooling that the gas temperature can be that which is dictated by thermodynamic considerations of maximum power and efficiency, more or less independently of materials considerations. With the cooling capacity available with liquids or by evaporation, the temperature of the material defining the gas flow path can be kept low enough that a much wider choice of engineering materials is available compared to the very expensive superalloys and other high temperature materials which are currently employed in gas turbines. For example it seems conceivable that aluminum alloys might be utilized for the stationary parts, and high strength low alloy steels for the rotating components, although the choice of materials and the mechanical details are outside the scope of this paper.

It is relatively easy to conceive of designs for liquid or evaporative cooling of the stationary components of the gas turbine. Depending on the location either liquid cooling or some form of heat pipe would be appropriate. Neither the cooling of these stationary parts nor the system aspects of the engine will be considered further here, although their importance to ultimate applications is appreciated. The principal subject of this paper is a technique for evaporatively cooling the rotating turbine blades, by means of what will be termed a return-flow cascade. It is proposed as the enabling element for a new class of heat engines.

This concept (for which US Patent number 5,299,418, entitled "Evaporatively Cooled Internal Combustion Engine" was issued on April 5, 1994) has been investigated experimentally, leading to proof of the conceptual viability of the return-flow cascade. Preliminary modeling has established some factors that control the heat flux limits. In addition some system studies have been carried out to assess the thermodynamic aspects of its application to aircraft engines. However, we wish to emphasize that the configurations built and tested are in no sense optimized, nor have the systems investigations as yet been carried to the point that the ultimate promise of this new technology can be assessed.

2.0 General Description of Vaporization-Cooled Gas Turbine

The general features of a gas turbine incorporating vaporization cooling are indicated schematically in Fig. 1. Liquid coolant might be circulated through cooling jackets which surround the combustion chamber and also through the stationary turbine blades. Alternatively, heat pipes could be used to cool these parts of the flow path. Since the technologies for cooling these parts are well established if the heat-pipe option is used (see Cotter, 1972) for a

Contributed by the International Gas Turbine Institute (IGTI) of The American Society of Mechanical Engineers for publication in the ASME Journal of Engineering for Gas Turbines and Power. Paper presented at the International Gas Turbine and Aeroengine Congress and Exhibition, Stockholm, Sweden, June 2–5, 1998; ASME Paper 98-GT-177.

Manuscript received by IGTI March 4, 1998; final revision received by the ASME Headquarters October 20, 1999. Associate Technical Editor: R. Kielb.

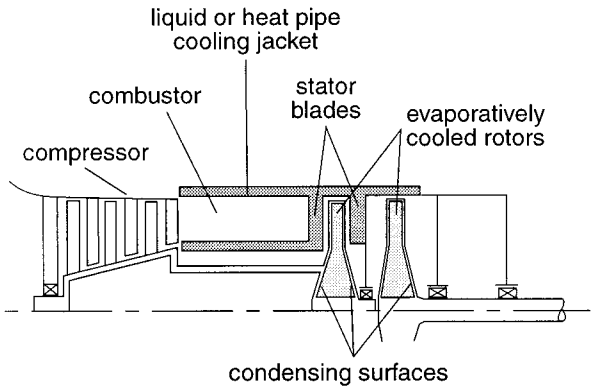

Fig. 1 Schematic of vaporization-cooled gas turbine

basic description of heat pipes), or need not be very different from those used in reciprocating engine practice if liquid cooling is used, they will not be discussed further here. Thus, the focus of the following discussion is on the cooling of the rotor blades. Although liquid thermosiphon or through-flow cooling have been considered in the past for the rotor, they have been found lacking for various reasons. For example, in the first case because of stresses induced by hydrostatic heads in the rotor passages and in the latter because of the high liquid consumption required. Nor did either of these concepts offer the self-regulating characteristic of vaporization cooling, as will be explained.

The conceptual basis for evaporatively cooling the turbine rotors is shown in Fig. 2. It comprises a closed heat transfer system, probably separate for each individual blade, in which the cooling fluid cascades outward in the centrifugal field of the rotating blade, falling from one capture shelf to another, with enough fluid being evaporated at each shelf to absorb the heat flux in its neighborhood. All fluid which is evaporated passes inward as vapor to the condensing section (conceptually) in the rotor disc, where it is reliquified, and then flows back outward in the centrifugal force field, to the cooling cascade in the blades. All the liquid passes to the first (most inward) shelf where some is evaporated and the remainder passes to the second and subsequent shelves, just enough being evaporated at each shelf to absorb the heat load at its location.

This concept has several important attributes. First, it is capable of accepting very high heat fluxes, comparable to those realized with heat pipes, the heat flux being limited only by the liquid flow rate or by the return flow of the vapor. Second, it enforces a nearly constant temperature of the cooled surfaces so long as there is liquid available over the whole surface covered by the shelves. That is, the shelves function as does the wick of a heat pipe.

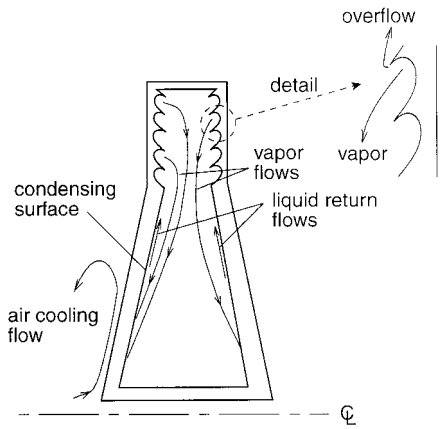

Fig. 2 Schematic diagram of evaporative-cooling system for rotor

Therefore, it is not necessary to predict the local heat flux accurately in order to maintain a nearly constant wall temperature. Thirdly, as conceived it is self controlling, both locally and globally. Any fluid which is vaporized returns to the cascade so that the flow rate of coolant is automatically that required by the total heat load to the blades. So long as there is fluid in the capture shelves, variations in the local heat load result only in variations in the local evaporation rate. The net result is to hold the blade approximately at a constant temperature set by the temperature of the condenser. The working fluid would be chosen so that its vapor pressure at the desired temperature is in a range appropriate from the viewpoints of the vapor pressure loads on the blade, and the vapor flow velocities required to carry the heat load to the condenser.

It has been noted repeatedly that this concept is similar in function to that of the now quite generally used heat pipe; however, it is important to note that the heat pipe as such is not suitable for application in the rotating system of a turbomachine because the capillary pumping that it depends upon to saturate the wick with fluid cannot distribute the fluid in the strong centrifugal field of the rotor. Typically, capillary pumping produces a few inches of rise with water against normal gravity (Cotter, 1972). In the several thousand G field of a turbine rotor this would become a few mils. As noted above, it may be that the heat pipe concept will be appropriate for cooling the stationary components of the gas turbine, in place of liquid cooling. This choice, while important to the design of a vaporization cooled gas turbine, is not critical to the concept addressed here.

The heat rejected by the vapor in the condenser can be removed in any number of ways. Convective cooling of the condenser by air which flows through the rotor cavity is one possibility, as shown schematically in Fig. 2. In this case, since the cooling air need not be at the pressure of the turbine working fluid, it could be extracted from the compressor at a lower pressure and temperature than is usual, reducing the amount of air required and the cycle penalty associated with its extraction. Alternatively, it could be desirable under some circumstances to introduce a liquid cooled condenser near the axis in the rotating system, the liquid coolant being fed to the rotor by some system of seals allowing its transfer to and from the rotating system. Again, though important in the application of the evaporative cooling concept, these considerations are not central to the concept, and a number of arrangements are possible.

2.1 Operating Characteristics. Assuming that the cooling system has come to some steady condition as described above, it is important to determine whether this operation is stable, and in particular what the response of the system is to a perturbation. Although the final determination of such stability must be experimental, and strong evidence for it will be presented below, some discussion of the mechanisms that may control the behavior of the cascade is in order at this point.

For example suppose the gas temperature is raised. This will occasion an increase in the evaporation rate in the blade, and hence an increase in the vapor flow. The increase in vapor flow to the condenser will cause an increase in its temperature, and therefore an increase in the vapor pressure in the blade, which will in turn cause an increase in the blade temperature, reducing the heat flow to it. But because of the very rapid increase of vapor pressure with temperature, the increase in blade temperature required to accommodate the increased heat load will be relatively small, and in most cases dominated by the cooling in the condenser. This argument indicates that the system should be stable to such perturbations.

A second question is how the system will behave during startup from an initially cold condition, during shutdown from hot operation, and during transients from one operating condition to another. In the cold startup the fluid in the rotor will be initially in liquid (or solid) form and when rotation begins it will tend to accumulate in the tip regions of the blades. The temperature being low, its vapor pressure will be low as well, and the vapor flow relatively small. As the blades heat up the fluid will vaporize,

liquefy in the condenser, and flow into the cascade, filling the capture shelves successively from the innermost radius. Eventually a steady state will be reached in which the capture shelves are full and the normal operation described above will continue. It is possible that the portions of the blades in which the capture shelves are unfilled at cold startup, could be overheated if the heating rate is initially too high, however, it appears that this situation can be avoided by gradually increasing the operating temperature at startup. Thus a general requirement is that the time required for adjustment of the cooling system to a new operating condition, be short compared to the time scale for changes in operating condition. The adjustment time is in fact determined by the flow times of the vapor to the condenser and the liquid from it. These are in the order of milliseconds, so it appears that the response of the cooling system should be sufficiently fast, in most situations. In the opposite case of cooling of the system, the liquid will be retained in the capture shelves until the rotation stops.

These plausibility arguments have been confirmed by the experimental results presented in section 3.

2.2 Cooling Limits. Some requirements for evaporative cooling systems can be understood from rough estimates of the heat flux which must be accepted by the cooled blades. In first approximation the heat flux to the blade is given by

$$q_w = \rho u c_p (T_t - T_w) \mathrm{St}, \tag{1}$$

where ρu is the mass flux density in the flow passage to be cooled, c_p is the specific heat of the gas, $T_t - T_w$ is the difference between the gas' stagnation temperature and the temperature of the cooled wall, and St is the Stanton number. For a typical gas turbine, with $\rho u = 2{,}000$ kg/m^{2}s, $c_p = 1{,}000$ J/kg K, $T_t - T_w = 500$ K, and St $= .001$, this gives an estimate of 100 watt/cm^2. In the vaporization cooled turbine this heat flux must be conducted through the wall of the turbine blade, to the coolant. This conduction process is governed by Fourier's law of heat conduction,

$$q_w = k \frac{\Delta T}{\Delta x}, \tag{2}$$

where k is the thermal conductivity of the blade material, ΔT is the temperature difference between the inside and the outside of the blade, and Δx is the thickness of the blade's skin. The objective of the cooling system being to maintain the blade material at as nearly as possible a constant temperature, this relation sets a limit on the permissible thickness of the blade's skin, Δx. For copper, $k = 480$ watt/m K, and for the above estimated heat flux, we find an allowable thickness of approximately 2.5 cm if the allowable temperature difference is 50 K. On the other hand, for an alloy with a conductivity of about one tenth that of copper, the allowable thickness is reduced to 0.25 cm. This seems still to be in a practical range.

2.3 Cascade Requirements. Since the heat must be conducted from all points on the blade to the immediate neighborhood of the fluid in the capture shelves in order that the evaporation of the fluid may absorb the heat, the spacing of the capture shelves, as well as the thickness of the blade's skin, must be as small as the dimension which has been estimated in the preceding paragraph. Thus an essential feature of the concept is a close spacing of the capture shelves, with spacing inversely proportional to the heat flux. This requirement for a close spacing in turn leads to further requirements on the structure of the cooling cascade.

In order that the cascade function as intended in the acceleration field of the rotor, it is necessary that the capture shelves be "level" in the "effective gravity" of the rotor, so that each shelf will fill before the liquid spills over its lip into the next shelf. This implies the two following requirements:

1 The lip of each capture shelf be at a nearly constant radius from the axis of rotation, over the entire internal circumference of the blade, the deviation being small compared to the spacing between shelves.
2 Disturbances of the rotational force field, by either gravity or rotational or lateral acceleration of the entire engine, be small compared to the rotational force field. That this second requirement is readily met may be seen from an estimate of the rotational force field. The centripetal acceleration is ν^2/r, where ν is the tangential velocity of the blade and r is the radius. A typical value of ν is 400 m/s or more, so for $r = 0.5$ m, the acceleration is 3×10^5 m/s^2 or about 3×10^4 times the acceleration of gravity. Thus gravity itself should introduce only very minor perturbations, and the system should be very insensitive to lateral accelerations as high as 100 times gravity. If the time for angular acceleration of the rotor is in the order of 1 s, the equivalent peripheral acceleration of the blades is on the order of 400 m/s^2, which is still a factor of 1000 below the acceleration due to the steady rotation.

The experiments to be described in the next section largely confirm the cascade behavior postulated and rationalized above.

3.0 Experimental Modeling

Since the return-flow cascade is a wholly new concept for cooling rotating blades, the first need is to define the factors controlling its feasibility and limiting the performance. This includes the interaction of fluid characteristics such as surface tension, wetting, and viscosity with acceleration forces in controlling fluid flow rate and distribution. Nor is the best geometry for such a cascade known. The model test sections used for the tests to be reported here were designed essentially to implement the idealized concept shown in Fig. 2. They consist of cylindrical evaporator sections with axisymmetric (about the radial direction) shelves on their inner surfaces, coupled to conical condensers. The evaporator sections which model the turbine blade are electrically heated on their outer surfaces while the condenser is air-cooled. The evaporators were approximately 2 cm in inner diameter and 5 cm in radial extent, the condensers of similar dimensions but tapered as shown. In light of the noted uncertainties about the liquid return behavior, the evaporators were provided with flow-control inserts designed to ensure that the liquid flowing from the condenser enters the first capture shelf and then passes sequentially through the remaining shelves, while at the same time allowing the vapor to enter the central passage through which it returns to the condenser. The arrangement for this purpose is shown in Fig. 3. It consists of a tubular insert, with hemispherical depressions on its outer surface that provide passages from one shelf to the next, and holes aligned with the inner portion of each space between the capture shelves to allow the venting of the vapor generated in the shelves. Two test models using this geometry have been tested, one with a shelf spacing of approximately 0.050 inches (TS1) and one with a spacing of 0.080 inches (TS2). In each case there were six of the liquid-passage depressions and six of the vapor holes, per shelf. It will be argued later that the liquid flow through the first (inner) set of depressions limited the heat flux capacity of these models under some conditions. Clearly, the capacity could be increased by providing more depressions for the inner shelves.

The instrumentation consisted primarily of several thermocouples distributed radially in grooves on the outer surface of the evaporator and three similarly distributed on the condenser. In addition the rotational speed, cooling air flow and its temperature at inlet to and exit from the condenser, were recorded.

These test models were mounted on the rotating arm of the MIT Rotating Heat Transfer Facility, which is shown schematically in Fig. 4, at location 1, labeled "test model." Briefly, the facility enables a test assembly to rotate in a vacuum, to eliminate external heat transfer and windage. Cooling fluid is provided through rotating seals and electrical power and electrical signals are carried through slip rings. The radius of the rotating arm is approximately

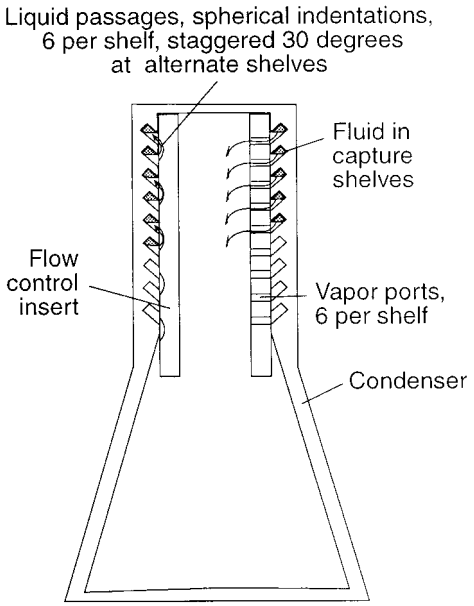

Fig. 3 Schematic of a typical evaporator and coupled condenser, showing flow control insert and capture shelves

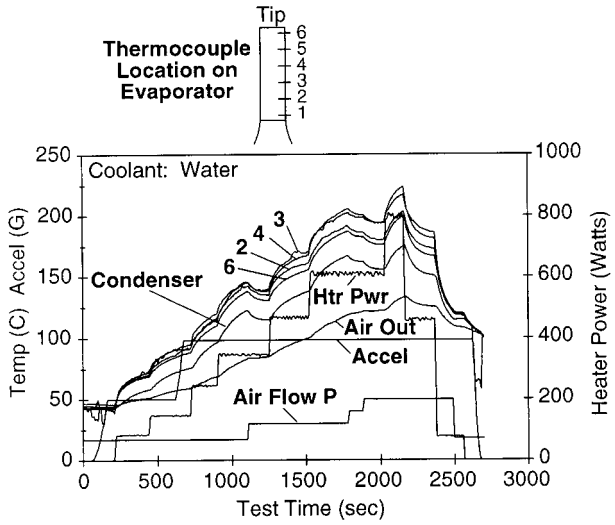

Fig. 5 Time history of an experiment with TS2 using water as working fluid

0.5 m and the rotation rate can be as high as 30 rps, although in the tests to be described it did not exceed 10 rps. The flow circuit includes counter-flow heat exchangers that operate between the incoming cooling air and that leaving the test section. This allows the test section to operate with elevated cooling air temperature without the need for high temperature airflow through the shaft and seals of the facility.

3.1 Test Procedures. The experiments were designed to explore the characteristics of the return-flow cascade, and in particular to determine if it is self regulating and capable of maintaining a nearly uniform evaporator temperature as described above. A typical experiment consisted in initiating rotation of the test model, and gradually increasing the electrical power to the evaporator while observing the variation of the evaporator and condenser temperatures. Typically these were closely coupled, showing that the thermal conductance of the cascade is very high (to be quantified below), as hypothesized. Due to the function of the counterflow heat exchangers the overall temperature level of the condenser, and, therefore, of the test section, would continue to rise even at constant heating power. After the cascade stabilized at some heat flux, (as high as 40 watt/cm^2 in the experiments reported) with the temperatures gradually rising as the heat exchangers heated up, the rotation rate was then gradually reduced (at about 0.025 rps per second) until the rapid (in a few seconds) rise of one or more of the temperatures on the evaporator signaled that the heat flux limit of the cascade had been reached. At this time the rotation rate was increased and generally the cascade recovered to its former temperature distribution. In this way the limits of the cascade were explored as a function of rotation rate and heat flux.

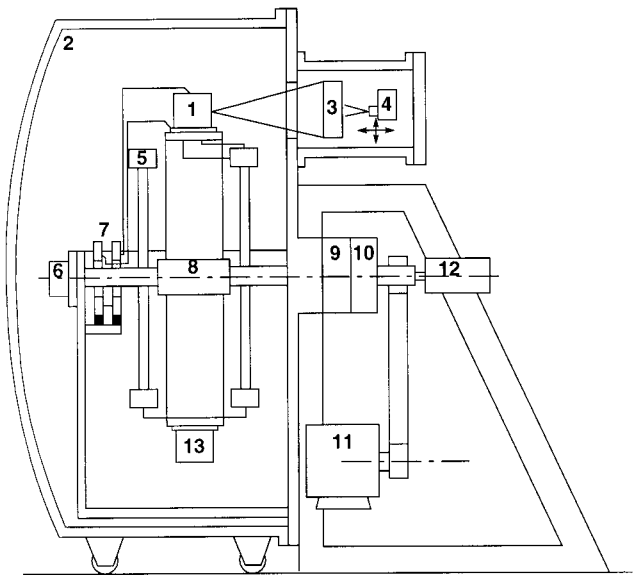

Legend:

1) Test model
2) Vacuum enclosure
3) Detection mirrors
4) Infrared detector
5) Counterflow heat exchanger
6) Shaft encoder
7) Power slip rings
8) Pressure transducer
9, 10) Shaft seals
11) Drive motor
12) Slip rings
13) Counterweight

Fig. 4 Overall schematic of rotating heat transfer facility

Most of the experiments have used water as the working fluid, but methanol was substituted for it in some experiments, to explore the effects of changes in the fluid properties. In high temperature gas turbine applications the most suitable working fluids are likely to be alkali metals, but for practical reasons they have not yet been used in these experiments.

3.2 Experimental Results. Time histories of two experiments conducted with the test section having 0.080 in. shelf spacing, along the lines described above, are shown in Figs. 5 and 6. In the case of Fig. 5 the working fluid was water, while for Fig. 6 it was methanol. For this test section, even at rotation rates as low as 1 rps it was not possible to reach the heat flux limit of the cascade within the available heating power with water as the working fluid. Hence Fig. 5 does not exhibit a heat flux limit. With methanol, the limit of the cascade was reached, as will be described in discussion of Fig. 6.

In Fig. 5, the variables of principal interest are the four temperatures measured on the evaporator, the condenser temperature, the heater power which was stepped up in increments of 50 to 100 watts, and the condenser cooling mass flow, which was also modulated as the power was increased. The spanwise acceleration was held at about 100 G's over most of the experiment. The evaporator temperatures are numbered increasing outward, 6 being near the tip and 2 about one third of the distance from the inner end of the evaporator to the tip. The primary result of the experiment

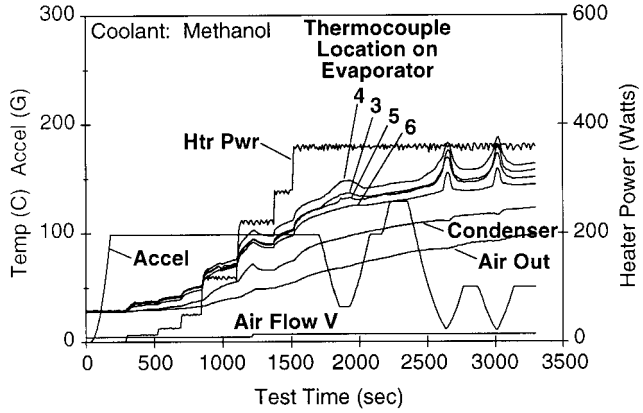

Fig. 6 Time history of an experiment with TS2 using Methanol as a working fluid and exhibiting heat flux limit

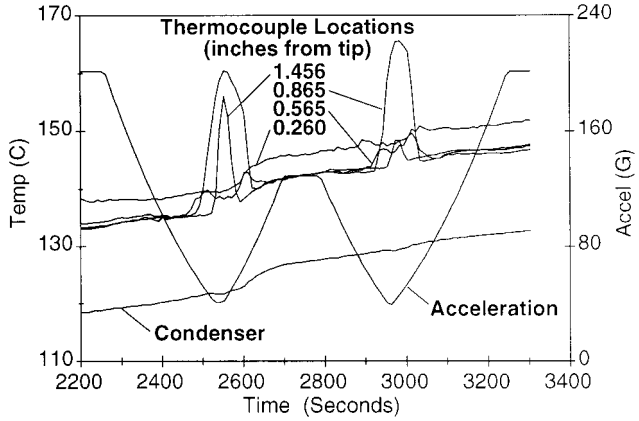

Fig. 7 Time history of an experiment with TS1 using water as a working fluid and exhibiting heat flux limit

is that the four temperatures measured in the evaporator are all nearly equal, the maximum difference being about 20 C at the highest power, and they all closely follow the condenser temperature, the difference between the lowest of them and the condenser being about 20 C. This low temperature difference indicates a very high thermal conductance, a characteristic typical of heat pipes. It is also significant that a step increase in the cooling flow, resulting in a drop of the condenser temperature, caused a corresponding drop in the evaporator temperatures. The time scale for response to step changes in power or cooling flow was of the order of a minute for these conditions, corresponding approximately to the thermal inertia of the test section.

The thermocouples in the evaporator are situated in grooves in its outer wall, adjacent the heater, and those in the condenser are several millimeters from the condensing surface, so a portion of the measured temperature difference between evaporator and condenser is due to conductive drop in the two walls. At a heat flux of 40 watt/cm^2, the highest value attained in Fig. 5, the conductive drop is estimated to be about 10 K, or half the temperature difference between the condenser and the coolest point of the evaporator.

Figure 6 shows the behavior of this same test model with methanol as working fluid, and in particular its response to changes in rotative speed (indicated by the radial acceleration in G's). After an initial heating period, the power and cooling flow were held constant. At about 1500 s the cascade had reached a stable operating point at about 350 watts and an acceleration of 100 G's, where the temperature differences within the evaporator and from evaporator to condenser were comparable to those found in Fig. 5. The rotative speed was then lowered linearly in time commencing at about 1800 s. At about 60 G's, two of the evaporator temperatures began to rise, indicating that the cascade had reached its heat flux limit at this speed. Increasing the speed caused it to recover to the former operating condition. The variation in speed was repeated at about 2400 and 2900 s with similar results.

Similar results are shown in more detail for the test section with 0.050 inch shelf spacing in Fig. 7. For this test water was the working fluid. Four evaporator temperatures are shown, the number indicating the distance in inches from the tip of the evaporator, so that the one labeled 1.456 is closest to the condenser. In this data sequence the heater power and condenser temperature were nearly constant, while the rotative speed was decreased until the heat flux limit was reached, then immediately ramped back up. This was done twice, at about 2500 and 2900 s. At the beginning of the first sequence (2500 s) all evaporator temperatures were nearly equal at about 140 C. As the speed was reduced the location at 0.865 in. showed signs of divergence at an acceleration of about 50 G's. The temperature at 1.456 in. similarly increased at about 45 G's, whereupon the speed was increased and both returned to their initial values. The same behavior occurred beginning at about 2930 s. That the cascades recovered after each of these divergences is taken as proof of the self-regulation capability and stability of the cooling mechanism of the cascade.

To further illuminate the general characteristics of the return-flow cascade an experiment was conducted with the test section with 0.080 in. shelf spacing, to compare its conductance in normal operation with the conductance of the metallic structure of the evaporator and condenser. As recorded in Fig. 8 this was done by applying power to the evaporator with it stationary and upright, so that the working fluid (methanol) was isolated in the condenser. As indicated by the time interval from about 100 to 700 s the evaporator temperatures rose rapidly, while the condenser temperature remained nearly constant at its initial value, until the temperature difference between evaporator and condenser was about 100 C and still rising rapidly. At 700 s, rotation was initiated, building to an acceleration of about 100 G's at 1000 s. The evaporator temperatures quickly dropped and the condenser temperature rose, till the temperature differences were on the order of 10 to 20 deg and stable. The rotation was then stopped with the test section pointed up as initially and the temperatures diverged again. It was then pointed down, giving the effect of a 1 G acceleration and the temperatures returned to the levels attained with rotation. The conclusion is that at this low heat flux, a 1 G acceleration is sufficient for operation of the cascade. More than that, the cascade quickly refills and resumes normal operation after having been

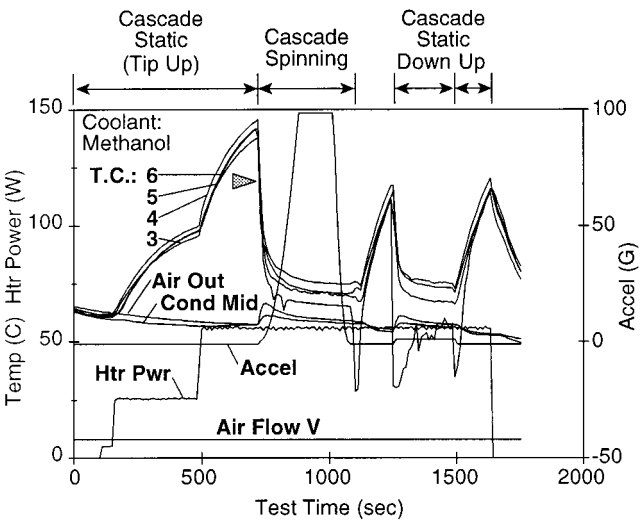

Fig. 8 Comparison of conductances of cascade when dry and in normal operation, with water as working fluid

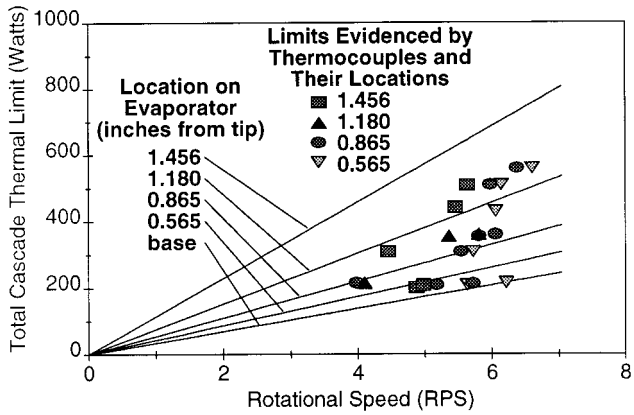

Fig. 9 Heat flux limit for TS1 with water as working fluid, as a function of rotative speed. Model results assume liquid flow rate through the inner end of the flow control insert as the limiting factor in heat flux.

dried out. This again confirms the self-regulating characteristic hypothesized earlier.

From a series of experiments such as those discussed above, the global characteristics of the two test models have been adduced. It is important that these are the characteristics of these test models only; no claim to generality can be made at this point in our investigation. On the other hand the observed characteristics are thus far as initially supposed.

3.3 Heat Flux Limits. In this section a simple flow and heat transfer model will be proposed that seems to provide a rationale for the observed heat flux limit.

The model is based on the assumption that in the configurations tested, the limiting heat flux is determined by the rate of liquid flow through the small passages that direct liquid from one shelf to the next. In this case the heat flux limit, Q, is given by the product of the liquid mass flow and the latent heat

$$Q \approx \dot{m} h_{fg}. \tag{3}$$

The head available to drive flow through the passages is approximately

$$\Delta p \approx \rho \omega^2 r \Delta r, \tag{4}$$

where an upper bound on Δr is defined by the spacing of the shelves. The flow velocity through the passages is then

$$u^2 \approx 2\Delta p/\rho = 2\omega^2 r \Delta r \tag{5}$$

and the resulting Q is

$$Q \approx h_{fg} \rho \omega A [2r\Delta r]^{1/2}. \tag{6}$$

For water and $r = 0.5$ m this becomes

$$Q \approx 2.3 \times 10^4 \omega A [\Delta r]^{1/2} \tag{7}$$

in watts where Δr is in cm and A is in cm^2.

Thus, according to this model the limiting heat flux should be proportional to the rotative speed, or the square root of the acceleration. It is a bit difficult to quantify A and Δr, but taking reasonable values of $A = 1$ mm^2 and $\Delta r = 1$ mm, we have an estimate for the total heat load allowable on the blade of

$$Q \approx 400\ n \approx 280\ g^{1/2}, \text{ watts}, \tag{8}$$

where n is the rotative speed in rps and g is the acceleration. The numerical factor however must be viewed strictly as an estimate, certainly subject to error by a factor of 3 or more.

The limiting heat flux given by this model is compared in Fig. 9 to a large number of limiting points identified for the test section with 0.050 in. shelf spacing, operating with water. The experimental points for each thermocouple are located on the abscissae at the rotational speed for which its temperature began to increase as the speed was decreased, at the heating power indicated on the ordinate. A series of lines indicate the limiting heat fluxes predicted by the above model with flow dimension defined by the actual cascade geometry. The assumption is that since all the liquid feeding the cascade must pass through the innermost row of depressions in the flow control insert, and some evaporates on each shelf, the outermost shelves should evidence the heat flux limit first as the rotative speed, and, therefore, the liquid supply is reduced.

The first point to be made from comparison of the model to the data is that the magnitude of the limiting heat flux is about right, suggesting that the liquid supply is in fact the limit on heat flux. Closer inspection shows that in general the thermocouples nearest the tip did usually exhibit the limit at the lower heat fluxes. On the other hand the trend of limiting heat flux with rotative speed does not seem to follow the simple proportionality suggested by the model.

A second test of the model is provided by the two sets of data from the test section with shelf spacing of 0.080 in., described above in Figs. 5 and 6, one with water and the other with methanol. With water this test section showed no heat flux limit within the range of heating available, up to about 800 watts. But with methanol the heat flux limit was identified at a power of about 350 watts. The heat flux limit for acceleration-driven methanol flow is about 0.4 that of water, so that other things being equal one would expect the cascade to be stable up to $800 \times 0.4 = 320$ watts with methanol. This is somewhat below the observed limit of 350 watts.

Clearly, more must be done to define the heat flux limits of the return-flow cascade, but it is important to note that the accelerations required to achieve stability in these experiments are far below those found in turbines. As indicated above a typical level is 3×10^4 G's. Thus it seems doubtful that the limits found here will be controlling in applications to gas turbines, particularly when use of alkali metals as coolants is considered.

4.0 Engine System Considerations

To judge the viability of the return-flow cascade in an engine application several factors must be considered. These include the mechanical details of incorporating it in the turbine rotor and the provision of cooling for the condenser and other matters that are quite specific to the particular engine. In addition, there are the more general effects on the engine's thermodynamic cycle of a higher permissible firing temperature, increased heat loss from the turbine due to lower blade temperatures, and the possibility of rejecting this heat elsewhere than to the turbine flow path. This last class of effects has been treated by Martinez-Tamayo (1995) for aircraft engine applications. Amongst his findings are the conclusion that in a turbofan engine there is considerable benefit in rejecting the heat from the turbine cooling system to the fan air stream, rather than to the turbine exhaust. He also found that the deleterious effects of the increased heat loss in the turbine can be more than offset by the beneficial effects of increased turbine inlet temperature, so that both the specific power and the thermal efficiency of the engine are improved by incorporation of vaporization cooling. In this analysis the return-flow cascade was treated as a replacement for air cooling, so that the basic architecture of the engine was assumed to be conventional.

Much remains to be done to achieve a full evaluation of the potential of the vaporization cooled gas turbine. As indicated in the introduction, if its characteristics are exploited fully the overall characteristics of the engine may be very different from those of present gas turbines. This is a subject for future discussion.

5.0 Conclusions

The primary conclusion of this work is that the return-flow cascade does function as conceived, to provide self-regulated heat flow from the evaporator to the condenser. While the experiments

reported have not fully covered the range of heat flux found in modern engines, when combined with simple models they indicate that these characteristics will be preserved at the very high heat fluxes that will exist in such modern engines if vaporization cooling is incorporated in them. The return-flow cascade therefore provides a means for cooling the rotating blades of a turbine to a very nearly constant temperature at temperature and pressure levels characteristic of modern gas turbines. In this sense it is the enabling element for the concept of the vaporization cooled gas turbine, which presents a new paradigm for gas turbine design.

Much remains to be done however, in examining both the detailed design issues and the system issues that must be resolved to incorporate the return-flow cascade in practical engines. These include the management of the waste heat from the condenser and the design of practical blades incorporating the evaporator and condenser, as well as the opportunities presented by new material choices.

6.0 Acknowledgments

This research has been supported by the Air Force Aeropropulsion Laboratory as a Phase II SBIR Contract, F33615-96-C-2617. Mr. Matthew Meininger is the Contract Monitor.

7.0 References

Cotter, T. P., 1972, "Theory of Heat Pipes," in Chang-Lin Tien, *Heat Pipes,* AIAA Selected Reprint Series, Vol. 16.

Martinez-Tamayo, F., 1995, "The Impact of Evaporatively Cooled Blades on Gas Turbine Performance," S.M. thesis, MIT Department of Aeronautics and Astronautics, Cambridge, MA.

US Patent No. 5,299,418, 1994, issued to Jack L. Kerrebrock.

Characteristics of MCrAlY Coatings Sprayed by High Velocity Oxygen-Fuel Spraying System

Y. Itoh

M. Saitoh

M. Tamura

Toshiba Corporation,
2-1, Ukishima-cho, Kawasaki-ku,
Kawasaki, Kanagawa, 210-0862,
Japan

High velocity oxygen-fuel (HVOF) spraying system in open air has been established for producing the coatings that are extremely clean and dense. It is thought that the HVOF sprayed MCrAlY (M is Fe, Ni and/or Co) coatings can be applied to provide resistance against oxidation and corrosion to the hot parts of gas turbines. Also, it is well known that the thicker coatings can be sprayed in comparison with any other thermal spraying systems due to improved residual stresses. However, thermal and mechanical properties of HVOF coatings have not been clarified. Especially, the characteristics of residual stress, that are the most important property from the view point of production technique, have not been made clear. In this paper, the mechanical properties of HVOF sprayed MCrAlY coatings were measured in both the case of as-sprayed and heat-treated coatings in comparison with a vacuum plasma sprayed MCrAlY coatings. It was confirmed that the mechanical properties of HVOF sprayed MCrAlY coatings could be improved by a diffusion heat treatment to equate the vacuum plasma sprayed MCrAlY coatings. Also, the residual stress characteristics were analyzed using a deflection measurement technique and a X-ray technique. The residual stress of HVOF coating was reduced by the shot-peening effect comparable to that of a plasma spray system in open air. This phenomena could be explained by the reason that the HVOF sprayed MCrAlY coating was built up by poorly melted particles.

Introduction

The increase in gas turbine firing temperature has driven the need to provide blade protection. Actually, as increases in the firing temperatures were made, a coating technology has been developed to protect gas turbine blades from oxidation and corrosion at high-temperature (Mevrel, 1989). There are two basic coating systems which are currently being used in gas turbine blades. These systems are diffusion coatings and overlay coatings. Diffusion coatings provide a surface enrichment layer of aluminium, chromium and/or silicon that results in the formation of protective surface oxides. Overlay coatings are a specifically designed oxidation and corrosion-resistant alloy that is deposited on to the blade surface. The overlay coatings based on the MCrAlY alloy system, where *M* can be iron, nickel, and/or cobalt, are commonly employed these days. The early production process was electron beam physical vapor deposition (EB-PVD). However, because of the high capital cost in setting up a commercial EB-PVD plant, plasma spraying systems such as air plasma spraying (APS) system have been widely accepted, particularly the argon shrouded plasma spraying and the vacuum plasma spraying (VPS) systems. In recent years, the vacuum plasma spraying system for overlay coatings has been established and is used for hot parts, such as blades and duct segments, etc., which are exposed to oxidizing and corrosive atmosphere at high-temperature.

As described above, the application of high integrity for chemical compositions, low oxygen content coatings was only successfully done in an inert gas atmosphere and/or vacuum pressure chamber. However, recently a high velocity oxygen-fuel (HVOF) system in open air has been established for producing the coatings with extremely low oxide content, low porosity, and high bonding strength (Parker and Kunter, 1994). Several investigations (Irons and Zanchuk, 1993; Irons, 1992) have been reported sprayed MCrAlY coatings with HVOF systems in open air and achieving near chamber quality. The superior coating performance is primarily a result of the higher particle velocities in comparison with the other thermal spraying systems (Russo and Dorfman, 1995). The HVOF system has been reported to be successfully applied to the gas turbine hot parts (Nestler et al., 1995; Clark et al., 1995). Also, it is well known that the thicker coatings can be sprayed for improving the residual stress in comparison with any other thermal spraying systems. However, the basic properties such as mechanical properties and residual stress characteristics of HVOF coatings have not been clarified. It is well known that the life of thermal sprayed blades are affected by the mechanical properties of coatings (Wood, 1989; Veys and Mevrel, 1987). The cracking and delamination of sprayed coatings is mainly affected by the residual stress (Ishiwata et al., 1995; Grunling et al., 1987).

In this paper, the mechanical properties of MCrAlY coatings sprayed by the high velocity oxygen-fuel (HVOF) system are investigated in comparison with the vacuum plasma sprayed MCrAlY coatings. Furthermore, the residual stress characteristics induced by HVOF system are analyzed using a deflection measurement method and a X-ray method in comparison with the air plasma spraying (APS) system.

Materials and Experimental Details

This investigation used as cast Ni-based super alloy (IN738LC) as a substrate for thermal sprayings and three kinds of commercial spraying powders such as CoCrAlY, CoNiCrAlY and NiCoCrAlY. The chemical compositions and powder size of these materials are given in Table 1.

The morphology of NiCoCrAlY powder before thermal spraying was examined at the cross-section using a scanning electron

Contributed by the Internal Combustion Engine Division (ICE) of The American Society of Mechanical Engineers for publication in the ASME Journal of Engineering for Gas Turbines and Power.

Manuscript received by the Gas Turbine Division May 1, 1997; final revision received by the ASME Headquarters July 30, 1999. Associate Technical Editor: D. Assanis.

Table 1 Chemical compositions of substrate and spraying powders

Materials	Chemical composition (mass %)										
	Cr	Aℓ	Y	W	Mo	Nb	Ta	Fe	Ti	Co	Ni
IN 738LC (As cast)	15.8	3.33	–	2.52	1.62	0.99	1.65	0.06	3.32	8.24	Bal.
CoCrAℓY (-400 Mesh)	28.9	5.84	0.35	–	–	–	–	–	–	Bal.	<.05
CoNiCrAℓY (-325 Mesh)	20.6	7.9	0.4	–	–	–	–	–	–	Bal.	32.5
NiCoCrAℓY (-325 Mesh)	17.2	12.6	0.65	–	–	–	–	–	–	21.7	Bal.

microscope (SEM) as shown in Fig. 1. The spraying powders used in this study were produced by rapid-cooling solidification technique using an argon gas atomizer. All of the particles appear to be mostly spherical and a lot of fine, precipitated (Ni, Co)Al metallic compounds can be observed in NiCoCr solid-solution matrix. In the same way, the particle morphologies of CoCrAlY and CoNiCrAlY appear to be mostly spherical and fine precipitated CoAl and (Ni, Co)Al metallic compounds can be observed, respectively.

The HVOF coatings were carried out with a JP-5000 system (Hobart Tafa Technologies) under the conditions of no preheating, kerosene + oxygen fuel, three kinds of combustion pressure, such as 483 kPa, 703 kPa, and 896 kPa, spray distance 400 mm, and traverse speed 500 mm/s. For the comparison of mechanical properties, the VPS coatings were carried out with a A-2000 V VPS system (Plasma Tecknik) under the conditions of preheating 843 K, voltage 64 V, current 685 A, spray distance 270 mm in argon gas atmosphere 6 kPa. A single face of IN738LC substrate was roughened by grit blasting after degreasing, and sprayed MCrAlY coatings with a coating thickness of about 2 mm. The bending test specimens ($50 \times 5 \times 1.5$ mm) were machined out of the thick coatings. In the same manner, the bending test specimens were machined out of the diffusion heat-treated (1393 K-2 h, 1116 K-24 h and argon gas cooled) coatings. In general, to densify the coating layer and improve the bonding strength, the coatings are subjected to the above high-temperature diffusion heat-treatment before mechanical finishing. The mechanical properties, such as Young's modulus, Poisson's ratio, bending strength, and Vicker's hardness are measured by four-point bending test using a strain gage method under the condition of cross-head speed 0.1 mm/min.

Figure 2 shows the testing apparatus to investigate the generating mechanism of residual stresses in case of HVOF system. The HVOF spraying condition is as same as described above. For comparison of residual stress characteristics, the APS coating was also carried out with a Metco system that employs a 7 MB gun under the conditions of no preheating, Ar + H_2 operating gases, voltage 78 V, current 500 A, spray distance 100 mm and traverse speed 500 mm/s. One side of strip-shaped substrate ($10 \times 130 \times 3$ mmt) was fixed, and the deflection of substrate at the center on

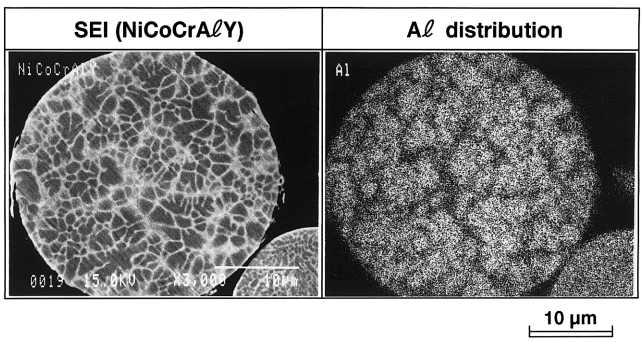

Fig. 1 EPMA analysis of NiCoCrAlY powder for thermal spraying

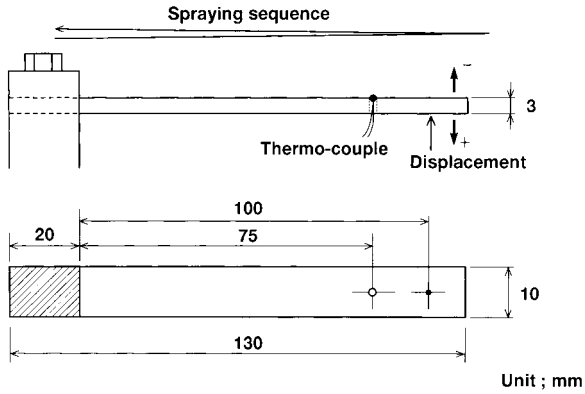

Fig. 2 Testing apparatus and configuration of test specimen

the rear face was measured in-situ during thermal spraying using dialgage as shown in Fig. 2. At the same time, the temperature change at the substrate surface was measured by a thermo-couple during thermal spraying. From the displacement, δ, and coating thickness, hc, the average residual stress can be calculated by the Stoney-Hoffman's equation (Stony, 1987; Kuroda and Clyne, 1991).

$$\sigma_R = Es' \cdot hs^2 \cdot \delta/(3 \cdot l^2 \cdot hc), \tag{1}$$

where $Es' = Es/(1 - \nu s)$: Es and νs are Young's modulus and Poisson's ratio of the substrate, respectively. hs and hc are the thickness of substrate and coating, respectively. l is substrate length. After thermal spraying, the longitudinal residual stress at coating surface (Irradiation area: 5×10 mm) was measured using an X-ray stress measurement equipment. Characteristic X-ray is Cr-K_α, and tube voltage and current was 30 kV and 300 mA, respectively. Diffraction plane was Cubic (2.2.0).

Macro and Microstructure of Sprayed Coatings

It was found that all of the MCrAlY coatings were composed of the Ni or Co-based solid-solution matrix and a lot of precipitated aluminum intermetallic compounds. Figure 3 shows the typical microstructure of MCrAlY coatings sprayed by HVOF system in case of (a) as-sprayed NiCoCrAlY and (b) heat-treated NiCoCrAlY observed by SEM and electron probe microanalysis (EPMA). The microstructure revealed that even the as-sprayed coatings were very dense with low oxide content. And also, the same microstructure as shown in Fig. 1 could be observed in Fig. 3(*a*). This caused concern since there are a lot of poorly melted particles. The same observation had been made before (Irons and Zanchuk, 1993). Therefore, it is recognized that the MCrAlY integrity, especially low oxide content, is maintained in spite of thermal spraying in open air. It is clear from these observations that HVOF guns produce particle velocities (or high kinetic energy), which are considerably higher than the other commercial thermal spraying systems. Furthermore, the diffusion heat treatment after thermal spraying transforms the coating into uniform microstructure with two predominant phases made up of (Ni, Co)Al metallic compounds and NiCoCr solid-solution matrix. The poorly melted particles can't be discriminated, and crack like pores are transformed into micropores in a line due to the progress of sintering.

The diffusion heat treatment of the MCrAlY coatings showed clearly the reduction of pores in the microstructure, as shown in Fig. 4, which was measured by a water submersion technique. The error in measurements is less than 0.01 percent and the scatter of datum in Fig. 4 is within ± 0.2 percent. The mean values of three-times measurement are shown in Fig. 4. The order of initial relative density of coatings was NiCoCrAlY > CoNiCrAlY > CoCrAlY independent of the coating systems, such as HVOF and

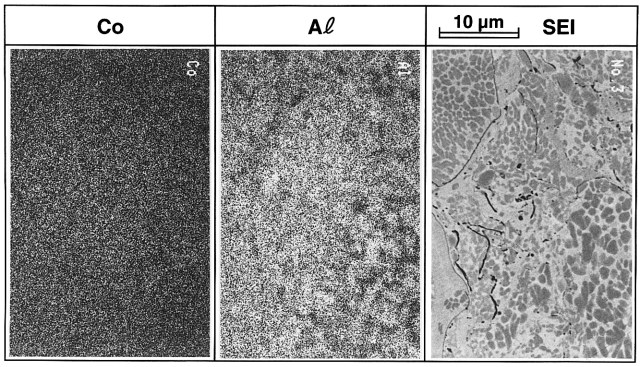

Fig. 3(*a*)

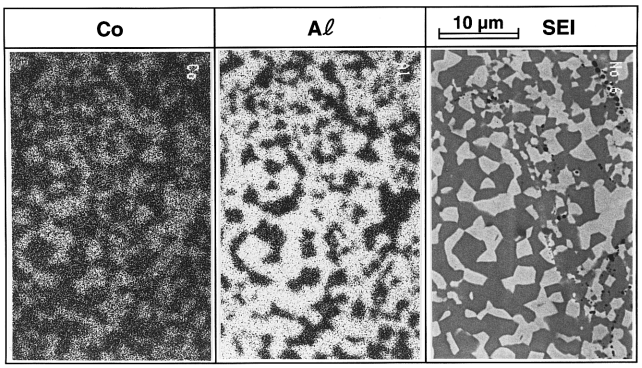

Fig. 3(*b*)

Fig. 3 EPMA analysis of NiCoCrAlY coating sprayed by HVOF process: (*a*) as-sprayed; (*b*) heat-treated (1393 K-2 h, 1116 K-24 h, Ar gas cooled).

VPS. It is thought this is because the MCrAlY coating with lower melting point (high nickel content) is sintered easily. The diffusion heat-treatment of the HVOF coatings removed a fair amount of porosity (>3 percent). From the view point of porosity content, it can be said that the HVOF system is a match for the VPS system.

Figure 5 shows the coating integrity for CoNiCrAlY and NiCoCrAlY during thermal spraying in terms of the aluminum and chromium content. The aluminum content is measured by inductively coupled plasma emission spectrometry. The chromium content is measured by $KMnO_4$-oxidation and $KMnO_4$-titration method. The error in measurements is less than 0.01 percent and the scatter of datum in Fig. 5 is within ± 0.5 percent. The effects of the various processes on the aluminum and chromium content are relatively clear by the mean values of five-samples measurement as shown in Fig. 5. The aluminum and chromium are well known elements for oxidation and corrosion resistance at high-temperature. Powder compositions with respect to the aluminum and chromium content before thermal spraying were reduced during thermal spraying process. The reduction tendency was large in case of the chromium element. However, it is clear that the coating integrity is almost held in the HVOF system, which is slightly inferior to the VPS system.

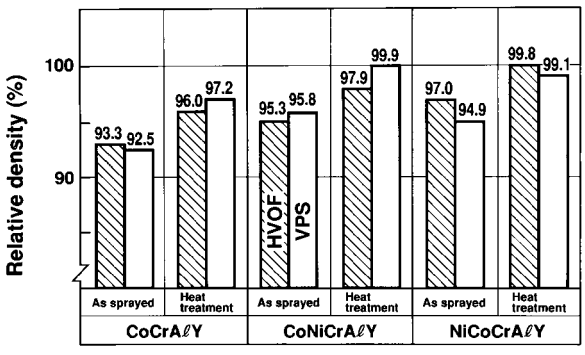

Fig. 4 Comparison of relative density between HVOF and VPS coatings

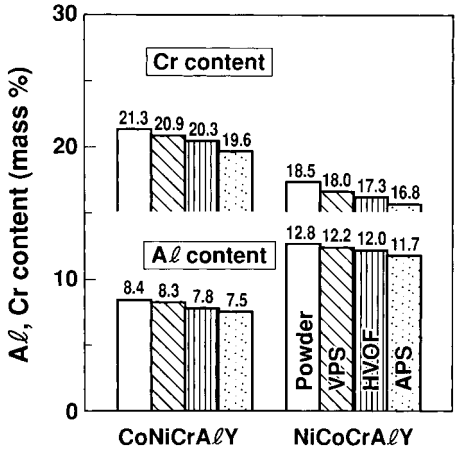

Fig. 5 Variation of chemical compositions for MCrAlY coatings due to various thermal spraying processes

Mechanical Properties of Sprayed Coatings

Figure 6 shows the mechanical properties of HVOF MCrAlY coatings in comparison with VPS MCrAlY coatings. (a) shows the results of CoCrAlY coating, and (b) shows the results of NiCoCrAlY coating. The error in measurements is less than 0.01 percent and the scatter of datum in Fig. 5 is within ± 3.5 percent. The mean values of three-times measurement are shown in Fig. 6(*a*) and (*b*).

All bending test specimens failed in an apparently brittle manner, and the load versus deflection curves were straight lines until their catastrophic failure. These brittle fractures are caused by the formation of aluminum metallic compounds inside the coatings. CoAl metallic compounds were formed in the CoCrAlY coating, and (Ni, Co)Al metallic compounds were formed in the NiCoCrAlY coating, respectively. It is considered that the kind of aluminum metallic compound and precipitated volume affects the mechanical properties of MCrAlY coatings (Itoh et al., 1994). In case of as-sprayed coatings, the bending strength of HVOF MCrAlY coatings were inferior ($\frac{1}{2} \sim \frac{1}{3}$) in comparison with the VPS MCrAlY coatings. However, the strength of HVOF MCrAlY coatings could be improved up to the level of the VPS MCrAlY coatings by the diffusion heat-treatment. This means that a lot of crack-like pores exist among the poorly melted particles. The HVOF MCrAlY coatings do not have excellent intergranular bonding. However, the reduction of pores by the diffusion heat-treatment improves the intergranular bonding of HVOF MCrAlY coatings. The difference of bending strength of as-sprayed HVOF MCrAlY is due to the coating structure which depended upon thermal spraying systems. For that reason, when the uniform microstructure can be obtained by the diffusion heat-treatment, it is recognized that there is no difference of the bending strength between HVOF and VPS MCrAlY coatings.

Typical examples of SEM observed fracture surfaces are shown in Fig. 7 for both the as-sprayed and heat-treated HVOF NiCoCrAlY coatings. A crack initiation site was not found clearly. However, there was a special feature in the photograph of as-sprayed HVOF NiCoCrAlY coating. Namely, some spherical particles about 20 $\sim$ 50 μm in diameter, could be observed in the fracture surface of as-sprayed coating. Actually, it is observed that

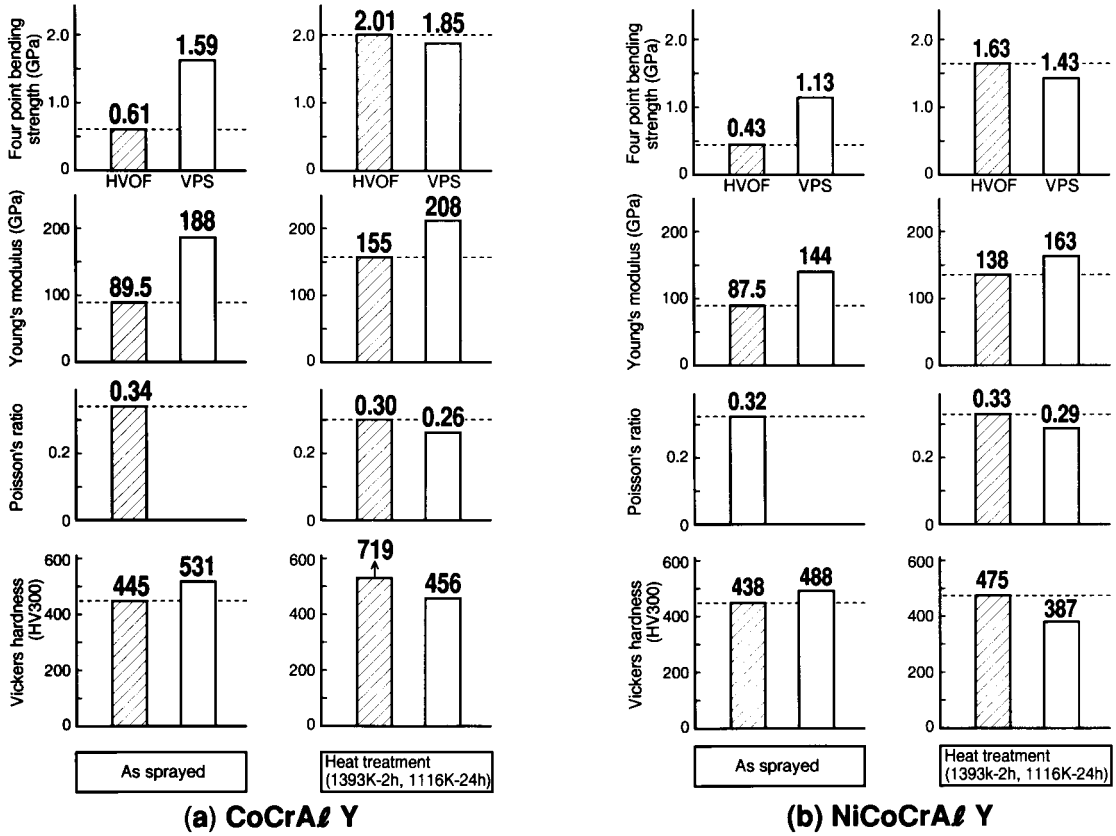

Fig. 6 Mechanical properties of MCrAlY coatings in comparison with HVOF process and VPS process: (*a*) CoCrAlY coatings; (*b*) NiCoCrAlY coatings.

the fracture goes forward along the crack-like pores. However, after the diffusion heat-treatment, the fracture surface becomes comparatively flat due to the progress of microstructural uniformity by sintering among the poorly melted particles.

In case of Young's modulus, the same tendency was confirmed for both CoCrAlY and NiCoCrAlY coatings. The Young's modulus of as-sprayed HVOF MCrAlY coatings was inferior ($\frac{2}{3} \sim \frac{1}{2}$) in comparison to the VPS MCrAlY coatings. However, the Young's modulus of HVOF MCrAlY coatings subjected to the diffusion heat-treatment could be improved up to the level of the VPS MCrAlY coatings. It is clear that the diffusion heat-treatment is effective in improving the Young's modulus of as-sprayed HVOF coatings for sintering among the HVOF sprayed particles.

There are no datum of as-sprayed VPS coatings for Poisson's ratio. However, the Poisson's ratio was nearly 0.3 for as-sprayed HVOF MCrAlY. These values are in agreement with the diffusion heat-treated MCrAlY coatings sprayed by both HVOF and VPS systems.

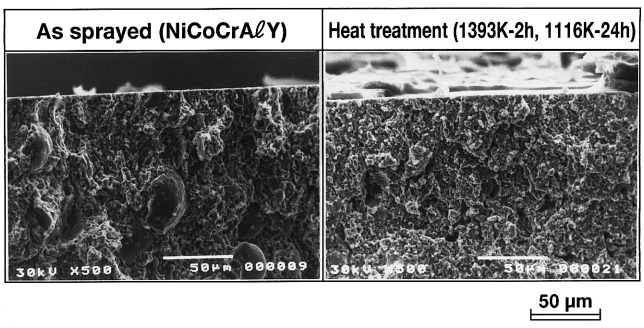

Fig. 7 SEM observation of fracture surface for NiCoCrAlY coating sprayed by HVOF process

On the other hand, a significant difference for Vickers hardness of coatings sprayed by HVOF and VPS systems could not be observed in case of as-sprayed. It seems that the crack like pores that exists in HVOF MCrAlY coatings do not affect the Vickers hardness, though they affect the strength and the Young's modulus as described above. It is well known that voluminous pores observed in APS sprayed MCrAlY coatings reduced the strength, Young's modulus and Vicker's hardness. This phenomenon is in agreement with the reason that the HVOF system is widely used to apply wear resistant coatings up to this time. Moreover, the Vickers hardness of heat-treated HVOF MCrAlY coatings shows high value in comparison with the VPS MCrAlY coatings. This phenomenon cannot been observed in the VPS MCrAlY coatings, and carbon content of spraying powders is less than 0.02 mass percent. It is considered that this is caused by the HVOF process for its own sake, such as carbonizing of some elements in MCrAlY coatings by the kerosene + oxygen fuel. The carbon contamination from the kerosene + oxygen fuel is thought to be generally important to application of the HVOF system to metal coatings, which contain a lot of carbide forming elements.

Residual Stress of Sprayed Coatings

Deflection measurement tests using a cantilever beam specimen as shown in Fig. 2 were conducted for investigating the generating mechanism of residual stress during thermal spraying (Kuroda and Clyne, 1991). The purpose of this test is to clarify the transient thermal stresses during thermal spraying. The typical measurement results for CoNiCrAlY coating are shown in Fig. 8(*a*) HVOF system and (*b*) APS system. Also, the temperature histories during thermal spraying of 15 cycles are shown in Fig. 8. While the HVOF gun traversed across the longitudinal direction of IN738LC substrate, both the displacement and the temperature of cantilever beam specimen made significant changes according to the gun

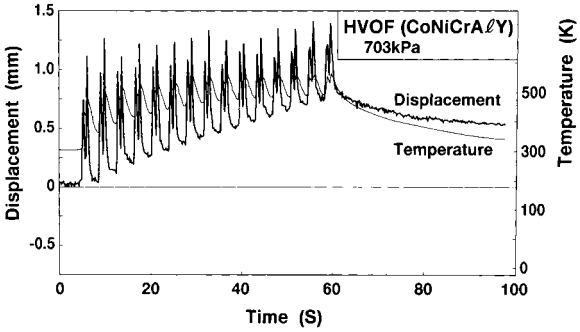

Fig. 8(*a*)

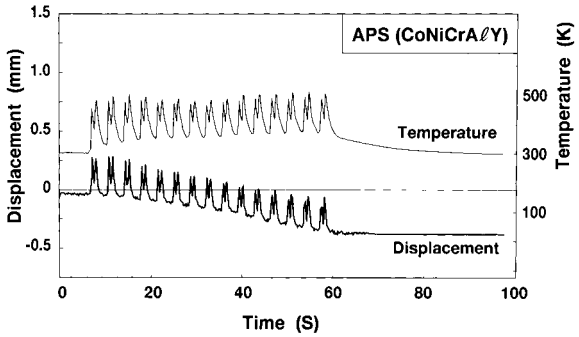

Fig. 8(*b*)

Fig. 8 Change of temperature and deflection of test specimens during thermal spraying: (*a*) HVOF process; (*b*) APS process.

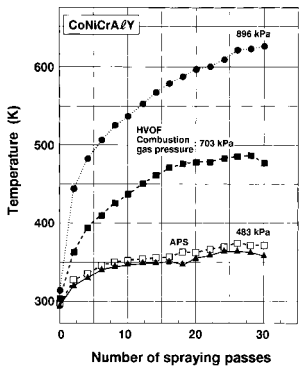

Fig. 9(*a*)

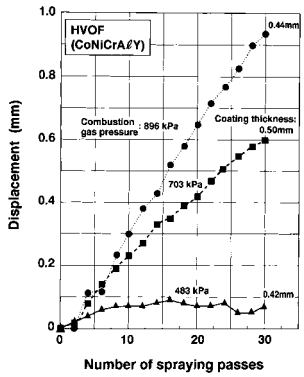

Fig. 9(*b*)

Fig. 9 Effect of combustion gas pressure on substrate temperature and deflection of test specimens during thermal spraying: (*a*) effect of spraying passes on substrate temperature; (*b*) effect of spraying passes on substrate deflection.

position. However, there was a tendency for the average displacement and the temperature to increase with buildup of the sprayed coating. The change of displacement by the HVOF system during one cycle of thermal spraying was significantly in comparison with the APS system. This shows the higher particle velocities achieved with the HVOF gun in comparison with the APS system. Also, it is very interesting that the average displacement of specimen sprayed by the HVOF system shows a plus sign (convex deflection), and on the contrary the average displacement of specimen sprayed by the APS system shows a minus sign (concave deflection). It seems that peening effect by poorly melted particles causes the substrate surface to induce compressive stresses in case of the HVOF system. The compressive stresses seem to be induced at not only the substrate surface but also the coating layer except for the final coating layer, namely surface layer. However, in case of the APS system, it is well known that the shrinkage force by thermal sprayed and fully melted particles causes the substrate surface to induce tensile stresses. According to the temperature rise during thermal spraying, the HVOF system shows high temperature in comparison with the APS system. It is thought that this temperature rise is caused by the very high particle velocity and the high deposit efficiency of HVOF system.

Figure 9(*a*) shows the effect of number of spraying passes and HVOF combustion gas pressure on the surface temperature of substrate. Figure 9(*b*) shows the effect on the displacement of substrate. It is clear that the surface temperature and the displacement increase with increasing the combustion gas pressure, which equates to the sprayed particle velocity. However, the rate of surface temperature rise has a tendency to decrease as shown in Fig. 9(*a*) as opposed to the displacement of the substrate. From this tendency, the deformation behavior of cantilever beam is strongly affected by the peening effect due to the poorly melted particles, not by the temperature rise. In Fig. 9(*b*), the final coating thickness for each of the spraying conditions is shown. When the combustion gas pressure was low, a porous coating was formed and the deposit efficiency became low. On the contrary, when the combustion gas pressure was high, a dense coating could be obtained by the peening effect and the deposit efficiency became high. But, the buildup speed of coating became lower due to crush action effect of coating layers. Figure 10 shows the macrophotographs of cross-section of coating layer in case of the HVOF CoNiCrAlY coating. There was a tendency for the coating layer to become denser with increasing the combustion gas pressure. Especially, in case of combustion gas pressure 483 kPa, a lot of poorly melted particles could be observed in the coating layer. In case of combustion gas

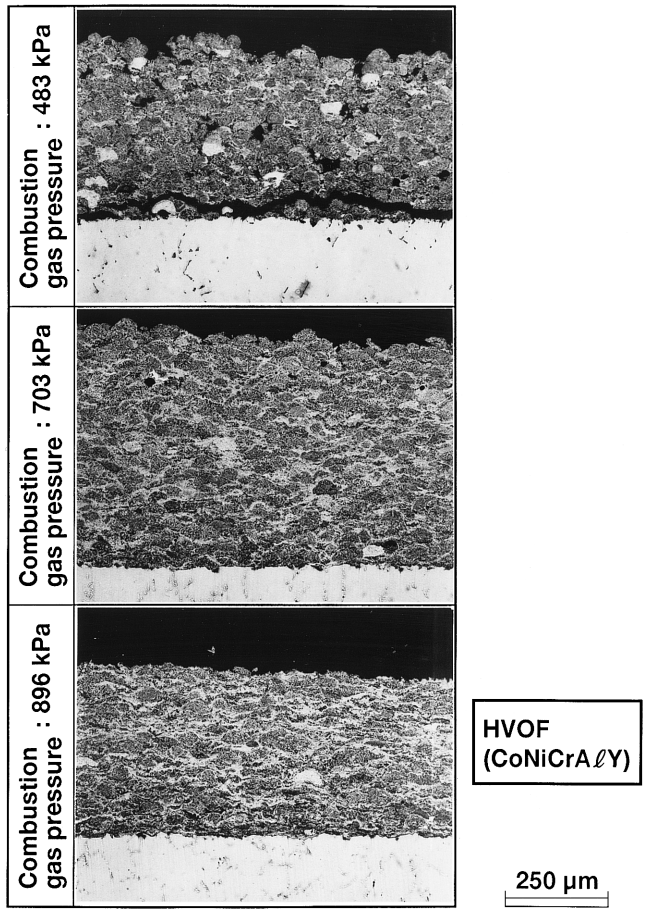

Fig. 10 Macrostructure of HVOF coating in the case of various combustion gas pressure

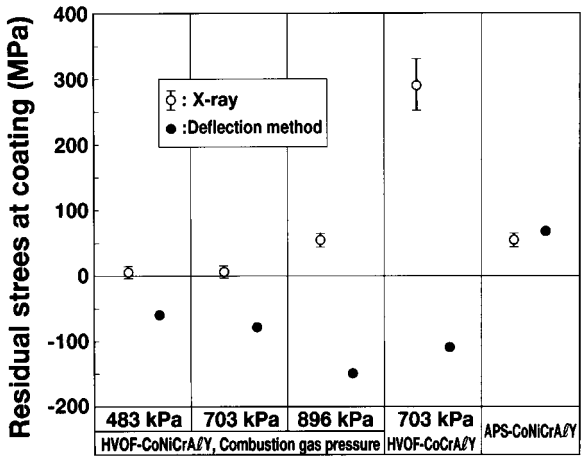

Fig. 11 Measurement results of residual stresses at the surface of MCrAlY coatings

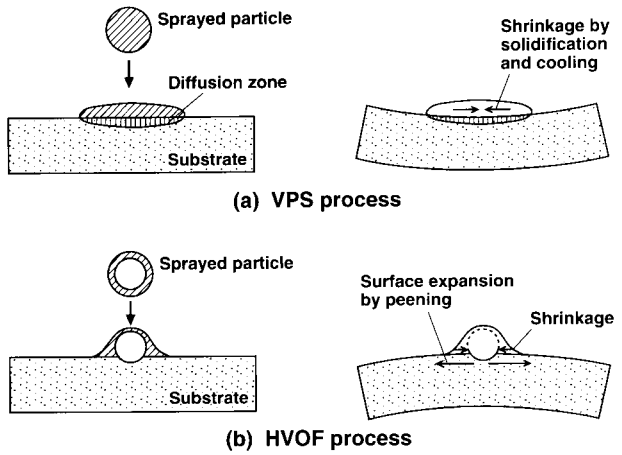

Fig. 12 Residual stress generating mechanism during thermal spraying

pressure 703 kPa, no porosity could be observed, and the spherical particles tended to become flat and the coating surface tended to become smoother. In case of any other MCrAlY, the same tendency could be observed.

The residual stresses calculated by Eq. (1) using the displacement of the cantilever beam are shown in Fig. 11. Also, the residual stresses at coating surface measured by a X-ray method is shown in Fig. 11. The diffraction peak of precipitated metallic compounds such as CoAl and (Ni, Co)Al is used to measure the residual stresses of CoCrAlY and CoNiCrAlY coatings, respectively. Elastic constants as shown in Fig. 6 are used for the calculation of residual stresses. The residual stresses which were obtained by two methods were good agreement in case of the APS CoNiCrAlY coatings. However, in case of the HVOF MCrAlY coatings, the residual stresses obtained by the displacement measurement method are not good agreement with the X-ray method. By the way, Eq. (1) is based on an assumption that the residual stresses are uniform in coating layer and the substrate shows elastic behavior. It is thought that the plastic deformation of substrate and coating layers except for the final coating layer due to the peening effect by poorly melted particles causes the disagreement between two measurement methods in case of the HVOF MCrAlY coating. As a matter of course, it seems that the nonuniformity of residual stress in the coating layer also arises. In Fig. 11, it is clear that the difference of residual stress become larger with increasing the peening effect. Therefore, the simple measurement method based on Eq. (1) is not effective in case of the HVOF system. As a result, the generating mechanism for residual stress is considered as follows from the above experiments. In case of the APS system, the residual stress induced in coating layer, σ_R is represented by the sum of the shrinkage stress of sprayed particles, σ_S and the thermal stress induced by the difference of temperature and material constants between coating and substrate, σ_T (Kuroda and Clyne, 1991).

$$\sigma_R = \sigma_S + \sigma_T \tag{2}$$

The shrinkage stress of sprayed particles, σ_S is due to the solidification of sprayed particles on the substrate as shown in Fig. 12. In case of HVOF system, almost all sprayed particles dash against the substrate in a poorly melted state. Therefore, compressive stress at substrate surface and coating layer except the final coating layer, $-\sigma_P$ is induced by the peening effect. The shrinkage stress, σ_S is slightly induced around the poorly melted particles ($\sigma_P > \sigma_S$). As a result, the residual stress induced in coating layer, σ_R is presented as follows.

$$\sigma_R = \sigma_S + \sigma_T - \sigma_P \tag{3}$$

By comparison with Eq. (2) and Eq. (3), it seems that the residual stress of HVOF coatings becomes lower than the APS coatings.

Based on the generating mechanism of residual stress described above, the residual stress distribution of the HVOF CoNiCrAlY (combustion gas pressure: 703 kPa) can be estimated as shown in Fig. 13. A numerical model had been presented simulating heat transfer and buildup of differential thermal contraction stresses during thermal spraying (Gill and Clyne, 1990). For this residual stress analysis, the usual finite element method program for analyzing thermoelastic problem was used, and material constants used are shown in Fig. 6. The thermal stress distribution is shown in Fig. 13 in case of two layered body with the uniform inherent strain of $\epsilon_1 = 0.048\%$ at coating layer. The inherent strain ϵ_1 is determined by the Eq. (1) and the convex displacement show in Fig. 9(*b*). It is clear that the compressive residual stress can be obtained at the coating surface. Namely, it is the case that the final coating layer is not affected by the peening effect. The straight line in Fig. 13 shows the residual stress at the final coating layer in case of three layered body with the inherent strain at the final coating layer of 0.0125 mm thickness. Namely, the inherent strain at final coating layer is a parameter in Fig. 13. As the residual stress measured by the X-ray method is 27 MPa, it seems that the inherent strain at final coating layer of 0.0125 mm thickness is $\epsilon_1 = -0.007\%$. The thickness of final coating layer can be ob-

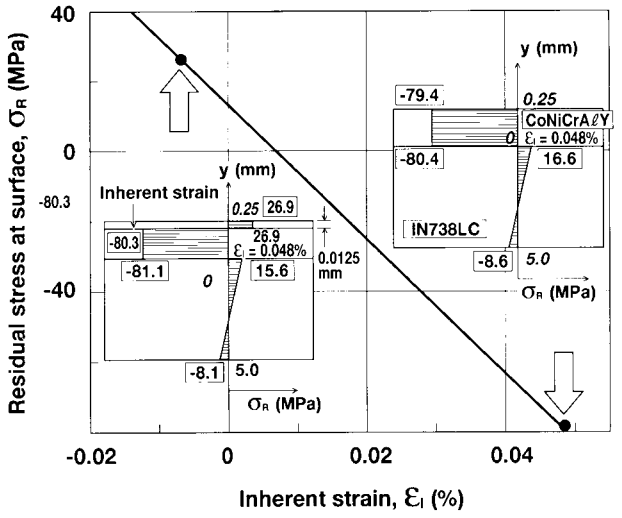

Fig. 13 Estimation of residual stress distribution by the inherent strain caused by thermal shrinkage and peening effect of coating layer

tained by dividing the total coating thickness by the coating passes. The inherent strain at final coating layer is affected by the peening conditions, such as the combustion gas pressure and the poorly melted particle size. The difference of residual stresses between the deflection measurement method and the X-ray method as shown in Fig. 11 can be explained by this consideration. Namely, it might be thought that the residual stresses of HVOF coatings was reduced by the peening effect in comparison with the APS coatings.

Conclusions

In case of the HVOF system, the microstructure revealed even the as-sprayed that coatings was very dense with low oxide content, as normally found in plasma sprayed coatings in open air. This caused concern since there are a lot of poorly melted particles in the HVOF coating. It is clear from these observation that HVOF guns produce high particle velocities (or kinetic energy), which are considerably higher than the other commercial thermal spraying systems. Furthermore, the diffusion heat treatment after thermal spraying transforms the coating layer into uniform microstructure with two predominant phases, which are made up of a lot of the precipitated aluminum metallic compounds and CoCr (or NiCoCr) solid-solution matrix. As a matter of course, the poorly melted particles can't be discriminated. And the diffusion heat treatment of the HVOF coatings reduced a fair amount of porosity (>3 percent). From the view point of porosity, it can be said that the HVOF system is a match for the VPS system.

Next, in case of as-sprayed coatings by the HVOF system, the Young's modulus and the bending strength of HVOF MCrAlY coatings were inferior in comparison with the VPS MCrAlY coatings. Some spherical particles, that were $20 \sim 50$ μm in diameter, could be observed in the cross-section of as-sprayed coating. However, the experimental results suggested that the Young's modulus and the bending strength of the HVOF MCrAlY coatings could be improved up to the level of the VPS MCrAlY coatings by the diffusion heat treatment. These phenomena could be considered by the reason that the HVOF MCrAlY coating was built up by poorly melted particles. When the uniform microstructure can be obtained by the diffusion heat treatment, it is recognized that there is no difference of the bending strength between the HVOF and the VPS MCrAlY coatings. On the other hand, the significant difference for Vickers hardness of coatings sprayed by HVOF and VPS systems could not be observed even as-sprayed coatings. It seems that the crack like pores that exists in the HVOF MCrAlY coatings do not affected on the Vickers hardness, though they affected on the strength and the Young's modulus. Moreover, the Vickers hardness of heat-treated HVOF MCrAlY coatings shows high value in comparison with the VPS MCrAlY coatings. It is thought that this is caused by the HVOF process for own sake, such as carbonizing of some elements in MCrAlY coatings from the kerosene + oxygen fuel.

According to the temperature rise during thermal spraying, the HVOF system revealed high temperature in comparison with the APS system. This means the high deposit efficiency of HVOF system due to very high particle velocity. It was clear that the surface temperature and the displacement became high values with increasing the combustion gas pressure, which equates to the sprayed particle velocity. The deformation behavior of cantilever beam is strongly affected by the peening effect due to the poorly melted particles, not by the temperature rise that causes to the concave deformation. In case of combustion gas pressure 483 kPa, a lot of poorly melted particles could be observed in the coating layer. The residual stress characteristics were analyzed using the deflection measurement method and the X-ray method. It was confirmed that the residual stresses of HVOF coatings was reduced by the peening effect in comparison with the plasma spray system in air. And the generating mechanism of residual stresses was investigated from the measurement results of deflection of cantilever beam specimens during the HVOF spraying. It was confirmed that the residual stress of HVOF coatings was reduced by the peening effect in comparison with the APS coatings.

References

Clark, R., Barbezat, G., Keller, S., and Nicoll, A. R., 1995, "A Review of HVOF System Process Considerations for Optimizing Coatings in Turbo-Machinery," Proceedings, 14th Inter. Thermal Spray Conf., JPN, pp. 1173–1178.

Gill, S. C., and Clyne, T. W., 1990, "Stress Distribution and Material Response in Thermal Spraying of Metallic and Ceramic Deposits," *Metallurgical Transactions*, B, 21B, pp. 377–385.

Grunling, H. W., Schneider, K., and Singheiser, L., 1987, "Mechanical Properties of Coated Systems," *Materials Science and Engineering*, Vol. 88, pp. 177–189.

Irons, G., 1992, "Higher Velocity Thermal Spray Proceeese Produce Better Aircraft Engine Coatings," paper presented at 28th Annual Aerospace/Airline Plating & Metal Finishing Forum & Exposition, CA, SAE Paper 920947.

Irons, G., and Zanchuk, V., 1993, "Comparison of MCrAlY Coatings Sprayed by HVOF and Low Pressure Processes," Proceedings, 1993 National Thermal Spray Conferences, CA, pp. 191–196.

Ishiwata, Y., Saitoh, M., and Itoh, Y., 1995, "Coating Design and Evaluation of High-Temperature Strength," Proceedings, 1995 Yokohama International Gas Turbine Congress, 95-Yokohama-IGTC-71, pp. 99–106.

Itoh, Y., Saitoh, M., and Miyazaki, M., 1994, "Mechanical Properties of Low-Pressure-Plasma Sprayed MCrAlY Coatings," *J. Soc. Mat. Sci. Japan*, Vol. 43, pp. 690–695.

Kuroda, S., and Clyne, T. W., 1991, "The Quenching Stress in Thermally Sprayed Coatings," *Thin Solid Films*, Vol. 200, pp. 49–66.

Mevrel, R., 1989, "State of the Art on High-Temperature Corrosion-Resistant Coatings," *Materials Science and Engineering*, Vol. A120, pp. 13–24.

Nestler, M. C., Hohle, H. M., Balbach, W. M., and Koromzay, T., 1995, "Economical Advantages of HVOF-Sprayed Coatings for the Land Based Gas Turbine Industry," Proceedings, 14th International Thermal Spray Conference, JPN, pp. 101–106.

Parker, D. W., and Kunter, G. L., 1994, "HVOF Moves Into the Industrial Mainstream," *Advanced Material & Processes*, Vol. 146, No. 1, pp. 31–35.

Russo, L., and Dorfman, M., 1995, "High Temperature Oxidation of MCrAlY Coatings Produced by HVOF," Proceedings, 14th International Thermal Spray Conference, JPN, pp. 1179–1184.

Stoney, G. G., 1909, "The Tension of Metallic Films Deposited by Electrolysis," *Surface Engineering*, Vol. 16-1, pp. 172–175.

Veys, J. M., and Mevrel, R., 1987, "Influence of Protective Coating on the Mechanical Properties of CMSX-2 and Contac784," *Materials Science and Engineering*, Vol. 88, pp. 253–260.

Wood, M. I., 1989, "Mechanical Interaction Between Coatings and Super Alloys Under Condition of Fatigue," *Surface and Coating Technology*, Vol. 39/40, pp. 29–42.

Cyclic Oxidation Behavior of Aluminide, Platinum Modified Aluminide, and MCrAlY Coatings on GTD-111

N. S. Cheruvu

K. S. Chan

G. R. Leverant

Electric Power Research Institute,
Materials Center for Combustion Turbines at
Southwest Research Institute,
6220 Culebra,
San Antonio, TX 78238-5166

Cyclic oxidation behavior of aluminide, platinum modified aluminide, and MCrAlY coatings has been investigated at three temperatures. Aluminide and platinum modified coatings were deposited on GTD 111 material using an outward diffusion process. CoCrAlY coating was applied on GTD-111 by Electron Beam Physical Vapor Deposition (EB-PVD). The oxidation behavior of these coatings is characterized by weight change measurements and by the variation of β phase present in the coating. The platinum modified aluminide coating exhibited the highest resistance to oxide scale spallation (weight loss) during cyclic oxidation testing. Metallographic techniques were used to determine the amount of β phase and the aluminum content in a coating as a function of cycles. Cyclic oxidation life of these coatings is discussed in terms of the residual β and aluminum content present in the coating after exposure. These results have been used to calibrate and validate a coating life model (COATLIFE) developed at the Material Center for Combustion Turbines (MCCT).

Introduction

The hot section components of advanced land based turbines operate at severe operating conditions—high thermal stresses and temperatures. Higher operating temperatures play a dominant role in the material and coating degradation, which in turn, adversely affects the service life of these components. The turbine blades are one of the most critical hot section components; thus, reliability and availability of a gas turbine depend on the blade life. Because of the higher operating temperatures encountered in these advanced turbines, the performance and durability of the coating system has now become one of the primary life limiting factors of coated blades.

In the mid 1960s, coatings were introduced in land based turbines to provide hot corrosion protection to superalloy (nickel and/or cobalt base alloy) blades and vanes. Nickel and cobalt base alloys are susceptible to hot corrosion (Type I and II) at the operating metal temperatures ranging from 1150° to 1700°F (621° to 927°C). The severity of hot corrosion increases with temperature up to 1600°F (871°C) and then decreases with temperature. Above 1700°F (927°C), oxidation supersedes hot corrosion. Furthermore, the source of corrodants is fuel and airborne salts carried by inlet air. However, airborne impurities can be prevented from entering into a turbine by effective use of air filters. As a result, hot corrosion problems are typically encountered in turbines that are fired with contaminated fuels. The advanced turbines are primarily fired with relatively clean natural gas and operate at higher temperatures. Degradation of coatings due to oxidation is the primary concern in these designs.

Coatings used on Row 1 and Row 2 turbine blades vary from one manufacturer to the other, but the generic types are similar and fall into three groups: aluminide, platinum modified aluminide (Pt-Al), and MCrAlY with or without an over aluminized layer. As part of an EPRI funded program, data on various coatings are being generated to calibrate and validate a coating life model developed at the MCCT (Chan et al., 1997). The objective of this program is to use the COATLIFE model to determine the coating refurbishment intervals for turbine blades and vanes. The results generated on aluminide, Pt-Al, and CoCrAlY coatings are presented in this paper. Post-test metallurgical evaluations were also performed on the specimens to understand degradation of these coatings due to exposure to thermal cycles at different temperatures.

Experimental Procedure

Specimen Geometry and Test Materials. Flat rectangular test specimens (30 × 15 × 1.5 mm) were machined from the shank section of a fully heat treated GTD-111 turbine blade using an electro discharge machining process. The specimens were ground and polished to remove the recast layer. GTD-111 has a nominal composition by weight: C 0.1%, Cr 14.0%, W 3.8%, Co 9.5%, Mo 1.5%, Al 3.0%, Ti 4.9% and Ta 2.8%. The heat treatment for GTD-111 blades consists of a partial solution treatment at 2050°F (1221°C) for two hours followed by aging at 1550°F (843°C) for 24 hours (Embley and Kallianpur, 1985).

Coating Application. Aluminide and Pt-Al coatings were applied on the test specimens using an outward diffusion process. The process is described elsewhere (Shankar, 1988; Smith and Boone, 1990). For Pt-Al coating application, the specimens were electroplated with approximately a 10 μm thick platinum plating prior to the aluminizing process. The CoCrAlY coating was applied using the Electron Beam Physical Vapor Deposition (EB-PVD) process.

Cyclic Oxidation. Tests were performed using a facility designed and fabricated at SwRI. This test facility consists of a furnace, a forced air cooling system, and a computer controlled moving arm that transfers specimens in and out of the furnace and to the cooling system. For cyclic oxidation tests, the specimens were inserted in a furnace that was maintained at the temperature of interest, and held in that furnace at that temperature for 55 min prior to moving them to the cooling system. The specimens were then cooled by forced air for 5 min prior to re-inserting them into

Contributed by the International Gas Turbine Institute (IGTI) of The American Society of Mechanical Engineers for publication in the ASME Journal of Engineering for Gas Turbines and Power. Paper presented at the International Gas Turbine and Aeroengine Congress and Exhibition, Stockholm, Sweden, June 2–5, 1998; ASME Paper 98-GT-468.

Manuscript received by IGTI March 24, 1998; final revision received by the ASME Headquarters October 20, 1999. Associate Technical Editor: R. Kielb.

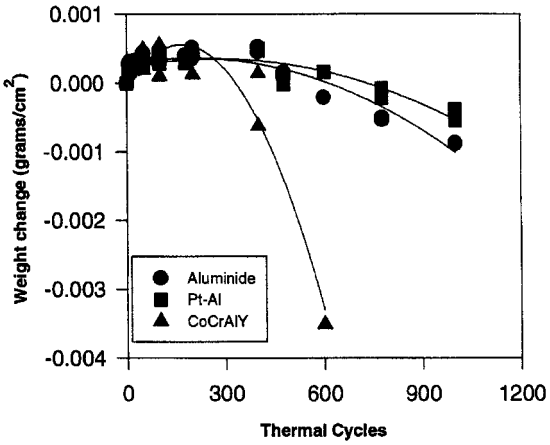

Fig. 1 Cyclic oxidation behavior of aluminide, Pt-Al and CoCrAlY coatings at 1950°F (1065°C)

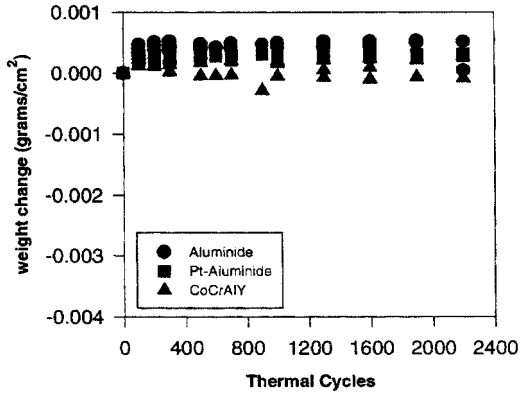

Fig. 3 Cyclic oxidation behavior of aluminide, Pt-Al and CoCrAlY coatings at 1750°F (954°C)

the furnace. The specimens took approximately four minutes to reach the test temperature and one minute to cool from the test temperature to room temperature. The tests were conducted at 1950°F (1065°C), 1850°F (1010°C), and 1750°F (955°C). Multiple specimens of each coating were tested at each temperature. Cyclic oxidation tests were interrupted periodically to weigh the specimens, and a specimen of each type of coating was removed from the test at predetermined cycles for post-test metallurgical evaluation. These specimens were sectioned and examined by optical and scanning electron microscopy to evaluate coating degradation. The composition of the phases in the coatings were determined using energy dispersive spectroscopy (EDS).

Results

As-Coated Microstructure. A specimen from each coating was sectioned in the as-coated condition to determine microstructure and coating thickness. The aluminide and Pt-Al coated specimens exhibited a single phase (β-NiAl) structure, while the CoCrAlY coated specimen exhibited approximately 50% β (CoAl-precipitates) and 50% γ (matrix). The γ phase is a solid solution of primarily cobalt and chromium. Thickness of aluminide, Pt-Al, and CoCrAlY coatings ranged from 1.0 to 1.8 mils, 2.0 to 3 mils, and 9.0 to 10 mils, respectively. The chemistry of these coatings was determined at three locations on each specimen; the top, the middle, and the bottom of the layer of each coating. The average chemistry of the coatings in weight percent is as follows:

Aluminide: 29.5% Al, 2.8% Cr, 7.0% Co, 0.7% Ti, 57.5% Ni, 0.4% Mo, and 2.4% Ta

Pt-Al: 19.9% Al, 4.1% Cr, 5.7% Co, 2.0% Ti, 51.2% Ni, 0.3% Mo, 2.9% Ta, and 15% Pt

CoCrAlY: 9.9% Al, 24.5% Cr, 60.3% Co, and 2.5% Ni

Cyclic Oxidation. Weight change of aluminide Pt-Al and CoCrAlY coated specimens as a function of thermal cycles at 1950°F (1065°C) is presented in Fig. 1. As expected, all these specimens initially gained weight due to formation of a protective

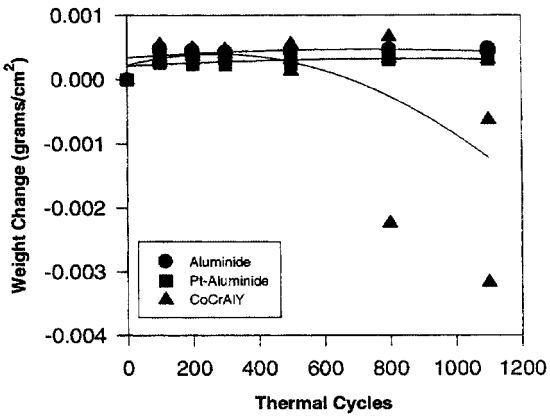

Fig. 2 Cyclic oxidation behavior of aluminide, Pt-Al, and CoCrAlY coatings at 1850°F (1010°C)

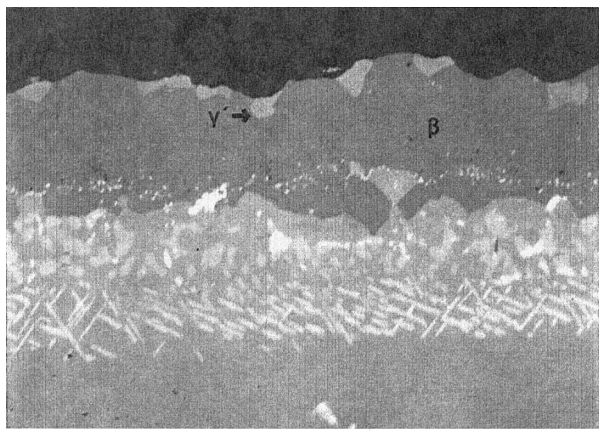

(a)

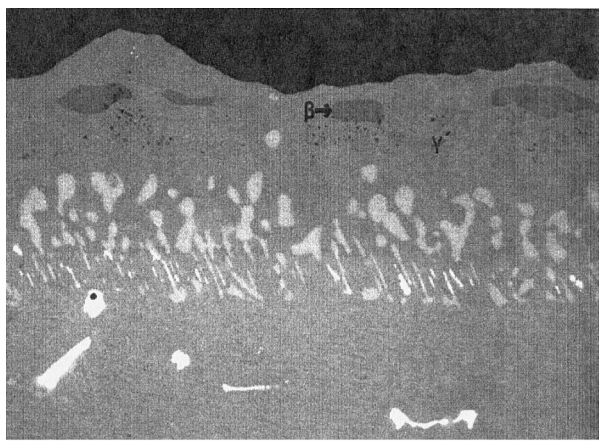

(b)

Fig. 4 β-phase variation in aluminide coating after exposure at 1950°F (1065°C) for (*a*) 400 cycles and (*b*) 1000 cycles

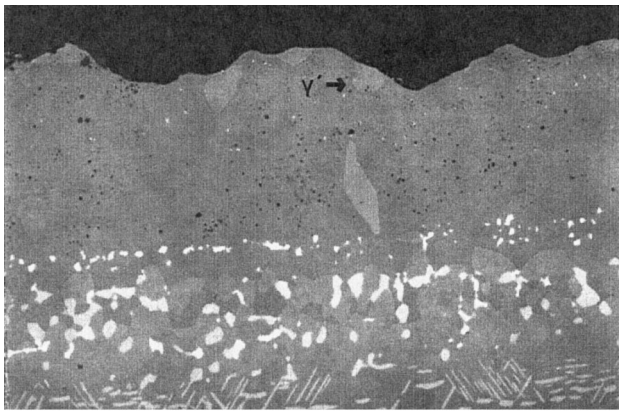

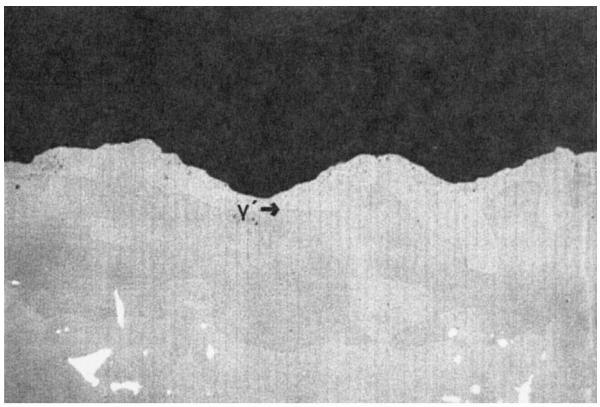

Fig. 5 *β*-phase variation in the Pt-Al coating after exposure at 1950°F (1065°C) for (*a*) 400 cycles and (*b*) 1000 cycles

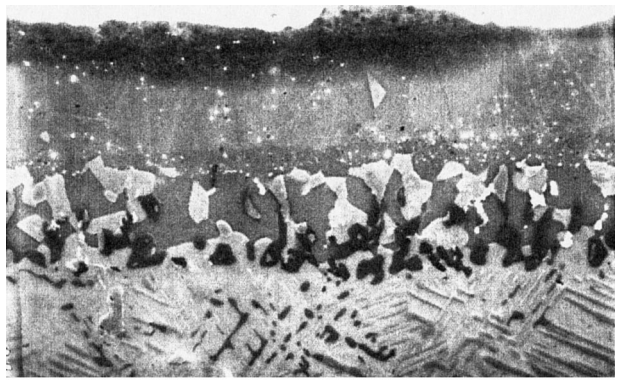

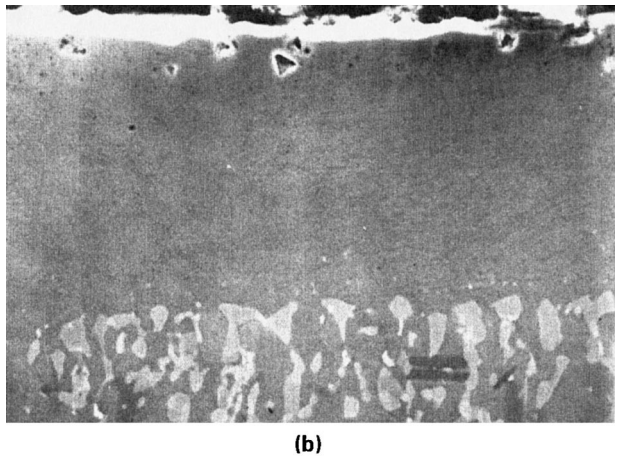

Fig. 7 Microstructure of aluminide and Pt-Al coatings after 1600 cycles at 1750°F (954°C)

oxide scale with thermal cycles, up to approximately 400 cycles for aluminide and Pt-Al coatings, and 200 cycles for CoCrAlY, reached a maximum value and the specimens then lost weight with increasing cycles, due to oxide spallation. The weight loss results show that Pt-Al offers slightly better resistance than aluminide coating. However the variation in weight loss results between the Pt-Al and aluminide coatings is not statistically significant. However, the CoCrAlY coating showed the least resistance among three coatings investigated.

Figure 2 shows weight change data of coatings as a function of thermal cycles at 1850°F (1010°C). The aluminide and Pt-Al coated specimens gained weight; no evidence of protective oxide spallation was noted among the specimens in 1100 thermal cycles. Weight loss due to oxide spallation was observed in two of three CoCrAlY coated specimens. However, the weight change data for CoCrAlY coated specimens exhibited significant scatter. Weight change data of coatings as a function of thermal cycles at 1750°F (954°C) is illustrated in Fig. 3. All three coatings predominantly gained weight. No evidence of weight loss due to oxide spallation was noted in these specimens which were run for 2200 cycles.

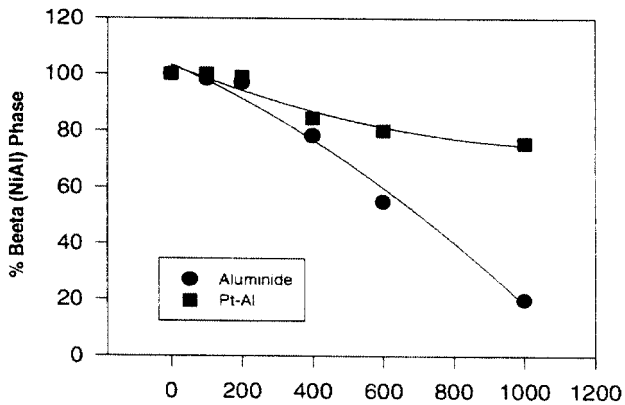

Fig. 6 Volume fraction of β in the aluminide and Pt-Al coatings as function of thermal cycles at 1950°F (1065°C)

Coating Microstructure. As expected, exposure to thermal cycles led to degradation of the microstructure of all three coatings. In the aluminide and Pt-Al coatings, the coating degradation is manifested by transformation of β-NiAl phase into γ'. In the CoCrAlY coating, degradation is manifested by the formation of β-CoAl phase depleted zones at the outer and the coating/substrate interface. The extent of degradation of coatings varied with the number of thermal cycles and the exposure temperature.

Aluminide and Pt-Al Coatings. Degradation of microstructure of aluminide and Pt-Al coatings after exposure to 400 and 1000 thermal cycles at 1950°F (1065°C) is illustrated in Figs. 4 and 5. In both coatings, β-NiAl phase is partly transformed into γ'. The γ' phase was identified based on nickel and aluminum contents, as determined by EDS. Aluminum content in the γ' phase ranged from 8 wt.% to 10 wt.%. In both aluminide and Pt-Al, the β to γ' transformation was greater for the specimen exposed to 1000 cycles than for the one exposed to 400 cycles. Volume fraction of β phase in aluminide and Pt-Al coatings as a function of the number of thermal cycles is presented in Fig. 6. Little or no transformation was noted in the first two hundred cycles in both coatings. As the number of cycles increased, the amount of β

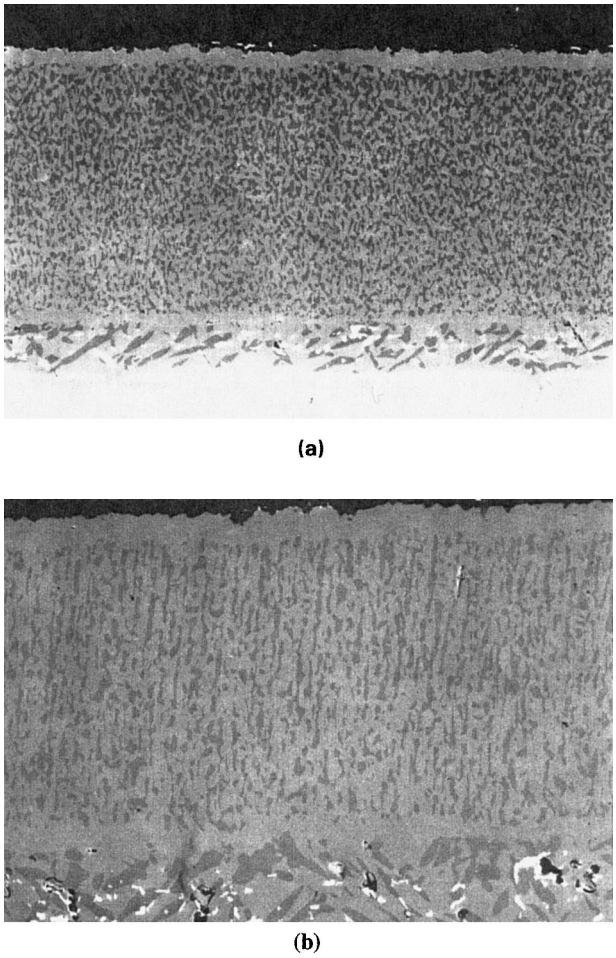

Fig. 8 Influence of exposure to thermal cycles at 1950°F (1065°C) on the width of β depleted and interdiffusion zones in the CoCrAlY coating after (*a*) 400 cycles and (*b*) 1000 cycles

phase decreased in both coatings. After 1000 cycles, the β phase content in the aluminide and Pt-Al coatings was reduced to 20 percent and 80 percent, respectively. For a given number of thermal cycles, the β to γ' transformation was more severe for the aluminide coating than for Pt-Al. Since β phase acts as a reservoir for aluminum, cyclic oxidation life of a coating is directly related to the amount of β phase present in the coating and thickness of the coating. Hence, these results show that the aluminide coating exhibits less cyclic oxidation resistance than Pt-Al. The Pt-Al would be capable of providing oxidation protection for several thermal cycles at this temperature.

Microstructure of aluminide and Pt-Al coatings after 1600 thermal cycles at 1750°F (954°C) is shown in Fig. 7. Consistent with the weight change results presented in the previous section, both aluminide and Pt-Al coatings have shown little or no evidence of degradation.

CoCrAlY Coating. Thermal exposure at 1950°F (1065°C) resulted in formation of β phase depleted zones at the outer surface of the coating and at the coating/substrate interface (Fig. 8). In addition, the width of the interdiffusion zone below the coating also increased due to inward diffusion of aluminum into the substrate during thermal exposure. The width of the β phase depleted zones increased with increasing number of cycles, and the β phase particles coarsened. As the number of cycles increased from 400 to 600, the volume fraction of the β phase decreased from 48.5 percent to 39.0 percent.

Similar coating degradation results were observed in the specimens exposed to 1850°F (1010°C) and 1750°F (954°C). However, the depleted zone widths were significantly smaller in these specimens.

Discussion

It is well known that both diffusion (aluminide and Pt-Al) and overlay (CoCrAlY) type coatings protect the substrate blade alloy against oxidation and corrosion by forming a protective-surface oxide layer. The β-NiAl or CoAl phase in these coatings acts as a reservoir, which provides aluminum for the formation of the protective oxide layer. As the protective oxide spalls during thermal cycling, aluminum in the coating diffuses outward to re-form the oxide layer at the surface. Aluminum also diffuses into the substrate alloy due to the composition gradient between the coating and the substrate. As a result, the coatings degrade due to inward and outward diffusion of aluminum present in the coatings. Inward and outward diffusion of aluminum leads to transformation of the β-NiAl phase into γ' or γ phase in aluminide and Pt-Al coatings. The extent of transformation, however, depends on the test temperature and number of thermal cycles. The higher the test temperature and/or the larger the number of thermal cycles accelerates transformation.

The present test results show that the β-phase in both aluminide and Pt-Al coatings was partly transformed into γ' as a result of thermal exposure. No evidence of γ phase was noted in the coating microstructure of the test specimens. However, Cheruvu and Leverant (1998) have reported that the β phase in the overaluminized layer transformed into γ, containing 3 wt.% aluminum, in a service run GT29+ coated GTD-111 blade after 25,834 hours of operation. A comparison of present results with the in-service degradation results suggests that long term tests will result in loss of aluminum in the γ' phase, which will lead to transformation of γ' into γ in these coatings. This suggests that even if the β phase completely transforms into γ', the latter phase will act as a reservoir for aluminum and will provide aluminum to reform the protective oxide layer.

CoCrAlY coatings also degrade due to inward and outward diffusion of elements. The diffusion of elements, in particular aluminum, results in dissolution of β phase particles at the outer surface of the coating and the coating/substrate interface, leading to the formation of β phase depleted zones in the coating (Daleo and Boone, 1997 and Srinivasan et al., 1995). As a result of exposure, nickel in the substrate also diffuses into the CoCrAlY coating. In addition to aluminum, cobalt and chromium in the coating also diffuse into the substrate. The outward diffusion of nickel from the base metal into the coating and inward diffusion of aluminum, cobalt, and chromium from the coating into the substrate results in coarsening of platelet precipitates in the interdiffusion zone and an increase in the width of this zone. Since diffusion is a thermally activated process, the widths of the depleted zones in the coating and the interdiffusion zone below the coating depend on the exposure temperature and time. The change in the width of the depleted zones and the interdiffusion zone are used to estimate operating temperature of service run blades (Srinivasan et al., 1995; Cheruvu and Leverant, 1998).

Though the weight change results showed an excessive weight loss after exposure to 600 thermal cycles at 1950°F (1065°C), only a small fraction of the original coating had degraded. The coating contained 39 percent β phase after exposure, suggesting that the cyclic oxidation life of the coating was not exhausted. The coating would be capable of surviving for many more thermal cycles at this temperature. For ranking coatings, consideration of weight change results, alone, may lead to an erroneous conclusion since these results are independent of coating thickness variations. Both weight change and post test metallurgical evaluation results need to be considered for ranking coatings. A more accurate indicator of a coating's condition for its residual life estimation is either the aluminum content or the volume fraction of the β-phase. The

volume fraction of this phase is a better measure of the coating's ability to re-form a protective oxide layer.

Conclusions

The following conclusions can be drawn from the results of this investigation:

- Loss of aluminum due to spallation and reformation of a protective-surface oxide layer during the cyclic oxidation testing led to transformation of β phase into γ' in both the aluminide and Pt-Al coatings. The extent of transformation was temperature and cycle dependent.
- The β to γ' transformation was more severe for the aluminide than for the Pt-Al coating, suggesting that former coating was less resistant to oxidation.
- Degradation of CoCrAlY coating due to exposure to thermal cycles was evidenced by formation of β-phase depleted zones at the outer surface and at the coating/substrate interface, and by enlargement of the interdiffusion zone.
- The volume fraction of the β-phase in the coating decreased with an increasing number of thermal cycles and/or exposure temperature.
- Though weight change results showed an excessive weight loss after 600 thermal exposure cycles at 1950°F (1065°C), a significant portion of the CoCrAlY coating, containing 39 percent β phase, was in good condition, suggesting that the coating can survive a larger number of cycles.
- Weight change results alone should not be considered for ranking the coatings since these results are not a good measure of the coating's ability to re-form a protective oxide layer.

Acknowledgments

This work was supported by the Electric Power Research Institute (EPRI) under contract WO-3643-01. The authors would like to thank EPRI for giving permission to publish this work. Cyclic oxidation tests were performed by Mr. A. Nagy. Ms. F. Cobia and Ms. M. Searles are thanked for performing microscopy work, and typing the manuscript, respectively.

References

Chan, K. S., Cheruvu, N. S., and Leverant, G. R., 1997, "Coating Life Prediction Under Cyclic Oxidation Conditions," ASME Paper 97-GT-389.

Cheruvu, N. S., Carr, T. J., Dworak, J., and Coyle, J., 1996, "In-service Degradation of Corrosion Resistant Coatings," ASME Paper 96-GT-429.

Cheruvu, N. S., and Leverant, G. R., 1998, "Influence of Metal Temperature on Base Material and Coating Degradation of GTD-111 Buckets," presented at the 1998 ASME Int'l. Gas Turbine and Aero Engine Congress and Exhibition, Stockholm, Sweden.

Daleo, J. A., and Boone, D. H., 1997, "Failure Mechanisms of Coating Systems Applied to Advanced Turbine Components," ASME Paper 97-GT-486.

Czech, N., Schmitz, F., and Stamm, W., 1995, "Thermal Mechanical Fatigue Behavior of Advanced Overlay Coatings," *Materials and Manufacturing Processes,* Vol. 10, pp. 1021–1035.

Embley, G. T., and Kallianpur, V. V., 1985, "Long-Term Creep Response of Gas Turbine Bucket Alloys," Proceedings, Life Prediction of High Temperature Gas Turbine Materials, August 27–30, Syracuse University, New York, V. Weiss, and W. T. Baker, eds., pp. 5–1.

Shankar, S., 1985, "Methods of Forming Protective Diffusion Layer on Nickel, Cobalt, and Iron Based Alloys," U.S. Patent No. 4,525,814.

Smith, J. S., and Boone, D. H., 1990, "Platinum Modified Aluminide-Present Status, ASME Paper 90-GT-319."

Srinivasan, V., Cheruvu, N. S., Carr, T. J., and O'Brien, C. M., 1995, "Degradation of MCrAlY Coating and Substrate Superalloy During Long-Term Thermal Exposure," *Materials and Manufacturing Process,* Vol. 10, pp. 955–969.

Dimensional Instability Studies in Machining of Inconel 718 Nickel Based Superalloy as Applied to Aerogas Turbine Components

B. K. Subhas

R. Bhat

K. Ramachandra

Gas Turbine Research Establishment,
Ministry of Defence C. V. Raman Nagar,
Bangalore, India

H. K. Balakrishna*
University Visvesvaraya,
College of Engineering,
Bangalore, 560001,
India

Inconel 718 alloy is used extensively in aerogas turbines and this alloy is most difficult to machine and highly prone to dimensional instability after machining. Such detrimental phenomenon poses an enormous problem in engine assembly and affects structural integrity. This paper highlights the systematic research work undertaken to study the plastic deformation characteristics of Inconel 718, and the effect of process variables on machined surface, subsurface, and dimensional instability. Also illustrated is the technique developed for simultaneous optimization of several process variables such as cutting speed, feed, depth of cut, rake angle, and tool nose radius to control the residual stresses and dimensional instability within the acceptable tolerance band of the component. Prediction equations were developed for residual stress, dimensional instability, tool life, surface finish, and material removal rate. Predicted data were validated experimentally. This paper also presents the qualitative and quantitative data on dimensional instability with specific case studies of jet engine components, and it clearly illustrates the approach followed to develop a technique to control such detrimental effect.

1 Introduction

The dimensional instability phenomenon is basically a change in dimension with respect to time without doing any further work on it. Two probable causes for dimensional instability have been identified. They are residual stresses and metallurgical alterations introduced by the machining processes. The primary and secondary machining process leads to surface layer changes such as a series of metallurgical changes, plastic deformation, and residual stresses, etc., which effect the surface integrity and results in dimensional instability of the finished part. The magnitude of the residual stresses and metallurgical alterations introduced during the machining process depends on the machinability parameters like speed, feed, depth of cut, cutting tool material and geometry, cutting fluid, etc. Normal practice in industry is to carry out the thermal stress relieving process to reduce the effect of residual stresses on dimensional instability at the machining stage.

The thermal stress relieving process is not supposed to change the properties or hardness of material, but, unfortunately, there is no stress reliving cycle for Inconel 718 alloy other than following with the solutionizing process, which changes the properties and hardness. Also, only a limited aging process is permitted on this material to avoid alloy degradation. This metallurgical restriction compels to control the residual stress by controlling the machinability parameters, which are the influencing factors for the introduction of residual stress. Therefore, dimensional instability could be controlled by understanding the metallurgy of Inconel 718, plastic deformation characteristics of Inconel 718, effect of process variables on machined surface and subsurface, and finally by controlling machinability parameters. Two aspects of the studies related to dimensional instability have been presented here. First is the plastic deformation characteristics of Inconel 718 and the effect of process variables on machined surface and dimensional instability; the second one is simultaneous optimization of various process parameters to control the dimensional instability.

A few studies on dimensional instability have been reported in the literature. Marschall and Maringer [1] have reported the various aspects of dimensional instability. According to them the major causes for a dimensional instability are the residual stress effects and metallurgical alteration. Israeli and Bendeck [2] have reported the instability parameters for machined parts. They also emphasized the effect of residual stress distribution on dimensional instability. They defined the specific instability potential as a parameter for specifying process operations. Komanduri et al. [3] reported that highly localized shear stress/strain and temperature in machining of Inconel 718 alloy produces the shear instability. Whereas Marschall [4] and Meyerson et al. [5] have studied the general effect of micro-structural changes on dimensional instability. Although they have not made any specific study on Inconel 718 alloys, they have emphasized the various mechanisms by which material may undergo dimensional changes as a result of internal changes at the micro-structural level. A few more researchers [6–7] have also reported the dimensional instability effect due to residual stress during the machining on conventional steel, but not on Inconel 718 superalloys. Subhas et al. [8] reported dimensional instability phenomenon on titanium alloys, but not on Inconel 718. The studies conducted by Subhas [9] on other nickel based superalloys like Nimonie-90 and Inconel 901 reveal no appreciable dimensional instability phenomenon. The literature review indicates that no systematic comprehensive studies have been reported on dimensional instability phenomenon of Inconel 718 alloy. The present work is therefore planned to study the plastic deformation characteristics of Inconel 718, and the effect of process variables on machined surface and dimensional instability in machined jet engine components.

Contributed by the International Gas Turbine Institute (IGTI) of THE AMERICAN SOCIETY OF MECHANICAL ENGINEERS for publication in the ASME JOURNAL OF ENGINEERING FOR GAS TURBINES AND POWER. Paper presented at the International Gas Turbine and Aeroengine Congress and Exhibition, Stockholm, Sweden, June 2–5, 1998; ASME Paper 98-GT-469.

Manuscript received by IGTI March 24, 1998; final revision received by the ASME Headquarters October 20, 1999. Associate Technical Editor: R. Kielb.

*Currently Dean, Sir M. Visvesvarayya Institute of Technology, Bangalore-562 157.

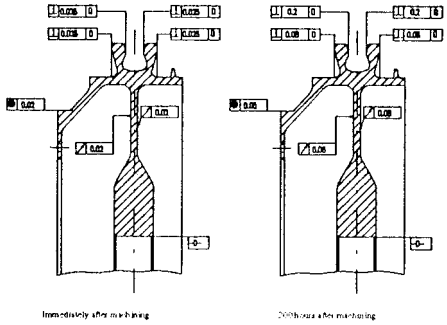

Fig. 1 Dimensional instability in IV stage compressor disc

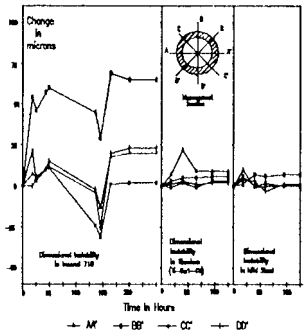

Fig. 2 Dimensional instability of Inconel 718, titanium alloy and mild steel

The second part of the study is related to optimization of machinability parameters to control the dimensional instability. Most of the studies reported on optimization of machinability parameters, are limited to speed, feed, and depth of cut by varying one parameter at a time with optimization criteria of maximum production rate and minimum cost. They generally followed Taylor's tool life equation for optimization. These methods do not consider the inter-related effect of machinability parameters, and are likely to be error-prone. Jose, et al. [10] and others [11–14] used the statistical method for the design of the experiment and optimization. This method considerably reduces the number of experiments and statistically accurate. Wu [11] applied response surface methodology for optimization of tool life. He fitted first and second-order equations and tested for adequacy, where as Albuelenga et al. [12] developed mathematical models representing metal cutting operations. Similarly, Shin et al. [13] presented a model for optimization of machining conditions. Optimization problem formulated by them is multi-variable nonlinear programming, where as Prasad et al. [14] used a combination of geometric and linear programming techniques. No data are reported to the knowledge of the authors on simultaneous optimization of all machining process parameters along with response functions, especially with criteria of minimum-residual stress and dimensional instability for application to aerogas turbine components. Although Harrington [15] and Derringer et al. [16] presented an approach of desirability function and simultaneous optimization for rubber industry application, such an approach is not followed for machining parameter optimization. Therefore, a simultaneous optimization technique is developed in this study to generate qualitative and quantitative data on optimum machinability parameters with criteria of least residual stress and dimensional instability as applied to aerogas turbine components.

2 Validation of Dimensional Instability Phenomenon

Although dimensional instability was experienced extensively on jet engine components (e.g., compressor disc shown in Fig. 1), for a better understanding and to validate the existence of dimensional instability problem, experimental studies were carried out by machining the ring-shaped specimen made of Inconel 718 alloy in a fully heat-treated condition.

Similar test specimens were machined out of titanium (Ti-6Al-4V) alloy and mild steel at identical machining conditions of Inconel 718 specimen, dimensional changes were measured with respect to time up to 220 hours after machining, the test results are presented in graphical form in Fig. 2.

Traditionally, titanium alloys are more prone to dimensional instability due to low modulus of elasticity, where, as the experimental values show, Inconel 718 is more prone to dimensional instability than titanium alloy, but this phenomenon was not noticed in other nickel based alloys. This experiment validates the existence of dimensional instability effect in Inconel 718.

3 Investigation on Plastic Deformation Characteristics

The literature review clearly indicates that further investigations are required—on deformation characteristics of Inconel 718—particularly to correlate the metal cutting variables, chip morphology, and their effect on structural phase transformation, residual stress, and dimensional instability. Therefore, experimental studies were carried out to investigate the following aspects of plastic deformation characteristics:

1 effect of machinability parameters on chip morphology
2 effect of cutting variables such as length of shear plane, tool geometry, etc. on pattern of residual stress
3 effect of direct machinability parameters on plastic deformation and resulting residual stresses

3.1 Experimental Setup and Procedure. The experimental procedure involved in the present work is two-fold. Machining experiments and a hole-drilling strain gauge experiment for determining the residual stresses.

3.1.1 Machining Experiment. Machining experiments are carried out to study the effect of machinability parameters on plastic deformation characteristics. The ring-shaped type Inconel 718 specimen machined to *ID* 55 mm and *OD* 76 mm, stress relieved, and aged to hardness 44 HRC was selected for the

Nomenclature

α = rake angle, deg.
d = depth of cut, mm
d_i = desirability of response variable
DIMI = dimensional instability, μm
f = feed, mm/rev
ID = inner diameter, mm
MRR = metal removal rate, mm^3/min
OD = outer diameter, mm
r = tool nose radius, mm
R_a = surface roughness, μm
σ_c = circumferential residual stress, MPa
σ_l = longitudinal residual stress, MPa
T = tool life, min
v = cutting speed, m/min
y = variable representing response variables
y_c = central value of response variable

Subscripts

max = indicating maximum value
min = indicating minimum value

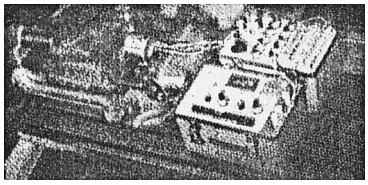

Fig. 3 Experimental set up for hole drilling method of residual stress measurement

machining experiment. The machining experiments were carried out on horizontal lathe. The specimen was held in mandrel to avoid clamping pressure. Kennametal-brazed-type carbide tools of K-68 grade ground to suitable tool geometry are used in machining experiments. The cutting fluid used is soluble oil (1:20). For every set of cutting parameters, chips were collected. Optical micrographs of the machined surface and the longitudinal midsection of the chips were taken. The dimensions of the specimen were measured on OD at a predetermined distance on the Mauser three-dimensional co-ordinate measuring machine. The dimensional instability is determined by taking measurements immediately after machining and after 200 hours or more. Tool flank wear and contact length at chip-tool interface are measured using a tool maker's microscope. A portable perthometer is used to measure the surface finish. Cutting forces were measured using Kistler 3 component tool force dynamometer.

3.1.2 Hole Drilling Strain Gauge Experiment. The experiment is carried out as per ASTM standard test method E 837 [17]. A special three-element strain gauge rosette (Measurement Group type A06-062RE-120) is installed on the machined surface of the test piece at the point where residual stresses are to be determined. The three gauge grids are wired and connected to a static strain indicator P-3000 thorough a switch and balance unit SB-10 of Measurement Group Inc., USA. A precision milling guide model RS-200 is attached to the test part and accurately centered over the drilling target on the rosette. After zero-balancing the gage circuits, a small shallow hole is drilled through the center of the rosette using a carbide cutter run by a high-speed air turbine unit. Relaxed strains are read for each predetermined incremental depth. The experimental setup and the close-up view of the gauge installed on the specimen are shown in Fig. 3 and Fig. 4.

3.2 Results and Discussion. Optical microscopic examination of the longitudinal midsection of chips produced at various speeds ranging from 10 m/min to 38 m/min show that there is a considerable deformation twinning. In Fig. 5 twinning can be seen in the deformed regions of Inconel 718 chips. Figure 6 also shows that even on the machined surface deformation twinning is noticed. This kind of deformation twinning is not generally the prevalent mode in machining other conventional steels and high temperature alloys [3]. Komanduri et al. [3] also observed similar phenomenon in Inconel 718 machined at a cutting speed of 100 m/min and titanium alloy machined up to 260 m/min. Their comparative studies of shear instability in machining of Inconel 718 and Ti-6Al-4V alloy show that the role of limited slip in the case of Ti-6Al-4V alloy can be considered to that of precipitates in Inconel 718. The higher resistance to deformation of Inconel 718 probably

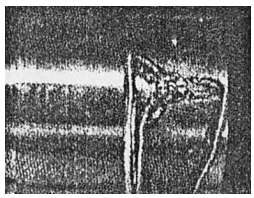

Fig. 4 Test specimen with strain gauge rosette mounted on it

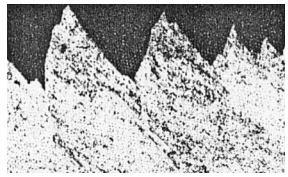

Fig. 5 Optical micrograph of longitudinal mid section of the chip (Magnification: 500×)

balances the slightly poor thermal properties of Ti-6Al-4V alloy. An h.c.p. structure titanium alloy provides limited slip and a f.c.c. structure material strengthened by precipitation phase (b.c.t.), such as Inconel 718, resist deformation up to high temperature. The experimental results show that shear localized chips formed with Inconel 718 were similar to the chips generated with titanium Ti-6Al-4V alloy [3].

The analysis of experimental results confirms that the primary deformation process of Inconel 718 is similar to titanium alloy; therefore, Inconel 718 also behaves in a similar way to titanium alloys in dimensional instability. However, the experimental results presented in Fig. 1 show that the magnitude of dimensional instability is more in Inconel 718 than titanium. This may be attributed to the presence of γ'' phase in Inconel 718, whereas a similar phenomenon was not noticed in other nickel based superalloys like Nimonic-90, Inconel-901 which are not precipitate strengthened with the presence of γ'' phase. This is very interesting observation resulted from this experimental investigation and analysis.

The analysis of experimental results related to studies on the influence of machinability parameters on plastic deformation mechanism resulting in residual stresses gives very interesting findings. Figure 7 shows experimental results on the effect of rake angle on residual stresses. The negative rake angle increases the residual stress, and the positive rake angle decreases the residual stress. These observed phenomena are logically correct because as the rake angle increases, shear angle increases, shear plane length decreases, cutting force decreases, and shear stress and strain decreases. Thus, the residual stresses decrease. These observations are further strengthened from experimental results presented in Fig. 8. The experiential results shown in Fig. 9 indicate that as the chip tool contact length decreases, the cutting forces decrease, that is, reduction in chip tool contact length reduces the plastic strains and the residual stresses. Figure 10 and Fig. 11 show the residual stress distribution for two different sets of cutting parameters. It is shown that the greater the distance from the machined surface, the lesser the amount of plastic deformation that occurs. Thus, the

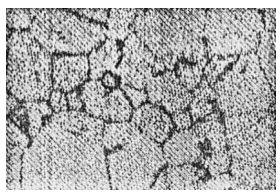

Fig. 6 Optical micrograph of machined specimen (Magnification: 500×)

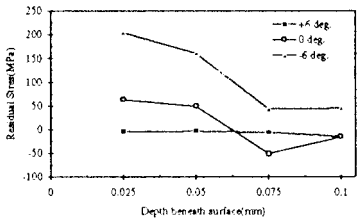

Fig. 7 Effect of rake angle on residual stress distribution (v = 13 m/min, f = 0.04 mm/rev, d = 0.5 mm)

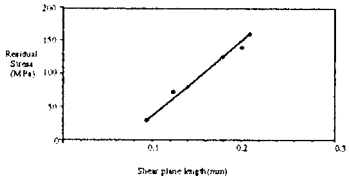

Fig. 8 Residual stresses in cutting direction versus shear plane length

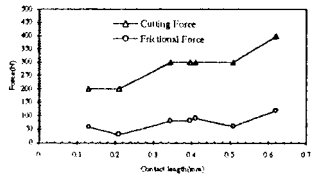

Fig. 9 Cutting Force and Frictional force versus Contact length

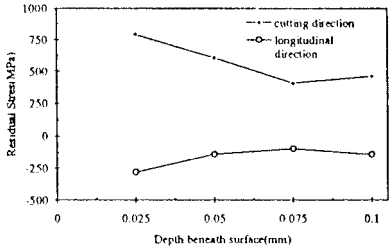

Fig. 10 Residual stress distribution (v = 32 m/min, f = 0.13 mm/rev, d = 1.0 mm, α = −6 deg)

lesser are the residual stresses. It is also clear that residual stresses in the cutting direction are more tensile than that in the longitudinal direction. This is qualitatively in agreement with results reported in [18].

Figure 12 shows the effect of feed on residual stress distributions. At the lower feeds, the surface residual stresses are compressive, but at the higher feeds they are tensile. The results obtained are consistent with that reported in [18]. The effect of depth of cut on the residual stress distribution is shown in Fig. 13. As the depth of cut increases, the volume of material being removed increases, which requires higher cutting energy to be expended. Therefore, the surface residual stresses increased with the depth of cut. The residual stress magnitude is the highest in Fig. 10. The cutting parameters used in this case is such that the combined effect of negative rake angle, higher feed rate, and depth of cut introduced a larger magnitude of stresses of mechanical origin. In addition, this higher cutting speed introduces stresses of thermal origin due to higher temperatures at the cutting region. This is responsible for the higher magnitude of surface residual stresses.

These investigations on plastic deformation aspects of Inconel 718 alloy clearly indicate that direct machinability parameters significantly influence the magnitude of residual stresses and residual stresses are primarily responsible for the dimensional changes. Hence, by optimization of machinability parameters, dimensional instability could be controlled. Therefore, a new methodology for optimization of machining process has been developed.

4 Optimization of Machining Process Parameters

This part of the study is related to the development of process parameter optimization technique to control the dimensional changes within the acceptable limits. An attempt is made to establish the appropriate technique to arrest this dimensional instability and to validate the established techniques experimentally.

4.1 Methodology. The steps involved in the proposed method are as follows:

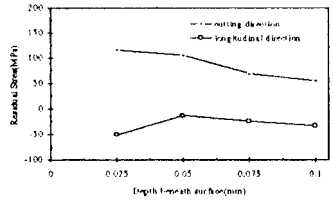

Fig. 11 Residual stress distribution (v = 13 m/min, f = 0.13 mm/rev, d = 1.0 mm, α = +6 deg)

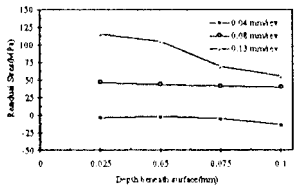

Fig. 12 Effect of feed on residual stress distribution (v = 13 m/min, d = 0.5 mm, α = 6 deg)

1 selection of machining process variables
2 design of statistical experiment
3 determination of predicting equation for the response functions such as residual stresses, tool life, surface finish and dimensional instability using response surface methodology and adequacy tests for the predicted equations
4 computation of machinability parameters such as cutting speed, feed, depth of cut, rake angle and tool nose radius by iterative search method for optimum combination of the responses using desirability function approach.

4.2 Selection of Process Variables. Most of the critical gas turbine components are axisymmetric in geometry; therefore, the turning process is used in this research work. The turning process variables such as speed, feed, depth of cut, rake angle, tool nose radius, side cutting edge angle, cutting tool material, and cutting fluids have varying degrees of influence on the residual stress. Of these, side cutting edge angle does not have significant influence. Already optimized data are available on the selection of cutting fluid as soluble oil (1:20) and cutting tool material as micro grain carbide for machining of nickel based superalloys [9]. Hence, these data are chosen form literature. In view of this, only five process variables-cutting speed, feed, depth of cut, nose radius and rake angle were chosen for optimization. The maximum and minimum levels were selected taking into account the recommended range of practical machining conditions used in finish machining of Inconel 718 as shown in Table 1.

4.3 Statistical Design of Experiment. The present investigation involves the study of the influence of speed, feed, depth of cut, rake angle, and tool nose radius on response properties namely residual stress, tool life, surface finish, dimensional instability, and material removal rate. Here the influence of process variables on response properties were assumed to be linear, and, hence, it was sufficient to study each variable at two levels only. The main effect of five factors were studied using half factorial design involving only sixteen experiments.

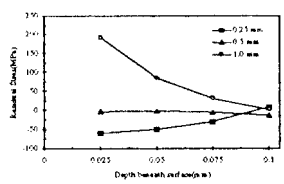

Fig. 13 Effect of depth of cut on residual stress distribution (v = 14 m/min, f = 0.04 mm/rev, α = 6 deg)

Table 1 Recommended range of practical machining conditions

Independent Variables	Maximum (+)	Minimum (-)
v	38	10
f	0.22	0.04
d	1.0	0.25
α	+6	-6
r	1.2	0.4

Experimental Procedure. The experimental procedure followed is same as that followed for the plastic deformation experiment given in the earlier paragraphs. Experimental data generated are given in Table 2. The trial numbers 17 to 20 are used for checking the adequacy of the predicted equations.

4.4 Prediction Equation for Process Responses. The effect of five independent machining parameters during turning operation on residual stress, tool life, dimensional instability, surface finish, and material removal rate were established by multiple regression analysis. The equation fitted is a first order with linear functional relationship. The two levels of independent variables are coded for convenience into -1 (low) and $+1$ (high) by the transforming equations. Typical transforming equations for the variables are of the following form:

$$\frac{2v - (v_{\max} + v_{\min})}{(v_{\max} - v_{\min})} \tag{1}$$

$$\frac{2(\ln v - \ln v_{\max})}{(\ln v_{\max} - \ln v_{\min})} + 1. \tag{2}$$

The transforming Eq. (1) is used for the independent variables when the prediction equations are required in polynomial form, and Eq. (2) is used when the prediction equations are required in exponential form. Similar transformation equations are used for other variables. These transformations were carried out by using a computer program and the following prediction equations were derived:

$$\sigma_c = -30.12 + 4.94v + 1477.34f + 76.23d - 10.55\alpha + 2.714r \tag{3}$$

$$\sigma_l = 2.24 + 0.31v + 1055f + 6.988d - 0.86\alpha + 0.676r \tag{4}$$

$$T = 9.95v^{-0.488}f^{-0.353}d^{-0.053}r^{-0.069}(\alpha + 7)^{0.022} \tag{5}$$

Table 2 Experimental data

Trial No.	v	f	d	α	r	σ_c	σ_l	R_a	T	DIMI
1	10	0.04	0.25	-6	0.4	190	18.5	0.35	11.5	47.0
2	38	0.04	0.25	-6	0.4	220	20.0	0.28	6.0	55.0
3	10	0.22	0.25	6	0.4	350	31.5	2.40	6.5	87.5
4	10	0.04	1.00	-6	0.4	280	26.0	0.90	11.0	70.0
5	10	0.04	0.25	+6	0.4	40	6.7	0.70	12.0	10.0
6	10	0.04	0.25	-6	1.2	200	19.0	0.30	10.5	50.0
7	38	0.22	0.25	-6	0.4	790	55.3	1.60	4.0	197.5
8	38	0.04	1.00	-6	0.4	300	28.5	0.40	5.0	75.0
9	38	0.04	0.25	+6	0.4	160	15.0	0.25	6.0	40.0
10	38	0.04	0.25	-6	1.2	230	22.5	0.28	5.5	57.5
11	10	0.22	1.00	-6	0.4	400	36.7	3.20	5.5	100.0
12	10	0.22	0.25	+6	0.4	290	27.5	2.00	6.5	72.5
13	10	0.22	0.25	-6	1.2	380	31.7	4.00	5.2	95.0
14	10	0.04	1.00	+6	0.4	100	8.5	0.80	12.0	25.0
15	10	0.04	1.00	-6	1.2	295	28.0	0.85	11.0	73.8
16	10	0.04	0.25	+6	1.2	50	7.7	0.60	12.0	12.5
17	24	0.13	0.625	0	0.8	325	25	1.8	7	80
18	24	0.13	0.625	0	0.8	267	23.9	2.6	8.1	67
19	24	0.13	0.625	0	0.8	290	27	1.2	7.5	82
20	24	0.13	0.625	0	0.8	310	23	1.0	8	65

Table 3 Constraints on response variables

Response variables	Maximum constraint	Minimum constraint
σ_c	200	0
σ_l	20	0
T	20	5
R_a	0.8	0.2

$$\text{DIMI} = -7.89 + 1.24v + 370.06f + 19.25d - 2.63\alpha + 0.858r \tag{6}$$

$$R_a = 4.157v^{-0.569}f^{1.52}d^{0.355}r^{0.113}(\alpha + 7)^{0.082}. \tag{7}$$

The following standard formula is used for material removal rate:

$$\text{MRR} = 1000.v.f.d. \tag{8}$$

Validity of Prediction Equations. These equations are valid when v, f, d, α, and r are within the minimum and maximum levels employed in the experiment as shown in Table 1. These equations were checked for adequacy by analysis of variance. The usual method is to find the ratio of lock of fit mean square to pure error mean square and compare this ratio with F-static. The pure error mean square is estimated from the repeated tests carried out at the midpoint of the machinability range chosen for this study. The tests were repeated four times (trial no. 17–20 in Table 2). The fitted equations are found to be adequate since no significance is observed at 99 percent confidence level.

4.5 Simultaneous Optimization. The technique of simultaneous optimization of several variables proposed by Derringer and Suich [16] for applications in rubber processing industry is extended for optimizing machining response variables such as dimensional instability, residual stress, surface finish, tool life, and material removal rate and derived corresponding independent variables such as v, f, d, α, and r for experimental validation and ready applications. In simultaneous optimization, the predicted σ_c, σ_l, T, R_a, MRR and DIMI are transformed into respective desirability functions. The individual desirabilities are then combined using the geometric mean to assess the desirability of the combined response. One-sided transformations of the form (9) for σ_c, σ_l, T, R_a, MRR and two-sided transformation of the form (10) for DIMI are used for obtaining the corresponding desirability functions.

$$d_i = \begin{cases} \left[\dfrac{y - y_{\max}}{y_{\min} - y_{\max}}\right], & y_{\min} < y < y_{\max} \\ 0 & y \geq y_{\max} \\ 1 & y \leq y_{\min} \end{cases} \tag{9}$$

$$d_i = \begin{cases} \left[\dfrac{y - y_{\min}}{y_c - y_{\min}}\right], & y_{\min} \leq y \leq y_c \\ \left[\dfrac{y - y_{\max}}{y_c - y_{\max}}\right], & y_c \leq y \leq y_{\max} \\ 0 & y < y_{\min},\ y > y_{\max} \end{cases} \tag{10}$$

Table 4 Optimized parameters

Acceptable dimensional Instability in microns	Independent parameters			Dependent or Response parameters			Composite Desirability
	v / α	f / r	d	σ_c / MRR	σ_l / DIMI	T / R_a	
Range II	14	0.04	0.4	62.6	8.54	10.2	
10 to 20 microns	6	0.4		196	15.6	0.516	0.296436
Range III	20	0.04	0.5	99.9	10.9	8.4	
20 to 30 microns	6	0.4		360	24.9	0.463	0.311526
Range IV	26	0.04	0.8	152.4	14.8	7.2	
30 to 50 microns	6	0.4		780	38.1	0.486	0.261750

Table 5 Dimensional instability measurements

Sl. No.	Specimen ID/OD location	Measurement immediately after machining in mm		Measurement after 360 hours in mm		Actual change in dimension in mm	
		Mean diameter	Roundness	Mean diameter	Roundness	Mean diameter	Roundness
1	ID at 5 mm	60.5569	0.0145	60.5569	0.0137	no hange	0.008
2	ID at 15 mm	60.5634	0.02157	60.5630	0.0186	0.001	0.0029
3	OD at 5 mm	66.3993	0.0151	66.3982	0.0136	0.0011	0.0015
4	OD at 15 mm	66.3948	0.0125	66.3939	0.0118	0.009	0.007
5	OD at 25 mm	66.3931	0.0117	66.3924	0.0094	0.007	0.0023

4.6 Optimization Criteria. Generally, the tolerance band of modern jet engine components is classified into the following four groups:

Group I: 5–10 microns range
Group II: 10–20 microns range
Group III: 20–30 microns range
Group IV: 30–40 microns range

There are only a very few components that call for the tolerance group of 5–10 microns, achieved either by jig boring or girding operations. Since the present study is limited to turning operation, only the Group II to Group IV tolerance range is considered for optimization. Simultaneous optimization is done for these three groups. These tolerance groups decide the maximum and minimum acceptable constraints on the dimensional instability. The midpoint of this range is taken as the central value for the dimensional instability where its desirability becomes unity. The maximum and minimum acceptable constraints on residual stress, tool life, and surface finish are selected based on the practical experience, and are given in Table 3. Minimum and maximum constraints on MRR are based on the minimum values of v, f, d, and limiting power of the lathe. Within the given tolerance group, individual desirability's are computed for different combinations of input machining parameters v, f, d, α, and r by varying them in discrete steps. Finally maximum composite desirability is searched by numerical comparison. A computer program is written in C-language to print the optimum values of σ_c, σ_l, T, R_a, MRR, and DIMI as soon as the maximum composite desirability is reached. The optimum parameters are listed in Table 4.

4.7 Experimental Validation of Optimum Parameters. To validate these derived optimum machinability parameters for the actual applications on critical components for the acceptable tolerance range of 10 to 20 microns, tests were conducted on ring-shaped specimen by following the same procedure that followed for generating initial experimental data. Measured response variables were compared with predicted. The inspection data are listed in Table 5. The inspection report clearly shows that the dimensional changes are well within the predicted limit. Repeated tests were conducted with same parameters and measured values scatter within 5 percent. This experiment validates that predicted optimum machinability parameters are most reliable. Similar validations have been done for other tolerance groups.

4.8 Validation of Optimum Parameters on Actual Components of Jet Engine. The predicted optimum parameters for the tolerance range of 10 to 20 microns were validated for practical application on compressor disc. By using these optimized v, f, d, α, and r the 400 (+0.02, 0.00) mm locating diameter was machined. Immediately after machining dimensions were checked, it was found to be 400 (+0.010, 0.00) mm. After 360 hours, the same dimension was 400 (+0.015, 0.00), which is within the acceptable tolerance band. Figure 14 and Fig. 15 show the effect of nonoptimized and optimized parameters on dimensional changes. The results prove the validity of this optimization technique and the parameters for the practical applications.

5 Conclusion

The following conclusions emerged form the present study:

1 Investigations on plastic deformation characteristics of Inconel 718 concludes that shear localized chips of Inconel 718 very similar with titanium Ti-6Al-4V alloy. Deformation twinning is noticed in Inconel 718 and titanium alloy. Inconel 718 also behaves similar way of titanium alloy in dimensional instability and magnitude is much higher than titanium alloys where as similar phenomenon is not noticed in other nickel based alloys.
2 The effect of machinability parameters on plastic deformation and resulting residual stresses was studied. A negative rake angle increases and a positive rake angle decreases the residual stresses.
3 As the chip tool contact length increases, cutting force and frictional forces increase; therefore, the controlled chip-tool contact length reduces residual stresses compared to natural chip tool contact length.
4 The empirical relationships for prediction of surface residual stresses, dimensional instability, surface finish, and tool life in machining by Inconel 718 superalloy have been established.
5 The cutting speed, feed, depth of cut, rake angle, and nose radius significantly influence the residual stresses, dimensional instability, surface finish and tool life.
6 The optimum machinability parameters (v, f, d, α, and r) have been established by simultaneous optimization of six response variables (σ_c, σ_l, T, R_a, MRR, and DIMI) using desirability function approach. The optimized results are verified with experimental results and it is found adequate.

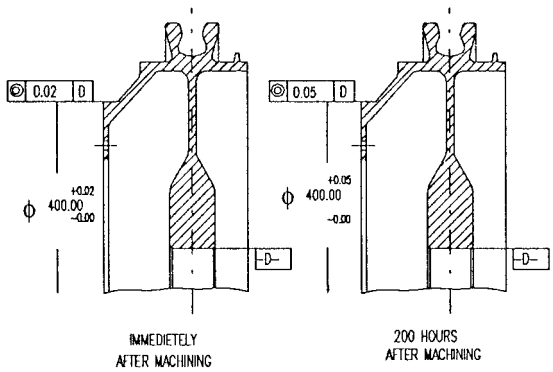

Fig. 14 Effect of non-optimized parameters on dimensional instability

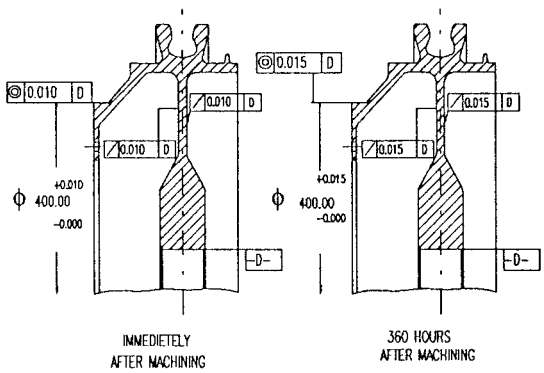

Fig. 15 Effect of optimized parameters on dimensional instability

7 Optimized machinability parameters for turning operations to control the dimensional instability on critical aerogas turbine engine components within the tolerance range of 10 to 20, 10 to 30, and 30 to 50 microns are established for shop floor applications.

Acknowledgment

The authors gratefully acknowledge Mr. V. Sundararajan, Director, GTRE for the permission given to publish this paper. Thanks are also to Mr. T. K. Sampathkumaran, Additional Director, for his encouragement during this developmental work.

References

1 Marshall, C. W., and Maringer, R. E., 1977, "Dimensional Instability—An Introduction," International series of Material Sci. & Tech., Vol. 22, Pergamon Press, New York.

2 Israeli, A., and Bendeck, 1983, *ASME J. of Engineering for Industry*, Vol. 105, pp. 133–135.

3 Komanduri, R., and Schroeder, T. A., 1986, *ASME J. Engineering for Industry*, Vol. 108, No. 2, pp. 93–100.

4 Marschall, C. W., and Maringer, R. E., 1971, *J. Inst. Materials*, Vol. 6, No. 2, pp. 373–387.

5 Meyerson, M. R., Frieman, L., and Cilles, P. M., 1969, *Trans. ASM*, Vol. 62, pp. 809.

6 Israeli, A., and Papier, R., 1981, *ASTM J. Testing and Evaluation*, Vol. 9, No. 6, pp. 348.

7 Kcanda, A. Z., and Wanhein, T., 1991, *Proc. IME*, Vol. 205, No. 83, pp. 207–214.

8 Subhas, B. K., and Katti, R. A., 1984, ASME Paper 84-GT-276.

9 Subhas, B. K., 1983, MS Research thesis, JNTU.

10 Jose, K. J., Philip, P. K., and Thomas, P., 1988, *13th AIMTDR Conf. Proceedings*, Jadhavapur University, pp. B-45–50.

11 Wu, S. M., 1964, *J. Engineering for Industry*, pp. 105–110.

12 Albuelenga, A. M., and Danidiery, M. A., 1983, *Int. J. MTDR*, Vol. 24, No. 1-B, pp. 11–18.

13 Shin, Y. C., and Joo, Y. S., 1992, *Int. J. Prod. Res.*, Vol. 30, No. 12, pp. 2907–2919.

14 Prasad, A. V. S. R. K., Rao, P. N., and Rao, U. R. K., 1994, *Proceedings of 19th AIMTDR Conference*, pp. 455–461.

15 Harrington, Jr., E. C., 1965, *Industrial Quality Control*, Vol. 21, No. 10, pp. 494–498.

16 Derringer, G., and Suich, R., 1980, Journal of Quality Technology, Vol. 12, No. 4, pp. 214–219.

17 *Standard Test Method for Determining Residual Stresses by the Holedrilling Strain-Gage Method*, 1987, Annual Book of ASTM Standards, Vol. 03-01, E837-85, pp. 991–997.

18 Tsuchida, K., Kawada, Y., and Kodama, S., 1975, *Bull. JSME*, Vol. 18, No. 116, pp. 123–130.

Isothermal Fatigue Behavior and Damage Modeling of a High Temperature Woven PMC

A. L. Gyekenyesi
NASA Glenn Research Center,
MS 6-1,
21000 Brookpark Road,
Cleveland, OH 44135

This study focuses on the fully reversed fatigue behavior exhibited by a carbon fiber/polyimide resin woven laminate at room and elevated temperatures. Nondestructive video edge view microscopy and destructive sectioning techniques were used to study the microscopic damage mechanisms that evolved. The elastic stiffness was monitored and recorded throughout the fatigue life of the coupon. In addition, residual compressive strength tests were conducted on fatigue coupons with various degrees of damage as quantified by stiffness reduction. Experimental results indicated that the monotonic tensile properties were only minimally influenced by temperature, while the monotonic compressive and fully reversed fatigue properties displayed greater reductions due to the elevated temperature. The stiffness degradation, as a function of cycles, consisted of three stages; a short-lived high degradation period, a constant degradation rate segment covering the majority of the life, and a final stage demonstrating an increasing rate of degradation up to failure. Concerning the residual compressive strength tests at room and elevated temperatures, the elevated temperature coupons appeared much more sensitive to damage. At elevated temperatures, coupons experienced a much larger loss in compressive strength when compared to room temperature coupons with equivalent damage. The fatigue damage accumulation law proposed for the model incorporates a scalar representation for damage, but admits a multiaxial, anisotropic evolutionary law. The model predicts the current damage (as quantified by residual stiffness) and remnant life of a composite that has undergone a known load at temperature. The damage/life model is dependent on the applied multiaxial stress state as well as temperature. Comparisons between the model and data showed good predictive capabilities concerning stiffness degradation and cycles to failure.

Introduction

Current objectives of the aeronautics community call for advanced aircraft that produce greater payload delivery and increased fuel efficiency. Of vital importance in the development of the propulsion systems for these aircraft is the utilization of cost effective advanced materials. Bowles et al. (1996) pointed out that one of the prevailing philosophies driving these programs is the utilization of lightweight polymer matrix composites (PMCs) in selected sections of newer engines where elevated temperatures prevail. These materials will serve both as load bearing and non-load bearing components. Anticipated service environments include temperature regimes that reach and maintain levels of 300°C (572°F) or more. These future requirements impose service temperatures approaching the glass transition temperature (T_G) of the resin. Whether the anticipated service requirements are stringent (e.g., aerospace) or mundane (where commercial success is driving technology) a data base of pertinent engineering properties must be developed. Therefore, one of the objectives of this study is to add to the existing property data base by providing information relative to fatigue and damage accumulation. This data has been obtained under conditions approaching the service conditions found in turbine engines.

With the increasing utilization of PMCs in structural components the need to predict service life under both static and cyclic loads becomes important. However, to predict life the design engineer must be able to detect the accumulated damage that occurs in a structural component under various service conditions. Once a dependable methodology has been established to detect damage, the design engineer must also be able to ascertain the effect damage has on engineering properties. This essentially leads to establishing a damage criterion. The damage criterion dictates when to remove a component from service.

In the past, successful fatigue life models for conventional materials would incorporate a relationship between microstructural damage (i.e., the defect state) and the mechanical properties of the materials. Similar models based on high quality fatigue data must be established for PMCs. Models that predict the rate of damage accumulation for PMCs would enable a design engineer to predict when a component should be removed from service. However, in order to construct a useful fatigue life model for PMC laminates constructed from either tapes, weaves or both, an extensive data base must be developed. While information relative to non-woven laminated PMCs has been added to the data base for a number of years, little effort has been invested augmenting the data base for woven PMCs. This study expands the data base of information regarding the fatigue life of a cross-woven PMC. The macroscopic and microscopic behavior of the material was documented at room and elevated temperatures under a fully reversed cyclic load. To accomplish this, advanced experimental techniques were developed and employed for the uniaxial tests. Finally, an isothermal, multiaxial fatigue life model was proposed that captures the reduction of stiffness under cyclic load for the aforementioned (0/90) weave. It should be noted that the primary objective of this study was to develop and establish a comprehensive fatigue model for PMCs that correlates well with experimental fatigue data. For a more detailed explanation concerning this research and its results, the reader is advised to see Gyekenyesi (1998).

Contributed by the International Gas Turbine Institute (IGTI) of THE AMERICAN SOCIETY OF MECHANICAL ENGINEERS for publication in the ASME JOURNAL OF ENGINEERING FOR GAS TURBINES AND POWER. Paper presented at the International Gas Turbine and Aeroengine Congress and Exhibition, Stockholm, Sweden, June 2–5, 1998; ASME Paper 98-GT-106.

Manuscript received by IGTI February 25, 1998; final revision received by the ASME Headquarters October 20, 1999. Associate Technical Editor: R. Kielb.

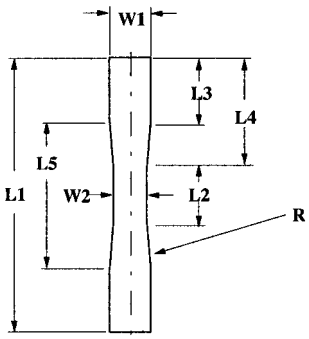

Fig. 1 Schematic of specimen geometry

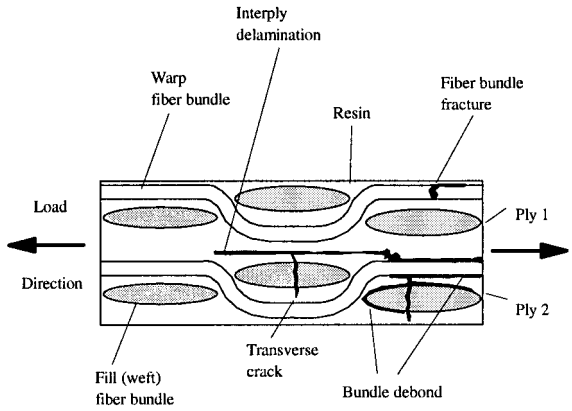

Fig. 2 Illustration of microscopic damage in a (0/90) weave: edge view

Material, Test Equipment, and Test Procedure

The high temperature PMC employed in this study carries the designation T650-35/PMR15. This material is a carbon fiber/polyimide composite with a two dimensional fiber architecture. An 8-harness satin balanced (0/90) cross-weave was utilized in fabricating each ply. Plate specimens were supplied in two different thicknesses, i.e., plates with a 10-ply thickness, and plates with 16 plies through the thickness. A glass transition temperature of 335°C (635°F) was obtained through a rheological analysis which was later verified by thermal mechanical analysis (TMA). The average fiber volume fraction of 0.64 was established through procedures set forth in ASTM Standard D 3171.

Two dog-bone specimen configurations were designed for this study. The first dog-bone configuration, identified as coupon A, was utilized in the monotonic tensile tests. The other dog-bone specimen, identified as coupon B, was utilized in monotonic compression tests and in fully reversed fatigue tests. The dimensions of the coupons are provided in Fig. 1 and Table 1. Finally, to assure the quality and reproducibility of the coupon B design, the standardized Wyoming Modified Celanese (WMC) test fixture was employed to provide benchmark data concerning the monotonic compressive strength.

The test rig utilized for this program is a closed-loop, servohydraulic system with a load capacity of 88.96 kN (20 kip). Specimens were gripped with hydraulic actuated, water cooled, diamond pattern serrated, wedge grips. Longitudinal strain measurements were obtained using an edge mounted, air cooled extensometer with a 1.27 cm (0.5 in) gage length. The monotonic and fatigue experiments were conducted under computer control. Specimens were heated utilizing six high intensity tungsten-filament quartz bulbs (500 watts/bulb).

The isothermal monotonic and fatigue experiments were conducted at two temperatures, i.e., 22°C (72°F) or room temperature (RT), and 316°C (600°F) which will be referred to as elevated temperature (ET). The ET was approximately 19°C (35°F) below the dry glass transition temperature, T_G. The monotonic tensile tests were conducted in load control using test coupon A and a load rate of 20.7 MPa/s (3 ksi/s). Displacement control was utilized for the monotonically increasing compression tests. Here test coupon B was employed with a displacement rate of −0.00254 cm/s (−0.001 in./s). Finally, to validate the monotonic compressive behavior of the coupon B design, the WMC fixture was employed at room temperature. Again, displacement control was utilized at a rate of −0.00254 cm/s (−0.001 in./s). Throughout this study, failure was defined as complete separation of a coupon into two pieces. The isothermal fatigue experiments were conducted at multiple levels of maximum stress. However, the stress ratio for all fatigue experiments was maintained at $R_\sigma = -1.0$ ($\sigma_{min}/\sigma_{max}$). A cyclic load frequency of 2 Hz was employed with a triangular load wave form. All the fatigue specimens were subjected to constant load limits and constant load rates, i.e., load control.

Table 1 Dimensions for flat, reduced gage section specimens

Dimension cm (in)	Coupon A* 10-ply Tensile	Coupon B** 16-ply Comp.
L1	17.78 (7.0)	15.24 (6.00)
L2	2.79 (1.10)	1.91 (0.75)
L3	4.45 (1.75)	5.72 (2.25)
L4	7.49 (2.95)	6.68 (2.63)
L5	8.89 (3.50)	3.81 (1.50)
W1	2.16 (0.85)	2.03 (0.80)
W2	1.19 (0.75)	1.91 (0.75)
R	36.83 (14.5)	7.19 (2.83)

*Average thickness = 0.323 cm (0.127 in)
**Average thickness = 0.533 cm (0.210 in)

Certain monotonic tests and certain fatigue tests were interrupted in order to ascertain information concerning microstructural damage, degraded moduli and residual strength. Selected monotonic tensile and compressive tests were interrupted to obtain sections for microstructural analysis. The destructive examination experiments were stopped at approximately 55 percent and 90 percent of the ultimate tensile and compressive strengths. In addition, selected fatigue tests were interrupted to acquire information regarding the relative state of the microstructure as well as obtaining values for the residual compressive strength. The tests were interrupted based on the degradation of the tensile and compressive moduli. The predetermined levels of moduli degradations were approximately 1, 5, and 10 percent stiffness loss. For each predetermined interruption point two coupons were obtained. One coupon was selected for destructive examinations while the other was used to obtain the residual compressive strength. Finally, the coupon edges' were monitored by live video to assess real time damage during testing.

Experimental Results

Elevated temperature had a statistically insignificant effect on composite tensile properties because the tensile behavior of the material was fiber dominated. While the behavior of the polyimide resin is significantly altered at ET, the carbon fibers are generally unaffected at the test temperatures in this study. The average ultimate tensile strength within ±1 standard deviation at 22°C (72°F) based on 11 specimens was 855 ± 17.0 MPa (124 ± 2.46 ksi). The average ultimate tensile strength within ±1 standard deviation at 316°C (600°F) utilizing 7 specimens was 831 ± 14.3 MPa (121 ± 2.07 ksi). The average tensile failure strain within ±1 standard deviation at 22°C (72°F) was 1.15 ± 0.0408 percent. The average tensile failure strain within ±1 standard deviation at 316°C (600°F) was 1.17 ± 0.0441 percent. In addition, the longitudinal moduli decreased approximately 2.3 percent due to the ET. At both temperatures the stress-strain curves were relatively linear to failure.

A schematic identifying the various damage mechanisms for this composite material is depicted in Fig. 2. During RT tensile

tests, transverse cracks were initiated at approximately 379 MPa (55 ksi), and these cracks continued to accumulate up to failure. Figure 3 illustrates an edge view of accumulated damage characterized by destructive examination of an interrupted tensile test at 758 MPa (110 ksi). At RT the transverse cracks appeared to be uniformly distributed through the width and the thickness. Warp bundle debonds and interlaminar delaminations were next in the sequence of damage events at RT. These events occurred at an approximate tensile stress value of 827 MPa (120 ksi). Debonds and delaminations were initiated near the intersection of the face and edge of the test specimen (i.e., the corner of the coupon). Stress concentrations in this region (a result of the Poisson's ratio mismatch between the bundles and resin) were the probable cause of the debonds. Although the debonds and delaminations appeared to occur simultaneously, bundle debonds probably occurred first. These debonds then branched to the resin rich interlaminar area which induced delaminations. Failure occurred shortly thereafter when isolated debonded warp bundles fractured causing the specimen to break into two pieces.

A slightly different pattern of microscopic damage was observed for the 316°C (600°F) tensile tests. Warp bundle debonds occurred simultaneously with transverse cracks along the edge of the coupon. These events were first detected via the edge view camera at approximately 414 MPa (60 ksi). Both mechanisms continued to accumulate up to failure. However, in contrast to RT tensile tests there was a relatively low density of transverse cracks which was most likely the result of increased ductility of the resin at ET. Relatively few transverse cracks were detected in the sectioned views taken from specimens at an interrupted stress level of 758 MPa (110 ksi), and none at all were detected at the lower interrupted stress level of 379 MPa (55 ksi). When observed, the transverse cracks were homogeneously distributed through the gage section. Again, tensile failure occurred when the isolated debonded warp bundles failed with increasing stress.

Elevated temperature had a more pronounced effect on the compressive properties of the composite. The average ultimate compressive strength within ± 1 standard deviation at 22°C (72°F) based on 4 specimens was -675 ± 5.21 MPa (-97.8 ± 0.756 ksi). The average ultimate compressive strength at 316°C (600°F) utilizing 4 specimens was -629 ± 26.4 MPa (-91.2 ± 3.82 ksi). Thus, the average ultimate strength was reduced by 6.7 percent as a result of the ET. At 22°C (72°F) the compressive failure strain within ± 1 standard deviation was -1.12 ± 0.0457 percent. At 316°C (600°F) the compressive failure strain was -1.04 ± 0.0465 percent. Thus, ET caused a 7.1 percent decrease in failure strain. The preceding statistical comparisons were based on a 95 percent confidence level using the *t*-test method. As was the case for the tensile behavior, the stress-strain curves for the monotonic compression tests at RT and ET were relatively linear to failure. Note

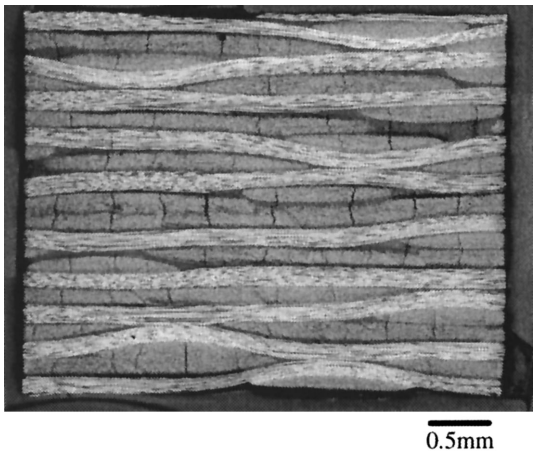

Fig. 3 Microscopic edge view of transverse cracks in a typical RT tensile specimen after loading to 758 MPa (110 ksi)

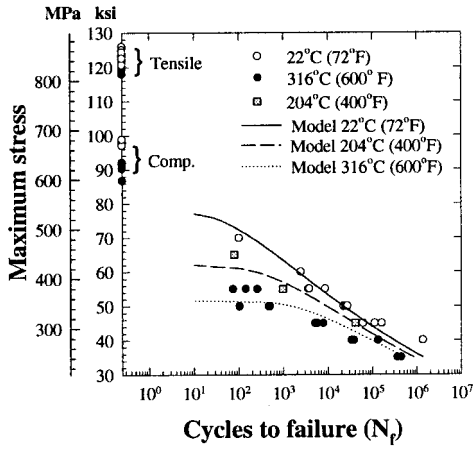

Fig. 4 Stress based isothermal fatigue life for T650-35/PMR15 (0/90) weave

that strain gage data (gages applied to both faces) verified that macroscopic buckling did not occur in the unsupported specimens.

As noted earlier, coupon B was used for the compression tests that generated the information presented above. To validate that coupon B produced acceptable compressive strength data, six monotonic compressive tests were conducted at room temperature utilizing the Wyoming Modified Celanese Fixture. The average ultimate strength obtained using this fixture was -668 MPa (-96.8 ksi) with a standard deviation of ± 46.5 MPa (± 6.78 ksi). Test results from the Celanese fixture showed acceptable agreement with the coupon B room temperature test results provided above (i.e., a statistically insignificant difference concerning the mean compressive strengths). This is a strong indication that the data obtained using the coupon B specimen geometry was reproducible.

At both room and elevated temperatures, neither the destructive microscopy nor the edge view monitoring indicated any signs of microstructural damage prior to failure for monotonic compressive loading. By viewing the edges of the specimens during the compressive tests, it was observed that the failures were instantaneous at both RT and ET. At both temperatures failure was likely the result of the simultaneous occurrence of massive bundle debonds and bundle buckling. The debonds were caused by the Poisson's induced out of plane tensile strain.

A graphical summary of the fatigue life data is presented in Fig. 4. As a reference, the monotonic tensile and absolute monotonic compressive data appear in this figure along the vertical axis. The maximum cyclic stress levels which ranged from 241 MPa (35 ksi) to 483 MPa (70 ksi) produced lives ranging from 10^1 to over 10^6 cycles to failure. The ET data showed a significant reduction in cycles to failure when compared to RT data tested at the same maximum stress level. For example, at the applied maximum stress of 345 MPa (50 ksi), the specimens exposed to RT had an average life 70 times greater than specimens exposed to ET (i.e., 24,314 versus 353 cycles to failure, N_f). As a final note, all the specimens failed during compressive regime of the fully reversed cycle at both temperatures.

Figure 5 depicts room temperature data for compressive stiffness (normalized with respect to the initial stiffness) versus accumulated cycles (normalized with respect to cycles to failure, N_f) for three specimens at a single maximum cyclic stress level of 379 MPa (55 ksi). Specimen identifications and respective cycles to failure are indicated in the figure. From this data, it is easily seen that normalized moduli as a function of normalized accumulated cycles is consistent from specimen to specimen, at a given temperature and stress level. Note that the specimens in Fig. 5 display three stages of degradation. The first damage stage occurred during the initial 1 percent of life (see Fig. 7 for close-up view of stage I). This was followed by a linear second stage (constant degradation

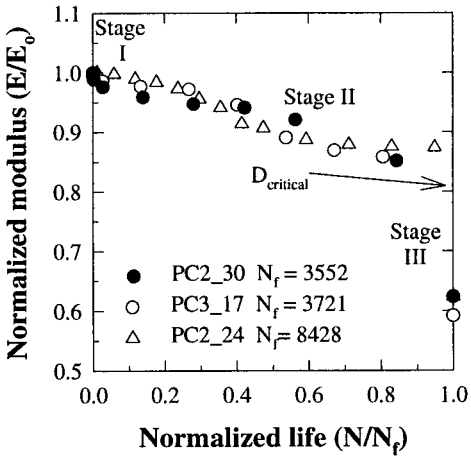

Fig. 5 Normalized compressive modulus degradation behavior for multiple specimens at 22°C (72°F): σ_{max} = 379 MPa (55 ksi)

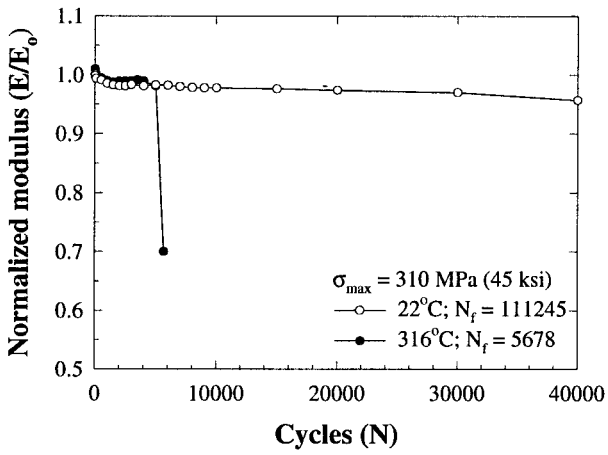

Fig. 7 Comparison of normalized compressive modulus degradation behavior between RT and ET at an equivalent stress

rate) which constituted the majority of life. As failure approached, a dramatic increase in the damage rate occurred. This increased rate of damage was reflected in the sudden loss of moduli prior to failure. Similar degradation rates were observed for both tensile and compressive moduli. This indicated an equivalent sensitivity of stiffness to the various microscopic damage mechanisms in either load direction. Here, the discussion focuses on the compressive modulus because failure always occurred during the compressive segment of the cycle. Figure 6 displays the normalized stiffness data for three specimens at 316°C (600°F) with an applied maximum cyclic stress of 310 MPa (45 ksi). Modulus degradation behavior similar to RT data was seen at each of the maximum applied cyclic stress levels at this temperature. Again, Stage II dominated the life of the coupons. However, the slope of the linear segments were relatively shallow in comparison to the room temperature data. Also, note in Fig. 6 that a slight increase was observed in some specimens during the early segments of life. Both the occasional early increase and the relatively shallow Stage II were likely influenced by an increase in resin stiffness due to cross-linking of the resin molecules at ET. The reader is directed to Bowles et al. (1996) for further discussions on this issue.

Figure 7 shows a typical comparison between the RT and ET compressive moduli (normalized with respect to the initial stiffness) for an equivalent maximum cyclic stress level. Notice that the normalized moduli degrade at the same rate, but the coupon tested at 316°C (600°F) failed much earlier than the coupon tested at room temperature. This artifact is incorporated into the analytical model.

Figure 8 depicts the average Stage II room temperature modulus degradation behavior at three stress levels as a function of accumulated cycles. Seen is the fact that the rate of modulus degradation is heavily dependent on the applied stress level. The multiple curves were obtained by fitting a first order linear regression curve to the Stage II data obtained from three specimens tested at a particular maximum stress level. For example, at σ_{max} = 379 MPa (55 ksi) a regression curve was obtained from the Stage II data appearing in Fig. 5. The average accumulated cycles were calculated by multiplying each specimen's normalized life by the average life of the three. It is clear from Fig. 8 that the rate of degradation of the normalized stiffness as a function of accumulated cycles is dependent on the applied maximum cyclic stress at RT.

At 1 percent stiffness loss, the damage in the RT fatigue coupons consisted of a few transverse cracks. No other forms of damage were apparent at this point in the fatigue life of the RT composite. The transverse cracks had a homogeneous distribution throughout the thickness and width. At 5 percent stiffness loss, the transverse cracks increased in density. Also, there were indications of bundle debonds at the roots of the transverse cracks. At 10 percent stiffness reduction, the bundle debonds propagated and coalesced into interlaminar delaminations. The debonds were concentrated along the face and edge of the coupons and expanded

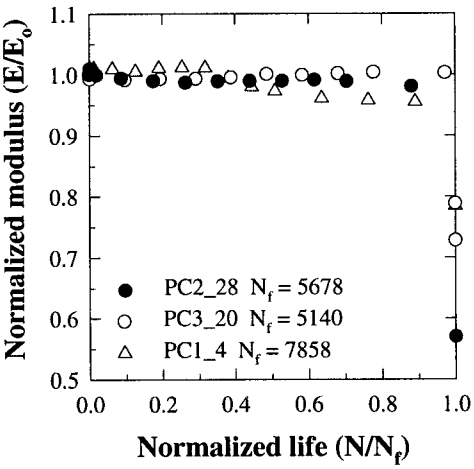

Fig. 6 Normalized compressive modulus degradation behavior for multiple specimens at 316°C (600°F): σ_{max} = 310 MPa (45 ksi)

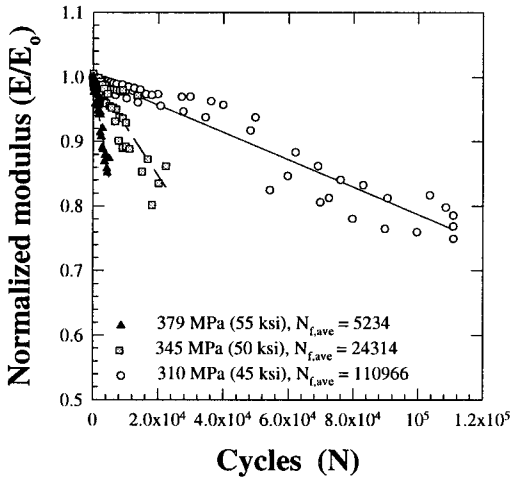

Fig. 8 Normalized compressive modulus at various maximum stresses for RT condition. Each line is an average of three specimens.

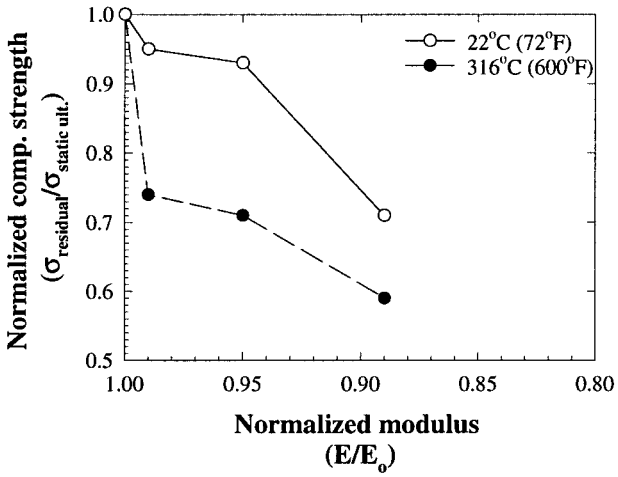

Fig. 9 Residual compressive strength behavior as a function of damage (i.e., current compressive modulus)

through the thickness. The transverse crack density did not increase after 5 percent stiffness loss. Because the count did not increase, it is likely that a saturation level was achieved. In-situ monitoring of the specimen edge indicated that delaminations grew ply by ply through the thickness until final failure occurred. Final fracture, which occurred during compression, was the result of massive debonds, bundle buckling and delaminations in the intact interior plies of the RT coupons.

At 316°C (600°F), no microscopic damage was observed in any of the sectioned views taken at a 1 percent stiffness reduction. However, the in-situ edge view showed initial bundle debonds and breaks occurred along the edge and face. The bundle debonds occurred within the first few cycles and progressed until failure. The damage level (i.e., the 1 percent decrease in the normalized stiffness) was maintained until a sufficient number of transverse cracks accumulated. The transverse cracks penetrated approximately one or two bundle widths from the edge. Interlaminar delaminations first appeared in the edge view when the composite reached a 4 percent stiffness reduction. The final damage mechanisms, initiated at 5 percent stiffness reduction, were interply delaminations. At this point an increased rate of bundle fractures were occurring due to buckling of the isolated bundles. All of these mechanisms initiated along the edge and face and then proceeded to propagate towards the midplane of the laminate (see Gyekenyesi, 1998, for discussion on edge effects). This indicated the start of Stage III (i.e., the drastic increase in degradation rate) behavior of the modulus curve. Failure occurred when the out-of-plane strain in the remaining intact plies caused massive debonding, delaminations, and bundle buckles.

Figure 9 shows the normalized residual compressive strength as a function of the normalized compressive modulus. Indicated in the figure is the fact that even a small amount of damage caused a significant reduction in strength at elevated temperature. For example, the damage which induced a 1 percent loss in stiffness caused a 25 percent reduction in residual compressive strength. For the RT case, a relatively large amount of damage, on the order of a 10 percent stiffness degradation, was required to reduce the residual strength by 25 percent. As a final note, the residual strength curve of Fig. 9 suggests a three stage pattern similar to that of the modulus degradation curves. However, there is insufficient data to make a conclusive statement. Future work that includes more residual compressive strength data is needed to make appropriate conclusions.

Damage Model and Life Prediction

The two macroscopic properties most often utilized as a measure of damage for PMCs are residual strength and residual modulus. The primary advantage of residual modulus over residual strength is the ability to readily follow modulus degradation via interrupted fatigue tests. For obvious reasons the residual strength can only be measured once during the fatigue life of a specimen. Wang and Chim (1983), Poursartip et al. (1982), Liu (1992), Ye (1989) as well as Lemaitre and Chaboche (1990) have focused on elastic moduli as a pertinent measure of the damage state. Poursartip et al. (1982) pointed out that elastic moduli are particularly attractive because as a fourth order tensor, elastic moduli offer the possibility of distinguishing and monitoring different components of damage. Yet, representing damage with a fourth order tensor has drawbacks as a result of its experimental complexities. Because of these limitations, the fatigue damage accumulation law proposed here incorporates a scalar representation for damage, but admits an anisotropic evolutionary law. The model predicts the current damage state (as quantified by current stiffness) and remnant life of a composite that has undergone a known cyclic load at temperature. The damage/life model is dependent on the applied multiaxial stress state. The model is also a function of the applied maximum fatigue stresses, the applied mean stresses, and temperature. The model is characterized using the uniaxial life and stiffness degradation data of the woven PMC employed in this study.

The measurement of damage is not directly accessible. Its quantitative evaluation, as with many properties, is linked to the definition of the variable chosen to represent the phenomenon. The inferred relationship is based on a link between deformation and damage, i.e., to the modification of the mechanical properties characterized. Here damage is defined as

$$D = 1 - \frac{E}{E_o}, \tag{1}$$

where E_o is the initial longitudinal stiffness and E is the current longitudinal stiffness. Thus, if the initial Young's modulus E_o is known, any measurement of the residual elastic stiffness can be used to determine the damage.

To describe the evolution of damage, a power law relationship is employed in a fashion similar to work by Wang and Chim (1983), Hwang and Han (1989) as well as Ye (1989). The evolutionary laws in those studies were developed for the case of uniaxially applied stresses with fixed R-ratios. Here, the general form of the evolutionary law is expressed as a power function in terms of Φ which is a function that accounts for multiaxial cyclic stress states. The evolutionary law is also a function of the current state of damage. The function Φ is dependent on the maximum cyclic stress and the cyclic mean stress. The damage rate is expressed as

$$\frac{dD}{dN} = A\,\frac{\Phi^C}{B(D + D_o)^{B-1}}, \tag{2}$$

where D_o is the initial damage state and A, B, and C are material constants. The functional dependence of Φ is stipulated as the difference between a function F (defined momentarily) evaluated at two different stress states, i.e.,

$$\Phi = [F(S^*_{\max}, \sigma^*_U) - F(S^*_{\text{mean}}, \sigma^*_U)]^{1/2}. \tag{3}$$

The vectors $S^*_{\max}$ and S^*_{mean} have components dependent on the maximum cyclic stresses ($\sigma_{L\max}$, $\sigma_{T\max}$, and $\tau_{LT\max}$) and cyclic mean stresses ($\sigma_{L\text{mean}}$, $\sigma_{T\text{mean}}$, and $\tau_{LT\text{mean}}$), respectively. Note that the components are referenced to the local L-T axis (i.e., longitudinal and transverse axis of the material). The vector σ^*_U is composed of ultimate strengths σ_{LU}, σ_{TU}, σ_{ZU} and τ_{LTU}.

The function Φ is a measure of the intensity of the applied multiaxial stress state with respect to the ultimate static failure envelope of the anisotropic composite. The ultimate strength values are defined by monotonic tests. The function F in Eq. (3) defines the monotonic failure surface for a two dimensional lamina. In essence, Φ utilizes the monotonic failure function to obtain

a scalar representation of the applied multiaxial cyclic stress, i.e., the stress environment. Therefore, as the applied multiaxial fatigue stress state moves closer to the monotonic failure surface it results in an increase in the rate of damage accumulation. Although there are many monotonic failure functions, this study employs a derivative of the Hill failure theory for anisotropic materials under plane stress because of its acceptance and wide use. Utilizing Hill's definition for multiaxial failure, the function F is defined as

$$F = \left(\frac{\sigma_L}{\sigma_{LU}}\right)^2 + \left(\frac{\sigma_T}{\sigma_{TU}}\right)^2 - \left(\frac{1}{\sigma_{LU}^2} + \frac{1}{\sigma_{TU}^2} - \frac{1}{\sigma_{ZU}^2}\right)\sigma_L\sigma_T + \left(\frac{\tau_{LT}}{\tau_{LTU}}\right)^2. \quad (4)$$

The Hill theory stipulates that for a plane stress environment the monotonic failure initiates when $F = 1$. Note that when the applied normal stresses are compressive, ultimate compressive strengths are used in Eq. (4).

Damage evolution can be obtained by integrating Eq. (2) and by assuming that $D = D_o$ when $N = 0$. Therefore, damage as a function of fatigue cycles is

$$D = [A\Phi^C N + (2D_o)^B]^{1/B} - D_o. \quad (5)$$

Modeling of property degradation is achieved by combining Eqs. (1) and (5).

At the end of the fatigue life of a specimen, where $N = N_f$, the damage parameter reaches a critical value defined as

$$D = D_o + D_{\text{critical}}. \quad (6)$$

Combining Eqs. (5) and (6) and solving for the number of cycles (N_f) associated with D_{critical}, the life model is expressed as follows:

$$N_f = \frac{(D_{\text{critical}} + 2D_o)^B - (2D_o)^B}{A\Phi^C}. \quad (7)$$

The stiffness degradation curves presented earlier indicate that the damage accumulation as a function maximum cyclic stress involved three stages. Since the second stage (linear portion) of the damage accumulation curves accounted for the majority of fatigue life for this PMC, it was reasonable to model damage for this stage. The following observations obtained from the fatigue data were used to simplify the characterization process. First, since the degradations were linear (i.e., constant rates regardless of the current level of damage as a result of only modeling Stage II), Eq. (2) was assumed to be dependent only on the cyclic stress state, Φ. Thus, the current level of damage was not altering the rate of damage accumulation. To eliminate the dependence on the current level of damage, the constant B was taken equal to 1 in Eq. (2). Second, Fig. 7 indicates that the modulus degradation rates were independent of temperature. Therefore, the room temperature and elevated temperature results were pooled for the characterization of the damage rate constants A, B, and C in Eq. (2). The damage rate for an individual specimen was calculated by fitting a linear regression curve to the stage II segment of the compressive modulus degradation curve. The log of the damage rates for each individual coupon (both room temperature and elevated temperature) were plotted as a function of the log of the multiaxial cyclic stress state Φ. The constant A represents the inverse log of the intercept and the constant C represents the slope of the line. From the regression analysis, the model constants for the current material system were

$$A = 0.1257$$

$$B = 1.000$$

and

$$C = 10.436. \quad (8)$$

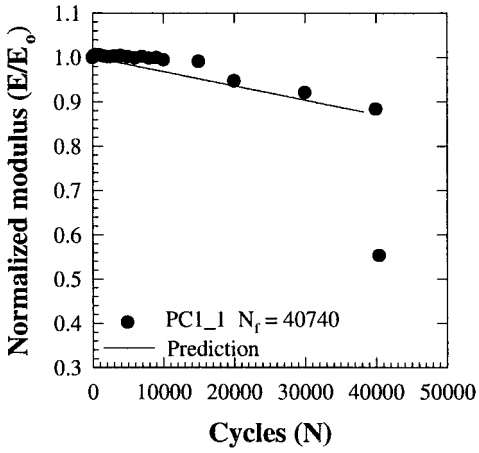

Fig. 10 Model versus data comparison of normalized compressive modulus as a function of cycles at 204°C (400°F)

Note that the cyclic mean stress term is 0 for this particular study since $R_\sigma = -1$. Therefore, Φ is simply the ratio of the applied maximum stress normalized by the RT monotonic tensile strength.

The fatigue life data (but not the damage rates) showed a significant decrease in cycles to failure as a result of the elevated temperature. This temperature dependence was a result of the material's lower tolerance to damage at elevated temperature. Although the specimens damage accumulation rates at a given maximum cyclic stress were approximately the same at either 22°C (72°F) or 316°C (600°F), the elevated temperature coupons failed at a much lower critical damage state. The critical damage values were defined as the lowest stiffness value on the stage II portion of the modulus degradation curves as indicated in Fig. 5. A linear relationship was obtained for D_{critical} after plotting D_{critical} versus Φ. The following equation describing the critical damage was defined for the current material

$$D_{\text{critical}} = P(T) + Q \cdot \Phi. \quad (9)$$

Based on the data, the constants are calculated as

$$P = (-6.510 \times 10^{-4}) \cdot T + 0.5776$$

$$Q = -8.877 \times 10^{-1} \quad (10)$$

for metric units (°C), and

$$P = (-3.625 \times 10^{-4}) \cdot T + 0.5894$$

$$Q = -8.877 \times 10^{-1} \quad (11)$$

for English units (°F). With the damage evolutionary law and D_{critical} defined, the focus is now turned to a comparison with experimental data. Note that it is assumed that the initial damage, D_o, is very small with respect to the damage which is induced during fatigue cycling. Thus, D_o is equated to 0. As a result, E_o is equal to the initial modulus at the test temperature prior to cyclic fatigue.

In addition to the data at 22°C (72°F) and 316°C (600°F), three coupons were tested at the intermediate temperature of 204°C (400°F) to further substantiate the predictive capabilities of the model. Figure 4 shows the theoretical results in comparison to the experimental data. Recalling that the model characterization was achieved using 22°C (72°F) and 316°C (600°F) data, the theoretical values at those temperatures show good agreement with the data as expected. The model also shows good agreement with the 204°C (400°F) cyclic fatigue data.

A comparison between the predicted compressive stiffness and the experimental data at 204°C (400°F) is displayed in Fig. 10. Equation (7) was utilized to define the total number of cycles to failure for the stiffness prediction at the respective stress and

temperature. As Fig. 10 depicts, the agreement was good concerning both the slope of the line and cycles to D_{critical}.

Conclusions

With respect to the experimental portion of this study, the monotonic and fatigue behaviors of a carbon fiber/polyimide weave (T650-35/PMR15) were studied at room and elevated temperatures. This involved investigating the effects of temperature on both the macroscopic and microscopic properties of the composite. The results indicated minimal influence of temperature concerning the monotonic tensile tests. This was expected due to the fiber domination under such loading. Elevated temperature had a more pronounced effect on the monotonic compression results. Finally, the fully reversed fatigue data showed significant reductions in cycles to failure as a result of temperature. The effect of temperature on monotonic compression and fully reversed fatigue was due to the increased role of the resin for a composite subjected to such modes of loading. Note that the fatigue tests always failed in compression.

The damage model quantitatively measures the degree of damage by establishing a functional relationship between the residual stiffness and the damage state of the laminate. The damage evolution law employs a power law relationship to model the damage rate as a function of the multiaxial cyclic stress environment and the current level of damage. The critical damage, which defines the level of damage at the time of failure, is dependent on the multiaxial cyclic stress environment and the temperature. Characterization of the model in respect to the T650-35/PMR15 (0/90) weave was achieved by the utilization of the fully reversed uniaxial fatigue life data and stiffness data. For the current material system, the damage was found to have a constant degradation rate dependent on the maximum cyclic stress. Because the stiffness data showed the degradation rates to be independent of temperature, the room and elevated temperature data were pooled in the characterization of the damage rate equation. However, the critical damage state was dependent on the both the cyclic stress level and temperature. Comparisons between the theoretical values and *S-N* data indicated good agreement between the model and experiment at 22°C (72°F) and 316°C (600°F). The predictive capabilities of the model were further substantiated by comparing the model to fully reversed fatigue data produced at an intermediate temperature of 204°C (400°F). The agreement at this intermediate temperature was good concerning both the modulus and cycles to failure. Lastly, the data generated here represents uniaxial loading applied at isothermal temperatures. Thus, a uniaxial formulation of the fatigue life model proposed in this study was characterized. Future work should encompass multiaxial testing and examine mean stress effects in order to enhance the modeling effort presented here.

References

Bowles, K. J., Roberts, G. D., and Kamvouris, J. E., 1996, "Long Term Isothermal Aging Effects on Carbon Fabric Reinforced PMR-15 Composites: Compression Strength," NASA TM-107129.

Gyekenyesi, A. L., 1998, "Isothermal Fatigue, Damage Accumulation, and Life Prediction of a Woven PMC," NASA CR-206593.

Hwang, W., and Han, K. S., 1989, "Fatigue of Composite Materials: Damage Model and Life Prediction," *Composite Materials: Fatigue and Fracture, Second Volume*, ASTM STP 1012, P. A. Lagace, ed., American Society for Testing and Materials, Philadelphia, PA, pp. 87–102.

Lemaitre, J., and Chaboche, J. L., 1990, *Mechanics of Solid Materials*, Cambridge University Press, New York.

Liu, B. Y., 1992, "Fatigue and Damage Tolerance Analysis of Composite Laminates: Stiffness Loss, Damage Modeling, and Life Predictions," Master's thesis, Dept. of Mech. Engineering, McGill University, Montreal, Quebec, Canada.

Poursartip, A., Ashby, M. F., and Beaumont, P. W. R., 1982, "Damage Accumulation During Fatigue of Composites," Proceedings, International Conference on Composite Materials IV, Tokyo.

Wang, S. S., and Chim, E. S. M., 1983, "Fatigue Damage and Degradation in Random Short-Fiber SMC Composites," *Journal of Composite Materials*, Vol. 17, p. 114.

Ye, L., 1989, "On Fatigue Damage Accumulation and Material Degradation in Composite Materials," *Composite Science and Technology*, Vol. 36, pp. 339–350.

Mechanical Property Scatter in CFCCs

M. Steen

C. Filiou

Institute for Advanced Materials,
Joint Research Centre,
European Commission,
P. O. Box 2,
NL-1755 ZG Petten,
The Netherlands

The tensile response of continuous fibre reinforced ceramic matrix composites (CFCCs) is not expected to show the large variation in strength properties commonly observed for monolithic ceramics. Results of recent investigations on a number of two-dimensional reinforced CFCCs have nevertheless revealed a considerable scatter in the initial elastic modulus, in the first matrix cracking stress and in the failure stress. One school of thought considers that the observed variability is caused by experimental factors. Elaborate testing programmes have been set up to clarify the origins of this scatter by investigation of the effects of control mode, loading rate, specimen shape, etc. Another school explains the scatter by the presence of (axial) residual stresses in the fibres and in the matrix. Although plausible, this hypothesis is difficult to verify because experimental determination of the residual stress state in CFCCs is not straightforward. In addition, with the available methods it is impractical to determine the residual stresses in every test specimen. This approach is indeed required for establishing the relationship between the magnitude of the residual stresses and the experimentally observed scatter. At IAM a method has been developed and validated which allows to quantify the axial residual stress state in individual CFCC specimens by subjecting them to intermittent unloading-reloading cycles. The method as well as the derived relationship between residual stress state and scatter in mechanical response will be presented.

Introduction

Although they exhibit very attractive properties, monolithic ceramics have not gained widespread application as structural materials because of their brittleness and lack of reliability. This is caused by the statistical distribution in strength, which in turn is governed by the distribution of flaws within the material. The introduction of a second phase with a known size decreases the range of the inherently present flaw sizes, and is hence expected to result in a narrower strength distribution and a higher reliability. Although this expectation has been confirmed to some degree on whisker and particulate reinforced CMCs, it has not been verified to the same extent for continuous fibre reinforced ceramic matrix composites (CFCCs). In the latter class of CMCs the introduction of a continuous fibre reinforcement with a tailored interface with the matrix has resulted in the appearance of a damage-tolerant instead of a brittle behavior under tensile loading conditions. This "tougher" behavior also renders the strength of CFCCs less size-dependent. However, the mechanical response is still characterized by a lot of scatter. As a support to the development of testing standards for CFCCs elaborate testing programs have therefore been set up to investigate whether the scatter in mechanical response is caused by experimental factors or by intrinsic material behavior (Piccola and Jenkins, 1995; Piccola et al., 1997). These investigations have shown that for a well-defined and carefully manufactured CFCC the scatter in strength obtained from tests within a single lab is rather small. Also, there does not seem to be a large influence of variations in the experimental procedures, although the failure strength under displacement control is lower than for load control (Piccola et al., 1997). It thus appears that the observed variability can not solely be caused by testing-related factors and that other causes also contribute to it.

For multi-directionally reinforced composites variations in volume fraction of the reinforcement and in porosity from specimen to specimen are obvious origins for scatter, and they have indeed been identified as such (Adami, 1992; Steen, 1995). However, an additional variability factor specific to multi-directionally reinforced CFCCs is the presence of a macroscopic residual stress state generated by the thermo-elastic mismatch between the fibres and the matrix. Whereas the residual stresses in particulate or whisker reinforced ceramics average out on the scale of the ceramic matrix grains, and are hence not expected to affect the macroscopic response to a large extent, this is not the case for CFCCs where longer-range residual stresses prevail. This paper presents a rationalisation of the scatter observed under short-term tensile loading of multidirectionally reinforced CFCCs in terms of the variations in axial residual stress state between specimens.

Scatter in Tensile Response

Experimental Evidence of Scatter. Examples of tensile stress versus strain curves for a satin weave two-dimensional C(f)/SiC(m) composite at room temperature are shown in Fig. 1. These tests have been performed on specimens taken from a single batch under nominally identical experimental conditions. The results clearly exhibit a considerable amount of scatter in the tensile response of this CFCC, both in terms of the overall shape of the stress-strain curve, and in terms of the values of individual parameters such as matrix cracking and failure stress, and to a lesser extent initial elastic modulus.

Effect of Volume Fraction of Reinforcement and Porosity. Although reinforcement volume fraction and porosity level are not independent, it is nevertheless possible to separately quantify their effect on the scatter by considering the variation in different parameters derived from the stress-strain curve. The volume fraction of reinforcement as a source of scatter is particularly evident from measurements of the tangent modulus immediately prior to failure for so-called class II composites where full interfacial debonding precedes failure (Evans et al., 1994). In this stage, matrix cracking has saturated and any deformation increment is solely borne by the fibres. The tangent modulus is hence $E_f V_f$, where V_f stands for the volume fraction of fibres oriented in the direction of load application. The results obtained in an in-house investigation on an Al_2O_3(f)/SiC(m) composite prepared by chem-

Contributed by the International Gas Turbine Institute (IGTI) of The American Society of Mechanical Engineers for publication in the ASME Journal of Engineering for Gas Turbines and Power. Paper presented at the International Gas Turbine and Aeroengine Congress and Exhibition, Stockholm, Sweden, June 2–5, 1998; ASME Paper 98-GT-319.

Manuscript received by IGTI March 16, 1998; final revision received by the ASME Headquarters October 20, 1999. Associate Technical Editor: R. Kielb.

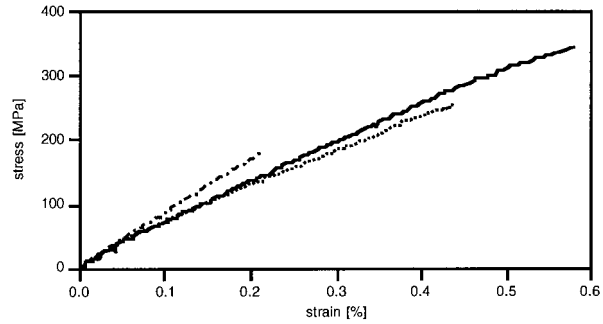

Fig. 1 Examples of tensile curves on satin weave C/SiC at room temperature

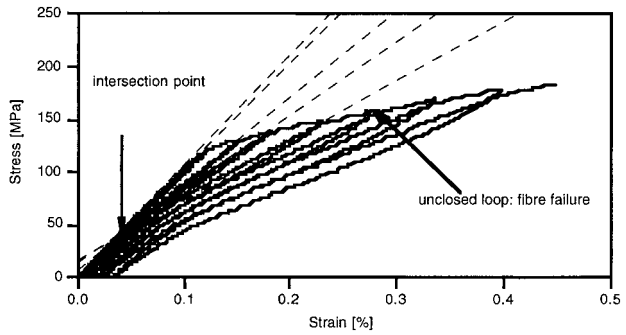

Fig. 3 Tensile curve with unloading-reloading cycles illustrating the determination of the common intersection point (Al_2O_3/SiC at room temperature)

ical vapour infiltration (CVI) are shown in Fig. 2 (Adami, 1992). Since the fibre modulus E_f only shows a small decrease over the investigated temperature range (Lesniewski et al., 1990), the larger part of the variation in the tangent modulus E_fV_f is caused by variations in V_f. The effect of porosity, on the other hand, is expected to show up primarily in the value of the initial elastic modulus E_c. For the same data set as used in Fig. 2, the initial modulus value ranges from 95 to 220 GPa.

Based on the rule of mixtures the initial modulus for the investigated two-dimensional CFCC with a symmetrical plain weave can be written as

$$E_c = 2E_fV_f + E_m(1 - 2V_f - V_p), \quad (1)$$

where E_m stands for the matrix modulus, and V_p is the porosity. Using this equation the porosity equals $V_p = 0.29 \pm 0.09$ based on literature values for E_m (Aubard et al., 1994). Such total porosity levels are too large to be physically realistic and cannot be substantiated by density measurements. Therefore, this indicates that other factor(s) contribute to the scatter in E_c.

Validation of a New Experimental Method to Determine Axial Residual Stresses in CFCCs

Experimental Determination of Fibre Axial Residual Stress and Strain. The presence of long-range residual stress fields arising from the thermo-elastic mismatch between the fibres (or fibre bundles) and the matrix is another factor that can contribute to the scatter in the tensile response of CFCCs. Particularly for CVI-processed CFCCs these residual stresses are expected to vary from specimen to specimen within the same batch in view of their different infiltration conditions. The difficulty of invoking the residual stress state as one of the factors causing scatter lies in the fact that it is experimentally very difficult to quantify the residual stress state in different specimens.

At IAM a method has been established to determine the average axial residual stresses in the fibres and in the matrix of a CFCC specimen by subjecting it to unload-reload cycles during testing.

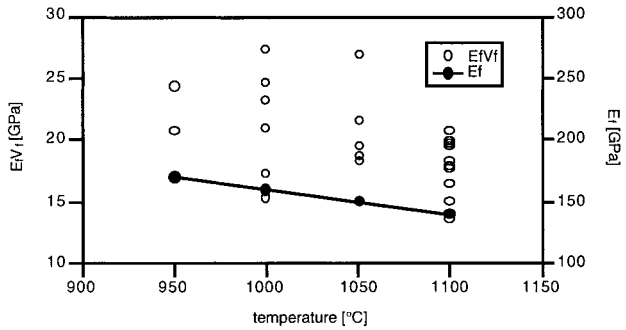

Fig. 2 Evolution of E_fV_f and E_f with temperature

The coordinates of the common intersection point of the average regression lines to consecutive unload-reload cycles represent the residual strain and stress (corrected for the volume fraction V_f oriented in the direction of load application) in the fibres (Steen, submitted). A graphical example of this evaluation is given in Fig. 3. An advantage of this method is that it not only allows the determination of the initial residual stresses before testing but also to follow how they evolve with the accumulation of damage during loading (Steen, 1997). To validate this method the axial residual stresses deduced from the common intersection point will be compared to results obtained by other experimental and analytical means, as well as with literature data where available.

Direct Experimental Comparison. Neutron diffraction is a suitable method for measuring average axial residual stresses in CFCCs (Majumdar et al., 1991) because no localized stress fields have to be measured. Hence, large volumes can be tested and the results correspond to the average axial residual stresses in each constituent. An Al_2O_3/SiC specimen from the earlier mentioned batch has been tested using a powder diffractometer in the high flux reactor at IAM (Youtsos et al., 1995). The results of the diffraction analysis are shown in Table 1, where they can be compared to the values of the intersection point strain. For the diffraction results the error values correspond to the uncertainty in the measurement performed on the single investigated specimen whereas for the intersection stresses they represent the standard deviation obtained from unloading-reloading cycles performed on a number of specimens. The diffraction results confirm both the sign and magnitude of the residual strains in the fibres and in the matrix as inferred from the common intersection point of consecutive unload-reload cycles.

Direct Analytical Comparison: Inverse Tangent Modulus Evaluation. The strain coordinate of the common intersection point represents the average residual strain in the fibres, whereas the stress coordinate is proportional to the average axial residual fibre stress. This interpretation is also given by Vagaggini et al., 1995, where the stress coordinate is called the negative misfit stress and is equal to the negative axial residual stress in the matrix, corrected by the factor E_c/E_m. The evaluation method proposed there uses analytical formulations of the unloading and reloading curves. The analysis can be performed on consecutive unloading and on consecutive reloading curves, through the dependence of the inverse tangent modulus on the applied stress

Table 1 Comparison of residual strains determined by neutron diffraction and from the intersection point (Al_2O_3/SiC at room temperature)

test	fibre	matrix
neutron diffraction	0.028 ± 0.01 %	-0.028 ± 0.006 %
intersection point	0.029 ± 0.008 %	-0.029 ± 0.008%

Table 2 Comparison of axial residual stresses (MPa) in a single specimen derived from hysteresis loop analysis by two different methods

method	plain weave C/SiC	satin weave C/SiC	Al_2O_3/SiC
intersection stress	-150	-330	35
acc. to Vagaggini (1995) unloading part of loop	-160 ± 5	-340 ± 23	34 ± 5
acc. to Vagaggini (1995) reloading part of loop	-161 ± 3	-306 ± 31	52 ± 8

(Domergue et al., 1995; Domergue et al., 1996). The results of the evaluation for individual room temperature tests on a satin and on a plain weave C(f)/SiC(m) composite, as well as on the Al_2O_3/SiC composite mentioned earlier are listed in Table 2. The standard deviations correspond to variations in the intersection point stress obtained from consecutive unloading or reloading curves within the same test. As can be observed the intersection point stresses obtained by both evaluation methods agree very well, indicating the equivalence of both analyses.

Indirect Comparison with Literature Data. Literature data on residual stresses in CFCC specimens are very scarce. Only a limited number of fibre-matrix combinations have been covered and the majority of the data refers to results obtained on micro-composites which represent a considerable simplification of the geometry compared to multidirectionally reinforced CFCCs. From the results of these tests the axial residual stresses in the fibre and the matrix are usually obtained by a finite element analysis. For Al_2O_3/SiC no literature data could be found, whereas those for C/SiC model composites using the same fibres and a CVI-SiC matrix as the two-dimensional composites investigated here are summarised in Table 3.

The residual stresses for the model composites depend on their fibre and matrix volume fractions. Hence, the results are not directly comparable to the average residual stresses for the two-dimensional CFCCs. However, using the value of the elastic modulus quoted in the different papers, the residual strains in the model composites can be determined, and are also listed. They agree well with the average residual fibre strain determined from the common intersection point for the satin weave composite, whose reinforcement texture is most akin to that of the one-dimensional configuration of the model composites. The higher "constraint" of the transverse bundles in the plain weave C/SiC explains the larger residual strains compared to the satin weave.

Axial Residual Stresses: An Additional Source of Variability

The variability in residual stress state manifests itself most prominently in stress-related properties such as the matrix cracking stress and the stress for first fibre failure. The former is derived from the stress-strain curve by the deviation from the initial modulus, whereas the latter from the stress above which unclosed unload-reload loops appear (see Fig. 3). Table 4 summarises the experimentally observed values for the intersection point stresses, the matrix cracking stress, and the first fibre failure stress for the investigated satin weave C/SiC composite. The important point to observe is that the large scatter in the nominal values for the matrix

Table 3 Comparison of residual stresses and strains in different types of C/SiC composites

test method	axial residual stress		residual fibre strain [%]	ref.
	matrix [MPa]	fibre [MPa]		
FEA microcomp.	180	-630	-0.286	Lamon et al., 1993
FEA microcomp.	300	-520	-0.236	Bobet et al., 1994
FEA 1D comp.	200 to 280	-550 to -620	-0.25 to -0.28	Bobet et al., 1994
2D plain weave		(-160 ± 12) / V_f	-0.198 ± 0.0177	Steen, unpubl.
2D satin weave		(-270 ± 66) / V_f	-0.262 ± 0.075	Steen, unpubl.

Table 4 Nominal and "true" values of stress-related parameters

parameter	nominal value [MPa]	value accounting for residual stresses [MPa]
intersection stress	-270 ± 66	
matrix cracking stress	18 ± 50	322 ± 18
fibre failure stress	313 ± 56	583 ± 42

cracking and fibre failure stress is matched by a similar scatter in the value of the intersection point stress. However, when the nominal stresses are corrected for the residual stress, as indicated by the intersection point stress, the scatter is considerably reduced. Moreover, the "true" (i.e., corrected) stresses for fibre failure in this satin weave C/SiC agree well with those obtained in a plain weave C/SiC with the same fibres, whereas the nominal stresses were totally different in the latter composite.

In addition to offering an explanation of the scatter in stresses for matrix cracking and fibre failure, the variation in the axial residual stress state from specimen to specimen also allows a rationalisation of the scatter observed for the initial elastic modulus. This is illustrated in Fig. 4 that shows the relation between the initial elastic modulus E_c and the intersection point strain, i.e., the average axial residual strain in the fibres for all the composites studied.

When the fibres are in axial residual tension and the matrix in axial compression (Al_2O_3/SiC) the initial modulus decreases with decreasing residual tensile fibre strain, or conversely with increasing residual tensile strain in the matrix. The explanation is that residual tensile stresses in the matrix promote the occurrence of first matrix cracking and hence of interfacial debonding, which results in a decrease of the initial modulus. Similarly, for C/SiC the large residual tensile stresses in the matrix corresponding to large residual compressive fibre strains have induced extensive matrix cracking and associated interfacial debonding. This has occurred to such an extent that the initial modulus does not seem to depend on the level of the residual stresses.

The discussion so far has shown that the scatter in stress parameters and in initial elastic modulus can be explained to a large extent by the variability of the axial residual stress state from specimen to specimen. In addition, and not shown here, accounting for the residual stresses also allows a rationalisation of the temperature dependence of the tensile response (Steen, 1996). Because the strength of both the fibres and of the CVI SiC matrix of the

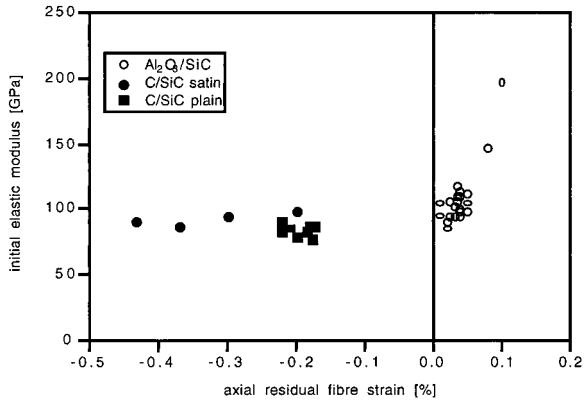

Fig. 4 Dependence of the initial elastic modulus on the residual fibre strain

investigated two-dimensional composites remains constant over a large temperature range one expects that also the tensile response of the CFCCs does not change with temperature, apart from the effect of thermal residual stresses. Individual stress-strain curves obtained at different temperatures can indeed be made to superimpose when they are translated so that their respective common intersection points coincide. This translation takes the sign and magnitude of the axial residual stresses into account. The resulting curve has been called the tensile "master curve" of the CFCC (Steen, 1996). It does not depend on temperature and represents the time-independent tensile response of the CFCC. The fact that a unique curve is obtained confirms the deterministic nature of the tensile properties of CFCCs, as inferred on a theoretical basis from the reduction in the range of inherent flaw sizes.

Conclusions

The co-ordinates of the common intersection point of the regression lines to consecutive unloading-reloading cycles represent the axial residual stress state in the fibres. The residual strains and stresses determined in this way agree well with results obtained by other independent techniques. A major advantage of this method is that it allows to monitor the change in the residual stresses and strains with the progression of damage within the specimen.

The scatter observed in tensile tests on multidirectionally reinforced CFCCs is caused by the combined effects of variations in volume fraction of the reinforcements, in porosity level, and in the axial residual stress state. These scatter origins are not independent from each other. Indeed, when applying the unloading-reloading method to determine the residual stresses in individual specimens the influence of variations in the fibre volume fraction and in the porosity are automatically taken into account.

The scatter in axial residual stress state from specimen to specimen can explain the observed variation in tensile response, in particular the matrix cracking stress, first fibre failure stress and initial elastic modulus. The lack of scatter in the "true" tensile behavior (i.e., taking into account the presence of axial residual stresses) indicates that the time-independent behavior of the investigated CFCCs is deterministic.

Acknowledgment

This work is performed under the Research and Development Programme of the EC. The authors thank SEP for providing the CFCC test specimens.

References

Adami, J. N., 1992, "Comportement en Fluage Uniaxial sous Vide d'un Composite à Matrice Céramique Bidirectional Al_2O_3-SiC," Institute for Advanced Materials, Joint Research Centre, European Commission, EUR 14425 FR.

Aubard, X., Lamon, J., and Allix, O., 1994, "Model of the Nonlinear Mechanical Behavior of 2D SiC/SiC Chemical Vapour Infiltration Composite," *J. Am. Ceram. Soc.*, Vol. 77, pp. 2118–2126.

Bobet, J. L., and Lamon, J., 1995, "Thermal Residual Stresses in Ceramic Matrix Composites—I. Axisymmetric Model and Finite Element Analysis," *Acta Metall. Mater.*, Vol. 6, pp. 2241–2253.

Domergue, J. M., Vagaggini, E., and Evans, A. G., 1995, "Relationship Between Hysteresis Measurements and the Constituent Properties of Ceramic Matrix Composites: II., Experimental Studies on Unidirectional Materials," *J. Am. Ceram. Soc.*, Vol. 78, pp. 2721–2730.

Domergue, J. M., Heredia, F. E., and Evans, A. G., 1996, "Hysteresis Loops and the Inelastic Deformation of 0/90 Ceramic Matrix Composites," *J. Am. Ceram. Soc.*, Vol. 79, pp. 161–170.

Evans, A. G., 1994, "Review—The Physics and Mechanics of Fibre-Reinforced Brittle Matrix Composites," *J. Mat. Sci.*, Vol. 29, pp. 3857–3896.

Lamon, J., Lissart, N., and Rechiniac, C., 1993, "Micromechanical and Statistical Approach to the Behavior of CMC's," *Ceram. Eng. Sci. Proc.*, pp. 1115–1124.

Lesniewski, C., Aubin, C., and Bunsell, A. R., 1990, "Property-Structure Characterisation of a Continuous Fine Alumina-Silica Fibre," *Comp. Sci. Techn.*, Vol. 37, pp. 63–78.

Majumdar, S., Singh, J. P., Kupperman, D., and Krawitz, A. D., 1991, "Application of Neutron Diffraction to Measure Residual Strains in Various Engineering Composite Materials," *J. Eng. Mat. Techn.*, Vol. 113, pp. 51–59.

Piccola, J. P., and Jenkins, M. G., 1995, "Effect of Test Parameters on Tensile Mechanical Behaviour of a Continuous Fibre Ceramic Composite (CFCC)," *Ceramic Engineering and Science Proceedings*, Vol. 16, No. 4, pp. 325–336.

Piccola, J. P., Jenkins, M. G., and Lara-Curzio, E., 1997, "Influence of Test Mode, Test Rate, Specimen Geometry and Bending on Tensile Mechanical Behavior of a Continuous Fiber Ceramic Composite," Proceedings, Thermal and Mechanical Test Methods and Behavior of Continuous-Fiber Ceramic Composites, M. G. Jenkins, S. T. Gonczy, E. Lara-Curzio, N. E. Ashbaugh, and L. P. Zawada, eds., ASTM 1309, pp. 3–15.

Steen, M., 1995, "Residual Stress State and Damage Mechanisms in Ceramic Matrix Composites Inferred from Uniaxial Tests Incorporating Unloading and Reloading Sequences," Proceedings, Fourth Euro Ceramics, S. Meriani and V. Sergo, eds., Vol. 3, pp. 63–70.

Steen, M., 1996, "Tensile Mastercurve of Ceramic Matrix Composites: Significance and Implications for Modelling," International Workshop on Modelling of the Mechanical Behaviour of Ceramic Matrix Composites MCMC'96, Petten, the Netherlands.

Steen, M., 1997, "Effect of Residual Stresses on the Mechanical Response of Continuous Fibre Reinforced Ceramic Matrix Composites," Proceedings, NATO Advanced Research Workshop on Multilayered and Fibre-Reinforced Composites: Problems and Prospects, Kiev.

Steen, M., 1999, "Residual Stresses and Their Effect on the Tensile Behaviour of Fibre Reinforced Ceramic Matrix Composites," submitted to Acta Mat.

Vagaggini, E., Domergue, J. M., and Evans, A. G., 1995, "Relationship Between Hysteresis Measurements and the Constituent Properties of Ceramic Matrix Composites: I., Theory," *J. Am. Ceram. Soc.*, Vol. 78, pp. 2709–2720.

Youtsos, A. G., Schröder, J., and Timke, T., 1995, "Residual Stress Investigations Near Material Interfaces by Neutron Diffraction at the JRC-Petten," Proceedings, High Technology Composites in Modern Applications, S. A. Paipetis and A. G. Youtsos, eds., University of Patras, Applied Mechanics Laboratory, pp. 374–390.

On the Performance of Hybrid Foil-Magnetic Bearings

H. Heshmat

H. Ming Chen

J. F. Walton, II

Mohawk Innovative Technology, Inc.,
1037 Watervliet-Shaker Road,
Albany, NY 12205

Recent technological advancements make hybridization of the magnetic and foil bearings both possible and extremely attractive. Operation of the foil/magnetic bearing takes advantage of the strengths of each individual bearing while minimizing each others weaknesses. In this paper one possible hybrid foil and magnetic bearing arrangement is investigated and sample design and operating parameters are presented. One of the weaknesses of the foil bearings, like any hydrodynamic bearing, is that contact between the foil bearing and the shaft occurs at rest or at very low speeds and it has low load carrying capacity at low speeds. For high speed applications, AMBs are, however, vulnerable to rotor-bending or structural resonances that can easily saturate power amplifiers and make the control system unstable. Since the foil bearing is advantageous for high speed operation with a higher load carrying capacity, and the magnetic bearing is so in low speed range, it is a natural evolution to combine them into a hybrid bearing system thus utilizing the advantages of both. To take full advantage of the foil and magnetic elements comprising a hybrid bearing, it is imperative that the static and dynamic characteristics of each bearing be understood. This paper describes the development of a new analysis technique that was used to evaluate the performance of a class of gas-lubricated journal bearings. Unlike conventional approaches, the solution of the governing hydrodynamic equations dealing with compressible fluid is coupled with the structural resiliency of the bearing surfaces. The distribution of the fluid film thickness and pressures, as well as the shear stresses in a finite-width journal bearing, are computed. Using the Finite Element (FE) method, the membrane effect of an elastic top foil was evaluated and included in the overall analytical procedure. Influence coefficients were generated to address the elasticity effects of combined top foil and elastic foundation on the hydrodynamics of journal bearings, and were used to expedite the numerical solution. The overall program logic proved to be an efficient technique to deal with the complex structural compliance of various foil bearings. Parametric analysis was conducted to establish tabulated data for use in a hybrid foil/magnetic bearing design analysis. A load sharing control algorithm between the foil and magnetic elements is also discussed.

Introduction

Advanced high speed rotating machinery designs are subjecting bearings to ever more severe mechanical and thermal environments, while in many instances also placing demands on the cleanliness of process gases. These conditions are requiring that new and innovative oil-free bearing systems be developed. Compliant foil bearings (CFBs) and active magnetic bearings (AMBs) are two technologies that have been investigated and fielded to meet these needs. For example, CFBs are suitable for a wide range of rotating machinery with operating speeds exceeding 100,000 rpm, such as cryogenic turboexpanders, air cycle machines, oil-free compressors and turbochargers. While CFBs appear quite simple, the simplicity does not necessarily imply ease of design. As a matter of fact, a thorough detailed systems oriented effort is necessary to successfully design and apply a set of CFBs in any advanced new application [1–8]. While CFBs have many advantages, like any hydrodynamic bearing, the shaft remains in intimate contact with the bearing smooth top foil when at rest or low speeds. Thus, a rub resistant coating is required to prevent wear of the journal and foil at low speeds during start-ups and shutdowns. To make a long lasting bearing, both wear resistant coatings and conformal CFBs must be provided by design. Furthermore, the introduction of Coulomb damping into the bearing design is a challenging issue that is crucial for rotor stability at high speeds. Active magnetic bearings (AMBs), on the other hand, are well suited for low speed operation because metal-to-metal contact is avoided, dynamic balancing is possible, and both stiffness and damping are electronically maneuverable. For high speed applications, AMBs are however vulnerable to rotor-bending or structural resonances that can easily saturate power amplifiers and make the control system unstable. This problem is mainly due to noncollocation of sensors and actuators. Another AMB problem for high speed applications is that reliable and long lasting backup bearings are not available. Conventional rolling-element-type backup bearings tend to produce skidding wear and last for only a few rotor drops due to electric failures. Worse yet, violent backward-whirl may occur and render a catastrophic system failure [9]. Since the foil bearing is advantageous for high speed operation and the magnetic bearing is so in low speed range, it is a natural evolution to combine them into a hybrid bearing taking the advantages of each. While there are many possible hybrid arrangements, this paper investigates one possible hybrid arrangement where the CFB and AMB are placed side by side. Figure 1 is a schematic representation of the hybrid bearing control system. For some applications such as aircraft gas turbines, the hybrid bearing can offer the following benefits:

1 For the same load capacity, the hybrid is potentially smaller and lighter and consumes less power than a pure AMB. The specific load capacity of foil bearings is more than 4000 Kg/Kg [2] of bearing weight while AMBs are about 18 Kg/Kg of bearing weight.
2 The rotor may be able to continue operating and subsequently

Contributed by the International Gas Turbine Institute (IGTI) of THE AMERICAN SOCIETY OF MECHANICAL ENGINEERS for publication in the ASME JOURNAL OF ENGINEERING FOR GAS TURBINES AND POWER. Paper presented at the International Gas Turbine and Aeroengine Congress and Exhibition, Stockholm, Sweden, June 2–5, 1998; ASME Paper 98-GT-376.

Manuscript received by IGTI March 22, 1998; final revision received by the ASME Headquarters October 20, 1999. Associate Technical Editor: R. Kielb.

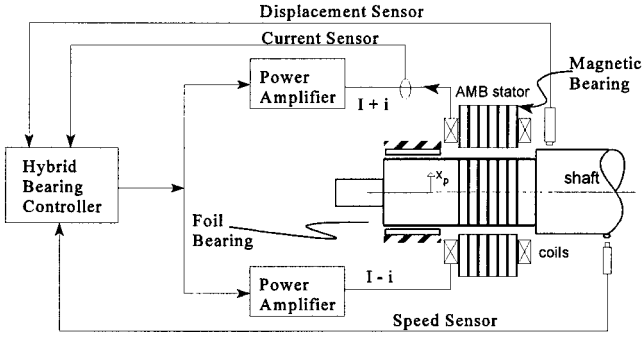

Fig. 1 Schematic of hybrid foil magnetic bearing concept

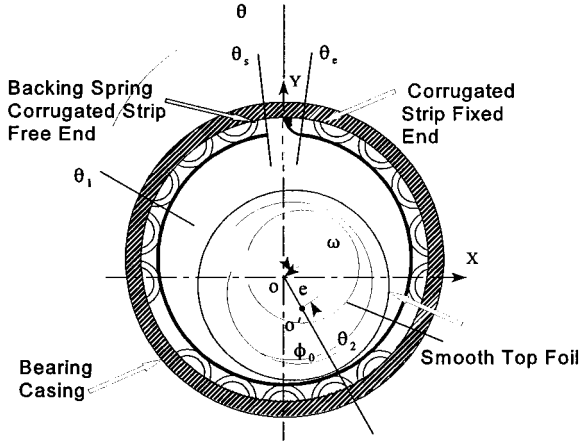

Fig. 2 Foil bearing assembly and nomenclature

be shut down if needed on the CFB alone in the event of an electrical system failure.

3 The foil bearing coating wear problem can be eliminated because the magnetic bearing supports the rotor loads at low speeds. Rotor system stability and response to unbalance can both be enhanced by the AMB through the use of electronically generated damping and in-situ balancing.

4 The tuning of the magnetic bearing in the high frequency range may be simplified because of the load sharing and Coulomb damping made possible by the CFB.

Hybrid Foil-Magnetic Bearings

An important design issue involved in a hybrid foil-magnetic bearing is the development of the control system to ensure proper system operation and load sharing between the two bearings. Note that a loaded AMB using a conventional PID control would typically locate the journal almost concentric with the bearing center. However, in a loaded foil bearing, as with any hydrodynamic bearing, the journal position is offset from the bearing center with some eccentricity and attitude angle. Thus to ensure functionality of the hybrid bearing, the designer must understand both the static and dynamic characteristics of both bearings. This paper first describes the development of a new analytical technique for evaluating the performance of CFBs. A load sharing control algorithm for hybrid bearing system is also presented.

Foil Bearing Characteristics. Figure 2 schematically presents the fundamental configuration and nomenclature for self acting hydrodynamic CFBs. One of the key features of the CFB is that it possesses a two fold mechanism for imparting stiffness and damping to a bearing. One mechanism is via the geometry and the materials used for the structural support elements and the smooth top foil, which the designer combines to provide a compliant spring support [3, 8]. The other mechanism is hydrodynamic, resulting from the gas film between the shaft and the smooth top foil. In CFBs, the clearance geometry required to generate load-carrying hydrodynamic films is provided by the elastic deflection of the foils. As speed increases, the smooth top foil and corrugated support foils are automatically forced radially outward, forming a converging wedge. Thus the optimum shape for hydrodynamic action is formed without having to use complex and expensive machining. Furthermore, with appropriate design, the converging

Nomenclature

A = area
Aij = foil bearing structural rigidity
C = radial clearance
C_g = gas constant
C_{ij} = two-dimensional influence coefficient
C_P = proportional gain coefficient
C_i = integral gain coefficient
C_D = derivative gain coefficient
D = diameter of CFB bearing for journal
e = eccentricity coefficient
f = coefficient of friction
F = force
$\bar{F}$ = $FC/(\pi\mu\omega LR^2)$, dimensionless force
g_{ij} = bearing geometric function
G_p = displacement sensitivity, (V/mm)
G_a = power amplifier sensitivity, (A/V)
h = film thickness
$\bar{h}$ = (h/C)
h_N = nominal film thickness
K = spring coefficient, bearing stiffness
$\bar{K}$ = (KC/P_aR^2)
K_B = structural stiffness of CFB
K_m = magnetic stiffness
K_i = current stiffness, function of bias current
L = width of bearing in the z direction
p_a = ambient pressure
P = pressure, unit load (W/LD)
R = radius of bearing or journal
S = Laplace variable
t = time, foil thickness
T = bearing torque
W = load
$\bar{W}$ = $W/(P_aR^2)$, Load parameter
x, y = rectangular coordinates
z = axial coordinate
α_{ij} = backing spring compliance coefficient
β = angular extent of bearing pad, $(\theta_E - \theta_S)$
ξ = normalized angular extent (θ/β)
δ = maximum surface deflection at midplane of CFB
δ_{ij} = surface deflection
ϵ = eccentricity ratio (e/C)
θ = angular coordinate
$\Re_{ij}$ = influence factor
θ_S = start of bearing pad
θ_E = end of bearing pad
θ_0 = angular position of $h_{\min}$
θ_1 = start of hydrodynamic film
θ_2 = end of hydrodynamic film
T_i, T_d = time constant of integrator and differentiator, (s)
μ = lubricant viscosity
υ = Poisson's Ratio
ϕ = attitude angle, $(\theta_0 - \pi)$
ϕ_L = load angle
ω = angular velocity
ω_n = natural frequency of system
Λ = speed parameter

Subscripts

a = ambient
E = end
Min = minimum
Max = maximum
r = radial
S = start

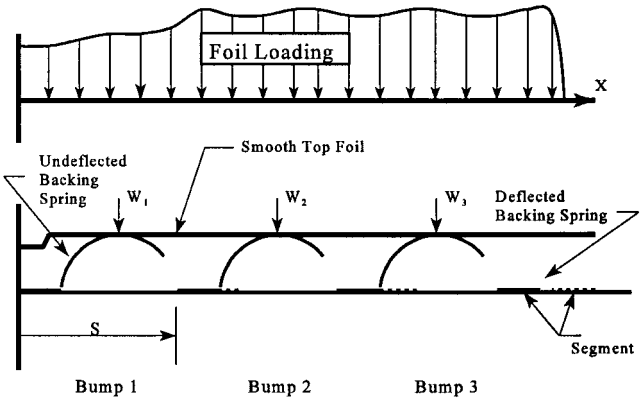

Fig. 3 Foil bump strip configuration and nomenclature

effects become more pronounced as a function of speed, and load, thereby increasing bearing load capacity.

Until very recently, the maximum load capacity of CFBs in air at 20°C and 1 ATM, was on the order of .345 Mpa at a speed of 60,000 rpm. Tests recently performed by the first author have demonstrated that CFBs can be designed with significantly increased load capacity to .669 Mpa. It has been shown that self acting CFBs have a steady-state load capacity proportional to journal speed [1–3].

Through analytic studies it has also been shown that CFB direct and cross-coupling stiffness are functions of applied load, speed, bearing dimensions, and number of pads similar to hydrodynamic bearings. However, unlike conventional hydrodynamic bearings, the stiffness of the CFBs is dominated by the stiffness of the structural elements and damping comes from the Coulomb friction forces generated between the bearing structural support elements and other interface regions resulting from their particular geometry and assembly. In addition to interface geometry and support configuration, damping is a strong function of the interacting materials, static load, frequency and amplitude of motion [4, 5]. As with all high speed rotor-bearing systems, damping is crucial for controlling sub-synchronous whirl.

Relevant to the hybrid bearing control are the following foil bearing parameters: load W, attitude angle ϕ, speed parameter Λ and stiffness coefficient K. These nondimensional parameters, as a function of journal eccentricity ratio ϵ, can be computed using an advanced computational technique. Given the journal speed, bearing dimensions, etc., the computed CFB performance data can be stored and applied to an on-line hybrid bearing control which will be discussed later.

Compliant Foil Bearing Analysis

Hybrid foil/magnetic bearing simulation requires accurate prediction of the foil bearing operating performance and stiffness characteristics to ensure that the bearings complement one another and produce the desired characteristics. In this section we are therefore concerned with evaluating the performance of a gas foil journal bearing using a compliant smooth top foil as the bearing surface supported by a compliant backing spring (corrugated strip foil). Figures 2 and 3 present the basic CFB and corrugated backing strip configurations. The foil is anchored at its trailing edge but is free at the leading end. The corrugated strip foil acts as a backing spring and the top foil, when loaded, deflects, conforming to the pressure profile. It must be stressed that in analyzing foil bearings, static force displacements play an important role, since the compliance of the bearing surface governs the operational characteristics. Due to the compliance of the bearing surface, to analyze foil journal bearings required the formation of a specialized nonlinear elasticity solution. A program has been developed and forms the basis of a coupled elastohydrodynamic solution to CFBs.

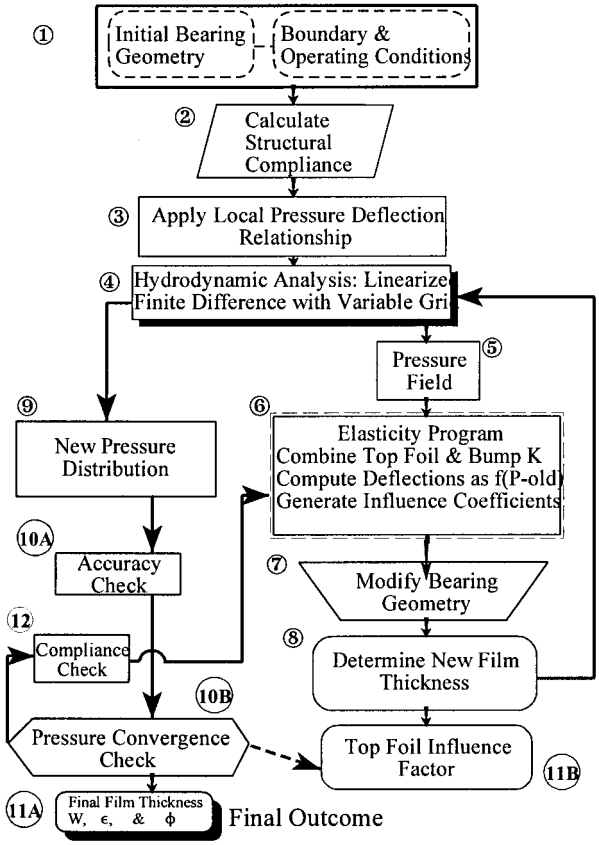

Fig. 4 Program flow chart including top foil influence

Theoretical Basis and Program Logic Flow Chart. Unlike conventional approaches, the solution of the CFB governing hydrodynamic equations must deal with a compressible fluid that is also coupled with a compliant bearing surface. The solution to the structural compliance is provided in two stages as presented in the flow diagram of Fig. 4.

In the first level elasticity solution formulation of the compliant element (backing spring) stiffness matrices it is assumed that the smooth foil (a) follows the global deflection of the backing springs, and (b) will not follow the indentation between bumps of the corrugated backing spring. It is also assumed that the deflection of the top foil and backing springs in responding to the hydrodynamic pressure is dependent on local effects only.

Based on past investigation of corrugated strip foils, Heshmat [1, 2] and Walton and Heshmat [3], it is shown that the bumps near the fixed end have a higher stiffness. In some cases the stiffness near the fixed end can be two to three times higher than near the free end. This phenomenon is related to the interacting forces that exist between bumps in a corrugated foil strip. A detailed analysis was developed to compute the stiffness, deflection, displacement and reacting forces, including friction forces for each bump for various geometries and load distributions [4, 5]. A sample solution for a corrugated foil consists of ten bumps given in Table 1. The compliance of an individual bump is represented in dimensionless form

$$\bar{\alpha}_n = C/(P_a[w_n/\delta_n]),$$

Table 1 Compliance as a function of number of bumps under uniform load distribution

	Bump Foil									
$\bar{\alpha}$	1	2	3	4	5	6	7	8	9	10
	0.2	0.6	1.0	2	5	8	11	14	17	20

where α is the compliancy factor, subscript n refers to the bump number from the fixed end, w designates load at the bump per unit transverse, δ is respective bump deflection.

It is apparent from Table 1 that this nonuniform circumferential stiffness distribution contributes greatly to the nonlinear stiffness characteristics of foil bearings.

Numerical Prediction of Foil Bearing Performance. With the nomenclature of compliant surface foil bearings (CFB) as given in Fig. 2 and 3, the two-dimensional compressible Reynolds equation can be written as

$$\frac{1}{R^2}\frac{\partial}{\partial\theta}\left[h^3\rho\frac{\partial p}{\partial\theta}\right]+\frac{\partial}{\partial z}\left[h^3\rho\frac{\partial p}{\partial z}\right]=6\mu\omega\frac{\partial\rho h}{\partial\theta} \tag{1}$$

However, the density is related to the pressure by an equation of state, generally of the form

$$p=C_g\rho^n, \tag{2}$$

where C_g is a constant, $n=1$ for isothermal conditions, and $n=\gamma=C_p/C_v$ for adiabatic conditions. The usual situation with a gas bearing is approximated by the isothermal case so it will be assumed in further analysis that $p=\rho C_g$, and considering the following nondimensional parameters:

$$\bar{Z}=(Z/R);\quad \bar{p}=(p/p_a);\quad \bar{h}=(h/C);\quad \Lambda=\frac{6\mu\omega}{p_a}\left(\frac{R}{C}\right)^2.$$

Normalizing the Reynolds Eq. (1), we obtain

$$\frac{\partial}{\partial\theta}\left[\bar{p}\bar{h}^3\frac{\partial\bar{p}}{\partial\theta}\right]+\frac{\partial}{\partial\bar{z}}\left[\bar{p}\bar{h}^3\frac{\partial\bar{p}}{\partial\bar{z}}\right]+\Lambda\frac{\partial}{\partial\theta}(\bar{p}\bar{h}). \tag{3}$$

Referring to Eq. (3), it should be noted that the film thickness variation h_{ij} is due both to bearing initial geometry $[g_{ij}]^{\text{int}}$ (eccentricity e and bearing initial surface shape) and to the deflection of the compliant surface under imposed hydrodynamic pressure. Since the latter is proportional to the local pressure, we have

$$h_{ij}=[g_{ij}]^{\text{int}}+[\alpha_{ij}][p_{ij}-p_a]. \tag{4}$$

Considering the initial CFB configuration with a single cylindrical top foil but disrupted at $\theta=0$ (Fig. 2) then

$$[g_{ij}]^{\text{int}}=C+e\cos(\theta-\phi_0), \tag{5a}$$

where normalized α_{ij},

$$\bar{\alpha}_{ij}=\frac{C}{p_a} \tag{5b}$$

reflects the structural compliancy coefficient of the backing spring. Consequently, the normalized film thickness is given by

$$\bar{h}_i=(h_{ij}/C)=1+\epsilon\cos(\theta-\phi_0). \tag{6}$$

Boundary Conditions. The construction of foil journal bearings does not permit the generation of sub-ambient pressures. Whenever diverging portions of the film tend to produce ambient pressure in the fluid film, i.e., on the surface of the top foil, the prevailing ambient pressure, P_a underneath the foil, along with preloading, lifts the foil until the pressures on both sides of the foil (including pressures from the springs) are equalized. This fact has the following implications for the start and end of the hydrodynamic film. When a relevant foil segment having a diverging film thickness, either at the start or the end of the arc, the foil continues to lift off, maintaining constant film thickness and constant ambient pressure.

In essence, this situation is similar to the trailing edge condition in cavitating liquid-lubricated bearings. Here, as with cavitation, the film ends at an unknown angular position, θ_2, (Fig. 2) which from continuity requirements must fulfill both the zero pressure and zero pressure gradient boundary conditions. Thus, the boundary conditions for the solution of Eq. (3) are

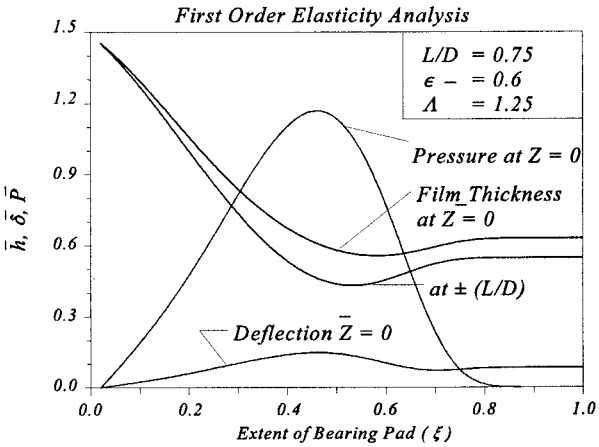

Fig. 5 Film thickness, deflection, and pressure

$$\text{at } \theta=\theta_{is} \quad \text{or} \quad \theta=\theta_1,\quad \bar{p}=1 \tag{7a}$$

$$\text{at } \theta=\theta_2\{\bar{p}=1 \tag{7b}$$

$$\text{at } \theta=\theta_2\left\{\frac{\partial\bar{P}}{\partial\theta}=0 \tag{7c}$$

$$\text{at } \bar{Z}=\pm\left(\frac{L}{D}\right)\bar{p}=1 \tag{7d}$$

Method of Solution. The range of analytical parameters and design variables involved in the present method of solution is fairly wide. The overall program therefore involved a number of computer codes, some of which had to be iterated on in order to arrive at integrated results for the bearing system as shown in Fig. 4.

For the numerical solution of Eq. (3), the dependent variable was represented by a finite number of points located at intersections of a grid mesh. By substituting Eq. (6) into Eq. (3) and with the grid network, the Reynolds Eq. (3) was written in finite difference form. The resultant form was linearized by the Newton–Raphson method and represented in matrix notation and solved by the column method (Heshmat et al., [7, 8]). The boundary conditions given in Eq. 7 were satisfied by setting negative pressures to 1 during the backsweep in the column method.

The resultant pressure field $[p_{ij}]$ was then taken to the next level of elasticity analysis, box no. 6, in Fig. 4, to include the effect of the top foil in the CFB analysis. In this higher level of elasticity analysis, the mathematical model of the foil bearing consisted of a staggered thin top foil supported via backing springs (α_{ij}) subjected to the resultant pressure field, p_{ij}.

The combined top foil and backing spring deflection was computed for the given p_{ij}, resulted in a deflection matrix, δ_{ij}. The overall structural stiffness is given by

$$[A_{ij}]=[P_{ij}]/[\delta_{ij}], \tag{8}$$

where A_{ij} is reflecting the structural rigidity of the top foil and backing spring. The new normalized influence coefficient can be written as

$$\bar{C}_{ij}=\frac{C}{p_a[A_{ij}]}. \tag{9}$$

The deflected shape of the foil (Fig. 5) along with the $\bar{C}_{ij}$, were used for the film thickness relationship, we have

$$[h_{ij}]^{\text{new}}=[\bar{g}_{ij}]^{\text{new}}+[\bar{C}_{ij}][\bar{P}_{ij}-1], \tag{10}$$

where

$$[\bar{g}_{ij}]^{\text{new}} = 1 + \epsilon \cos(\theta - \phi_0) + [\delta_{ij}]/C.$$

The new film thickness relationship, Eq. (10), was substituted in Reynolds Eq. 3. Referring to the diagram of Fig. 4, iteration between elasticity analysis and governing hydrodynamic analysis required few iterations to achieve final film thickness. The performance parameters as well as membrane stress contours were obtained, when numerical convergence based on error criteria was satisfied.

Performance Parameters. With the solution of $p(\theta, z)$ accomplished, the performance quantities of the bearing can then be obtained by proper integration. The load capacity is given in dimensionless form as follows:

$$\bar{F}_{yx} = \frac{F_{yx}}{p_a R^2} = \int_{+(L/D)}^{-(L/D)} \int_{\theta_{ij}}^{\theta_{ji}} (\bar{p} - 1)(-\cos\theta \text{ or } \sin\theta) d\theta d\bar{z}. \quad (11)$$

The dimensionless load is then given by

$$\bar{W} = \frac{W}{p_a R^2} = 4\left(\frac{L}{D}\right)\left(\frac{P}{p_a}\right) = \sqrt{\bar{F}_y^2 + \bar{F}_x^2}. \quad (12)$$

The torque on the journal is normalized form

$$\bar{T} = \frac{T}{p_a R^2} \int_{-(L/D)}^{+(L/D)} \int_{\theta_{ij}}^{\theta_{ij}} \left\{ \frac{\bar{h}}{2} \left(\frac{\partial \bar{p}}{\partial \theta} \right) + \frac{\Lambda}{6} \frac{1}{\bar{h}} \right\} d\theta d\bar{z} \quad (13)$$

Bearing Stiffness Coefficient. For small displacements from the bearing equilibrium position (e, θ_0) the stiffness coefficient is given by the general term

$$k = \frac{\partial F}{\partial e} \sin\theta_0 + \frac{1}{e} \frac{\partial F}{\partial \theta_0} \cos\theta_0 \quad (14)$$

Properly normalized, the collinear and cross-coupled spring coefficients are thus given by

$$\bar{K}_{xx} = \frac{\partial \bar{F}_x}{\partial \epsilon} \sin\theta_0 + \frac{1}{\epsilon} \frac{\partial \bar{F}_x}{\partial \theta_0} \cos\theta_0 \quad (15)$$

$$\bar{K}_{xy} = \frac{\partial \bar{F}_x}{\partial \epsilon} \cos\theta_0 + \frac{1}{\epsilon} \frac{\partial \bar{F}_x}{\partial \theta_0} \sin\theta_0 \quad (16)$$

$$\bar{K}_{yx} = \frac{\partial \bar{F}_y}{\partial \epsilon} \sin\theta_0 + \frac{1}{\epsilon} \frac{\partial \bar{F}_Y}{\partial \theta_0} \cos\theta_0 \quad (17)$$

$$\bar{K}_{yy} = \frac{\partial \bar{F}_y}{\partial \epsilon} \cos\theta_0 + \frac{1}{\epsilon} \frac{\partial \bar{F}_y}{\partial \theta_0} \sin\theta_0. \quad (18)$$

Sample Solutions. To demonstrate the aforementioned analytical model and numerical procedure, the following example problem is used. The journal foil bearing parameters are $D = 100$ mm, $L = 75$ mm, $C = 0.1$ mm, single pad configuration with an operating condition: $P_a = 100$ kPa, $\mu = 0.02$ *cp*, and $\epsilon = 0.6$, $n = 10{,}000$ rpm, $t = 0.15$ mm. For simplicity α_{ij} matrix is developed from data given in Table 1. The results of the intermediate solution, which neglects bending and membrane stresses on the smooth top foil, are presented in Fig. 5. Figure 5 is a composite plots of hydrodynamic pressure, film thickness and deflections taken at the bearing center line ($\bar{z} = 0$) along the normalized angular extent of bearing pad, ($\xi = \theta/\beta$), with an additional film thickness profile at the edge of the bearing ($\bar{z} = L/D$).

The resultant film and pressure profiles are the inputs to our second level elasticity equation as called for in box no. 6 of the flow diagram (Fig. 4). For an aligned journal/bearing condition, it is sufficient to model only one-half of the bearing (symmetric about the mid-plane, $\bar{z} = 0$). The top foil (membrane) grid net work was prepared for elasticity analysis via FEA. The top foil is considered symmetric about the bearing centerline (i.e., $\bar{z} = 0$) and relevant boundary conditions such as leading edge of the foil is free and its trailing end is anchored to the bearing housing (fixed end) were also applied. Not shown in this figure are distributed backing springs α_{ij} at the nodal points. Figure 6 depicts the top foil model with applied hydrodynamic pressure vectors taken from the previously computed pressure profile. The compliant structural elements (top smooth and backing spring system) FEA was conducted with the above input variables. Intermediate results are plotted in Fig. 7.

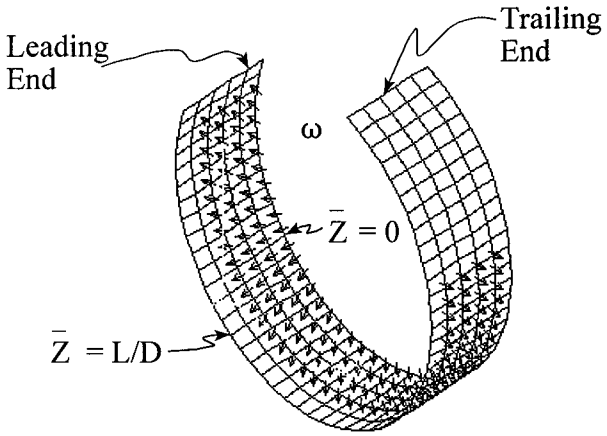

Fig. 6 Pressure profile applied to top foil

Using Eqs. 8 through 10 and iterating and following numerical scheme sequences as numbered in Fig. 4, after several passes pressure convergence was achieved. Using the relationship

$$\bar{\Re}_{ij} = [\alpha_{ij}]/[C_{ij}]^{\text{final}} \quad (19)$$

at the end of successful completion of the computation, $\bar{\Re}_{ij}$, an influence factor was obtained (box no. 11B, Fig. 4), which is a measure of the top foil's membrane effect. The magnitude of the influence factor, $\bar{\Re}_{ij}$, can be interpreted as a stiffening effect of the top smooth foil due to the membrane effect on the overall structural compliancy of the bearing. Figure 8 shows a composite plot of $\bar{\Re}_{ij}$ as a function extent of the large bearing pad for four different values of $\bar{z}$. As can be seen from the plots of Fig. 8, the stiffening effect of the top foil is greater at the middle of the bearing than at its edge. In fact, the top foil appears to be having

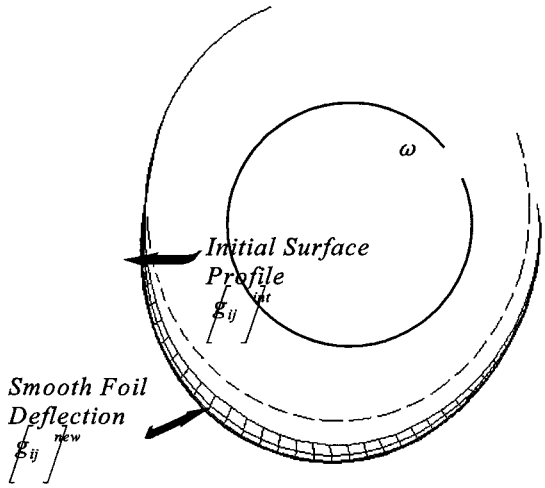

Fig. 7 Top foil deflections

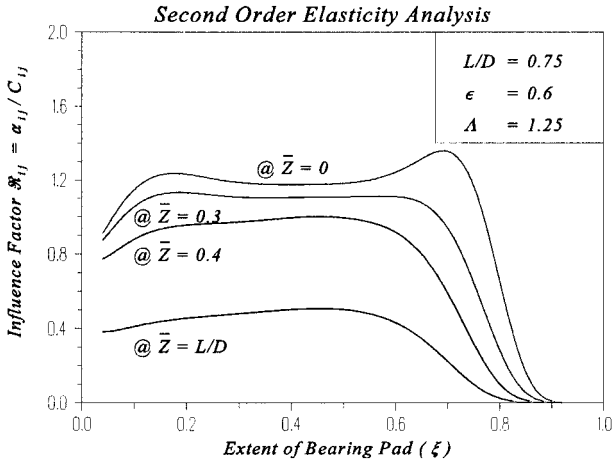

Fig. 8 Top smooth foil influence factors

a softening effect at the bearing surface near the edge (about 40 percent to 50 percent).

Furthermore, the top foil near the trailing end where hydrodynamic pressure approaches to zero, $\bar{\Re}_{ij}$ also approaches zero. These data ($\bar{\Re}_{ij}$) were stored and utilized to reduce a computation time via by passing second level elasticity analysis for similar top foil thickness and dimensions.

Parametric Study—Performance Characteristics. In the parametric study, a set of standard conditions of $L/D = 0.75$ and $\beta = 350$ deg with variable α given in Table 1 and $t = 3$ will be used, and any parametric variation will commence from this set of reference values. Due to the nature of CFB, unlike rigid journal bearings, the film thickness varies in both the θ and z directions. Since pressures cause proportional deflections of the bearing surface, the film thickness in the interior of the bearing, where pressures are highest, will be larger than at the edges ($z = \pm L/D$); also, since the maximum pressures occur near the line of center ($z = 0$), the film thickness in the interior of the $\theta = \phi_0$ line will not be necessarily the smallest. Therefore, a nominal film thickness, h_N, will be defined as the minimum film thickness that occurs along the bearing centerline, i.e., at $z = 0$. In Fig. 9, this central film thickness is plotted for a centerline $z = 0$ at various values of Λ. This value of h_N, shifts downstream and increases in value by increasing Λ. This should be kept in mind when h_N values are plotted as a function of ϵ and Λ. Similarly, the apex of the pressures slightly shifts downstream as a function of Λ.

Table 2 gives a detailed listing of the performance of a vertically loaded single pad bearing as a function of Λ and ϵ. Some of the noteworthy points emerging from these tabulations which are needed for the hybrid bearing control are plotted in Figs. 10 through 14.

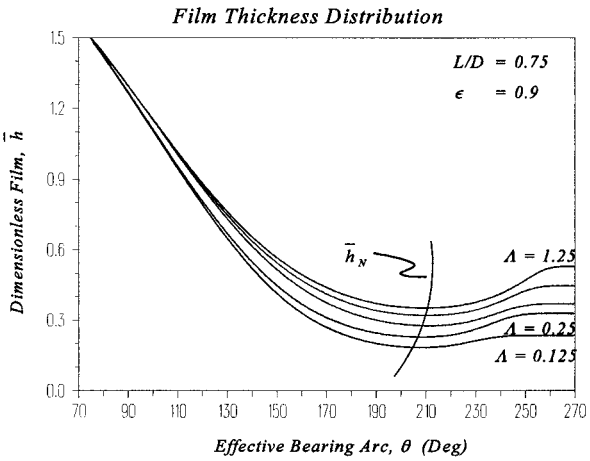

Fig. 9 Location of minimum film thickness

Table 2-A Performance of a vertically loaded single pad bearing

	ε	W x 10³	ϕ	F	h_N	ζ	β
Λ = .125	.200	0.7	69	1.889	.800	.007	.095
	.400	24.9	59	2.262	.605	.019	.266
	.600	57.5	46	3.092	.410	.021	.707
	.800	162.3	28	4.928	.245	.057	2.210
	.950	378.4	16	6.907	.176	.123	4.750
Λ = 0.25	.200	19.5	68	1.889	.800	.008	.190
	.400	50.1	58	2.259	.606	.021	.530
	.600	114.9	43	3.009	.421	.035	1.360
	.800	290.4	26	4.360	.283	.091	3.550
	.950	559.5	16	5.375	.221	.163	6.310
Λ = 0.63	.200	49.1	65	1.881	.805	.013	.4730
	.400	125.2	53	2.219	.618	.033	1.290
	.600	271.9	37	2.821	.461	.075	2.950
	.800	561.3	23	3.500	.354	.151.	5.910
	.950	894.3	15	4.084	.296	.229	8.870
Λ = 0.88	.200	68.8	63	1.875	.808	.018	.660
	.400	173.1	50	2.195	.629	.045	1.750
	.600	361.4	35	2.742	.485	.096	3.760
	.800	693.5	22	3.280	.385	.178	6.950
	.950	1047.5	15	3.679	.329	.257	0.960
Λ = 1.25	.200	97.5	60	1.865	.813	.025	.920
	.400	240.3	46	2.158	.645	.060	.236
	.600	477.4	32	2.585	.515	.121	4.740
	.800	853.3	20	3.032	.421	.209	8.140
	.950	1227.6	15	3.297	.365	.289	11.200

Magnetic Bearing Characteristics

Magnetic bearings [14] can be broadly classified into those that use either repulsive or attractive forces. Repulsive force systems most often use permanent magnets while attractive force systems use electromagnets. Attraction electromagnets are by far the most

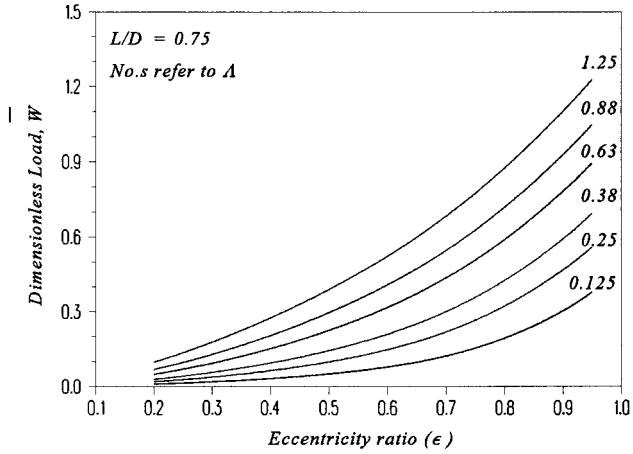

Fig. 10 Load capacity versus eccentricity ratio

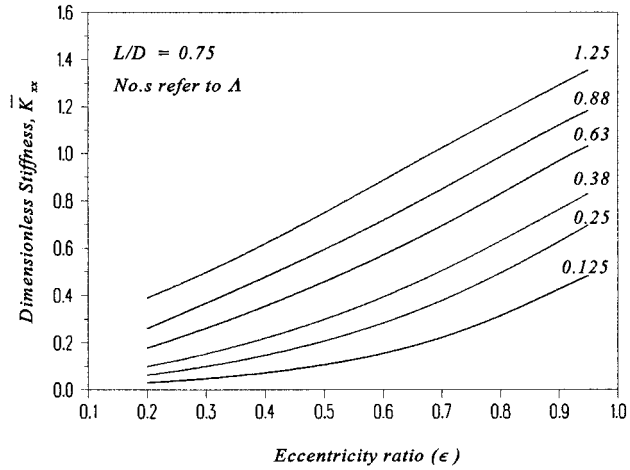

Fig. 11 Stiffness K_{xx} versus eccentricity ratio

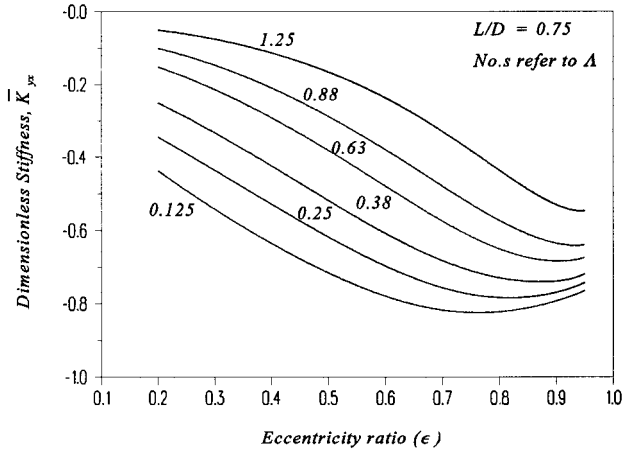

Fig. 12 Stiffness K_{yx} versus eccentricity ratio

widely used approach for magnetic suspension systems, since stiffness nearly comparable to rolling element bearings can be achieved and active control permits variation of parameters as dictated by rotor system dynamics [10–13, 16]. In general, an actively controlled electromagnetic bearing (AMB) consists of a stator which is wound with coils to create the magnetic field and ferromagnetic laminations mounted on the rotor to interact with the stator magnetic field.

Figure 1 shows a homopolar AMB [15] with position sensors, used to provide feedback control of the system. Conventional AMBs apply bias currents to electromagnets to support static loads and set up an operating flux field for linearized control. The dynamic control modulates the bias currents to create stiffness and damping. The bias currents form a flux field equivalent to a negative spring, and thus the bearing is inherently unstable. Stability is established by a negative feedback control of the rotor displacements. The feedback controller is typically a gain and phase compensation network which sets up proportional, integral and derivative (PID) functions. The PID functions provide respectively, the dynamic stiffness, the static stiffness and the damping. High static stiffness keeps the rotor centered in the bearing. The dynamic stiffness of a magnetic bearing can be represented by (1) in a normalized form

$$K/K_m = (G_p G_a K_i/K_m)[C_p + C_i/(\tau_i S + 1) + . \qquad (20)$$

Equation (1) indicates that the magnetic bearing stiffness and damping can be varied by three gains and two time constants. Lead-lag or notch filter circuits can be added in series to the PID circuit making gain and phase compensation possible at resonant frequencies not covered by the PID circuit. By varying the magnetic bearing DC stiffness, we can put more or less load onto the foil bearing. DC stiffness reduction can be accomplished by reducing the integral gain C_i.

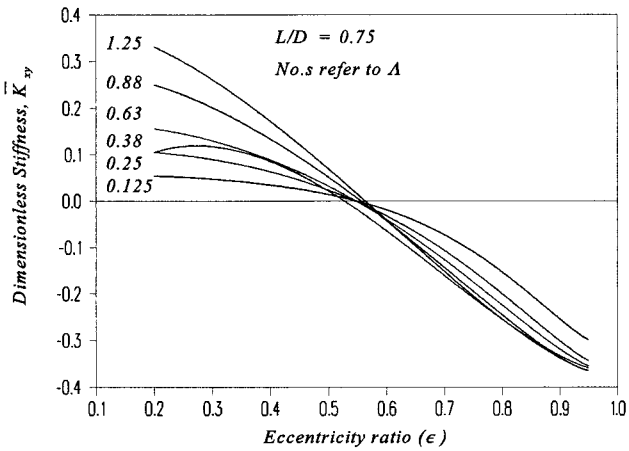

Fig. 13 Stiffness K_{xy} versus eccentricity ratio

Hybrid Foil-Magnetic Bearing Control Algorithm. Based on the above discussion, one may specify the following AMB functions in the hybrid bearing: the magnetic bearing will (1) initially center the shaft to minimize rubbing between the foil bearing and shaft at start-up and during low speeds, (2) release the load gradually to the CFB by following its preferred eccentricity locus, (3) provide synchronous balancing forces, and (4) provide additional damping for enhanced high speed rotor stability.

To reap the many potential benefits of a hybrid foil/magnetic bearing, an approach defining the steady-state load sharing as a function of operating conditions needs to be made. Note that a share of steady-state load directly implies a unique eccentricity in the foil bearing. The control reference of the magnetic part may or may not have to follow this eccentric location, depending on whether the integral control is exercised or not. Indeed, steady-state load sharing is complicated, but is the most crucial control problem of the hybrid bearing. Establishing the load sharing ratio is important because the dynamic properties of both the foil and magnetic bearings depend on their operating steady-state load. A possible control scheme including the load sharing logic is presented as follows:

- Foil and magnetic bearing data are stored for on-line calculations.
- **Step 1.** at a given speed let the magnetic bearing take all the steady state load so that the total load and direction can be determined.
- **Step 2.** using stored data, determine the eccentricity and attitude angle of the foil bearing for a predetermined share of the load.
- **Step 3.** move the magnetic bearing reference to the calculated eccentric location predicted for the foil bearing. Once the rotor center has been relocated, measure the currents in coils and the journal true location and calculate the steady-state load actually bearing supported by the magnetic bearing.
- **Step 4.** adjust the integral gains to make the steady-state load sharing correct, if necessary.
- **Step 5.** recalculate the current stiffness K_i, magnetic stiffness K_m (because both coil steady-state currents and air gaps have been changed) and the dynamic stiffness as a function of excitation frequency according to the existing PID gains.
- **Step 6.** calculate the stiffness and damping of the foil bearing for the steady-state load. These dynamic coefficients are added to those of the magnetic bearing.
- **Step 7.** check the adequacy of the total dynamic properties in terms rotor stability. If not satisfied, adjust the PID controller to improve them.

Numerical Example. The load-sharing mechanism is demonstrated below by a hybrid bearing design example. This hybrid bearing has the following specifications:

Part	Foil Part	Magnetic
Diameter (mm)	100	100
Length (mm)	75	75
Radial clearance (mm)	0.051	0.572
Share of Static Load (Kg)	9.53	6.35

The load sharing is performed at a $\Lambda = 1.25$. At this speed parameter, the foil bearing nondimensional data are given in Table 2. For the load of 9.5 Kg, the foil bearing eccentricity, altitude angle and stiffness values were calculated by interpolation using the above table, and the results were as follows:

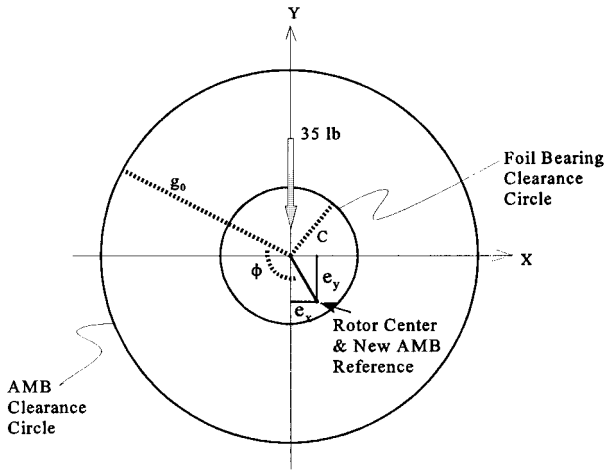

Fig. 15 Hybrid foil/magnetic bearing coordinate system

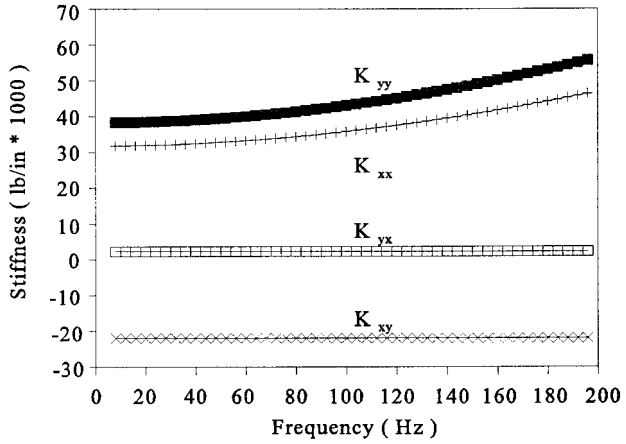

Fig. 16 Hybrid bearing stiffness

ϵ, .4925
ϕ(°) 9.5
e (mm), 0.985E-03
e_x (mm), 0.627E-03
e_y (mm), −760E-03
K_{xx} (mm), 3.80×10^6
K_{xy} (N/M), -3.85×10^6
K_{yx} (N/M), 0.41×10^6
Kyy (N/M), 4.8×10^6

Initially, the magnetic bearing supported all the 35 lb load and its reference was set at $X = Y = 0$ (Fig. 15). The relevant magnetic bearing parameters are as follows:

Initial bias currents: I_{10}, I_{30}, I_{20}, I_{40} = 4.20 A (top), 3.00 A (bottom), 3.00 A (right), 3.00 A (left)
Pid gains: C_p, C_i, C_d = 1.70, 7.60, .0035
Time constants: τi, τ_d = 1.59 s, .16 msec
Control loop constants: G_p, G_a + 7.87 V/mm, 1.0 A/V

Since the rotor center is shifted to ($X = e_x$, $Y = e_y$), the magnetic bearing reference center should be also shifted to that eccentric point. With less load (i.e., 6.35 Kg) to support, the new magnetic bearing bias currents, air gaps and magnetic quadrant forces were calculated and the results are tabulated as follows:

$$I_1 = 3.963A$$

$$I_2 = 2.916AI$$

$$I_3 = 3.237A$$

$$I_4 = 3.084A$$

$$g_1, g_2, g_3, g_4 = .592, .556, .551, .587 \text{ (mm)}$$

$$F_1, F_2, F_3, F_4 = 26.86, 16.45, 20.51, 16.45 \text{ (Kg)}$$

Without changing the PID gains, the magnetic bearing stiffness and damping coefficients were calculated over a frequency range 0 to 200 Hz. Note that these coefficients are frequency dependent while those of the foil bearing are not. Adding the two coefficients together, we have the hybrid bearing coefficients as presented in Figs. 16 and 17.

It is always informative in rotor-bearing system design to know where the bearing natural frequencies are located for a given supported mass (M). For the hybrid bearing, a simple way to locate the frequencies is simply by plotting K_{xx}, K_{yy}, and $M\omega^2$ as shown in Fig. 18. In this figure, the mass supported by the hybrid bearing was 15.88 Kg. The interception between K_{xx} and $M\omega^2$ is at 100 Hz, while the interception between K_{yy} and $M\omega^2$ is at 112 Hz. Note that the rotor was running at 10,000 rpm or 167 Hz which is far above the natural frequencies. A more precise calculation of damped frequencies has yielded the following eigenvalues:

$$-124 \pm j629 \quad \text{and} \quad -241 \pm j645 \text{ (rad/s)}.$$

The corresponding modal frequencies are 100 Hz and 103 Hz, not too far away from those estimated by Fig. 18. Note that the foil bearing damping has not been included in the above calculations.

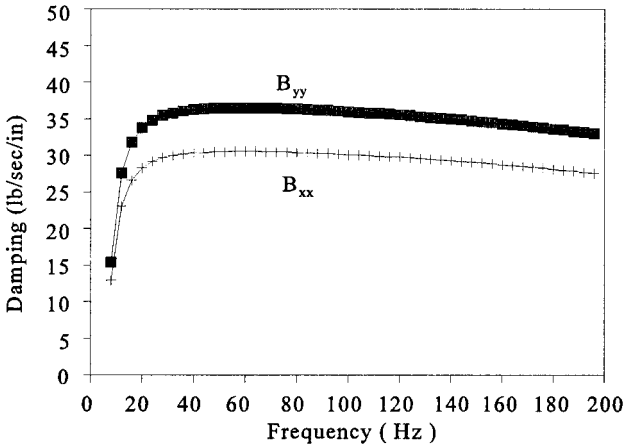

Fig. 17 Hybrid bearing damping

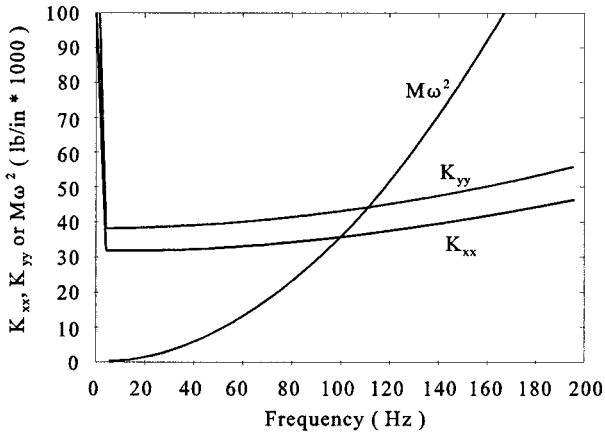

Fig. 18 Foil-magnetic bearing natural frequencies adjusting the PID gains

These two modes are reasonably damped and more damping can be achieved by adjusting the PID gains.

Conclusion

Operation of the foil/magnetic bearing takes advantage of the strengths of each individual bearing while minimizing each others weaknesses. A possible hybrid foil and magnetic bearing arrangement is investigated and sample design and operating parameters are presented. A new numerical technique was developed to investigate the performance of a class of gas-lubricated journal bearings. Parametric analysis was conducted to establish tabulated data for use in a hybrid foil/magnetic bearing design analysis. A load sharing control algorithm for hybrid foil-magnetic bearings was also discussed.

An analytical model of bending dominated compliant surface hydrodynamic foil gas journal bearings were developed to account for the variation of structural stiffness in θ and the z direction and to provide a solution to investigate the effects of top smooth foil on the bearing performance. The two-dimensional distribution of the compressible fluid film thickness and pressure, as well as the shear losses in foil bearings of finite length, was computed in line with structural elasticity of the bearing compliant surfaces. Structural stiffness characteristics of the foil bearing's backing spring and membrane effects of the top foil were included and integrated in the numerical scheme and were dealt with in two levels of iteration. As for the first level numerical analysis, deformation of the bearing surface without the effect of the top foil was formulated in relationship to the pressure. In line with the deflection of the bearing surface, the film thickness was substituted into the Reynolds equation and solved using the finite difference method. This technique provided the advantages of utilizing variable structural stiffness characteristics of the backing spring, numerical stability, and rapid convergence in obtained intermediate solutions.

Using the FE method, the membrane effect of the elastic top foil was included in the overall analysis. Further, the combined smooth top foil and elastic foundation was formulated as an influence coefficient to accelerate the numerical solution. The overall program logic proved to be an efficient and sound technique to handle the complex structural compliance of various foil bearings.

Parametric analysis was conducted to establish tabulated data for use in a hybrid foil magnetic bearing system. The technique reported herein can readily be adapted to deal with various foil bearing configurations and can evaluate the performance of innovative foil bearing designs. Future efforts are needed to experimentally verify and validate the analysis developed and presented.

Acknowledgments

The authors would like to acknowledge Mohawk Innovative Technology, Inc. for providing the primary funding necessary to make this effort possible. The U.S. Army Applied Research Laboratory is also acknowledged for their support through the Small Business Innovation Research program.

References

1 Heshmat, H., and Hermel, P., 1992, "Compliant Foil Bearing Technology and Their Application to High Speed Turbomachinery," Proceedings, 19th Leeds-Lyon Symposium on Thin Film in Tribology—From Micro Meters to Nano Meters, Leeds, U.K., Sep. 1992.

2 Heshmat, H., 1993, "Advancements In The Performance of Aerodynamic Foil Journal Bearings: High Speed and Load Capability," ASME Paper 93-Trib-32.

3 Walton, J. F., and Heshmat, H., 1994, "Compliant Foil Bearings For Use In Cryogenic Turbopumps," NASA CP3282 Vol. 1, Sept. 19, 1994, pp. 372–381.

4 Heshmat, H., and Ku, C-P. R., 1994, "Structural Damping of Self-Acting Compliant Foil Journal Bearings," ASME *Journal of Tribology*, Vol. 116, No. 1, January 1994, pp. 76–82.

5 Ku, C-P. R., and Heshmat, H., 1993, "Structural Stiffness and Coulomb Damping in Compliant Foil Journal Bearings: Theoretical Consideration," STLE Annual Meeting, Calgary, Canada, May 17–20, 1993.

6 Heshmat, H., Walowit, J., and Pinkus, O., 1983, "Analysis of Gas-Lubricated Compliant Journal Bearings," ASME *J. Lubr. Tech. Trans.*, Vol. 105, No. 4, pp. 647–655.

7 Heshmat, H., 1991, "Analysis of Compliant Foil Bearings with Spatially Variable Stiffness," Paper No. AIAA-91-2102.

8 Heshmat, C. A., and Heshmat, H., 1994, "An Analysis of Gas Lubricated, Multi-Leaf Foil Journal Bearings With Backing Springs," ASME Paper 94-Trib-61.

9 Ehrich, F. F., 1969, "The Dynamic Stability of Rotor/Stator Radial Rubs in Rotating Machinery," ASME *Journal of Engineering for Industry*, Vol. 91, pp. 1025–1028.

10 Chen, H. M., 1988, "Magnetic Bearings and Flexible Rotor Dynamics," STLE Annual Meeting at Cleveland, Ohio, May 9–12, 1988.

11 Chen, H. M., 1988, "Active Magnetic Bearing Design Methodology—A Conventional Rotordynamics Approach," presented at the 15th Leeds-Lyon Symposium on Tribology, Sept. 6–9, 1988, at Leeds, UK.

12 Chen, H. M., Wilson, D., Lewis, P., and Hurley, J., 1990, "Stability Analysis for Rotors Supported by Active Magnetic Bearings," presented at the 2nd International Magnetic Bearing Symposium, Japan, July 12–16, 1990.

13 Chen, H. M., and Ku, C. P., 1991, "Virtual Balancing of Rotors Supported by Magnetic Bearings," presented at the 13th Biennial ASME Conference on Mechanical Vibration & Noise, Sept. 22–25, 1991, Miami, Florida.

14 Schweitzer, G., et al., 1994, *Active Magnetic Bearings*, vdf Hochschulverlag AG an der ETH, Zurich.

15 Dirusso, E., Brown, G. V., and Provenza, A. J., 1994, "Test of a Cryogenic Electromagnet Biased Homopolar Magnetic Bearing," *Advanced Earth-to-Orbit Technology*, R. J. Richmond and S. T. Wu, eds., NASA, CP-3282 Vol. II, pp. 385–394.

16 Chen, H. M., 1995, "Design and Analysis of a Sensorless Magnetic Damper," ASME Paper 95-GT-180.

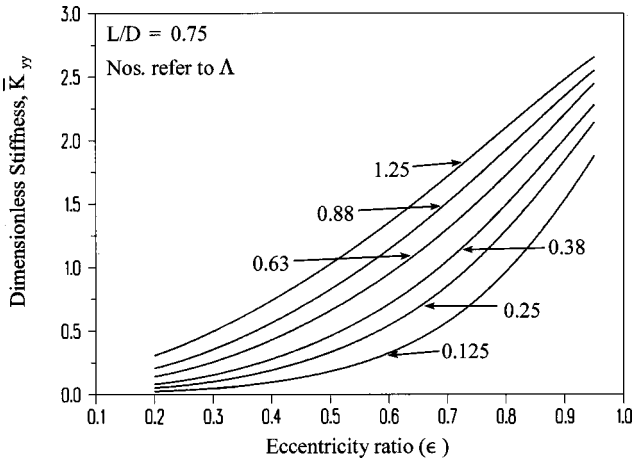

Fig. 14 Stiffness K_{yy} versus eccentricity ratio

Flutter Mechanisms in Low Pressure Turbine Blades

M. Nowinski
Swiss Federal Institute of Technology,
EPFL-DGM-LTT, Ecublens 1015,
Lausanne, Switzerland

J. Panovsky
Honeywell Aerospace,
P.O. Box 52181,
Phoenix, AZ 85072-2181

The work described in this paper is part of a comprehensive research effort aimed at eliminating the occurrence of low pressure turbine blade flutter in aircraft engines. The results of fundamental unsteady aerodynamic experiments conducted in an annular cascade are studied in order to improve the overall understanding of the flutter mechanism and to identify the key flutter parameters. In addition to the standard traveling wave tests, several other unique experiments are described. The influence coefficient technique is experimentally verified for this class of blades. The beneficial stabilizing effect of mistuning is also directly demonstrated. Finally, the key design parameters for flutter in low pressure turbine blades are identified. In addition to the experimental effort, correlating analyses utilizing linearized Euler methods demonstrate that these computational techniques are adequate to predict turbine flutter.

Introduction

This paper summarizes the results of a series of experiments conducted in an annular cascade facility to investigate torsional flutter in low pressure turbine (LPT) blades. The development of improved design guidelines for LPT flutter is an active research area because there have been several recent occurrences of instability in this class of blades. Because of these concerns, a research project was initiated with the goal of eliminating flutter in LPT blades.

To date, several forced vibration experiments similar to those described in this paper have been conducted in both linear and annular cascades (Bölcs and Schläfli, 1984; Buffum and Fleeter, 1990). In general, this work has been focused on a characterization of the aerodynamic stability of the cascade based on measurements of the blade surface unsteady pressures. For the current LPT cascade, this topic was the general focus of a previous paper (Panovsky et al., 1997). In addition, comparisons were presented between the measured unsteady pressures and predictions from computational fluid dynamics (CFD) codes.

The current paper represents an extension of this work. The primary objective of the tests presented here is to investigate the influence of the reduced frequency, inlet flow incidence, location of the torsion axis, and other key parameters on the cascade unsteady response. In addition, an enhanced understanding of the unsteady behavior of the cascade is obtained based on unsteady pressure measurements made along the test section outer wall. Tests were also performed to check the applicability of the influence coefficient technique to these cases, as well as to study the effects of cascade mistuning. Computational predictions are included to compare with the experimental measurements.

Experimental Facility and Data Analysis

In this section, a brief description of the experimental facility, test article, and data analysis technique is provided. A more complete presentation can be found in Panovsky et al. (1997). The experimental measurements were conducted in the nonrotating annular test facility (Bölcs, 1983) at the Ecole Polytechnique Fédérale de Lausanne (EPFL). This is a continuous flow, open cycle facility with a test section measuring 160 mm (inner radius) by 200 mm (outer radius). The flow conditions at the test section inlet can be varied over a wide range of Mach numbers (0.3 to 1.6) and flow angles (20 deg to 70 deg). The general intent of the facility is to provide two-dimensional flow conditions. In addition, it provides important advantages for oscillating blade measurements due to its inherent circumferential flow periodicity and absence of lateral boundaries.

The test cascade is composed of an annular arrangement of twenty blades. The LPT blade shape used for this series of tests corresponds to a latter stage of a modern commercial turbofan engine. Each airfoil in the cascade is imbedded within a base whose curved surface also forms the inner boundary of the test section. Each base is attached to its own mass and spring element, and the resulting blade assemblies are mounted to a common core.

The individual blades in the cascade are excited using an array of electromagnets. Control of the vibration amplitude and interblade phase angle (IBPA) is accomplished electronically based on feedback signals provided by inductive displacement transducers placed over each individual blade assembly (Kirschner et al., 1980). The frequency and mode shape are based on the torsional mode of the actual blade. To permit the investigation of the effects of changes in the mode shape, provisions for three locations of the torsion axis were made. These locations are shown in the blade schematic of Fig. 1. The nominal blade vibration amplitude is approximately 0.5 deg.

The upstream and downstream steady-state flow conditions are determined from spanwise-circumferential traverse data obtained using 3-hole aerodynamic probes. In addition, throughflow information is provided by a series of static pressure taps located along the outer wall of the test section. A parallel line of taps are available for unsteady pressure measurements. Two neighboring blades in the cascade are also instrumented with a total of 18 static pressure taps at midspan to measure the steady blade surface pressure distribution. A second pair of blades are instrumented with 18 miniature piezoresistive pressure transducers at midspan to measure the unsteady blade surface pressures. These measurement locations are also shown in Fig. 1.

The raw, time-dependent data derived from the pressure transducers and the inductive displacement transducers is composed of small amplitude, continuous voltage signals. These analog signals are treated through a chain of filters and amplifiers, and, subsequently, digitized and stored. The data sample is then subdivided into blocks, and an FFT decomposition, including the application of a data window to reduce leakage effects, is performed on each block. The frequency component corresponding to the blade vibration reference frequency is extracted from each data block, and an average complex value is calculated. The transducer sensitivi-

Contributed by the International Gas Turbine Institute (IGTI) of The American Society of Mechanical Engineers for publication in the ASME Journal of Engineering for Gas Turbines and Power. Paper presented at the International Gas Turbine and Aeroengine Congress and Exhibition, Stockholm, Sweden, June 2–5, 1998; ASME Paper 98-GT-573.

Manuscript received by IGTI December 12, 1997; final revision received by the ASME Headquarters October 20, 1999. Associate Technical Editor: R. Kielb.

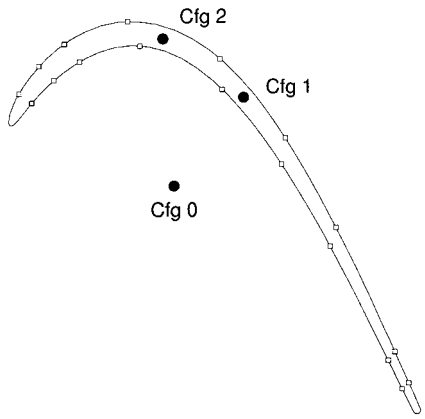

Fig. 1 Blade Profile with torsion axes and transducer locations

Table 1 Summary of test cases

Cfg. #	Cond. #	M_1	M_2	k	i (°)
0	1	0.37	0.74	0.31	0.7
0	2	0.50	1.00	0.24	1.1
0	3	0.46	0.95	0.25	4.9
0	4	0.47	0.83	0.28	10.4
1	1	0.38	0.77	0.16	0.6
1	2	0.50	0.76	0.17	6.3
1	3	0.46	0.77	0.16	3.6
1	4	0.47	0.67	0.19	9.3
2	1	0.39	0.66	0.18	0.4
2	2	0.49	0.68	0.17	5.8
2	3	0.46	0.54	0.21	5.4
2	4	0.36	0.45	0.25	6.2
2	5	0.42	0.52	0.22	0.7

ties, and any other calibration corrections are applied to these average values. The standard deviations for each data set are calculated using the average and individual block values. The 95 percent confidence intervals are calculated from the standard deviation estimates assuming a Student's *t*-distribution. For these measurements, typical 95 percent confidence intervals are on the order of ± 3 percent for the unsteady pressure amplitude, and ± 4 deg for the unsteady pressure phase angle.

Computational Program

Computational results using a quasi-three-dimensional linearized Euler code called NOVAK (Holmes and Chuang, 1993) have been obtained for all of the experimental cases. These predictions are compared to the experimental results in terms of the unsteady pressure, work, and damping coefficients (Bölcs and Fransson, 1986). All presented calculations were performed without streamtube contraction, which was found to only slightly affect the unsteady predictions (Panovsky, 1997). The primary purpose of the analytical investigations is for comparison with the experimental measurements to determine whether inviscid methods are applicable to LPT flutter.

In linearized Euler methods, the unsteadiness in the flowfield is assumed to be a small harmonic perturbation to the nonlinear steady flow governed by the Euler equations. The linearized Euler approaches seem to be the best compromise of accuracy and efficiency available at the present time. These methods can include the effects of the geometry of the blades, and model the most pertinent physics of the flowfield. Shocks can be directly captured by the steady solutions, and their effects on the unsteadiness determined. Because of the assumptions inherent in the linearization, variations in the flow parameters are limited to small harmonic perturbations. The determination of incipient flutter meets this requirement, since actual LPT blades vibrate at very small amplitudes. Obviously, Euler methods cannot model the boundary layers and other viscous regions accurately. The numerical solutions for blades operating at high incidence angles, as sometimes required of LPT blades, may not be accurate.

Results

Description of Test Cases. Measurements for four to five steady flow conditions were conducted for each of the three torsion axis locations mentioned previously. The most significant parameters are summarized in Table 1. The sets of tests corresponding to each of the torsion axis locations will be collectively referred to as "configurations". The range of steady conditions shown reflects primarily variations to incidence angle, although changes to other steady flow parameters were also addressed.

Three different types of unsteady experiments were conducted. The first is the traveling wave mode, where each blade is driven to a constant amplitude and there is a constant temporal phase difference between adjacent blades. This mode simulates the dominant characteristics of the system mode behavior of the actual rotor assembly (Lane, 1956). A total of twelve interblade phase angles are used for each of the steady conditions.

The second type of experiment will be called the single blade vibration test, where each blade in the cascade is vibrated individually. Measuring the unsteady pressures generated on the instrumented (reference) blade while vibrating single blades in the cascade gives a direct determination of the influence coefficients (Crawley, 1988). These coefficients define the relative importance of each blade in the cascade to the generation of unsteady pressures on a given reference blade.

The final type of experiment is referred to as the alternating blade test, where only every other blade in the cascade is excited in a traveling wave mode. This test is a simulation of mistuning, which studies the effect of the small frequency variations of actual blades on the overall vibratory response of the rotor. The driven blades model those that would be at a system mode natural frequency while the undriven blades simulate those that are detuned from the system frequency. The arrangement selected is considered the most stable mistuning pattern, at least from a robust design viewpoint (Crawley and Hall, 1985).

Traveling Wave Tests. A representative case from the traveling wave results, corresponding to the design point conditions (condition 1) for configuration 1, is presented in this section. The distribution of the first harmonic of the unsteady pressure mea-

Nomenclature

c = chord length
C_p = coefficient of unsteady pressure, $\tilde{p}/\alpha(p_{t1} - p_1)$
CFD = computational fluid dynamics
i = inlet incidence angle
IBPA = interblade phase angle
k = reduced frequency, $\omega c/2U_2$
LPT = low pressure turbine
M_1 = inlet Mach number
M_2 = outlet Mach number
$\tilde{p}$ = unsteady pressure
PS = pressure side of the blade
p_{t1} = inlet total pressure
p_1 = inlet static pressure
s = normalized blade surface distance
SS = suction side of the blade
U_2 = outlet velocity
α = blade angular displacement
ω = blade vibration angular frequency

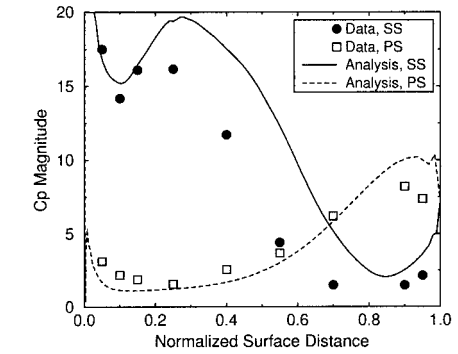

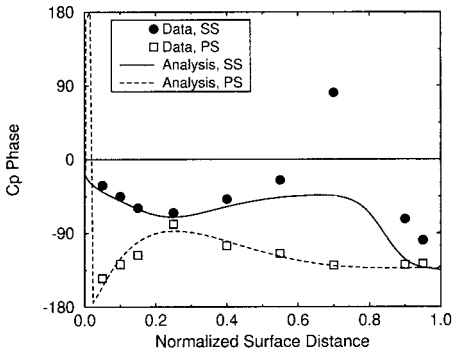

(a)

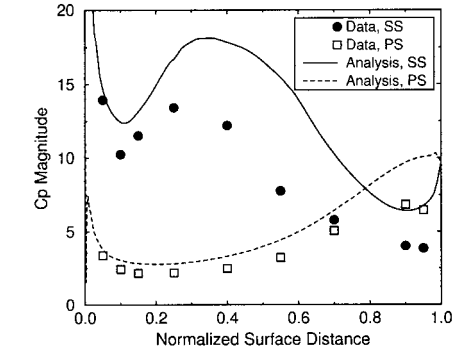

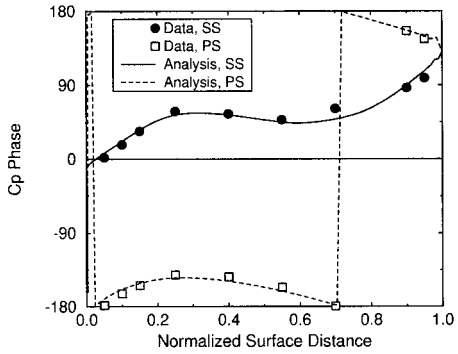

(b)

Fig. 2 Magnitude and phase of unsteady pressure: (*a*) IBPA = −90 deg and (*b*) IBPA = +90 deg.

sured along the blade surface is given in Fig. 2 for two interblade phase angles, IBPA = −90 deg and IBPA = +90 deg. It can be observed from these plots that, in general, the highest amplitude unsteady pressures occur in the leading edge region up to $s = 0.5$ on the suction side, and near the trailing edge on the pressure side. Computational results calculated by the NOVAK code are also included in these figures. These results are in reasonably good agreement with the experimental data and, in particular, accurately capture the trends exhibited along the blade surface and the effects of changing IBPA. Some differences are evident, especially in the magnitude of the unsteady pressures.

Additional insight into the influence of IBPA is provided by the contour plots in Fig. 3 which show the measured distribution of the unsteady pressure amplitude on the blade surface as a function of IBPA. On both blade surfaces, the unsteady pressure peak regions illustrated in Fig. 2 are most prominent near IBPA = 180 deg, and tend to disappear near IBPA = 0 deg. This behavior points to the important influence of the direct neighbor blades on the instrumented blade unsteady pressures.

Further information concerning the interaction of the neighboring blades can be obtained from the unsteady pressure measurements obtained along the outer wall of the test section. Such measurements have been previously presented by Körbächer (1996) and represent a unique opportunity to investigate the unsteady interaction of the blades in the cascade by experimental means. Figure 4 shows the instantaneous pressure distribution within two blade passages for IBPA = 180 deg. Three different positions of the blades are shown: (a) largest throat area between the two blades; (b) mean throat area; and (c) smallest throat area. The mean position of the blade is indicated by the black profile, and the instantaneous position is indicated by the white profile. Due to the torsional motion of the blade, the trailing edge experiences the largest linear displacement. This can lead to fairly significant changes in the throat area of the blade passage during cascade vibration, particularly for IBPA = 180 deg. It can be observed in Fig. 4(*a*) that for the largest throat area, the measured unsteady pressures in the center passage are small. Figures 4(*b*) and 4(*c*) illustrate an increase in the instantaneous unsteady pressure as the two blade trailing edges approach one another. For the smallest throat area, the aforementioned peak unsteady pressure regions along the leading edge on the suction side and along the trailing edge of the pressure side become apparent. It can also be observed from this series of plots that these peak regions are coupled to the same basic unsteady flow phenomenon.

The aerodynamic damping coefficient can be calculated from the unsteady pressure measurements using the standard expression (Bölcs and Fransson, 1986). In Fig. 5, the damping distribution along the blade surface as a function of IBPA is shown. The zero damping contour is represented in these plots by a black line. Note that the maximum damping contributions occur near $s = 0.25$ on the suction surface and near the trailing edge on both surfaces. The primary destabilizing influences (negative damping) occur near IBPA = +90 deg.

The damping distribution can be integrated over the blade surface to obtain the overall damping as a function of IBPA, as shown in Fig. 6. This plot indicates there is only a small range of IBPA near +90 deg where the cascade is unstable. Comparison of the test measurements and computational predictions are shown to be in very good agreement. Similar comparisons for all of the steady conditions listed in Table 1 have been conducted, and indicate that linearized Euler methods are sufficient for the prediction of LPT flutter.

Single Blade Tests. The unsteady pressures which occur on a given blade surface represent a combination of the contributions made by the individual vibrating blades in the cascade. These contributions are generally referred to as the influence coefficients. It is also possible to define influence coefficients for local and overall work and damping. The blade numbering convention utilized in this paper defines the reference blade as blade 0, with the +1 blade immediately to the pressure side, the −1 blade immediately to the suction side, and so on to define the entire cascade.

The contribution from each blade in the test cascade can be directly determined by vibrating only single blades and measuring the unsteady pressures generated on the instrumented (reference) blade. The influence coefficients can also be obtained mathematically from the traveling wave results by assuming a linear super-

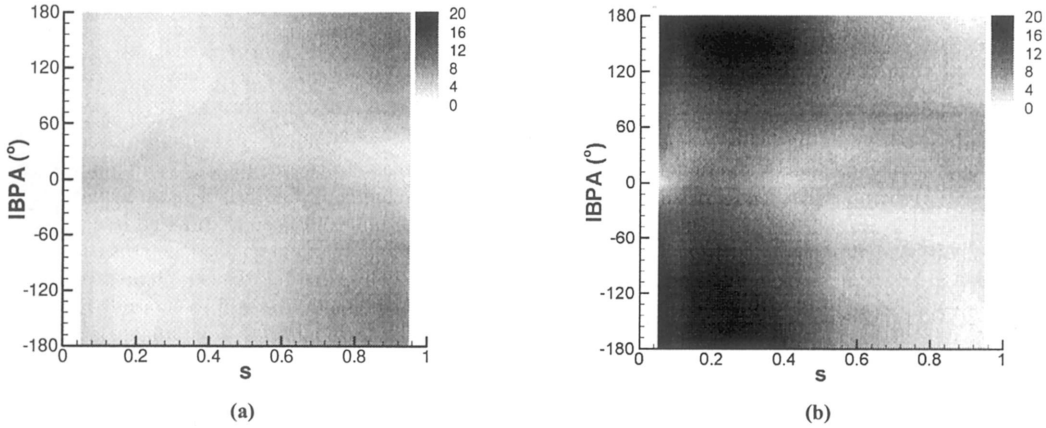

Fig. 3 Measured C_p magnitude: (*a*) *PS* and (*b*) *SS*.

position of the unsteady pressures in the cascade. By comparing the single blade and traveling wave influence coefficients, the validity of this assumption can be verified. For configuration 1, condition 1, the results of this comparison are shown in Fig. 7 for a single unsteady pressure transducer located at $s = 0.25$ on the suction surface. Both the magnitude and the phase are shown to be in excellent agreement. Other locations and conditions (refer to Table 1), give similar correlations. Thus, the influence coefficient technique is demonstrated to be valid for the case of LPT flutter. Similar linearity validations were reported by Bölcs et al. (1989) and Körbächer and Bölcs (1996) for annular turbine and compressor cascades, respectively, vibrating in the bending mode. However, to the authors' knowledge, this is the first time that the superposition principle has been validated for LPT blades vibrating in torsion. This determination also provides a potential opportunity to greatly simplify the experimental setup, as it implies that the traveling wave results can be accurately simulated by vibrating only a single blade in the cascade and measuring the unsteady pressures on the various neighboring blades.

The influence coefficients also provide important information regarding the relative importance of the motion of individual blades in the cascade to the generation of time-dependent pressures at a given location. In general, for this cascade, only the contributions from the 0 or reference blade and the neighboring $+1$ and -1 blades have a significant influence on the unsteady pressures. Along the suction surface, the 0 blade exerts the largest influence near the leading edge. The neighboring -1 blade (which faces the suction side of blade 0) also exerts a significant influence at this location. Near the mid-section of the blade, the influence of the -1 blade substantially increases, becoming larger than that of the 0 blade. The important influence of this neighboring blade was cited in the previous section. Near the trailing edge, the influence of the -1 blade diminishes greatly and the largest influences are derived from the 0 and $+1$ blades. Along the pressure side, the primary influence is due to the 0 blade except near the trailing edge. Here, the influence of the $+1$ blade (which faces the pressure side of blade 0) is also significant.

Alternating Blade Tests. The effects of mistuning were evaluated by vibrating only alternate blades in the cascade in a traveling wave pattern. Unsteady pressures were recorded as for the other tests. It was found that this vibration mode had a powerful stabilizing effect on the cascade, as has been indicated by previous research (Kaza and Kielb, 1982; Crawley and Hall, 1985).

The reason for this stabilizing effect is clearly evident when analyzing the unsteady pressure distribution on the blade. The unsteady pressures near $s = 0.25$ on the suction side for IBPA $= +90$ deg are the most destabilizing on the blade (see Figs. 3 and 5). As mentioned previously, this unsteadiness is primarily due to the relative motion of the -1 blade. By not allowing the -1 blade to vibrate, this source of unsteadiness is essentially removed, and an improvement in the overall stability of the blade results.

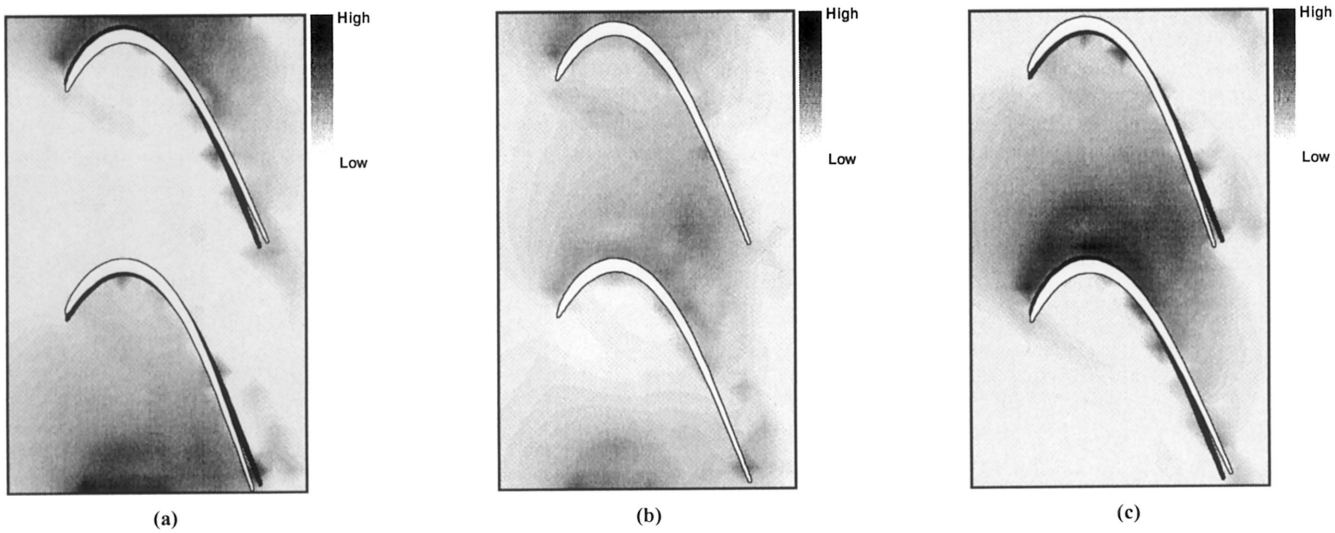

Fig. 4 Instantaneous pressures from outer wall measurements for IBPA = 180 deg

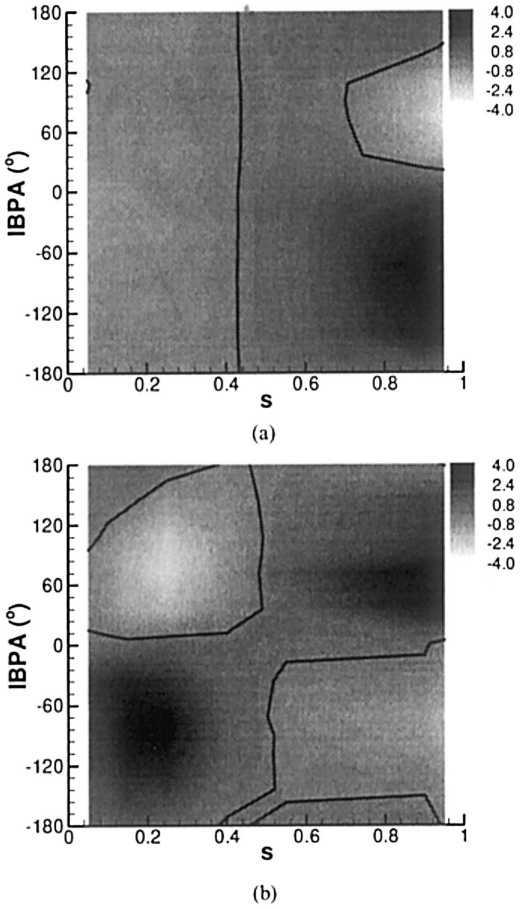

Fig. 5 Experimental damping coefficient distribution: (*a*) *PS* and (*b*) *SS*.

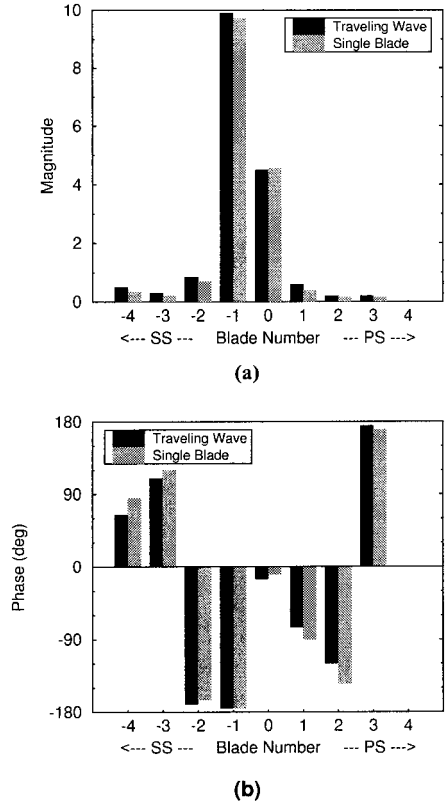

Fig. 7 Comparison of influence coefficients for $s = 0.25$ on the *SS*: (*a*) magnitude and (*b*) phase.

The stabilization can also be explained by a consideration of the influence coefficients of the overall damping from the normal traveling wave experiments. The contribution from the reference blade is the average damping value across the IBPA range. The influence coefficients show that the only significant contribution from other blades is from the immediate neighbors, the -1 and $+1$ blades. In the traveling wave domain, these contributions will appear as the first harmonic variations with IBPA. If these contributions are removed by fixing these blades, the minimum stability over all IBPA will increase. Since only the minimum stability is of concern in a practical sense, the stability of the blade improves.

An example of the results of the mistuning experiments is shown in Fig. 8 for configuration 1, condition 1. The effect of removing the contributions of the neighboring blades is readily apparent, as the damping coefficient over the entire IBPA range approaches the average value. It is worth noting that the unsteady pressures produced by this vibration pattern and, in fact, any arbitrary vibration pattern, can be also accurately determined from the influence coefficients.

Key Design Parameters

We now utilize the experimental results to identify the effect of key design parameters on the stability characteristics of the cascade. To conduct this study, the least stable point from the curve of damping versus IBPA is identified for each of the steady conditions summarized in Table 1. This minimum damping value is the primary value of interest from a stability evaluation standpoint. These damping values were then plotted as a function of every significant steady and unsteady parameter associated with the various steady conditions.

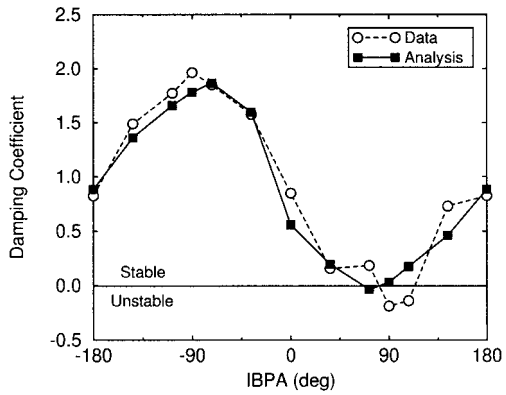

Fig. 6 Overall damping coefficient

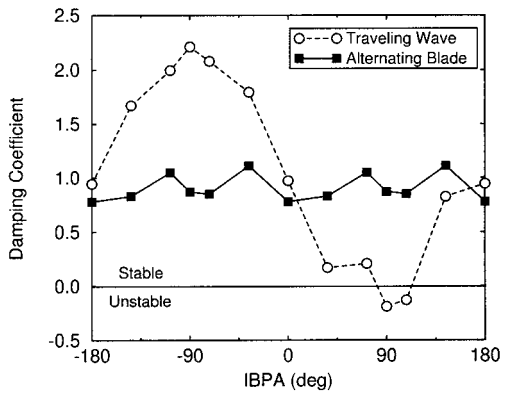

Fig. 8 Effect of mistuning on overall damping coefficient

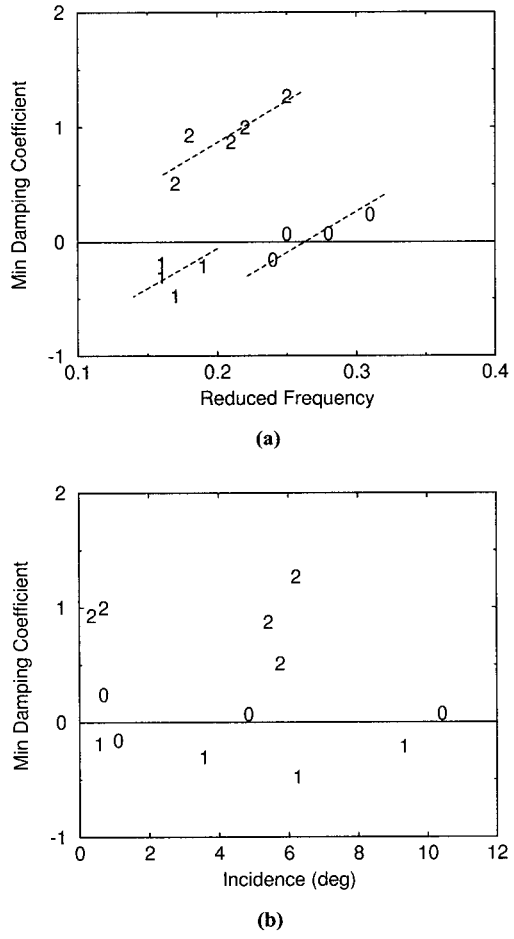

Fig. 9 Trends of minimum damping versus key parameters: (*a*) reduced frequency and (*b*) incidence.

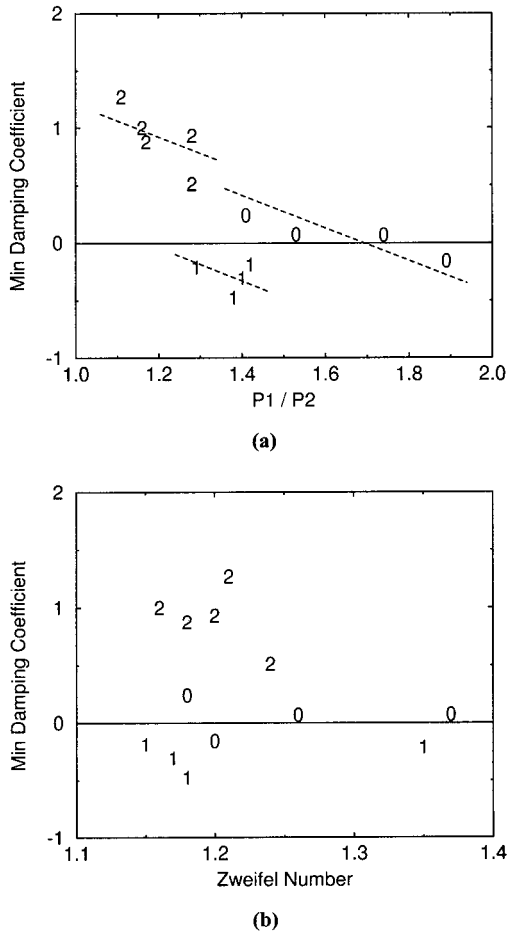

Fig. 10 Trends of minimum damping versus key parameters: (*a*) static pressure ratio and (*b*) Zweifel number.

An example is shown in Fig. 9 for two of the parameters which are usually considered to be the most important, reduced frequency and incidence. Each steady condition is denoted by a numerical index which corresponds to the configuration number. Thus, there are four data points for configurations 0 and 1, while configuration 2 has five points. Acknowledging that the available data set does not reflect independent variations of these parameters, it is nevertheless surprising that neither of these plots indicates a clear trend in the damping. The primary trend shown is that the conditions are grouped into configurations, implying that the primary driver is mode shape. If we consider the data points within a particular configuration, a secondary trend is observed for the reduced frequency. For example, within the five data points for configuration 2, there is a clear trend toward lower damping as the reduced frequency drops. A dotted line is used to indicate this trend for each of the configurations. The incidence plot, however, does not exhibit even this secondary trend.

Loading in general, in terms of higher pressure ratio or higher exit Mach number or other similar measure, seems to have a secondary influence, but no single parameter could be identified as having the dominant contribution. In fact, the Zweifel number (Zweifel, 1945), which is the primary loading guideline, shows no trend at all. Examples of the effect of loading are shown in Fig. 10 using the ratio of the inlet and exit static pressures and the Zweifel number as parameters. Average trends are again indicated by dotted lines in the pressure ratio plot. In summary, this study indicates that the most dominant contribution to overall stability for LPT blades is the mode shape, followed by reduced frequency, and finally some type of loading parameter.

The influence coefficients of the overall stability can also be used to assess the importance of the individual blades to the observed trends. It is found that the mode shape strongly affects contributions from the neighboring -1 and $+1$ blades. The reduced frequency affects contributions from both the reference blade and the adjacent blade pair. Loading variations solely affect the reference blade. Incidence variations did not seem to have a significant effect on the stability characteristics of the cascade through the range tested. These results are summarized in Table 2. It should be noted that these conclusions have been drawn based on the experimental data only, and mostly serve to highlight the important design parameters. A more detailed parameter study employing computational methods is presented by Panovsky and Kielb (1998).

Summary and Conclusions

Detailed measurements of the unsteady pressures generated by the vibratory motion of a modern LPT blade in an annular cascade have been completed. A total of thirteen steady conditions were investigated using three torsion axis locations. Several types of unsteady tests were conducted, including traveling wave, single blade, and alternating blade modes.

The traveling wave results demonstrated that the highest ampli-

Table 2 Dependence of the damping influence coefficients on key parameters

Blade(s)	Mode Shape	*k*	Incidence	Loading
Reference	secondary	secondary	none	secondary
Adjacent pair	primary	secondary	none	none

tude unsteady pressures were typically generated on the front half of the blade along the suction side, and near the trailing edge on the pressure side. The important role that these regions play in determining the overall stability of the blade was also shown. In addition, using the outer wall unsteady pressure measurements and the blade influence coefficients, the interaction of the direct neighbor blades was identified as the primary source for these peak unsteady pressures.

By comparing the influence coefficients from the traveling wave and single blade mode tests, the validity of the linear superposition approach for unsteady pressures was demonstrated for LPT blades. The alternating blade mode tests explicitly demonstrate the benefits of mistuning for flutter. The resulting stabilization is expected based on the work of previous researchers, and the reason for this behavior becomes particularly obvious when considering the important influence on the stability attributed to the adjacent blades, as indicated by the influence coefficients and outer wall measurements.

Correlating analyses for all of the experimental data have been completed using a quasi-three-dimensional linearized Euler code. Detailed comparisons of the measured and predicted unsteady pressures and damping coefficients were provided and discussed. The results indicate that this type of method can be used to reliably assess the stability of LPT blades.

Results of the experimental data were used to determine the key parameters for LPT flutter. This investigation indicates that there is a fairly small range of IBPA where flutter can occur for this blade. This range is a function of mode shape, frequency, and steady conditions. However, the most significant factor in determining stability was shown to be the mode shape. While all of the tests conducted used a torsion mode, relatively small changes to the location of the torsion axis had a dramatic effect on the stability behavior. This is an extremely important conclusion because the primary design parameter up to this time has been the reduced frequency. Reduced frequency and loading were also found to have an influence, though to a lesser degree than mode shape. Incidence angle did not have a significant effect on stability over the range tested. The importance of these parameters was also expressed in terms of the corresponding influence coefficients. This led to the conclusion that variations in the reference blade contributions are driven primarily by reduced frequency and loading. The adjacent blade pair contributions vary primarily due to changes in mode shape, though reduced frequency has a secondary effect.

Acknowledgments

The authors wish to thank GE Aircraft Engines and Ecole Polytechnique Fédérale de Lausanne for permission to publish this paper. The first author would like to thank Dr. Peter Ott and Dr. Heiko Körbächer for their valuable technical comments. The second author would like to thank Dr. Graham Holmes, Dr. Christopher Lorence, Dr. Steven Manwaring, and especially Dr. Robert Kielb; thanks are also extended to Prof. Torsten Fransson of the Royal Institute of Technology in Sweden.

References

Bölcs, A., 1983, "A Test Facility for the Investigation of Steady and Unsteady Transonic Flows in Annular Cascades," ASME Paper 83-GT-34.

Bölcs, A., and Fransson, T. H., 1986, "Aeroelasticity in Turbomachines: Comparison of Theoretical and Experimental Cascade Results," Air Force Office of Scientific Research, AFOSR-TR-87-0605.

Bölcs, A., Fransson, T. H., and Schläfli, D., 1989, "Aerodynamic Superposition Principle in Vibrating Turbine Cascades," presented at the AGARD 74th Specialists' Meeting of the Propulsion and Energetics Panel on Unsteady Aerodynamic Phenomena in Turbomachines, Luxembourg, August 28–September 1, 1989.

Bölcs, A., and Schläfli, D., 1984, "Flutter Phenomena in a Transonic Turbine Cascade," *Unsteady Aerodynamics of Turbomachines and Propellers*, Proceedings, Symposium, Cambridge, England, pp. 411–425, September 24–27, 1984.

Buffum, D. H., and Fleeter, S., 1990, "Aerodynamics of a Linear Oscillating Cascade," NASA Technical Memorandum 103250.

Crawley, E. F., 1988, "Aeroelastic Formulation for Tuned and Mistuned Rotors," chapter 19 in *AGARD Manual on Aeroelasticity in Axial-Flow Turbomachines, Vol. 2, Structural Dynamics and Aeroelasticity*, M. F. Platzer and F. O. Carta, eds., AGARD-AG-298.

Crawley, E. F., and Hall, K. C., 1985, "Optimization and Mechanisms of Mistuning in Cascades," ASME Journal of Engineering for Gas Turbines and Power, Vol. 107, No. 2, pp. 418–426.

Holmes, D. G., and Chuang, H. A., 1993, "2D Linearized Harmonic Euler Flow Analysis for Flutter and Forced Response," in *Unsteady Aerodynamics, Aeroacoustics, and Aeroelasticity of Turbomachines and Propellers*, H. M. Atassi, ed., Springer-Verlag, New York.

Kaza, K. R. V., and Kielb, R. E., 1982, "Flutter and Response of a Mistuned Cascade in Incompressible Flow," *AIAA Journal*, Vol. 20, No. 8, pp. 1120–1127.

Kirschner, A., Fosco, B., and Muller, E., 1980, "Control of Vibration in Aeroelastic Experiments," Communication de l'ITA/EPFL, No. 10, pp. 285–295.

Körbächer, H., 1996, "Experimental Investigation of the Unsteady Flow in an Oscillating Annular Compressor Cascade," Ph.D. dissertation, Laboratoire de Thermique Appliquée et de Turbomachines, Swiss Federal Institute of Technology, Lausanne, Switzerland.

Körbächer, H., and Bölcs, A., 1996, "Steady-State and Time-Dependent Experimental Results of a NACA-3506 Cascade in an Annular Channel," ASME Paper 96-GT-334.

Lane, F., 1956, "System Mode Shapes in the Flutter of Compressor Blade Rows," *Journal of the Aeronautical Sciences*, pp. 54–66.

Panovsky, J., 1997, "Flutter of Aircraft Engine Turbine Blades," Ph.D. dissertation, University of Cincinnati, Cincinnati, OH.

Panovsky, J., Nowinski, M., and Bölcs, A., 1997, "Flutter of Aircraft Engine Low Pressure Turbine Blades," presented at the 8th International Symposium of Unsteady Aerodynamics and Aeroelasticity of Turbomachines, Stockholm, Sweden, Sept. 14–18, 1997.

Panovsky, J., and Kielb, R., 1998, "A Design Method to Prevent Low Pressure Turbine Blade Flutter," presented at the ASME Gas Turbine Conference and Exhibition, Stockholm, Sweden, June, 1998.

Zweifel, O., 1945, "The Spacing of Turbomachinery Blading, Especially with Large Angular Deflection," Brown Boveri Rev., Vol. 32, p. 12.

A Design Method to Prevent Low Pressure Turbine Blade Flutter

J. Panovsky[1]

R. E. Kielb

GE Aircraft Engines,
1 Neumann Way, MD A413
Cincinnati, OH 45215

A design approach to avoid flutter of low pressure turbine blades in aircraft engines is described. A linearized Euler analysis, previously validated using experimental data, is used for a series of parameter studies. The influence of mode shape and reduced frequency are investigated. Mode shape is identified as the most important contributor to determining the stability of a blade design. A new stability parameter is introduced to gain additional insight into the key contributors to flutter. This stability parameter is derived from the influence coefficient representation of the cascade, and includes only contributions from the reference blade and its immediate neighbors. This has the effect of retaining the most important contributions to aerodynamic damping while filtering out terms of less significance. This parameter is utilized to develop a stability map, which provides the critical reduced frequency as a function of torsion axis location. Rules for preliminary design and procedures for detailed design analysis are defined.

Introduction

The development of improved design rules and approaches to avoid flutter of low pressure turbine (LPT) blades has become a high priority because of several recent occurrences of torsional flutter. A combined experimental and computational effort to address this issue, utilizing a representative blade geometry in an annular cascade facility, has been described by Panovsky et al. (1997) and Nowinski et al. (1998). One of the key outcomes from this previous effort is that the most important contributor to flutter is the location of the torsion axis. Of secondary importance are the reduced frequency and, to a lesser extent, the steady blade loading. The effect of the inlet flow incidence angle was negligible. While the importance of mode shape has been identified previously by many authors (e.g., Bendiksen and Friedmann (1980); Försching (1989)), reduced frequency has remained the primary design parameter for flutter.

Another major conclusion, which resulted from comparisons of test data and analytical predictions, is that computational fluid dynamics (CFD) methods based on a linearized Euler approach (Hall and Crawley, 1989) are adequate to reliably predict flutter behavior in LPT blades. The codes can now be used to consider other cases of interest and to perform systematic parameter studies. The method assumes tuned blades, so that only a single passage is analyzed with phase-lagged conditions on the periodic boundaries. The prediction of incipient flutter is sufficient since our goal is to develop design rules.

The focus of the present paper is to study the flutter sensitivity to the key parameters identified through the earlier efforts. The studies summarized here include the effects of reduced frequency and mode shape. The findings are compared to previous investigations by Kirschner, Pelet, and Gyarmathy (1976) and Whitehead (1987). All of the computational results utilize the quasi-three-dimensional linearized Euler code NOVAK by Holmes and Chuang (1993). Unique approaches are introduced to allow these studies to be done in a practical manner, and to provide additional insight. The first step is to define a new parameter for stability which addresses the entire range of interblade phase angle (IBPA) in a single relevant value.

Derivation of Stability Parameter

The unsteady pressures which arise on a blade surface during its vibratory motion are due to contributions from all of the blades in the cascade. The contribution of each blade to an arbitrary reference blade is defined as its influence coefficient (e.g., Crawley, 1988). Influence coefficients can also be determined for the aerodynamic work.

The influence coefficients can be defined by the transformation

$$w_l = \sum_{k=-(N/2)}^{N/2} W_k e^{ik\sigma_l} \tag{1}$$

where

$$\sigma_l = \frac{2\pi l}{N}. \tag{2}$$

Note that lower case indicates the IBPA (or traveling wave) domain and upper case denotes the influence coefficients. This relation is in the form of a Discrete Fourier Transform. Each complex influence coefficient can be written in terms of its magnitude and phase,

$$W_k = \bar{W}_k e^{i\phi_k}. \tag{3}$$

These expressions show that the contribution of each blade is in the form of a sine wave in the IBPA domain. The 0 blade contribution is the average value, and corresponds to the contribution of the reference blade on itself. A single-period sinusoidal variation in the curve of work versus IBPA corresponds to contributions from the adjacent blades on either side of the reference. The $+1$ blade is adjacent to the pressure side of the reference blade, while the -1 blade is on the suction side. Higher frequency components are due to blades which are the corresponding number of passages away from the reference blade. This behavior has special significance for the aerodynamic damping. Only the constant value corresponding to the 0 blade can be absolutely stable or unstable. All other blades will give equal stabilizing and destabilizing contributions.

[1] Current address: Honeywell Engines and Systems, P.O. Box 52181, M/S 553-10, Phoenix, AZ 85072.

Contributed by the International Gas Turbine Institute (IGTI) of The American Society of Mechanical Engineers for publication in the ASME Journal of Engineering for Gas Turbines and Power. Paper presented at the International Gas Turbine and Aeroengine Congress and Exhibition, Stockholm, Sweden, June 2–5, 1998; ASME Paper 98-GT-575.

Manuscript received by IGTI December 9, 1997; final revision received by the ASME Headquarters October 20, 1999. Associate Technical Editor: R. Kielb.

All of the experimental and computational results that have been obtained through this flutter research project indicate that the reference blade and its immediate neighbors are the dominant contributors to the unsteady behavior of the LPT cascade (Panovsky et al., 1997; Nowinski et al., 1998). This behavior is typical of most other cascades, whether they are fans, compressors, or turbines. The more-distant blades do have some contribution, but for the purpose of developing design rules, the 0 and ± 1 blades are the important contributions to understand and control.

To maximize stability, the 0 blade contribution to the damping would be maximized to the stable side, while the ± 1 blade pair influence is minimized, since any stabilizing contribution necessarily causes an equally de-stabilizing contribution at another IBPA. The magnitude of the influence coefficient indicates the importance of each blade, but the overall amplitude of the fundamental harmonic (in terms of IBPA) of the damping curve depends on the magnitude of both the $+1$ and -1 blades and their relative phase. This is because both of these contributions are in the form of a single-period sine wave in the IBPA domain. The phasing of the individual influence coefficients can be such that they superpose constructively, which would lead to less stability, or destructively, which would cancel the contribution and tend toward the 0 blade stability level.

In light of these considerations, a criterion will be defined to better assess stability and the important contributions. For this stability criterion, the damping versus IBPA curve is approximated by including only contributions from the reference blade and the adjacent blade pair. The stability parameter is defined as the least stable point on this approximating curve. To obtain an expression for the stability parameter, we first note that the portion of the work at the kth harmonic (in terms of IBPA) will be due to contributions from the $\pm k$ conjugate pair. The contribution of each pair can be separated into real and imaginary terms

$$W_{+k}e^{+ik\sigma_l} + W_{-k}e^{-ik\sigma_l} = \bar{S}_k^R \sin(k\sigma_l + \phi_k^R) + i\bar{S}_k^I \sin(k\sigma_l + \phi_k^I). \quad (4)$$

Only the real part of the right-hand side of Eq. (4) contributes to the aerodynamic damping. The magnitude of this real part for the $\pm k$ pair is

$$\bar{S}_k^R = \sqrt{\bar{W}_{+k}^2 + 2\bar{W}_{+k}\bar{W}_{-k}\cos(\phi_{+k} + \phi_{-k}) + \bar{W}_{-k}^2}. \quad (5)$$

A special expression is needed for the 0 blade

$$\bar{S}_0^R = \bar{W}_0 \cos\phi_0. \quad (6)$$

The stability parameter, S, is defined as the minimum point on the approximating curve to the overall damping. This point is given by subtracting the magnitude of the contribution due to the adjacent pair from the average value due to the reference blade,

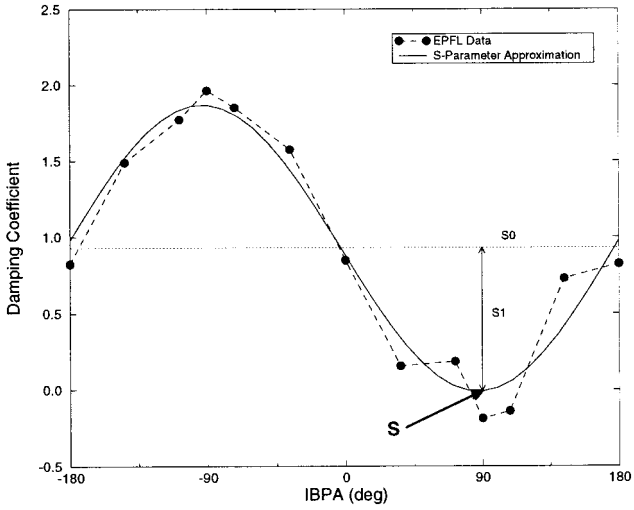

Fig. 1 Definition of the stability parameter

$$S = \bar{W}_0 \cos\phi_0 - \sqrt{\bar{W}_{+1}^2 + 2\bar{W}_{+1}\bar{W}_{-1}\cos(\phi_{+1} + \phi_{-1}) + \bar{W}_{-1}^2}. \quad (7)$$

If S is positive, the blade will be stable for all IBPA. If it is negative, then there is some range of IBPA where the blade will be unstable. The corresponding expression for the phase angle of S can be used to define the most unstable IBPA, but this is of secondary importance. Using Eq. (7), it is possible to summarize the overall stability of the cascade for the entire IBPA range in terms of a single parameter.

The contributions to the stability parameter are shown schematically in Fig. 1. The damping versus IBPA curve resulting from the experimental data for design point conditions is used in this example (Panovsky et al., 1997). The approximation using only the reference blade and its immediate neighbors is indicated by the solid line. The average value is denoted "$S0$" and corresponds to the contributions from the blade on itself. The ± 1 blade pair contribution is in the form of a sine wave of a single period. This has an amplitude denoted "$S1$" in the figure. The least stable point on the curve is obtained by subtracting this magnitude from "$S0$".

There are actually two ways to consider the stability criterion:

1 $S > 0$ stable
  $S < 0$ unstable
2 $S_0^R > S_1^R$ stable
  $S_0^R < S_1^R$ unstable

Nomenclature

A = matrix of aerodynamic coefficients
a = modal amplitude vector
B = work matrix in influence coefficient domain
b = work matrix in traveling wave domain
c = chord
CFD = computational fluid dynamics
F = discrete Fourier transform operator
h = bending deflection
i = imaginary component
IBPA = interblade phase angle
k = reduced frequency
LPT = low pressure turbine
N = total number of blades
n = normal vector
p = pressure
q = dynamic pressure
S = stability parameter
S_k = contribution of kth conjugate pair
s = normalized distance along surface
u = physical deflection vector
W = work in influence coefficient domain
w = work in traveling wave domain
x = axial coordinate
y = tangential coordinate
α = torsional amplitude
Φ = matrix of fundamental mode shapes
ϕ = phase of complex variable
η = coordinate normal to chord
σ = interblade phase angle
Ξ = damping coefficient
ξ = coordinate along chord

Subscripts

k = blade number
l = index in traveling wave domain

Superscripts

I = imaginary component
R = real component
-- = magnitude of complex variable

The first has the advantage of giving a single quantity which provides a direct measure of the stability of a design. With the second measure, both sides of the inequality could be plotted versus some parameter of interest. The intersection of the lines indicates the stability boundary. This second measure has the advantage that the importance of the reference blade compared to the adjacent blade pair is apparent in such parameter studies.

The advantage of the stability parameter is that it captures the important contributions to the damping versus IBPA curve while filtering out the smaller variations. While these details are important for the assessment of a particular design, they may obscure the more global behavior which is the goal of the present study. Additionally, the influence coefficients for the 0 and ± 1 blades can be determined fairly accurately with analyses run at just a few IBPA, using as few as three distinct IBPA. The parameter S can be determined from this small set of analyses and the overall stability determined without the need to run many IBPA to see if the damping curve crosses over the stable/unstable boundary. This presents an efficient method for doing parameter studies. An alternative calculation is to design a computer code around the stability parameter, determining the unsteady pressures on the reference blade due to motions of this blade and its immediate neighbors. These three solutions give the influence coefficients directly, and then S can be calculated to determine the overall stability. The solution in the traveling wave domain could easily be plotted if desired, by using Eq. (1). This approach may be even more efficient than using three traveling wave solutions, though most computational codes are not written with the necessary conditions on the periodic boundaries. Buffum and Fleeter (1990) have proposed this type of approach and, in fact, modified a CFD code to perform calculations in terms of influence coefficients.

The experimental results from the cascade tests were used to verify the ability of the stability parameter to reliably approximate the minimum damping value. Comparisons such as the example given in Fig. 1 were constructed for each of the thirteen steady conditions described in Nowinski et al. (1998). These comparisons indicated that the stability parameter is a very good estimate of the minimum damping value over a wide range of steady conditions and for three mode shapes. Now that the stability parameter has been validated using experimental data, it can be applied with confidence in additional studies.

Effect of Frequency on Fundamental Modes

The first parametric study describes stability trends of the blade in three fundamental modes as a function of reduced frequency. The fundamental modes are defined as bending along and normal to the chord, and torsion about the blade leading edge. Figure 2 is a sketch of the geometry and coordinate systems. Bending normal to the chord, in the η direction, will be referred to as the "flex" mode while bending along the chord, in the ξ direction, is referred to as the "axial" mode. For comparison, and to point out some contrasts, bending along the cascade axial and tangential directions (x and y) are also considered. These directions are more representative for system modes of tip-shrouded LPT blades. The steady flow in all of these studies is defined by the design point operating conditions of the actual blade. The range of reduced frequency assessed is from 0.05 to 0.5, a range which extends beyond standard designs for both bending and torsion.

Damping Versus IBPA. A summary of the damping coefficient versus IBPA is shown in Fig. 3 for the three fundamental modes, with the reduced frequency as a parameter. The most surprising feature about these curves is the critical (or "flutter") reduced frequency, that where the modes become unstable, is almost identical for each of these modes. This critical reduced frequency is between 0.2 and 0.3 in each case. This is quite surprising, since experience suggests that the bending modes are much more stable than torsion. For each mode, note the smooth shifting of the curves with reduced frequency. The torsion and flex

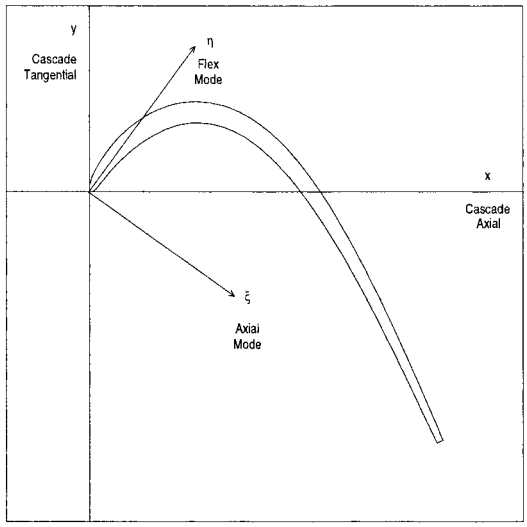

Fig. 2 Definition of fundamental mode shapes

modes are least stable near an IBPA of -90 deg while the least stable IBPA for the axial mode is near $+90$ deg.

Because of the surprising result for these fundamental modes, the analyses were repeated for bending along the cascade axial and tangential directions (x and y in Fig. 2). A considerable difference in the flutter reduced frequencies was found in these cases, with values near 0.1 for cascade axial and 0.4 for cascade tangential. These results, plus the value found for torsion, are consistent with engine experience.

The conclusion is that the fundamental modes all having the same flutter reduced frequency is coincidental, though it may have some presently unknown physical significance. For any other set of bending axes, this consistency will not hold. Bending in an arbitrary direction can be thought of as a combination of the two fundamental axial and flex bending modes. It is the difference in the least stable IBPA for these fundamental modes, as shown in Fig. 3, which causes the flutter reduced frequency to vary for an arbitrary bending direction.

Influence Coefficients. Influence coefficients have been determined from the traveling wave results, and their magnitudes are summarized in Fig. 4. These results show that the primary contributions in all cases are dominated by the reference blade and its immediate neighbors. It is interesting, though, that the relative importance of the neighbor blades does change for the various modes, and the trend with reduced frequency is not always the same. The reference blade contributions increase with increasing reduced frequency, indicative of the increased stability expected. The change in the reference blade with reduced frequency is similar to the overall trends found by Szechenyi (1985) for fan blade flutter.

The -1 blade is the dominant contribution for the axial mode and it, too, increases in magnitude for increasing reduced frequency. Recall, though, that this is de-stabilizing. There is little change in the -1 blades' contribution in the flex mode, while the influence decreases with increased reduced frequency for torsion. For all modes, the contribution of the $+1$ blade grows as the reduced frequency increases. But the overall importance of this $+1$ blade and the sensitivity to reduced frequency does vary with mode shape.

Stability Parameter. The stability parameter can be calculated from the influence coefficients using Eq. (7). As mentioned previously, it is also worthwhile to consider the contributions from the reference blade and from the adjacent blade pair individually, and this is done in Fig. 5 for the fundamental modes. This plot is more useful than the influence coefficients of Fig. 4 because it

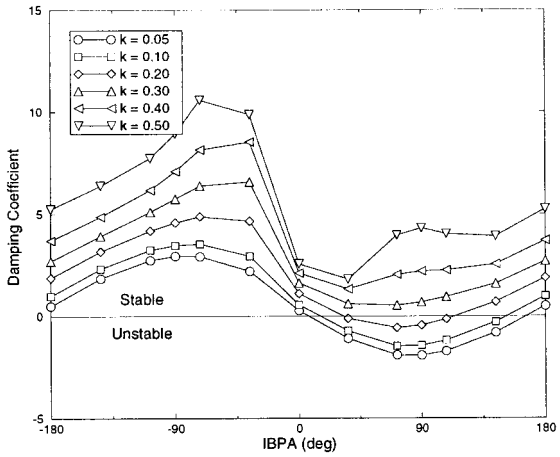

(a) Axial

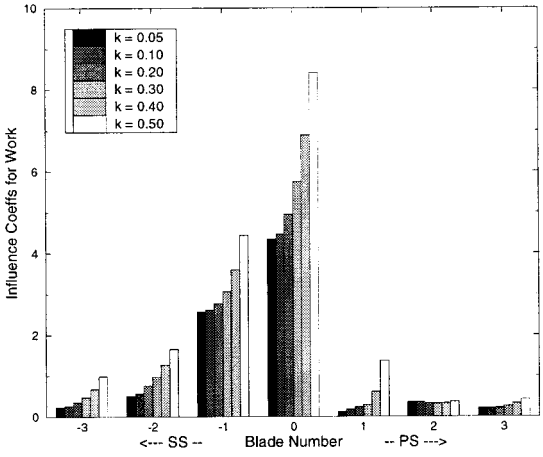

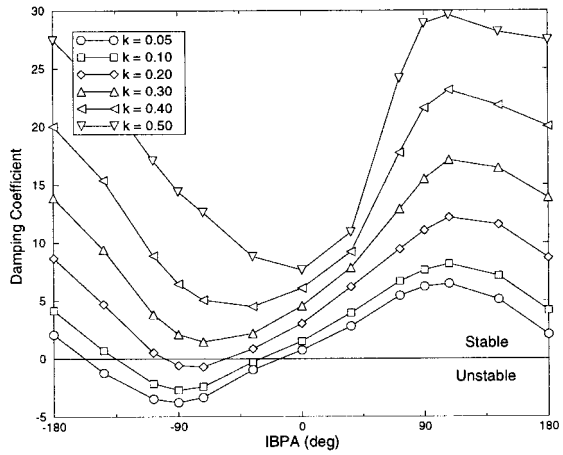

(b) Flex

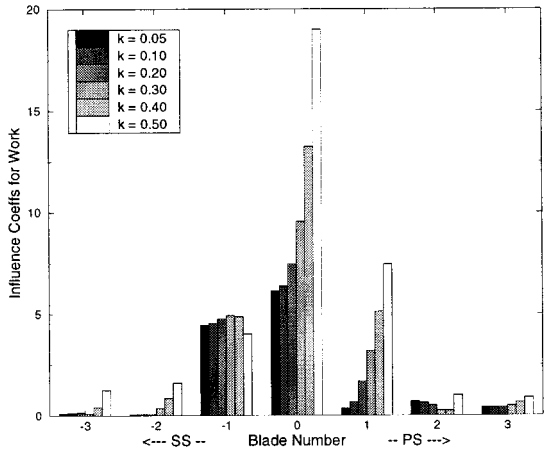

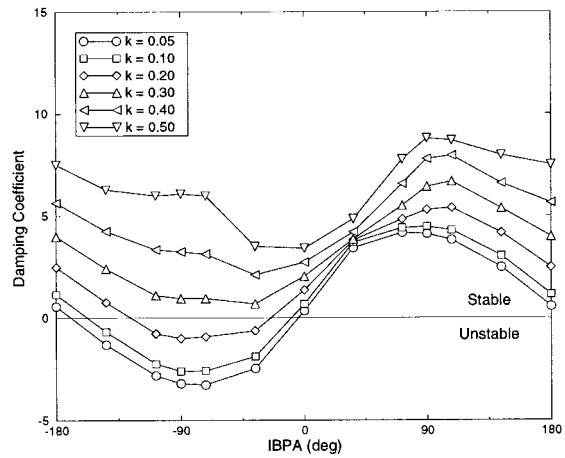

(c) Torsion

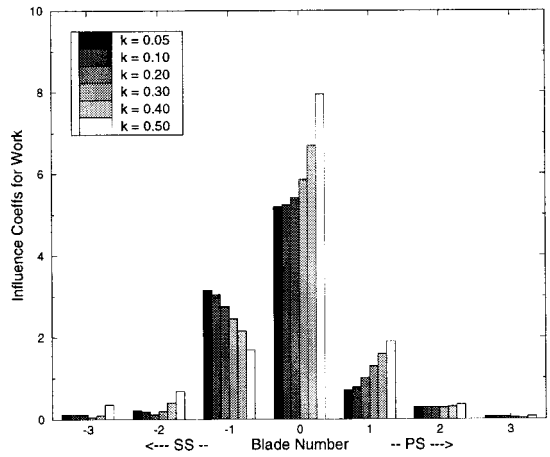

Fig. 3 Damping as a function of IBPA for the three fundamental modes

Fig. 4 Magnitudes of the influence coefficients for the fundamental modes

isolates the contribution of these blades to the damping portion of the complex work term. Recall that stability benefits from maximizing the S_0 contribution and minimizing the S_1 contribution. Significant features of the resulting trends is that they are nearly linear with reduced frequency, and the variation of stability (S) is almost totally a function of the reference blade. The slope of the S parameter is nearly the same as that for S_0, while the S_1 contribution is much less affected by the reduced frequency. So one of the most important outcomes from this study is that the dependence of flutter on reduced frequency is primarily a reference blade contribution.

For each of these modes, both S and S_0 increase with increasing reduced frequency. The S_1 contribution varies from a slight in-

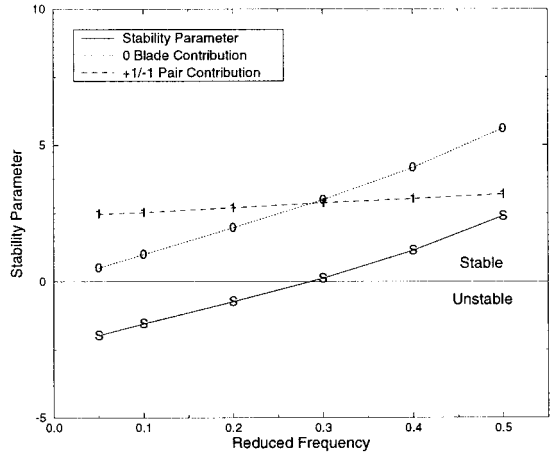

(a) Axial

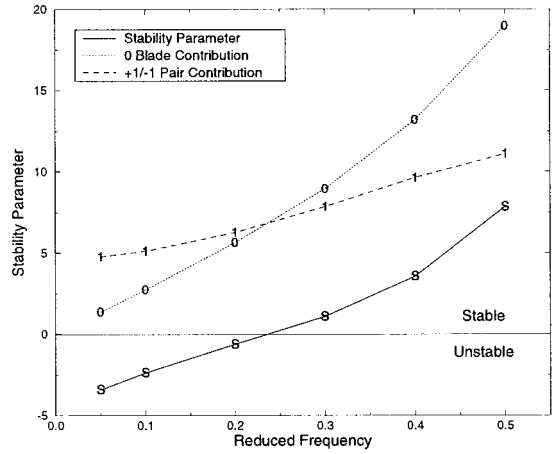

(b) Flex

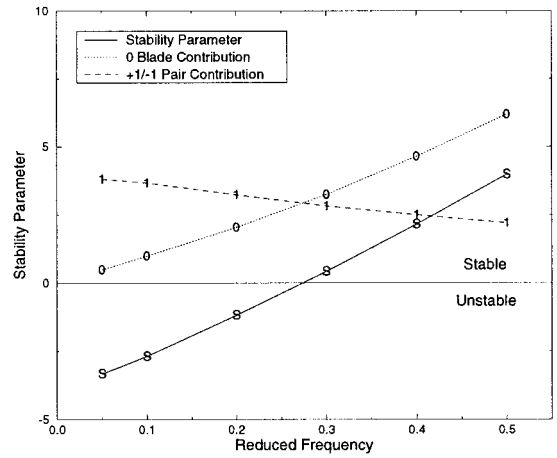

(c) Torsion

Fig. 5 Stability parameter versus reduced frequency, including contributions due to reference blade and adjacent blade pair

crease in de-stabilizing influence for the axial mode, to a significant increase for flex, to a significant decrease for torsion. This behavior can be contrasted to the trends found in Fig. 4. For example, the influence coefficients shown in Fig. 4 for torsion decrease with increasing reduced frequency for the -1 blade, but increase for the $+1$ blade. It is unclear whether the combination will increase or decrease the stability. But the benefit to stability is clear in Fig. 5, since the magnitude of the de-stabilizing S_1 influence is diminishing.

Effect of Mode Shape

The most important design parameter identified through the experimental correlation effort is the mode shape (Panovsky et al., 1997; Nowinski et al., 1998). One of the keys to conducting a complete study of mode shape in a practical and systematic manner is the ability to superpose the three fundamental modes defined in the previous section to get the equivalent of the torsion axis at any location. This study also addresses bending modes, since a torsion axis at infinity generates a pure bending mode. In this section, this superposition is coupled directly with the stability parameter S.

Superposition of Fundamental Modes. By exploiting linearity, we can determine the unsteady solution for torsion of amplitude α about any arbitrary location (ξ, η) by the superposition of the three fundamental modes. If the aerodynamic work for a number of locations is to be determined, it is much more efficient to use superposition rather than direct calculation. Using vector relations, it is straightforward to show (Panovsky, 1997) that the amplitude of these fundamental modes is given by

$$\{a(\xi, \eta; \alpha)\} = \begin{Bmatrix} h_\xi \\ h_\eta \\ \alpha \end{Bmatrix} = \alpha \begin{Bmatrix} \eta \\ -\xi \\ 1 \end{Bmatrix}. \tag{8}$$

Following Whitehead (1987) and Holmes and Cedar (1995), the work for a torsion axis at the point (ξ, η) can be obtained directly by superposing the solutions for the three fundamental modes through the expression

$$w_l = \{a\}^T [b_l] \{a\}. \tag{9}$$

The derivation of this expression is contained in the Appendix. The matrix $[b_l]$ is called the work matrix. Each entry of this (3×3) matrix is the work done by combining the pressures from each fundamental mode with the displacement of each of these modes. This matrix is calculated once for the fundamental modes, then the work for rotation about any point in space is given by substituting for the $\{a\}$ in Eq. (9). Note, though, that the work matrix is a function of IBPA.

Similarly, it is also possible to determine each influence coefficient

$$W_k = \{a\}^T [B_k] \{a\}, \tag{10}$$

where $[B_k]$ is the matrix of influence coefficients for the fundamental modes for the kth blade. This expression is also derived in the appendix.

The general procedure, then, is to run the unsteady code in the three fundamental modes with unit amplitudes through the range of interblade phase angles. As few as three IBPA's can be used. The mode shapes and unsteady pressures from these solutions are then used to determine the work matrix at each IBPA. From this series of work matrices, the influence coefficient matrices can be calculated. Finally, the influence coefficients at an arbitrary point can be determined using Eq. (10), and then the stability parameter is found using Eq. (7). Note that it is now very efficient to map out the stability over an arbitrary range of (ξ, η). For a choice of steady conditions and vibration frequency, all that is necessary is to repeat Eqs. (10) and (7) for any (ξ, η) of interest. A note on the normalization of the aerodynamic work to obtain the damping coefficient is also discussed in the Appendix.

Damping Coefficient Map. An intermediate step in this process is to determine the damping values as a function of torsion axis location for each value of IBPA. While this step is not necessary to determine the overall stability, it does provide useful

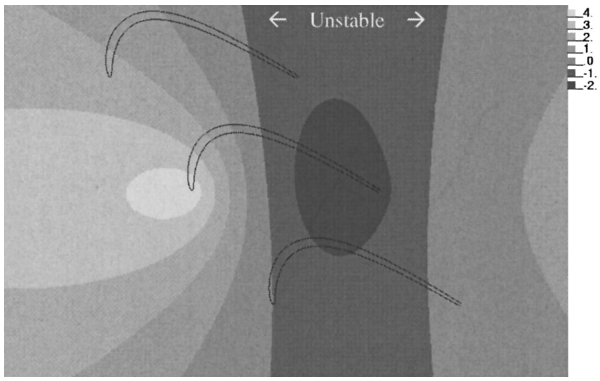

Fig. 6 Damping as a function of torsion axis location for $k = 0.2$ and IBPA = 90 deg. The reference blade is in the center.

information. An example in Fig. 6 shows contours of damping as a function of torsion axis for design point conditions at IBPA = +90 deg for a reduced frequency of 0.2. This type of plot will be used extensively in the studies which follow. To construct this plot, the damping at each location in a fine (ξ, η) grid is calculated by superposing the results from the three fundamental modes, as given by Eq. (9). This calculation is repeated over the range of torsion axis locations shown, then contours of these damping values are produced. For clarity and interpretation, blade profiles to represent the cascade are included. The reference blade is in the center of the plot.

The effect of torsion axis is quite evident from this plot. The aerodynamic damping changes significantly over the plotted range of axis locations. A large region of instability is centered near the trailing edge of the reference blade, denoted by the darker shading and bounded by the nearly vertical zero-damping contours in the plot. A mode with a torsion axis within this region will be unstable, while a torsion axis located outside the region will be stable at this IBPA. The most stable region is for a torsion axis at the leading edge of the reference blade. Stability also increases as the torsion axis moves beyond the trailing edge of the reference blade in the chordwise direction.

The drawback to this type of plot is that it only applies to a single IBPA. The main goal of a flutter analysis is to determine whether the design is stable or not. If a design is unstable, the IBPA at which it flutters is of little consequence. To determine overall stability, plots such as Fig. 6 would have to be constructed for each IBPA, and then unstable locations on any plot would have to be identified. This would obviously be quite tedious and time-consuming.

Stability Regions Near the Reference Blade. To overcome the limitations of the damping map, the stability parameter defined earlier is used. The value of S corresponds to the least stable damping value over the entire IBPA range, so that each torsion axis location can be represented by a single value. A stability parameter map is generated for the range of torsion axis locations through superposition using Eqs. (7) and (10). In Fig. 7, stable and unstable regions are shown for a series of reduced frequencies. The reference blade is again at the center. At the lowest value of reduced frequency, $k = 0.05$, the entire domain is unstable except a small region which begins near the true chord line of the reference blade, passes through the blade's high-curvature region, and extends along the cascade tangential direction (y direction, from Fig. 2). As the reduced frequency increases, this stable region expands, and a second stable region downstream of the blade row becomes evident. Both of these regions continue to expand with further increases in the reduced frequency. At the highest value of reduced frequency investigated, the unstable region lies off the blade along a line normal to the aft surface of the blade.

These results seem to imply that reduced frequency is a critical parameter, while the experimental results indicate that it is of secondary importance. The study summarized in Fig. 7 can be somewhat misleading because of the range of reduced frequency covered. Realistically, only a very small portion of this reduced frequency range would be within the possible range of variation for any particular design. In summary, mode shape is the most important parameter from a design perspective, but reduced frequency must also be taken into account.

Critical Reduced Frequency Map Near the Reference Blade. The results from the previous section can be overlaid to determine the value of reduced frequency for which each torsion axis location becomes unstable. The contour plot of the results is shown in Fig. 8. The contour shading pattern is set up such that a darker shade indicates less stability. The contour levels in these plots are cut off at $k = 0.6$ to emphasize the range of interest. This is an extremely useful and enlightening plot. The region toward the lower left is the least stable, as shown previously in Fig. 7. The most stable region is toward the upper left corner of this plot, with stability also increasing to the right. On the reference blade itself, a torsion axis on the forward portion of the blade is much more stable than the aft portion.

Figure 8 can be used as a basic design tool. One interpretation is that by controlling the torsion axis location, it would be possible to allow much lower reduced frequency than the current guidelines. It is quite interesting that at the leading and trailing edges as well as at mid-chord, the critical reduced frequency is nearly identical. There is a significant difference between the critical reduced frequency at the most stable location on the blade (at approximately 20 percent true chord) and the least stable (at approximately 60 percent true chord). This leads to a high gradient between these locations. Since this region is the most likely location for the torsion axis of an actual blade, it is not surprising that previous engine experience has been so erratic while using reduced frequency as a design criterion. Small changes in these contours as a function of blade shape or operating conditions for other blade designs could lead to large differences in critical reduced frequency.

The contours of flutter reduced frequency are roughly aligned normal to the blade meanline at all locations along the blade surface. As a result, changes in torsion axis location along the meanline are much more significant than a shift normal to the surface. Note that many of the contours coalesce at a point between the reference blade and its nearest neighbor to the pressure side. The region around this point contains very high gradients in the critical reduced frequency contours. This location appears to be a pivotal point in determining the primary stable and unstable regions, and is the apex of the stable region toward the upper left of the plot.

A question which naturally arises from these results is the source of the changes in stability that occur. The two constituents of the stability parameter—the contribution from the reference blade and that from the adjacent blade pair—were interrogated. The goal was to determine whether the isolated blade effects or the cascade effects are the key driver in the sensitivity to flutter, because such insight is a key to developing realistic design approaches. While considering the contributions for the reference and the adjacent blade pairs did help to explain the patterns found in the critical reduced frequency maps, they did not provide any overwhelming insight. The interested reader is referred to Panovsky (1997) for details.

Critical Reduced Frequency Map Far From Reference Blade. The behavior in a more global sense is also investigated by considering a much larger range of possible torsion axis locations. This larger range provides the behavior for bending-dominated modes, though the analysis is still performed by considering torsion about these points. This must be kept in mind when interpreting the results. For example, if a stable region aligns itself with some geometric feature, the motion of the blade is

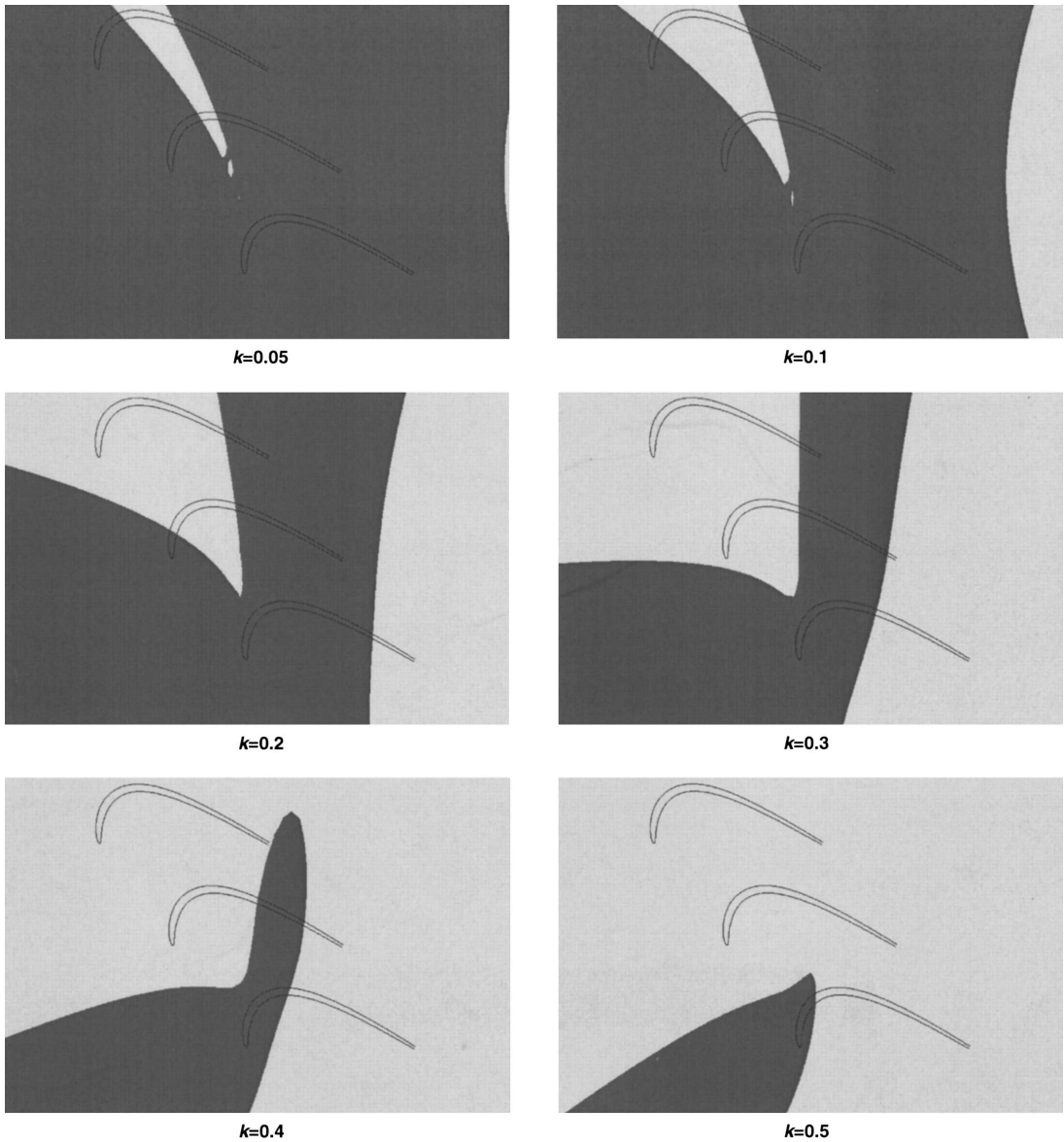

Fig. 7 Unstable regions (shaded) for various levels of reduced frequency

actually perpendicular to this feature. The descriptions given here will refer to the location of the torsion axis.

Table 1 summarizes the relationships between the location of torsion axis, the equivalent bending direction, and the descriptive name for the mode. The definitions are consistent with the coordinate systems introduced in Fig. 2. As an example, the first entry indicates the torsion axis is approaching infinity along the ξ axis. This is equivalent to a translation of the blade section in the η direction, which has been previously defined in the fundamental mode study as the "blade flex" mode.

Regions of instability for this expanded range were determined as previously presented in Fig. 7. These results were then overlaid to produce contours of critical reduced frequency, shown in Fig. 9. The reference blade is again at the center of the domain. Many blades from the row are included for subsequent interpretation

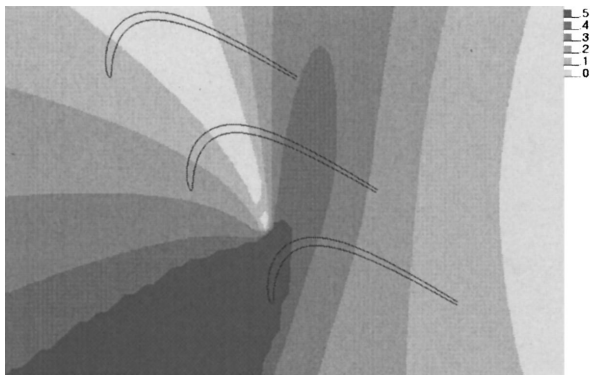

Fig. 8 Critical (flutter) reduced frequency as a function of torsion axis location near the reference blade

Table 1 Equivalent bending modes for torsion axes approaching infinity

Location of Torsion Axis	Direction of Translation	Equivalent Bending Mode Name
$\xi \to \pm\infty$	η	blade flex (normal to chord)
$\eta \to \pm\infty$	ξ	blade axial (along chord)
$x \to \pm\infty$	y	cascade tangential
$y \to \pm\infty$	x	cascade axial

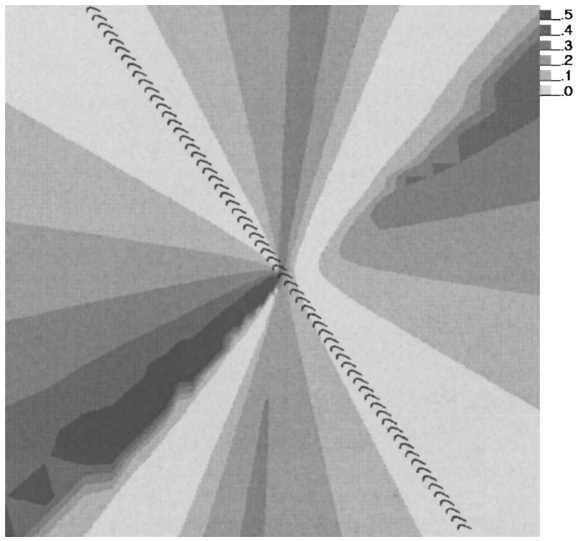

Fig. 9 Critical (flutter) reduced frequency as a function of torsion axis location for the expanded range

purposes. Note that the stability behavior at infinity is symmetric about the origin (at the center of the plot). This is expected, since torsion about mirror image pairs of locations correspond to bending modes with 180 deg temporal phase shifts but no change in the IBPA. As in the previous plots for torsion axes nearer the reference blade, small changes in mode shape can give drastically different flutter frequencies. These results clarify some of the trends seen in the more-local results shown in Fig. 8 and, in fact, change the conclusions dramatically from those that would be reached by considering only that local plot.

In general, there is a highly stable region which lies along the cascade tangential direction. Since these plots are for the torsion axis location, the blade motion is normal to this line. Another stable region lies along a line normal to the aft surface of the blade, which is close but not quite perpendicular to the previous direction. The least stable region lies along the cascade axial, with another region of low stability along the blade axial direction. These regions converge at the origin, resulting in the high gradients seen earlier for the truly torsion-dominated modes. Note that large gradients persist far from the origin. These gradients help to explain the differences found earlier for the various bending modes.

Comparisons to Previous Research. The effect of torsion axis location has been studied previously by other researchers, though in a much less comprehensive manner than presented here. Two of these investigations will be summarized, since they are closely related to the findings of the present study.

Kirschner et al. (1976) conducted an experimental study in a linear cascade on important parameters for flutter of a turbine blade, including three different torsion axis locations. The torsion axes are at approximately 20 percent, 40 percent, and 60 percent chord, all within the airfoil profile. The experimental results indicate that moving the torsion axis forward is quite stabilizing while moving the torsion axis rearward is de-stabilizing.

Whitehead (1987) conducted a numerical study using the geometry of the standard configuration 4 turbine blade (Bölcs and Fransson, 1986), which included a study comparing the effect of a small amount of torsion in a predominately bending mode. The stability for a torsion axis located several chords up and downstream in the cascade axial direction is compared to the stability for a purely bending mode. Whitehead finds that the torsion axis upstream is very de-stabilizing, while a downstream location is very stabilizing.

Note that the results of these two investigations are opposite in trend. However, both outcomes can be explained by the stability maps of Figs. 8 and 9. For the Kirschner study, moving the torsion axis forward along the meanline from 40 percent to 20 percent chord places the torsion axis near the most stable region, as shown in Fig. 8. Moving from 40 percent chord toward the trailing edge results in lower stability. In the Whitehead study, all of the torsion axes are located a few chords from the blade profile along the cascade axial direction. From Figs. 8 and 9, the region upstream of the blade is the least stable region overall. Moving downstream a few chords will give increasing stability. Note that this trend changes if the torsion axis is pushed farther downstream.

These results show that it is critical to conduct a complete study which considers all rigid body modes. Extrapolation of the trends from a small number of torsion axis locations can result in significant errors. Moving the torsion axis in the upstream and downstream directions must eventually produce the same stability behavior, because the torsion axis at positive and negative infinity corresponds to the same bending mode. This is true for any arbitrary direction, as well. Therefore, any trends obtained from limited studies must be restricted to the range of torsion axis locations used. By utilizing the superposition approach, this restriction is eliminated.

Limitations on Parameter Studies

Note that only a single two-dimensional airfoil shape was considered at its design point conditions. A relevant question is the ability to generalize these results to other blade geometries or even other flow conditions. It is believed that the trends shown here will remain valid for most LPT cases. Changes in geometry and conditions will change the precise local values, of course, and for this reason some amount of margin must be included in designs which are based on the proposed criteria. But there has been no indication from any of these studies that LPT flutter behavior is analogous to "falling off a cliff" as some design parameter is varied. Rather, all indications are that there is a slow diminishing of stability and then a smooth transition into the unstable regime. Such behavior indicates that small changes to blade shape or design conditions will probably have small influences on flutter behavior.

Another qualifier on these studies is that the experimental data used to validate the inviscid analysis did not cover ranges of parameters where viscous effects could become more important, such as at very large incidence angles. For this reason, results from the inviscid analyses should not be blindly accepted in these regimes until they have been verified through experiments. In general, LPT blades do not typically deviate significantly from the design point incidence for aircraft applications. However, larger incidence angles do occur in power generation applications. Future studies should address these concerns as well as other factors associated with actual LPT blades, such as endwall effects on the steady flow and structural coupling due to shrouds.

Summary and Conclusions

A stability parameter based on the influence coefficients of only the reference blade and its two closest neighbors was presented. This parameter retains the most important contributions to the overall stability while filtering out small perturbations, giving a clearer picture of the sensitivity of the blade stability to design parameters. The entire IBPA range is addressed by this single parameter, which can be determined from as few as three unsteady analyses. The stability parameter is more useful than the influence coefficients because it isolates the contribution of the reference and adjacent blades to the damping portion of the complex work term.

A study of the fundamental bending and torsion modes showed that each of these modes becomes unstable for a reduced frequency in the range 0.2 to 0.3. The flutter reduced frequency for bending along the cascade axial is considerably lower, which is consistent with previous engine experience. By utilizing the stability parameter, the dependence of flutter on the reduced frequency was shown to be primarily a contribution from the reference blade.

The methodology to utilize the stability parameter in conjunction with a superposition of these fundamental bending and torsion modes was also presented. This allows a complete and systematic study of all rigid body modes to be conducted in a very efficient manner. The use of the stability parameter allows significant stability trends to be easily identified. The results were presented as stability maps of the torsion axis location as a function of reduced frequency. Also provided were similar maps of the flutter reduced frequency as a function of the torsion axis location.

These studies were summarized in two sets, corresponding to torsion-dominated and bending-dominated mode shapes. Regions of maximum and minimum stability were identified. For the torsion-dominated modes, a torsion axis located on the forward portion of the airfoil is much more stable than one on the aft portion. The most stable location is at approximately 20 percent chord, while the least stable location is near 60 percent chord. For modes which are dominated by bending, the most stable region is for torsion axes along the cascade tangential direction. The least stable region lies along the cascade axial direction.

These stability maps indicate the flutter reduced frequency is extremely sensitive to the precise location of the torsion axis. Because performance goals are continually pushing the reduced frequency to lower values, the sensitivity of stability to mode shape must be acknowledged. The mode shape must be controlled in a manner to allow performance to be optimized while maintaining adequate flutter margins. To allow for inevitable blade-to-blade variations, the torsion axis must also be placed in regions of low gradients, or additional margin must be included.

The results of the parameter studies presented in this paper reveal relevant trends which must be taken into account when designing new blades or when assessing flutter behavior. The studies indicate a new approach to designing for flutter, namely by controlling mode shape rather than reduced frequency. This new design approach can be implemented by the use of the stability parameter and application of the superposition techniques presented here.

Acknowledgments

The authors wish to thank GE Aircraft Engines for permission to publish this paper. They also acknowledge the technical contributions of Dr. Graham Holmes, Dr. Christopher Lorence, and Dr. Steven Manwaring at GE Aircraft Engines, Mr. Matthew Nowinski at Ecole Polytechnique Fédérale de Lausanne, and Prof. Torsten Fransson of the Royal Institute of Technology in Sweden.

References

Bendiksen, O., and Friedmann, P., 1980, "Coupled Bending-Torsion Flutter in Cascades," *AIAA Journal*, Vol. 18, pp. 194–201.

Bölcs, A., and Fransson, T. H., 1986, "Aeroelasticity in Turbomachines Comparison of Theoretical and Experimental Cascade Results. Appendix A5: All Experimental and Theoretical Results for the 9 Standard Configurations," Communication du Laboratoire de Thermique Appliquee et de Turbomachines, EPF-Lausanne, No. 13.

Buffum, D. H., and Fleeter, S., 1990, "Aerodynamics of a Linear Oscillating Cascade," NASA Technical Memorandum 103250.

Crawley, E. F., 1988, "Aeroelastic Formulation for Tuned and Mistuned Rotors," chap. 19 in *AGARD Manual on Aeroelasticity in Axial-Flow Turbomachines, Vol. 2, Structural Dynamics and Aeroelasticity*, M. F. Platzer and F. O. Carta, eds., AGARD-AG-298.

Försching, H., 1989, "A Parametric Study of the Flutter Stability of Two-Dimensional Turbine and Compressor Cascades in Incompressible Flow," Zeitschrift für Flugwissenschaften und Weltraumforschung, Vol. 13, pp. 351–364.

Hall, K. C., and Crawley, E. F., 1989, "Calculation of Unsteady Flows in Turbomachinery Using the Linearized Euler Equations," *AIAA Journal*, Vol. 27, No. 6, pp. 777–787.

Holmes, D. G., and Cedar, R. D., 1995, personal communication.

Holmes, D. G., and Chuang, H. A., 1993, "2D Linearized Harmonic Euler Flow Analysis for Flutter and Forced Response," in Unsteady Aerodynamics, Aeroacoustics, and Aeroelasticity of Turbomachines and Propellers, H. M. Atassi, ed., Springer-Verlag, New York.

Kirschner, A., Pelet, C., and Gyarmathy, G., 1976, "Investigation of Blade Flutter in a Subsonic Turbine Cascade," Proceedings, International Union of Theoretical and Applied Mechanics and Association Technique pour la Turbine a Gaz, Symposium sur l'Aeroelasticite dans les Turbomachnes, Paris, France, Oct. 18–23, 1976; *Revue Francais de Macanique, Special Issue*, pp. 97–104.

Nowinski, M. C., Panovsky, J., and Bölcs, A., 1998, "Flutter Mechanisms in Low Pressure Turbine Blades," to be presented at ASME Gas Turbine Conference and Exhibition, Stockholm, Sweden, June, 1998.

Panovsky, J., 1997, "Flutter of Aircraft Engine Turbine Blades," Ph.D. thesis, University of Cincinnati, Cincinnati, OH.

Panovsky, J., Nowinski, M., and Bölcs, A., 1997, "Flutter of Aircraft Engine Low Pressure Turbine Blades," presented at the 8th International Symposium of Unsteady Aerodynamics and Aeroelasticity of Turbomachines, Stockholm, Sweden, Sept. 14–18, 1997.

Szechenyi, E., 1985, "Fan Blade Flutter—Single Blade Instability or Blade to Blade Coupling?" ASME Paper 85-GT-216.

Whitehead, D. S., 1987, "Flutter of Turbine Blades," *Unsteady Aerodynamics and Aeroelasticity of Turbomachines and Propellors*, Proceedings, Fourth International Symposium, Aachen, Germany, pp. 437–452, Sept. 6–10, 1987.

APPENDIX

Derivation of Superposition Relations

We can represent a torsion mode about an arbitrary location by obtaining scale factors for the three fundamental modes (refer to Fig. 2). Linearity and small displacements are assumed. Computational solutions for the pressures and work are taken to be available for the fundamental modes run at unit amplitudes, with the torsion axis located at the origin of the coordinate system. The term "unit amplitude" implies one chord displacement for the bending modes and one radian for the torsion.

The scale factors for each of the fundamental modes can be determined from straightforward geometric relations (Panovsky, 1997), following previous work by Whitehead (1987) and Holmes and Cedar (1995). It can be shown that given a rotation α about the (ξ, η) location, the amplitude of the fundamental torsion mode must also be α. The scale factors for the fundamental bending modes are given by

$$h_\xi = +\alpha\eta$$

$$h_\eta = -\alpha\xi. \tag{A.1}$$

Torsion about this arbitrary point can then be written in terms of the fundamental modes as

$$\{a(\xi,\ \eta;\ \alpha)\} = \begin{Bmatrix} h_\xi \\ h_\eta \\ \alpha \end{Bmatrix} = \alpha \begin{Bmatrix} \eta \\ -\xi \\ 1 \end{Bmatrix}. \tag{A.2}$$

Note that the functional notation used is meant to imply that torsion of amplitude α about some point (ξ, η) is equivalent to scaling the fundamental modes by the indicated amounts. The motion of the grid points on the blade surface for rotation about this arbitrary point is then

$$\{u\} = [\Phi]\{a\}, \tag{A.3}$$

where $[\Phi]$ is the matrix of mode shapes for the fundamental modes (i.e., the first column is for unit translation in the ξ direction, the second column is for unit translation in the η direction, and the third column is for unit rotation about the origin).

The unsteady pressures for a general motion can be written

$$\{p\} = [A]\{u\}. \tag{A.4}$$

These expressions can be substituted into the work expression given by

$$w = \int \pi p^I \bar{u} \cdot \hat{n} ds. \tag{A.5}$$

The right-hand side can be re-written in its discrete form and expanded

$$\begin{aligned} w &= \pi\{p^I ds\}^T\{\bar{u} \cdot \hat{n}\} \\ &= \pi\{\mathrm{Im}[A][\Phi]\{a\}ds\}^T\{[\Phi]\{a\} \cdot \hat{n}\}, \end{aligned} \tag{A.6}$$

which can be simplified to

$$w = \{a\}^T[b]\{a\} \tag{A.7}$$

through some basic linear algebra. This is the same as Eq. (9) presented earlier.

This expression can be used to determine the damping (by suitable normalization of the work) for torsion about an arbitrary point by appropriate superposition of the solutions for the fundamental modes. The major limitation is that similar plots would be required for each IBPA to determine regions of stability throughout the entire IBPA range. This limitation, though, has been overcome by extending this approach to obtain similar results for the influence coefficients and the stability parameter.

The influence coefficients are given by the Discrete Fourier Transform of the traveling wave components, which will be denoted in operator notation as

$$W_k = F(w_l). \tag{A.8}$$

Note that the convention adopted earlier of using k for blade contributions and l for traveling wave contributions has been retained. The Fourier Transform is a linear operator and substituting from (A.7) gives

$$F(w_l) = \{a\}^T F([b_l])\{a\}. \tag{A.9}$$

The Fourier Transform of the work matrix is a matrix of the transforms of the individual work terms,

$$F(w_l) = \{a\}^T[F(b_{ij})]\{a\}. \tag{A.10}$$

It is then possible to determine each influence coefficient

$$W_k = \{a\}^T[B_k]\{a\}, \tag{A.11}$$

where $[B_k]$ is the matrix of influence coefficients for the fundamental modes for the kth blade.

Normalization for Work

Before conducting the calculations of the damping values using superposition of the fundamental modes, an inadequacy in definitions must be overcome. Following Bölcs and Fransson (1986), the damping coefficient for a purely bending mode is related to the dimensional work by

$$\Xi_h = -\frac{w}{\pi q c^2 \bar{h}^2}, \tag{A.12}$$

where h is the plunging amplitude normalized by the chord. The damping coefficient for torsion is

$$\Xi_\alpha = -\frac{w}{\pi q c^2 \bar{\alpha}^2}. \tag{A.13}$$

In the superposition results, we want to consider every rigid body mode as a torsion about some axis. In the limit, a torsion axis approaching infinity corresponds to a bending mode of the blade. A problem arises in that the damping coefficient in Eq. (A.13) is basically the work per radian of rotation. For a torsion axis at infinity, the translation of the blade becomes infinite, as does the damping coefficient. Ideally, the damping coefficient for torsion would asymptote to the coefficient for bending, which would require a translational motion of one chord.

Clearly, an alternative approach must be used, and an additional normalization is employed here. Constraints on the normalization are that it cannot affect the algebraic sign on the damping coefficient, and it must be a continuous function. The condition chosen is that, regardless of the torsion axis location, the sum of the displacements of the leading edge and the trailing edge must be one chord. This is obviously satisfied by a unit radian rotation about the leading edge, trailing edge, and mid-chord (linear mode shapes are used, as always). The derivation of the general expression is straightforward (Panovsky, 1997), and is given by

$$\alpha = \frac{1}{\sqrt{\xi^2 + \eta^2} + \sqrt{(\xi - 1)^2 + \eta^2}}. \tag{A.14}$$

This normalization does not quite reach the desired goal of consistency with the definition of the damping coefficient for bending. As the torsion axis approaches infinity, the leading and trailing edge each move one-half chord with the current normalization, rather than the full chord obtained by using Eq. (A.12). As a result, the damping coefficient is different by a factor of four. Note that this will not change the location of any of the resulting stability boundaries.

Q. Wang
Department of Mechanical Engineering,
Northwestern University,
Evanston, IL 60208

Y. Cao

R. Wang

F. Mignano

Department of Mechanical Engineering,
Florida International University,
Miami, FL 33174

G. Chen
Department of Mechanical Engineering,
Northwestern University,
Evanston, IL 60208

Studies of a Heat-Pipe Cooled Piston Crown

Designing pistons with effective cooling is crucial to preventing piston failure and improving engine service life. A piston design that incorporates the heat-pipe cooling technology may provide a new approach that could improve the thermal-tribological performance of heavy-duty diesel engine pistons. A simplified piston crown with an annular reciprocating heat pipe is constructed to demonstrate this concept. The piston crown is experimentally tested on a specially designed reciprocating apparatus. Experimental data indicate that the annular heat-pipe cooling can greatly assist in reducing the temperature gradient and peak temperature along the ring bank. In order to predict the performance in a more realistic piston working condition, a three-dimensional finite element modeling is used to analyze the thermal performance of this annular heat-pipe cooled crown (AHPCC). The heat-transfer coefficient under the reciprocal environment of the experimental apparatus and the effective thermal conductance of the heat pipe are determined by correlating the numerical calculations with the experimental measurements. The results indicate that the heat-pipe-cooling concept presented in this paper can provide an effective means for piston temperature control under real piston operating conditions.

1 Introduction

Effective piston cooling is crucial to preventing engine failures and improving its thermal efficiency and service life. A higher temperature of charge in an engine combustion chamber may be preferred for higher engine efficiency. However, this high temperature may adversely affect engine elements and cause considerable thermal-tribological problems. Piston scuffing in diesel engines, particularly at the piston/piston-ring/cylinder-liner interface, is a serious problem which degrades engine performance and shortens engine life. Among the assembly elements, the piston is the most vulnerable one. Because of the reciprocating motion of the piston assembly, efficient piston cooling is difficult to achieve through conventional cooling methods, such as crankcase oil splashing and internal gallery circulation for heavy duty diesel engines, as described by Law and Day (1969) and Mihara and Kidoguchi (1992). Because of the combustion and the nonuniform cooling conditions, the temperature in the piston is nonuniform. The maximum temperature difference in the ring area may be as large as 100–140°C, depending on the cooling conditions (Monro and Griffiths, 1979). This nonuniformity contributes to the piston structural distortion and variation of the piston working clearance, which eventually affects the tribological performance of the piston.

For the aforementioned reasons it is necessary to search for a new piston design that is able to tolerate a higher temperature in the combustion chamber and at the same time retain a reasonably low temperature level at tribological interfaces with improved temperature uniformity. Development of pistons by incorporating heat-pipe-cooling technique suggests a direction to achieve these goals because of the superb heat transfer capability of the heat pipe. The piston motion requires that the heat pipe be subject to the same reciprocal motion that the piston experiences. For this reason, reciprocating heat pipes have been developed and extensively studied (Cao and Wang, 1995a, 1995b; Wang et al., 1995). The reciprocating heat pipe, like many conventional heat pipes (Cotter, 1965; Cao and Faghri, 1992), has an evaporator at the heat input section and a condenser at the cooling section. Evaporation in the evaporator section and condensation in the condenser section result in a very effective heat transfer path and a very high heat conductance. The return of the condensate to the evaporator section in a reciprocating heat pipe is achieved by means of the dynamic action of the heat pipe. Because of this dynamic motion, the liquid phase convection is also an effective means of heat transfer. It has been proven that the reciprocating heat pipe has a similar or higher thermal conductance compared to that of conventional heat pipes (Ling et al., 1996).

This paper reports the development and modeling of a simplified annular heat-pipe cooled piston crown (AHPCC). The annular heat pipe is an extension of the reciprocating heat pipes mentioned above. Due to its cylindrical shape, the heat pipe can comply with the piston structure and the engine-operating environment. This annular heat pipe has the potential to cool the piston ring area effectively and thus maintains the piston ring-bank at a reasonably uniform temperature. The AHPCC serves as a prototype for proving the possibility of using such an annular heat pipe in a real piston for the piston temperature control. In addition to experimental tests, a finite element modeling (FEM) is employed to simulate the AHPCC operation under severe working conditions. Models for a simplified crown without the heat-pipe working fluid and a solid-wall crown were also developed for experimental correlation and comparisons with those of the AHPCC.

2 Description of the Simplified Piston Crown Incorporating an Annular Reciprocating Heat Pipe

The annular heat pipe is a cylindrically shaped element with an annular cavity that is vacuumed and filled with a working fluid. A simplified piston crown with an annular heat pipe was fabricated and shown in Fig. 1, which consists of an inner adapter and an outer ring. This simplified crown has the basic features of a real engine piston crown of a two-piece articulated diesel-engine piston, which usually has a steel crown and an aluminum-alloy skirt. The current piston crown would simplify the complex geometry of a real steel crown and can be used to evaluate the cooling effectiveness of the annular heat pipe. The inner adapter and outer ring were assembled through a tight fit and welding at two ends to form the "crown" that has a top land (the top flat end) and a ring-bank area (the side grooved region). The clearance between the shoulders of these two pieces results in an annular heat-pipe cavity

Contributed by the Internal Combustion Engine Division (ICE) of THE AMERICAL SOCIETY OF MECHANICAL ENGINEERS for publication in the ASME JOURNAL OF ENGINEERING FOR GAS TURBINES AND POWER.

Manuscript received by the ICE February 26, 1998; final revision received by the ASME Headquarters January 19, 1999. Associate Technical Editor: D. Assanis.

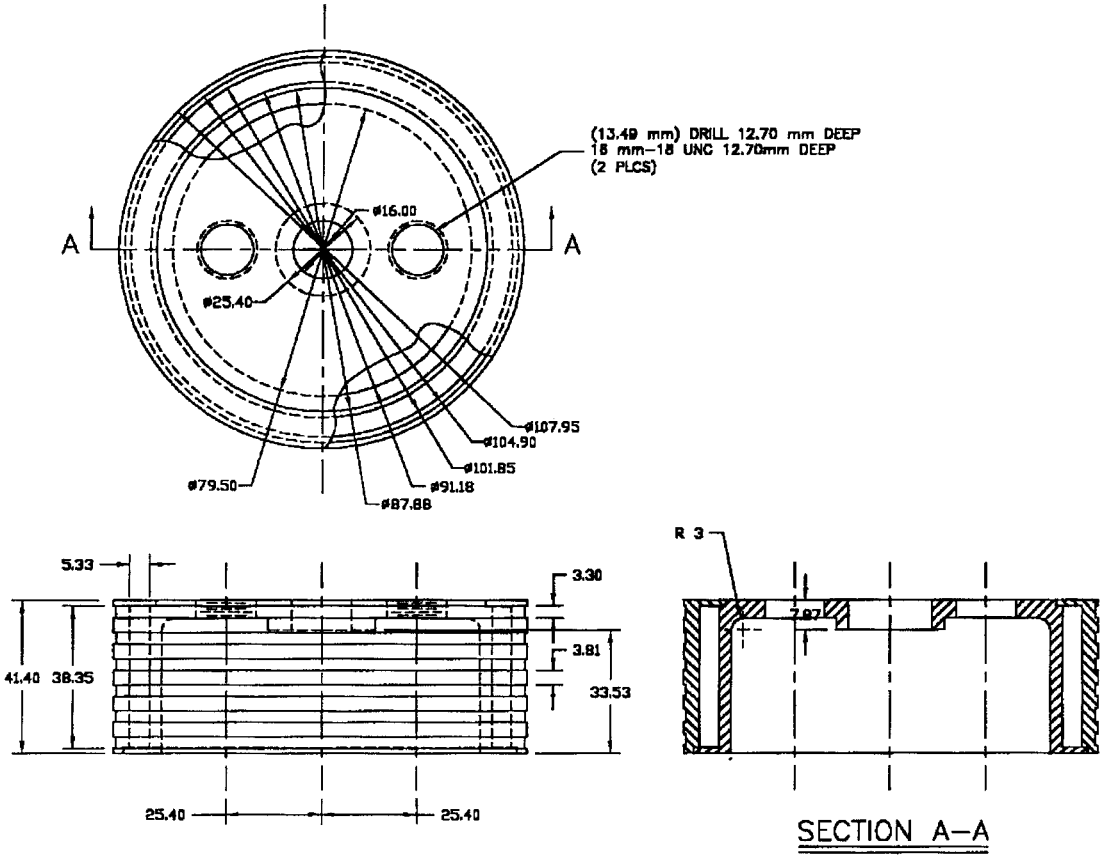

Fig. 1 Structure of the simplified piston crown with an annular heat pipe

parallel to the piston ring bank, complying with the piston geometry. A central hole on the top land was made for connecting the "crown" onto a reciprocating tester for experimental study.

The AHPCC was made of stainless steel 316. After properly evacuating the heat-pipe cavity, an amount of liquid methanol was filled into the heat pipe as the working fluid. It was expected that the chaotic fluid-vapor motions in the heat pipe due to the piston reciprocation could facilitate an enhanced heat transfer process in the heat pipe both circumferentially and longitudinally. As a result of this enhanced heat transfer in both the longitudinal and circumferential directions, the piston ring-bank area could become isothermal at a desired temperature level.

In order to simulate a non-symmetric heat-transfer condition as it would occur in a real engine piston, an offset heater, as shown in Fig. 2, was used. Two additional holes were made on the top land near the central hole to reduce the heat conduction rate from the heater to the opposite side of the top land, which would create a more severe nonsymmetric heat input condition on the top land.

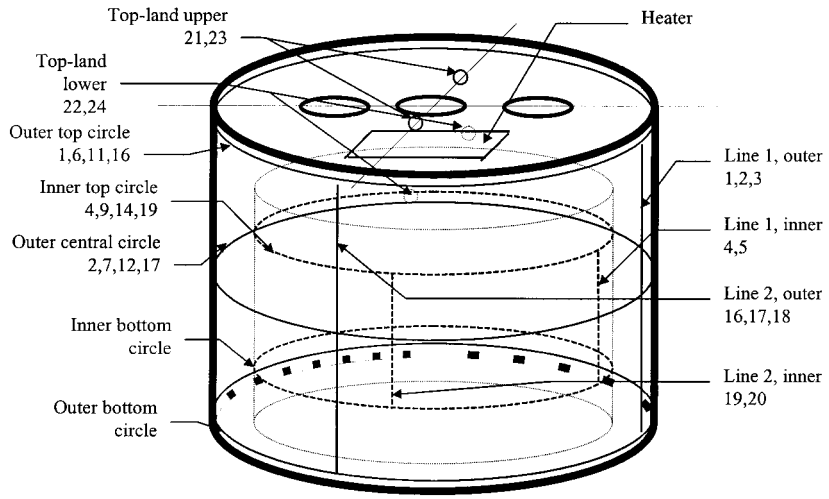

Fig. 2 Heat input and temperature measurement. (A total of 24 thermocouples were used. They were in five circles, three of them were on the outer surface and the other two were on the inner surface. The thermocouples on each circle were 90 apart forming eight lines in the longitudinal direction.)

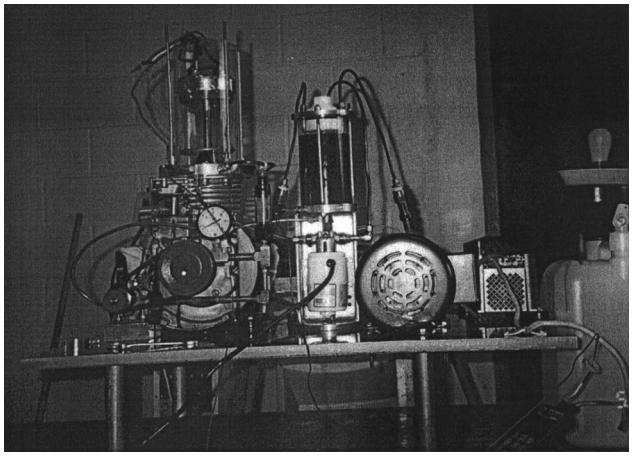

Fig. 3 Photograph of the reciprocating engine-simulation tester

To test the heat-spreading effectiveness of the annular heat pipe, the top land of the simplified crown was covered by a heat-insulation layer to minimize the heat loss there.

3 Experimental Setup and Results

The simplified crown shown in Fig. 1 was fabricated and tested under the conditions of with and without the heat-pipe cooling. It was expected that with the same structure and heater arrangement for the heat pipe crown and nonheat pipe crown, the testing data obtained should yield an accurate comparison.

A piston reciprocation tester was used for the experimental investigation. Figure 3 shows a photograph of the apparatus. It utilizes the piston reciprocal motion of a single-cylinder internal combustion engine, Briggs and Stratton model 1904009 with a piston stroke of 69.85 mm. The testing crown was connected to the piston of the apparatus through a thread adapter so that it could experience the same motion as that of the piston. A Balder electric motor, model M3559T, was used to drive the engine through a belt. The speed of the motor, which is the same as that of the engine crank, was controlled by a Toshiba motor controlling driver, model VFSX-2022p. A plastic cylindrical chamber was built to facilitate the observation and for the safety considerations.

An electric heater (Omega KH 212/10 flexible heater) was used as the heat source, and the heat input was controlled by a variable auto-transformer (type 3PN1010V). Both the ring-bank and top-land temperatures were measured through thermocouples. A total number of 24 thermocouples were used to obtain the temperature distributions in the piston crown, and their dispositions are given in Fig. 2. The thermocouples were located along five measurement circles at both inner and outer crown surfaces, namely, outer-top, outer-central, outer-bottom, inner-top, and inner bottom. They were also arranged along eight lines in the longitudinal direction, namely, lines 1 through 4 at the inner surface and lines 1 through 4 at the outer surface. The thermocouples along each circle were 90 deg apart with line 3 being opposite to line 1 and line 4 opposite to line 2. The vertical distance between the top and bottom circles was about 39 mm. The inner measurement circles were in between the adjacent outer measurement circles and were separated by the same distance as that of the outer measurement circles. In addition, four other thermocouples, numbered 21 through 24, were attached to the top-land area, as indicated in Fig. 2. An automatic temperature data acquisition was achieved through an Omega Tempscan/1000A high-speed temperature measurement system.

In the present experiments, the top land of the simplified crown is the heat-receiving region. As a result, the end of the annular heat pipe adjacent to the top land would work as the evaporator and the rest of the heat pipe portion would work as the condenser. In a static state, the heat transfer mechanisms of the annular heat pipe in the longitudinal direction should be similar to that of a conventional heat pipe. The reciprocal motion of the annular heat pipe with the piston would overcome the adverse effect of the gravity and facilitate the liquid return from the condenser section to the evaporator section. It was expected that both the vapor flow and the liquid impingement in the heat pipe could greatly enhance the heat transfer in both circumferential and longitudinal directions.

Figure 4 shows the maximum temperature differences in the ring-bank area of the piston crown with and without the heat pipe cooling. For all of the tests, the electric heater was fixed at the same location on the top-land area as indicated in Fig. 2. During the reciprocating tests, the simplified crown was heated to a desired temperature prior to starting the reciprocating motion. The reciprocating-test results indicate that the annular heat pipe can quickly react to power changes and effectively control the temperature distribution in the ring-bank area. The results also show that the heat-pipe cooling can lead to a uniform ring-bank temperature distribution without significantly affecting the top-land temperature level. It can be anticipated that this uniform temperature will greatly benefit future engine development for a higher power density and better thermal-tribological performance. The testing results show in Fig. 4 are for those with a power input of 51 W and a reciprocating frequency of 7 Hz. Additional experimental results at different power inputs and reciprocating frequencies have been reported by Mignano et al. (1998), and all those results give the same trend as that shown in Fig. 4.

Although the experimental data have proven the feasibility of the heat pipe cooling concept and the cooling effectiveness of the heat pipe, a direct application of the data to the piston design is limited. First, the experiments were conducted at a much lower temperatures than that of a piston working under a real engine condition because of the power capacity of the heater. Second, the reciprocating frequencies of the tester is limited to an extent that the heater and thermocouples would not be torn apart. Finally, the working fluid used in the heat pipe might not be practical for a real piston crown. The selection of methanol as the heat pipe working fluid is based on the compatibility of the working fluid and the material of the tested piston crown. In a future study, a working fluid such as water should be used in the heat pipe, which would allow the piston crown to work at a higher temperature. A finite element analysis should be conducted to remedy the aforementioned shortcomings and provide more information for the piston crown design. The experimental data collected in this study could be used to verify the finite element model and determine the unknowns in the modeling. Once the numerical model is verified, it could be used to predict the cooling effectiveness of the heat pipe under wider working conditions.

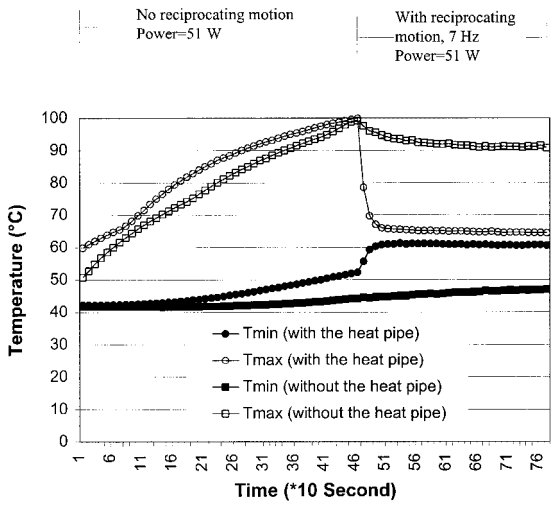

Fig. 4 Comparisons of the maximum temperature differences in the ring-bank area of the simplified piston with and without the heat pipe

4 FEM Modeling

In this study, an ANSYS-based FEM analysis is conducted with the assistance of experimental measurements described earlier. Three simplified piston crowns based on two structures were numerically studied. The first crown structure is illustrated in Fig. 5(*a*) with an annular heat pipe channel. After the heat pipe channel is evacuated and filled with an amount of working fluid, the piston crown becomes an annular heat-pipe cooled crown (AHPCC). For the purpose of benchmark comparison, two additional piston crowns were also studied. The first crown for this purpose is based on the same crown structure as shown in Fig. 5(*a*) but without charging any working fluid. Because of the lack of working fluid in the heat pipe channel, the heat transfer in the crown is due to pure heat conduction without heat pipe cooling effect. The second piston crown for the comparison purpose is a solid piston structure shown in Fig. 5(*b*). For convenience, the three piston crowns mentioned above are referred to as models 1, 2, and 3 in this paper. As mentioned earlier, both model 2 and model 3 are for the benchmark comparisons with model 1 (AHPCC) to illustrate the heat-pipe cooling effectiveness. Each modeled structure includes the simplified crown and an insolating material on the top land for (Fig. 6). For all three models, the ring grooves were neglected for simplicity. The thermal analysis of the simplified crowns is basically to solve heat conduction equations subject to appropriate convective heat-transfer boundary condition due to the reciprocating motion of the piston. In the numerical modeling, the heat source applied to the heating area shown in Fig. 2 was actually sandwiched in between the top land of the simplified piston crown and the insolating material. The annular heat pipe can be treated as an isotropic conductor whose effective thermal conductance should be determined by correlating numerical results with the experimental measurements. The governing equations and the corresponding boundary conditions are given as follows.

For model 1, the general steady-state heat transfer can be described by the following heat-conduction equation:

$$\frac{\partial}{\partial x}\left(k\frac{\partial T}{\partial x}\right)+\frac{\partial}{\partial y}\left(k\frac{\partial T}{\partial y}\right)+\frac{\partial}{\partial z}\left(k\frac{\partial T}{\partial z}\right)=0 \quad (x, y, z)\in\Omega \tag{1}$$

Since the numerical model includes three regions, i.e., piston crown material, annular heat pipe, and insulating material on the top land, the thermal conductivity in the above equation would vary as follows:

$$k=k_{hp},\ (x, y, z)\in\Omega_{hp} \tag{2}$$

$$k=k_{inso}(x, y, z)\in\Omega_{inso} \tag{3}$$

$$k=k_{cr},\ (x, y, z)\in\Omega_{cr}, \tag{4}$$

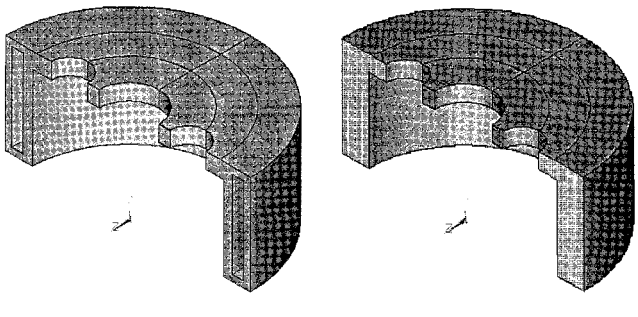

(a) (b)

Fig. 5 Simplified piston crowns with and without the heat-pipe channel, (*a*) with the annular heat-pipe channel; and (*b*) without the annular heat-pipe channel.

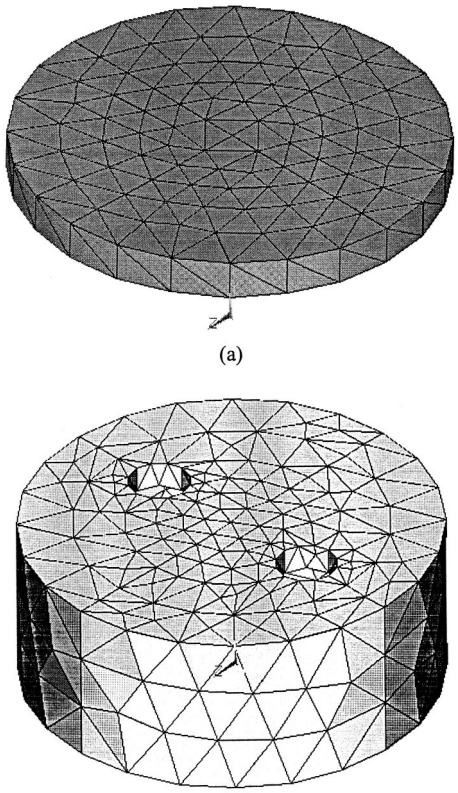

(a)

(b)

Fig. 6 FEM meshes for the simplified crown and the isolator on the top land: (*a*) the isolator; (*b*) the simplified crown.

where k_{cr}, k_{hp}, and k_{inso} are, respectively, the thermal conductivity of crown material, effective thermal conductance of the annular heat pipe, and thermal conductivity of the insulating material, and the subscripts, $_{hp}$, $_{inso}$, and $_{cr}$ refer to the heat pipe, insolating and crown materials. In the heat input region, a given heat generation rate Φ is specified. On the boundary surfaces that are exposed to the air, the following boundary conditions are given:

$$k_i\frac{\partial T}{\partial n_j}=-\beta(T-T_\infty), \tag{5}$$

where n_j is the normal of boundary j. The heat conductivity, k_i, would take a different value at different regions. The value of heat transfer coefficient, β, would also vary at different locations due to different cooling conditions. In the current study, β was considered as an average of the heat-transfer coefficient.

Equations (1) through (5) completely describe the heat transfer problem for the AHPCC (model 1). For models 2 and 3, the governing equations and boundary conditions are similar except for the annular heat pipe region. Figure 6 presents the FEM meshes for the crown and the isolator. A total of 2700 isoparametric tetrahedral elements were used in the modeling. The same group of equations and meshes should be applied to model 2 without the heat-pipe working fluid by setting k_{hp} to be zero and to model 3 for the solid-wall crown by changing k_{hp} into k_{cr} in the annular heat pipe region. In all three models, the thermal conductivity of the crown material, k_{cr}, is taken to be 16.6 W/m°C based on the actual material used. The convective heat transfer coefficient, β, with respect to the reciprocating environment and the effective thermal conductance of the annular heat pipe, k_{hp}, are unknown. These values can be determined, however, by employing the reciprocating test results reported earlier. In this study, the experimental results obtained at 51 W heat input and 7 Hertz reciprocating motion, which are presented in Fig. 4, were employed to determine

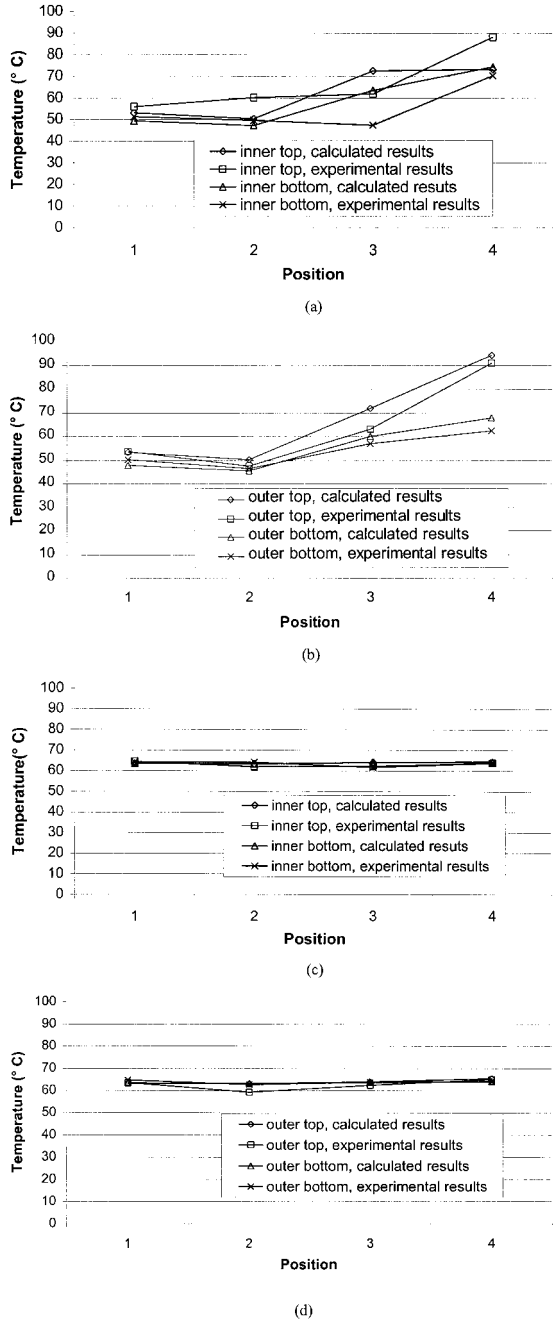

Fig. 7 Comparison between the calculated and measured ring-bank temperatures for the simplified crown represented by the solid model structure in Fig. 5(*a*): (*a*) on the inner surface of the ring area, without the annular heat pipe (model (2)); (*b*) on the outer surface of the ring area, without the annular heat pipe (model (2)); (*c*) on the inner surface of the ring area, AHPCC (model (1)); and (*d*) on the outer surface of the ring area, AHPCC (model (1)).

the values of the heat transfer coefficient, β, and the heat-pipe effective thermal conductance, k_{hp}. The measured temperature distribution from the crown without the heat-pipe working fluid (model 2) were used first to determine the heat transfer coefficient, β, by minimizing the root-mean-square (RMS) errors of the calculated temperatures, T_c, relative to the measured ones, T_m, simply using the trial and error method:

$$\text{Error } (\beta) = \sqrt{\frac{1}{n}\sum_{l=1}^{n} (T_{cl} - T_{ml})^2}, \tag{6}$$

where n is the number of data compared. A value of 30 W/(m^2°C) was obtained for β corresponding to the experimental reciprocating environment with a RMS error of 6.9°C. This β was then applied to the model for the AHPCC (model 1) to determine the effective heat conductance, k_{hp}, for the annular heat pipe. The same methods of correlating the experimental data with the numerical results and minimizing the RMS errors at the same reciprocating and heat input conditions were adopted:

$$\text{Error } (k_{hp}) = \sqrt{\frac{1}{n}\sum_{l=1}^{n} (T_{cl} - T_{ml})^2}. \tag{7}$$

The nearly uniform temperature in the ring area obtained from experiments suggests that it is appropriate to treat the annular heat pipe as an isotropic material having a very high effective heat conductance. With an RMS error of 1.33°C, the value of k_{hp} was found to be about 3980 W/m°C, which is about 240 times that of the crown material, k_{cr}.

5 Numerical Results and Discussion

Once the values of β and k_{hp} are obtained, the numerical models can be used for a comparative study of the thermal performance of the simplified crown. Before the numerical model is actually used to predict the performance of an AHPCC, however, the accuracy of the model must be verified in comparison with the corresponding experimental data. Figure 7 presents the calculated and measured ring-bank temperatures for the AHPCC (model 1). The comparisons indicate that the FEM models thus developed can closely predict the performance of the simplified crown for thermal analyses.

After the verification, these finite element models described above were employed to analyze the thermal performance of the simplified crown at higher heat inputs and working temperatures. It should be noticed that the effective thermal conduc-

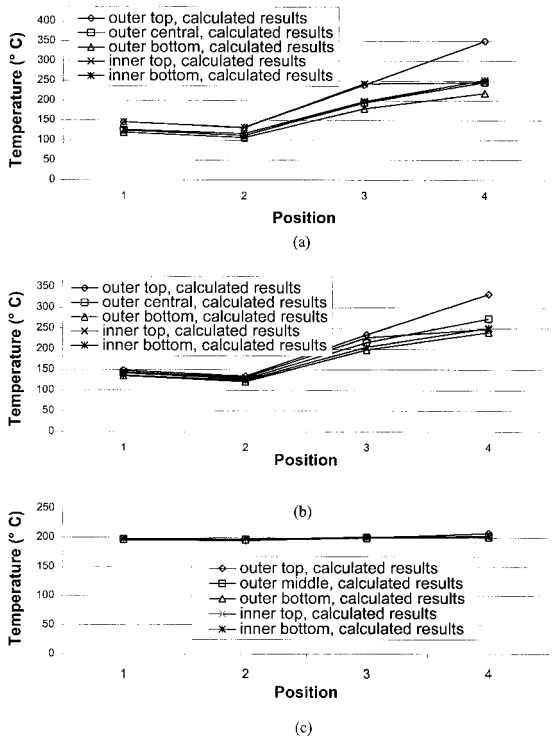

Fig. 8 Calculated ring-bank temperatures for the crowns with a heat input of 255 W: (*a*) without the annular heat pipe (model (2)), solid structure shown in Fig. 5(*a*); (*b*) without the annular heat pipe (model (2)), solid structure shown in Fig. 5(*b*); and (*c*) with the annular heat pipe (AHPCC, model (1)).

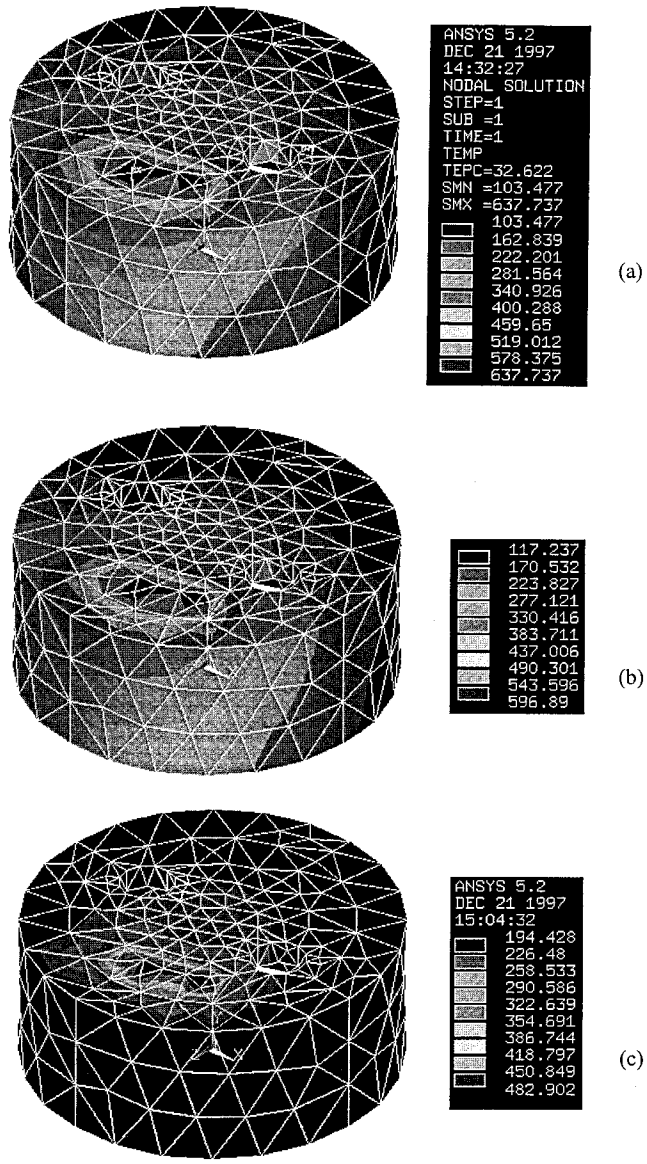

Fig. 9 Isotherms for the crowns when the heat input is 255 W: (*a*) without the annular heat pipe, solid model shown in Fig. 5(*a*); (*b*) without the annular heat pipe, solid model shown in Fig. 5(*b*); and (*c*) with the annular heat pipe.

tance of the heat pipe might increase as the heat input is increased (Chen et al., 1998). However, using the thermal-conductance value determined at a lower heat input for higher heat-input cases would yield conservative estimations on the heat-pipe performance. Temperature distributions for the AHPCC (model 1), the crown without the heat-pipe working fluid (model 2), and the crown with a solid-wall (model 3) were analyzed at 255 W and 510 W heat inputs. Figures 8 through 11 present the results in terms of temperature distributions (Figs. 8 and 10) and isotherms (Figs. 9 and 11). As can be seen, models 2 and 3 without the heat pipe cooling yield similar thermal performances with very high ring-bank temperature gradients. As expected, the heat-pipe cooling significantly contributes to the temperature uniformity and peak-temperature reduction (model 1). The maximum temperature difference for the simplified crown with the solid wall (model 3) at 255 W is about 215°C. This difference is reduced to 13°C by the heat-pipe cooling (model 1), which is only 6 percent of the former. Similarly, the maximum temperature difference in the AHPCC for the case with a 510 W power input is only about 6 percent of that for the solid-wall crown having the same heat input. The temperature distribution can also be clearly viewed through isotherm maps, which reveal that the annular heat pipe makes the ring-bank area almost isothermal. For both heat inputs, the peak temperatures along the ring bank are reduced to about 60 percent of the peak values in the conventional crown as a result of the annular heat pipe cooling. Because the current analyses are based on conservative values of the heat pipe effective thermal conductance, the trend of temperature uniformity and peak-temperature reduction for real pistons with combustion heat input should be similar or even more favorable.

Operation of the simplified crown under higher frequencies of reciprocation was not conducted. However, previous studies revealed that at a higher reciprocating frequency, the working fluid impingement inside a reciprocating heat pipe is enhanced and as a result, the heat-pipe performance can be more notably improved (Wang et al., 1996a).

6 Conclusions

A simplified piston crown with an annular reciprocating heat pipe has been developed to investigate the effect of heat-pipe cooling on the piston-crown temperature distribution. Experimental investigations were conducted to verify the working mechanisms of the annular heat pipe under a reciprocating motion and confirm the effect of heat-pipe cooling on piston temperature control. Ansys-based FEM models have been developed by correlating the numerical results with the experimental measurements. The effective thermal conductance of the annular heat pipe was found to be about 3980 W/m-°C, about 240 times that of the crown material.

The FEM models were then applied to analyze the performance of the simplified crowns at higher power inputs. The results indicate that the annular heat-pipe cooling can greatly assist in reducing the temperature gradient and peak tempera-

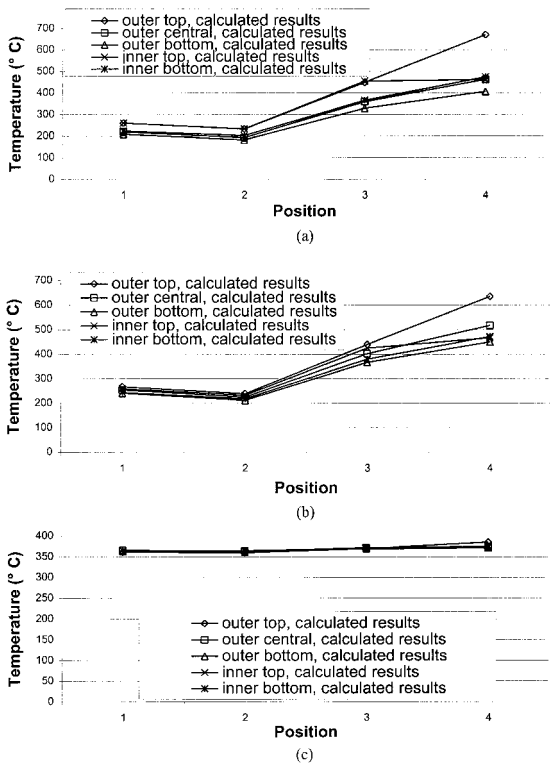

Fig. 10 Calculated ring-bank temperatures for the crowns when the heat input is 510 W: (*a*) without the annular heat pipe, solid model shown in Fig. 5(*a*); (*b*) without the annular heat pipe, solid model shown in Fig. 5(*b*); and (*c*) with the annular heat pipe.

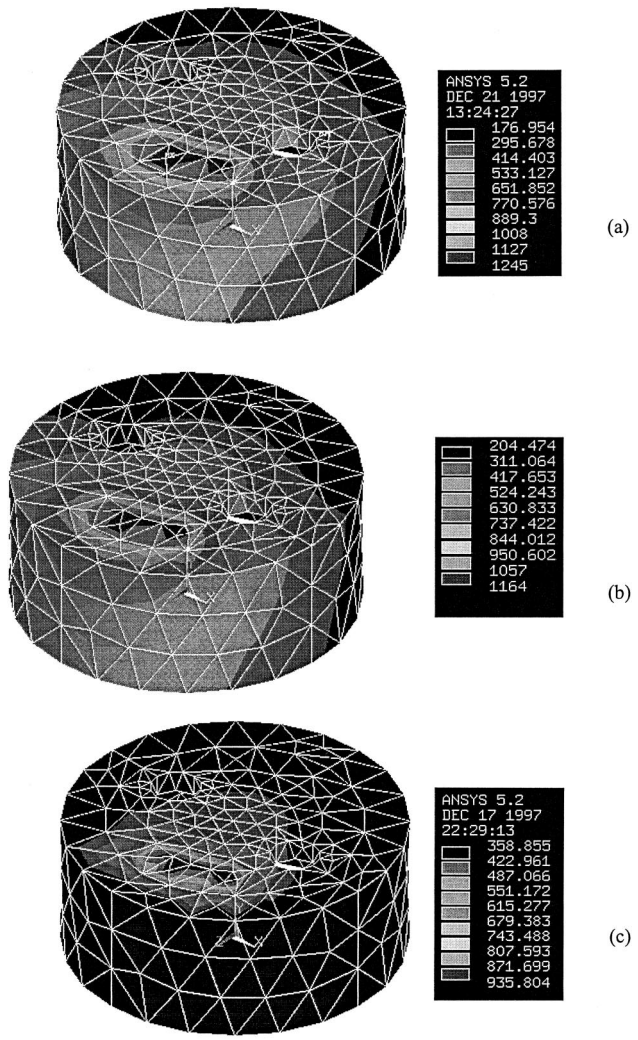

Fig. 11 Isotherms for the simulated crown when the heat input is 510 W: (*a*) without the annular heat pipe, solid model shown in Fig. 5(*a*); (*b*) without the annular heat pipe, solid model shown in Fig. 5(*b*); and (*c*) with the annular heat pipe.

ture along the ring bank. It is anticipated that this heat-pipe cooling technique can function well under the working conditions of a real engine. It may also be expected that the uniform ring-bank temperature will significantly benefit the development of future engines with a high power density and excellent thermal-tribological performance.

Acknowledgments

The authors would like to acknowledge the Office of Naval Research for financial support and Dr. Peter Schmidt for his interest in this research work.

References

Cao, Y., and Faghri, A., 1992, "Transient Multidimensional Analysis of Nonconvetional Heat Pipes With Uniform and Nonuniform Heat Distributions," *ASME Journal of Heat Transfer*, Vol. 113, pp. 995–1002.

Cao, Y., and Wang, Q., 1995a, "Reciprocating Heat Pipes and Their Applications," *ASME Journal of Heat Transfer*, Vol. 117, No. 2, pp. 1094–1096.

Cao, Y., and Wang, Q., 1995b, "Thermal Analysis of the Piston Cooling System With Reciprocating Heat Pipes," *Heat Transfer Engineering*, Vol. 16, pp. 50–57.

Chen, G., Wang, Q., Cao, Y., and Tso, C., 1998, "Development of an Isothermal Journal Bearing by Utilizing the Heat-Pipe Cooling Technology," *Tribology Transactions*, accepted for publication.

Cotter, T. P., 1965, *Heat Pipe Theory and Practice*, Hemisphere Publishing, Washington D.C.

Law, D. A., and Day, R. A., 1969, "Oil Cooled Aluminum Alloy Diesel Engine Pistons — A New Approach," SAE Paper 690749.

Ling, J., Cao, Y., and Wang, Q., 1996, "Experimental Investigations and Correlations for the Performance of Reciprocating Heat Pipes," *Heat Transfer Engineering*, Vol. 17, pp. 34–45.

Mignano, F., Wang, R., Chen, G., Wang, Q., Cao, Y., and Vargas, A., 1998, "Development of a Diesel-Engine Piston by Incorporating Heat Pipe Technology—Experimental Simulation of Piston Crown," to be presented at the 1998 SAE International Congress, Detroit, MI.

Mihara, K., and Kidoguchi, I., 1992, "Development of Nodular Cast Iron Pistons With Permanent Molding Process for High Speed Diesel Engines," SAE Paper 921700.

Monro, R., and Griffiths, W. J., 1979, "Development and Operating Experience of Pistons for Medium Speed Diesel Engines," presented at the general meeting of the Diesel Engineers and Users Association in London.

Wong, T. Y., Scott, C. G., and Ripple, E. D., 1993, "Diesel Engine Piston Scuffing: A Preliminary Investigation," SAE Paper 930687.

Wang, Q., Cao, Y., and Velasquez, A., 1996a, "A Study of the Impingement Frequency of Fluid in Curved Pipes for Piston Applications," *Applications of New Diesel Engine and Component Design*, pp. 13–18.

Wang, Q., Cao, Y., and Souto, A., 1995, "Development of a New Engine Piston Incorporating Heat Pipe Cooling Technology," *Analysis of New Diesel Engine and Component Design*, pp. 19–25.

Wang, Q., Cao, Y., and Chen, G., 1996b, "Piston Assembly Design for Improved Thermal-Tribological Performance," *Tribology Transactions*, Vol. 39, pp. 483–489.

Emission Control Through Cu-Exchanged X-Zeolite Catalysts: Experimental Studies and Theoretical Modeling

S. Bhattacharyya[1]

R. K. Das

Department of Mechanical Engineering,
Indial Institute of Technology,
Kharagpur 721 302,
India

Catalysts based on X-zeolite have been developed by exchanging its Na^+ ion with Copper ions and its effectiveness in reducing NO_X in an actual SI engine exhaust has been tested. Unlike noble metals, the doped X-zeolite catalysts, studied here, exhibit significant NO_X reduction for a wide λ range and exhibit a slow rate of decrease with increase in λ ratio. Back pressure developed across the catalyst bed was found to be well-affordable and power loss due to back pressure is only minimal. During 30 hours of testing of the catalyst, no significant deactivation was observed. Additionally a mathematical model has been developed to predict the performance of the catalyst and to validate that against experimental results. Results predicted by the mathematical model agree well with the experimental results and absolute average deviation of experimental conversion efficiency is found to be less than 5 percent of the predicted value.

Introduction

Three-way catalytic (TWC) converters containing noble metal catalysts are extensively used for simultaneous control of all the three principal pollutants in automobile exhaust, carbon monoxide (CO), oxides of nitrogen (NO_X), and unburnt hydrocarbons (HC) (Taylor, 1983). Besides high and rapidly increasing prices, TWCs are handicapped by their limited effectiveness only within a very narrow range of air-fuel ratio near stoichiometric ($\lambda = 1$) (Held et al., 1990). During lean A/F ratio operation, NO_X conversion falls drastically due to competition for adsorption sites on catalyst surfaces with excess oxygen ($\lambda > 1$) present in the feed gas or released by the decomposition of NO_X. Thus the fuel economy improvement potentiality of the currently developing lean-burn gasoline engines, which can improve engine efficiency up to 15 percent compared to current SI engines with TWC and even greater for DI-gasoline engines (König, 1993), can only be utilized if a suitable catalytic system for converting NO_X even in an oxidizing atmosphere is available. In recent studies, metal-doped zeolite catalysts have been reported to be a strong candidate for selective catalytic reduction (SCR) of NO_X in presence of different reducing agents. Several researchers have reported high NO_X conversion by hydrocarbons such as ethylene and propylene in a net-oxidizing atmosphere over metal-exchanged ZSM-5 catalyst (Table 1). A recent comprehensive review (Bhattacharyya and Das, 1999) exhaustively summarizes the studies that have been reported in this area.

Presence of reducing agents like HC, CO, ammonia, urea etc. in the exhaust gas feed increases the selectivity of NO_X reduction over zeolite catalysts. Held et al. (1990) have reported detailed results of selective NO_X reduction over different zeolites in presence of HC, NH_3, and urea. At present it appears more economical to look for a catalyst to reduce NO_X by a reducing agent like CO and/or HC which are already present in auto engine exhausts. Iwamoto and Mizuno (1993) observed that presence of hydrocarbons like C_2H_4, C_3H_6, C_3H_8, and CO enhanced the performance of Cu-ZSM-5 catalyst even in presence of oxygen in the exhaust feed.

The present work was undertaken with a view to study the potentiality of copper-exchanged X-zeolites for reduction of NO_X in an actual SI engine exhaust and to develop a mathematical model for predicting the performance of a packed bed catalytic reactor containing this catalyst. Although X-zeolite is characterized by similar properties as Y-zeolite, very little work have been reported on application of X-zeolite in automotive emission control.

Experimental Study

Zeolites are crystalline, hydrated aluminosilicates of group I and group II element, as formed in nature or in synthesized form. Zeolites are formed of AlO_4 and SiO_4 tetrahedra, bonded together via the oxygen atoms and assembled in such a way as to constitute cavities, cages and channels, uniformly penetrating the entire lattice volume and thus generating a high internal surface area available for adsorption and catalytic processes (Breck, 1974). The properties of zeolites or molecular sieves which make them particularly suitable for use as catalysts are their large surface area, well defined and uniform pore structure, well defined crystal structure, temperature stability, easy ion-exchange method and reproducibility in various forms.

The copper-exchanged X-zeolite (Cu-X) has been developed by ion-exchanging of 13X zeolites in pelleted form (3.0 mm average diameter) with cupric chloride ($CuCl_2$, $2H_2O$). When the molecular sieves are slurried with distilled water, the pH rises to between 10 and 11, which is sufficient to precipitate the hydroxides of many transition metals. Thus, to avoid producing a catalyst with a supported oxide component, it is necessary to reduce the pH before attempting ion-exchange, but not to a value less than 5, where the removal of aluminum from the sieve itself would lead to collapse of the structure. The transition metal salts were dissolved in distilled water and added to the zeolite slurry and the pH value was maintained at ~6 by adding HCl. The mixture was continuously stirred at warm temperatures. When the supernatant liquid became colorless, indicating complete ion-exchange, the zeolites were filtered and washed with distilled water. Finally, the solid was oven dried in air and then activated by heating for several hours. The degree of ion-exchange of the catalyst, calculated assuming that all the metal ions used were completely exchanged, is 49.6

[1] Currently with Department of Mechanical Engineering, University of Canterbury, Christchurch, New Zealand; souvik@mech.canterbury.ac.nz

Contributed by the Internal Combustion Engine Division (ICE) of The American Society of Mechanical Engineers for publication in the ASME Journal of Engineering for Gas Turbines and Power.

Manuscript received by the ICE February 18, 1997; final revision received by the ASME Headquarters October 7, 1999. Associate Technical Editor: D. Assanis.

Table 1 Selective reduction of NO over metal-exchanged zeolite catalysts

Catalyst	NO Reduction achieved	Reference
Cu-MFI-143	> 95%	Iwamoto et al., 1991
Cu-ZSM-5	90%	
Cu-ZSM-5 -12-140	97% & 80% without & with O_2 72% with O_2 & 2% H_2O	Li and Hall, 1991
Cu-ZSM-5	30 – 40% on vehicle test	Monroe et al., 1993
Cu-ZSM-5	40% in CI engine exhaust at 250°C 26% with 1.4% water 18% with 7% water in exhaust	Konno et al., 1992
Cu-ZSM-5	35% with 800 ppm C_3H_6 & 7% O_2 60% with 1200 ppm C_2H_4 & 7% O_2	Cho, 1993
Cu-ZSM-5 Ce-ZSM-5 Ce-ZSM-5	20.5% with 166 ppm C_3H_6 at 523 K 32% with 166 ppm C_3H_6 at 623 K 59% with 1000 ppm C_3H_6 at 673 K	Misono and Kondo, 1991
Cu-ZSM-5	52% with 800 ppm C_2H_4 at < 473 K	Heimrich and Deviney, 1993

percent for Cu-X catalyst. The crystallinity of the zeolites remains fairly unaffected by the various treatments that they have to undergo for metal exchange, as is evident from the X-ray diffraction studies of the exchanged catalysts. The test conditions including inlet exhaust gas composition is shown in Table 2.

A commercial 3-cylinder, water-cooled, 4-stroke, 800 cc spark ignition engine test rig (Fig. 1), coupled to a hydraulic dynamometer, was employed for studying the performance of the catalysts. The catalyst bed was attached to the exhaust manifold of the stationary engine with the provision for heating and regulating the exhaust gas flow rate through the catalyst bed. A mild steel tube, 5 cm in diameter and 60 cm long, was used for housing the catalyst. As the catalyst bed was kept at a distance of about 1 m from the engine exhaust manifold, it was sometimes difficult to get the higher temperatures, particularly during lower flow rates of gas. To overcome this problem, a heating element was employed to heat the exhaust gas, when required, within the first 30 cm length of the tube, before it entered the catalyst bed. NO_x concentrations upstream and downstream of the catalyst bed are measured on-line by an electro-chemical type gas analyzer. The catalyst has been investigated for a wide range of engine A/F ratio, space velocity (SV) and temperature of exhaust gas. Detailed description of the test rig has been reported in Das et al. (1997).

Model Development

A mathematical model has been developed from fundamental heat and mass transfer considerations to predict the composition of exhaust gas at the outlet of a cylindrical packed bed reactor with radius R and length L. The exhaust gas is composed of different

Table 2 Catalyst test conditions

Gas composition	
O_2	1% – 10%
CO	0.2% – 1%
CO_2	13%
H_2O	0% – 10%
NO	500 – 2000 ppm
HC	500 – 3000 ppm
N_2	Balance
Space Velocity	10,000 /h – 50,000 /h
Temperature	150°C – 400°C
Engine Speed	2,000 – 3,000 rpm
Air/Fuel Ratio	14.0 – 16.5
Engine Load	Idle to Maximum

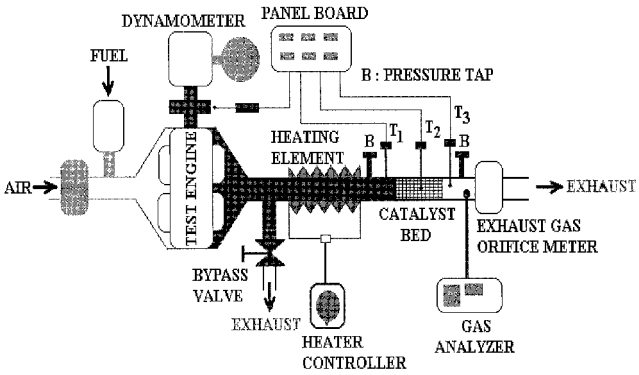

Fig. 1 Experimental test set-up

gas species and concentrations of each of these species as well as temperature and flow rate of the gas mixture upstream of the reactor are inputs to the model which, in turn, predicts the concentrations and percentage conversion of each of the gases downstream of the reactor bed.

The conversion performance and thermal responses of a catalytic converter are coupled. The rates of chemical reactions in converters are highly nonlinear functions of temperature. Conversely, heat released during reactions contributes to the thermal response. This coupling implies that a realistic converter model must solve chemical and thermal problems simultaneously. Complex physical/chemical phenomena occurring in a converter include the heat and mass transfer between the exhaust gas and catalyst surface, convective heat and mass transport, chemical reactions and the attendant heat release, heat conduction to the solid and heat loss to the surroundings.

The present model is a two-dimensional heterogeneous model which considers radial and axial variation of temperature and concentration of each species in the bulk gas phase and those inside or at the surface of the solid catalyst. Thus there are two sets of equations: one for the bulk gas phase and another for the solid phase. The model also considers intraparticle gradients of temperature and concentrations by making use of the effectiveness factor, η, which is defined as the ratio of the actual rate of reaction to that in the absence of the diffusional limitations, that is, when the surface conditions prevail throughout the particle. Thus,

$$\eta = \frac{\text{Actual reaction rate at conditions inside the particle}}{\text{Reaction rate at surface conditions}}$$

$$= \frac{R_i(C,\ T)}{R_i(C_s,\ T_s)}$$

Governing Equations

A particular species i in a mixture of gas is considered to be consumed by chemical reaction in a cylindrical reactor of radial co-ordinate r and axial co-ordinate z. Neglecting axial dispersion effect and radial velocity of gas, the steady-state gas and solid phase mass conservation equation of the species and the energy conservation equation for the fully developed gas mixture in a packed bed with void fraction ϵ, can be written as follows (Wasch and Froment, 1971).

Gas Phase.

$$\epsilon \mathcal{D}_{er,i}\left(\frac{\partial^2 C_{g,i}}{\partial r^2} + \frac{1}{r}\frac{\partial C_{g,i}}{\partial r}\right) - U_s \frac{\partial C_{g,i}}{\partial z} = k_{g,i} a_v (C_{g,i} - C_{s,i});$$

$$i = 1,\ 2,\ 3,\ \ldots,\ 9 \quad (1)$$

$$\lambda_{er}^{g}\left(\frac{\partial^2 T_g}{\partial r^2} + \frac{1}{r}\frac{\partial T_g}{\partial r}\right) - \rho_g C_{p_g} U_s \frac{\partial T_g}{\partial z} = h_g a_v (T_g - T_s) \quad (2)$$

Solid Phase.

$$k_{g,i}a_v(C_{g,i} - C_{s,i}) = \eta_i R_i \rho_b; \quad i = 1, 2, 3, \ldots, 9 \qquad (3)$$

$$\lambda^s_{er}\left(\frac{\partial^2 T_s}{\partial r^2} + \frac{1}{r}\frac{\partial T_g}{\partial r}\right) + \rho_b \sum_{i=1}^{n} [(-\Delta H)_i \eta_i R_i] = h_g a_v (T_s - T_g) \qquad (4)$$

In the above equations, subscripts g and s are used to differentiate between solid and gas phases and the subscript i represents a specific species in the exhaust gas which is considered to be a mixture of nine different species with i = 1:CO, 2:NO, 3:H_2, 4:C_3H_6, 5:CH_4, 6:O_2, 7:CO_2, 8:H_2O, and 9:N_2. $\mathcal{D}_{er,i}$ is the effective radial diffusivity of the ith species of gas, λ^g_{er} and λ^s_{er} are effective radial conductivities of gas and solid, respectively, k_g and h_g are gas-to-solid mass and heat transfer coefficients, a_v is the total external surface area of catalyst per unit catalyst volume, U_s is the superficial flow velocity which actually is the velocity through the empty bed, ρ_g and C_{pg} are density and specific heat at constant pressure of gas, respectively. In the solid phase, ρ_b is the bulk density of the catalyst bed, R_i is the rate of the reaction involving the ith species and η_i and $(-\Delta H)_i$ are the corresponding effectiveness factor and heat of reaction, respectively.

Boundary Conditions

At $z = 0$ and $0 \le r \le R$:

$$C_{g,i} = C_{0,i}, \quad T_g = T_0.$$

At $r = 0$ and $0 \le z \le L$:

$$\frac{\partial C_g}{\partial r} = 0, \quad \frac{\partial T_g}{\partial r} = \frac{\partial T_s}{\partial r} = 0.$$

At $r = R$ and $0 \le z \le L$:

$$\frac{\partial C_g}{\partial r} = 0, \quad -\lambda^g_{er}\frac{\partial T_g}{\partial r} = \alpha^g_w (T_g - T_w),$$

and

$$-\lambda^s_{er}\frac{\partial T_s}{\partial r} = \alpha^s_w (T_s - T_w).$$

At the catalyst bed inlet, concentration and temperature of the gas are given by the inlet conditions, $C_{0,i}$ and T_0, and at the axis of the cylindrical reactor, mass transfer in gas and heat transfer in gas and solid are zero because of symmetry. At the cylinder wall, mass transfer is again zero and total heat transfer to the wall is logically split to consider heat transfers from gas and solid phases separately.

Determination of Model Parameters

Instead of considering one lumped effective conductivity as done in two-dimensional pseudohomogeneous model (Yagi and Kunii, 1957), the radial effective conductivity for the gas phase, λ^g_{er}, and that for the solid phase, λ^s_{er} is distinguished and consequently the following expressions may be derived for λ^g_{er} and λ^s_{er}:

$$\lambda^g_{er} = \epsilon(\lambda_g + \beta d_p h_{rv} + \rho_g C_{p_g} \mathcal{D}_{er}) \quad \text{and}$$

$$\lambda^s_{er} = \frac{\beta(1-\epsilon)}{\dfrac{\gamma}{\lambda_s} + \dfrac{1}{\lambda_g/\phi + h_p d_p + h_{rs} d_p}},$$

where λ_g and λ_s are thermal conductivities of gas and solid, respectively.

The theoretical expression for the effectiveness factor, η, can be written as (Satterfield, 1970)

$$\eta = \frac{3\phi'\coth(3\phi') - 1}{3\phi'^2} \quad \text{where,} \quad \phi' = \frac{V_p}{S_p}\sqrt{\frac{k\rho_s}{\mathcal{D}_e}},$$

where ϕ' is the modified Thiele modulus. The effective diffusivity inside catalyst, $\mathcal{D}_e$, can be computed by means of Bosanquet relation, as

$$\mathcal{D}_e = \left(\frac{1}{\mathcal{D}_{K_{\text{eff}}}} + \frac{1}{\mathcal{D}_{M_{\text{eff}}}}\right)^{-1}.$$

Effective radial diffusivity, $\mathcal{D}_{er}$, is obtained from the correlation of Fahien and Smith (1955) given by

$$\text{Pe}_{mr} = \frac{d_p U_s}{\mathcal{D}_{er}} = 10\left[1 + 19.4\left(\frac{d_p}{d_t}\right)^2\right] \quad \text{for} \quad \text{Re} > 10.$$

Empirical correlations (Bird et al., 1994) have been employed to calculate gas-to-solid heat and mass transfer coefficients, h_g and k_g:

$$J_H = J_D = 0.91\ \text{Re}^{-0.51}\psi \quad \text{for} \quad \text{Re} < 50$$

$$= 0.61\ \text{Re}^{-0.41}\psi \quad \text{for} \quad \text{Re} > 50,$$

where J_H and J_D are Colburn factors for heat and mass transfer respectively, from which h_g and k_g can be obtained.

The gas-to-wall heat transfer coefficient, α^g_w, is correlated by Dixon and Cresswell (1979) as follows:

$$\text{Nu}^g_w = \frac{\alpha^g_w d_p}{\lambda_g} = 0.6\ \text{Pr}^{1/3}\ \text{Re}^{1/2} \quad \text{for} \quad \text{Re} < 40$$

$$= 0.2\ \text{Pr}^{1/3}\ \text{Re}^{0.8} \quad \text{for} \quad 40 < \text{Re} < 2000.$$

After determining α^g_w, the solid-to-wall heat transfer coefficient, α^s_w, can be calculated from the following relation:

$$\alpha^s_w = \frac{\lambda^s_{er}}{\lambda^g_{er}}\alpha^g_w.$$

Kinetics and coverage of (NO + CO) reactions are accurately fit by a modified Langmuir-Hinshelwood model which assumes that the major reaction steps are rate limited by NO decomposition followed by CO scavenging of the resulting adsorbed oxygen. The overall reaction

$$\text{NO} + \text{CO} \rightarrow \text{N}_2 + \text{CO}_2$$

has been reported to follow the reaction mechanism given by

$$\text{CO}(g) \rightleftharpoons \text{CO}(s)$$

$$\text{NO}(g) \rightleftharpoons \text{NO}(s)$$

$$\text{NO}(s) \rightarrow \tfrac{1}{2}\text{N}_2(s) + \tfrac{1}{2}\text{O}_2(s)$$

$$\text{CO}(s) + \tfrac{1}{2}\text{O}_2(s) \rightarrow \text{CO}_2(g)$$

$$\tfrac{1}{2}\text{N}_2(s) + \tfrac{1}{2}\text{N}_2(s) \rightarrow \text{N}_2(g).$$

Rate of different reactions considered in this model are obtained in the Langmuir-Hinshelwood form given by

$$R_i = \frac{C_{s,i}k_i}{G_i},$$

where k_i is the specific reaction rate and G_i is a factor representing the inhibition of reactions because of adsorption and depends on temperature and adsorption equilibrium constants of different species on the catalyst surface. Noting that both specific reaction rate, k_i, and adsorption equilibrium constant, K_i, can be represented in the Arrhenius form, G_i can be written as

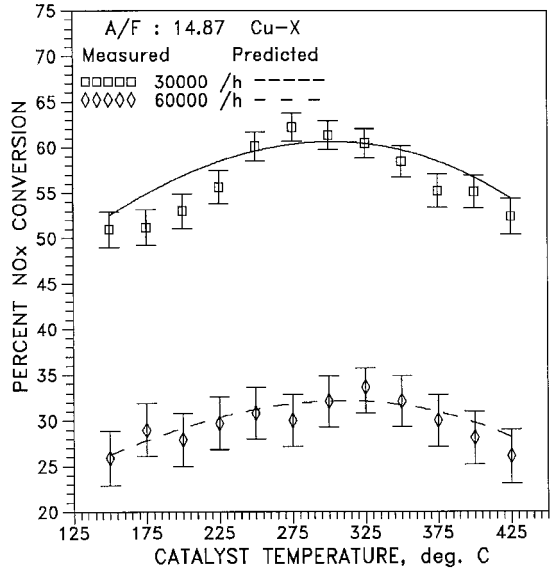

Fig. 2 Comparison of experimental and predicted NOx conversion efficiency for varying temperature and surface velocity at A/F of 14.87

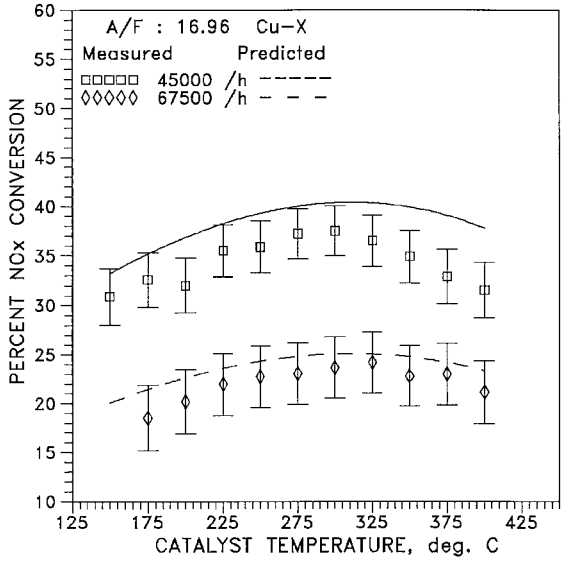

Fig. 3 Comparison of experimental and predicted NOx conversion efficiency for varying temperature and surface velocity at A/F of 16.96

$$G_i = G_i'/k_i$$

$$\Rightarrow R_i = C_{s,i}/G_i,$$

where

$$G_i = T_s\left[A_i \exp\left(\frac{B_i}{T_s}\right) + C_i \exp\left(\frac{-D_i}{T_s}\right)\right],$$

where A_i, B_i, C_i, and D_i are constants for different species of gas on the solid surface and depends on the catalyst being used.

Method of Solution

This set of coupled, nonlinear, two-dimensional, parabolic partial differential equations have been solved by an implicit, finite difference method. Solution of these equations provides the gas temperature and concentration of each gas species at any location of the reactor. Thus, the temperature and composition of the exhaust gas at the outlet of the reactor bed, and, hence, the conversion efficiency of the pollutants can be predicted. In this context, NO_X conversion or reduction efficiency is defined as

$$\text{Conversion Efficiency (CoE)} = \left[1 - \frac{\text{Outlet concentration}}{\text{Inlet concentration}}\right].$$

Qualitatively, the task of solving the problem numerically consists of starting from the initial condition at $z = 0$, and marching the solution along the z-direction. Since gas phase and solid phase equations are coupled, solution of gas phase equation involves solid temperature and concentrations and vice versa. Thus it is required to solve the gas and solid phase equations simultaneously. Additionally, mass conservation equations for different species of gas are to be solved separately.

Results and Discussions

In case of heterogeneous catalysis, increase in temperature has two opposing effects on the reaction velocity which increases due to increase in specific reaction rate and decreases due to partial destruction of the catalyst by coagulation of catalyst surface. Thus, there must be an optimum temperature at which the efficiency of the catalyst is maximum. In conformation to this theory, NO_X conversion efficiency exhibit peaks at a particular temperature depending on the testing conditions.

It is noteworthy that CoEs do not reach the peaks sharply, rather CoEs close to the peak values are maintained through a certain range around the temperature for peak efficiency. These temperature for peak CoE of NO_X is observed to increase with rise in SV. At an A/F ratio of 14.87, NO_X CoE peaks at 275°C when SV is 30000/h, but when SV is changed to 60000/h, the same occurs at 325°C (Fig. 2).

From Figures 2 and 3, it also appears that the NO_X CoE curves become flatter with increase in SV, i.e., the rate of change of CoE with temperature decreases making NO_X conversion less temperature dependent. At an A/F ratio of 14.87 and a SV of 30000/h (Fig. 2), NO_X CoE reaches the peak at an average rate of change of 0.09 percent per degree temperature change; whereas at a SV of 60000/h, this rate is observed to be 0.044.

As certain amount of uncertainty is inherent in each measurement, it is required to specify the precise degree of accuracy with which the variables are measured (Holman, 1971). The uncertainty in the calculated result is estimated on the basis of the uncertainties in primary measurements.

The uncertainties involved in the experimental results and the corresponding results predicted by the mathematical model are also shown in the figures. It is seen that for higher measured CoEs, the corresponding uncertainties are relatively less. At an A/F ratio of 14.87 and SV of 30000/h, average uncertainty is ± 3 percent in measured NO_X CoE, while at an A/F ratio of 16.96 and SV of 67500/h the same is ± 5.5 percent.

It can be seen from the figures that the model overpredicts the NO_X CoEs during low temperature range 150–250°C and again during high temperature range 325–400°C, but slightly underpredicts for temperatures around 300°C. absolute average deviation of CoE is found to be less than 5 percent, where, deviation of CoE is defined as

$$\text{Deviation, } \Delta\eta(\%) = \left[1 - \frac{\text{Experimental CoE}}{\text{Predicted CoE}}\right] \times 100.$$

Effect of Space Velocity

Space velocity (SV), defined as the gas flow rate per unit reactor volume, is actually the inverse of residence time of gases on the catalyst bed. Thus increase in SV reduces the residence time of gases on the catalyst bed; hence, less time is available for the reaction among the gas molecules to occur, causing lower conversion of the gases. Again, very low SV for an existing engine,

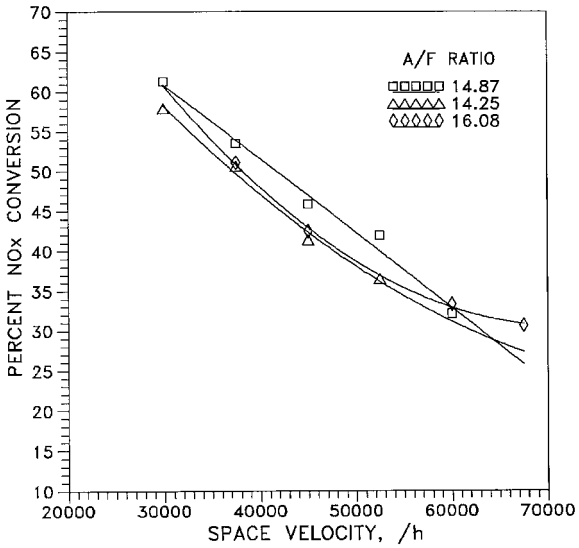

Fig. 4 Effect of space velocity on NOx conversion efficiency at various A/F values

requires large volume of catalyst bed which not only increases the cost of the catalytic converter but also causes greater pressure drop across the bed resulting in degradation of engine performance. Hence, it is required to find an optimum SV considering the catalyst and engine economy and also NO_X reduction performance of the catalysts. Effect of SV on the NO_X reduction over Cu-X catalyst is shown in Fig. 4. The figures have been plotted at a temperature of 300°C and for three different A/F ratios: 14.87, 14.25 and 16.08. For all three A/F ratios, the fall of NO_X and CO CoEs are almost linear. It can be seen that although for the first two A/F ratios, there are similar changes in CoEs, for A/F ratio of 16.08, CoEs fall at a slower rate.

Effect of A/F Ratio

The Cu-exchanged X-zeolite catalyst maintain their catalytic activity over a wide range of A/F ratio and have the potentiality to solve the problems of controlling NO_X in a net oxidizing atmosphere. Figure 5 shows effect of A/F ratio on the performance of the catalyst for three different SVs. The general trend of the figures is that NO_X CoE increase with change in A/F ratio from rich to stoichiometric, maintain respective high performance up to certain range of A/F ratio in the lean side and then decrease for leaner mixtures. Peak NO_X and CO CoEs are shown to occur at an A/F ratio of 15.4 and performances close to the peaks are maintained within an A/F ratio range of 14.6–16.4.

Zeolites have been identified as unstable under hydrothermal conditions because of its low Si/Al ratio. However several reported studies on ZSM-5 (Bhattacharyya and Das, 1999) has been found to be satisfactory from applications point of view. In the present study, although each catalyst was tested for more than 30 h, no appreciable change in NO_X reduction efficiency was noticed during this test period. Variation found between the results of tests conducted at different times with identical test conditions were only within 2–5 percent, which may be attributed to the change of atmospheric conditions, humidity, in particular. Although the deactivation and durability of the catalysts cannot be properly evaluated based on this short period testing, the catalysts may be expected to maintain good performance over a long period. Nevertheless, long endurance tests are necessary to evaluate catalyst durability.

Effect on Back Pressure

Under the two-fold requirements of improved automobile performance and stringent allowable tailpipe emissions, not only conversion efficiency but also back pressure or pressure drop across the catalyst bed is an important criterion for catalyst selection. The flow of exhaust gas through the catalyst bed is restricted by the catalyst particles which gives rise a pressure drop across the catalyst bed and this back pressure has negative effect on the engine performance. Day and Socha (1991) have observed the percent power loss per unit back pressure to be insensitive to the particular engine being tested. Percent HP loss per mm of Hg back pressure has been reported by them to be 0.032. Consequently, power losses in this present study are calculated using this data, i.e., 2.353×10^{-3}% HP loss per mm of water back pressure. It has been observed that there is a maximum power loss of only 0.4 percent at a SV of 67500/h when 1.6 mm diameter particles are used and in case of 3.0 mm diameter particles maximum power loss is even less.

Conclusions

A Cu-exchanged X-zeolite catalyst has been developed and its effectiveness in reducing NO_X in an actual SI engine exhaust has been tested. A mathematical model has been developed additionally to predict the performance of the catalyst and the predictions of the model are compared with experimental results. From the study, the following conclusions can be drawn:

1 Depending on the operating conditions, NO_X CoE exhibits peak at a certain temperature which tends to increase during higher SV operation. NO_X CoEs, close to the peak values, are maintained through a certain range around the temperature for peak efficiency.
2 The Cu-X catalyst maintains its catalytic activity over a wide A/F ratio range of 14.6–16.4.
3 NO_X CoE appears to decrease almost linearly with increase in SV. At higher SV, NO_X CoE also becomes less temperature dependent.
4 Results predicted by the mathematical model agree well with the experimental results and absolute average deviation of experimental CoE is found to be less than 5 percent of the predicted CoE.

Notation

a_v = external particle surface area per unit reactor volume, cm^{-1}
C_g = gas phase concentration, moles/cm^3

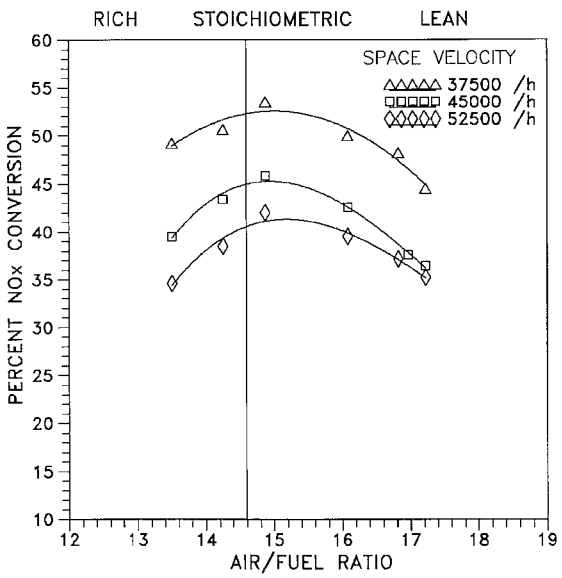

Fig. 5 Effect of A/F on NOx conversion efficiency at various space velocities

C_s = gas concentration on the solid, moles/cm^3
$C_{0,i}$ = concentration of species i in feed, moles/cm^3
C_{pg} = specific at constant pressure of gas, J/gm K
C_s = solid phase concentration on the surface, moles/cm^3
d_p = particle diameter, cm
d_t = internal tube diameter, cm
$\mathcal{D}_e$ = effective diffusivity inside catalyst, cm^2/s
$\mathcal{D}_K$ = Knudsen diffusivity, cm^2/s
$\mathcal{D}_M$ = molecular diffusivity, cm^2/s
$\mathcal{D}_{er}$ = effective diffusivity in radial bed direction based on superficial flow velocity, cm^2/s
G = superficial mass flow velocity, gm/cm^2 s
h_g = gas-to-solid heat transfer coefficient in a fixed bed, W/cm^2 K
h_p = coefficient for heat transfer through the contact surfaces between solid particles, J/cm^2.s.K
h_{rs} = radiation coefficient between particles, W/cm^2 K
h_{rv} = radiation coefficient between voids, W/cm^2 K
k = reaction rate coefficient; for the first order, e.g., cm^3/gm cat s
k_g = gas-to-solid mass transfer coefficient in a fixed bed, cm/s
L = total length of the reactor, cm
l_p = average length between the centres of two neighbouring solids in the direction of heat flow, cm
l_s = average length of solid affected by thermal conductivity, cm
Nu = Nusselt number $[h_g d_t/\lambda_g]$
Pe_{mr} = Péclet number for radial effective diffusion in fixed bed, $[d_p U_s/\mathcal{D}_{er}]$
Pr = Prandtl number, $[C_{pg}\mu_g/\lambda_g]$
r = radial position, cm
R_i = reaction rate of i per unit catalyst weight, mol/gm cat s
R_t = tube radius, cm
Re = Reynolds number, $[d_p G/\mu]$
S_p = surface area of a particle, cm^2
Sh = Sherwood number, $[k_g d_t/\mathcal{D}_m]$
T_g = gas temperature, K
T_0 = feed gas temperature, K
T_s = solid temperature, K
U_s = superficial flow velocity, cm/s
V_p = particle volume, cm^3
z = axial distance in a reactor, cm
α_w^g = wall heat transfer coefficient from the gas phase, W/cm^2 K
α_w^s = wall heat transfer coefficient from the solid phase, W/cm^2 K
$\beta = l_p/d_p$
$(-\Delta H)$ = heat of reaction, J/mol
$\gamma = l_s/d_p$
ϵ = void fraction of bed,
η = catalyst effectiveness factor based on surface conditions,
λ_{er}^g = effective radial conductivity for gas phase, W/cm K
λ_{er}^s = effective radial conductivity for solid phase, W/cm K
λ_g = conductivity of gas, W/cm K
μ = dynamic viscosity, gm/cm s
ρ_b = bulk density of bed, gm cat/cm^3
ρ_g = gas phase density, gm/cm^3
ρ_s = catalyst density, gm cat/cm^3
ϕ = Thiele modulus

Reference

Bhattacharyya, S., and Das, R. K., 1999, "Catalytic Control of Automotive Nox: A Review," *International Journal of Energy Research*, Vol. 23, pp. 351–369.

Bird, R. B., Stewart, W. E., and Lightfoot, E. N., 1994, *Transport Phenomena*, Wiley, Singapore.

Breck, D. W., 1974, *Zeolite Molecular Sieves*, Wiley, New York.

Cho, B. K., 1993, "Nitric Oxide reduction by Hydrocarbons over Cu-ZSM-5 Monolith under Lean Conditions: Steady-State Kinetics," *Journal of Catalysis*, Vol. 142, pp. 418–429.

Das, R. K., Ghosh, B. B., Bhattacharyya, S., and Datta Gupta, M., 1997, "Catalytic Control of SI Engine Emissions over Ion-exchanged X-Zeolites," presented at ASME-ASIA 97, Singapore.

Day, J. P., and Socha, L. S., (Jr.), 1991, "The Design of Automotive Catalyst Supports for Improved Pressure Drop and Conversion Efficiency," SAE Paper 910371, Vol. 100, pp. 105–114.

Dixon, A. G., and Cresswell, D. L., 1979, "Theoretical Prediction of Effective Heat Transfer Parameters in Packed Beds," *AIChE Journal*, Vol. 25, pp. 663–676.

Fahien, R. W., and Smith, J. M., 1955, "Mass Transfer in Packed Beds," *AIChE Journal*, Vol. 1, pp. 25–32.

Heimirch, M. J., and Deviney, M. L., 1993, "Lean NO_X Catalyst Evaluation and Characterization," *SAE Transactions*, 930736, Vol. 102, Sec. 4, pp. 564–573.

Held, W., König, A., Richtel, T., and Puppe, L., 1990, "Catalytic NO_X Reduction in Net oxidizing Exhaust Gas," *SAE Transactions*, 900496, Vol. 99, Sec. 4, pp. 209–216.

Holman, J. P., 1971, *Experimental Methods for Engineers*, Mc-Graw Hill, New York.

Iwamoto, M., Yahiro, H., Tanda, K., Mizuno, M., and Mine, Y., 1991, "Removal of Nitrogen Monoxide Through a Novel Catalytic Process. 1. Decomposition on Excessively Copper Ion-Exchanged ZSM-5 Catalysts," *Journal of Physical Chemistry*, Vol. 95, No. 9, pp. 3727–3730.

Iwamoto, M., and Mizuno, N., 1993, "NO_X Emission Control in Oxygen-Rich Exhaust through Selective Catalytic Reduction by Hydrocarbons," *Proceedings of The Institution of Mechanical Engineers, Journal of Automobile Engineering*, Part D, Vol. 207, pp. 23–33.

König, A., 1993, "A Cooperative Research Project on NO_X Catalysis for Lean Automotive Engines," presented at the Automotive Conference, Brussels.

Konno, M., Chikahisa, T., Murayama, T., and Iwamoto, M., 1992, "Catalytic Reduction of NO_X in Actual Diesel Engine Exhaust," *SAE Transactions*, 920091, Vol. 101, Sec. 4, pp. 11–18.

Li, Y., and Hall, K., 1991, "Catalytic Decomposition of Nitric Oxide over Cu-Zeolites," *Journal of Catalysis*, Vol. 129, pp. 202–215.

Misono, M., and Kondo, K., 1991, "Catalytic Removal of Nitrogen Monoxide over Rare-Earth Ion-Exchanged Zeolites in the Presence of Propene and Oxygen," *Chemistry Letters*, Vol. 6, pp. 1001–1002.

Monroe, D. R., DiMaggio, C. L., Beck, D. D., and Metekunas, F. A., 1993, "Evaluation of a Cu/Zeolite Catalyst to Remove NO_X from Lean Exhaust," *SAE Transactions*, 930737, Vol. 102, Sec. 4, pp. 574–582.

Satterfield, S. N., *Mass Transfer in Heterogeneous Catalysis*, M. I. T. Press, Cambridge.

Taylor, K. C., 1983, "Automotive Catalytic Converters," *Catalysis Science and Technology*, Springer-Verlag, Berlin, Vol. 5, pp. 120–170.

Wasch, A. P., and Froment, G. F., 1971, "A Two-Dimensional Heterogeneous Model for Fixed Bed Catalytic Reactors," *Chemical Engineering Science*, Vol. 26, pp. 629–634.

Yagi, S., and Kunii, D., 1957, "Studies on Effective Thermal Conductivities in Packed Beds," *AIChE Journal*, Vol. 3, pp. 373–381.

Thermal Response of Automotive Hydrocarbon Adsorber Systems

G. C. Koltsakis

A. M. Stamatelos

Mechanical Engineering Department,
Aristotle University Thessaloniki,
540 06 Thessaloniki, Greece

Modern hydrocarbon adsorbers for gasoline engines are promising candidates for cold start emission control. In this paper, the flow and heat transfer in a typical complex system, comprising a "barrel type" adsorber and two conventional catalysts is studied. A mathematical model is developed and applied for the computation of the flow and pressure distribution, as well as transient heat transfer in the system. The model is aimed at understanding and quantifying the particular thermal response behavior of hydrocarbon adsorber systems. Illustrative results with variable geometric parameters under realistic input conditions are presented.

Introduction

Future emission regulations require drastic improvements of the current emission control systems. The conventional catalytic converter used in automobile exhaust is effective only after the catalyst temperature exceeds a characteristic "light-off" temperature, which is usually around 550 K. For this reason, the major portion of the hydrocarbon (HC) emissions occur during the cold start phase. The HC adsorber (trap) is a promising technology to minimize the cold start HC emissions. The key component of such a system is the zeolite based HC adsorber catalyst, which is able to adsorb hydrocarbons at low temperatures ($<$420 K). At higher temperatures the hydrocarbons are desorbed and subsequently oxidized in a downstream placed conventional 3-way catalyst.

A variety of HC trap configurations have been developed and evaluated in the last years (Hochmuth et al., 1993; Abthoff et al., 1998; Noda et al., 1998; Patil et al., 1998; Silver et al., 1998). A basic problem faced by these systems is the undesired hydrocarbons breakthrough during the desorption phase. To avoid this, the downstream 3-way catalyst should be sufficiently warmed up before the HC adsorber exceeds the critical desorption temperature. A number of techniques have been proposed to overcome this problem. Flow management techniques seem to be more efficient compared to complex heat exchanger systems (Hochmuth et al., 1993). The exhaust gas flow through the adsorber should be maximized during the cold start phase. After the adsorber reaches the desorption temperature, the flow should be directed through the downstream catalyst. In the system presented by Buhrmaster et al. (1997), this is achieved by creating a central passage in the adsorber ("barrel type" adsorber) and managing the exhaust flow through the passage using a fluidic air diverter. In the system of Noda et al. (1998), the fluidic air diverter is dispensed of and the diameter of the central passage is experimentally optimized to attain best overall emission performance.

The flow field in conventional catalytic converters has been extensively studied experimentally and numerically, in order to minimize undesired flow maldistributions at converter inlet (Wendland and Matthes, 1986; Lai et al., 1992). The prediction of the flow field and the heat transfer in HC trap systems with "barrel type" adsorbers is more complicated and presents a challenge for the involved engineer. No relevant numerical studies have appeared in the known literature. In the following, a characteristic trap system will be studied numerically, using a mathematical model for the flow and pressure distribution as well as heat transfer. Neglecting the exothermic reactions, which are not significant during cold start, the model will be applied in different realistic operating modes and the results will be discussed.

Problem Definition

Figure 1 shows the arrangement of the hydrocarbon trap system considered in the present study. The system consists of a small volume "start catalyst" followed by the HC adsorber with a central passage and the "main catalyst." The substrates of the catalysts and the adsorber are ceramic honeycomb monoliths with square channels.

In order to specify the test conditions to be examined, the flow rate and temperature levels met in real world operation should be considered. Figure 2 presents the vehicle speed during the first 150 seconds of the standard driving procedure FTP (Federal Test Procedure). The experimentally measured exhaust gas flow rate and temperature at trap inlet for a 2.0 liter gasoline car under these driving conditions are also given in the same figure as functions of time.

For this study, we choose three representative test conditions. The first corresponds to the idle operation point immediately after engine cold start (0–25 s in FTP). The second simulates the step change in inlet conditions in the first acceleration of the driving cycle (40–60 s in FTP). The third operation mode corresponds to real FTP transient conditions regarding inlet flow rate and temperature. The above test modes are tabulated in Table 1.

In the present analysis the start and main-catalyst geometry will not be varied as well as the external dimensions of the HC adsorber. On the other hand, the effect of the adsorber central passage diameter will be studied for selected diameter values. The geometric parameters, which will be used in the simulations, are summarized in Table 2. In the same table, the thermophysical properties of the monoliths are also included.

Before proceeding to the model description and results, it may be necessary to summarize the main design goals of the HC trap system as follows:

- The main catalyst should reach light-off temperature (about 550 K) before desorption from HC trap initiates (around 420 K). Practically, acceptable conversion efficiency is expected, even if only part (e.g., 30 percent) of the main catalyst volume is over 550 K (Mondt, 1987).
- Before the main catalyst lights-off, as much as possible exhaust gas should be passed through the HC adsorber to maximize cold start HC reduction.

Contributed by the Internal Combustion Engine Division (ICE) of THE AMERICAN SOCIETY OF MECHANICAL ENGINEERS for publication in the ASME JOURNAL OF ENGINEERING FOR GAS TURBINES AND POWER.

Manuscript received by the ICE January 17, 1998; final revision received by the ASME Headquarters June 9, 1999. Associate Technical Editor: D. Assanis.

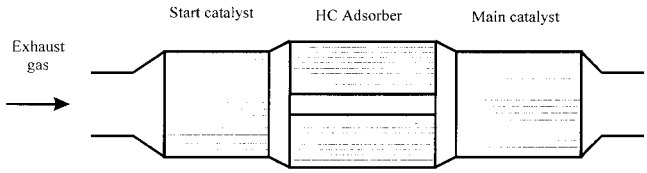

Fig. 1 Arrangement of a typical hydrocarbon adsorber system

Model Description

Flow Distribution. Each monolith is divided in n concentric ring-form sections. We choose that the first section ($i = 1$) of all monoliths, has an outer diameter equal to that of the central passage of the HC adsorber. Thus for every monolith j, the frontal area of the first ring section is

$$A_{1j} = 0.25\pi d_{cp}^2. \tag{1}$$

All other $n - 1$ ring sections of each monolith j are chosen to have equal frontal area

$$A_{ij} = \frac{A_{fr,j}}{n-1}. \tag{2}$$

To estimate the mixing conditions between the flow elements exiting the monoliths from each ring section, we may consider them acting as co-flowing jets. For the conditions of interest, the length of the "initial mixing region" of the jet amounts 10–15 "nozzle" diameters (Blevins, 1984). This is about an order of magnitude higher compared to the length of the air gaps between the monoliths. Therefore, it is reasonable to assume negligible mixing between the flow elements travelling in the small gaps between the monoliths. Thus, for every i, the flow elements through the i section of the start catalyst will pass through the i sections of the adsorber and the main catalyst.

The axial and radial temperature gradients in the monoliths are significant during warm-up. Since pressure drop also depends on the local temperature, we employ a two-dimensional discretization for the flow field calculation. Flow entrance effects will be also taken into account. An iterative procedure is employed consisting of the following steps.

Step 1. Assumption of initial arbitrary values for total back-pressure Δp_{tot} and individual flow rates $\dot{m}_i$. Assuming initially equal values of $\dot{m}_i$ and satisfying the mass balance $\dot{m} = \sum_{i=1}^{n} \dot{m}_i$, we have

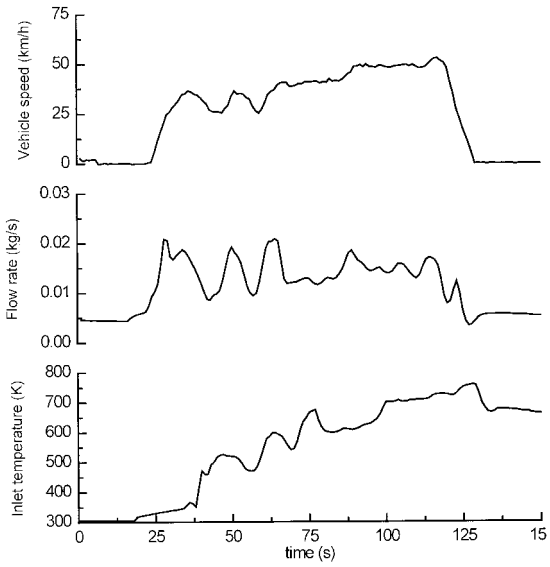

Fig. 2 Typical flow rate and temperature versus time in the standard federal test procedure (FTP)

$$\dot{m}_i = \frac{\dot{m}}{n}, \quad i = 1 \ldots n. \tag{3}$$

Step 2. With the inlet pressure and flow rates given, the pressure field can be computed step-wise along the system for each section with suitable pressure drop relations. For each node (i, k) the pressure drop depends on whether the flow is laminar or turbulent.

For laminar flow, taking into account a correction for the entrance effect (Wendland and Matthes, 1986; Day, 1997) we have

$$\Delta p_{\text{lam},ik} = p_{i,k} - p_{i,k+1} = (1 + 0.06/x^*)^{0.5} \frac{28.5\mu u_{ik}}{d_{h,ik}^2} \Delta x, \tag{4}$$

with

$$u_{ik} = \frac{\dot{m}_i}{\rho A_{ik} \epsilon_{ik}}. \tag{5}$$

For turbulent flow the entrance region is negligibly short and the pressure drop relation is (Incropera and DeWitt, 1996),

$$\Delta p_{ik} = p_{i,k} - p_{i,k+1} = ff \frac{\rho_{ik}}{2} \frac{u_{ik}^2}{d_{h,ik}} \Delta x, \tag{6}$$

Nomenclature

A = surface
3WCC = three-way catalytic converter
c_p = specific heat capacity, J/kg K
d = diameter, m
h = convective heat transfer coefficient, W/m^{2}K
l = length, m
$\dot{m}$ = mass flow rate, kg/s
Nu = Nusselt number, Nu = $(h \cdot d_h/\lambda_g)$
$\dot{q}$ = heat transfer volumetric rate, W/m^3
r = radius, m
S = specific surface area per unit monolith volume, m^{-1}
t = time, s
T = temperature, K
x = axial distance from monolith entrance, m
x^* = dimensionless axial distance, $x^* = (x/d_h \cdot \text{Re} \cdot \text{Pr})$

Greek Letters

ϵ = void fraction
μ = dynamic viscosity, kg/ms
ν = kinematic viscosity, m^2/s
ρ = density, kg/m^3
ζ = empirical factor for diffuser pressure loss
λ = thermal conductivity, W/mK
ξ = dimensionless length, $\xi = (\text{Nu}\lambda_g S_i A_i \epsilon_i / d_{h,i} \dot{m}_i c_{p,g}) x$

Subscripts

cp = central passage
conv = convection
g = exhaust gas
h = hydraulic
i = radial node index
j = monolith index
k = axial node index
m = mass
out = outer
s = solid

Table 1 Exhaust flow rate and temperature at the test conditions studied

	Test Condition	FTP time (appr.)	Flow rate (kg/s)	Exhaust gas temperature (K)
1.	Isothermal (Cold start – Idle)	0-20s	$5\ 10^{-3}$	300
2.	Step response	40-60s	$20\ 10^{-3}$	500
3.	Fully transient	0-150	variable	variable

with

$$u_{ik} = \frac{\dot{m}_i}{\rho_{ik} A_{ik} \epsilon_{ik}} \tag{7}$$

and

$$ff = 0.316 \cdot \mathrm{Re}^{-0.25}. \tag{8}$$

Between the monolith gaps, we assume ideal flow and the pressure variation is due to the flow cross-area difference. From Bernoulli's law,

$$\Delta p_{\mathrm{gap},ij} = \left[\frac{1}{2\rho} \left(\frac{1}{A_{ij}^2} - \frac{1}{A_{i,j+1}^2} \right) \right] \dot{m}_i^2. \tag{9}$$

An additional pressure loss due to flow separation effects in the inlet diffuser is taken into account based on a semi-empirical factor ζ (Waermeatlas, 1988),

$$\Delta p_{i1} = p_{in} - p_{i,1} = \frac{\zeta}{2} \left(1 - \frac{A_{i,0}}{A_{i,1}} \right)^2 \frac{\dot{m}_i^2}{\rho_{i,1} A_{i1}^2}. \tag{10}$$

The velocity profiles in conical converter canisters measured by Will and Bennett (1992) were employed to evaluate ζ as function of the radial distance. For the geometry considered here, the following step function correlates the experimental data of the above reference quite closely: $\zeta = 0$ for $0 \le r \le 20$ mm, $\zeta = -600 + 3 \cdot 10^4 r$ for 20 mm $\le r \le$ 30 mm, and $\zeta = 300$ for 30 mm $\le r \le$ 50 mm.

Based on the pressure drop relations, we can compute stepwise the pressure along the monoliths and thus the pressure at the final axial node for each ring section, $p_{i,k\max}$. The resulting computed pressure loss for each ring section is

$$\Delta p_i = p_{\mathrm{in}} - p_{i,k\max}. \tag{11}$$

Step 3. If the computed pressure losses Δp_i for all ring sections are numerically equal to Δp_{tot} the flow and pressure field has been solved. In the opposite case, the assumed values for total pressure loss and flow rates should be corrected, according to step 4.

Step 4. The following corrections for the flow distribution and total pressure loss are applied:

$$\Delta p'_{\mathrm{tot}} = \frac{\dot{m}}{\sum_{i=1}^{n} \frac{\dot{m}_i}{\Delta p_i}}, \tag{12}$$

$$\dot{m}'_i = \frac{\Delta p'_{\mathrm{tot}}}{\Delta p_i} \dot{m}_i. \tag{13}$$

It may be easily shown that the above equations satisfy the mass balance $\dot{m} = \sum_{i=1}^{n} \dot{m}'_i$.

We then repeat the computation procedure starting from step 2. The iterative algorithm converges quickly. The computed values for total backpressure and individual flow rates are provided as input for the next time step, to minimize the required iterations.

Table 2 Geometrical and thermophysical data of the HC adsorber system used in the present study

Parameter	Start catalyst	HC Adsorber	Main catalyst	Units
Monolith diameter	100	120	100	mm
Monolith length	100	140	120	mm
Channel density	62	46.5	62	channels/cm^2
Substrate wall thickness	0.1	0.3	0.1	mm
Channel hydraulic diameter	1.17	1.17	1.17	mm
Central passage diameter	0	0,20,35	0	mm
Substrate density	1800	1800	1800	kg/m^3
Substrate conductivity	1.5	1.5	1.5	W/m K
Other parameters				**Units**
Gap between monoliths			30	mm
Inlet diffuser length			50	mm
Outlet cone length			40	mm
Inlet pipe diameter			50	mm
Outlet pipe diameter			50	mm

Heat Transfer

In this study, we confine our interest in the warm-up operation of the system during cold start, where CO and hydrocarbon oxidation rates are practically insignificant and the associated exothermy may be neglected. The convective and radiative heat losses to ambient are significant for relatively high surface temperatures (Koltsakis et al., 1997). In thermal response studies of insulated trap systems, they can be also neglected for simplification purposes, without accuracy sacrifices. Therefore, the trap system is considered adiabatic. However, axial and radial temperature gradients inside the monoliths may occur and are taken into account by the model.

The basic heat transfer mode is convection between exhaust gas and solid phase in the channels of the monolithic substrates (Koltsakis, 1997). Although the flow in the exhaust piping of an engine is normally turbulent, the Re numbers in the converter monolith channels are always safely in the laminar region (typical values range from 20 to 300). The Nu number for the laminar flow in the channels approximates the solution of the Graetz-Nusselt problem for constant wall temperature. The methodology employed to deposit the active washcoat in the initially square monolith channels results in a circular channel geometry. For laminar flow in circular channels with the introduction of a correction for entrance effects (Hawthorn, 1974) we have

$$\mathrm{Nu} = 3.66 \left(1 + \frac{0.095}{x^*} \right)^{0.45}. \tag{14}$$

Due to the larger diameter of the central passage of the HC adsorber the flow conditions may well be turbulent. Thus for Re $>$ 2300 the following Nu number correlation is employed (Incroperra and DeWitt, 1996):

$$\mathrm{Nu} = 0.022\ \mathrm{Pr}^{0.5}\ \mathrm{Re}^{0.8}. \tag{15}$$

The two-dimensional axi-symmetric grid described above is used to model the heat transfer. Each radial ring-section contains a large number of internal channels. With a given temperature and velocity distribution at the monolith inlet, representative inlet conditions can be defined for all channels contained in each monolith radial section.

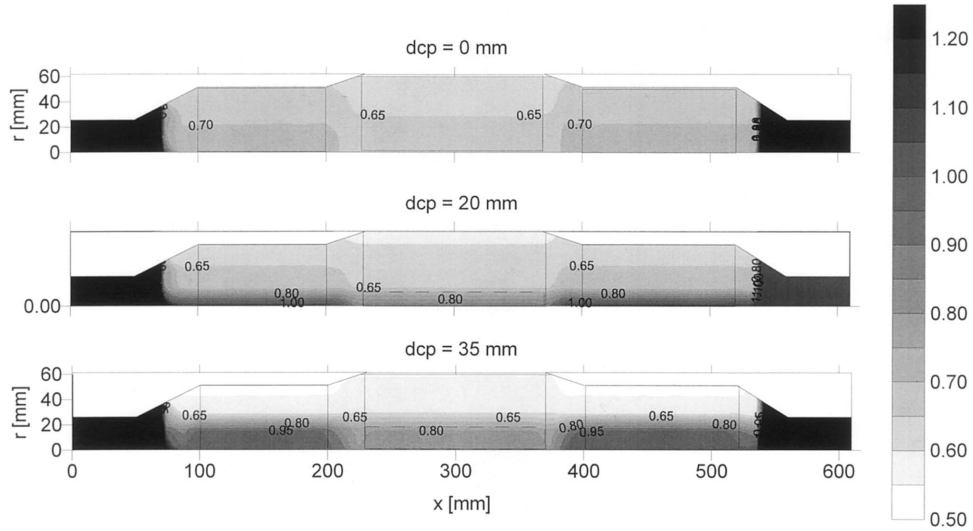

Fig. 3 Isothermal test: computed axial velocity for different central passage diameters (d_{cp} = 0, 20, 35 mm).

The transient thermal response of each monolith is computed as a series of quasi steady-states (Chen et al., 1988; Koltsakis et al., 1998). Thus, the solution procedure followed in each time marching comprises the following steps:

- Computation of the convective heat transfer from the exhaust gas to the monolith surface for each ring section.
- Computation of the two-dimensional transient temperature field in the cylindrical converter, taking into account the heat conduction in the monolith. The contribution of the convective heat transfer in the channels (computed in the previous step) is taken into account by respective source terms.

The first step involves the computation of the gas temperature for each node $(i, k + 1)$ given the conditions in the node (i, k). Employing locally analytical solutions (Mondt, 1987; Koltsakis, 1997), with the dimensionless length ξ defined in the Nomenclature, we obtain

$$T_{g,k+1} = T_{s,k} + (T_{g,k} - T_{s,k})e^{-\Delta\xi}. \tag{16}$$

After the determination of the temperature distribution along the channel, the corresponding convective heat rates on a volume basis may be computed for each space step according to the following balance equation:

$$\dot{q}_{\text{conv},ik} = \frac{\dot{m}_i \cdot c_{p,g}}{A_i \Delta\xi} \cdot (T_{g,ik+1} - T_{g,ik}). \tag{17}$$

In the second computational step, the temperature field in the converter is described by the transient heat equation with heat sources in cylindrical co-ordinates,

$$\rho_s C_{p,s} \frac{\partial T_s}{\partial t} = \lambda_{s,x} \frac{\partial^2 T_s}{\partial x^2} + \lambda_{s,r} \frac{1}{r} \frac{\partial}{\partial r}\left(r \frac{\partial T_s}{\partial r}\right) + \dot{q}_{\text{conv}}. \tag{18}$$

The values of ρ_s, $C_{p,s}$, $\lambda_{s,x}$, and $\lambda_{s,r}$ depend on the respective grid node. For the nodes included in the monoliths, bulk values are computed for the above parameters, according to the respective void fraction. The boundary conditions for the heat conduction equation in the radial direction result from the adiabatic conditions at the outer radius and the symmetry line,

$$\left.\frac{\partial T}{\partial r}\right|_{r=r_{\text{out}}} = 0 \tag{19}$$

and

$$\left.\frac{\partial T}{\partial r}\right|_{r=0} = 0. \tag{20}$$

In the axial direction, heat transfer from the monolith edges is also negligible. The respective boundary conditions for each monolith are

$$\left.\frac{\partial T}{\partial x}\right|_{x=x,\text{first}} = 0 \tag{21}$$

and

$$\left.\frac{\partial T}{\partial r}\right|_{x=x,\text{last}} = 0. \tag{22}$$

The two-dimensional transient temperature field in each monolith is solved using the "alternate direction implicit" (ADI) technique, which offers stability advantages with moderate computation effort.

Results

Isothermal Operation. Figure 3 presents a contour plot of the exhaust gas axial velocity inside the HC trap adsorber system in the steady-state, isothermal test case (Table 1, test condition 1) for different values of the adsorber central passage diameter (d_{cp}). In the case with no central passage (first plot), the radial velocity variations are due to the inlet diffuser effects, which typically produce a parabolic velocity profile at the catalyst front face. The lower velocities in the adsorber monolith are due to the higher frontal face and its higher porosity (lower cell density).

The presence of a central passage in the adsorber monolith reduces the flow resistance and concentrates the flow in the core region. Local values of the axial velocity in the core region are about 40 percent higher than those in the channels at the periphery. As expected, this effect is more pronounced for the smaller passage.

For engineering purposes, it is useful to know the flow rate through the central passage relative to the total flow rate. This is actually presented in Fig. 4 for different values of the central passage diameter as function of the exhaust gas flow rate. For a 45 mm diameter the flow rate percentage may reach 30 percent, which is double the value expected for a radially uniform flow distribu-

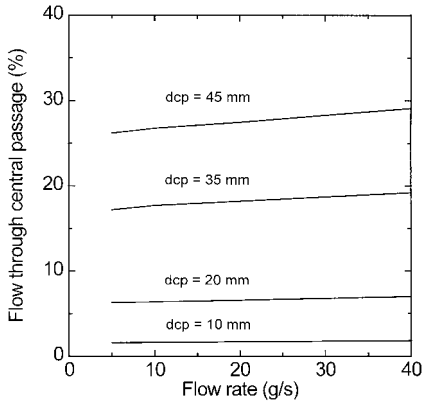

Fig. 4 Isothermal test: relative flow through central passage for different flow rates; (T = 300 K).

tion. In general, the dependence of this percentage on flow rate is only minor for the value range met in real-world applications.

Step Temperature Change. Figure 5 presents the computed temperature fields in the system with 20 mm adsorber passage, at selected times of the step response test (Table 1, test condition 2). At 10 s only a small portion of the adsorber has actually sensed the step temperature change at inlet. For the first 30 s, the enthalpy of the exhaust gas flowing through the adsorber channels is almost entirely consumed to warm-up the adsorber. On the other hand, the exhaust gas flowing through the adsorber passage retains much of its enthalpy to warm-up a significant portion of the main converter core, even at time = 10 s. The radial conduction in the main converter is not sufficient to transfer the heat to the periphery, which continuously experiences convective heat transfer from cooler gas arriving from the adsorber channels.

The effect of the adsorber passage on the thermal response is illustrated in Fig. 6, which presents the temperature fields for the three systems tested at time = 40 s. With no adsorber passage, the main converter is practically under 350 K, whereas the adsorber has already reached desorption temperatures (<420 K). In the systems with adsorber passages, the adsorber has also reached desorption temperatures, although somewhat lower than in the no-passage system. However, the core regions of the main converters are already sufficiently warmed-up. Since radial thermal conduction is quite slow, the main converter periphery is not affected from the presence of the adsorber passage significantly.

The evolution of the exhaust gas temperature at the core and the periphery at adsorber exit are presented in Fig. 7 for different values of passage diameters. Exhaust gas temperatures in the monolith channels generally tend to approximate the local temperatures of the solid phase (Chen et al., 1988). Thus, the results can be associated with the contour plots of Fig. 5 and 6 to explain the much faster gas temperature response in the core region, in the presence of an adsorber passage. Interestingly, the response curves for the two different diameters tested are very close. Indeed, as shown in the isothermal case (Fig. 3) the axial gas velocities in the adsorber passages, which mainly control the response times, are less than 10 percent different. The same has been also verified by the model for the step response test. As shown above (Fig. 3), the existence of the adsorber passage results in lower axial gas velocities in the periphery. This explains the somewhat slower exhaust gas temperature rise in the periphery for non-zero adsorber passage diameters.

Driving Cycle Conditions. The results presented so far were intended to provide a basic idea of the main physical phenomena affecting the thermal behavior of complex HC adsorber systems. For system design and optimization purposes it is rational to perform calculations with realistic input conditions corresponding to real engine operation. A basic optimization parameter is the temperature of the exhaust gas entering the main converter, which is directly related with its activation.

Based on the input data presented in Fig. 2 for FTP driving conditions, the computed temperatures at the core and periphery of main catalyst inlet are presented in Fig. 8. With no adsorber passage, the main catalyst will remain inactive even 150 s after engine start-up. On the other hand, the core region of the main catalyst will be subjected to sufficiently high temperatures (>550 K) at least 60 s earlier. In practice, this can be very crucial for the elimination of cold start emissions.

Evaluating systems in terms of HC emissions would require a complete reactor model with a kinetic mechanism to simulate of HC adsorption—desorption as function of the local temperature. However, some first implications can be seen even from the

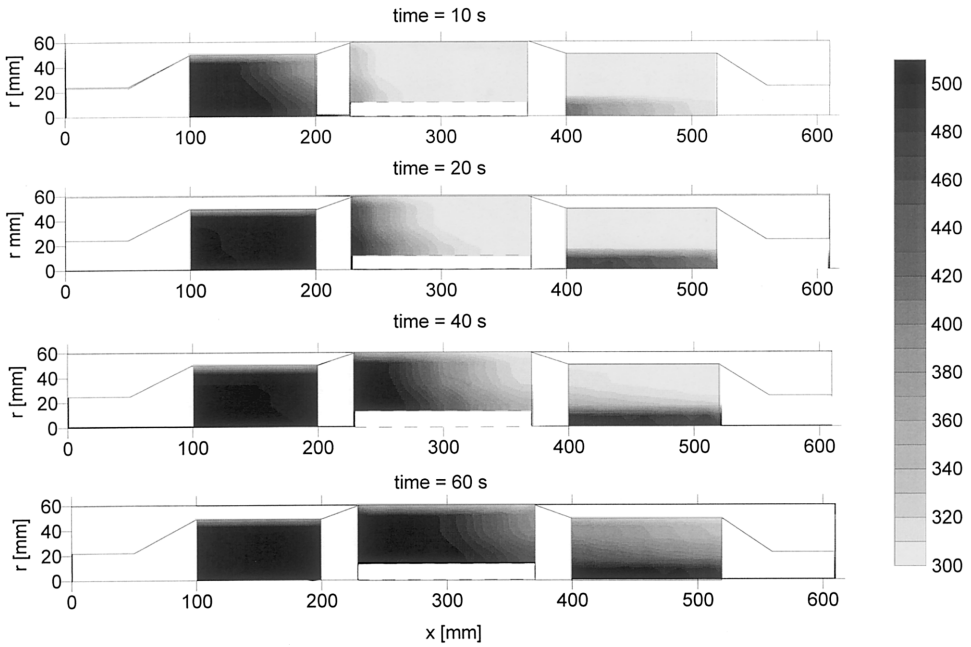

Fig. 5 Step response test: temperature fields at selected times (d_{cp} = 20 mm).

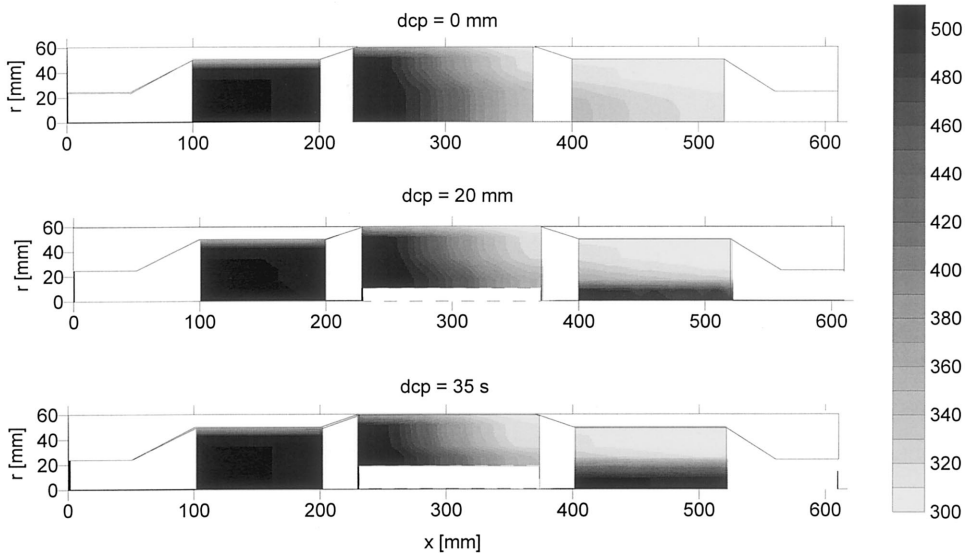

Fig. 6 Step response test: temperature fields at time = 40 s for different central passage diameters (d_{cp} = 0, 20, 35 mm).

present study. For example, it is shown in Fig. 8 that the periphery of the main catalyst is quite cold to achieve oxidation of desorbed hydrocarbons even after 150 s in the driving cycle. Design modifications such as variation of the main catalyst aspect ratio or even flow management techniques could be considered as possible solutions to this potential problem.

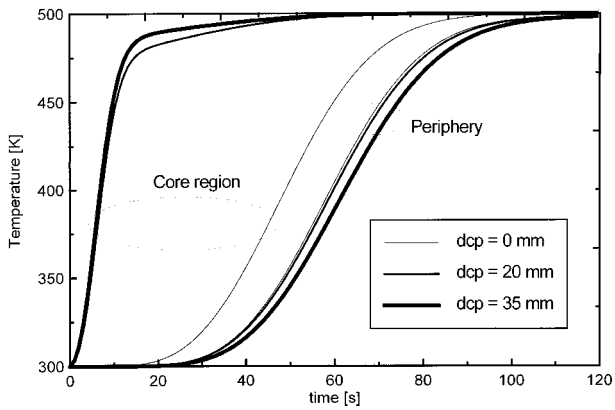

Fig. 7 Step response test: exhaust gas temperature at the HC adsorber exit at two points (d_{cp} = 0, 20, 35 mm).

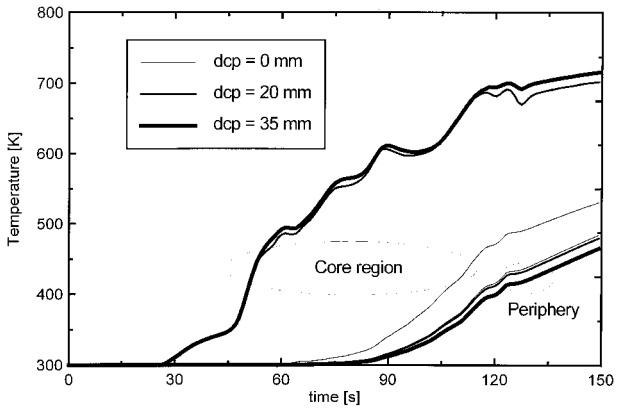

Fig. 8 Driving cycle simulation: computed exhaust gas temperature at main converter inlet at two points (d_{cp} = 0, 20, 35 mm).

Conclusions

Computer aided methods for the design of emission control devices are especially important in the case of complex HC adsorber systems. "Barrel type" adsorbers exhibit a particular thermal response behavior, which is actually very critical for the successful control of HC adsorption, desorption, and oxidation in the main catalyst. Flow and heat transfer effects in a typical three-component system were studied, using an engineering mathematical model. The model was initially applied in simple test cases simulating isothermal operation and step temperature response. The results were useful to identify the critical physical and geometric parameters controlling the system thermal response. The cold start phase of an FTP driving scenario was also simulated, to illustrate model application in realistic cases. It is sensed that the design optimization of such systems for real world applications relies on a large number of individual parameters including geometry of individual monoliths, catalyst properties, additional air management, flow diversions, etc. A more effective computer aided methodology would also involve simulation of the adsorber adsorption–desorption kinetics, which is a subject of work-in-progress.

References

Abthoff, J., Kemmler, R., Klein, H., Matt, M., Robota, H. J., Wolsing, W., Wiehl, J., and Dunne, S. R., 1998, "Application of In-Line Hydrocarbon Adsorber Systems," SAE Paper 980422.

Bella, G., Rocco, V., and Maggiore, M., 1991, "A Study of Inlet Flow Distortion Effects on Automotive Catalytic Converters," ASME JOURNAL OF ENGINEERING FOR GAS TURBINES AND POWER, Vol. 113, pp. 419–426.

Blevins, R. D., 1984, *Applied Fluid Dynamics Handbook*, Van Nostrand Reinhold Company, New York.

Buhrmaster, C. L., Locker, R. J., Patil, M. D., Nagel, J. N., and Socha, L. S., 1997, "Evaluation of In-Line Adsorber Technology," SAE Paper 970267.

Chen, D. K. S., Oh, S. H., Bissett, E. J., Van Ostrom, D. L., 1988, "A Three-Dimensional Model for the Analysis of Transient Thermal and Conversion Characteristics of Monolithic Catalytic Converters," SAE Paper 880282.

Day, J. P., 1997, "Substrate Effects on Light-Off—Part II: Cell Shape Contributions," SAE Paper 971024.

Hawthorn, R. D., 1974, "Afterburner Catalysts—Effects of Heat and Mass Transfer Between Gas and Catalyst Surface," AIChE Symposium Series No. 137, Vol. 70, pp. 428–438.

Hochmuth, J. K., Burk, P. L., Tolentino, C., and Mignano, M. J., 1993, "Hydrocarbon Traps for Controlling Cold Start Emissions," SAE Paper 930739.

Incropera, F. P., DeWitt, D. P., 1996, *Fundamentals of Heat Transfer*, 3rd ed., John Wiley & Sons, New York.

Koltsakis, G. C., Konstantinidis, P. A., and Stamatelos, A. M., 1997, "Development and Application Range of Mathematical Models for 3-Way Catalytic Converters," Applied Catalysis-B: Environmental, 12, pp. 161–191.

Koltsakis, G. C., 1997, "Warm-Up Behavior of Monolithic Reactors Under Non-reacting Conditions," *Chemical Engineering Science*, Vol. 52, No. 17, pp. 2891–2899.

Koltsakis, G. C., Kandylas, I. P., and Stamatelos, A. M., 1998, "Three-Way Catalytic Converter Modeling and Applications," *Chemical Engineering Communications*, Vol. 164, pp. 153–189.

Lai, M. C., Lee, T., Kim, J. Y., Cheng, C. Y., Li, P., and Chui, G., 1992, "Numerical and Experimental Characterizations of Automotive Catalytic Converter Internal Flows," *Journal of Fluids and Structures*, Vol. 6, pp. 451–470.

Mondt, J. R., 1987, "Adapting the Heat and Mass Transfer Analogy to Model Performance of Automotive Catalytic Converters," ASME JOURNAL OF ENGINEERING FOR GAS TURBINES AND POWER, Vol. 109.

Noda, N., Takahashi, A., Shibagaki, Y., and Mizuno, H., 1998, "In-Line Hydrocarbon Adsorber for Cold Start Emissions—Part II," SAE Paper 980423.

Patil, M. D., Peng, L. Y., and Morse, K. E., 1998, "Airless In-Line Adsorber System for Reducing Cold Start HC Emissions," SAE Paper 980419.

Silver, R. G., Dou, D., Kirby, C. W., Richmond, R. P., Balland, J., and Dunne, S., 1997, "A Durable In-Line Hydrocarbon Adsorber for Reduced Cold Start Exhaust Emissions," SAE Paper 972843.

Wendland, D. W., and Matthes, W. R., 1986, "Visualization of Automotive Catalytic Converter Internal Flows," SAE Paper 861554.

Waermeatlas, 1988, VDI-Verlag GmbH, Duesseldorf.

Will, N. S., and Bennett, C. J., 1992, "Flow Maldistributions in Automotive Converter Canisters and Their Effect on Emission Control," SAE Paper 922339.

Modeling the Lubrication, Dynamics, and Effects of Piston Dynamic Tilt of Twin-Land Oil Control Rings in Internal Combustion Engines

T. Tian

V. W. Wong

Sloan Automotive Laboratory,
Massachusetts Institute of Technology,
77 Massachusetts Avenue,
Building 31-166,
Cambridge, MA 021392

A theoretical model was developed to study the lubrication, friction, dynamics, and oil transport of twin-land oil control rings (TLOCR) in internal combustion engines. A mixed lubrication model with consideration of shear-thinning effects of multigrade oils was used to describe the lubrication between the running surfaces of the two lands and the liner. Oil squeezing and asperity contact were both considered for the interaction between the flanks of the TLOCR and the ring groove. Then, the moments and axial forces from TLOCR/liner lubrication and TLOCR/groove interaction were coupled into the dynamic equations of the TLOCR. Furthermore, effects of piston dynamic tilt were considered in a quasi three-dimensional manner so that the behaviors of the TLOCR at different circumferential locations could be studied. As a first step, variation of the third land pressure was neglected. The model predictions were illustrated via an SI engine. One important finding is that around thrust and anti-thrust sides, the difference between the minimum oil film thickness of two lands can be as high as several micrometers due to piston dynamic tilt. As a result, at thrust and anti-thrust sides, significant oil can pass under one land of the TLOCR along the bore, although the other land perfectly seals the bore. Then, the capabilities of the model were further explained by studying the effects of ring tension and torsional resistance on the lubrication and oil transport between the lands and the liner. The effects of oil film thickness on the flanks of the ring groove on the dynamics of the TLOCR were also studied. Friction results show that boundary lubrication contributes significantly to the total friction of the TLOCR.

Introduction

As the oil control ring is the first barrier for the oil supply to the upper regions and it has much higher ring tension than the top two rings, it is arguably the most critical part to the oil consumption and friction from the piston ring-pack in internal combustion engines. Understanding dynamic behavior of oil control rings is a necessary step for quantifying oil transport rate, oil consumption, and friction in the piston ring pack.

Twin-land oil control rings are commonly used in diesel engines and some of the gasoline engines. Nowadays, a TLOCR is implemented with two pieces—a twin-land ring and a spring (Fig. 1). The spring is used to supply high tension for increasing the conformity of the ring to a distorted bore, and small axial height of two lands further gives high unit pressure on the running surfaces to reduce oil film thickness passing the TLOCR. The lubrication between the lands and the liner as well as the interaction between the TLOCR and the groove are the keys for understanding the behavior of the TLOCR for the following reasons. First, oil paths through the TLOCR include (1) the interface of the liner and the running surfaces of the two lands, governed by the lubrication between the lands and the liner, and (2) the groove of the TPOCR, governed by the dynamics of the TLOCR and the gas flow through the groove. Secondly, lubrication between the lands and the liner determine the friction of the TLOCR.

Some theoretical and experimental work has been done to study the lubrication and dynamics of the TLOCR. A theoretical model was developed by Ruddy et al. (1981a, b), where the twist of the TLOCR and the lubrication between the two lands and the liner were coupled. It was found that the constraint from the radial pressure on the two lands controls the twist of the TLOCR. Inversely, twist of the TLOCR, along with running surface profiles, radial height difference of the lands, and surface roughness, has significant effects on the lubrication between the lands and the liner. A similar model was also developed by Sui et al. (1993). Axial dynamics of the TLOCR, interaction between the flanks of the TPOCR and the groove, and effects of piston dynamic tilt were not considered in these modeling studies.

On the other hand, experimental results showed the effects of TLOCR axial motion on oil transport in the TLOCR groove and the dependency of the behavior of the TLOCR on the circumferential locations. Along with other in-cylinder variables, axial positions of the TLOCR and piston tilt were simultaneously measured in a diesel engine by Ariga (1996). Axial lift of the TLOCR indicated that under certain operating conditions, there could be a large amount of oil between the flanks of the TLOCR and the groove, which could significantly increase the oil transport rate through the oil control ring. The measurement also showed a sudden change of the axial positions of the TLOCR at both thrust and anti-thrust sides when piston tilt switches direction. Takiguchi et al. (1998) measured oil film thickness of the piston ring pack and found that the oil film thickness of the two lands behave differently at thrust and anti-thrust sides.

A unique feature of the TLOCR is the constraint of the two lands to each other. Piston dynamic tilt creates a difference in the oil film thickness of two lands with the liner and thus unbalanced

Contributed by the Internal Combustion Engine Division (ICE) of The American Society of Mechanical Engineers for publication in the ASME Journal of Engineering for Gas Turbines and Power.

Manuscript received by the ICE October 22, 1998; final revision received by the ASME Headquarters March 18, 1999. Associate Technical Editor: D. Assanis.

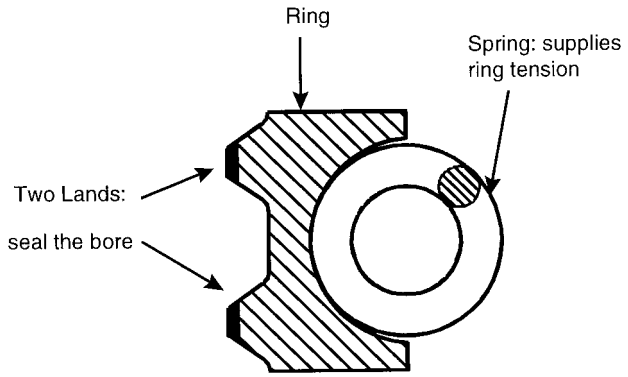

Fig. 1 Twin land oil control ring (TLOCR)

radial forces on two lands. How the TLOCR responds to piston dynamic tilt has significant impact on oil transport through the TLOCR. In this work, dynamics and lubrication of the TLOCR are modeled with consideration of the effects of the piston dynamic tilt. The model incorporates the lubrication between the two lands and the liner, and the interaction between the flanks of the TLOCR and the groove into the dynamic equations of the TLOCR so that oil transport through the interface of the two lands and the liner as well as through the interface of the flanks of the TPOCR and the groove can both be studied. Variation of the third land pressure is currently neglected to avoid involvement with the top two ring analysis.

The model predictions are illustrated via a SI engine in this paper. Oil film thickness, ring lift, ring twist, friction, and the effects of piston tilt at different circumferential locations are explained. Then discussions are primarily focused on the oil film thickness difference between the two lands due to piston dynamic tilt and the implications to oil transport through the TLOCR.

Model Formulation

As shown in Fig. 2, one section of the TLOCR at a particular circumferential location is considered. The piston is chosen as the reference, and the axial and angular dynamics of one section of the TLOCR inside the groove is modeled. Forces and moments from the following sources are considered:

- *Lubrication between two lands and the liner:* it creates friction force and radial pressure distribution on the running surfaces of the two lands.
- *Interaction between the flanks of the TLOCR and the groove:* it includes pressure generated in the oil between the flanks of the TLOCR and the groove due to the motion of the TLOCR and pressure generated from the asperity contact between the TLOCR and the groove.
- *Inertia force due to piston acceleration and deceleration.*

The pressure from the interaction between the flanks of the TLOCR and the groove can be directly calculated according to the position of the TLOCR. However, lubrication condition, film thickness, and all the pressure distributions between the running surfaces of the two lands and the liner have to be solved according to extra conditions. In the following, sub-models on lubrication between the lands and the liner as well as the interaction between the flanks of the TLOCR and the groove will be briefly described. Before doing that, the method to incorporate piston dynamic tilt effects is explained.

Incorporating Piston Dynamic Tilt. Dynamically, the entire TLOCR spends most time sitting on either upper or lower side of the groove during engine operation. Statically, the clearance of the TLOCR in its groove is between 20 μm and 40 μm. Therefore, the maximum possible relative angle between the neutral plane (non-stressed) of the TLOCR and the piston is about 0.02 deg across an 80 mm bore (Fig. 3), which is much less than the magnitude of piston dynamic tilt angle (>0.1 deg). Based on these dynamic and geometrical considerations, the neutral plane of the TLOCR was assumed to follow piston dynamic tilt.

Following this assumption, the relative angle (α) of the neutral axis of a section of the TLOCR to the axis perpendicular to the liner can be expressed as

$$\alpha = -\alpha_{\text{piston}} \cos(\theta), \tag{1}$$

where α_{piston} is the piston tilt angle and θ specifies the location of the section in the circumferential direction ($\theta = 0$ is the anti-thrust side). Throughout this work, relative angle to the liner actually means relative angle to the axis that is perpendicular to the liner.

From geometrical relations, one can see that the relative angle between the neutral axis of the TLOCR and the liner would create a difference in the clearance between the two lands and the liner, and thus unbalanced radial forces on two lands. This difference between two lands is most pronounced at thrust and anti-thrust sides and diminishes at the pin sides. Furthermore, the torsional stiffness of any section of the TLOCR was assumed to be same as that of a complete ring without a gap and is expressed as

$$T_r = \epsilon E b^3 \ln\left(\frac{D_O}{D_I}\right)/3(D_O + D_I), \tag{2}$$

where E is the Young's modulus of the TLOCR, b is the axial width of the TLOCR, D_O and D_I are outer and inner diameters of the TLOCR, respectively, and ϵ is a factor ($0 < \epsilon < 1$). A factor ϵ was used since some parts of the TLOCR are removed compared to a rectangular ring ($\epsilon = 1$).

With all the above assumptions, the present model, which is essentially a two-dimensional model, is able to incorporate piston dynamic tilt, and the dynamic behavior of different sections can be analyzed by specifying the circumferential location of a section in the input.

Interaction Between TLOCR and the Groove. Asperity contact between the flanks of the TLOCR and the groove as well as the squeezing pressure in the oil between the flanks of the TLOCR and the groove were all considered for the interaction between the TLOCR and the groove. Currently, a uniform roughness and oil film thickness are assumed to exist on the flanks of the TLOCR and the groove. However, this assumption can be easily relaxed.

Asperity Contact Between the TLOCR and the Groove. As shown in Fig. 4, a uniform roughness distribution is assumed to

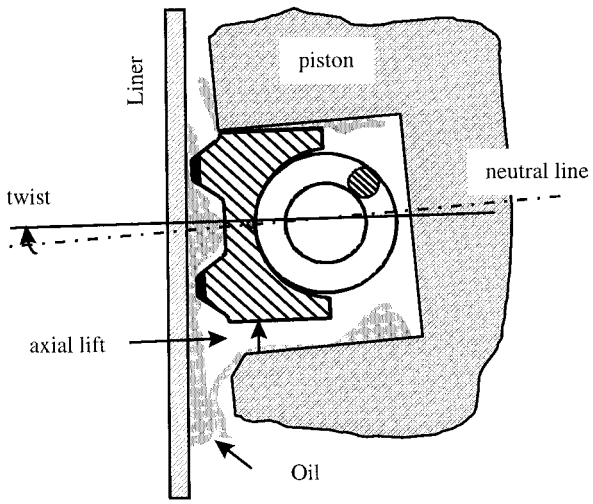

Fig. 2 References and variable definitions for the dynamics of the TLOCR

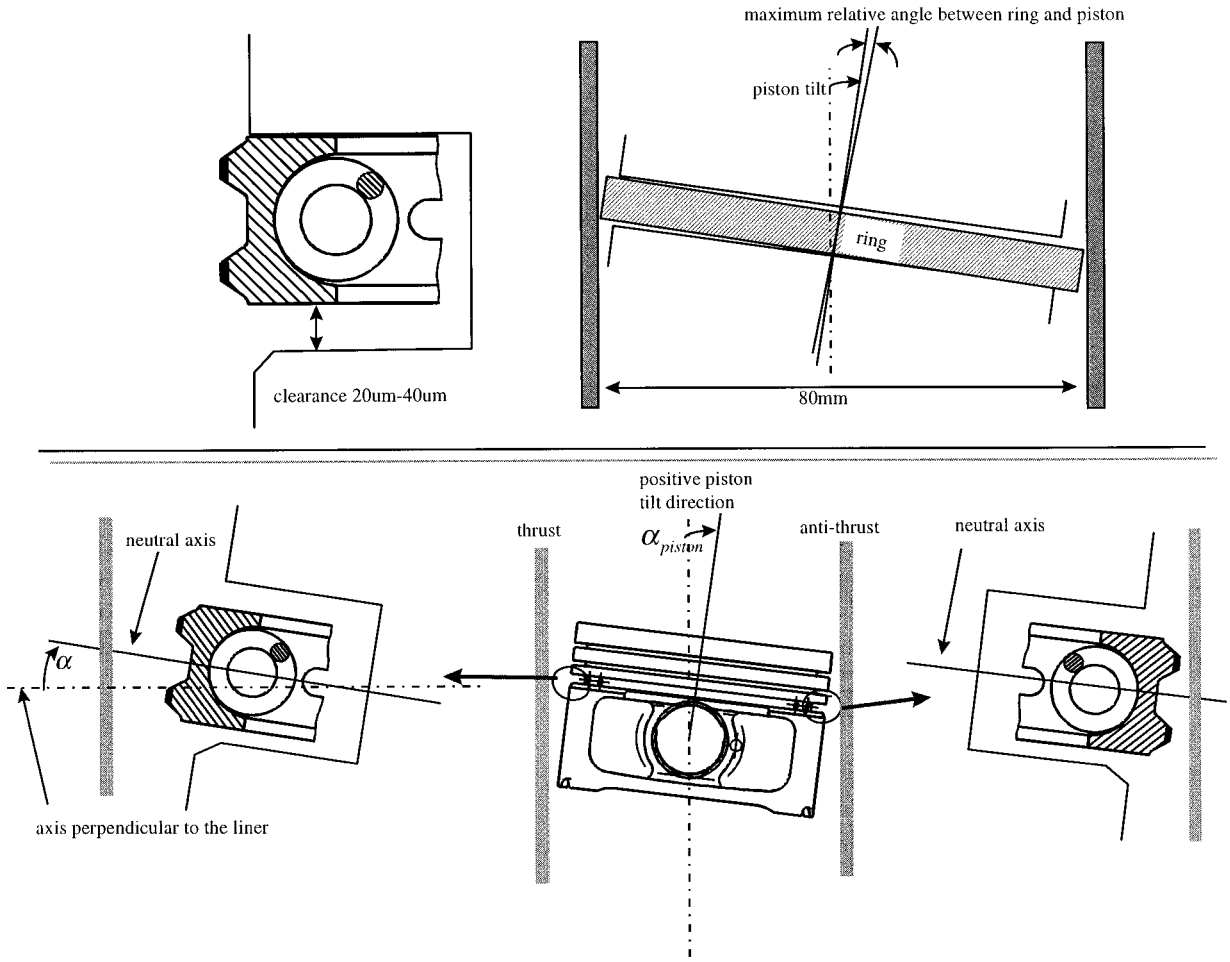

Fig. 3 Assumptions on the position of the TLOCR in a tilted piston

exist on the flanks of the TLOCR and the groove, and asperity contact pressure distribution was modeled by using Greenwood and Tripp's model (Greenwood et al., 1971). With given surface roughness, the contact area and pressure-distribution are calculated according to the axial and twist positions of the TLOCR. In return, the integrated moment and axial force from this asperity contact pressure are incorporated in the dynamic equations of the TLOCR. One can find the detailed description of this sub-model from earlier works by Tian et al. (1998a, 1997a) where this submodel was used for modeling the dynamics of the top two rings.

Oil Squeezing Between the TLOCR and the Groove. Two assumptions were made to model the hydrodynamic pressure in the oil between the TLOCR and the groove.

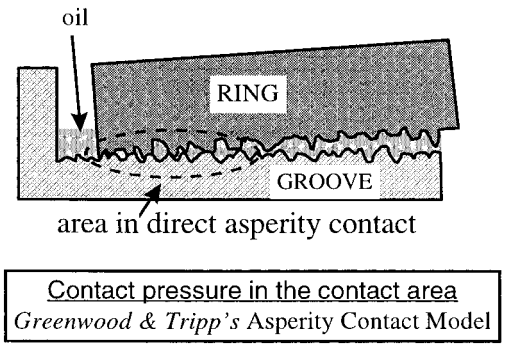

Fig. 4 Asperity contact between the flanks of the TLOCR and the groove

I First, the oil on either the upper or lower side of the groove is assumed to have a uniform thickness. Thus, the pressure generated in the oil is only estimated in the region where the clearance between the flanks of the TLOCR and the groove is less than the specified oil film thickness on the flank of the groove.

II Even in the region where the clearance between the TLOCR and the groove is less than the specified oil film thickness, the pressure in the oil is evaluated differently depending on the moving direction of the TLOCR. As shown in Fig. 4, the second assumption is that the pressure rise in the oil only occurs in the region where the ring is approaching the groove. The hydrodynamic pressure distribution due to squeezing oil in Region II (Fig. 4) is obtained by solving the Reynolds equation. In the region where the ring is moving away from the groove, the oil pressure is assumed to be the same as the gas pressure.

In the second assumption, assuming the pressure in Region I to be the same as the gas pressure (Fig. 5) is based on two considerations. First, in Region I where the TLOCR is moving away from the groove, oil pressure may drop below 1 bar and cavitation occurs. However, even cavitation does occur, the pressure in the cavitation region should be close to the gas pressure in the groove that is assumed to be 1 bar. Secondly, when the TLOCR moves away from the groove, there might not be oil immediately filling the vacuumed region. Therefore, the pressure in Region I should be the gas pressure inside the groove. Thus, in any cases, the pressure in Region I should be close to the gas pressure inside the

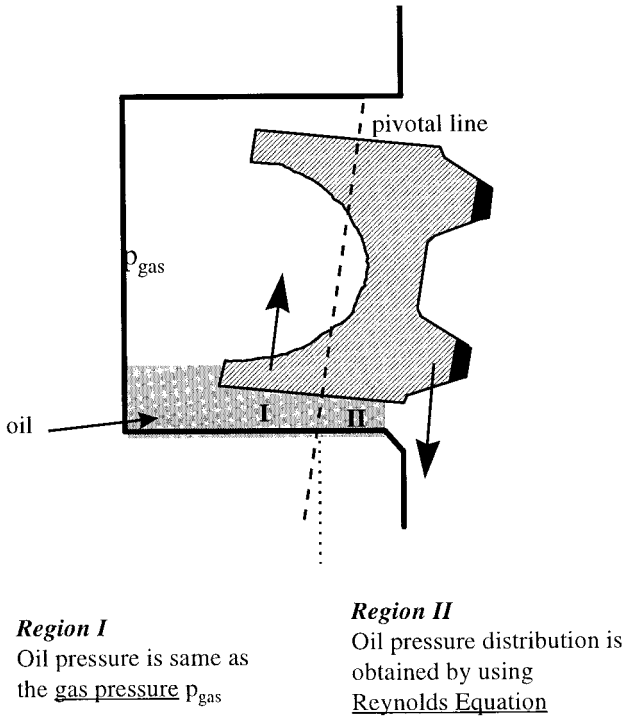

Fig. 5 Pressure in the oil between the flanks of the TLOCR and the groove

groove. One can find the detailed description of this submodel from earlier works by Tian et al. (1998a, 1997a).

In reality, the oil film thickness on the flanks of the groove is neither uniform in the radial direction nor steady from cycle to cycle. Nonetheless, using the current model, one is able to obtain such important oil transport information as the oil flow rates in and out of the TLOCR groove within a cycle due to the dynamics of the TLOCR with given amount of the oil film on the flanks of the groove. In the future, this assumption of a uniform oil film thickness on the flanks of the TLOCR groove can be relaxed after gaining better understanding of oil transport between the TLOCR and the adjacent regions.

Lubrication Between the Lands and the Liner. Lubrication between the two lands and the liner determines not only the oil flow rate, minimum oil film thickness, and asperity contact between the lands and the liner, but also friction and radial pressure distribution that affect the dynamics of the TLOCR. Both hydrodynamic and boundary lubrication were considered for the interaction between the lands and the liner. Using the method developed by Tian et al. (1997a, 1996), the Averaged Reynolds equation of Patir et al. (1978, 1979) was modified to take into account the effects of shear thinning of multi-grade oils. Additionally, dynamic twist of the TLOCR not only changes the land running surface profiles relative to the liner but also introduces an extra squeezing term. These two effects of TLOCR dynamic twist on hydrodynamic lubrication between lands and the liner were taken into account in the present model.

Greenwood and Tripp's asperity model (1971) was used to describe the boundary lubrication between the lands and the liner.

The dynamics of the TLOCR in the radial direction is negligible and force balance in the radial direction was thus applied. It was assumed that there is always sufficient oil supply from the liner to the two lands, i.e., the leading edge was assumed to be always fully flooded, as shown in Fig. 6. Despite assuming sufficient oil supply, hydrodynamic lubrication can still disappear and pure boundary lubrication occurs. Thus, the model considers three different lubrication modes, namely, pure hydrodynamic lubrication, mixed lubrication, and pure boundary lubrication. The existence of these three lubrication modes largely depends on the minimum point on the running surface of the land, defined as the location where the clearance between the land and the liner reaches the minimum (Tian et al., 1997b).

As shown in Fig. 6(*b*), if the minimum point locates at the leading edge of a land, for most of time, pure boundary lubrication occurs, because hydrodynamic pressure cannot be generated and only asperity contact supports the radial load from the expander. Hydrodynamic lubrication could only appear for a few crank angles around the TDC or BDC when squeezing effects is more dominant than sliding effects.

On the other hand, if the minimum point of a land does not locate at the leading edge, hydrodynamic lubrication occurs along with possible asperity contact. To obtain all the land/liner lubrication information, one has to solve the clearance between the lands and the liner and the wetting extent through iteration by applying radial force balance and outlet conditions. Three outlet conditions were applied, namely, Reynolds exit condition, film nonseparation condition, and fully flooded trailing edge. Film nonseparation condition was developed by Tian et al. (1997a, 1996) and it is used to replace Reynolds exit condition when the unsteady squeezing effects become dominant around TDC and BDC and further applying Reynolds exit condition results in violation of mass conservation.

The clearances between the two lands and the liner are not independent to each other. Here, any section of the TLOCR is assumed to be rigid, i.e.,

$$h_{0,u} = h_{0,l} + \alpha_1 l, \tag{3}$$

where $h_{0,l}$, $h_{0,u}$ are the nominal clearance between the liner and the reference points on the running surfaces of the lower land and the upper land, respectively; α_1 is the relative angle between the center

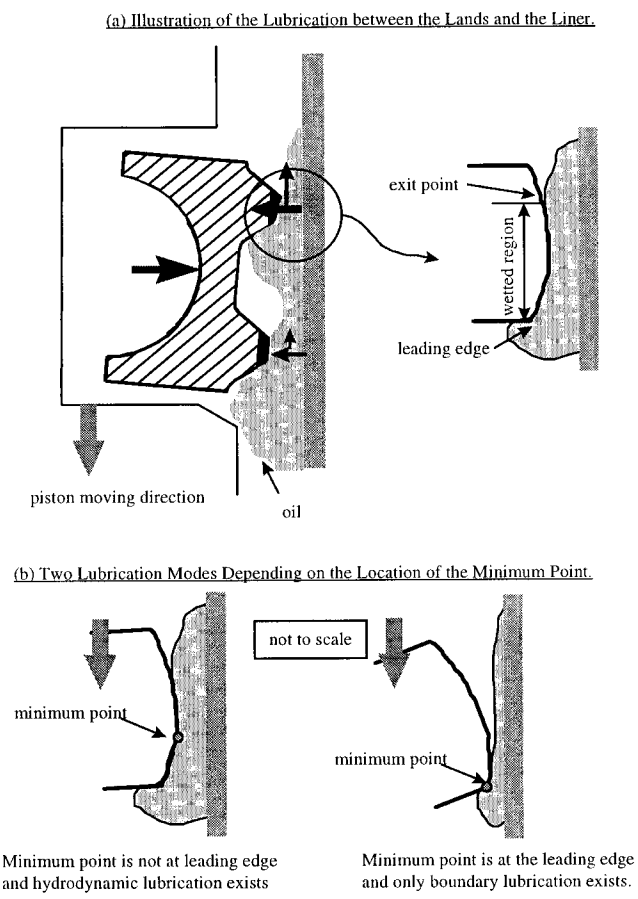

Fig. 6 Lubrication between the lands and the liner

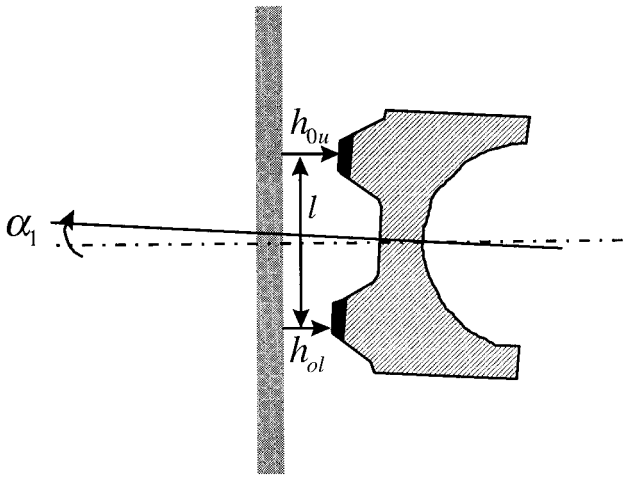

Fig. 7 Relation between the clearances of the two lands

line of the TLOCR and the liner, and l is the axial distance between the reference points of the two lands (Fig. 7).

Computation Algorithm. The dynamic equations of the TLOCR are solved via implicit method in time. Two levels of iteration were performed. At each time step, the outer level iteration is used to obtain the axial position and twist value of the TLOCR. Then, at each step of an outer level iteration, an inner level iteration has to be performed to solve land/liner lubrication. Newton's iteration and a globally convergent scheme were applied for both outer and lower level iterations and Jacobians were derived analytically for better computation speed and accuracy.

Illustration of the Model Predictions

The model was applied to a gasoline engine. The TLOCR used (Table 1) is a typical one for this size of engines. Engine speed 2500 rpm was chosen for this study. The piston tilt result of a similar engine was used to illustrate the effects of piston dynamic tilt (Fig. 9(*b*)). The piston tilt was calculated with a numerical model (Wong et al., 1994) under 2500 rpm/WOT.

One of the primary purposes of this paper is to illustrate the effects of piston dynamic tilt. Thus, all the parameters related to running surface profiles and the radial height difference between two lands were kept simple. As listed in Table 2, surface roughness of the land running surfaces and the liner were assumed to be 0.15 μm (rms value) to simulate smooth TLOCR and liner. The running surface profiles were assumed to be symmetrical with an exit height of 0.06 μm (Fig. 8) to simulate flat running surfaces of the two lands that are usually found in TLOCR. The radial height difference of the two lands was assumed to be zero in order to isolate the piston tilt effects. A final note is that the ring tension is assumed being evenly applied to all the circumferential locations.

In the following, predictions for the baseline parameters are explained first. Then ring tension, torsional stiffness, and the oil film thickness on the flanks of the groove are arbitrarily varied to illustrate their effects on the lubrication between the TLOCR and the liner as well as the interaction between the TLOCR and the groove.

Table 1 Major parameters of the engine and TLOCR

Bore×Stroke	87.2mm × 79.1mm
Nominal TLOCR Groove Axial Width	3 mm
Nominal Axial Clearance of the TLOCR	36μm
Tangential Tension of the TPOCR	50N (Baseline)
Axial Width of the Lands	0.35mm

Table 2 Other parameters

Roughness of the Liner (rms)	0.15μm
Roughness of the Running Surfaces of the Lands	0.15μm
Combined Roughness of the Flanks TLOCR Lands and the Groove	0.5μm
Oil Film Thickness on the Upper Side of the Groove	5μm (Baseline)
Oil Film Thickness on the Lower Side of the Groove	10μm (Baseline)
ε (in Equation 2)	0.5 (Baseline)

Lubrication Between the TLOCR and the Liner. First, the calculation was conducted for the section of the TLOCR at the thrust side since the effects of the piston dynamic tilt is most pronounced at the thrust side according to Eq. 1.

Minimum Oil Film Thickness of the Two Lands. Figure 9(*a*) shows the minimum clearance of between each land and the liner. Throughout this work, the term minimum oil film thickness (MOFT) is used as the minimum clearance between a land and the liner, and the term "clearance" by default, represents the nominal clearance between two rough surfaces. One can immediately find the correlation between the MOFT of the two lands and the piston dynamic tilt as shown in Fig. 9(*b*). When the piston tilt is positive, the MOFT of the lower land is less than the one of the upper land. Conversely, the MOFT of the lower land is greater when the piston tilt is negative. This relation between the MOFT of the two lands and the piston tilt qualitatively reflects the geometrical relation of the TLOCR in a tilted piston and the liner, as shown in Fig. 10(*d*). Further examining the radial force distribution on two lands shows the dynamic response of the TLOCR to piston dynamic tilt.

Figure 10(*a*) shows the integrated radial force on the running surface of each land. One can see that the ring radial load is primarily supported by one land. This uneven distribution of the radial forces thus creates a moment. As a result, the TLOCR is twisted in a direction such that the relative angle between the centerline of the TLOCR and the liner is reduced, compared with the static relation between the TLOCR and the liner (Fig. 10(*c*) and 10(*d*)). In Fig. 10(*c*) "Twist" represents the dynamic twist of the TLOCR relative to the neutral line ("Neutral" in Fig. 10(*c*)) that follows piston tilt, "Neutral" represents the relative angle of the neutral line to the liner, and "TLOCR/Liner" represents the relative angle of the centerline of the TLOCR to the liner after the dynamic twist of the TLOCR is taken into account (see Definition in Fig. 10(*d*)). Therefore, in Fig. 10(*c*), the value of "TLOCR/Liner" is essentially summation of "Twist" and "Neutral." Notice that the positive direction of all the angles defined in Fig. 10(*d*) is clockwise. Certainly the dynamic twist of the TLOCR is created by

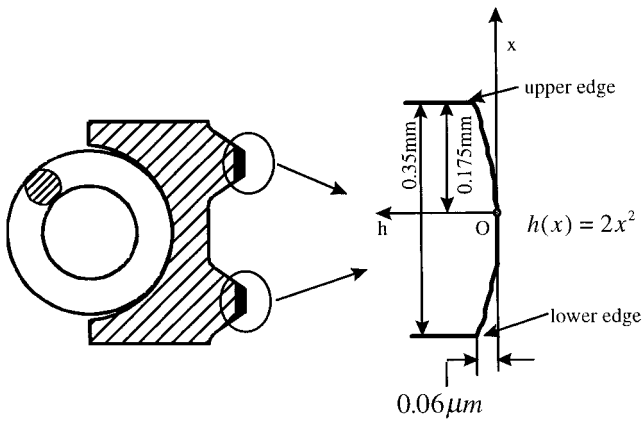

Fig. 8 Definition of the running surface profiles used in this work

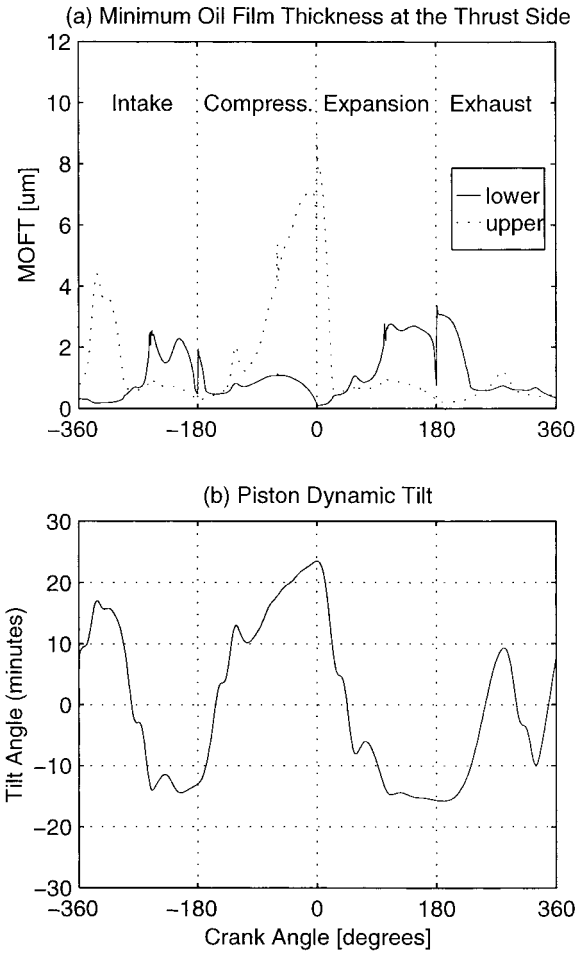

Fig. 9 Minimum oil film thickness of the two lands and piston dynamic tilt

unbalanced moment from all the sources such as radial forces, friction, and the pressures of TLOCR/groove interaction. In the above arguments, only the moment from the radial forces is mentioned. Figure 10(*b*) shows that the uneven radial forces are indeed the primary source for the dynamic twist of the TLOCR as the torsional resistance (the sign is switched for comparison) of the TLOCR is pretty close to the moment from the uneven radial forces in magnitude. Hereafter, the moment on the TLOCR always means the moment about the center of gravity of the TLOCR that includes the spring. Figure 10(*d*) graphically illustrates the static and dynamic positions of the TLOCR in a tilted piston.

The significance of these results shown in Figures 9 and 10 is that at the thrust side, large MOFT difference between the two lands still exists although the relative angle between the TLOCR and the liner caused by piston tilt is much reduced due to the dynamic twist. As a result, bore sealing is primarily performed by one land at a time, and the MOFT of the other land can be as high as several microns despite the high ring tension applied on the TLOCR. High MOFT on either land is detrimental to the sealing ability of the TLOCR as a large amount of oil might either be transported into the region between the two lands of the TLOCR or pass by the TLOCR along the bore.

As indicated in Eq. 1, the relative angle between the neutral line of the TLOCR and the liner varies along the circumferential direction. Figure 11 shows the MOFT of two lands at five equally spaced locations. One can see that the MOFT difference of the two lands decreases from the thrust side to the pin side. The MOFT of the two lands are almost identical at the pin side since the piston tilt effects vanish at the pin side ($\theta = 90$ deg in Eq. 1). Then, the

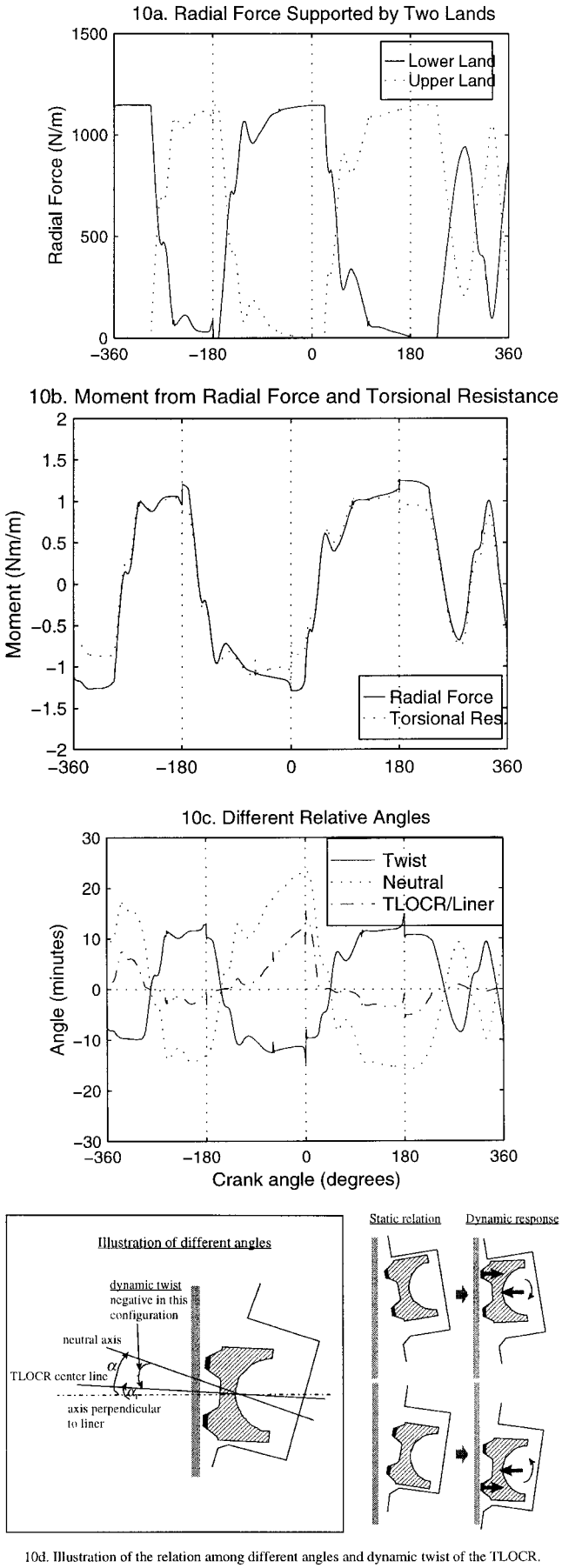

10d. Illustration of the relation among different angles and dynamic twist of the TLOCR.

Fig. 10 Integrated radial forces on two lands and all the different relative angles

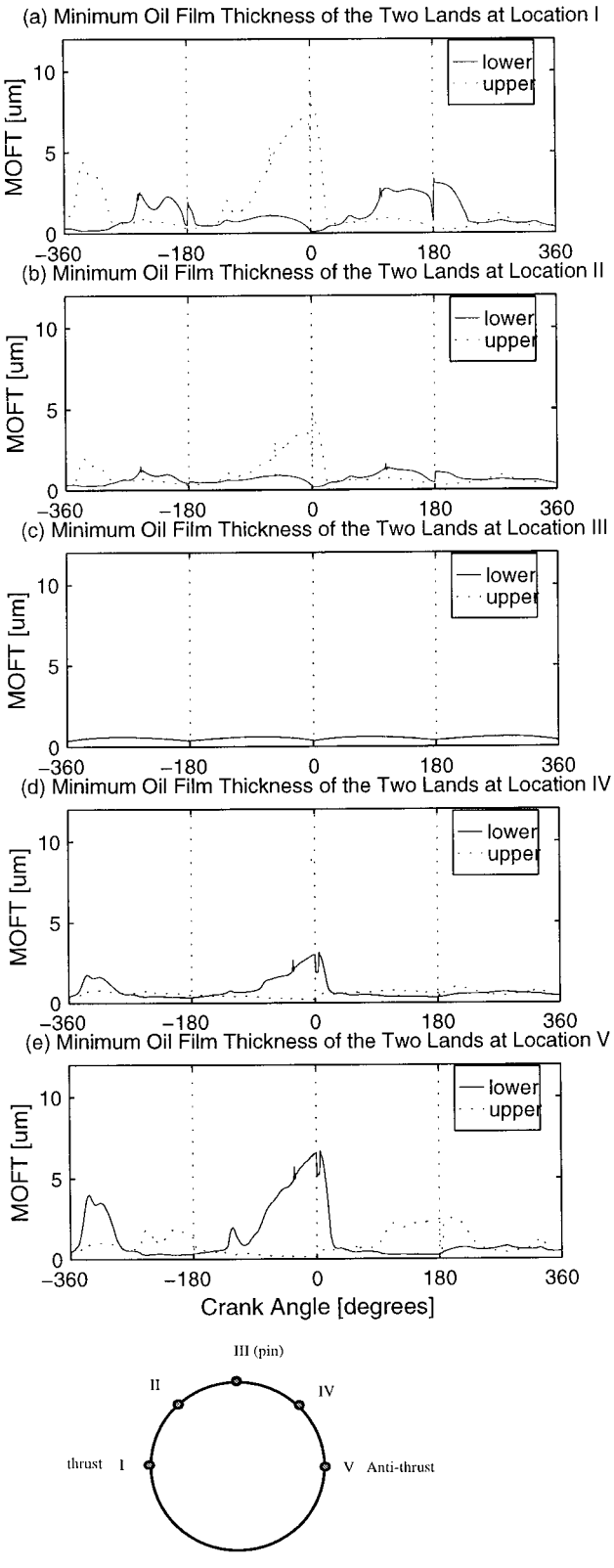

Fig. 11 MOFT at five locations

MOFT difference of the two lands increases from the pin side to the anti-thrust side. Furthermore, the MOFT difference displays opposite trend comparing thrust and anti-thrust sides, i.e., at one moment, if the MOFT of the lower land is higher than the one of the upper land at one side of the bore, the opposite must be true at the other side of the bore.

Lubrication Conditions. The lubrication condition between the lands and the liner at the thrust side is plotted in Fig. 12. The vertical axis is the axis on the running surface of each land in the axial direction (Fig. 12(*c*)). The solid line in Fig. 12 is the minimum point of the running surface of each land, defined as the location where the clearance between the running surface and the liner reaches the minimum (Tian et al., 1997b). The region between the two dotted lines is where hydrodynamic lubrication occurs (marked as "wetted region" in the graph). The lubrication condition is largely controlled by the variation of the minimum point, which is determined by the original running surface profile and the varying relative angle between the TLOCR and the liner. When the minimum point becomes the leading edge, e.g., during early intake and early expansion strokes, hydrodynamic lubrication disappears and only boundary lubrication exists. If the minimum point moves to the trailing edge or close to the trailing edge, e.g., during the late part of compression stroke, hydrodynamic lubrication exists in the entire running surface. When the minimum point is varying within the running surface, the location of the trailing edge is determined according to the outlet conditions. One can see the complexity of the lubrication conditions on the running surfaces of the two lands as a result of flat land running surface profiles and large variation of dynamic twist of the TLOCR. Determining the lubrication between the lands and the liner is in fact the most difficult and time-consuming part of the computation.

Oil Transport. The MOFT difference between two lands may result in oil accumulation inside the TLOCR and further oil flow to the upper regions. Detailed discussion on oil transport around the TLOCR is beyond the scope of this paper. Here, it is only intended to show implications of the model predictions on oil transport. Figure 13 plots the thickness of the oil film on the liner at the thrust

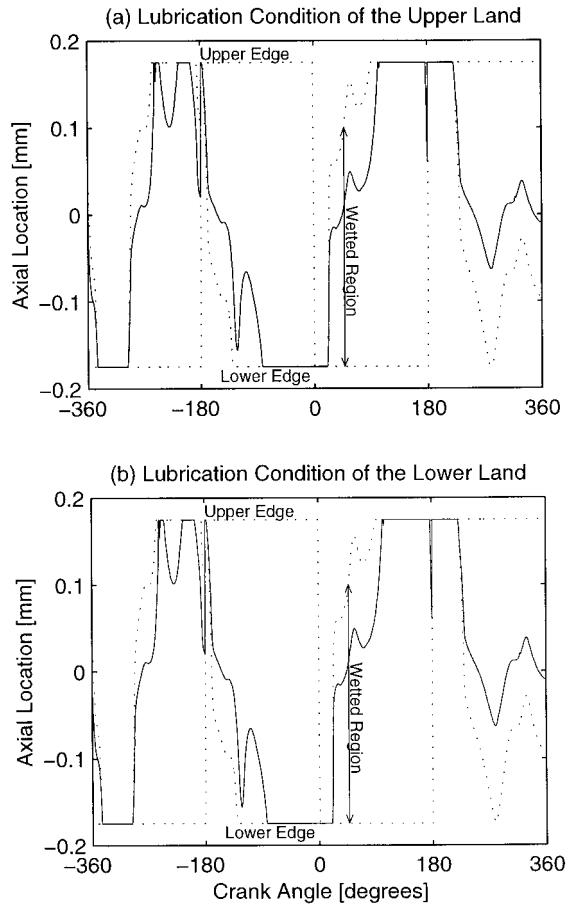

Fig. 12 Lubrication conditions of two lands

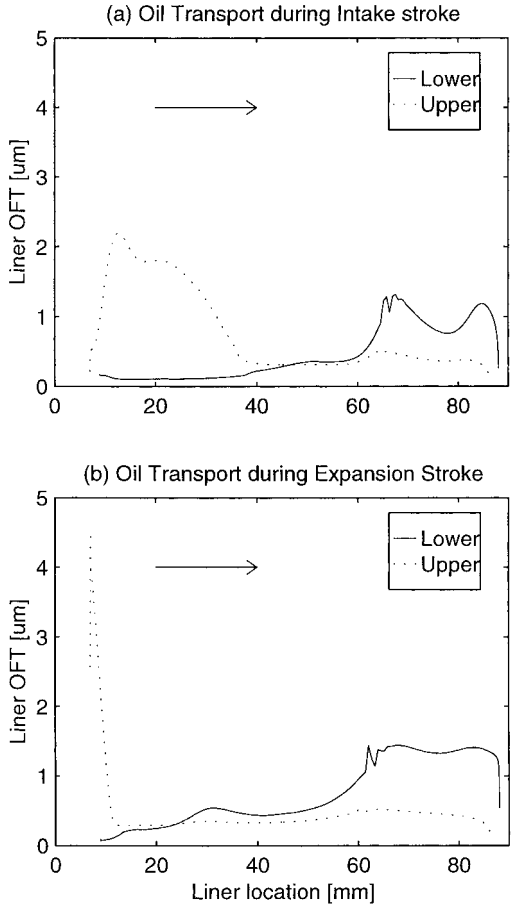

Fig. 13 Oil film thickness left by the two lands during down-strokes

side after passage of each land during different down-strokes. The horizontal axis is the liner location with the origin being the TDC position of the top ring. Since it is assumed that the two lands always have sufficient oil supply, the liner oil film thickness can also be understood as the maximum amount of the oil that is allowed to pass the lands. As seen in Fig. 13(*a*), down along the liner from 60 mm, there is more oil allowed to pass by the lower land than the upper land. As a result, the upper land scrapes the oil on the liner left by the lower land and oil accumulation inside the TLOCR may be created. On the other hand, during the early intake stroke, high liner oil film thickness that passes through the upper land (Fig. 13(*a*)) indicates that the oil accumulated inside the TLOCR can be released by the upper land and may result in oil accumulation in the upper piston regions. All these studies on oil transport and influence of the piston third land pressure will be discussed in future works. Here, through this simple study, one can see that piston dynamic tilt is able to create oil accumulation in different regions and may result in irreversible oil transport to upper piston regions.

Friction. Integrated friction force from the five locations defined in Fig. 11 is plotted in Fig. 14. Two values of boundary lubrication friction coefficient (f) were used to show the effect of boundary lubrication on total friction power loss of the TLOCR. One can see that reducing the friction coefficient from 0.1 to 0.05 can bring as much as 15 percent reduction to the FMEP of the TLOCR. Additionally, comparison of two friction traces in Fig. 14 indicates that boundary lubrication exists throughout the entire cycle. As stated earlier, pretty small roughness values were assumed here on both liner and the running surfaces of the two lands. One would expect more contribution from the boundary lubrication to the total friction of the TLOCR with rougher liner and lands.

Dynamics of the TLOCR and TLOCR/Groove Interaction. The clearances between the lower side of the TLOCR and the groove at ID and OD locations at the thrust side are plotted in Fig. 15(*a*). Also marked in Fig. 15(*a*) are the oil film thickness on the lower and upper sides of the groove and the roughness contact line with thickness of four (4) times of the combined roughness of the flanks of the TLOCR and the groove. First, one can see that lift of the TLOCR is dominated by the inertia force of the TLOCR since in general the inertia force is greater than the other driving force—friction, as shown in Fig. 15(*b*). In Fig. 15(*b*), the unit of the forces is Newton per unit length in the circumferential direction. Secondly, switch of the clearances at ID and OD occurs exactly at the same time as the piston tilt changes the sign (Fig. 9(*b*)) due to the dynamic twist of the TLOCR as discussed in the earlier section (Fig. 10(*c*)).

With detailed description of the interaction between the flanks of the TLOCR and groove in the vicinity of the groove, the model not only predicts the overall up and down motion of the TLOCR but also the detailed motion when the TLOCR moves to the vicinity of the groove. This detailed motion in the vicinity of the groove determines the reaction force from the groove, asperity contact between the TLOCR and the groove, and the oil transport through the groove. As can be seen in Fig. 15(*a*), when the TLOCR first makes contact with the oil film either on the upper or lower groove, the oil resistance is low because of thick oil film and small contact area between the TLOCR and the oil. Then, the penetration of the TLOCR into the oil becomes much more gradual as the film thickness decreases and the contact area increases. The oil flow rates in and out of the groove can also be calculated based on the model predictions and will be discussed in future works along with the oil transport from the land/bore interface.

The integrated axial forces and moments from the interactions of TLOCR and the groove are plotted in Fig. 16. One can see from Fig. 15(*a*) and Fig. 16 that the penetration of the TLOCR into the roughness is not significant and there is little contribution from the asperity contact to the total reacting force and moment. Additionally, the magnitude of the moment from TLOCR/groove interaction is much less than the moment from the radial forces comparing Fig. 16(*b*) with Fig. 10(*b*). However, when engine speed increases, much increased inertia force should result in greater reaction force and moment from TLOCR/groove interaction.

Figure 17 shows the lift of the TLOCR with two different sets of oil film thickness on the flanks of the groove. In Fig. 17(*a*), 10 μm and 20 μm were used for the film thickness on the upper and lower flanks, respectively. With this set of oil film thickness, the clearance (36 μm) between the TLOCR and the groove is almost

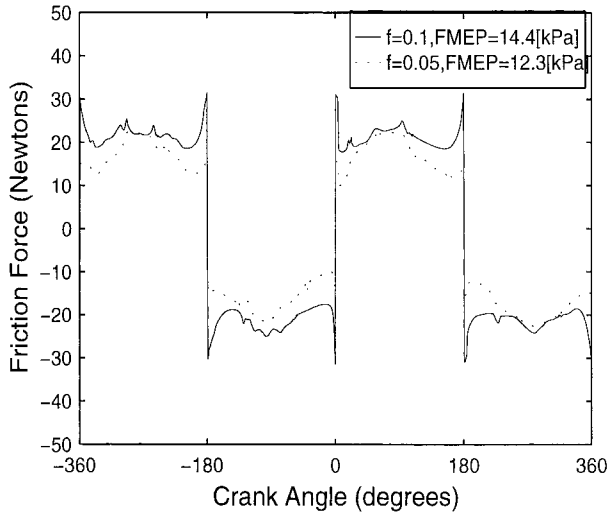

Fig. 14 Integrated friction force of the TLOCR from five locations under two different friction coefficients

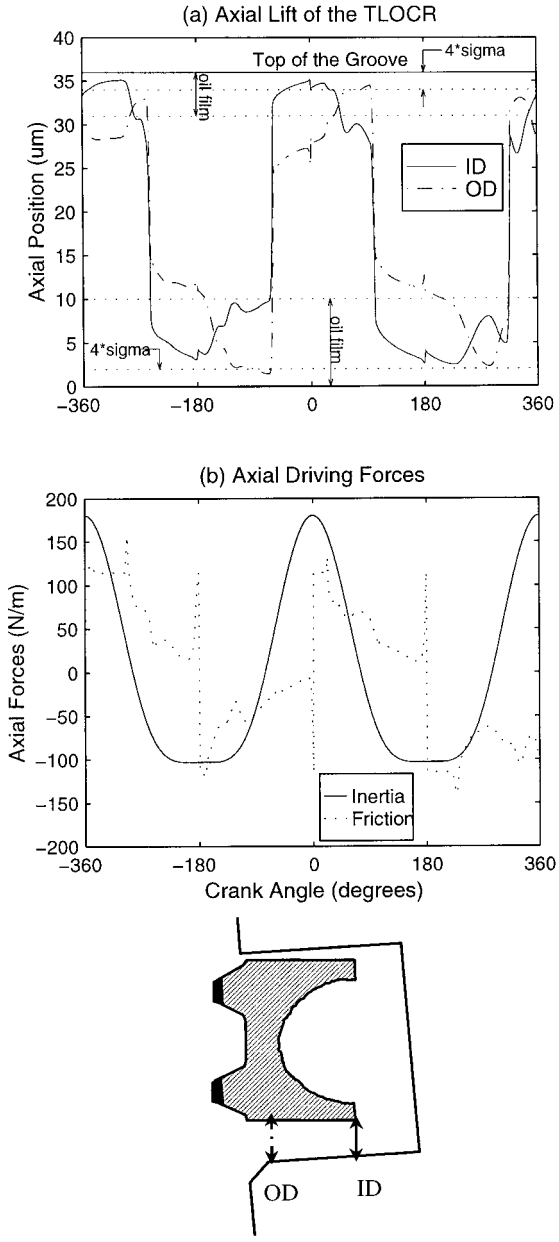

Fig. 15 Axial position of the TLOCR inside the groove and the driving forces

full of the oil. Compared with the one in Fig. 15(*a*), the motion of the TLOCR in Fig. 17(*a*) is much more gradual and the TLOCR almost always floats in the groove. On the other hand, with the oil film thickness of 2 μm on both upper and lower flanks of the groove in Fig. 17(*b*), up-and-down transition of the TLOCR position is steep until the TLOCR makes contact with thin oil layer and roughness. In this case, pressures from oil squeezing and asperity contact between the TLOCR and the groove occur at the same time when the clearance between the TLOCR and the groove is less than 2 μm. One can see from Fig. 18 that the magnitude of integrated asperity contact force is significant when the oil film thickness on the upper and lower flanks of the groove is 2 μm.

MOFT Under Different Torsional Stiffness and Ring Tension. As discussed earlier, uneven radial forces from two lands as a primary source create dynamic twist on the TLOCR and reduces the MOFT difference at both thrust and anti-thrust sides caused by piston dynamic tilt. However, large MOFT difference at the thrust side still exists when the piston tilt is high since dynamic twist is limited by the torsional stiffness of the TLOCR. Therefore, two key parameters that control the MOFT difference are the torsional stiffness of the TLOCR and the radial forces on the two lands. In this study, the torsional stiffness and the tension of the TLOCR were arbitrarily varied, and the maximum of the MOFT of the two lands at the thrust side is plotted in Fig. 19. The maximum of the MOFT of the two lands exactly reflects the MOFT difference of the two lands since the minimum of the MOFT is always very small. In Fig. 19(*a*), two other torsional stiffness values (ϵ = 0.3, 0.8) were used. Not surprisingly, the maximum of the MOFT decreases with reduction of torsional stiffness as the uneven radial forces can create greater dynamic twist. Similar trend can be found in Fig. 19(*b*) where the tension of the TLOCR was varied. Greater tension can create greater moment and thus dynamic twist. As a result, the maximum of the MOFT is reduced when the ring tension is increased.

Although simple, these results demonstrate a different way to have a better bore sealing for a TLOCR. A unique feature of a TLOCR is its two lands being geometrically separated. Thus, under a tilted piston, a MOFT difference is created on both thrust and anti-thrust sides. With adequate ring tension, the MOFT of one land is very low and the efforts for having a better bore sealing from the TLOCR should perhaps be focussed on how to reduce the maximum MOFT of the two lands. As demonstrated in Fig. 19, reducing torsional stiffness can achieve the same level of bore sealing as increasing ring tension without potentially increasing friction as the maximum of the MOFT of the two lands is reduced by either methods. Even considering bore distortion, all the results here seem to indicate that it is much easier to obtain a small MOFT for one land than for both lands under a tilted piston. In conclusion, while ring tension of the TLOCR is certainly an important param-

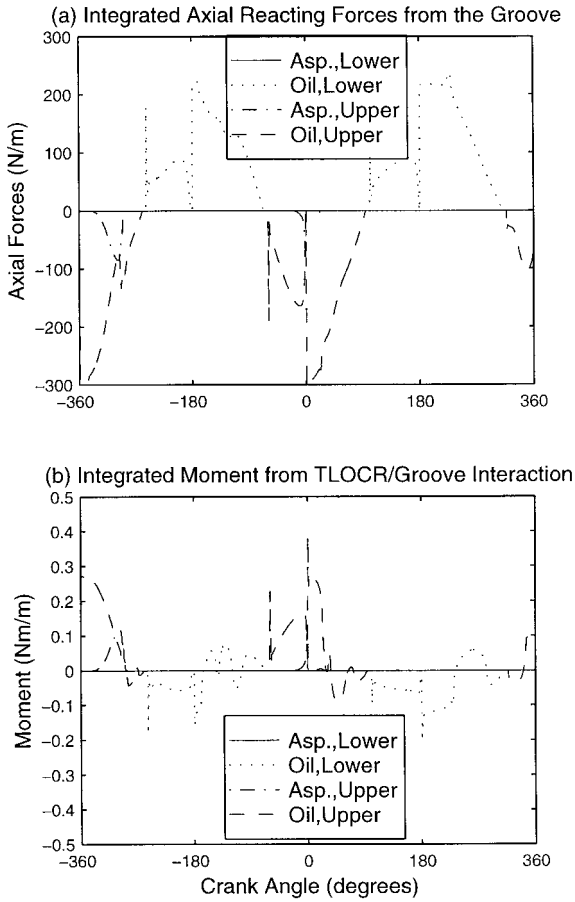

Fig. 16 Axial forces and moments generated from TLOCR/groove interactions

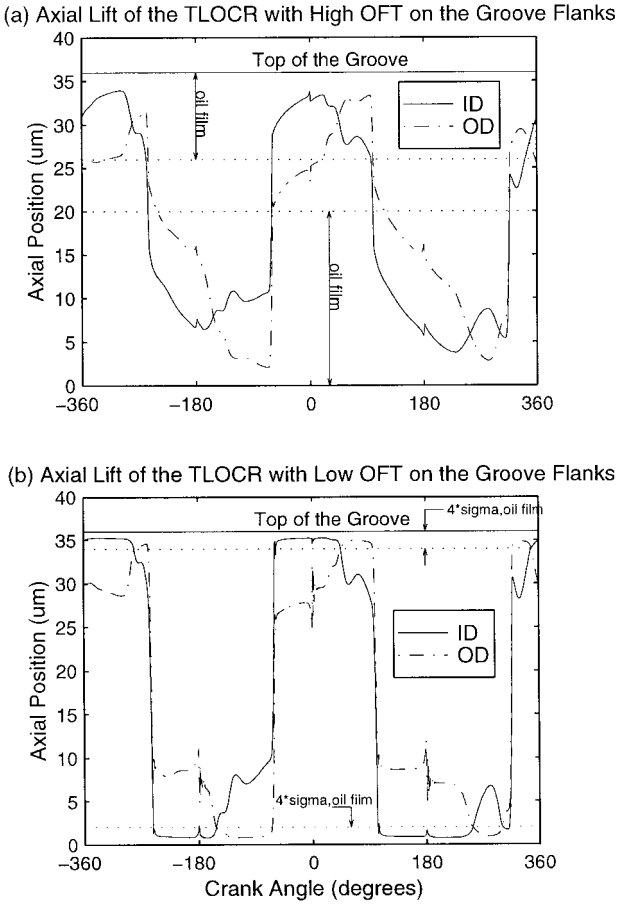

Fig. 17 Motion of the TLOCR under two different assumed oil film thickness on the flanks of the groove

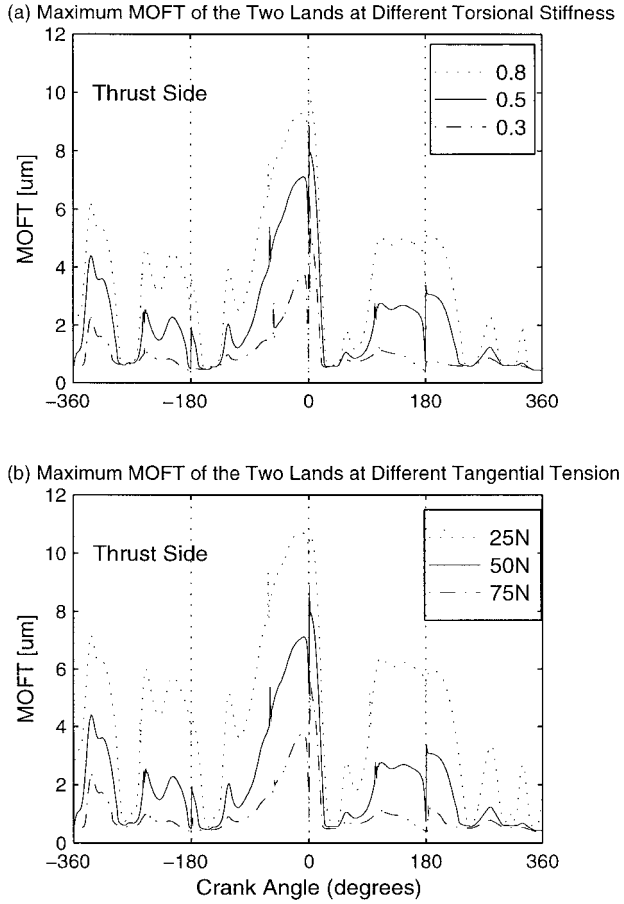

Fig. 19 Maximum of the MOFT of the two lands under different torsional stiffness and ring tensions

eter and easy to modify in reality, other parameters such as torsional stiffness are perhaps equally critical to the bore sealing ability of the TLOCR.

Discussions and Conclusions

A theoretical model for the lubrication and dynamics of twin-land oil control rings (TLOCR) has been presented. The model takes into account a number of important aspects of the TLOCR that have never been discussed before such as the effects of piston dynamic tilt and detailed interaction between the TLOCR and the groove when the TLOCR moves close to the flanks of the groove. The sample results demonstrate the effectiveness of the model in revealing oil film thickness, dynamics, and the friction of the TLOCR as well as oil transport through the interfaces of TLOCR/liner and TLOCR/groove.

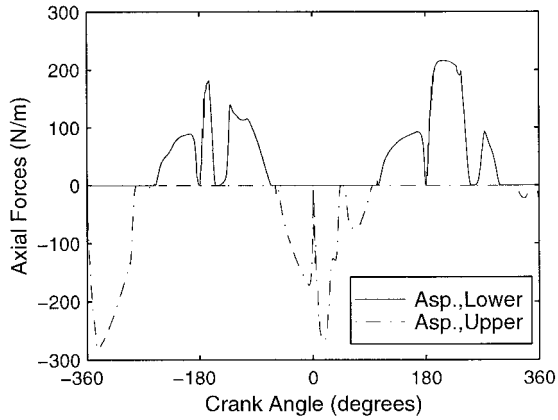

Fig. 18 Integrated axial forces from TLOCR/groove asperity contact under thin oil film thickness

The most important finding is the existence of MOFT difference between two lands under a dynamically tilted piston and this MOFT difference is most pronounced at both thrust and anti-thrust sides. As there is plenty of oil below and within the TLOCR, a large MOFT on either land may cause oil leakage to upper piston regions. A simple study showed that reducing torsional stiffness and increasing ring tension can both reduce the MOFT difference of the two lands and give better TLOCR bore sealing. The results also show that the model, with its detailed description on oil behavior between the flanks of the TLOCR and the groove, has potential for studying oil transport through the flanks of the groove. With further incorporation of gas flow, a complete oil transport model for twin-land oil control rings can be established. Oil transport through oil control rings is one of the most critical elements for understanding oil consumption from piston system because an oil control ring controls the amount of oil supply to top two rings and upper piston regions. Along with the model on three-piece oil control rings (Tian et al., 1998b), better understanding can be gained on the oil transport in the piston ring-pack.

Many aspects of the model predictions qualitatively match the experimental measurements of Ariga (1996) and Takiguchi et al. (1998). Ariga's measurements clearly indicate change of relative angle between the TLOCR and the groove due to change of the direction of piston tilt as predicted by the present model (Fig. 15(*a*)). Additionally, the damping effects of oil film thickness inside the TLOCR groove shown in Fig. 17 of the present paper

can be found in Fig. 12 of Ariga's work (Ariga, 1996). Takiguchi's LIF measurements at mid-stroke (Takiguchi et al., 1998) show that the film thickness of the two lands of the TLOCR has different relationship at thrust side and anti-thrust side. For instance, in Takiguchi's work (Takiguchi et al., 1998), it is shown that the film thickness of the lower land is higher than the upper land at mid expansion stroke at the thrust side. On the other hand at the anti-thrust side, the film thickness of the upper land is actually slightly higher than the lower land at mid expansion stroke. This difference in oil film thickness between thrust and anti-thrust sides may be due to the piston tilt effects, as indicated by the present model. As one knows, piston tilts toward the thrust side during mid expansion stroke. However, caution has to be made when comparing the predictions of the present model with the LIF. As described earlier, fully flooded inlet condition was used in the present model. Therefore, to be more precise, in practice, the maximum MOFT of two lands predicted by the present model should be interpreted as the clearance between the land and the liner because there might be no sufficient oil to feed high clearance between the land and the liner. On the other hand, LIF measurement is not able to tell if there is only oil between the land and the liner.

The current model is essentially a two-dimensional model for one section of the TLOCR that neglects the stress constraint from other sections and existence of the gap by using a constant torsional stiffness for different sections. The accuracy of the model and necessity for extending the model into a three-dimensional one will be determined by further validation with experiments and engine tests.

Acknowledgments

This work was sponsored by the MIT Consortium on Lubrication in IC Engines with financial and technical support from Dana Corp., Shell, Renault, Peugeot SA, Volvo, and MAHLE. The authors would like to thank Remi Rabute at Dana for supplying engine test data during the course of model development.

References

Ariga, S., 1996, "Observation of Transient Oil Consumption With In-Cylinder Variables," SAE Paper 961910.

Greenwood, J. A., and Tripp, J. H., 1971, "The Contact of Two Nominally Flat Surfaces," *Proc. Inst. Mech. Engrs.*, Vol. 185, p. 625.

Patir, N., and Cheng, H. S., 1978, "An Average Flow Model for Determining the Effects of Three-Dimensional Roughness on Partial Hydrodynamic Lubrication," ASME *Journal of Lubrication Technology*, Vol. 100, No. 1, p. 12.

Patir, N., and Cheng, H. S., 1979, "Application of Average Flow Model to Lubrication Between Rough Sliding Surfaces," ASME *Journal of Lubrication Technology*, Vol. 101, pp. 220–230.

Ruddy, B. L., Dowson, D., and Economou, P. N., 1981a, "Theoretical Analysis of the Twin-Land Type of Oil Control Piston Ring," *Journal of Mechanical Engineering Science*, Vol. 23, No. 2.

Ruddy, B. L., Dowson, D., and Economou, P. N., 1981b, "The Influence of Running-in of the Twin-Land Type of Oil-Control Piston Ring Upon Long-Term Engine Oil Consumption," Proceedings, 8th Leeds-Lyon Symposium on Tribology, pp. 162–169.

Sui, P. C., and Ariga, S., 1993, "Piston Ring Pack Friction and Lubrication Analysis of an Automotive Engine Using a Mixed Lubrication Model," SAE Paper 931937.

Takiguchi, M., Nakayama, K., Furuhama, S., and Yoshida, H., 1998, "Variation of Piston Ring Oil Film Thickness in an Internal Combustion Engine—Comparison between Thrust and Anti-Thrust Sides," SAE Paper 980563.

Tian, T., 1997a, "Modeling the Performance of the Piston Ring-Pack in Internal Combustion Engines," Ph.D. thesis, Department of Mechanical Engineering, MIT, Boston, MA.

Tian, T., Noordzij, L. B., Wong, V. W., and Heywood, J. B., 1998a, "Modeling Piston-Ring Dynamics, Blowby, and Ring-Twist Effects," ASME JOURNAL OF ENGINEERING FOR GAS TURBINES AND POWER, Vol. 120, pp. 843–854.

Tian, T., Rabute, R., Wong, V. W., and Heywood, J. B., 1997b, "Effects of Piston-Ring Dynamics on Ring/Groove Wear and Oil Consumption," SAE Paper 970835.

Tian, T., Wong, V. W., and Heywood, J. B., 1996, "A Piston Ring-Pack Film Thickness and Friction Model for Multigrade Oils and Rough Surfaces," SAE Paper 962032.

Tian, T., Wong, V. W., and Heywood, J. B., 1998b, "Modeling the Dynamics and Lubrication of Three Piece Oil Control Rings in Internal Combustion Engines," SAE Paper 982657.

Wong, V. W., Tian, T., Lang, H., Ryan, J. P., Sekiya, Y., Kobayashi, Y., and Aoyama, S., 1994, "A Numerical Model of Piston Secondary Motion and Piston Slap in Partially Flooded Elastohydrodynamic Skirt Lubrication," SAE Paper 940696.

The Potential for LNG as a Railroad Fuel in the U.S.

S. G. Fritz
Southwest Research Institute,
6220 Culebra Road,
P.O. Drawer 28510,
San Antonio, TX 78228-0510

Freight railroad operations in the United States represent a substantial opportunity for liquefied natural gas (LNG) to displace diesel fuel. With the promise of achieving an overwhelming economic advantage over diesel fuel, this paper presents some discussion to the question, "Why is the application of LNG for railroad use in the U.S. moving so slowly?" A brief overview of the freight railroad operations in the U.S. is given, along with a summary of several railroad LNG demonstration projects. U.S. Environmental Protection Agency and California Air Resources Board exhaust emission regulations may cause the railroad industry to move from small-scale LNG demonstration projects to using LNG as a primary freight railroad transportation fuel in selected regions or route-specific applications.

Introduction

A quiet renaissance is occurring within the freight railroad industry in North America. After decades of downsizing, the industry has recently been faced with the unfamiliar challenge of accommodating record growth. When the U.S. Congress passed the Staggers Railroad Act in 1980, deregulating railroads, the industry took painful steps needed to increase competitiveness. Over the next decade, employment was reduced from 532,000 to 292,000, while intercity revenue freight increased from 1,350 to 1,560 billion tonne-km. The industry reduced its locomotive fleet from 28,000 to 18,800, and eliminated older, less fuel-efficient models in favor of new, efficient, higher power locomotives. This resulted in a remarkable improvement in fuel economy, from 1,290 to 1,822 revenue tonne-km per liter of diesel fuel.

The U.S. Interstate Commerce Commission (ICC), which was dissolved in December 1995, classified U.S. railroads by their level of operating revenue. In 1994, there were twelve freight railroad companies that had revenues greater than the $255.9 million threshold for "Class I" railroads.

Much of the recent growth in railroad freight movement is a result of problems within the long-haul trucking industry, which has seen rapid cost increases and nationwide shortage of qualified drivers. The economic situation of the trucking industry has encouraged use of intermodal shipping, where truck trailers or containers are transported long distances by train, then transferred to trucks for local distribution. Railroads are responding to the increased demand by buying new locomotives and freight cars, hiring people, and investing in new facilities.

Deregulation has led all freight (and passenger) modes to lower their rates per tonne-km (passenger-km) since the late 1970's. The Association of American Railroads (AAR) reports that railroad revenue per tonne-km for selected years is as follows

Year	Current $	Constant$
1984	0.044	0.044
1989	0.038	0.032
1993	0.036	0.027

Market forces continue pushing transportation companies to find ways to reduce costs to keep prices down yet maintain profitability. As discussed below, diesel fuel costs are the second largest operating cost item for railroads (after labor), and therefore, the railroads are working hard to reduce fuel costs.

Contributed by the Internal Combustion Engine Division (ICE) of THE AMERICAN SOCIETY OF MECHANICAL ENGINEERS for publication in the ASME JOURNAL OF ENGINEERING FOR GAS TURBINES AND POWER; ICE Paper No. 97-ICE-12.

Manuscript received by the ICE April 1, 1997; final revision received by the ASME Headquarters July 27, 1999. Associate Technical Editor: D. Assanis.

Railroad Energy Consumption and LNG Market Potential

When considering the U.S. freight railroads as a potential LNG market it is interesting to first put the size of the freight railroad industry of the U.S. into perspective with other world freight railway systems. Figure 1 compares the size of the U.S. Class I railroads to selected world railways based on revenue tonne-km in 1992. The Russian railroads are big. Very big. However, traffic has decreased dramatically since 1990, when the former USSR railroads moved 3717 billion tonne-km of freight, to 1993 when Russia moved 1607 billion tonne-km. The Russian railway system is roughly 75 percent electrified, with the remainder diesel-electric. Even the 25 percent that is diesel electric represents an attractive market for LNG use.

In 1997, the U.S. Class I railroads operated 224,374 km of track, using 13.64 billion liters of diesel fuel (0.49 quads) in 19,682 diesel-electric locomotives to move 2270 billion tonne-km of freight (Railroad Facts, 1998). If there were a 100 percent conversion to LNG by the U.S. freight railroads, it would result in roughly a 2 percent increase in total U.S. natural gas consumption.

The average cost in 1997 of the ASTM No. 2-D diesel fuel used by the U.S. railroads was $0.18 per liter ($0.68 per U.S. gallon). Fuel costs represent an average operating expense of 7.4 percent of total revenue. Therefore, the cost of fuel is a fundamental variable in the profitability of the railroads.

Although a comprehensive discussion on the economics of LNG as compared to diesel fuel is beyond the scope of this paper, several feasibility studies have been performed in recent years (Bepple, 1987; Para, 1992; SwRI-5285, 1994). The underlying conclusions of these studies are similar: LNG, under a given set of economic and operating assumptions, has a direct economic advantage over diesel fuel. However, capital requirements for wide scale conversion to LNG are very large, and the assumptions modeled contain enough uncertainty to cause the railroads in the U.S. to be very cautious in their consideration of LNG. These facts, coupled with the uncertainty in gas engine availability and durability, have slowed, but not stopped, progress toward introduction of LNG into this market. Several LNG-fueled engine and locomotive demonstration programs are currently underway; and locomotive exhaust emission regulations, especially for the Los Angeles, California area, could provide the necessary incentives for selected railroads to opt for LNG.

LNG Locomotive Demonstration Projects in the U.S.

The use of LNG in U.S. locomotive engines was demonstrated by SwRI in 1986 in a project funded by the U.S. Department of Energy (Wakenell, 1987; Wakenell, 1988). A model 567B two-

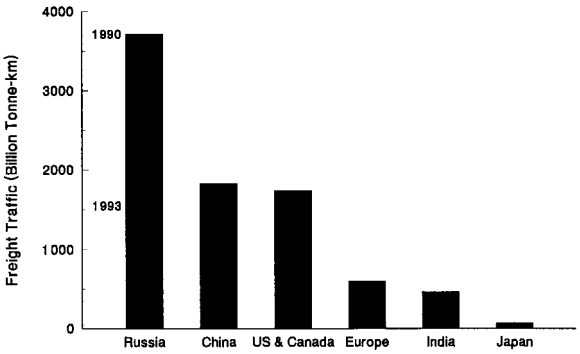

Fig. 1 Relative size of major freight railway systems

cylinder research engine manufactured by the Electro-Motive Division of the General Motors Corporation (EMD), was modified for dual-fuel operation using LNG as the primary fuel (up to 99 percent), and diesel fuel as the pilot charge to ignite the gas. The project demonstrated that high pressure, late cycle gas injection could yield engine performance that matched that of the unmodified diesel, with only slightly lower thermal efficiency. However, the exhaust emission tests revealed that the diesel pilot and natural gas fuel injection systems needed further development. Excessive smoke, particulate matter (PM), and carbon monoxide (CO) emissions at high power conditions indicated over-fueling and incomplete combustion.

Burlington Northern Railroad. While SwRI was demonstrating high pressure, late cycle gas injection, the Burlington Northern Railroad (BN) was well into proof-of-concept testing using natural gas as a locomotive fuel. In 1983, BN modified an EMD model GP-9 locomotive, powered by a naturally aspirated 16-cylinder, 1300 kW, model 567C engine, to run on natural gas (dual-fuel). A compressed natural gas (CNG) highway trailer mounted on a flat car was used to haul the fuel. From 1985 through 1987, on-the-rail tests of BN No. 1961 on a route between Minneapolis, Minnesota and Superior, Wisconsin (approximately 240 km) proved that a natural gas-powered locomotive could be operated safely. BN also established that the relatively low energy density of CNG made it impractical for wide-scale railroad use, and BN's focus shifted to LNG.

In 1987, BN entered into an agreement with Air Products and Chemicals, Inc. (APCI) to develop fuel tender cars, storage, and refueling facilities for railroad application of refrigerated liquid methane (RLM, a purified form of liquid natural gas). They also explored the various types of technology available to convert high power turbocharged locomotives to use RLM. The BN and APCI settled on engine conversion equipment and technology developed by Energy Conversions, Inc. (ECI) of Tacoma, Washington. BN and APCI, working with ECI, applied the ECI dual-fuel conversion system for a EMD model SD40-2 locomotive equipped with a turbocharged 2,237 kW model 16-645E3B engine (Stolz, 1992; Olson, 1993; Jensen, 1994). The combined efforts resulted in a locomotive that achieved BN's goal of producing 100 percent of the diesel power rating using dual-fuel operation, while maintaining diesel-only capability for operation when RLM was not available (Gillispie, 1994).

In October 1991, BN contracted with SwRI to perform exhaust emission measurements on the first of two dual-fuel SD40-2 locomotives converted by ECI. BN locomotive No. 7890 had just successfully completed a 500-hour durability test, and BN wanted to understand the modified engines' exhaust emission characteristics before operation in revenue service. A mobile SwRI emissions test facility was transported to Tacoma, Washington where gaseous (HC, CO, NO_x, O_2, and CO_2) and particulate emission measurements were made. A gas chromatograph was used to measure methane (CH_4) content of the exhaust to compute nonmethane hydrocarbon (NMHC) emissions. The full load emissions data from those tests, given in Fig. 2, show that NO_x emissions from the dual-fuel locomotive were well below the baseline level of 16.4 g/kW-hr, and PM emissions were also lower than diesel levels. However, the conversion dramatically increased NMHC and CO emissions over diesel levels, with CO emissions about seven times higher, and NMHC levels about two times higher. The results clearly demonstrated the trade-off of achieving NO_x reductions at the expense of increased HC and CO emissions. Although natural gas is generally considered a "clean" fuel, the emissions data indicated that the BN locomotive needed additional development for emissions optimization. Though economic concerns were primary motivations for BN's dual-fuel demonstrations, a fuel consumption penalty of about nine percent at rated power was observed during dual-fuel operation.

In 1992, two BN SD40-2 dual-fuel locomotives were placed in revenue service, hauling 13,500 tonne coal trains from the Powder River Basin of Montana to an electric power plant in Superior, Wisconsin. RLM was supplied from a 95,000 liter

Nomenclature

List of Abbreviations

AAR = Association of American Railroads
API = American Petroleum Institute
ASME = American Society of Mechanical Engineers
ASTM = American Society for Testing and Materials
AT&SF = The Atchison, Topeka and Santa Fe Railway Company
BNSF = Burlington Northern Santa Fe Corporation
BSFC = brake specific fuel consumption
CAA = Clean Air Act Amendments of 1990
CARB = California Air Resources Board
CFR = Code of Federal Regulations
cm = centimeter
CO = carbon monoxide
CO_2 = carbon dioxide
EMD = Electro-Motive Division of General Motors Corporation
EPA = U.S. Environmental Protection Agency
°F = degrees Fahrenheit
g = gram
H_2O = water
HC = hydrocarbons
hr = hour
ICC = U.S. Interstate Commerce Commission
ISO = International Organization for Standardization
L = liter
LNG = liquefied natural gas
min = minute
mm = millimeter
NO_x = oxides of nitrogen
O_2 = Oxygen
OEM = original equipment manufacturer
PM = particulate matter
rpm = revolutions per minute
SAE = Society of Automotive Engineers
sec = seconds
SP = Southern Pacific Transportation Company
SwRI = Southwest Research Institute
ton = U.S. ton = 2,000 lbs
tonne = metric ton = 1,000 kg
UP = Union Pacific Railroad
U.S. = Unites States of America
wt = weight
% = percent

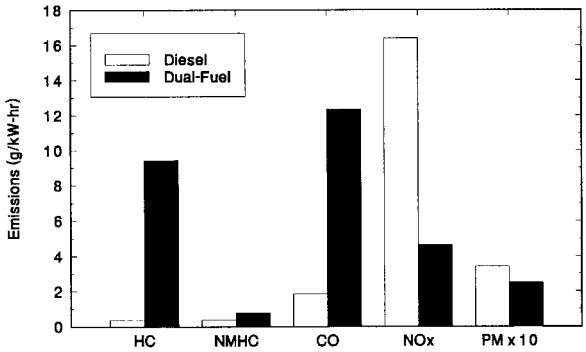

Fig. 2 Full load exhaust emissions results of BN No. 7890

tender car located between two dual-fuel locomotives. This allowed the locomotives to make the 2700 km round trip with one fueling stop at an RLM facility established by APCI near Staples, Minnesota. One of the two locomotives with the RLM tender car is shown in Fig. 3.

The two RLM-fueled locomotives were used in revenue service until late 1995, when the BN Railroad merged with the AT&SF Railroad to become the Burlington Northern Santa Fe Railway Company (BNSF). The new management at the BNSF made the decision that enough had been learned from the BN demonstration, and that future efforts should focus on the current generation of high-power locomotives. When BN's LNG project began in the mid 1980's, the 2237 kW EMD model SD40-2 was the "backbone" of the U.S. locomotive fleet. It was the logical candidate at that time for conversion to LNG, with expectations that these locomotives would be primary power for the railroads for the next 20 years. During the 5–7 year period while the BN LNG-fueled locomotives matured into reliable locomotives, the makeup of the BN's fleet began to change rapidly. New microprocessor-controlled locomotives from both EMD and GE offered dramatic improvements in power, adhesion (wheel slip control), reliability, and fuel consumption. The scale of the differences was such that BN placed the largest single locomotive order ever in the U.S., 350 EMD model SD70MAC locomotives. Three of these new 3000 kW locomotives could replace five of the SD40-2s. GE now offers 3356 kW locomotives as their standard power level. Both EMD and GE are introducing new 4,475 kW locomotives. The model SD40-2 locomotive, the mainstay of most Class I locomotive rosters just a few years ago, is rapidly being displaced by these new high power locomotives. Any LNG engine development for today and tomorrow must focus on the new high power locomotives. BNSF is now considering development of the EMD model 710 engine with ECI.

MK Rail. In 1993, MK Rail Corporation (now MotivePower Industries) introduced the MK 1200G switcher locomotive. This was an LNG mono-fuel locomotive powered by a Caterpillar model 3516G turbocharged, aftercooled, spark-ignited, lean-burn engine producing 1000 kW. The exhaust emissions characteristics of this LNG engine made it particularly attractive for use in the Los Angeles area, where the Union Pacific Railroad (UP) and BNSF each have successfully operated two of these locomotives in daily revenue switching service. MK Rail reports that these engines have NO_x levels of 2.7 g/kW-hr, CO levels of 2.5 g/kW-hr, total HC levels of 3.8 g/kW-hr, and PM levels of 0.11 g/kW-hr, measured in accordance with ISO 8178-1. These emission levels clearly demonstrate the potential for natural gas fuel to achieve very low exhaust emission levels, but reported performance also demonstrates the limited power density inherent with lean-burn spark-ignited gas engines. The Cat 3516G engine, rated at 1,000 kW on natural gas, is typically rated at nearly 1,900 kW on diesel fuel. As the railroads push for freight locomotives of higher and higher power capacity, spark-ignited lean-burn gas engines simply do not provide enough power density for high power applications.

Union Pacific Railroad. In March of 1992, EMD and the UP announced an agreement for modifying two EMD 3000 kW model SD60M locomotives which would run either on diesel fuel alone, or on dual-fuel with diesel and high pressure natural gas. In May of 1992, the Transportation Systems Division of the General Electric Company (GE) announced that they would develop a dual-fuel 3000 kW model Dash-8 locomotive for the UP. At that time, delivery and testing of these prototype locomotives were scheduled for mid 1993. Work progressed on demonstration units at both companies until 1995, when technical difficulties with the high pressure fuel injection systems on both designs, combined with the introduction of many other technologies on diesel locomotives, resulted in both builders suspending their LNG freight locomotive programs. EMD, however, has remained active in LNG locomotive developments for passenger applications.

GasRail USA. GasRail USA is a multi-year, cooperative industry research project, initiated in 1993 by SwRI to develop natural gas engine technology for U.S. railroad freight and passenger locomotives, and to demonstrate that the use of LNG can lower exhaust emissions. Participants in the program represent a wide range of organizations: the federal government, state agencies, freight and passenger railroads, original equipment manufacturers, and the natural gas industry. Members of the project have included the U.S. Department of Energy, South Coast Air Quality Management District, Southern California Regional Rail Authority, California Air Resources Board, Union Pacific Railroad, Electro-Motive Division of General Motors Corporation, Southern California Gas Company, Gas Research Institute, and Amoco Petroleum Products.

The GasRail project grew out of SwRI's extensive experience in developing engines that can operate on natural gas and other alternative fuels. The research and development phases of the project included both single and multi-cylinder engine development. Work is continuing with multi-cylinder engine development, and integration of an LNG-fueled engine and its associated fuel storage and handling systems into a 2250 kW EMD model F59PHI passenger locomotive. Following integration, on-track demonstrations of the passenger locomotive will be conducted in Los Angeles by the Southern California Regional Rail Authority (SCRRA), through its heavy-rail passenger service known as Metrolink. A photograph of the Metrolink F59PHI locomotive is given in Fig. 4.

Exhaust Emission Regulations—The Driving Force?

In 1988, the California Clean Air Act required the California Air Resources Board (CARB) to regulate a broad category of off-highway mobile sources, including locomotives. In response, the focus of the ongoing AAR research programs at SwRI shifted from fuel studies and engine durability issues to exhaust emissions testing. Gaseous and particulate emission measurements were performed the following year at SwRI on two 12-cylinder locomotive

Fig. 3 BN No. 7890 natural-gas fueled locomotive

Fig. 4 Metrolink F59PHI passenger locomotive before conversion to LNG

Table 1 Locomotive exhaust emissions summary

Diesel Locomotive Model	Engine Model	Number of Units Tested	AAR 3x3 Average Composite Emissions (g/kW-hr)[a]			
			HC	CO	NO_x	PM
EMD						
GP35	16-645D3A	1	0.68	3.8	9.9	0.6
MP15AC	12-645E	5	0.80 to 1.05	4.7 to 6.2	14.1 to 16.8	0.66 to 0.83[b]
SD40-2	16-645E3	4	0.93 to 1.3	2.0 to 3.0	14.6 to 15.2	nd
SD40-2	16-645E3B	5	0.31 to 0.43	1.3 to 2.4	15.6 to 17.2	nd
F40-PH	16-645E3B	1	0.36	0.67	16	0.38
SD50	16-645F3B (A.O.)	4	0.35 to 0.44	1.0 to 3.2	11.9 to 13.1	0.38 to 0.46
SD60	16-710G3	2	0.35	2.7	13.7	0.32
F59-PH[c]	12-710G3A	1	0.4	1.2	15.6	0.27
SD70MAC[d]	16-710G3C EFI	1	0.38	0.76	17.4	0.31
SD75M[d]	16-710G3EC EFI	1	0.38	1.2	17.6	0.31
GE						
C40-8	7FDL16	4	0.54 to 0.75	5.6 to 7.2	16.0 to 17.3	nd
B32-8	7FDL12J8	1	0.72	4.2	16.8	0.58
AMD-103	7FDL16N6	1	0.54	2	16.2	0.47
C44-9	7FDL16N6 EFI	1	0.28	1.9	15.2	0.16
C40-9[d]	7FDL16N19 EFI	1	0.36	1.2	19.3	0.15
Republic						
RD-20	DDC 16V-149	1	0.5	3.2	18	0.2
MK Rail						
MK 5000C[d]	Cat 3612 MUI	1	0.58	1.3	19.6	0.15

[a] Results presented as ranges represent 95 percent confidence intervals for the AAR 3x3 duty-cycle average weighted emissions at standard injection timing.
[b] PM data on MP15AC locomotives based on data from 4 of the 5 locomotives tested.
[c] Data on the EMD F59PH locomotive funded by Caltrans (Fritz 1992, Fritz 1994).
[d] Data based on EPA-funded testing (Fritz 1995)

research engines. The emission results were used as the basis for much of the California locomotive emissions inventory to determine what percentage of air pollution in the state was attributable to locomotives (Fritz, 1989; Booz-Allen, 1991). In 1990, work for the AAR progressed from emissions characterization to emissions reduction programs, which investigated the effects of retarded fuel injection timing, enhanced aftercooling, and use of low-aromatic, low-sulfur diesel fuel (Markworth, 1992; Cataldi, 1992).

The Federal Clean Air Act Amendments of 1990 directed the U.S. Environmental Protection Agency (EPA) to promulgate emission regulations for new locomotive engines by 1995. This action brought exhaust emission regulations to the attention of railroads nationwide, not just those operating in California. EPA estimates that current unregulated locomotives contribute about four percent of the total nationwide NO_x emissions, which is about nine percent of the total nationwide mobile source NO_x emissions. This makes locomotives one of the largest remaining unregulated sources of NO_x emissions in the U.S.

Because the service life of a locomotive is relatively long—typically 30 years or more—EPA regulations address both new and in-use locomotives. This process deviates significantly from other EPA mobile source regulations, in which only new automobile, truck, and bus engines are directly regulated. In addition, the resulting burden of compliance testing rests solely with the original equipment manufacturers (OEM). The railroad industry faces many of the same responsibilities as OEMs regarding emissions certification of their rebuilt or remanufactured engines.

In response to pending regulations at both the state and federal level, the railroad industry shifted the focus of research and development efforts at SwRI from laboratory engine work to field testing of in-use locomotives. The industry recognized that emission regulations were being developed without technical support information, and set out to develop in-use emissions data on which effective regulations could be based. Sponsored by the AAR, SwRI began field testing in-use locomotives at a temporary facility established at the UP Railroad switchyard in San Antonio. Between October 1992 and February 1993, SwRI tested 13 locomotives, covering three different engine models (Fritz, 1994; Fritz, 1995). On completion of these tests, it became apparent that future test requirements were such that a more permanent facility was needed, one which included particulate emissions measurement capability. In October 1993, locomotive exhaust emissions testing began at a new test site located near downtown San Antonio. The SwRI Locomotive Exhaust Emissions Test Center was developed in cooperation with the AAR and the Southern Pacific Railroad, and is located at a former SP repair shop. Since this facility opened, over 50 revenue-service locomotives, including some 18 engine models, have been tested (Fritz, 1995; Fritz, 1995). Presented in Table 1 is a summary of the locomotive exhaust emissions for the various engine models tested.

Table 2 gives the EPA locomotive emission levels for the following locomotive engines (Federal Register, 1998):

Exempt Pre-1973 engines: any engine manufactured before January 1, 1973 would be exempt from emissions regulation.

Tier 0 1973–2001 engines: any engine manufactured between January 1, 1973 and December 31, 2000.

Tier 1 2002–2004 engines: engines manufactured between January 1, 2002 and December 31, 2004.

Tier 2 2005 + engines: Engines manufactured after January 1, 2005.

NO_x emissions are the target of the Tier 0 and Tier 1 regulations. In general, the Tier 0 regulations represent roughly a 25 percent reduction in NO_x emissions for current locomotives, and a 40 percent NO_x reduction from today's levels for new locomotives manufactured between 2002 and 2005. HC, CO, and PM levels are already below the proposed levels for these locomotives. New locomotives manufactured after 2005 will have roughly a 60 percent reduction in NO_x, and also significant reductions in HC, CO, and PM. The proposed HC and CO levels for these locomotives will require the use of advanced engine or aftertreatment (catalyst) technologies for LNG-fueled engines, and maybe also for diesel-fueled engines.

Although California first proposed locomotive exhaust emission standards, their progress has been slowed by the EPA rulemaking, and specifically over jurisdictional issues of when a "new" locomotive, subject to EPA regulations, becomes "used," and therefore

Table 2 EPA locomotive emission standards

Engine Model Year	EPA Freight Duty-Cycle Composite (g/kW-hr)				
	HC	CO		NO_x	PM
		Diesel	NG		
1973 - 2001	1.20	6.4	15.4	12.7	0.80
2002 - 2004	0.74	3.0	13.4	9.9	0.60
2005 +	0.40	2.0	2.0	7.4	0.27

potentially regulated while operating in California. It appears that there will likely be a "Southern California" fleet of low emission locomotives beginning around 2010, in which the entire fleet of locomotives operating in a defined area would have to meet the 2005 Tier 2 standards. The relatively strict NO_x limits proposed present the best opportunity for application of widespread use of LNG in locomotives.

The U.S. railroads expect that in 2010, locomotives operating in the South Coast District will average no more than the EPA 2005 emissions limits of 7.4 g/kW-hr. One method the railroads could apply to meet the average is simply operating only locomotives manufactured after 2004. Alternatively, they could operate a mixed fleet that has some older power (switchers), some 2005 + units, and some locomotives that are lower in emissions than 2005 + locomotives, that are averaged against those that are higher than the 2005 + standards. The methodology used to "average" the emissions from different types of locomotives has not yet been determined. The South Coast average is a separate agreement between the BNSF and UP railroads and CARB.

Observations

Significant locomotive market penetration of LNG faces many challenges. U.S. government funding for research and development (primarily through the DOE) is getting smaller and smaller. The railroads are merging, and in the process, reducing or eliminating internal R&D groups. The industry is also changing the way it views locomotives. Prior to the 1980s, U.S. railroads purchased locomotives outright. In the 1980's, leasing locomotives became popular. Today, more and more railroads are simply buying MW-hrs, with locomotive ownership and maintenance provided by third parties, often the locomotive builders themselves. This current trend complicates the economic models for considering LNG.

As the EPA locomotive exhaust emission regulations are implemented, LNG will have to compete against low emission diesel technology which has been developed for on-highway truck-sized engines in the U.S. Furthermore, EPA regulations for HC and CO for locomotives built after 2005 will likely require advanced emission control systems for LNG-fueled engines. Also, the reliability of low-emission LNG-fueled engines in locomotive applications has yet to be proven.

Even in the face of these obstacles, LNG-fueled locomotives are likely to play a role in the future. California emission regulations will likely provide necessary incentives for introducing LNG into wide scale locomotive use. Future crude price/supply disruptions could trigger interest on a broader scale. The price of "reformulated" diesel fuel, if its use is required by the railroads, could also affect interest. Market economics will continue to push the railroads to reduce operating costs, and LNG may be an attractive alternative to diesel fuel.

In summary, unless there is a dramatic change in the price relationship between diesel fuel and LNG, emission regulations in Southern California will drive need for LNG-fueled locomotives, starting in 2010. For the next ten years, LNG use will be limited to small scale locomotive demonstrations. However, this is an important step in developing the necessary low-emission engine technologies, and to assess the capital requirements for LNG use in everyday railroad operations.

References

Bepple, G., et al., 1987, "The Economics of Natural Gas in Railway Locomotive Applications," Transport Canada Report No. TP8765E, International Rail Consultants.

Cataldi, G. R., and Widell, G. W., 1992, "Locomotive Exhaust Emissions: Combined Effects of Low-Sulfur, Low-Aromatic, High-Cetane Fuel; Retarded Injection Timing; and Increased Aftercooling," AAR Technology Digest TD 92-012.

Federal Register, 1998, Vol. 63, No. 73, pp. 18798–19084.

Fritz, S. G., et al., 1989, "Diesel Fuel Specification and Locomotive Improvement Program, Tenth Research Phase Final Report," SwRI Report No. 03-2695, AAR Report No. R-771.

Fritz, S. G., et al., 1994, "Locomotive Exhaust Emission Field Tests: Phase I—EMD SD40-2 and GE C40-8 Locomotives," SwRI Report No. 03-4171-C, AAR Report No. R-877.

Fritz, S. G., et al., 1995, "Exhaust Emissions From In-Use Locomotives," ASME Paper No. 95-ICE-4.

Fritz, S. G., Markworth, V. O., and Mason, R. L., 1995, "Exhaust Emission Field Tests of Several Locomotives: Phase II—EMD MP15AC, GP35, F40PH, SD60 and GE AMD-103, DASH8-32BWH, DASH9-44CW EFI, and Republic RD20 Locomotives," final report for the Association of American Railroads (AAR), SwRI Report No. 03-4171-D, AAR Report No. R-885.

Fritz, S. G., 1995, "Emission Measurements—Locomotives," draft final report submitted to the U.S. Environmental Protection Agency under work assignment 2-4 of EPA Contract No. 68-C2-0144, SwRI Project No. 08-5374-024.

Fritz, S. G., 1992, "Exhaust Emissions From Two Intercity Passenger Locomotives," SwRI Report No. 08-4976.

Fritz, S. G., 1994, "Exhaust Emissions From Two Intercity Passenger Locomotives," ASME JOURNAL OF ENGINEERING FOR GAS TURBINES AND POWER, Vol. 116, No. 4, pp. 774–783.

Gas-Fueled Railway Feasibility Study, 1994, SwRI Final Report No. 5285.

Gillispie, M. J., and Jensen, M. A., 1994, "Effects of Fuel Gas Mixtures on Power Limits in a Dual-Fuel Engine," *Natural Gas and Alternative Fuels in Engines*, ASME Publication No. ICE-Vol. 21.

Jensen, S. C., 1994, "A Retrofit System to Convert a Locomotive to Natural Gas Operation," *Natural Gas and Alternative Fuels in Engines*, ASME Publication No. ICE-Vol. 21.

Locomotive Emission Study, 1991, final report submitted to the California Air Resources Board by Booz-Allen & Hamilton, Inc.

Markworth, V. O., and Fritz, S. G., 1992, "The Effect of Injection Timing, Enhanced Aftercooling, and Low-Sulfur, Low-Aromatic Diesel Fuel on Locomotive Exhaust Emissions," ASME JOURNAL OF ENGINEERING FOR GAS TURBINES AND POWER, Vol. 114, pp. 488–495.

Olson, L. E., 1993, "The Natural Gas Locomotive at Burlington Northern Railroad," paper presented at the International Association of Railway Operating Officers, September 12–15, 1993, Chicago, Illinois.

Para, C. J., and Moyer, C. B., 1992, "LNG as a Fuel for Railroads: Assessment of Technology Status and Economics," Accurex Environmental Corporation for the Gas Research Institute under contract 0591-292-2153.

Railroad Facts: 1998 Edition, 1998, published by the Association of American Railroads, L.C. Card No. A66-7305.

Stolz, J. L., 1992, "Operating a Diesel Locomotive with Liquid Methane Fuel," ASME Paper No. 92-ICE-5.

Wakenell, J. F., 1987, "High-Pressure Late Cycle Direct Injection of Natural Gas in a Rail Medium Speed Diesel Engine," SAE Paper No. 872041.

Wakenell, J. F., et al., 1988, "An Investigation of High Pressure/Late Cycle Injection of CNG as a Fuel for Rail Applications," final report no. ORNL/Sub/85-22032/1 for the U.S. Department of Energy under contract No. DE-AC05-840R21400.

Variable Composition Hydrogen/ Natural Gas Mixtures for Increased Engine Efficiency and Decreased Emissions

R. Sierens
roger.sierens@rug.ac.be

E. Rosseel

University of Gent,
Laboratory for Transporttechnology,
Sint-Pietersnieuwstraat B-9000 Gent, Belgium

It is well known that adding hydrogen to natural gas extends the lean limit of combustion and that in this way extremely low emission levels can be obtained: even the equivalent zero emission vehicle (EZEV) requirements can be reached. The emissions reduction is especially important at light engine loads. In this paper results are presented for a GM V8 engine. Natural gas, pure hydrogen and different blends of these two fuels have been tested. The fuel supply system used provides natural gas/hydrogen mixtures in variable proportion, regulated independently of the engine operating condition. The influence of the fuel composition on the engine operating characteristics and exhaust emissions has been examined, mainly but not exclusively for 10 and 20 percent hydrogen addition. At least 10 percent hydrogen addition is necessary for a significant improvement in efficiency. Due to the conflicting requirements for low hydrocarbons and low NO_x, determining the optimum hythane composition is not straight-forward. For hythane mixtures with a high hydrogen fraction, it is found that a hydrogen content of 80 percent or less guarantees safe engine operation (no backfire nor knock), whatever the air excess factor. It is shown that to obtain maximum engine efficiency for the whole load range while taking low exhaust emissions into account, the mixture composition should be varied with respect to engine load.

Introduction

Hydrogen-enriched natural gas has been the subject of several research projects. These mixtures of natural gas and hydrogen are commonly named "Hythane" (a registered trademark of Hydrogen Consultants Inc.).

Main point of interest is that with the addition of hydrogen, the lean limit of natural gas operation can be extended, without going into the lean misfire region. This results in low and even extremely low NO_x levels with only a slight increase in hydrocarbons. The low exhaust emission levels are obtained without emission control equipment (without a catalytic convertor). The CO and CO_2 values are lower for any gaseous fuel compared to gasoline, and for hydrogen no CO or CO_2 is formed at all (from the fuel itself).

Although hydrogen is an alternative fuel with very clean burning characteristics, a high flame propagation speed and wide flammability limits, it also has disadvantages. The complexity and weight of hydrogen storage, the loss of power associated with the use of pure hydrogen and the backfire phenomenon are the most important ones. The addition of natural gas to hydrogen (also hythane, but with a high percentage of hydrogen) can solve the backfire problem. In many cases backfire restricts the operating region of the air-fuel mixture on the "rich" side. With natural gas addition stoichiometric mixtures can be run without any other precautions.

The proposition of an Equivalent Zero Emission Vehicle (EZEV) at 10 percent of the 1997 ULEV (ultra low emission vehicle) requirements by the California Air Resources Board (CARB) has encouraged the research in lean burn hydrogen or hythane spark ignited engines.

In the literature similar trends are found using hythane blends. When comparing the results in detail, one has to keep in mind that the composition of natural gas can be quite different (for different countries). The methane content can change from 90 to 98 percent, with sometimes high nitrogen concentrations (1 to 8 percent). This will of course influence the experimental results.

Hoekstra et al. (1994, 1995) examined a V8 Chevrolet 350 engine at one particular speed (12.7 kW, 1700 rpm, $\epsilon = 9{:}1$) with different hydrogen enriched compressed natural gas mixtures (0, 11, 20, 28, 36 percent H_2) to simulate a light-duty truck traveling along a level paved road at 55 mph. They found extremely low NO_x values at $\lambda = 1.6$ ($\phi = 0.625$) for the 28 and 36 percent H_2 blends (with 28 percent H_2 : NO_x = 28 ppm or 0.21 g/bhph and with 36 percent H_2 : NO_x = 12 ppm or 0.10 g/bhph).

In Hoekstra et al. (1996) described test results concerning the NO_x emissions and the efficiencies of two engines. They conclude that with a 30 percent hydrogen–70 percent natural gas mixture the NO_x levels can be less than 10 ppm. With negligible efficiency penalty relative to MBT spark timing: the first engine (the same as described above running at the same speed) operated at $\lambda = 1.54$ ($\phi = 0.65$); for the second engine (tests at Sandia National Laboratory on a single cylinder Onan engine; 0.49 l, $\epsilon = 14{:}1$) the air-fuel ratio λ was increased to 1.91 (or the equivalence ratio ϕ diminished to 0.52) to obtain this low NO_x level.

Swain et al. (1993) and Yusuf et al. (1997) made tests with a 20 percent hydrogen–80 percent natural gas blend on two engines (2 l Nissan and 1.6 l Toyota) under light load conditions. The increase in flame front propagation speed by H_2 enrichment was measured (up to 29 percent), with a lean limit of combustion for the hythane blend at $\lambda = 1.85$ ($\lambda = 1.56$ for pure methane). For hythane a 10 to 14 percent improvement in the brake thermal efficiencies over methane was found.

Larsen and Wallace (1997) and Cattelan and Wallace (1994) tested a turbocharged 3.1 l V6 engine under mid and high load conditions with a 15 percent H_2 hythane blend and found similar trends (for the exhaust concentrations in ppm) as the light load tests by Swain et al. (1993) and Yusuf et al. (1997). It was clearly

Contributed by the Internal Combustion Engine Division (ICE) of THE AMERICAN SOCIETY OF MECHANICAL ENGINEERS for publication in the ASME JOURNAL OF ENGINEERING FOR GAS TURBINES AND POWER.

Manuscript received by the ICE June 25, 1992; final revision received by the ASME Headquarters July 5, 1999. Associate Technical Editor: D. Assanis.

demonstrated that hythane reduces the exhaust concentrations of regulated pollutants and increases the efficiency of a spark ignition engine.

Raman et al. (1994) described lean burn and stoichiometric combustion tests with a three-way catalyst. The latter under steady state and transient conditions. For the lean burn (5.7 l GM V8) engine it was again shown that hydrogen extends the lean limit of natural gas, thereby enabling lower NO_x emissions without excessive THC. When the BMEP advantage of hythane is sacrified by retarding the spark advance until methane and hythane produce equal BMEP the NO_x concentrations drop significantly.

Bell and Gupta (1997) described tests with lean mixtures of natural gas blended with 5, 10, and 15 percent hydrogen on a 4 cylinder 2.5 l GM engine at 2200 rpm and 50 percent WOT. Engine performance parameters, heat release analyses and exhaust emissions of CO, NO, and HC were presented. Again the subject of the research was to extend the lean operating limit of the engine and to investigate the performance and emissions characteristics of the SI engine at these conditions. In the air-fuel ratio range 1.11 to 1.33 (equivalence ratio range of 0.75 to 0.90) the hydrogen addition did not result in a significant increase in BHP. At the natural gas lean operating limit $\lambda = 1.56$ ($\phi = 0.64$) hydrogen addition allowed an increase in power (up to 47 percent again with 15 percent H_2) due to an increase in the average flame speed maintaining a sufficient heat release rate for good combustion quality. The lean operating limit (15 percent H_2) was reached around $\lambda = 2.38$ ($\phi = 0.42$). Brake thermal efficiencies (15 percent H_2) were higher than for the other fuelling cases at corresponding equivalence ratios. A maximum BTE of 37 percent was found at $\lambda = 1.54$ ($\phi = 0.65$) and at $\lambda = 1.89$ ($\phi = 0.53$), an equal value compared to the use of pure natural gas at $\lambda = 1$. With the addition of H_2 and the extension of the lean limit, a minimum value of 0.11 g/bhph was obtained for NO_x over a relatively broad range of equivalence ratio. A smaller quench zone as the flame is able to propagate closer to the wall and a reduction of partial burning with H_2 addition results in a reduction of HC emissions. A significant change in the combustion process was observed with 10 and 15 percent H_2 addition (improvement in engine performance and a marked extension of the lean limit). With 5 percent H_2 addition the improvement was only small. It was envisioned that a minimum concentration of H_2 addition is required to result in an energy release rate increase large enough to affect performance.

Description of the Test Rig

Engine. A Crusader T7400 spark ignited engine (based on the GM 454 engine, best known as the Chevrolet Big Block) was adapted for gaseous fuels.

The engine specifications are as follows:

—8 cylinders in V
—bore: 107.95 mm
—stroke: 101.60 mm
—swept volume: 7.41 (454 in^3)
—compression ratio: 8.5:1
—engine speed: 1000–4500 rpm
—ignition sequence: 18436572

The engine is connected to a water (Froude) brake.

The gas (natural gas, hydrogen or hythane) is mixed with the air in a gas carburettor. The venturi of the gas carburettor is slightly under-dimensioned, which causes a lower volumetric efficiency and some power loss. For the comparison of the different fuels, this has no importance.

The composition of the natural gas consists of 91 percent methane, 6 percent ethane, 1.5 percent propane, 0.8 percent nitrogen and smaller fractions of higher hydrocarbons. The ignition is done by a single-firing system (one spark for each cycle of 720°ca), which is necessary to avoid backfire when using hydrogen. The ignition timing is regulated by a special disc on the distributor.

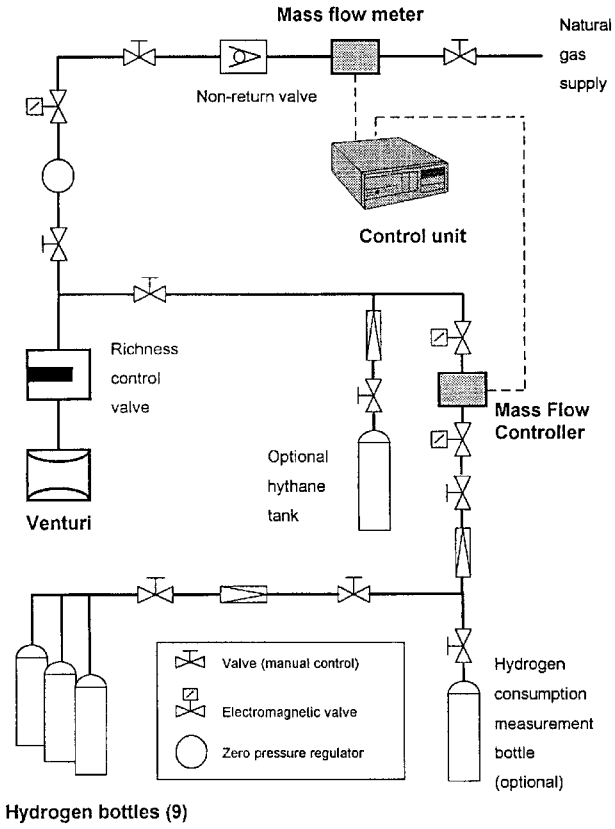

Fig. 1 The fuel preparation system

The Fuel Supply System. The layout of the system is shown in Fig. 1. The fuel is delivered to the engine through a gas venturi, which is supplied with the fuel mixture at a slight overpressure. The richness is controlled using a control valve in the supply line.

Both pure hydrogen and natural gas as well as mixtures of these fuels can be used with this system. The hydrogen is stored in 9 steel bottles at a pressure of 200 bar; the natural gas is obtained from the city gas net at 30 mbar overpressure. Measurement of the fuel flow rate is made using mass flow meters in both of the supply lines. The extra bottle in the hydrogen line was used previously to measure the hydrogen flow: the main supply line is shut off so that the hydrogen is consumed from the bottle.

If hythane is used, the hydrogen flow is controlled by a mass flow controller (the same device is used as mass flow meter for pure hydrogen). From the measured natural gas flow the necessary hydrogen flow is computed and supplied as input signal to the mass flow controller. This results in a constant hydrogen content (accuracy of flow meter and flow controller each 1 percent FS at calibrated conditions), independent of engine speed and load. The hydrogen concentration is given in volume percent (the term mass flow meter/controller only means that the measurement is automatically compensated for temperature and pressure changes, the reading is in Nm^3/h). Alternatively, hythane (or any other fuel) from a high pressure tank (200 bar) can be used for short runs: it contains a very limited amount of hythane and freezing problems can occur. By putting this tank on a scale fuel consumption can be measured as well.

Apparatus. The engine is fully equipped with the usual sensors. The measurement/control signals are read and controlled by a PLC system (programmable logic controller). This system monitors engine speed, oil and coolant temperature, exhaust gas temperatures, etc. and shuts off the engine when necessary. With a Microsoft Excel worksheet all values are stored and can be made visible on a screen.

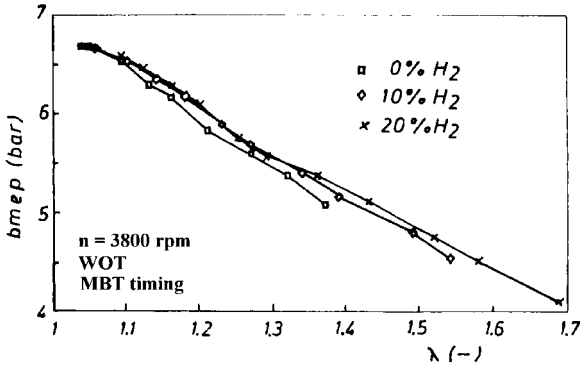

Fig. 2 The influence of the air-fuel ratio λ on bmep

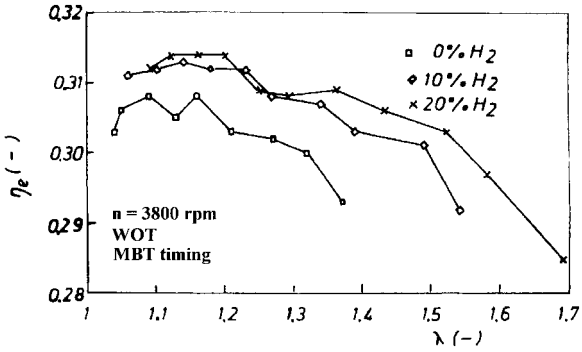

Fig. 3 The influence of the air-fuel ratio λ on the efficiency

The exhaust temperatures and the exhaust gas composition can be measured at the exhaust of each cylinder and at the end of each bank (V engine). Two O_2 (λ)-sensors are installed at the common exhaust pipe of each bank, which allows an immediate value of the air-fuel ratio of each bank. The λ-sensors and the exhaust temperatures give the possibility to check if all cylinders behave the same.

The exhaust gas components are measured with the following methods of measurement: CO, CO_2, NO, NO_2 (multor 610, non dispersive infra red); O_2 (servomex model OA 1100, paramagnetic), HC (Signal model 3000, flame ionization).

Experimental Results and Discussion

All measurements were made at 3800 rpm, with the throttle wide open (WOT). These conditions are chosen because at that engine speed maximum power is reached. No other throttle positions were used because for hythane and hydrogen the best efficiency is achieved when regulating power through adjustment of the air fuel ratio instead of the inlet pressure (this doesn't necessarily hold true for very low percent H_2 concentrations of hythane and for the very low loads in which we are not interested in this study). This is not the case for natural gas because its combustion becomes so slow at lean mixtures that efficiency suffers and even misfire occurs below a certain equivalence ratio (however, this depends to great extent on the engine considered). Therefore, the lean limit as such has not been investigated here.

The measurements are analysed with respect to mean effective pressure instead of power, to make the results less dependent on engine size and speed. For a similar reason, exhaust emissions are represented in g/kWh instead of ppm or volume percent: this way the dependence on effective engine power is avoided. More specifically, this also avoids the effect of the dilution with air of the noxious emissions in lean mixtures.

Natural Gas and Hythane With 10 and 20 Volume Percent Hydrogen.

Brake Mean Effective Pressure, Fuel Consumption, Thermal Efficiency, Volumetric Efficiency and Ignition Advance. In a first set of measurements a comparison is made between natural gas and two blends of hythane (hythane with 10 and 20 volume percent hydrogen, respectively). Each time, spark timing was optimised for maximum power (MBT).

Figure 2 shows how the air-fuel ratio λ ($\lambda = 1/\phi$) influences bmep. As can be seen clearly, the different fuel mixtures give very similar results: the only major difference is the ability of hythane to run leaner, the more so the higher the hydrogen content. For pure natural gas the lean limit gives a large reduction in engine power (however, no significant benefit is to be expected from such lean running: low efficiency and large hydrocarbon emissions).

The specific fuel consumption b_e (expressed in g/kWh) for the same conditions as in Fig. 2 has a lowest value between 1.1 and 1.2 for each of the fuels. Because of the very different lower heat values of combustion (for hydrogen 120 MJ/kg and for methane 50 MJ/kg), efficiency comparisons should be made using Fig. 3. This shows that a hydrogen addition of 10 percent increases efficiency moderately, whereas 20 percent hydrogen gives no significant extra benefit (for the same λ-value). This result is in agreement with Bell and Gupta (1997), they also found a significantly higher efficiency when adding 10 percent hydrogen, and no further improvement when going to 15 percent hydrogen.

Figure 4 gives the efficiency as a function of bmep for the fuels considered. This shows that at lower loads higher hydrogen contents always give a significantly higher efficiency.

Figure 5 shows that the volumetric efficiency, defined as the volume air and gas aspirated into the engine divided by the swept volume, is nearly independent of the fuel and only slightly dependent on the air fuel ratio (increases from 0.70 to 0.72). This is to be expected since the inlet manifold contains mainly air whatever the mixture used (more than 80 volume percent even with hydrogen). The low volumetric efficiency is due to the suboptimal inlet system (obstruction by the venturi), as mentioned before. The small influence of the air-fuel ratio can be explained by different flow losses in the venturi at different fuel flows.

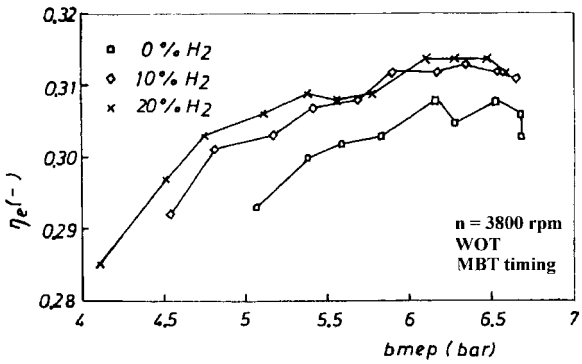

Fig. 4 Efficiency versus bmep

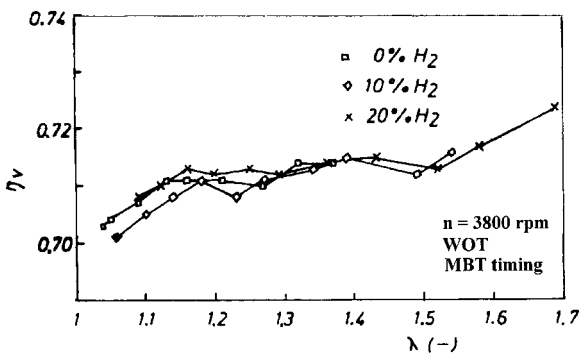

Fig. 5 The volumetric efficiency as a function of the air-fuel ratio λ

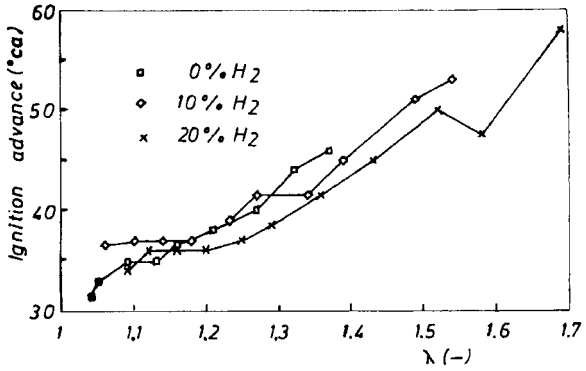

Fig. 6 The optimum ignition advance as a function of the air-fuel ratio λ

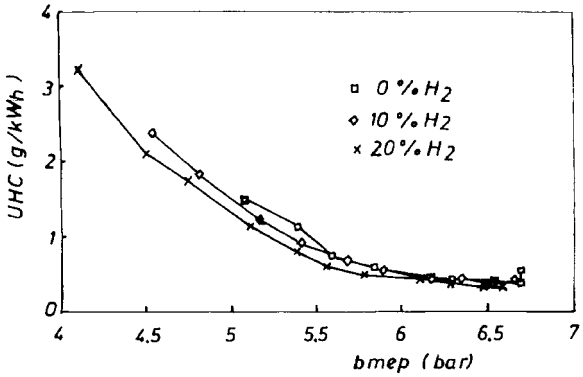

Fig. 9 The hydrocarbon emissions versus bmep

As can be seen in Fig. 6, the optimum ignition advance (MBT timing) decreases when hydrogen is added, because of the higher flame speed of hydrogen (Yusuf et al., 1997; Milton and Keck, 1984; Karim, 1996). Similarly, as is known from the literature (Heywood, 1988), leaner mixtures need more ignition advance (slower combustion).

Emissions. The hydrocarbon (UHC) and the NO_x emissions as functions of the air excess factor are shown in Fig. 7 and Fig. 8. Minimum hydrocarbon and maximum NO_x emissions are found for an air-fuel ratio of about 1.1. This result is in agreement with the literature, and holds for any fuel (see for example Heywood (1988) for gasoline and Bell and Gupta (1997) for hythane).

For leaner mixtures the combustion temperature is lower because of the lower heat of combustion available in the mixture, which reduces NO_x, and for richer mixtures less oxygen is available for the formation of NO_x. Hydrocarbon emissions are at minimum at an air-fuel ratio point slightly greater than stoichiometric (equivalence ratio point slightly less than stoichiometric) point because it's at this point that both adequate oxygen exists to ensure complete oxidation and temperatures are high, hence promoting complete combustion and good post combustion oxidation of crevice gases that escape the main combustion event. For very lean mixtures the flame may be unable to travel through the whole combustion chamber and in some cases the spark may be unable to ignite the mixture at all.

The Fig. 9 and Fig. 10 give the hydrocarbon and NO_x emissions as a function of bmep. They show that "at the same bmep" hydrogen addition increases NO_x and decreases unburned hydrocarbons, irrespective of bmep level. This result seems to disagree with results from the literature, which claim lower NO_x emissions when adding hydrogen. On inspection however, it becomes clear they compare natural gas with hythane with the latter running leaner (see for example Bell and Gupta (1997)), or with a reduced spark advance (see for example Raman et al. (1994)). Both these measures have the disadvantage of increasing unburned hydrocarbon emissions as well as decreasing efficiency. Also, the NO_x emissions can be reduced by retarding the spark from MBT for any fuel and therefore also for pure natural gas.

For comparison purposes, measurements with pure hydrogen are included in Fig. 8 and Fig. 10. Finally, Fig. 11 shows the NO_x versus efficiency, and Fig. 12 the NO_x versus UHC, for the different hythane mixtures. Figure 11 is a combination of the Fig. 2 and Fig. 8 and Fig. 12 is a combination of Fig. 7 and Fig. 8 or of the Fig. 9 and Fig. 10. It is reminded that all runs are done for 3800 rpm, WOT and the ignition timing set at MBT. The Fig. 11 and Fig. 12 show the definite advantage in NO_x for the same efficiency by increasing the H_2 content, with no HC penalty.

Hythane With 50, 67, 84 Volume Percent Hydrogen and Pure Hydrogen. In a second set of tests a preliminary investigation was made on the use of higher hydrogen fractions. Due to time constraints (high hydrogen consumption) the ignition advance was not optimized for each condition in this set of measurements,

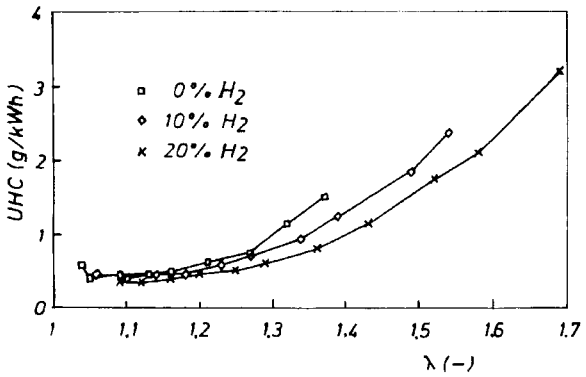

Fig. 7 The hydrocarbon emissions as a function of the air-fuel ratio λ

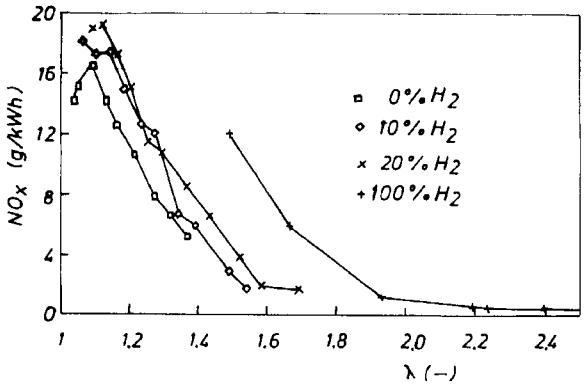

Fig. 8 The NO_x emission as a function of the air-fuel ratio λ

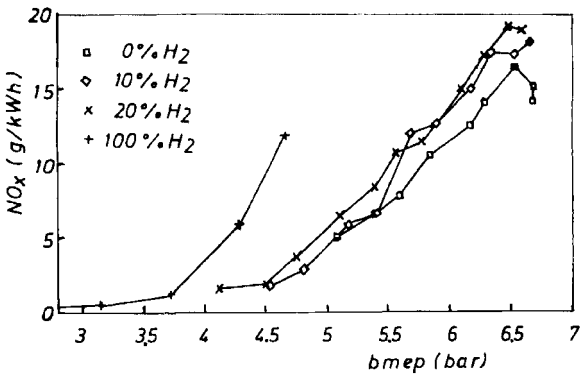

Fig. 10 The NO_x emission versus bmep

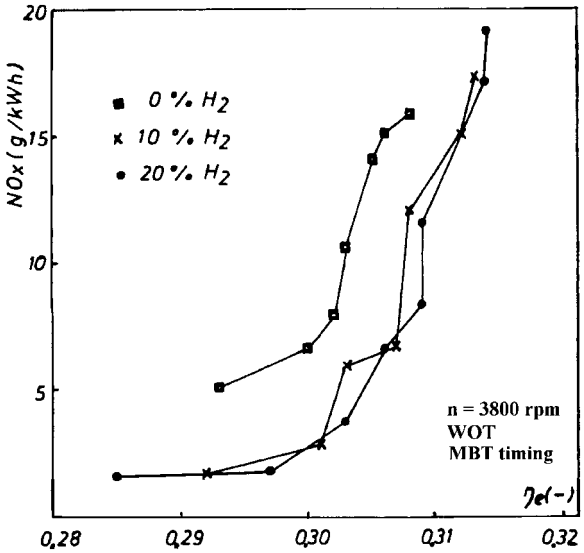

Fig. 11 The NO_x emissions versus efficiency

but was kept constant at 20 deg before TDC, except for pure hydrogen where the optimal spark advance was used (which varies from 12 deg at $\lambda = 1.5$ to 22 deg at $\lambda = 3.5$).

For pure hydrogen, the engine could function reliably (without backfire) for $\lambda \geq 1.5$. Hythane with less than 79 percent hydrogen never causes backfire nor knock in this engine, whatever the richness. During the measurements with 84 percent hydrogen knock (without backfire) occurred for $\lambda = 1.06$. This suggests that a hydrogen content of 80 percent or less guarantees safe operation of the engine, whatever the air-fuel ratio.

In Fig. 13 the bmep achieved by pure hydrogen and hythane with 50, 67, and 84 percent hydrogen is shown. Remarkably, all hythane mixtures give a very comparable output for λ between 1 and 1.3. This is in agreement with the results presented by Raman et al. (1994), who compared pure natural gas with hythane (30 percent hydrogen) and found the same bmep at $\lambda = 1.3$ and only 2 percent bmep loss at stoichiometry with hythane. The reason for this behavior is that increasing the hydrogen content

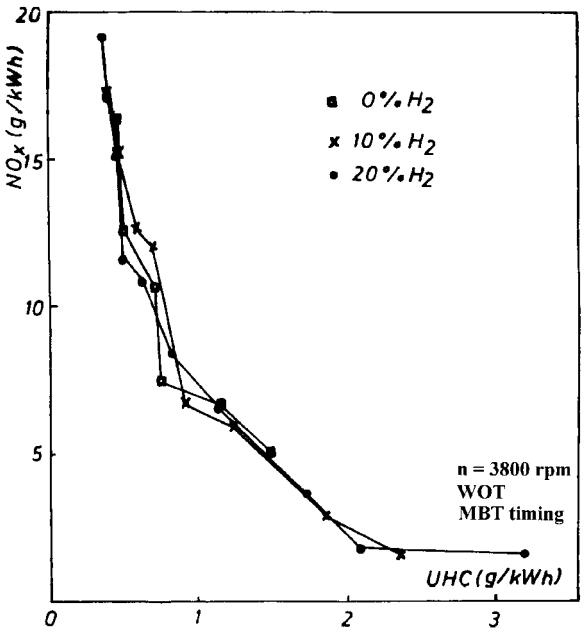

Fig. 12 The NO_x emissions versus hydrocarbon emissions

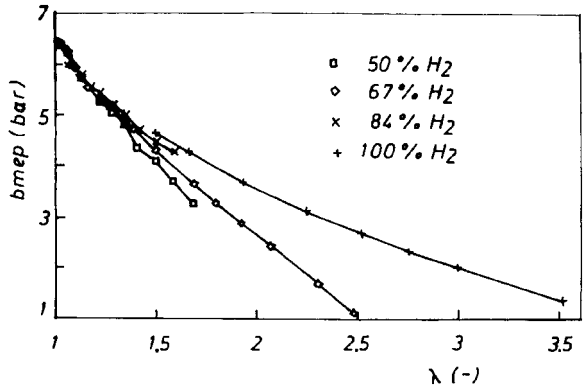

Fig. 13 The bmep for high hydrogen concentrations as a function of λ

increases flame speed (increasing bmep) but decreases the volumetric energy content (for $\lambda < 1.43$) (decreasing bmep). In the λ region considered both effects compensate each other largely. For $\lambda > 1.43$ the volumetric energy content as well as the flame speed increase with higher hydrogen contents, which causes higher bmep for those mixtures. At these air-fuel ratios the bmep drops significantly though.

For strongly lean mixtures pure hydrogen gives the highest output, as it is the only fuel capable of fast combustion at these conditions. For the high hydrogen content leaner mixtures are possible as given in Fig. 13. The lean limit as such has not been the goal of this study.

The Low Emission Potential of Hythane

Most if not all of the literature about the use of hythane concerns the possibility to achieve extremely low emissions. We will now investigate how this can be done.

Assuming that an ultra low emission vehicle (ULEV) with a fuel consumption equivalent to 10 l gasoline per 100 km (fuel density of 0.75 kg/l) during a test cycle has to be designed, the emissions performance of the engine can be estimated. The following analyses holds for any test cycle as the engine load is regulated without a trottle but by the air-fuel ratio (no loss of control of the air-fuel ratio during transient conditions). If we take the average engine efficiency equal to 20 percent, the ULEV limits (1.7 g CO per mile, 0.04 g NMOG per mile and 0.2 g NO_x per mile) convert to an average engine emission level of no more than 15 g CO per kWh, 0.35 g NMOG per kWh and 1.75 g NO_x per kWh. These average engine emission levels are roughly calculated as follows: 10 l/100 km $\times$ 0.75 kg/l $\times$ 0.20 (η_e) $\times$ 43.5 10^6 J/kg (H_u) $\cdot$ (3600 10^3)$^{-1}$ kWh/J gives 0.181 kWh/km. For CO one finds 1.7 g/mile $\times$ 1.609 mile/km/0.181 kWh/km $\cong$ 15 g/kWh.

Looking at the emission graphs, it seems that the hydrocarbon emissions are always too high. However, because the unburned hydrocarbons (UHCs) originate mainly from the fuel and more specifically from the natural gas fraction of the fuel, they are mostly methane. Because the ULEV limits concern nonmethane organic gases (NMOG; methane is not relevant with respect to the formation of tropospheric ozone), this improves the chances to comply with the limits. Unfortunately, the exhaust gas analysis equipment available for the experiments described here, didn't allow the measurement of NMOG directly.

The CO emissions from the tested engine are very low, as is the case for any gaseous fuel, and therefore it doesn't cause major problems when trying to comply with the limits.

As can be seen from Fig. 8, the NO_x emissions are only low enough for very lean hydrogen and lean hythane mixtures. In the case of hythane, the higher the hydrogen fraction, the leaner the engine has to run and the lower the achievable bmep. At these conditions the engine produces a lot of UHC (see Fig. 7), which makes it extremely unlikely that the NMOG limit can be attained

without exhaust gas treatment. The use of pure hydrogen gives no problem with NMOG, since only a negligible amount of UHC is emitted (no hydrocarbons in the fuel).

For lean mixtures, it is however possible to reduce CO and UHC (and therefore NMOG) emissions by using an oxidation catalyst. If we take into account that the NMOG fraction is reduced more strongly than the methane fraction, it is very probable that in this way the NMOG limits can be fulfilled.

Therefore, the following strategy to run the engine can be proposed.

- At low loads, pure hydrogen is used ($\lambda > 2$), limiting NO_x and eliminating NMOG and CO emissions.
- At intermediate loads, hythane is used in such a way that NO_x remains low. The oxidation catalyst reduces CO and NMOG emissions to acceptable levels.
- At full load (nearly) pure natural gas is used, providing high maximum bmep.

Although this means high emissions at full load conditions, this is not a major concern with respect to the legal limits since these conditions don't occur in the test cycles used to measure emissions. Also, during everyday vehicle use the engine is mainly operated at part load reducing the need to optimize emissions at full load. If low emissions are to be reached at all operating conditions, a three way catalyst may be used with $\lambda = 1$ operation at high loads. This necessitates the use of a throttle to regulate power in the high load region and is unpractical without a drive by wire system. A less complicated solution would be to make the high load region simply unavailable for the driver (not an acceptable solution to the end user).

Such a system has the following advantages:

- *High Efficiency.* WOT is used at all but the lowest loads, avoiding throttling losses. Figure 4 shows that near optimal efficiency is reached. Spark advance is set at MBT.
- *Low emissions.*
- *Low Knock Sensitivity.* At high loads pure natural gas with a high ON is used; at lower loads lean running avoids knock. This opens the possibility for high compression ratios, which increase efficiency.
- *Backfire is Avoided.* Since hydrogen is not used at $\lambda < 1.5$, backfire can be avoided without taking any special precautions.

The disadvantages are as follows:

- *Weight and Volume.* Two fuels must be stored.
- *Complexity and Cost.* A mixing system is necessary to control the hydrogen/natural gas ratio.

Conclusions

A fuel supply system was designed and implemented that provides the engine with a hydrogen/natural gas mixture in a variable proportion. The composition of this mixture can be set independently of engine operation. For future practical applications, minimal modifications should allow this variable mixture composition with respect to engine load for maximum efficiency and minimal pollution.

For hythane with low hydrogen content (up to 20 percent) a limited improvement in emissions can be obtained. Because of the conflicting requirements for low hydrocarbons and low NO_x extremely low emissions are not possible without exhaust aftertreatment: to reduce hydrocarbon emissions λ must be less than 1.3, while for low NO_x λ must be at least 1.5.

For lower bmep, high efficiency can be achieved by increasing the hydrogen content and thus avoiding throttling losses. At the same time unburned hydrocarbon emissions are minimized, while (for lean mixtures) NO_x emissions stay limited. This means that for optimal results the composition of the fuel should depend on load.

References

Bell, S. R., and Gupta, M., 1997, "Extension of the Lean Operating Limit for Natural Gas Fuelling of a Spark Ignited Engine Using Hydrogen Blending," *Combustion Science and Technology*, Vol. 123, pp. 23–48.

Cattelan, A. I., and Wallace, J. S., 1994, "Hythane and CNG Fuelled Engine Exhaust Emission and Engine Efficiency Comparison," Proceedings, 10th World Hydrogen Energy Conference, Cocoa Beach, Vol. 3, pp. 1761–1770.

Dhooge, D., and Pussemier, B., 1997, "Ombouwen van een GM-motor tot een waterstofmotor (Converting a GM-engine into a Hydrogen Engine)," end of year thesis, Laboratory for Machines, University of Gent, Gent, Belgium.

Heywood, J., 1988, *Internal Combustion Engine Fundamentals*, McGraw-Hill, New York.

Hoekstra, R. L., Collier, K., and Mulligan, N., 1994, "Demonstration of Hydrogen Mixed Gas Vehicles," Proceedings, 10th World Hydrogen Energy Conference, Cocoa Beach, Vol. 3, pp. 1781–1796.

Hoekstra, R. L., Collier, K., Mulligan, N., and Chew, L., 1995, "Experimental Study of a Clean Burning Vehicle Fuel," *Int. J. Hydrogen Energy*, Vol. 20, No. 9, pp. 737–745.

Hoekstra, R. L., Van Blarigan, P., and Mulligan, N., 1996, "NO_x Emissions and Efficiency of Hydrogen, Natural Gas and Hydrogen/Natural Gas Blended Fuels," SAE Paper 961103.

Karim, G. A., 1996, "Hydrogen as an Additive to Methane for Engine Applications," Proceedings, 11th World Hydrogen Energy Conference, Stuttgart, Vol. 2, pp. 1921–1926.

Larsen, J. F., and Wallace, J. S., 1997, "Comparison of Emissions and Efficiency of a Turbocharged Lean-Burn Natural Gas and Hythane-Fuelled Engine," ASME Journal of Engineering for Gas Turbines and Power, Vol. 119, pp. 218–226.

Milton, B. E., and Keck, J. C., 1984, "Laminar Burning Velocities in Stoichiometric Hydrogen and Hydrogen-Hydrocarbon Gas Mixtures," *Combustion and Flame*, Vol. 58, pp. 13–22.

Raman, V., Hansel, J., Fulton, J., Lynch, F., and Bruderly, D., 1994, "Hythane—An Ultra Clean Transportation Fuel," Proceedings, 10th World Hydrogen Energy Conference, Cocoa Beach, Vol. 3, pp. 1797–1806.

Sierens, R., 1993, "Comparative Tests on a SI Engine Fuelled With Natural Gas or Hydrogen," ASME Winter meeting Houston 93, ASME/ICE Engine Symposium at the Energy-Sources Technology Conference, ASME Paper 93-ICE-15.

Swain, M. R., Yusuf, M., Dülger, Z., and Swain, M. N., 1993, "The Effects of Hydrogen Addition on Natural Gas Engine Operation," SAE Paper 932775.

Yusuf, M., Swain, M. R., Swain, M. N., and Dülger, Z., 1997, "An Approach to Lean Burn Natural Gas Fuelled Engine Through Hydrogen Addition," Proceedings, 30th ISATA Conference, Florence, paper 97EL081.

Analysis of Combustion in Diesel Engines Fueled by Directly Injected Natural Gas

P. G. Hill

B. Douville

Department of Mechanical Engineering,
University of British Columbia,
2324 Main Hall,
Vancouver B.C., V6T 1Z4,
Canada

A single-cylinder two-stroke (DDC 1-71) diesel engine has been fueled with natural gas directly injected at high pressure into the engine cylinder. Prior to injection of the natural gas, a quantity of diesel fuel is injected into the cylinder (from the same injector) to provide for gas ignition. Tests have been conducted at medium load and speed over a wide range of injection timing, and with both conventional diesel and gas/diesel operation. With natural gas fueling, significant reduction in nitrogen oxide emissions have been measured without significant loss in efficiency, relative to conventional diesel operation. Using measurements of cylinder pressure development, a new method of combustion analysis has been used to estimate mass burning rate, burned gas temperature, and rate of nitrogen oxide (NO) generation. The method uses a nonlinear regression technique to determine the distribution with crank angle of the cylinder heat loss rate. The method assumes that NO formation takes place within one turbulent mixing time following combustion of each fuel-air increment. Comparison of measured and calculated NO concentration in the exhaust over the whole range of injection timing shows that for both conventional diesel and gas/diesel operation the effective turbulent mixing period is equivalent to 4 degrees of crank angle at 1250 RPM. The results demonstrate that a mass burned method can be used to infer cylinder temperature distributions and NO formation rate as well as the progress of combustion.

Introduction

Natural gas as a fuel for diesel engines offers the advantage of reduced emissions of nitrogen oxides, particulate matter, and carbon dioxide while retaining the high efficiency of the conventional diesel engine. Direct injection of natural gas at high pressure (late cycle injection) retains the characteristic features of diesel combustion without the need for throttling or reduced compression ratio. With high pressure direct injection the engine is not vulnerable to knock since the fuel is not mixed with air during compression. Thus the engine can operate at high compression ratio with a wide range of natural gas composition, e.g., with high propane content.

A disadvantage of natural gas use in diesels is the high autoignition temperature of the mostly methane mixtures. The autoignition temperature of methane under diesel-like conditions has been shown by Naber et al. (1994) to exceed 1200 K, much above the maximum compression temperature in conventional diesel engines. Thus, ignition assistance is needed and possible methods include prior combustion of a pilot quantity of diesel fuel, glow plugs (Fukuda et al., 1993; Aesoy and Valland, 1996) or other possible methods such as spark discharge or plasma jet injection.

With pilot-ignited natural gas a quantity of diesel fuel is needed at all loads to ignite the natural gas by direct contact with the products of the diesel pilot combustion. The required proportion of diesel pilot fuel to natural gas may vary from a few percent at high load to a large fraction at low load. The natural gas and pilot liquid enter the chamber through different nozzles, with the liquid injection being a few degrees in advance of the gaseous one. The ignition delay with combined fueling is addressed in this paper by examining in a single-cylinder two-stroke engine the result of using natural gas together with a relatively large proportion of diesel pilot liquid fuel at medium and light load where the combustion pattern can be easily inferred from cylinder pressure and other measurements.

A central purpose of this paper to demonstrate a new method of determining burning rate and tracking NO formation in two-stroke diesel engines. The method uses cylinder pressure and intake and exhaust measurements to determine simultaneously, via a nonlinear regression technique, the cylinder heat loss, and the mass burning rate. With the assumption of locally stoichiometric combustion the procedure determines the temperature development of each increment of combustion product. The method includes a model for NO formation which allows the kinetics of the extended Zeldovich mechanism to operate during one turbulent mixing time subsequent to combustion of each incremental quantity of fuel. Experimental and analytical results are compared over a range of injection timing and substantial differences are found between 100 percent diesel and gas/diesel operation.

The Experimental Program

The measurements were made on a single-cylinder Detroit Diesel (DDC) engine whose specifications are given in appendix A. The engine has been instrumented to indicate mass flow rates of air and fuel, airbox temperature and pressure, cylinder pressure, and exhaust temperature as well as torque and speed. In addition NO*x* measurements were made and recorded as NO equivalent.

For conventional diesel fueling, the commercially available electronic DDC injector was used. For sequential injection of both conventional diesel fuel and natural gas, the injector shown in Fig. 1 was used. It is a modified version of the electronically controlled DDC injector. As shown, it is cam actuated to produce hydraulic lifting pressure whose buildup is controlled by a solenoid-operated valve on the liquid fuel return line. In the modified injector two concentric needle valves are operated; the inner (liquid fuel) needle opens first, followed by the outer gas needle. The diesel pilot quantity injected is limited by the stroke of the pilot plunger. The delay in opening of the outer gas needle relative to the inner liquid fuel needle is controlled by selection of needle closing springs.

Tables 1 and 2 show the range of test conditions for both diesel

Contributed by the Internal Combustion Engine Division (ICE) of The American Society of Mechanical Engineers for publication in the ASME Journal of Engineering for Gas Turbines and Power.

Manuscript received by the ICE, December 4, 1997; final revision received by the ASME Headquarters July 27, 1999. Associate Technical Editor: D. Assanis.

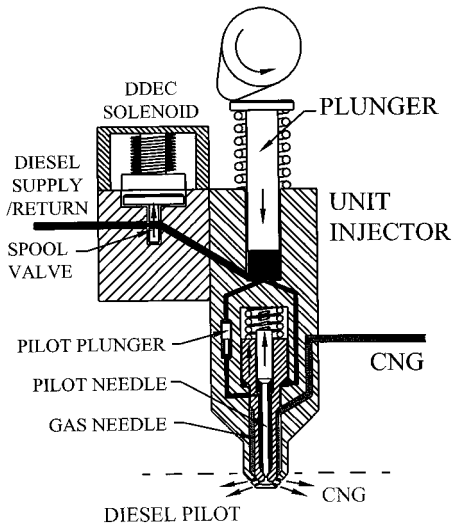

Fig. 1 Electronically controlled injector for natural gas and diesel pilot fuel

and diesel/gas fueling at 1250 rpm and 3 bar brake mean effective pressure (bmep), which is about 60 percent of rated load for this engine. The natural gas injection pressure was 140 bar. The composition of the natural gas was approximately the following percentages by volume: methane 95.5; ethane 3.0; propane 0.5; butane plus heavier hydrocarbons 0.2; nitrogen 0.6; carbon dioxide 0.2. In the column captions of Tables 1 and 2 boi signifies beginning of injection, pw pulse width, Mair the air flow rate (including scavenged air), Mdsl the liquid fuel rate, Mgas the natural gas flow rate, Tairbox the airbox temperature, Pairbox the air box pressure, and Texh the exhaust temperature.

Cylinder pressure measurements were made with a PCB112A10 piezo-electric pressure transducer whose readings were adjusted in two respects. To provide a static datum the dynamic indications were uniformly shifted to agree with airbox pressure at inlet port closure. This measure was found to be consistent with an apparent average polytropic compression coefficient of 1.30 ± 0.02 in each case. To correct for crank angle phasing it was found necessary to shift crank angle indications by -1 degree to provide peak compression pressure (in the absence of combustion) about one degree

Table 1 Conventional diesel fueling: 3 bar bmep and 1250 rpm

boi deg atdc	pw deg	Mair kg/h	Mdsl kg/h	Mgas kg/h	NOx ppm (wet)	Tairbox K	Pairbox kPa	Texh K
-7	11.0	111.6	2.45	0	294	353.0	123.7	613
-9	10.2	110.9	2.42	0	344	352.7	123.5	586
-11	9.8	111.5	2.39	0	420	352.9	123.1	569
-13	9.4	110.9	2.39	0	477	352.7	123.1	557
-15	9.3	109.9	2.40	0	568	351.7	122.8	549
-17	9.5	109.8	2.47	0	662	352.4	122.9	553
-19	9.6	111.5	2.52	0	720	352.8	122.9	555
-21	9.2	108.8	2.56	0	797	352.8	123.1	564

Table 2 Gas/diesel fueling: 3 bar bmep and 1250 rpm

boi deg atdc	pw deg	Mair kg/h	Mdsl kg/h	Mgas kg/h	NOx ppm (wet)	Tairbox K	Pairbox kPa	Texh K
-7	14.6	110.9	0.611	1.776	258	352.8	120.3	608
-9	12.5	108.8	0.554	1.616	320	352.9	120.5	583
-11	12	110.1	0.570	1.573	381	352.2	120.0	575
-13	12	110.8	0.574	1.630	441	352.1	119.7	569
-15	12.1	111.5	0.606	1.613	509	352.1	119.7	566
-17	12.2	111.4	0.572	1.606	591	351.0	119.5	561
-19	12.5	109.8	0.543	1.620	684	351.0	119.6	561
-21	13.1	110.0	0.576	1.594	779	351.6	119.6	561

before top dead center. Due possibly to thermal effect on the pressure transducer during the expansion process the polytropic indices for the last 20 degrees of expansion before exhaust valve opening were as low as 1.30, i.e., considerably lower than the average isentropic index for the interval in question. This effect was corrected for by use, between maximum pressure and exhaust valve opening, of the formula

$$P' = P[1 - C\sqrt{(\theta - \theta_{max})}].$$

Here P is the measured pressure, P' is the corrected pressure, θ is crank angle, and θ_{max} is crank angle at the location of maximum pressure. The constant C was determined in each case so that the polytropic expansion index for the last 20 degrees of expansion before exhaust valve opening was 1.35, somewhat above the isentropic index for expansion and thus qualitatively consistent with the effect of heat loss during expansion. The square root dependence of the correction on crank angle difference corresponds to the impulse of a thermal wave impinging on the transducer at θ_{max}.

The cylinder pressure measurements for the operating conditions shown in Tables 1 and 2 are displayed in Fig. 2. The heating values of the fuel were taken to be 43,500 kJ/kg for diesel fuel and 50,000 for natural gas. Each pressure curve represents the results of averaging, over 20 consecutive cycles, the indicated pressures at each crank angle. Figures 2(*a*) and 2(*b*) both show that highest peak pressure corresponds to earliest beginning of injection. However, for the same injection angle (and the same load and speed in all cases) pressure development with the gas/diesel fueling is appreciably delayed relative to the conventional diesel case.

Thermodynamic Analysis

The method of analysis, which is described in detail by Hill and Douville (1997), consists of the following elements.

(1) Determination of the Composition and Temperature of the Cylinder Contents at Inlet Port Closure. This in turn requires determination of the trapped air quantity and the composition and temperature of the residual gases, which are deduced from overall stoichiometry and the exhaust gas temperature measurement. The assumption is made that the only residual gas constituents of importance for heat balance calculations are O_2, N_2, CO_2, and H_2O.

The manufacturer has determined that the trapped air quantity can be calculated from

Nomenclature

bmep = brake mean effective pressure
boi = beginning of injection
Mair = air flow rate (including scavenged air)
Mdsl = liquid fuel flow rate
Mgas = natural gas flow rate
P = measured pressure
P' = corrected pressure
Pairbox = air box pressure
pw = pulse width,
Q = instantaneous heat loss rate (kW)
r = scavenge ratio
Tairbox = airbox temperature
Texh = exhaust temperature
V_D = piston displacement
ρ_{airbox} = air density at airbox pressure and temperature
θ = crank angle
θ_{max} = crank angle at maximum cylinder pressure

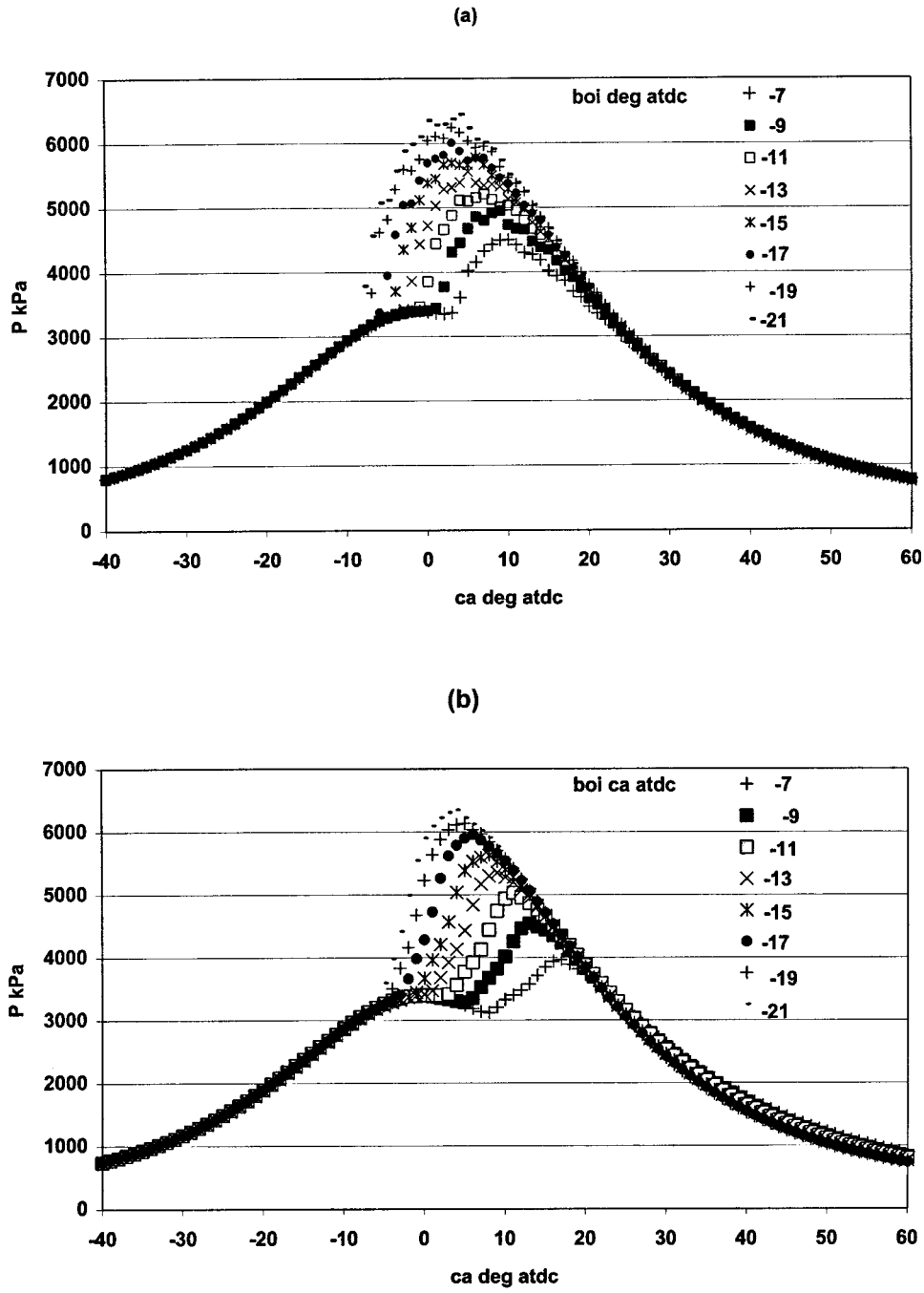

Fig. 2 Cylinder pressures: (*a*) 100 percent diesel fueling; (*b*) gas/diesel fueling

$$m_{\text{atrap}} = m_{\text{ideal}}[0.9 - (1.0 - 0.34)r \exp(-1.11r)]$$

in which r is the scavenge ratio $m_{\text{air}}/m_{\text{ideal}}$ and

$$m_{\text{ideal}} = \rho_{\text{airbox}} V_D$$

in which ρ_{airbox} is the air density at airbox pressure and temperature and V_D is the piston displacement volume.

(2) Determination of Cylinder Heat Loss and Bulk Gas Temperature During the Compression Period. With the gas composition known and constant during the compression process, the cylinder conditions at the beginning of injection, as well as the heat loss during compression are calculated from the measured cylinder pressures, and known variations of isochoric specific heats with temperature.

(3) Determination of Cylinder Heat Loss During the Combustion Period. The distributions of heat loss rate which Dent and Sulaimon (1977) have measured in diesel engine cylinders can be used to show that heat loss intensity can be well represented by skewed Gaussian curves such as are defined by

$$Q = Q_o \exp[-\tau^2/(1 + C_1\tau + C_2\tau^2)],$$

in which

$$\tau = \frac{\theta - C_3}{C_4},$$

and Q is the instantaneous heat loss rate (kW) and θ is crank angle after top dead center (atdc).

The four constants C_1 through C_4 and the constant Q_o are

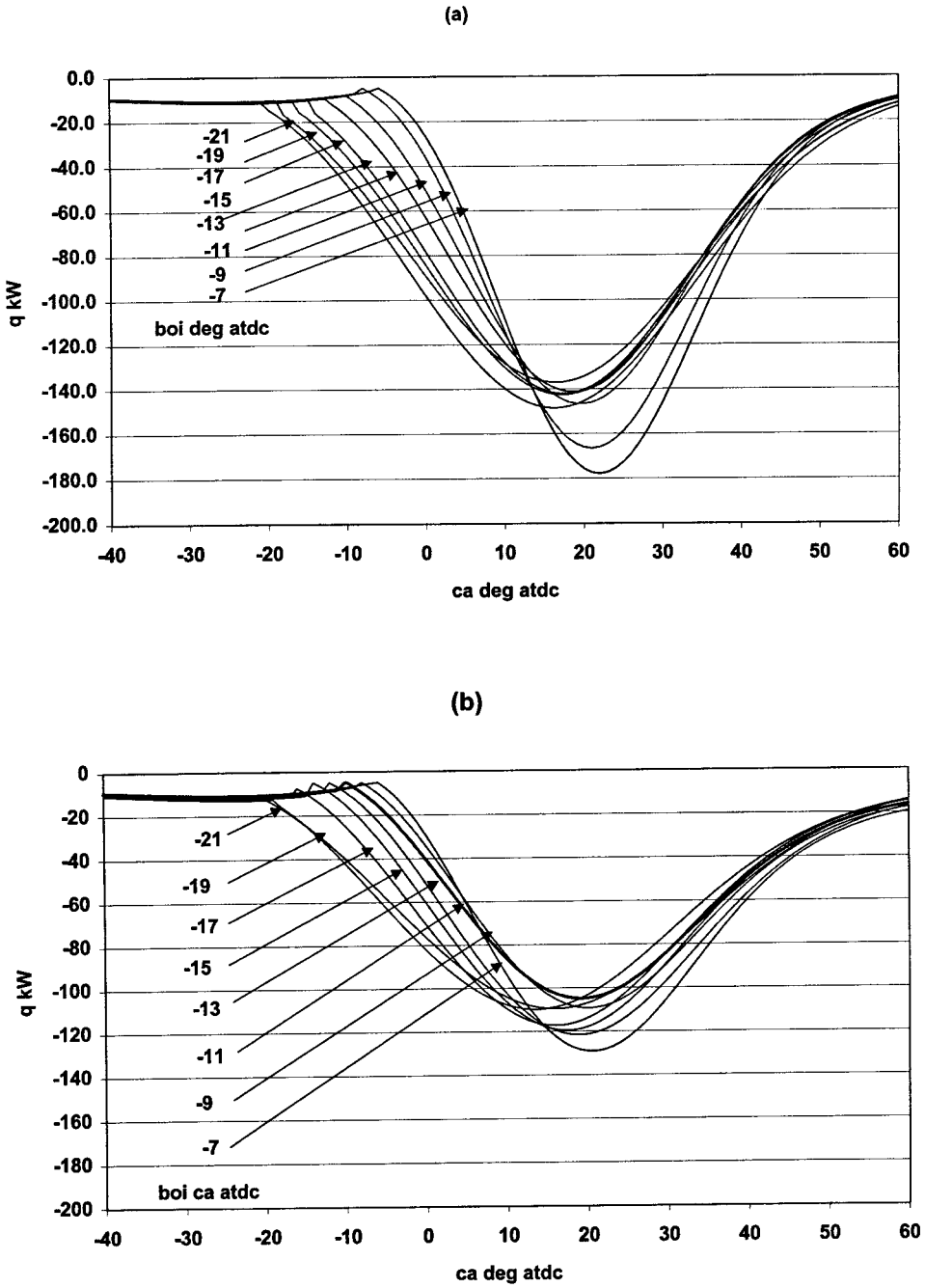

Fig. 3 Wall heat loss rate: (*a*) 100 percent diesel fueling; (*b*) gas/diesel fueling

determined by a nonlinear optimization procedure, which also determines the crank angle at the end of the combustion period. At the beginning of the injection period the form of the heat loss function is constrained to be consistent with a zero value of $dX/d\theta$, where X is the mass burned fraction.

The objective function for the optimization process consists of the weighted sum of the squares of (a) the difference between the calculated mass-burned fraction at the end of combustion and the one deduced from exhaust emission measurements, (b) the same difference for halfway between the end of combustion and exhaust valve opening, (c) the same mass-fraction difference for exhaust valve opening, (d) the difference between the integrated heat loss per cycle and the heat loss determined from an overall engine heat balance, and (e) the difference between the heat loss rate at the point at which the mass burned fraction was 0.975 and 15 per cent of the value of Q_o. It is typical that the heat loss from the cylinder during exhaust and intake processes is very much smaller than the heat loss during the combined compression and combustion period.

Beginning with assumed values of the heat loss parameters to be optimized, perhaps 50 iterations of the complete mass burned calculation procedure may be required to satisfy the objective function within what are believed to be the experimental uncertainties. Subroutine AMOEBA by Press et al. (1986) is used for the optimization process.

(4) Determination, During the Burning Period, of the Mass of Fuel Burned During Each Crank Angle Increment and of the Temperature of the Product Increment of Burned Gas. These two quantities are determined by satisfying the conservation of energy and mass while assuming locally stoichiometric combustion and equilibrium gas composition for products other than

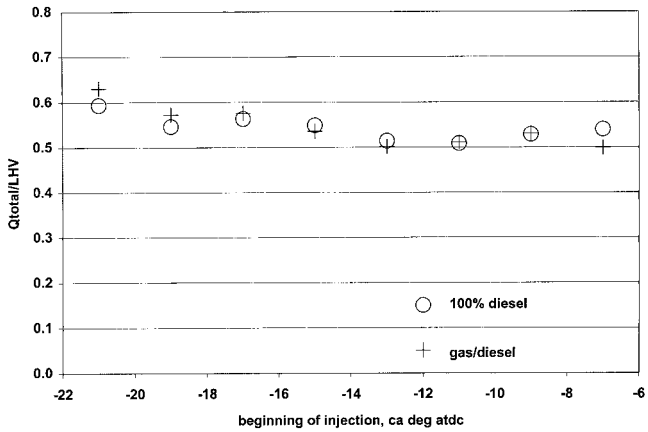

Fig. 4 Total relative heat loss to the wall

NO or NO_2. (The concentration of NO is far from equilibrium in the immediate post flame gas but is sufficiently small to have negligible effect on the conservation equations.) The equilibrium product compositions are obtained as functions of temperature and pressure by interpolation of tables created by the STANJAN program (due to Reynolds (1986)) for determining equilibrium product composition.

(5) Determination of the Generation of NO in the Post-Flame Combustion Gas Prior to Mixing. Subsequent to combustion but within one turbulent mixing time (thought of as L/u', where L is the integral length scale and u' the rms fluctuation velocity), the temperature of each increment of combustion product will change isentropically with pressure. During this period the rate of generation of NO is calculated using the extended Zeldovich mechanism (see Heywood (1988)). At the end of this period

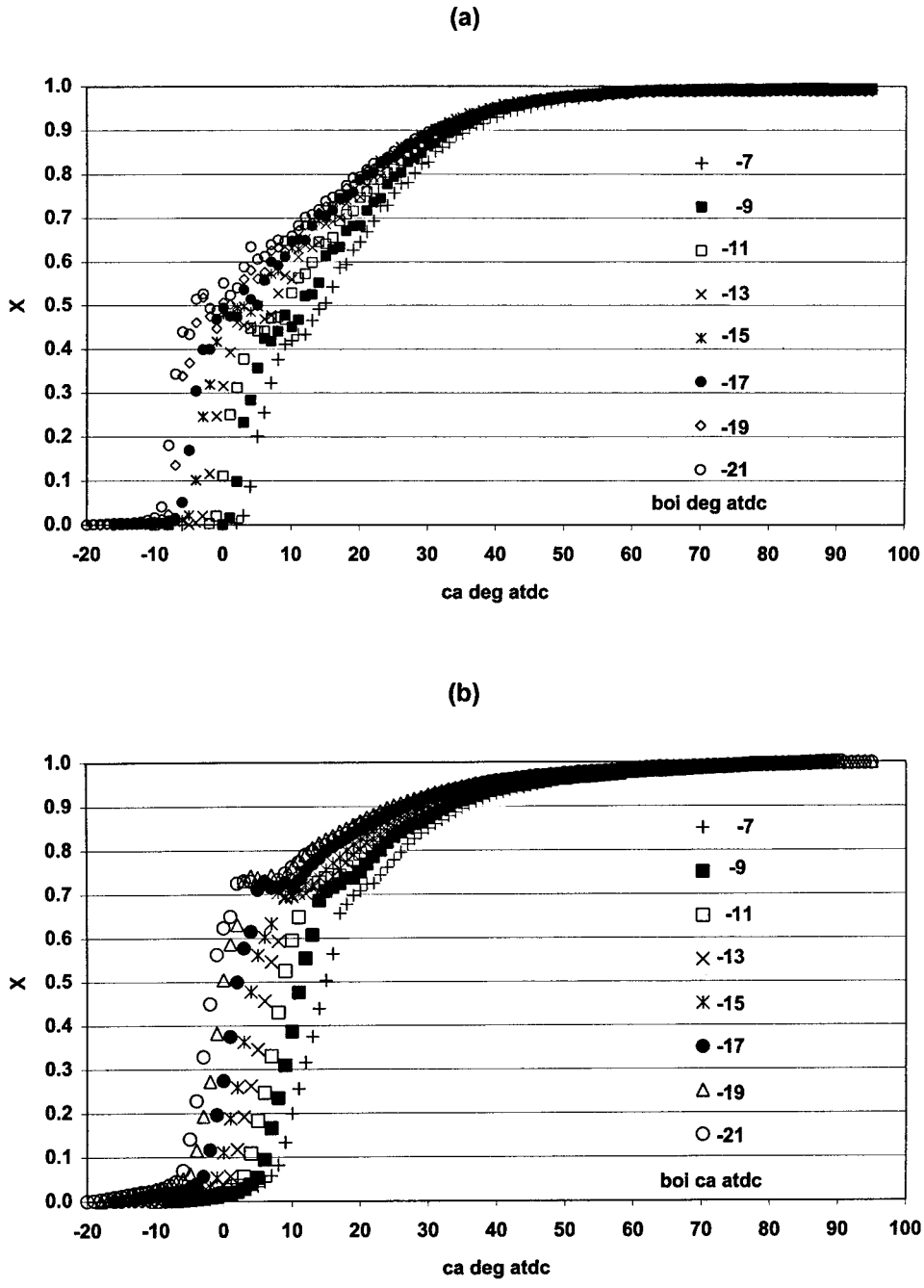

Fig. 5 Mass burn rates: (*a*) 100 percent diesel fueling; (*b*) gas/diesel fueling

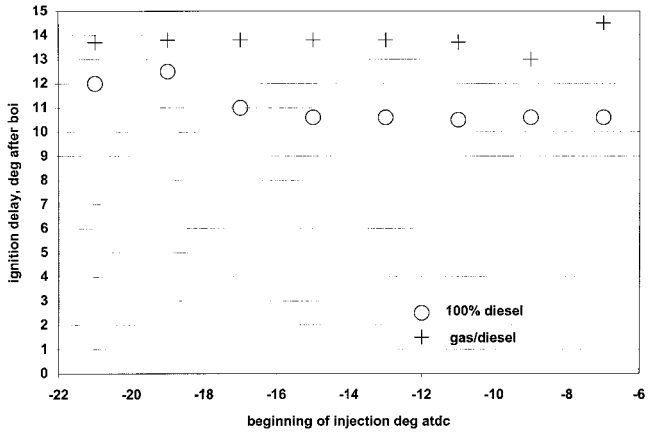

Fig. 6 Ignition delay: (*a*) 100 percent diesel fueling; (*b*) gas/diesel fueling

sudden mixing is assumed with the resultant temperature so low that no further NO is formed in the mixed increment. As will be shown, comparison of the total average concentration of NO produced in this way with the measured exhaust values shows that there is a characteristic mixing period for this engine at this rpm of about 4 degrees and that the NO concentration at the end of the mixing period is far from equilibrium.

(6) Determination of the Properties of the Burned-and-Mixed Gas Increments of Combustion Product. The mass mixing ratio of unburned gas to product gas is taken to be the same for all increments of combustion product and set so that all of the combustion products and remaining unburned gas are fully mixed at the end of combustion plus one mixing period. During the combustion period the masses and energies of all increments of burned gas and burned-and-mixed gas, as well as the remaining

(a)

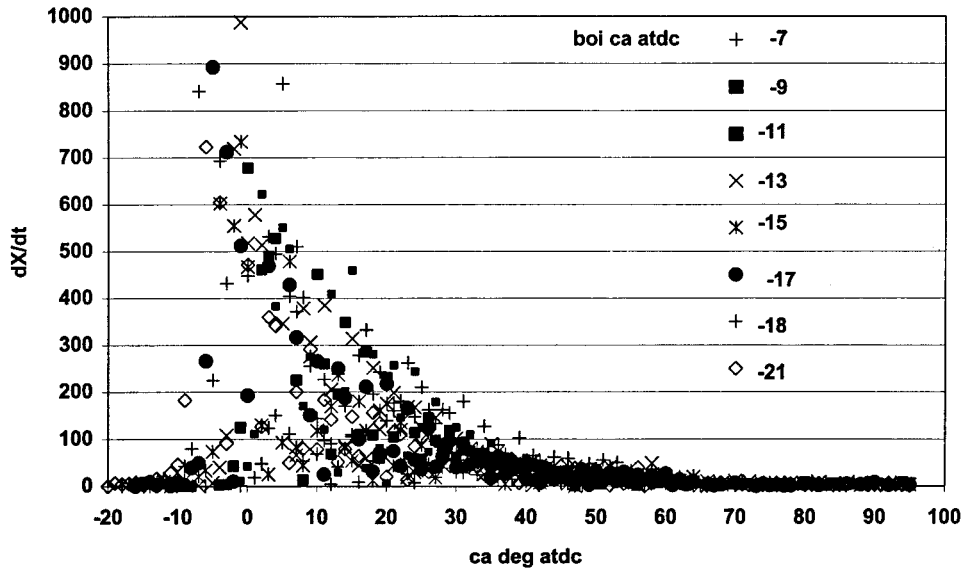

(b)

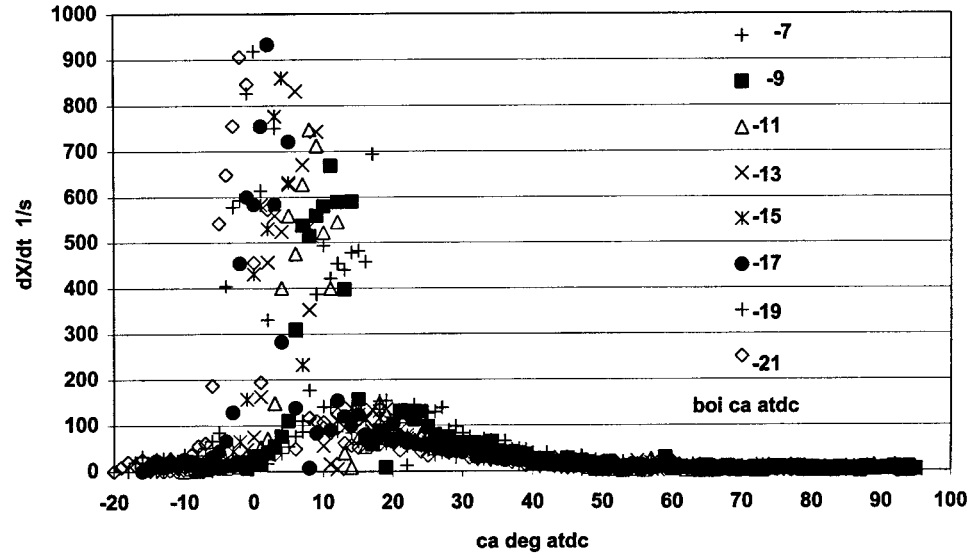

Fig. 7 Rates of change of mass burn rates: (*a*) 100 percent diesel fueling; (*b*) gas/diesel fueling

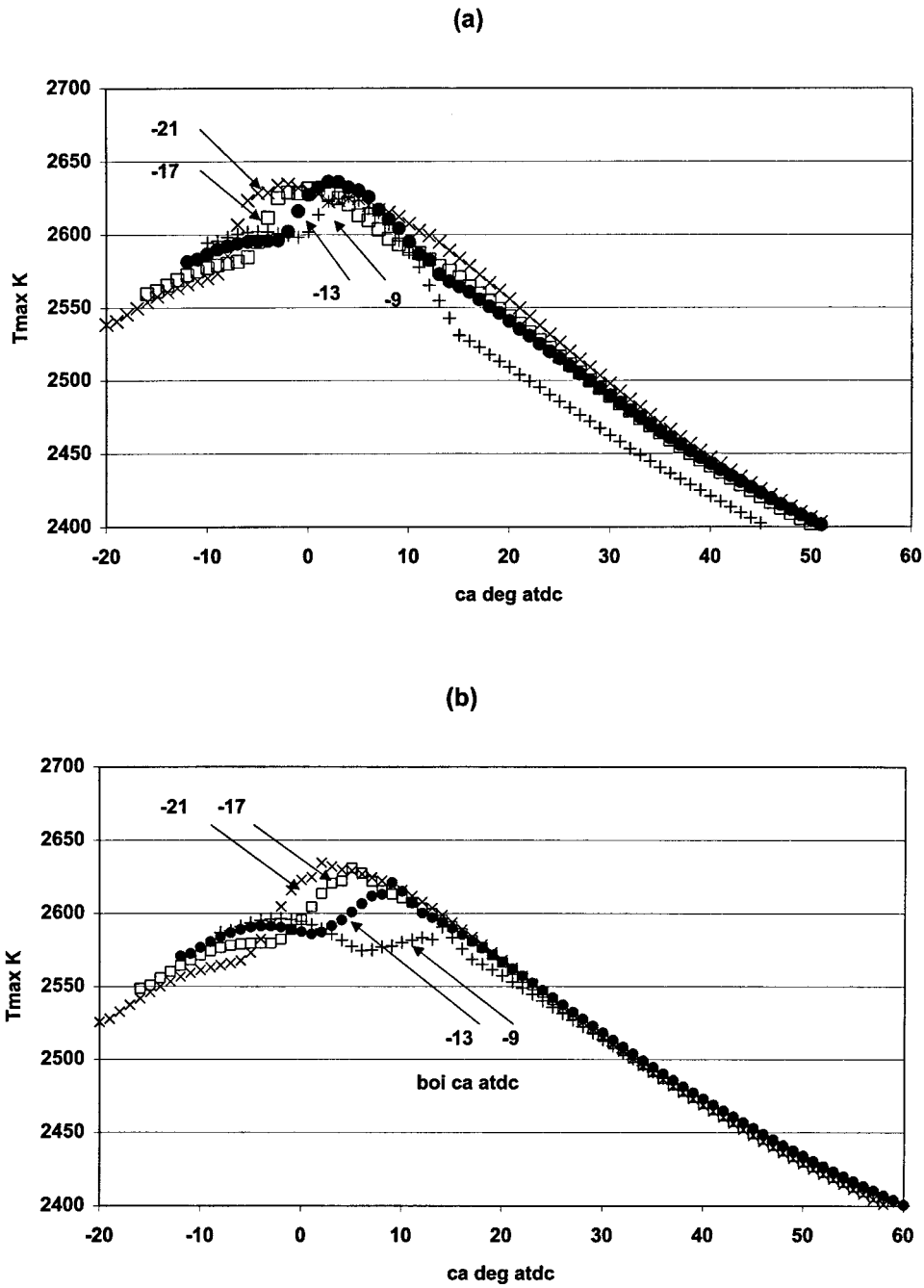

Fig. 8 Maximum burned gas temperature: (*a*) 100 percent diesel fueling; (*b*) gas/diesel fueling

unburned and unmixed gas, must be recognized in satisfying the conservation equations at the end of each crank angle increment.

The equations that express all of these requirements are given explicitly in Hill and Douville (1997)

Results

Figure 3 shows the calculated heat loss rate distributions for each of the injection timings for both diesel and gas/diesel operation. The magnitude of the heat loss rate decreases somewhat as the piston approaches top dead center and the surface area of the chamber decreases. This is followed however by a sharp increase in heat loss during the combustion period. Toward the end of the combustion period the apparent heat loss rate decreases to a small value. In this part of the process the surfaces of the combustion chamber are heated to quite high temperature while the bulk temperature of the gaseous content of the cylinder is decreasing due to expansion. The gradual shift with injection timing of the heat loss distribution is qualitatively the same for the conventional diesel case as for gas/diesel fueling. With the latter the peak heat loss rates are lower, partly due to relative delay in peak burning rate. The integrated total heat loss varies little with injection timing, as shown in Figure 4; the integrated heat loss as a proportion of the fuel heating value for each of the injection timings is essentially the same for both fueling cases.

Associated with the heat loss distributions displayed in Fig. 3, the calculated mass-burned fractions are shown in Fig. 5. A systematic variation of the distributions of mass-burned fraction is seen for the conventional diesel case and also for the gas/diesel case with generally more rapid rates of burning seen in the latter. From these curves the ignition delays, here defined as the crank

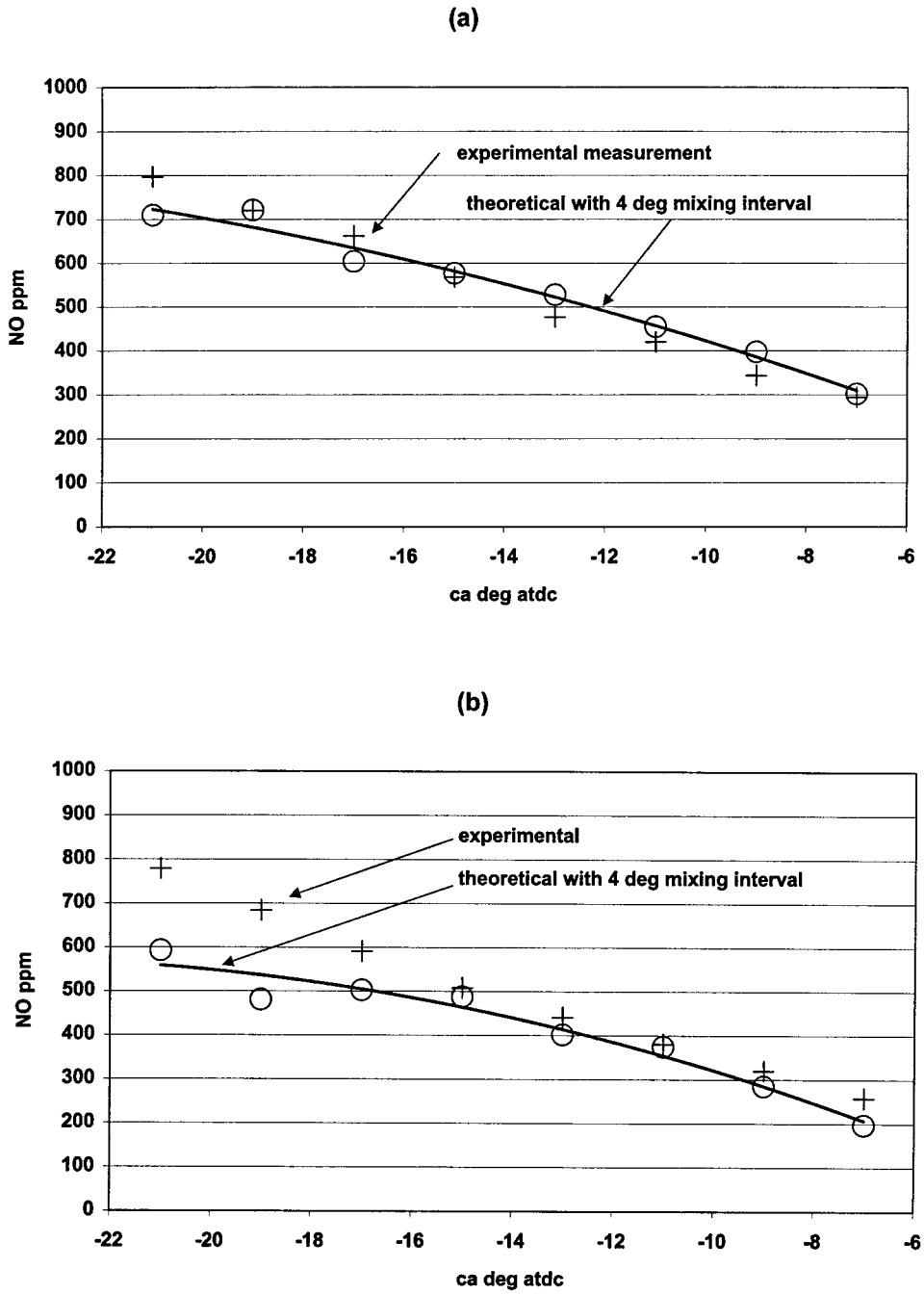

Fig. 9 NO*x* formation: (*a*) 100 percent diesel fueling; (*b*) gas/diesel fueling

angle differences between the electronically signalled beginning of injection and 5 percent burned have been measured and are displayed in Fig. 6. Though it may appear that, for the same injection timing the presence of the natural gas significantly delays the ignition of the diesel fuel, it should be noted that two quite different injectors were used with differing hydraulic responses. Thus differences in hydraulic response as well as in liquid atomization could account for most of the differences in ignition delay shown in Fig. 6.

It is may be seen from Fig. 7 that peak rates of burning are much the same for 100 percent diesel and gas/diesel fueling. However, in the latter case the peak rates appear to be associated with the diesel liquid portion of the fuel. When the diesel liquid combustion is complete there appears to be a sudden drop in burning rate. Such an effect will of course depend strongly on relative diesel liquid and gas injection timing and on the relative proportions of these two fuels.

Figure 8 indicates calculated peak temperatures associated with the increments of burned products formed at each crank angle. The peak temperatures are, as one would expect, highest for earliest injection timing but the variation in peak temperature is not large. It is notable, however, that for the case with highest peak temperature there is considerably more rapid subsequent decline in temperature than with other cases. For natural gas fueling the peak temperatures are, for the given injection parameters, somewhat delayed but much the same as with conventional diesel fueling.

Figure 9 shows the measurements of the concentrations of NO and NO_2 (taken as equivalent NO) in the exhaust. Here one sees a strong decline in total integrated NO concentration which is larger than one might expect from the peak temperature calculations.

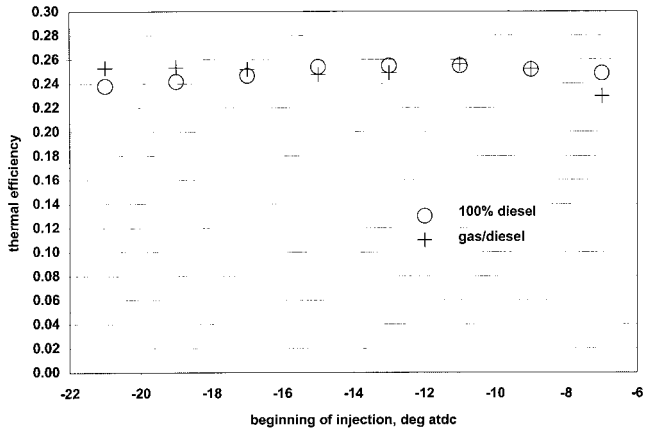

Fig. 10 Thermal efficiency: (*a*) 100 percent diesel fueling; (*b*) gas/diesel fueling

Evidently peak temperature by itself is not a sufficient indicator of the tendency toward NO production: NO is simultaneously being generated in regions of burned products over which there can be at any one time a wide distribution of temperature prior to mixing. It appears necessary to take into account the distributions of temperature and NO generation rate in the immediate post-flame gases.

Figure 9 shows quite close agreement over the range of injection timings between measured NO*x* in the exhaust and the calculated values based on the extended Zeldovich mechanism. For both fueling conditions it has been assumed that one mixing time is equivalent to 4 degrees crank angle. The decrease in NO production (of the order of 100 ppm) due to the partial use of natural gas is shown by comparison of Figs. 9(*a*) and 9(*b*).

Figure 10 shows the measured engine efficiency for both fueling conditions; the calculated efficiency for the gas/diesel case does not include the work of compression of the natural gas. Though the gas injection pattern in this case has not been optimized and the relative injection timing between liquid diesel fuel and natural gas was arbitrarily chosen, there is little difference in efficiency. Other measurements in our laboratory have shown that with natural gas fueling over a range of loads, speeds and gas/diesel fueling ratios, there need be no loss in efficiency with directly injected natural gas relative to conventional diesel fueling. A notable feature evident from Figs. 9 and 10 is that for this engine delayed injection can greatly reduce NO production with little or no loss in efficiency. For operation with small quantities of pilot liquid fuel, where particulate formation should not be of great concern, natural gas fueling should be able to take advantage of late injection timing as an effective means of NO*x* reduction.

Conclusions

1 A new method of using cylinder pressure data and intake and exhaust measurements has been used to determine ignition delay, cylinder heat loss, and peak combustion temperatures in a two-stroke diesel engine fueled with conventional diesel fuel and also with a combination of diesel fuel and natural gas over a range injection timings.
2 The observation of longer ignition delay with natural gas being present in the latter part of the pilot injection period does not necessarily indicate an inhibiting effect due to the presence of the natural gas; it could be due to differences in hydraulic response of the two injectors or in atomization. Further work is needed on this question.
3 With conventional diesel fueling the calculated cylinder heat loss rate distributions shift in a regular manner with injection timing. At light load with gas/diesel fueling the heat loss rate distribution shifts markedly with injection timing; however the integrated total heat loss varies little with timing within a broad range.
4 It is possible to track the formation of NO in the chamber using calculated flame temperatures and the extended Zeldovich post-flame within one turbulent mixing time after the incidence of combustion. Over a range of injection timings and for both fueling conditions the effective average mixing period in this engine appears to correspond to 4 degrees of crank angle.

References

Aesoy, V., and Valland, H., 1996, "The Influence of Natural Gas Composition on Ignition in a Direct Injection Gas Engine Using Hot Surface Assisted Compression Ignition," SAE Paper 961934.

Dent, J. C., and Sulaiman, S. J., 1977, "Convective and Radiative Heat Transfer in a High Swirl Direct Injection Diesel Engine," SAE Technical Paper 770407.

Fukuda, T., Komoda, T., Furushima, K., Yangihara, M., and Ito, Y., 1993, "Development of the Highly Efficient Gas Injection Diesel Engine with Glow Plug Ignition Assist for Cogeneration Systems," Proceedings, JSME-ASME International Conference on Power Engineering—93 (ICOPE-93), Tokyo, Japan, Vol. 1, Sept. 12–16, 1993.

Heywood, J. B., 1988, *Internal Combustion Engine Fundamentals*, McGraw Hill, New York.

Hill, P. G., and Douville, B., 1997, "Relating Burning Rate and NO Formation to Pressure Development in Two-Stroke Diesel Engines," *ASME J. of Ener. Res. Tech.*, Vol. 119, pp. 129–136.

Naber, J. D., Siebers, D. L., Di Julio, S. S., and Westbrook, C. K., 1994, "Effects of Natural Gas Composition on Ignition Delay Under Diesel Conditions," *Combustion and Flame*, Vol. 99, pp. 192–200.

Press, W. H., Flannery, B. P., Teukolsky, S. A., and Vetterling, W. T., 1986, *Numerical Recipes*, Cambridge University Press, Cambridge, United Kingdom.

Reynolds, W. C., 1986, STANJAN Chemical Equilibrium Solver Version 3.93 IBM-PC, computer program, Department of Mechanical Engineering Stanford University, Stanford, CA.

APPENDIX A

DDC 1-71 Engine Specifications

Bore, mm	108
Stroke, mm	127
Conrod length, mm	254
Displacements, litres	1.162
Compression ratio	16:1
Rated power	11.2 kW @ 1200 rpm
Rated bmep	4.8 bar @ 1200 rpm
Rated torque	76 Nm @ 1200 rpm
Inlet port closure	60 deg abdc
Exhaust valve open	95 deg atdc

W. Wagner[1]

J. R. Cooper[2]

A. Dittmann[3]

J. Kijima[4]

H.-J. Kretzschmar[5]

A. Kruse[6]

R. Mareš[7]

K. Oguchi[4]

H. Sato[8]

I. Stöcker[5]

O. Šifner[9]

Y. Takaishi[4]

I. Tanishita[4]

J. Trübenbach[3]

Th. Willkommen[3]

The IAPWS Industrial Formulation 1997 for the Thermodynamic Properties of Water and Steam

In 1997, the International Association for the Properties of Water and Steam (IAPWS) adopted a new formulation for the thermodynamic properties of water and steam for industrial use. This new formulation, called IAPWS Industrial Formulation 1997 for the Thermodynamic Properties of Water and Steam (IAPWS-IF97), replaces the previous industrial formulation, IFC-67, that had formed the basis for power-plant calculations and other applications in energy engineering since the late 1960's. IAPWS-IF97 improves significantly both the accuracy and the speed of the calculation of the thermodynamic properties compared with IFC-67. The differences between IAPWS-IF97 and IFC-67 will require many users, particularly boiler and turbine manufacturers, to modify design and application codes. This paper summarizes the need and the requirements for such a new industrial formulation and gives the entire numerical information about the individual equations of IAPWS-IF97. Moreover, the scientific basis for the development of the equations is summarized and the achieved quality of IAPWS-IF97 is presented regarding the three criterions accuracy, consistency along region boundaries, and computation speed. For comparison, corresponding results for the previous standard IFC-67 are also presented.

1 Introduction

In the 1960s an industrial formulation for the thermodynamic properties of water and steam was developed. This was called "The 1967 IFC Formulation for Industrial Use" (IFC-67) [1]. IFC-67 was formally recognized for the calculation of thermodynamic properties of water and steam for official use such as performance guarantee calculations of power cycles. In addition to this, IFC-67 was used for innumerable other industrial applications. However, compared with today's requirements IFC-67 contains a number of weaknesses. Moreover, because of the progress that has been achieved in mathematical methods to develop accurate equations of state, a number of reasons warranted the development of a new industrial formulation.

This newly developed formulation was adopted by the International Association for the Properties of Water and Steam (IAPWS) at its meeting in Erlangen (Germany), September 1997, under the name "IAPWS Industrial Formulation 1997 for the Thermodynamic Properties of Water and Steam" abbreviated to "IAPWS Industrial Formulation 1997" or even shorter IAPWS-IF97 [2]. Since this date IAPWS-IF97 has been officially valid. However, due to the need to modify design and application codes, IAPWS has recommended an introductory period, lasting until January 1, 1999, during which IAPWS-IF97 should not be used for contractual commitments.

This article contains details relevant to the development of IAPWS-IF97, the full numerical information on the individual equations needed for their use, details of their accuracy, consistency along region boundaries, and results of computing-time investigations in comparison with IFC-67.

[1] Ruhr-Universität Bochum, Lehrstuhl für Thermodynamik, D-44780 Bochum, Germany, corresponding author

[2] Queen Mary and Westfield College, Department of Engineering, London, United Kingdom

[3] Technische Universität Dresden, Institut für Thermodynamik und Technische Gebäudeausrüstung, Dresden, Germany

[4] Kanagawa Institute of Technology, Faculty of Engineering, Atsugi, Japan

[5] Hochschule Zittau/Görlitz (FH), Fachgebiet Technische Thermodynamik, Zittau, Germany

[6] Ruhr-Universität Bochum, Lehrstuhl für Thermodynamik, Bochum, Germany
Current address: Bayern Innovativ GmbH, Nürnberg, Germany

[7] University of West Bohemia, Department of Thermodynamics, Plzen, Czech Republic

[8] Keio University, Faculty of Science & Technology, Yokohama, Japan

[9] Academy of Sciences of Czech Republic, Institute of Thermomechanics, Prague, Czech Republic

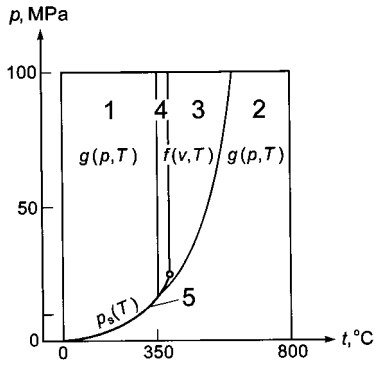

Fig. 1 Regions and equations of IFC-67. The boundary between regions 2 and 3 is described by the L-function

Those who are only interested in the numerical information needed to use the equations of IAPWS-IF97 can find this information in compact form in several steam tables, for example [3, 4, 4a], or in the release on IAPWS-IF97 [2].

2 Need for the Development of the New Industrial Formulation IAPWS-IF97

In order to demonstrate the need for a new industrial formulation, the characteristics of the industrial formulation IFC-67 are considered. As shown in Fig. 1, the entire range of validity ($0°C \leq t \leq 800°C$ for $p \leq 100$ MPa) was divided into five regions with separate equations. For each of the regions 1 (liquid) and 2 (vapor) there was an equation of the specific Gibbs free energy g as function of pressure p and temperature T, namely $g(p, T)$. Each of the regions 3 and 4 was covered by an equation of the specific Helmholtz free energy f as function of specific volume v and temperature T, namely $f(v, T)$. The fifth region was the saturation curve for which a saturation-pressure equation $p_s(T)$ was given.

Based on the equations for the industrially most important regions 1, 2, and 5, the following properties could be directly calculated with IFC-67 as a function of p and T: specific volume v, specific enthalpy h, specific entropy s and specific isobaric heat capacity c_p, and in addition the saturation pressure p_s as a function of T. If other combinations of variables were of interest, for example the combinations $v(p, h)$, $T(p, h)$, $s(p, h)$, $h(p, s)$, $T(p, s)$, and $T_s(p)$ for turbine-expansion calculations, these had to be determined via corresponding iterations. Due to these iterations in combination with a relatively complex structure of the equations, calculations for the complete power cycle with the whole set of the IFC-67 equations required relatively long computing times.

Nowadays, with modern mathematical tools to establish effective structures of such property formulations [5], the long process-calculation times with the IFC-67 equations became a real weakness of this formulation. Besides this main disadvantage of IFC-67 there were several other deficiencies which are summarized as follows:

1 For certain regions IFC-67 no longer met the present standard of accuracy.
2 For some properties there were considerable inconsistencies at region boundaries.
3 The technically important property speed of sound w was not incorporated in the set of the IFC-67 equations.
4 IFC-67 was not based on the current temperature scale ITS-90 [6].
5 IFC-67 was based on earlier data and was therefore not connected to the current scientific standard of IAPWS for the thermodynamic properties of ordinary water substance, the IAPWS-95 formulation [7, 8].

More details concerning the above mentioned items can be seen in the figures of Section 5.5.

3 Administrative Measures of IAPWS for the Development and Examination of IAPWS-IF97

Due to the weaknesses of the IFC-67 formulation listed in the previous section, at the IAPWS meeting in Buenos Aires in 1990 it was decided that a set of new fast equations should be developed for industrial calculations. This new industrial formulation, later called IAPWS-IF97, should then replace the industrial formulation IFC-67. In order to develop the entire equation package in an international collaboration, the Task Group "New Industrial Formulation" was established. It consisted of the following 12 members from seven countries: W. Wagner (Chairman, Germany), A. Alexandrov (Russia), J. R. Cooper (United Kingdom), A. Dittmann (Germany), J. Gallagher (USA), P. G. Hill (Canada), H.-J.

Nomenclature

a, b, c = adjustable parameters
c_p = specific isobaric heat capacity
c_v = specific isochoric heat capacity
d = adjustable parameter
f = specific Helmholtz free energy, $f = u - Ts$
g = specific Gibbs free energy, $g = h - Ts$
h = specific enthalpy
I = exponent
i = serial number
J = exponent
j = serial number
M = molar mass
n = coefficient
p = pressure
R = specific gas constant
R_m = molar gas constant
s = specific entropy
T = thermodynamic temperature[10]
t = Celsius temperature, $t = T - 273.15$ K
u = specific internal energy
v = specific volume
w = speed of sound
β = transformed pressure, Eqs. (27*a*) and (55*a*)
γ = dimensionless Gibbs free energy, $\gamma = g/(RT)$
Δ = difference in any quantity
δ = reduced density, $\delta = \rho/\rho^*$
η = reduced enthalpy, $\eta = h/h^*$
θ = reduced temperature, $\theta = T/T^*$
ϑ = transformed temperature, Eq. (27*b*)
π = reduced pressure, $\pi = p/p^*$
ρ = mass density
σ = reduced entropy, $\sigma = s/s^*$
τ = inverse reduced temperature, $\tau = T^*/T$
ϕ = dimensionless Helmholtz free energy, $\phi = f/(RT)$

Superscripts

o = ideal-gas part; ideal gas
r = residual part
$*$ = reducing quantity
$'$ = saturated liquid state
$''$ = saturated vapor state

Subscripts

b = normal boiling point
c = critical point
max = maximum value
s = saturation state
t = triple point
tol = tolerated

[10] All temperature values given in this article are temperatures according to the International Temperature Scale of 1990 (ITS-90)

Kretzschmar (Germany), R. Mareš (Czech Republic), K. Oguchi (Japan), H. Sato (Japan), O. Šifner (Czech Republic), and J. T. R. Watson (United Kingdom). This group was responsible for the development of IAPWS-IF97 with respect to organizational questions of scientific nature (structure of the formulation, selection of the individual equations, official report to IAPWS, etc.). The final form of IAPWS-IF97 is based on contributions and equations by the scientists who form the group of authors of this article.

The entire project was continuously supervised by the IAPWS Working Group "Industrial Calculations" of which many members are representatives of international companies involved in the power industry. This working group, chaired by B. Rukes (Germany), is the successor of the IAPWS "Subcommittee on Industrial Calculations." The progress of the development of IAPWS-IF97 was continuously discussed in joint sessions of this group with the IAPWS Working Group "Thermophysical Properties of Water and Steam" which was chaired by J. R. Cooper (United Kingdom).

Finally, at the IAPWS meeting in Paris in 1995 the Task Group "New Industrial Formulation-Evaluation" was founded. This group was responsible for the examination of IAPWS-IF97 and consisted of the following members: K. Miyagawa, (Chairman, previously Fuji Electric, Japan), H. W. Bradly (Bradly Associates, United Kingdom), R. B. McClintock (previously General Electric, USA), I. Kodl (Skoda, Czech Republic), W. T. Parry (General Electric, USA), C. Perstrup (Elsam Project, Denmark), B. Rukes (Siemens KWU, Germany), M. Scala (Ansaldo, Italy), P. F. Smith (GEC Alstom Power Generation, United Kingdom), and R. C. Spencer (previously General Electric, USA).

4 Requirements for IAPWS-IF97

The requirements for the industrial formulation IAPWS-IF97 are based on the proposal of the former "Subcommittee on Industrial Calculations," which was agreed with the Task Group "New Industrial Formulation." The main items are summarized in the following sections.

4.1 Range of Validity. The entire set of equations of IAPWS-IF97 should have the same range of validity as given for IFC-67, which is defined by the following temperature and pressure range:

$$0°C \le t \le 800°C \quad p \le 100 \text{ MPa}.$$

For high-temperature applications such as in gas turbines the following extension of the range of validity was requested:

$$800°C \le t \le 2000°C \quad p \le 10 \text{ MPa}.$$

4.2 Accuracy. For the properties specific volume v, specific enthalpy h, and saturation pressure p_s, IAPWS-IF97 should generally meet the corresponding values from the scientific standard, the "IAPWS Formulation 1995 for the Thermodynamic Properties of Ordinary Water Substance for General and Scientific Use" [7, 8], hereafter abbreviated to IAPWS-95, within the tolerances of the International Skeleton Tables IST-85 in its version of 1994 [9]. Roughly summarizing, the relevant IST-85 tolerances are, dependent on the state range, for v between ± 0.01 percent and ± 0.3 percent, for h between ± 0.1 percent and ± 0.3 percent, and for p_s $\pm$ 0.025 percent. Based on extremely accurate experimental data, in the liquid region for $p < 1$ MPa the IST-85 tolerances [9] for v and h and on the saturation curve for $t < 100°C$ the tolerances for p_s are extraordinarily small; here, the smallest tolerances are ± 0.001 percent in v, ± 0.03 percent in h, and ± 0.002 percent in p_s. However, in view of the technical demands in this range, the permitted tolerances to the IAPWS-95 values were increased to ± 0.01 percent in v, to ± 0.1 percent in h, and to ± 0.025 percent in p_s. For the specific isobaric heat capacity c_p and the speed of sound w, IAPWS-IF97 should represent the values from IAPWS-95 to within ± 1 percent except for the range very near the critical point where clearly larger deviations were allowed. By taking as reference the IAPWS-95 formulation [7, 8] the agreement between the industrial formulation and the scientific formulation of IAPWS is ensured.

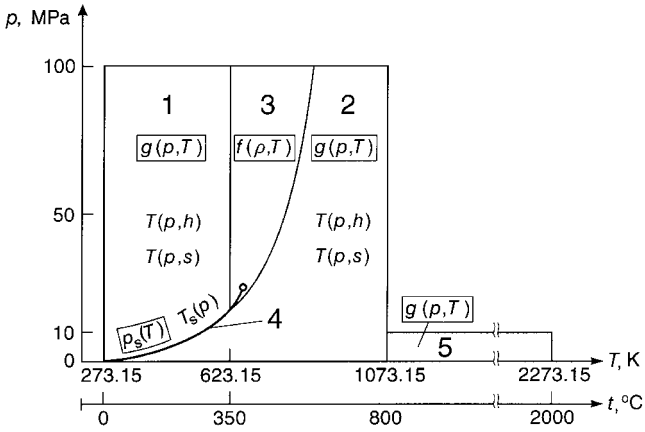

Fig. 2 Regions and equations of IAPWS-IF97. The boundary between regions 2 and 3 is described by the B23-equation, see section 5.3

Besides the representation of v, h, c_p, and w for the (stable) homogeneous regions including saturation, the specification included the requirement that the equations should also yield reasonable values for metastable states close to the stable regions.

4.3 Maximum Inconsistencies at Region Boundaries. With regard to the continuity at the region boundaries (see Fig. 2), reference is made to the so-called Prague values [10]. These Prague values, established for IFC-67, give permissible differences in the property values along the region boundaries when calculating these properties from all equations valid at the corresponding boundary. The continuity requirements are as follows:

(a) Single Phase.

Specific volume:	$\Delta v = \pm 0.05$ percent
Enthalpy:	$\Delta h = \pm 0.2$ kJ kg^{-1}
Heat capacity:	$\Delta c_p = \pm 1$ percent
Entropy:	$\Delta s = \pm 0.2$ J kg^{-1} K^{-1}
Gibbs free energy:	$\Delta g = \pm 0.2$ kJ kg^{-1}
Speed of sound:	$\Delta w = \pm 1$ percent

(b) Saturation.

Saturation pressure:	$\Delta p_s = \pm 0.05$ percent
Saturation temperature:	$\Delta T_s = \pm 0.02$ percent
Gibbs free energy:	$\Delta g = \pm 0.2$ kJ kg^{-1}

4.4 Increase of Computation Speed. This item was the most important demand for IAPWS-IF97. The main requirement regarding the computation speed was that the calculation of all property functions listed in Table 1 for regions 1, 2, and 4 should be altogether three times faster than with IFC-67; for the definition of the individual regions of IAPWS-IF97 see Fig. 2. Table 1 is based on a survey made by the "Subcommittee on Industrial Calculations" among the international power-cycle companies and related industries. In addition to the most important property functions for these regions the table also gives the average frequencies of use of the corresponding functions.

For regions 3 and 5 of IAPWS-IF97 the computation-speed requirements only related to a few functions (see Table 18), where these functions are not combined with frequency-of-use values. For region 3, corresponding to regions 3 and 4 of IFC-67, it was only necessary that IAPWS-IF97 was not slower than with IFC-67. For region 5, the computing-time requirements related only to 1073.15 K, the maximum temperature for which IFC-67 was valid. For this isotherm IAPWS-IF97 should be three times faster than with IFC-67.

Table 1 Most important property functions and their frequency of use

Region [a]	Function	Frequency of use [b] %	
1 (Liquid)	$v(p,T)$	2.9	
	$h(p,T)$	9.7	
	$\boxed{T(p,h)}$	3.5	3.5
	$\boxed{h(p,s)}$	1.2	1.2
2 (Vapor)	$v(p,T)$	6.1	
	$h(p,T)$	12.1	
	$s(p,T)$	1.4	
	$\boxed{T(p,h)}$	8.5	13.3
	$\boxed{v(p,h)}$	3.1	
	$\boxed{s(p,h)}$	1.7	
	$\boxed{T(p,s)}$	1.7	6.6
	$\boxed{h(p,s)}$	4.9	
4 (Saturation)	$p_s(T)$	8.0	
	$\boxed{T_s(p)}$	30.7	35.2
	$\boxed{h'(p)}$	2.25	
	$\boxed{h''(p)}$	2.25	
	Σ:	100.0	59.8

[a] For the definition of the regions see Fig. 2

[b] Functions with values less than 1 % have been neglected; these sum up to 8 %, the remaining values have been scaled up to 100 %

In order to perform all these computing-time investigations, special benchmark programs for a specified PC and compiler were developed. These programs took into account the frequencies of use (if any) of the corresponding property functions.

5 The IAPWS Industrial Formulation 1997

This section gives full information about the IAPWS Industrial Formulation 1997 (IAPWS-IF97) covering all numerical details needed for the use of the individual equations, statements on their development and details concerning accuracy, consistency along the region boundaries, and computation speed of IAPWS-IF97 compared with the previous industrial standard IFC-67.

5.1 Concept and Structure of IAPWS-IF97. The IAPWS Industrial Formulation 1997 consists of a set of equations for different regions which cover the following range of validity:

$$273.15\ \mathrm{K} \le T \le 1073.15\ \mathrm{K} \quad p \le 100\ \mathrm{MPa}$$

$$1073.15\ \mathrm{K} \le T \le 2273.15\ \mathrm{K} \quad p \le 10\ \mathrm{MPa}.$$

Figure 2 shows in which way the entire range of validity of IAPWS-IF97 is covered by its equations. The division into individual regions is very similar to IFC-67. One difference is that the middle density range is covered by only one region, namely by region 3. The other difference is that there is additionally a high-temperature region, region 5. Region 4 corresponds to the saturation curve. The boundaries of the regions can be directly taken from Fig. 2 except for the boundary between regions 2 and 3; this boundary is defined by the so-called B23-equation given in Section 5.3. Both regions 1 and 2 are individually covered by a fundamental equation for the specific Gibbs free energy $g(p, T)$, region 3 by a fundamental equation for the specific Helmholtz free energy $f(\rho, T)$, and the saturation curve, corresponding to region 4, by a saturation-pressure equation $p_s(T)$. The high-temperature region 5 is also covered by a $g(p, T)$ equation. These five equations, shown in rectangular boxes in Fig. 2, form the so-called *basic equations.*

In order to meet the main requirement of a short computing time, the entire set of the IAPWS-IF97 equations was developed based on the following two-step concept:

1 After finding convenient functional terms, the structure of the four basic equations for the homogeneous regions was optimized using the method by Setzmann and Wagner [5] in such a way that the requirements regarding accuracy and consistency along region boundaries were met with equation structures allowing short computing times. In this optimization process, the equations were fitted to input values calculated from the IAPWS-95 formulation [7, 8]. In this way IAPWS-IF97 was coupled with the current scientific standard IAPWS-95.

2 All those thermodynamic properties which are not direct functions of the independent variables of the basic equations are not found by iteration from the basic equations. Instead of this, so-called *backward equations* were developed, namely equations $T(p, h)$ and $T(p, s)$ for regions 1 and 2 and $T_s(p)$ for the saturation curve. With these backward equations, shown in Fig. 2 for the corresponding regions, all the functions shown in rectangular boxes in Table 1 can be calculated without any iteration. For example, if $h(p, s)$ is to be calculated in region 2, first the temperature T is calculated from the backward equation $T(p, s)$ and then $h(p, T)$ can be directly obtained from the corresponding basic equation $g(p, T)$.

However, this entire concept required that the numerical consistency between the backward and the basic equations was extremely good. Otherwise it would have caused numerical problems when "jumping" back and forth between the basic and the backward equations, for example, when calculating the turbine-expansion line of a power-cycle process. Based on test calculations with characteristic power cycles via iterations with IFC-67, the following numerical consistency requirements were finally set up:

(*a*) The temperature determined from the backward equation $T(p, h)$ for given values of p and h had to agree with the temperature value calculated for the same p and h from the corresponding basic equation $g(p, T)$ within a tolerated temperature difference ΔT_{tol}. This ΔT_{tol} value amounts to ± 25 mK for the entire region 1 and for region 2 at entropy values not greater than 5.85 kJ kg^{-1} K^{-1}. For region 2 at entropy values greater than 5.85 kJ kg^{-1} K^{-1}, the permissible ΔT_{tol} value amounts to ± 10 mK; the smaller ΔT_{tol} inconsistency value in this part of region 2 (turbine expansion) is particularly important for the power industry.

(*b*) The temperature determined from the backward equation $T(p, s)$ for given values of p and s had to agree with the temperature calculated for the same p and s from the corresponding basic equation $g(p, T)$ within a tolerated temperature difference ΔT_{tol}. For the tolerated ΔT_{tol} inconsistency values with regard to the $T(p, s)$ equation, the same statement held as given for the $T(p, h)$ equation under item (*a*).

(*c*) The saturation pressure calculated from the saturation-temperature equation $T_s(p)$ was not allowed to deviate by more than $\Delta p_s = \pm 0.003$ percent from the p_s value determined from the saturation-pressure equation $p_s(T)$.

The permissible numerical inconsistencies between the basic and backward equations, summarized under items (*a*) to (*c*), were extremely small, namely about one tenth of the uncertainties of the scientific standard IAPWS-95.

5.2 Reference Constants. This section summarizes all reference constants needed for evaluating the equations given in Section 5.5.

The specific gas constant of ordinary water,

$$R = 0.461\ 526\ \mathrm{kJ\,kg^{-1}\,K^{-1}}, \tag{1}$$

results from the recommended values of the molar gas constant [11],

$$R_m = 8.314\ 51\ \mathrm{J\,mol^{-1}\,K^{-1}}, \tag{2}$$

and from the molar mass of ordinary water,

$$M = 18.015\ 257\ \mathrm{g\,mol^{-1}}. \tag{3}$$

The value of M results from the molar masses obtained from isotopic molar masses in [12] and representative isotopic compositions given in [13].

The values of the critical parameters

$$T_c = 647.096 \text{ K}, \tag{4}$$

$$p_c = 22.064 \text{ MPa}, \tag{5}$$

$$\rho_c = 322 \text{ kg m}^{-3} \tag{6}$$

are from the corresponding IAPWS release [14]. The triple-point temperature is

$$T_t = 273.16 \text{ K} \tag{7}$$

according to the International Temperature Scale of 1990 (ITS-90) [6] and the triple-point pressure

$$p_t = 611.657 \text{ Pa} \tag{8}$$

was determined by Guildner et al. [15]. According to the scientific standard of the thermodynamic properties of ordinary water, the IAPWS-95 formulation [7, 8], the temperature of the normal boiling point (at a pressure of 0.101 325 MPa (1 atm)) amounts to

$$T_b = 373.124\ 3 \text{ K}. \tag{9}$$

5.3 Auxiliary Equation for the Boundary between Regions 2 and 3. The boundary between regions 2 and 3 (see Fig. 2) is defined by the following simple quadratic pressure-temperature relation, the B23-equation

$$\pi = n_1 + n_2\theta + n_3\theta^2, \tag{10}$$

where $\pi = p/p^*$ and $\theta = T/T^*$ with $p^* = 1$ MPa and $T^* = 1$ K. The coefficients n_1 to n_3 of Eq. (10) are listed in Table A1 of the appendix. Equation (10) describes roughly an isentropic line; the entropy values along this boundary line are between $s = 5.047$ kJ kg^{-1} K^{-1} and $s = 5.261$ kJ kg^{-1} K^{-1}.

Alternatively Eq. (10) can be expressed explicitly in temperature as

$$\theta = n_4 + [(\pi - n_5)/n_3]^{0.5} \tag{11}$$

with θ and π as defined for Eq. (10) and the coefficients n_3 to n_5 listed in Table A1. Equations (10) and (11) cover the range from 623.15 K at 16.5292 MPa up to 863.15 K at 100 MPa.

5.4 Functional Forms Adopted for Short Computing Times. Wide-range equations of state in reference quality are nowadays explicit in the Helmholtz free energy as function of density and temperature [7, 8, 16, 17]. As functional forms for such equations pure polynomials in density and temperature and particularly such polynomials combined with exponential functions in density have proved very successful.

Since, however, for IAPWS-IF97 a short computing time was one of the most important criterions, the computing times of selected arithmetic operations were investigated [18]. Compared with the two most important basic operations addition and multiplication, all the other operations are slower by a factor of ten or more. After these tests it was clear that it was only possible to use polynomials in the form of series of additions and multiplications as basic functional forms for the new equations. Based on many tests for the general functional dependency

$$z = z(x, y), \tag{12}$$

where, for example, $z = f$, $x = \rho$, and $y = T$, the following general functional expression has proved most effective [18]:

$$z(x, y) = \sum_i n_i \left(\frac{x}{a} + b\right)^{I_i} \left(\frac{y}{c} + d\right)^{J_i}. \tag{13}$$

This general expression forms the basis for the majority of the equations of IAPWS-IF97.

The final form of all equations (except for the saturation curve, region 4) of IAPWS-IF97 was found by using the structure-optimization method of Setzmann and Wagner [5] or a modified version of Wagner's method [19]. These procedures require a so-called bank of terms from which the best combination of an optimum number of terms is determined. For the development of the backward equations, these procedures were combined with further optimization tools, see later.

5.5 The Basic Equations for Regions 1 to 5. For those homogeneous regions of IAPWS-IF97 for which it is thermodynamically reasonable the corresponding equations of state were established as function of the "technical" variables pressure p and temperature T; this is the case for regions 1, 2, and 5. For these regions, the equations are formulated explicit in the specific Gibbs free energy g which is, as a function of p and T, a fundamental equation. Since region 3 contains the critical point, this region cannot be reasonably covered by an equation with p and T as independent variables. However, it can be represented by an equation as a function of density ρ and temperature T. Thus, for region 3 an equation explicit in the specific Helmholtz free energy as a function of ρ and T is used which is a fundamental equation, also. One advantage of using fundamental equations (instead of equations of state in form of $p(v, T)$ and $v(p, T)$, respectively) is that all thermodynamic properties can be calculated from derivatives of the equations, no integrations with further information are needed. If the first and second derivatives of g with respect to p and T and of f with respect to ρ and T, respectively, are correctly represented, then any thermodynamic property, based on these derivatives (which is the case for the vast majority of properties), can be correctly calculated from such fundamental equations.

Proceeding from Eq. (13) with $z = g/(RT)$, $x = p$, $a = p^*$, $y = T^{-1}$, and $c = (T^*)^{-1}$ one obtains the following general form of a so-called combined polynomial for the $g(p, T)$ equations:

$$\frac{g}{RT} = \sum_i n_i \left(\frac{p}{p^*} + b\right)^{I_i} \left(\frac{T^*}{T} + d\right)^{J_i}, \tag{14}$$

where p^* and T^* are reducing parameters.

In the following sections first the final form of the corresponding basic equation is given including all numerical information for its use, then details of its development are summarized and finally its accuracy is discussed; all table numbers starting with an "A" are listed in the appendix.

5.5.1 The Gibbs Free Energy Equation for Region 1. The basic equation for this region is a fundamental equation for the specific Gibbs free energy g. This equation is expressed in dimensionless form, $\gamma = g/(RT)$, and reads

$$\frac{g(p, T)}{RT} = \gamma(\pi, \tau) = \sum_{i=1}^{34} n_i (7.1 - \pi)^{I_i} (\tau - 1.222)^{J_i}, \tag{15}$$

where $\pi = p/p^*$ and $\tau = T^*/T$ with $p^* = 16.53$ MPa and $T^* = 1386$ K; R is given by Eq. (1). The coefficients n_i and exponents I_i and J_i of Eq. (15) are listed in Table A2.

All thermodynamic properties can be derived from Eq. (15) by using the appropriate combinations of the dimensionless Gibbs free energy γ and its derivatives. The relations of the relevant thermodynamic properties to γ and its derivatives are summarized in Table 2. All required derivatives of the dimensionless Gibbs free energy γ, Eq. (15), are explicitly given in Table 3.

Since the 5th International Conference on the Properties of Steam in London in 1956, the specific internal energy and the specific entropy of the saturated liquid at the triple point have been set equal to zero, as follows:

$$u'_t = 0; \quad s'_t = 0. \tag{16}$$

Table 2 Relations of thermodynamic properties to the dimensionless Gibbs free energy γ and its derivatives when using Eq. (15)[a]

Property	Relation
Specific volume $v=(\partial g/\partial p)_T$	$v(\pi,\tau)\frac{p}{RT}=\pi\gamma_\pi$
Specific internal energy $u=g-T(\partial g/\partial T)_p-p(\partial g/\partial p)_T$	$\frac{u(\pi,\tau)}{RT}=\tau\gamma_\tau-\pi\gamma_\pi$
Specific entropy $s=-(\partial g/\partial T)_p$	$\frac{s(\pi,\tau)}{R}=\tau\gamma_\tau-\gamma$
Specific enthalpy $h=g-T(\partial g/\partial T)_p$	$\frac{h(\pi,\tau)}{RT}=\tau\gamma_\tau$
Specific isobaric heat capacity $c_p=(\partial h/\partial T)_p$	$\frac{c_p(\pi,\tau)}{R}=-\tau^2\gamma_{\tau\tau}$
Specific isochoric heat capacity $c_v=(\partial u/\partial T)_v$	$\frac{c_v(\pi,\tau)}{R}=-\tau^2\gamma_{\tau\tau}+\frac{(\gamma_\pi-\tau\gamma_{\pi\tau})^2}{\gamma_{\pi\pi}}$
Speed of sound $w=v\left[-(\partial p/\partial v)_s\right]^{0.5}$	$\frac{w^2(\pi,\tau)}{RT}=\frac{\gamma_\pi^2}{\frac{(\gamma_\pi-\tau\gamma_{\pi\tau})^2}{\tau^2\gamma_{\tau\tau}}-\gamma_{\pi\pi}}$

$\gamma_\pi=\left(\frac{\partial\gamma}{\partial\pi}\right)_\tau,\ \gamma_{\pi\pi}=\left(\frac{\partial^2\gamma}{\partial\pi^2}\right)_\tau,\ \gamma_\tau=\left(\frac{\partial\gamma}{\partial\tau}\right)_\pi,\ \gamma_{\tau\tau}=\left(\frac{\partial^2\gamma}{\partial\tau^2}\right)_\pi,\ \gamma_{\pi\tau}=\left(\frac{\partial^2\gamma}{\partial\pi\partial\tau}\right)$

[a] A general procedure how to obtain the relation of any property and any differential quotient to γ and its derivatives when using Eq. (15) can be found in [19a]

In order to meet this condition at the temperature and pressure of the triple point, see Eqs. (7) and (8), the coefficients n_3 and n_4 in Eq. (15) have been adjusted accordingly. As a consequence, Eq. (15) yields for the specific enthalpy of the saturated liquid at the triple point

$$h'_t = 0.611\ 783\ \mathrm{J\,kg^{-1}}. \tag{17}$$

Equation (15) covers region 1 of IAPWS-IF97 defined by the following range of temperature and pressure (see Fig. 2):

$$273.15\ \mathrm{K} \le T \le 623.15\ \mathrm{K} \quad p_s(T) \le p \le 100\ \mathrm{MPa}.$$

In addition to the properties in the stable single-phase liquid region, Eq. (15) also yields reasonable values in the metastable superheated-liquid region close to the saturated liquid line. For temperatures between 273.15 K and 273.16 K at pressures below the melting pressure [20] (metastable subcooled liquid) all values are calculated by extrapolation from Eqs. (15) and (28).

To assist the user in computer-program verification of Eq. (15), Table A3 contains test values of the most relevant properties.

5.5.1.1 Development of Eq. (15). Based on test calculations with Eq. (14) regarding the maximum ranges of the exponents I_i and J_i, the values for the reducing parameters p^* and T^* and the shifting parameters b and d, the following general functional expression of 911 terms (bank of terms) was used as a starting point for the development of the equation for the dimensionless Gibbs free energy for region 1 [18]:

$$\gamma = \sum_{i=0}^{8}\sum_{j=-18}^{18} n_{ij}(7.1-\pi)^i(\tau-1.222)^j + \sum_{i=16}^{32}\sum_{j=-43}^{-10} n_{ij}(7.1-\pi)^i(\tau-1.222)^j, \tag{18}$$

Table 3 The dimensionless Gibbs free energy γ, Eq. (15), and its derivatives

$\gamma = \sum_{i=1}^{34} n_i(7.1-\pi)^{I_i}(\tau-1.222)^{J_i}$	$\gamma_\tau = \sum_{i=1}^{34} n_i(7.1-\pi)^{I_i} J_i(\tau-1.222)^{J_i-1}$
$\gamma_\pi = \sum_{i=1}^{34} -n_i I_i(7.1-\pi)^{I_i-1}(\tau-1.222)^{J_i}$	$\gamma_{\tau\tau} = \sum_{i=1}^{34} n_i(7.1-\pi)^{I_i} J_i(J_i-1)(\tau-1.222)^{J_i-2}$
$\gamma_{\pi\pi} = \sum_{i=1}^{34} n_i I_i(I_i-1)(7.1-\pi)^{I_i-2}(\tau-1.222)^{J_i}$	$\gamma_{\pi\tau} = \sum_{i=1}^{34} -n_i I_i(7.1-\pi)^{I_i-1} J_i(\tau-1.222)^{J_i-1}$

$\gamma_\pi=\left(\frac{\partial\gamma}{\partial\pi}\right)_\tau,\ \gamma_{\pi\pi}=\left(\frac{\partial^2\gamma}{\partial\pi^2}\right)_\tau,\ \gamma_\tau=\left(\frac{\partial\gamma}{\partial\tau}\right)_\pi,\ \gamma_{\tau\tau}=\left(\frac{\partial^2\gamma}{\partial\tau^2}\right)_\pi,\ \gamma_{\pi\tau}=\left(\frac{\partial^2\gamma}{\partial\pi\partial\tau}\right)$

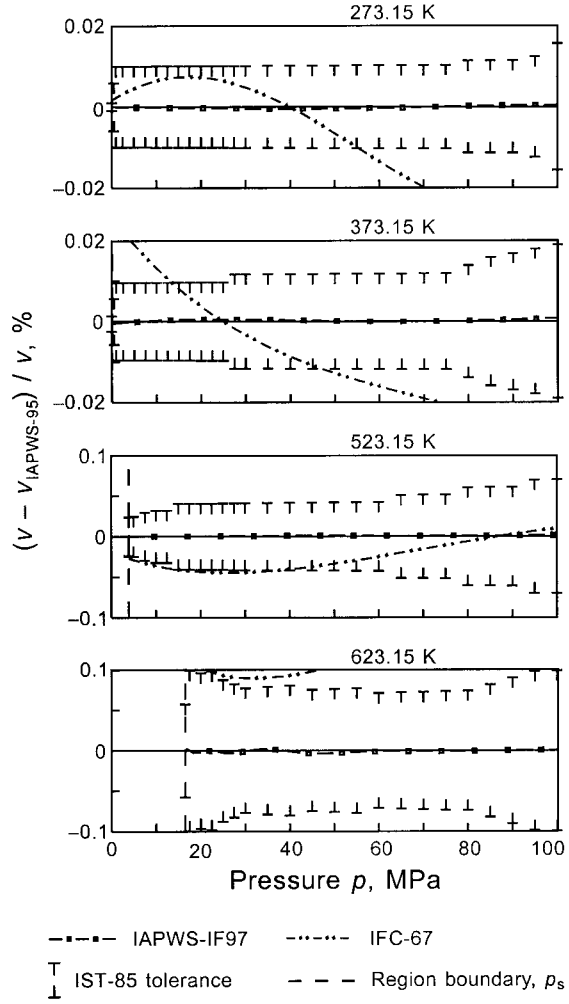

Fig. 3(*a*) Percentage deviations of the specific volumes v calculated from Eq. (15) and IFC-67, respectively, from values $v_{IAPWS-95}$ calculated from IAPWS-95 [7, 8]

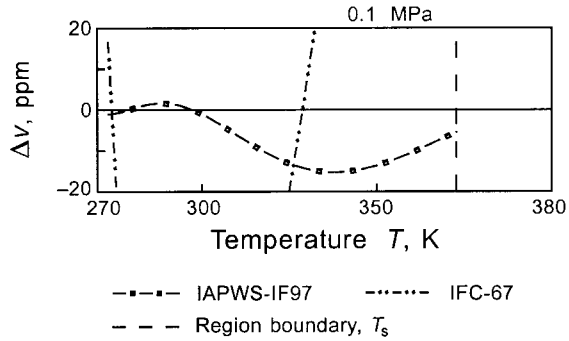

Fig. 3(*b*) Relative deviations in ppm of the specific volumes v calculated from Eq. (15) and IFC-67, respectively, from values $v_{IAPWS-95}$ calculated from IAPWS-95 [7, 8]; $\Delta v = (v - v_{IAPWS-95})/v$.

where $\pi = p/p^*$ and $\tau = T^*/T$ with $p^* = 16.53$ MPa and $T^* = 1386$ K. Equation (15), obtained from Eq. (18) by the method of Setzmann and Wagner [5] for optimizing the functional structure of the final γ equation, was fitted to values of the properties v, h, c_p, s, and the two partial derivatives $(\partial v/\partial p)_T$ and $(\partial v/\partial T)_p$. All these values were calculated from IAPWS-95 [7, 8] for given values of p and T distributed as selected grid points over region 1. Details of this fitting process (formulation of the sums of squares based on the relations given in Table 2, weighting factors, etc.) are given by Kruse and Wagner [18]. The inclusion of the partial

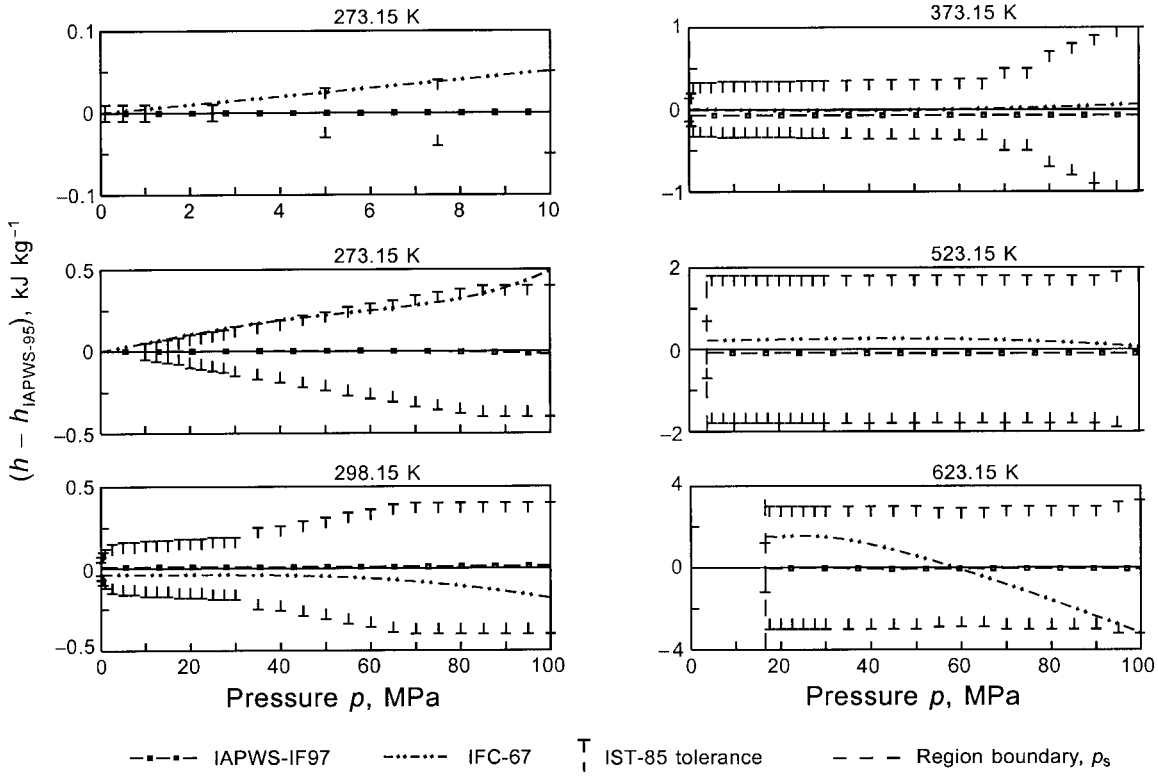

Fig. 4 Absolute deviations of the specific enthalpies h calculated from Eq. (15) and IFC-67, respectively, from values $h_{IAPWS-95}$ calculated from IAPWS-95 [7, 8]; see the spread pressure scale up to $p = 10$ MPa in the first deviation diagram for 273.15 K.

derivatives of v with respect to p and T made it unnecessary to fit the equations to the corresponding values of c_v and w which would have led to a nonlinear system of normal equations when minimizing the sum of squares. Such a nonlinear fitting process could not have been combined with the procedure of optimizing the structure of the equations because this procedure can only cope with sums of squares which are linear in the coefficients n_{ij}. Moreover, fitting Eq. (15) to the properties mentioned above ensures that Eq. (15) yields reasonable values for any property based on the first and second derivatives of g, see also the general statement at the beginning of Section 5.5.

5.5.1.2 Accuracy of Eq. (15). Equation (15) clearly meets the accuracy requirements listed in Section 4.2. However, this statement on the formal fulfillment of the requirements gives an insufficient impression of the accuracy of Eq. (15). Therefore, the quality of representing the IAPWS-95 values [7, 8] by Eq. (15) is illustrated by Figs. 3(*a*) to 6 for the relevant properties v, h, c_p, and w along four isotherms considered to be characteristic for the entire region 1. All the diagrams show the deviations of the values calculated from Eq. (15) from the corresponding IAPWS-95 values. In the deviation diagrams for v and h, Figs. 3(*a*) to 4, the IST-85 tolerances [9] are plotted related to the IAPWS-95 values at the p-T values of the Skeleton Tables IST-85 [9]. For comparison, the figures also contain the corresponding lines generated from IFC-67. Figure 3(*a*) shows that Eq. (15) represents the values of the specific volume from IAPWS-95 so well that the v line from Eq. (15) is nearly identical with the zero line. Even for $T \leq 398.15$ K and $p \leq 0.5$ MPa, where the IST-85 tolerances are clearly smaller than the requirements (see Section 4.2), the IAPWS-95 values are represented to within the original tolerances; the only exception is the v value at 323.15 K and 0.1 MPa where the deviation is just outside the IST-85 tolerance. For the greatest part of region 1 the deviations are less than 10 ppm and the maximum deviation amounts to 44 ppm at about 16 MPa and 621 K. In larger ranges of region 1 IFC-67 does not meet the present requirements. Figure 3(*b*) illustrates the accuracy of Eq. (15) along the 0.1 MPa isobar which might be of interest for calibration purposes. The maximum deviation from the IAPWS-95 values, of which the uncertainty in v for this isobar is ± 1 ppm [7, 8], is less than 15 ppm and for $T \leq 300$ K even less than 2 ppm.

Figure 4 gives an impression of how Eq. (15) represents the specific enthalpy values from IAPWS-95 [7, 8]. It can be seen that Eq. (15) meets all enthalpy values from IAPWS-95 within the original IST-85 tolerances. This is also the case for pressures below 1 MPa where two to three times larger enthalpy deviations would have been allowed (see Section 4.2). For temperatures up to 423.15 K the absolute deviations from the IAPWS-95 values remain within ± 0.1 kJ kg^{-1} and for higher temperatures they are in most cases less than ± 0.2 kJ kg^{-1} which is 10 to 20 times smaller than the IST-85 tolerances; considering the entire region 1, the maximum deviation occurs at 569 K very close to the phase boundary and amounts to 0.24 kJ kg^{-1}. The enthalpy is the only property for which the IFC-67 values remain everywhere in this region within the tolerances. However, it should be pointed out that a good representation of the absolute enthalpy values is not the decisive criterion for practical applications, whereas a reasonable representation of enthalpy differences is the most important point. If one is interested in estimating the maximum uncertainties in isobaric enthalpy differences, one has to look at the uncertainties in the isobaric heat capacity.

Figure 5 illustrates the representation of the isobaric heat capacity by Eq. (15). In the entire region 1, the deviations from c_p values from IAPWS-95 are clearly smaller than the permitted tolerances of ± 1 percent, in most cases they are even smaller than ± 0.1 percent; the maximum deviation amounts to 0.15 percent at about 15 MPa and 618 K. A very high accuracy along the 623.15 K isotherm, the boundary to region 3, was the decisive precondition for meeting the consistency requirement along this region boundary.

Figure 6 gives an impression of the behavior of Eq. (15) regarding the speed of sound. This property was the most difficult one to

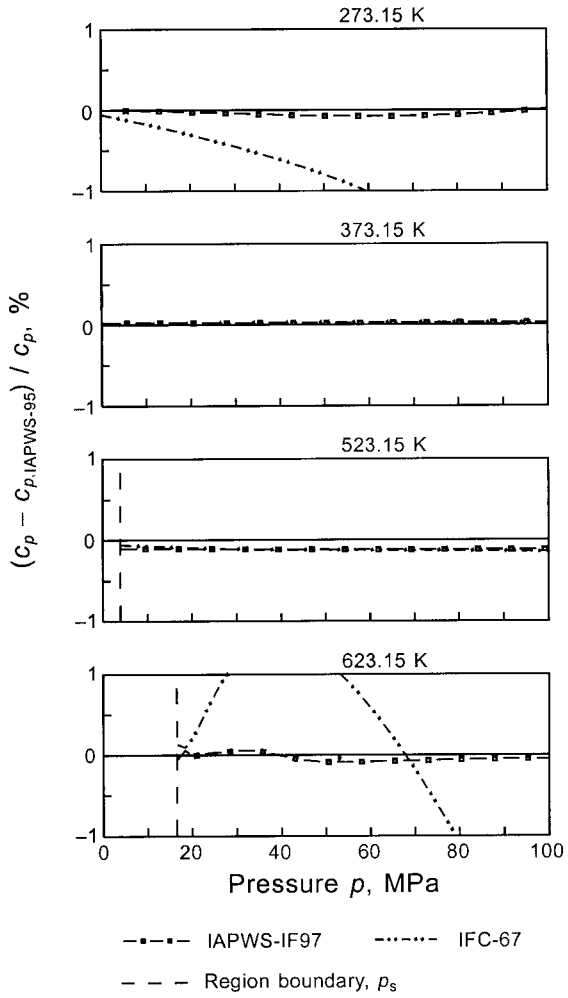

Fig. 5 Percentage deviations of the specific isobaric heat capacities c_p calculated from Eq. (15) and IFC-67, respectively, from values $c_{p,\text{IAPWS-95}}$ calculated from IAPWS-95 [7, 8]

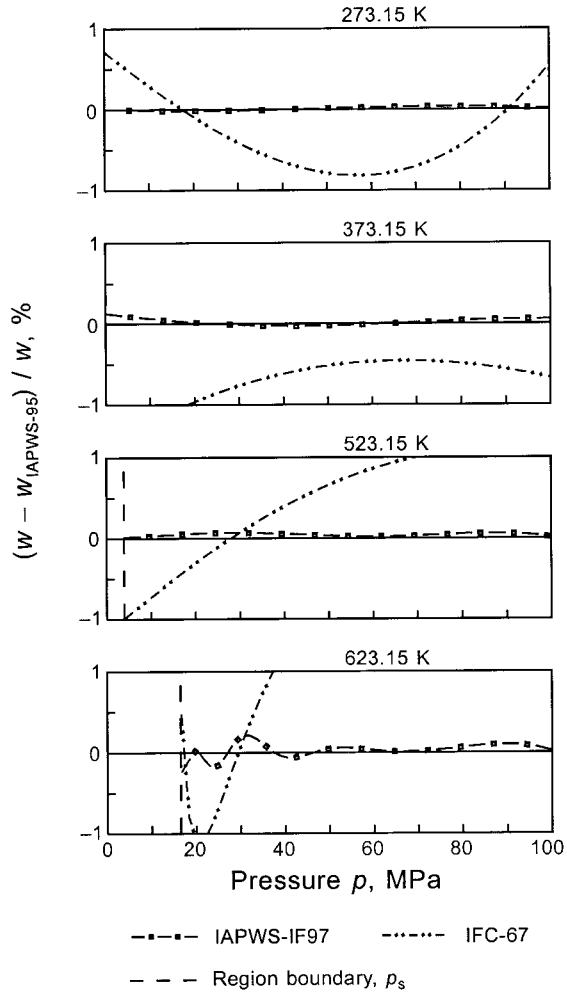

Fig. 6 Percentage deviations of the speeds of sound w calculated from Eq. (15) and IFC-67, respectively, from values $w_{\text{IAPWS-95}}$ calculated from IAPWS-95 [7, 8]

be represented in this region. Nevertheless, in most cases the deviations are less than ± 0.1 percent. The maximum deviation from the IAPWS-95 values occurs at 619 K near the phase boundary and amounts to -0.5 percent. Based on the wish to keep the deviations regarding the speed of sound everywhere below ± 0.5 percent and to keep the maximum inconsistency with respect to this property at the region boundaries definitely below ± 0.5 percent, it was not possible to have less than 34 terms for Eq. (15).

Metastable states. In addition to the properties in the stable single-phase liquid region, Eq. (15) also yields reasonable values in the metastable superheated-liquid region close to the saturated liquid line. Investigations yielded that for temperatures up to 573.15 K and pressures down to zero the deviations from the IAPWS-95 values remain practically the same as they are at the saturation curve (region 4). For 623.15 K, Eq. (15) can be extrapolated into the superheated-liquid region for pressures $|p - p_s| \leq 1.5$ MPa without showing deviations from IAPWS-95 greater than 0.1 percent in v.

5.5.2 The Gibbs Free Energy Equation for Region 2. The basic equation for this region is probably the most important equation of the entire package of IAPWS-IF97 because in actual plant the important processes, e.g., the expansions in steam turbines, occur in this region.

The auxiliary equation for defining the boundary between regions 2 and 3 is given as Eqs. (10) and (11) in Section 5.3.

The basic equation for this region is a fundamental equation for the specific Gibbs free energy g. This equation is expressed in dimensionless form, $\gamma = g/(RT)$, and is separated into two parts, an ideal-gas part γ^o and a residual part γ^r, so that

$$\frac{g(p, T)}{RT} = \gamma(\pi, \tau) = \gamma^o(\pi, \tau) + \gamma^r(\pi, \tau), \tag{19}$$

where $\pi = p/p^*$ and $\tau = T^*/T$ with R given by Eq. (1).

The equation for the ideal-gas part γ^o of the dimensionless Gibbs free energy reads

$$\gamma^o = \ln \pi + \sum_{i=1}^{9} n_i^o \tau^{J_i^o}, \tag{20}$$

where $\pi = p/p^*$ and $\tau = T^*/T$ with $p^* = 1$ MPa and $T^* = 540$ K. The coefficients n_1^o and n_2^o were adjusted in such a way that the values for the specific internal energy and specific entropy, calculated from Eq. (19), relate to Eq. (16). Table A4 contains the coefficients n_i^o and exponents J_i^o of Eq. (20).

The form of the residual part γ^r of the dimensionless Gibbs free energy is as follows:

$$\gamma^r = \sum_{i=1}^{43} n_i \pi^{I_i} (\tau - 0.5)^{J_i}, \tag{21}$$

Table 4 Relations of thermodynamic properties to the ideal-gas part γ^o and the residual part γ^r of the dimensionless Gibbs free energy and their derivatives when using Eqs. (19), (23), and (29)[a]

Property	Relation
Specific volume $v=\left(\partial g/\partial p\right)_T$	$v(\pi,\tau)\frac{p}{RT}=\pi\left(\gamma_\pi^o+\gamma_\pi^r\right)$
Specific internal energy $u=g-T\left(\partial g/\partial T\right)_p-p\left(\partial g/\partial p\right)_T$	$\frac{u(\pi,\tau)}{RT}=\tau\left(\gamma_\tau^o+\gamma_\tau^r\right)-\pi\left(\gamma_\pi^o+\gamma_\pi^r\right)$
Specific entropy $s=-\left(\partial g/\partial T\right)_p$	$\frac{s(\pi,\tau)}{R}=\tau\left(\gamma_\tau^o+\gamma_\tau^r\right)-\left(\gamma^o+\gamma^r\right)$
Specific enthalpy $h=g-T\left(\partial g/\partial T\right)_p$	$\frac{h(\pi,\tau)}{RT}=\tau\left(\gamma_\tau^o+\gamma_\tau^r\right)$
Specific isobaric heat capacity $c_p=\left(\partial h/\partial T\right)_p$	$\frac{c_p(\pi,\tau)}{R}=-\tau^2\left(\gamma_{\tau\tau}^o+\gamma_{\tau\tau}^r\right)$
Specific isochoric heat capacity $c_v=\left(\partial u/\partial T\right)_v$	$\frac{c_v(\pi,\tau)}{R}=-\tau^2\left(\gamma_{\tau\tau}^o+\gamma_{\tau\tau}^r\right)-\frac{(1+\pi\gamma_\pi^r-\tau\pi\gamma_{\pi\tau}^r)^2}{1-\pi^2\gamma_{\pi\pi}^r}$
Speed of sound $w=v\left[-\left(\partial p/\partial v\right)_s\right]^{0.5}$	$\frac{w^2(\pi,\tau)}{RT}=\frac{1+2\pi\gamma_\pi^r+\pi^2\gamma_\pi^{r2}}{\left(1-\pi^2\gamma_{\pi\pi}^r\right)+\frac{\left(1+\pi\gamma_\pi^r-\tau\pi\gamma_{\pi\tau}^r\right)^2}{\tau^2\left(\gamma_{\tau\tau}^o+\gamma_{\tau\tau}^r\right)}}$

$\gamma_\pi^r=\left(\frac{\partial\gamma^r}{\partial\pi}\right)_\tau,\ \gamma_{\pi\pi}^r=\left(\frac{\partial^2\gamma^r}{\partial\pi^2}\right)_\tau,\ \gamma_\tau^r=\left(\frac{\partial\gamma^r}{\partial\tau}\right)_\pi,\ \gamma_{\tau\tau}^r=\left(\frac{\partial^2\gamma^r}{\partial\tau^2}\right)_\pi,\ \gamma_{\pi\tau}^r=\left(\frac{\partial^2\gamma^r}{\partial\pi\partial\tau}\right),\ \gamma_\tau^o=\left(\frac{\partial\gamma^o}{\partial\tau}\right)_\pi,\ \gamma_{\tau\tau}^o=\left(\frac{\partial^2\gamma^o}{\partial\tau^2}\right)_\pi$

[a] A general procedure how to obtain the relation of any property and any differential quotient to γ^o and γ^r and their derivatives when using Eqs. (19), (23), and (29) can be found in [19a]

where $\pi = p/p^*$ and $\tau = T^*/T$ with $p^* = 1$ MPa and $T^* = 540$ K. The coefficients n_i and exponents I_i and J_i of Eq. (21) are listed in Table A5.

All thermodynamic properties can be derived from Eq. (19) by using the appropriate combinations of the ideal-gas part γ^o, Eq. (20), and the residual part γ^r, Eq. (21), of the dimensionless Gibbs free energy and their derivatives. The relations of the relevant thermodynamic properties to γ^o and γ^r and their derivatives are summarized in Table 4. All required derivatives of the ideal-gas part and of the residual part of the dimensionless Gibbs free energy are explicitly given in Table 5 and Table 6, respectively.

Equation (19) covers region 2 of IAPWS-IF97 defined by the following range of temperature and pressure, see Fig. 2:

$$273.15\ \text{K} \le T \le 623.15\ \text{K} \quad 0 < p \le p_s(T)_{\text{Eq.(28)}}$$

$$623.15\ \text{K} < T \le 863.15\ \text{K} \quad 0 < p \le p(T)_{\text{Eq.(10)}}$$

$$863.15\ \text{K} < T \le 1073.15\ \text{K} \quad 0 < p \le 100\ \text{MPa}$$

Table 5 The ideal-gas part γ^o of the dimensionless Gibbs free energy, Eq. (20), and its derivatives

$\gamma^o = \ln\pi + \sum_{i=1}^{9} n_i^o \tau^{J_i^o}$	$\gamma_\tau^o = \sum_{i=1}^{9} n_i^o J_i^o \tau^{J_i^o-1}$
$\gamma_\pi^o = \pi^{-1}$	$\gamma_{\tau\tau}^o = \sum_{i=1}^{9} n_i^o J_i^o (J_i^o-1)\tau^{J_i^o-2}$
$\gamma_{\pi\pi}^o = -\pi^{-2}$	$\gamma_{\pi\tau}^o = 0$

$\gamma_\pi^o=\left(\frac{\partial\gamma^o}{\partial\pi}\right)_\tau,\ \gamma_{\pi\pi}^o=\left(\frac{\partial^2\gamma^o}{\partial\pi^2}\right)_\tau,\ \gamma_\tau^o=\left(\frac{\partial\gamma^o}{\partial\tau}\right)_\pi,\ \gamma_{\tau\tau}^o=\left(\frac{\partial^2\gamma^o}{\partial\tau^2}\right)_\pi,\ \gamma_{\pi\tau}^o=\left(\frac{\partial^2\gamma^o}{\partial\pi\partial\tau}\right)$

Table 6 The residual part γ^r of the dimensionless Gibbs free energy, Eq. (21), and its derivatives

$\gamma^r = \sum_{i=1}^{43} n_i \pi^{I_i}(\tau-0.5)^{J_i}$	$\gamma_\tau^r = \sum_{i=1}^{43} n_i \pi^{I_i} J_i(\tau-0.5)^{J_i-1}$
$\gamma_\pi^r = \sum_{i=1}^{43} n_i I_i \pi^{I_i-1}(\tau-0.5)^{J_i}$	$\gamma_{\tau\tau}^r = \sum_{i=1}^{43} n_i \pi^{I_i} J_i(J_i-1)(\tau-0.5)^{J_i-2}$
$\gamma_{\pi\pi}^r = \sum_{i=1}^{43} n_i I_i(I_i-1)\pi^{I_i-2}(\tau-0.5)^{J_i}$	$\gamma_{\pi\tau}^r = \sum_{i=1}^{43} n_i I_i \pi^{I_i-1} J_i(\tau-0.5)^{J_i-1}$

$\gamma_\pi^r=\left(\frac{\partial\gamma^r}{\partial\pi}\right)_\tau,\ \gamma_{\pi\pi}^r=\left(\frac{\partial^2\gamma^r}{\partial\pi^2}\right)_\tau,\ \gamma_\tau^r=\left(\frac{\partial\gamma^r}{\partial\tau}\right)_\pi,\ \gamma_{\tau\tau}^r=\left(\frac{\partial^2\gamma^r}{\partial\tau^2}\right)_\pi,\ \gamma_{\pi\tau}^r=\left(\frac{\partial^2\gamma^r}{\partial\pi\partial\tau}\right)$

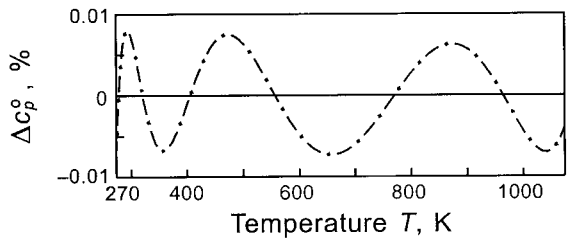

Fig. 7 Percentage deviations of the specific isobaric heat capacities in the ideal-gas state c_p^o calculated from Eq. (20) from values $c_{p,\text{IAPWS-95}}^o$ calculated from IAPWS-95 [7, 8]; $\Delta c_p^o = ((c_p^o/R) - (c_p^o/R)_{\text{IAPWS-95}})/(c_p^o/R)$.

In addition to the properties in the stable single-phase vapor region, Eq. (19) also yields reasonable values in the metastable-vapor region for pressures above 10 MPa. Equation (19) is not valid in the metastable-vapor region at pressures $p \le 10$ MPa; for this part of the metastable-vapor region see Section 5.5.2.3. For temperatures between 273.15 K and 273.16 K at pressures above the sublimation pressure [20] (metastable subcooled vapor) all values are calculated by extrapolation from Eqs. (19) and (28).

To assist the user in computer-program verification of Eq. (19), Table A6 contains test values of the most relevant properties.

5.5.2.1 Development of Eqs. (20) and (21). When developing an equation of state which should cover the typical gas-phase region starting from zero pressure, it is necessary to separate the part responsible for the behavior of the ideal gas from the rest of the equation. Thus, for region 2 the fundamental equation for the specific Gibbs free energy g in its dimensionless form, $\gamma = g/(RT)$, is separated into an ideal-gas part γ^o and a residual part γ^r according to Eq. (19). The relation for the ideal-gas part $\gamma^o(\pi, \tau)$, Eq. (20), consists of the pure pressure-dependent part $\gamma^o(\pi) = \ln\pi$ and of a pure temperature dependent part $\gamma^o(\tau)$. Keeping in mind a short computing time and the limited range of validity of Eq. (19), namely from 273.15 K to 1073.15 K, $\gamma^o(\tau)$ is expressed by a simple polynomial so that the entire equation for the ideal-gas part γ^o of the dimensionless Gibbs free energy has the form of Eq. (20). Its coefficients n_3 to n_9 were determined by fitting Eq. (20) to (c_p^o/R) values from IAPWS-95 [7, 8]; details of this fitting process, which was also combined with optimizing the structure of Eq. (20), can be found in reference [18]. The coefficients n_1^o and n_2^o were determined as described for Eq. (20).

Again, the development of the residual part γ^r of the dimensionless Gibbs free energy, Eq. (21), started with the formulation of the general functional expression based on the general form of the combined polynomial according to Eq. (14) and on similar considerations and test calculations as carried out for Eq. (18). Here, the shifting parameter b in Eq. (14) was set to zero to ensure a reasonable transition to the ideal gas. Thus, the final bank of terms consisted of 955 terms and had the following form [18]:

$$\gamma^r = \sum_{i=1}^{10}\sum_{j=0}^{33} n_{ij}\pi^i(\tau-0.5)^j + \sum_{i=11}^{25}\sum_{j=20}^{60} n_{ij}\pi^i(\tau-0.5)^j, \quad (22)$$

where $\pi = p/p^*$ and $\tau = T^*/T$ with $p^* = 1$ MPa and $T^* = 540$ K. Equation (21), obtained from Eq. (22) by the procedure of Setzmann and Wagner [5] for optimizing the functional structure of the final γ^r equation, was fitted as a part of Eq. (19) (i.e., in combination with Eq. (20)) to values of the properties v, h, c_p, s, $(\partial v/\partial p)_T$, and $(\partial v/\partial T)_p$. All these values were calculated from IAPWS-95 [7, 8] for given values of p and T distributed as selected grid points over region 2. The reasoning for including the partial derivatives of v in these properties is given for Eq. (18). Further details of the fitting process are given by Kruse and Wagner [18].

5.5.2.2 Accuracy of Eq. (19). Figure 7 shows that the γ^o equation, Eq. (20), represents the (c_p^o/R) values from IAPWS-95 [7, 8] with maximum deviations of ± 0.0081 percent. In order to

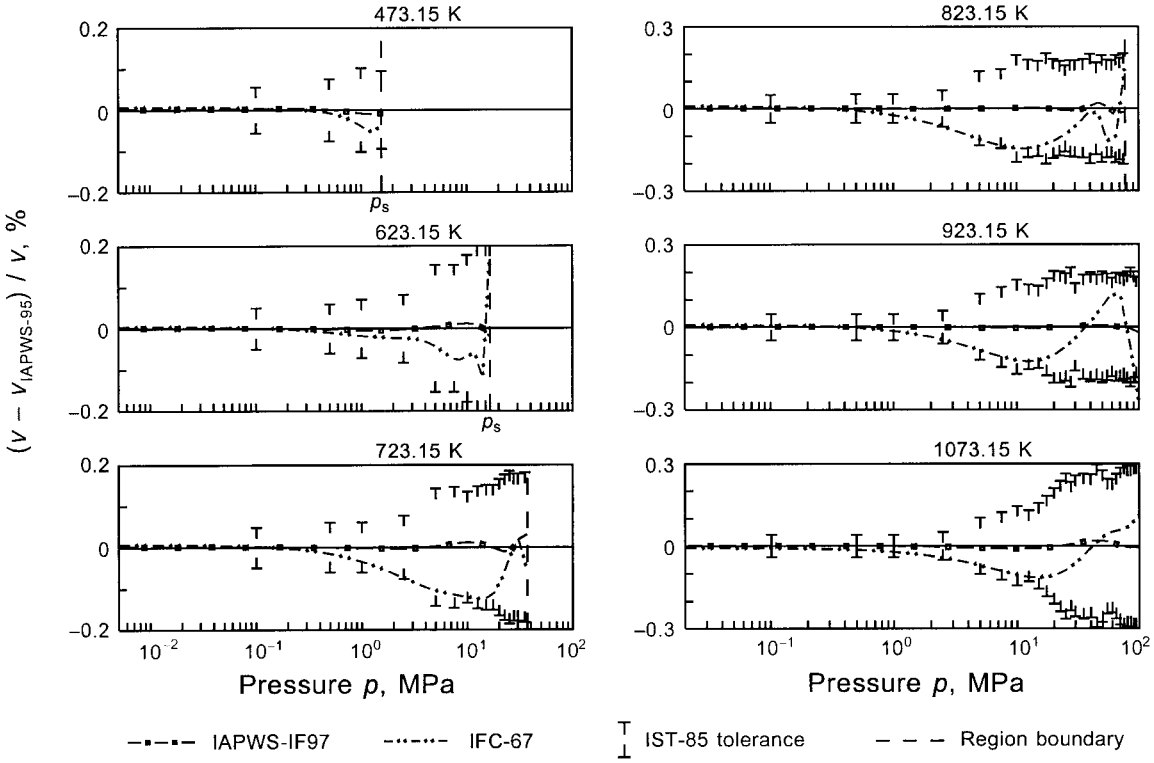

Fig. 8 Percentage deviations of the specific volumes v calculated from Eq. (19) and IFC-67, respectively, from values $v_{IAPWS-95}$ calculated from IAPWS-95 [7, 8]

obtain the difference in c_p^o itself between IAPWS-IF97 and IAPWS-95 a constant amount of $+0.0017$ percent has to be added to the deviations plotted in Fig. 7. This constant offset is caused by the older value of the gas constant used for IAPWS-95.

Equation (19) clearly meets the accuracy requirements listed in Section 4.2. The quality of representing the IAPWS-95 values [7, 8] by Eq. (19) is illustrated in Figs. 8 to 12 for the relevant properties v, h, c_p, and w. The figures show the deviations of the values calculated from Eq. (19) from the corresponding IAPWS-95 values along six isotherms and along the boundary between regions 2 and 3 described by the B23-equation corresponding to Eq. (10). These seven lines are considered to be characteristic examples for the behavior of Eq. (19) in the entire region 2. The corresponding values from IFC-67 are plotted for comparison.

Figure 8 provides information on the representation of the specific volumes by Eq. (19) which is better than the requirements by far; considering the entire region 2, the maximum deviation from the IAPWS-95 values amounts to 0.038 percent which occurs near 39 MPa and 750 K. In contrast to this, at higher temperatures IFC-67 makes full use of the tolerances reaching up to ± 0.3 percent.

Figure 9 shows that the behavior of Eq. (19) regarding the representation of the specific enthalpies is very similar to that of the specific volumes. When considering the entire region, for $T \leq 750$ K the deviations from the IAPWS-95 values are less than ± 0.2 kJ kg^{-1}, whereas for $T > 750$ K and $p > 10$ MPa the deviations increase up to about 0.4 kJ kg^{-1}; the maximum deviation occurs at 100 MPa near 900 K and amounts to 0.41 kJ kg^{-1}. Thus, for the largest part of region 2 the deviations are 20 to 40 times less than the IST-85 tolerances [9]. In contrast to this, the IFC-67 values show more systematic deviations from the values of IAPWS-95 which increase up to the IST-85 tolerances at the highest pressures of the corresponding isotherm.

Figure 10 illustrates the percentage difference between the isobaric heat capacities from IAPWS-95 and Eq. (19). In this region c_p was the property which gave the most problems. The most difficult problem was to keep the deviations along the boundary to region 3 within ± 0.5 percent (see Fig. 12). This was the decisive precondition for meeting the consistency requirement along this region boundary. Nevertheless, apart from the boundaries to regions 3 and 4 the deviations are less than ± 0.1 percent. However, when approaching the boundary to region 3 at higher temperatures, the deviations in c_p increase up to ± 0.5 percent in a few cases; the maximum deviation amounts to 0.59 percent at about 56 MPa and 780 K. It can be seen that IFC-67, even for moderate pressures, does not meet the requirements set for IAPWS-IF97, although its enthalpy representation in this range does not seem to be too bad (see, however, the statement on this matter given in context with Fig. 4 in Section 5.5.1.2).

From Fig. 11 it can be seen that Eq. (19) does not have any difficulty in representing the speeds of sound. Along the entire boundary to region 4 (saturation curve) the deviations from the IAPWS-95 values remain within ± 0.1 percent. When approaching the boundary to region 3, it is only at higher temperatures that the deviations increase to ± 0.25 percent. Considering the entire region 2, the maximum deviation from the IAPWS-95 values amounts to 0.33 percent at 100 MPa near 900 K.

Figure 12 shows the deviations of the properties v, h, c_p, and w from the corresponding IAPWS-95 values along the boundary to region 3. It can be seen that Eq. (19) does not have any problems along this "difficult" boundary, neither for c_p nor for w. In contrast to this, the c_p values from IFC-67 deviate from IAPWS-95 by up to about 6 percent.

After looking at all these deviation diagrams and realizing that the accuracy requirements are clearly exceeded, it should be emphasized that the quality of Eq. (19) is absolutely necessary in order to meet for certain the requirements regarding the consistency along the boundary between region 2 and regions 3 and 4, respectively. The large differences in c_p at the equivalent boundaries were one of the greatest weaknesses of IFC-67.

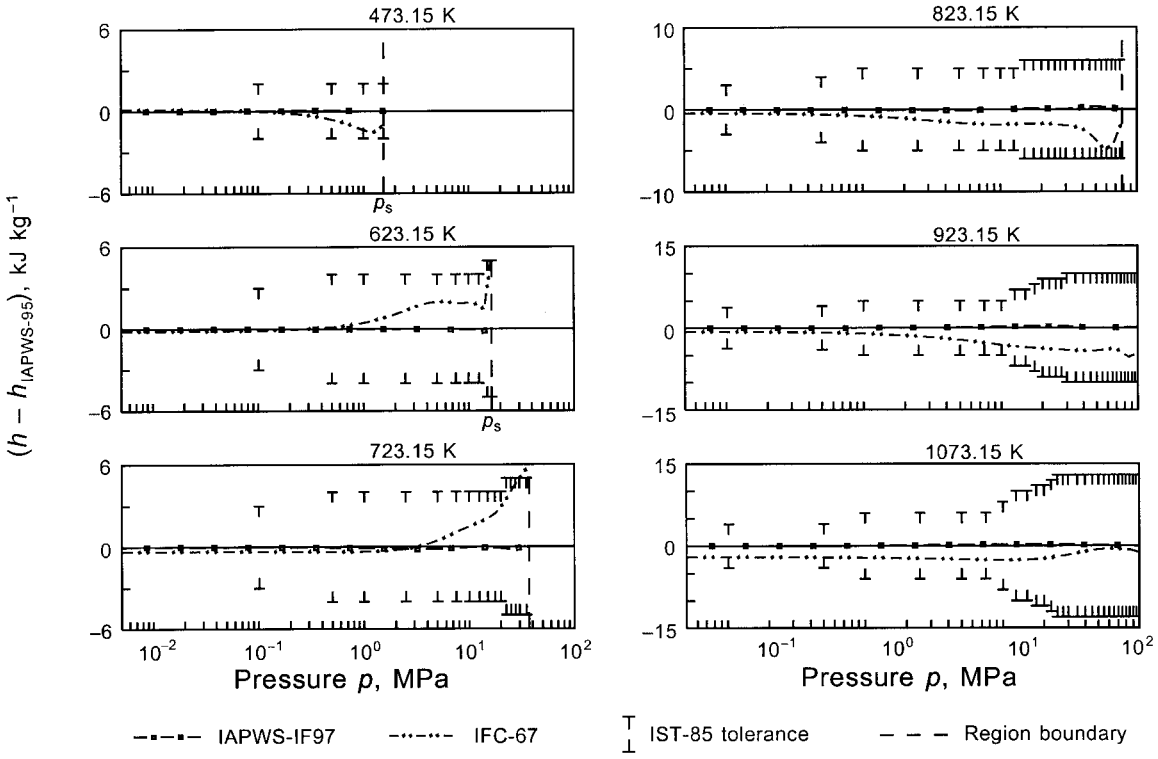

Fig. 9 Absolute deviations of the specific enthalpies h calculated from Eq. (19) and IFC-67, respectively, from values $h_{IAPWS-95}$ calculated from IAPWS-95 [7, 8]

5.5.2.3 Supplementary Equation for the Metastable-Vapor Region. As for the basic equation, Eq. (19), the supplementary equation for a part of the metastable-vapor region is given in the dimensionless form of the specific Gibbs free energy, $\gamma = g/(RT)$, consisting of an ideal-gas part γ^o and a residual part γ^r, so that

$$\frac{g(p, T)}{RT} = \gamma(\pi, \tau) = \gamma^o(\pi, \tau) + \gamma^r(\pi, \tau), \qquad (23)$$

where $\pi = p/p^*$ and $\tau = T^*/T$ with R given by Eq. (1).

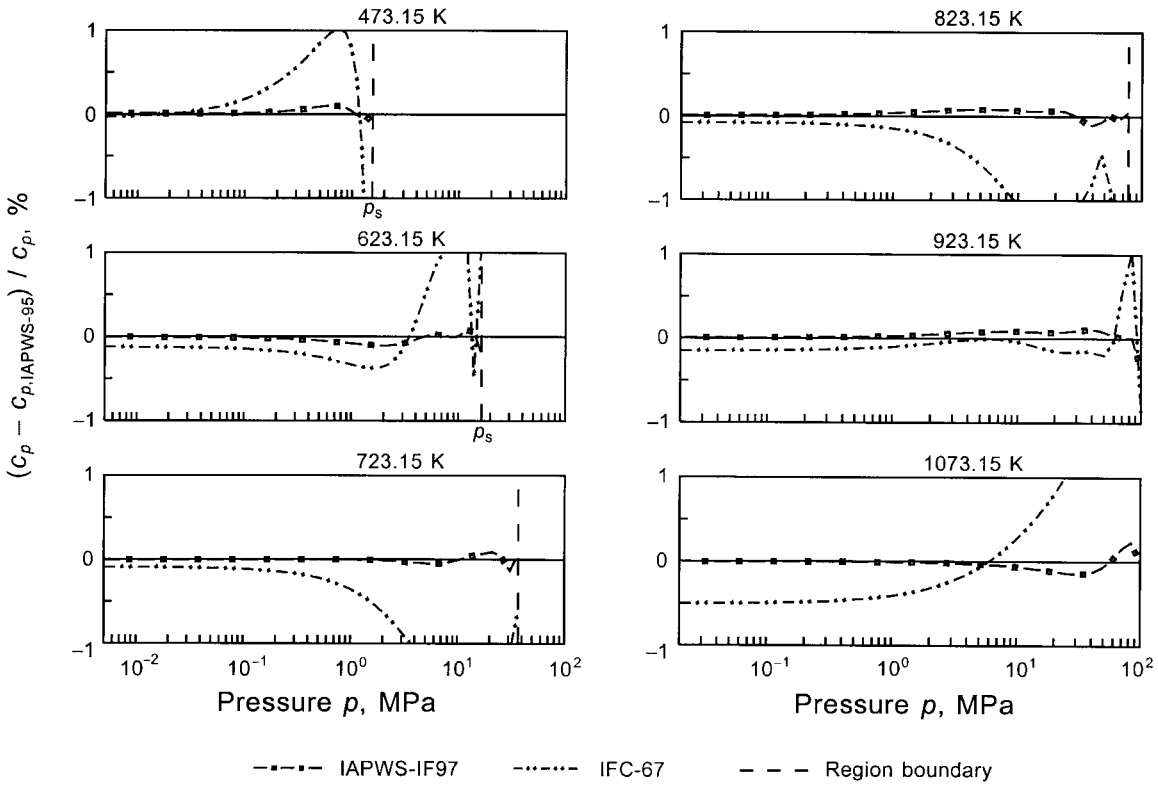

Fig. 10 Percentage deviations of the specific isobaric heat capacities c_p calculated from Eq. (19) and IFC-67, respectively, from values $c_{p,IAPWS-95}$ calculated from IAPWS-95 [7, 8]

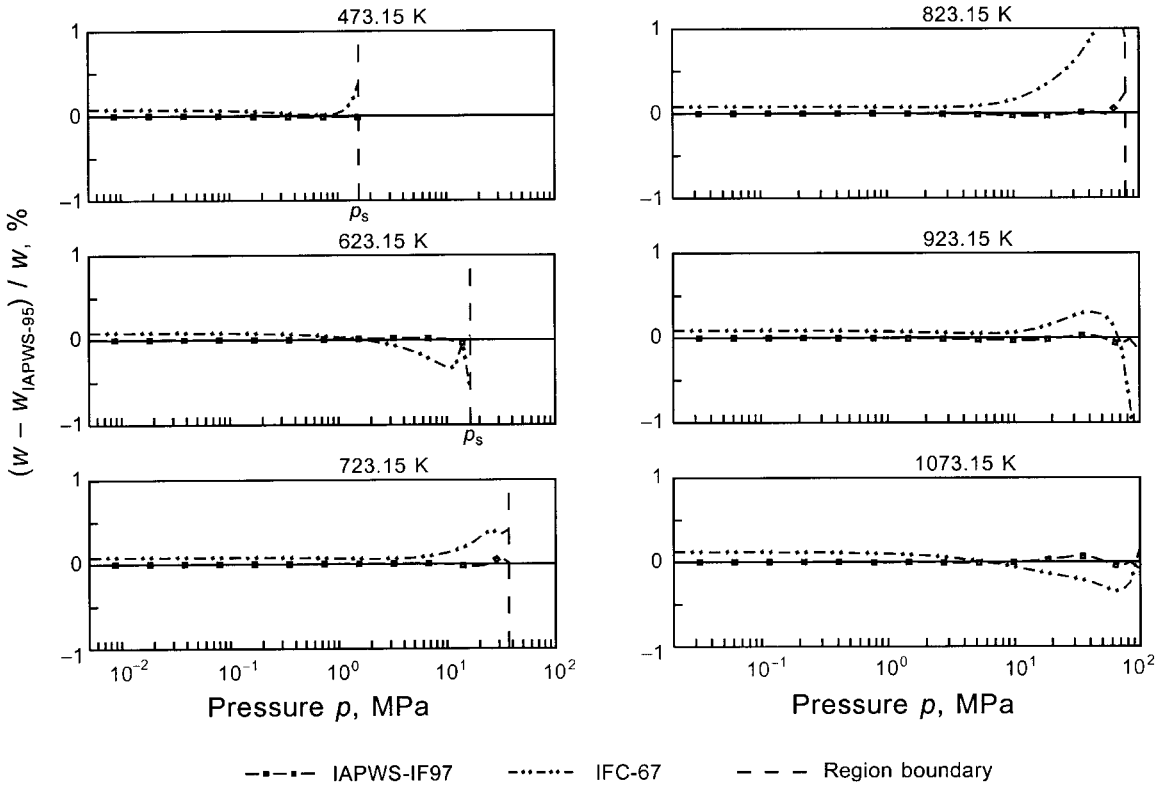

Fig. 11 Percentage deviations of the speeds of sound w calculated from Eq. (19) and IFC-67, respectively, from values $w_{IAPWS-95}$ calculated from IAPWS-95 [7, 8]

The equation for the ideal-gas part γ^o is identical with Eq. (20) except for the values of the two coefficients n_1^o and n_2^o, see Table A4. For the use of Eq. (20) as part of Eq. (23) the coefficients n_1^o and n_2^o were readjusted to meet the high consistency requirement between Eqs. (23) and (19) regarding the properties h and s along the saturated vapor line, see below.

The equation for the residual part γ^r reads

$$\gamma^r = \sum_{i=1}^{13} n_i \pi^{I_i} (\tau - 0.5)^{J_i}, \tag{24}$$

where $\pi = p/p^*$ and $\tau = T^*/T$ with $p^* = 1$ MPa and $T^* = 540$ K. The coefficients n_i and exponents I_i and J_i of Eq. (24) are listed in Table A7.

All thermodynamic properties can be derived from Eq. (23) by using the appropriate combinations of the ideal-gas part γ^o, Eq. (20), and the residual part γ^r, Eq. (24), of the dimensionless Gibbs free energy and their derivatives. The relations of the relevant thermodynamic properties to γ^o and γ^r and their derivatives are summarized in Table 4. All the required derivatives of the ideal-gas part and of the residual part of the dimensionless Gibbs free energy are explicitly given in Table 5 and Table 7, respectively.

Equation (23) is valid in the metastable-vapor region from the saturated vapor line to the 5 percent equilibrium moisture line at pressures from the triple-point pressure, see Eq. (8), up to 10 MPa. The 5 percent moisture line is determined from the equilibrium h' and h'' values where these enthalpy values at saturation belong to the pressure (not to the temperature) after the corresponding expansion.

To assist the user in computer-program verification of Eq. (23), Table A8 contains test values of the most relevant properties.

Reasons for Eq. (23). Initially the thermodynamic properties in the metastable-vapor region between the saturated vapor line and the 5 percent equilibrium moisture line were calculated from Eq. (19). Therefore, Eq. (19) was not only fitted to the properties of the stable part of region 2 calculated from IAPWS-95 [7, 8] but also to the corresponding properties in the metastable part adjacent to region 2. However, after the development of Eq. (19) it became clear that in the metastable region for pressures below 10 MPa Eq. (19) showed unexpected behavior [21]. In this range the vapor spinodal of IAPWS-95 is too close to the saturated vapor line [7, 8] and as a consequence Eq. (19) also displayed the same trend. Thus, it was decided to develop a supplementary equation for the metastable-vapor region for pressures up to 10 MPa. Since there are no experimental data in the metastable-vapor region to which such an equation could be fitted, the needed input values were determined by extrapolating a so-called gas equation into the metastable-vapor region for $p \leq 10$ MPa. This gas equation which provides a reliable representation of the thermodynamic properties of the gas region of H_2O at low densities ($\rho \leq 55$ kg m^{-3}) is described in reference [8]; it was used as an auxiliary equation for the development of IAPWS-95 [7, 8]. Besides fitting Eq. (23) to values of v, h, c_p, and s in the metastable-vapor region extrapolated from the gas equation, it was also fitted to corresponding values on the saturated vapor line calculated from Eq. (19).

Behavior of Eq. (23). Figure 13 shows in an h-s diagram the section of the metastable-vapor region which covers the temperature range from 300 K to 420 K corresponding to a pressure range from 0.0036 MPa to 0.44 MPa. The 5 percent moisture line is also shown which indicates approximately the lowest location of such Wilson lines which are considered to be the lower limit of the metastable region required for steam-turbine engineering. It can be seen that the paths of the isotherms calculated from the various equations considered are significantly different. Due to several thermodynamic reasons the IFC-67 isotherms seem to be too linear whereas the isotherms calculated from the basic equation of this region, Eq. (19), have a too strong curvature. The course of the isotherms calculated from the supplementary equation, Eq. (23), and the gas equation [8] to which Eq. (23) was fitted, are in very good agreement. Equation (23) is considered to yield reasonable

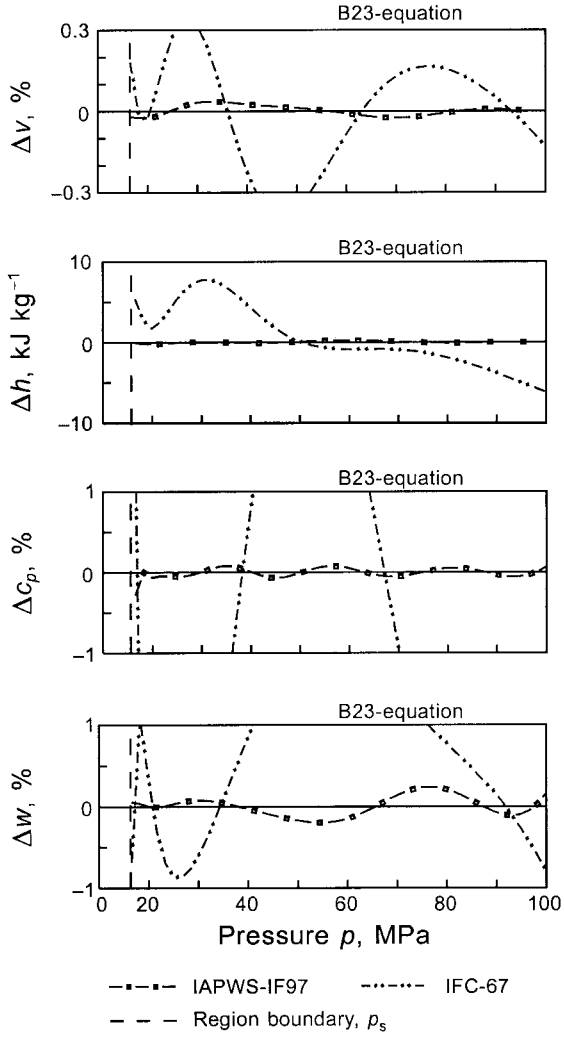

Fig. 12 Percentage deviations of the values of v, c_p, and w and absolute deviations of h values calculated from Eq. (19) and IFC-67, respectively, from the corresponding values calculated from IAPWS-95 [7, 8] along the boundary between regions 2 and 3 defined by the B23-equation: $\Delta v = (v - v_{\text{IAPWS-95}})/v$; $\Delta c_p = (c_p - c_{p,\text{IAPWS-95}})/c_p$; $\Delta h = h - h_{\text{IAPWS-95}}$; $\Delta w = (w - w_{\text{IAPWS-95}})/w$.

predictions for steam properties for industrial use in the metastable-vapor region.

The consistency of Eq. (23) with the basic equation, Eq. (19), along the saturated vapor line is characterized by the maximum and root-mean-square (RMS) inconsistencies regarding the properties v, h, c_p, s, g, and w; these values are listed in Table 8. The maximum inconsistencies are clearly smaller than the consistency requirements at the single-phase region boundaries corresponding to the so-called Prague values [10], which are given in Section 4.3.

Table 7 The residual part γ^r of the dimensionless Gibbs free energy, Eq. (24), and its derivatives

$\gamma^r = \sum_{i=1}^{13} n_i \pi^{I_i} (\tau - 0.5)^{J_i}$	$\gamma^r_\tau = \sum_{i=1}^{13} n_i \pi^{I_i} J_i (\tau - 0.5)^{J_i - 1}$
$\gamma^r_\pi = \sum_{i=1}^{13} n_i I_i \pi^{I_i - 1} (\tau - 0.5)^{J_i}$	$\gamma^r_{\tau\tau} = \sum_{i=1}^{13} n_i \pi^{I_i} J_i (J_i - 1)(\tau - 0.5)^{J_i - 2}$
$\gamma^r_{\pi\pi} = \sum_{i=1}^{13} n_i I_i (I_i - 1)\pi^{I_i - 2} (\tau - 0.5)^{J_i}$	$\gamma^r_{\pi\tau} = \sum_{i=1}^{13} n_i I_i \pi^{I_i - 1} J_i (\tau - 0.5)^{J_i - 1}$

$$\gamma^r_\pi = \left(\frac{\partial \gamma^r}{\partial \pi}\right)_\tau, \quad \gamma^r_{\pi\pi} = \left(\frac{\partial^2 \gamma^r}{\partial \pi^2}\right)_\tau, \quad \gamma^r_\tau = \left(\frac{\partial \gamma^r}{\partial \tau}\right)_\pi, \quad \gamma^r_{\tau\tau} = \left(\frac{\partial^2 \gamma^r}{\partial \tau^2}\right)_\pi, \quad \gamma^r_{\pi\tau} = \left(\frac{\partial^2 \gamma^r}{\partial \pi \partial \tau}\right)$$

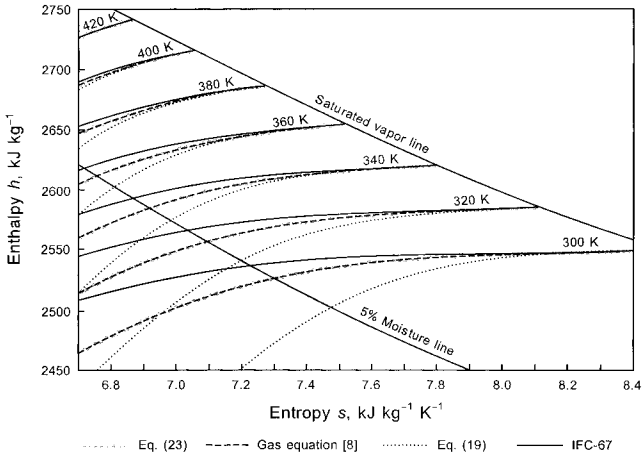

Fig. 13 Mollier *h-s* diagram for the metastable-vapor region with isotherms calculated from the equations given above

Along the 10 MPa isobar in the metastable-vapor region, the transition between Eqs. (23) and (19) is not smooth but for practical calculations unimportant.

5.5.3 The Helmholtz Free Energy Equation for Region 3. The basic equation for this region is a fundamental equation for the specific Helmholtz free energy f. This equation is expressed in dimensionless form, $\phi = f/(RT)$, and reads

$$\frac{f(\rho, T)}{RT} = \phi(\delta, \tau) = n_1 \ln \delta + \sum_{i=2}^{40} n_i \delta^{I_i} \tau^{J_i}, \qquad (25)$$

where $\delta = \rho/\rho^*$, $\tau = T^*/T$ with $\rho^* = \rho_c$, $T^* = T_c$, and R, T_c, and ρ_c given by Eqs. (1), (4), and (6). The coefficients n_i and exponents I_i and J_i of Eq. (25) are listed in Table A9.

Due to fitting Eq. (25) to the phase-equilibrium condition in the form of the Maxwell criterion for given values of T or p all properties along that part of the saturation curve belonging to region 3 can be calculated from Eq. (25) alone. Moreover, Eq. (25) reproduces exactly the critical parameters according to Eqs. (4) to (6) and yields zero for the first two pressure derivatives with respect to density at the critical point.

All thermodynamic properties can be derived from Eq. (25) by using the appropriate combinations of the dimensionless Helmholtz free energy ϕ and its derivatives. The relations of the relevant thermodynamic properties to ϕ and its derivatives are summarized in Table 9. All required derivatives of the dimensionless Helmholtz free energy are explicitly given in Table 10.

Equation (25) covers region 3 of IAPWS-IF97 defined by the following range of temperature and pressure, see Fig. 2:

$$623.15 \text{ K} \le T \le T(p)_{\text{Eq.(11)}} \quad p(T)_{\text{Eq.(10)}} \le p \le 100 \text{ MPa}.$$

Table 8 Inconsistencies between Eqs. (19) and (23) along the saturated vapor line given as maximum and root-mean square (RMS) values

Inconsistency	Prague value [10]	Maximum value[a]	RMS value
Δv, %	0.05	0.014	0.006
Δh, kJ kg^{-1}	0.2	0.043	0.020
Δc_p, %	1	0.78	0.357
Δs, J kg^{-1}K^{-1}	0.2	0.082	0.044
Δg, kJ kg^{-1}	0.2	0.023	0.009
Δw, %	1[b]	0.051	0.025

[a] Absolute value

[b] The permitted inconsistency value for w is not included in the Prague values

Table 9 Relations of thermodynamic properties to the dimensionless Helmholtz free energy ϕ and its derivatives when using Eq. (25)[a]

Property	Relation
Pressure $p = \rho^2(\partial f/\partial\rho)_T$	$\frac{p(\delta,\tau)}{\rho RT} = \delta\phi_\delta$
Specific internal energy $u = f - T(\partial f/\partial T)_\rho$	$\frac{u(\delta,\tau)}{RT} = \tau\phi_\tau$
Specific entropy $s = -(\partial f/\partial T)_\rho$	$\frac{s(\delta,\tau)}{R} = \tau\phi_\tau - \phi$
Specific enthalpy $h = f - T(\partial f/\partial T)_\rho + \rho(\partial f/\partial\rho)_T$	$\frac{h(\delta,\tau)}{RT} = \tau\phi_\tau + \delta\phi_\delta$
Specific isochoric heat capacity $c_v = (\partial u/\partial T)_\rho$	$\frac{c_v(\delta,\tau)}{R} = -\tau^2\phi_{\tau\tau}$
Specific isobaric heat capacity $c_p = (\partial h/\partial T)_p$	$\frac{c_p(\delta,\tau)}{R} = -\tau^2\phi_{\tau\tau} + \frac{(\delta\phi_\delta - \delta\tau\phi_{\delta\tau})^2}{2\delta\phi_\delta + \delta^2\phi_{\delta\delta}}$
Speed of sound $w = \left[(\partial p/\partial\rho)_s\right]^{0.5}$	$\frac{w^2(\delta,\tau)}{RT} = 2\delta\phi_\delta + \delta^2\phi_{\delta\delta} - \frac{(\delta\phi_\delta - \delta\tau\phi_{\delta\tau})^2}{\tau^2\phi_{\tau\tau}}$
Phase-equilibrium condition (Maxwell criterion)	$\frac{p_s}{RT\rho'} = \delta'\phi_\delta(\delta',\tau)$; $\frac{p_s}{RT\rho''} = \delta''\phi_\delta(\delta'',\tau)$
	$\frac{p_s}{RT}\left(\frac{1}{\rho''} - \frac{1}{\rho'}\right) = \phi(\delta',\tau) - \phi(\delta'',\tau)$

$\phi_\delta = \left(\frac{\partial\phi}{\partial\delta}\right)_\tau$, $\phi_{\delta\delta} = \left(\frac{\partial^2\phi}{\partial\delta^2}\right)_\tau$, $\phi_\tau = \left(\frac{\partial\phi}{\partial\tau}\right)_\delta$, $\phi_{\tau\tau} = \left(\frac{\partial^2\phi}{\partial\tau^2}\right)_\delta$, $\phi_{\delta\tau} = \left(\frac{\partial^2\phi}{\partial\delta\partial\tau}\right)$

[a] A general procedure how to obtain the relation of any property and any differential quotient to ϕ and its derivatives when using Eq. (25) can be found in [19a]

In addition to the properties in the stable single-phase region defined above, Eq. (25) also yields reasonable values in the metastable regions (superheated liquid and subcooled steam) close to the saturated liquid and saturated vapor line, see Section 5.5.3.2.

To assist the user in computer-program verification of Eq. (25), Table A10 contains test values of the most relevant properties.

5.5.3.1 Development of Eq. (25). In contrast to the fundamental equation of the Gibbs free energy g the fundamental equation of the Helmholtz free energy f chosen for region 3 of IAPWS-IF97 is suitable for the critical and supercritical region covered by region 3. The independent variables of such an f equation are the density ρ and the temperature T. When establishing an equation of state in the form of the fundamental equation of the Helmholtz free energy, the expression is usually separated into a part for the ideal gas and a residual part [8, 16, 17]. However, such a separation is not necessary for the special application only to the critical and supercritical region. Comprehensive test calculations yielded that there was no need to use the shifting parameters b and d as given in Eq. (14) for the general functional form of the $g(p, T)$ equations but to use the critical parameters ρ_c and T_c as reducing parameters ρ^* and T^*. Moreover, in addition to the pure polynomial in δ and τ the incorporation of $(\ln\delta)\tau^j$ terms proved favorable. As a result of all these considerations and test calculations the following general functional expression of 362 terms was used for the subsequent optimization process [18]:

$$\phi = \sum_{j=0}^{10} n_j(\ln\delta)\tau^j + \sum_{i=0}^{12}\sum_{j=0}^{26} n_{ij}\delta^i\tau^j, \qquad (26)$$

Table 10 The dimensionless Helmholtz free energy ϕ, Eq. (25), and its derivatives

$\phi = n_1\ln\delta + \sum_{i=2}^{40} n_i\,\delta^{I_i}\,\tau^{J_i}$	$\phi_\tau = \sum_{i=2}^{40} n_i\,\delta^{I_i}\,J_i\,\tau^{J_i-1}$
$\phi_\delta = n_1\delta^{-1} + \sum_{i=2}^{40} n_i\,I_i\,\delta^{I_i-1}\,\tau^{J_i}$	$\phi_{\tau\tau} = \sum_{i=2}^{40} n_i\,\delta^{I_i}\,J_i(J_i-1)\,\tau^{J_i-2}$
$\phi_{\delta\delta} = -n_1\delta^{-2} + \sum_{i=2}^{40} n_i\,I_i(I_i-1)\,\delta^{I_i-2}\,\tau^{J_i}$	$\phi_{\delta\tau} = \sum_{i=2}^{40} n_i\,I_i\,\delta^{I_i-1}\,J_i\,\tau^{J_i-1}$

$\phi_\delta = \left(\frac{\partial\phi}{\partial\delta}\right)_\tau$, $\phi_{\delta\delta} = \left(\frac{\partial^2\phi}{\partial\delta^2}\right)_\tau$, $\phi_\tau = \left(\frac{\partial\phi}{\partial\tau}\right)_\delta$, $\phi_{\tau\tau} = \left(\frac{\partial^2\phi}{\partial\tau^2}\right)_\delta$, $\phi_{\delta\tau} = \left(\frac{\partial^2\phi}{\partial\delta\partial\tau}\right)$

where $\delta = \rho/\rho^*$, $\tau = T^*/T$ with $\rho^* = \rho_c$, $T^* = T_c$ and T_c and ρ_c given by Eqs. (4) and (6). The incorporation of the ln δ term (which looks similar to an ideal gas term but is not) proved so effective that it was used in spite of its clearly slower computation speed; this is, however, not so bad because for region 3 the requirements regarding the computing time were clearly weaker than for regions 1, 2, and 4 (see Section 4.4).

Equation (25), obtained from Eq. (26) by the method of Setzmann and Wagner [5] for optimizing the functional structure of the final ϕ equation, was fitted to values of the properties p, h, c_v, s, and the two partial derivatives $(\partial p/\partial\rho)_T$ and $(\partial p/\partial T)_\rho$. These values were calculated from IAPWS-95 [7, 8] for given values of ρ and T distributed as selected grid points over region 3. The inclusion of the partial derivatives of p with respect to ρ and T made it unnecessary to fit the equations to the corresponding values of c_p and w which would have led to a nonlinear system of normal equations when minimizing the sum of squares. Such a nonlinear fitting process could not have been combined with the structure-optimization procedure [5] because this procedure can only cope with sums of squares which are linear in the coefficients n_j and n_{ij}, respectively. Moreover, fitting Eq. (25) just to the properties mentioned above ensures that Eq. (25) yields reasonable values for any property based on the first and second derivatives of ϕ, see also the general statement at the beginning of Section 5.5. In addition to the properties calculated from IAPWS-95 within region 3 the equations were also fitted to the corresponding properties calculated from the g equation of region 1, Eq. (15), along the boundary between regions 1 and 3 and from the g equation for region 2, Eq. (19), along the boundary between regions 2 and 3. In this way, Eq. (25) was fitted with good numerical consistency with the g equations of regions 1 and 2.

Moreover, for temperatures from 623.15 K to T_c = 647.096 K (see Eq. (4)) the equations were fitted to the phase-equilibrium condition $g'(T, p) = g''(T, p)$ in form of the Maxwell criterion (see Table 9). Simultaneously to this fitting process, the equations were also constrained to the conditions at the critical point, see the corresponding statement on Eq. (25). Details of this entire fitting process are given by Kruse and Wagner [18].

5.5.3.2 Accuracy of Eq. (25). Equation (25) meets clearly the accuracy requirements listed in Section 4.2. The quality of representing the IAPWS-95 values [7, 8] by Eq. (25) is illustrated in Figs. 14(*a*) to 17 for the relevant properties v, h, c_p, and w. The figures show the deviations of the values calculated from Eq. (25) from the corresponding IAPWS-95 values along five isotherms and along the boundary between regions 2 and 3 described by the B23-equation corresponding to Eq. (10). Since the 623.15 K isotherm is included in these isotherms, the behavior of Eq. (25) along the boundaries to the two adjacent regions 1 and 2 is recognizable. These six lines are considered to be characteristic examples for the behavior of Eq. (25) in the entire region 3. Where necessary, special deviation diagrams for the behavior of Eq. (25) in the critical region are given. Figure 14(*a*) illustrates how well Eq. (25) represents the specific volumes from IAPWS-95. For the largest part of region 3 including the "difficult" range along the boundary to region 2, the deviations from the IAPWS-95 values remain within ±0.03 percent whereas the IST-85 tolerances [9] are mostly between ±0.1 percent and ±0.2 percent. Even in the critical and enlarged critical region the deviations were kept within the tolerances, see Fig. 14(*b*). As a matter of course, the largest deviations from IAPWS-95 occur in the immediate vicinity of the critical point, but Fig. 14(*b*) shows that even for T = 648.15 K (T_c = 647.096 K) at about p = 22.3 MPa (p_c = 22.064 MPa) the deviation from IAPWS-95 only increases up to about 3 percent. Figure 14(*a*) also shows that over the entire region IFC-67 does not meet the present requirements.

As can be seen from Fig. 15 there is practically no difference between the specific enthalpies from Eq. (25) and from IAPWS-95. With very few exceptions along the critical isochore, Eq. (25) represents the IAPWS-95 values to within ±0.25 kJ kg^{-1}; the

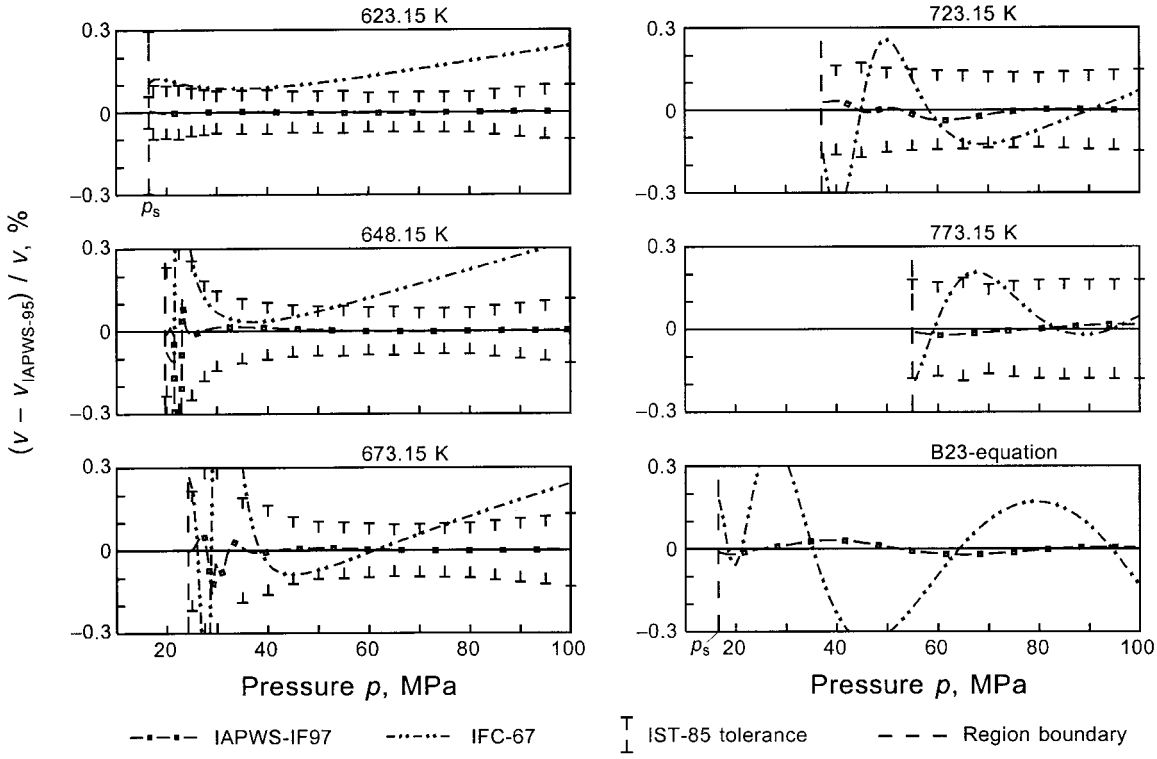

Fig. 14(*a*) Percentage deviations of the specific volumes *v* calculated from Eq. (25) and IFC-67, respectively, from values $v_{IAPWS-95}$ calculated from IAPWS-95 [7, 8]

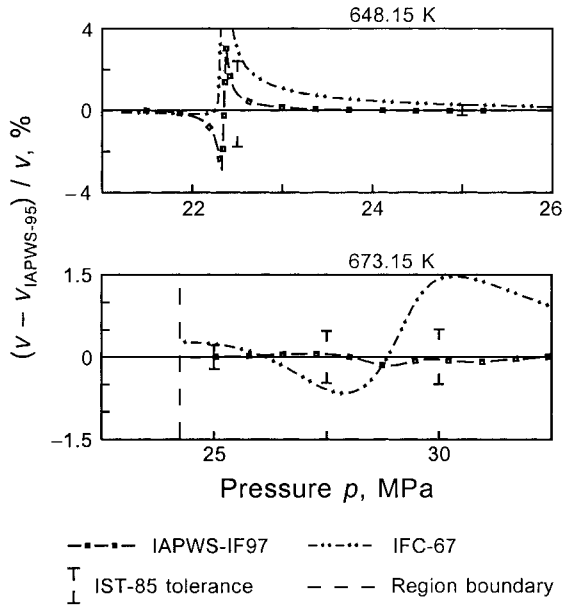

Fig. 14(*b*) Percentage deviations of the specific volumes *v* calculated from Eq. (25) and IFC-67, respectively, from values $v_{IAPWS-95}$ calculated from IAPWS-95 [7, 8]; spread pressure scale for the enlarged critical region.

maximum deviation is less than 0.6 kJ kg^{-1} occurring near 24 MPa and 650 K.

Figures 16(*a*) and 16(*b*) summarize the behavior of Eq. (25) with regard to the representation of the isobaric heat capacities which gave the most problems in region 3. Except for the critical region, Eq. (25) represents the values from IAPWS-95 to within ± 0.5 percent, in wide ranges even to within ± 0.1 percent. In contrast to this, the c_p values from IFC-67 deviate over large parts of this region by more than ± 2 percent from the IAPWS-95 values. When approaching the critical point the values of c_p increase drastically and directly at the critical point c_p is infinite. Thus, it is not surprising, but one should be aware, that in the critical range c_p values calculated from different equations of state deviate considerably from each other. This fact is illustrated in Fig. 16(*b*) where the systematic deviations in this region are shown in more detail. For 648.15 K (T_c = 647.096 K) it can be seen that in a small pressure range slightly above the critical pressure (p_c = 22.064 MPa) the c_p values from Eq. (25) deviate considerably from the IAPWS-95 values, where the maximum deviation reaches up to -53 percent. The diagram also shows that the pressure range in which such significant deviations from IAPWS-95 occur is much wider for IFC-67 than for Eq. (25); the maximum deviation of the IFC-67 values amounts to -62 percent. For all these considerations it should not be forgotten that the uncertainty of IAPWS-95 in c_p in the immediate vicinity of the critical point is also relatively large. The lower diagram of Fig. 16(*b*) shows that at the border of the critical region, e.g., at 673.15 K, the c_p values from Eq. (25) deviate from the IAPWS-95 values by at most 1.7 percent.

In order to check whether these extraordinarily large deviations of c_p from Eq. (25) from those from IAPWS-95 in the near-critical region have consequences for practical calculations, isobaric enthalpy differences according to a temperature difference of 10 K were calculated from Eq. (25) and from IAPWS-95 in this region. These investigations covered a pressure range from 22.1 MPa to 24 MPa, where the isobaric enthalpy differences were calculated for the temperature difference between 652 K and 642 K for pressures up to 23 MPa and between 662 K and 652 K for 23.5 MPa and 24 MPa. For 22.1 MPa, 22.2 MPa, 22.3 MPa, 22.5 MPa, and 24 MPa the differences between the Δh values from IAPWS-95 and from Eq. (25) remained below 0.1 percent whereas for 22.7 MPa, 23 MPa, and 23.5 MPa the corresponding $\Delta(\Delta h)$ values increased to 0.23 percent, 0.85 percent, and 1.62 percent, respectively. These test calculations show that the very large c_p deviations hardly affect Δh values over temperature intervals of 10 K.

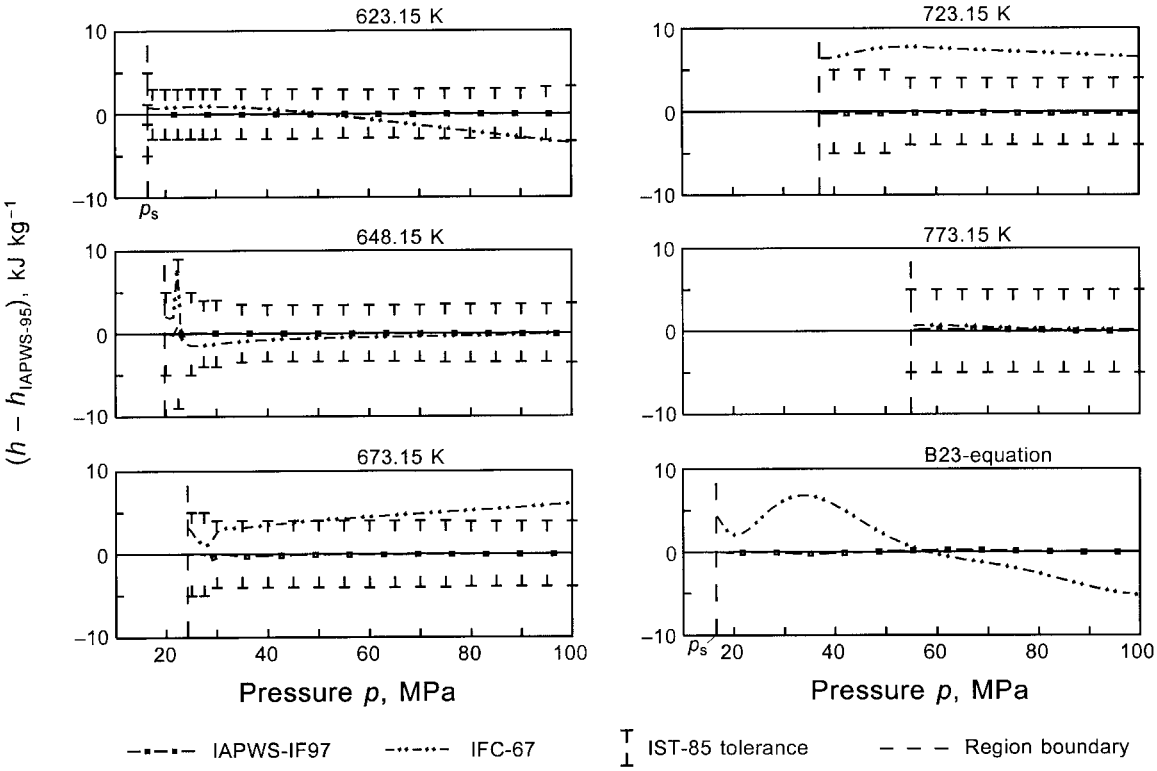

Fig. 15 Absolute deviations of the specific enthalpies h calculated from Eq. (25) and IFC-67, respectively, from values $h_{IAPWS-95}$ calculated from IAPWS-95 [7, 8]

From Fig. 17 it can be seen that the quality of Eq. (25) in representing the speeds of sound w from IAPWS-95 is very similar to that of c_p discussed above. Apart from the critical region, the deviations of the w values from Eq. (25) from those of IAPWS-95 remain within ± 0.3 percent whereas in the critical region the deviations increase, as expected, to values greater than ± 1 percent. It can also be seen that IFC-67 is not able to meet the present requirements of ± 1 percent regarding the representation of the speed of sound.

Metastable States. Figure 18 illustrates the behavior of Eq. (25) within the two-phase region along representative isotherms for the temperature range 623.15 K $\leq T \leq$ 647.096 K $= T_c$ and in addition along the 648.15 K isotherm in the single-phase region. All isotherms in the two-phase region have only one minimum and one maximum which are points of the spinodals meeting in the critical point. There are no further extrema and the two inflection points (instead of one) on the lower isotherms do not have any physical or practical meaning because they are within the unstable region. Thus, Eq. (25) predicts reasonable values in the metastable vapor and liquid region of region 3.

5.5.4 The Saturation-Pressure Equation for Region 4. For several reasons (see section 5.5.4.1) instead of a saturation-pressure equation, an implicit equation was developed describing the saturation curve. This equation can be solved directly for either saturation pressure p_s or saturation temperature T_s.

The equation for describing the saturation curve is an implicit bi-quadratic equation which reads

$$\beta^2\vartheta^2 + n_1\beta^2\vartheta + n_2\beta^2 + n_3\beta\vartheta^2 + n_4\beta\vartheta + n_5\beta + n_6\vartheta^2 + n_7\vartheta + n_8 = 0, \quad (27)$$

where

$$\beta = (p_s/p^*)^{0.25} \quad (27a)$$

and

$$\vartheta = \frac{T_s}{T^*} + \frac{n_9}{(T_s/T^*) - n_{10}} \quad (27b)$$

with $p^* = 1$ MPa and $T^* = 1$ K; for the coefficients n_1 to n_{10} see Table A11.

The explicit form of the saturation-pressure equation (basic equation) is obtained from the solution of Eq. (27) with respect to p_s as follows[11]:

$$\frac{p_s}{p^*} = \left[\frac{2C}{-B + (B^2 - 4AC)^{0.5}}\right]^4, \quad (28)$$

where $p^* = 1$ MPa and

$$A = \vartheta^2 + n_1\vartheta + n_2$$

$$B = n_3\vartheta^2 + n_4\vartheta + n_5$$

$$C = n_6\vartheta^2 + n_7\vartheta + n_8$$

with ϑ according to Eq. (27*b*). The coefficients n_i of Eq. (28) are listed in Table A11.

Equations (27) and (28) reproduce exactly the p-T values at the triple point according to Eqs. (7) and (8), at the normal boiling point according to Eq. (9) and at the critical point according to Eqs. (4) and (5). Due to the special fitting process of Eq. (27) with respect to Eq. (25), the specific volumes of the saturated liquid and vapor, v' and v'', can be simply calculated directly up to the critical point from the intersection of the saturation pressure from Eq. (28) with the pressure from the Helmholtz free energy equation, Eq. (25), for the temperature considered. Therefore, it is not necessary to calculate v' and v'' by solving Eq. (25) using the Maxwell criterion which is a complex iteration process.

[11] This solution is not quite simple, for details see [22]. The saturation-temperature equation (backward equation) which follows from Eq. (27) by solving it with respect to T_s is given in Section 5.6.4.

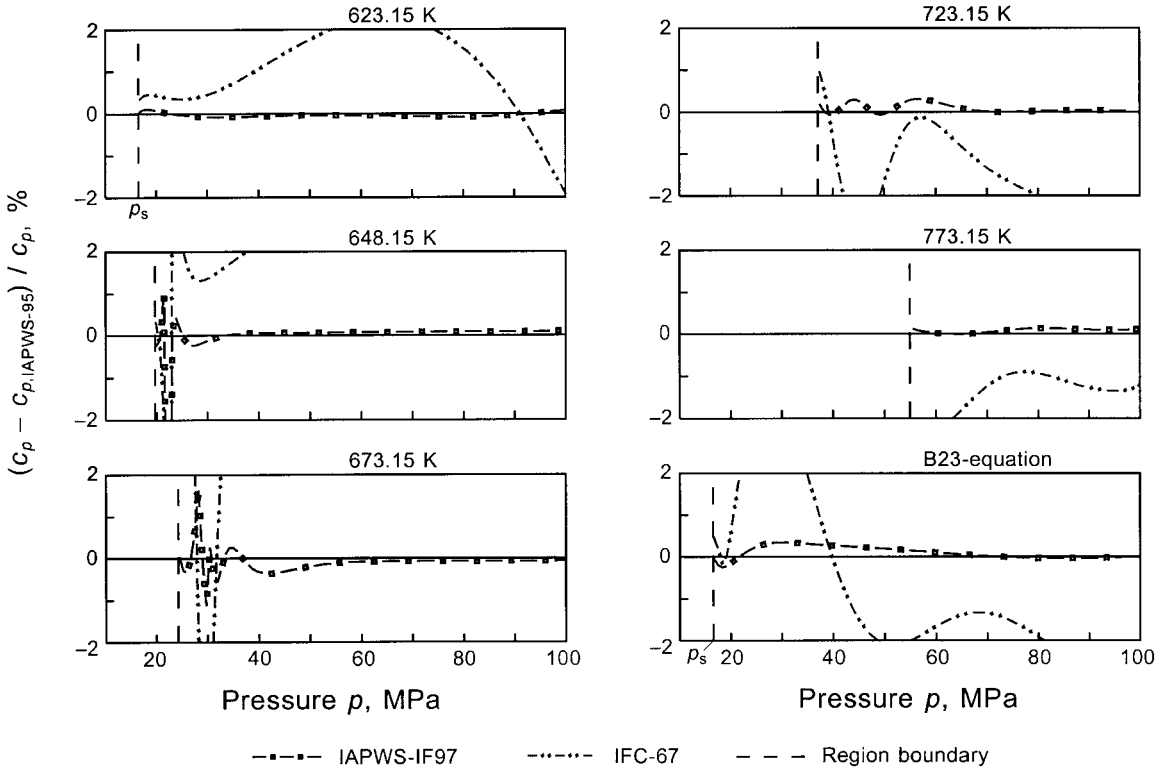

Fig. 16(*a*) Percentage deviations of the specific isobaric heat capacities c_p calculated from Eq. (25) and IFC-67, respectively, from values $c_{p,\text{IAPWS-95}}$ calculated from IAPWS-95 [7, 8]

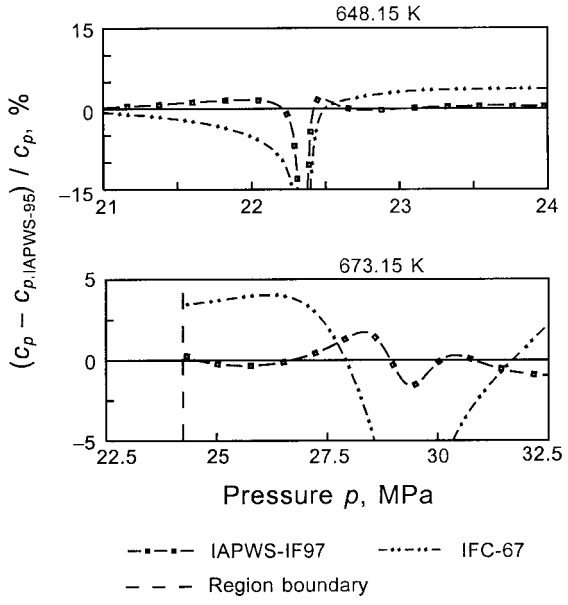

Fig. 16(*b*) Percentage deviations of the specific isobaric heat capacities c_p calculated from Eq. (25) and IFC-67, respectively, from values $c_{p,\text{IAPWS-95}}$ calculated from IAPWS-95 [7, 8]; spread pressure scale for the enlarged critical region.

Equation (28) is valid along the entire vapor-liquid saturation curve from the triple-point temperature T_t to the critical temperature T_c and can be simply extrapolated to 273.15 K so that it covers the temperature range

$$273.15\ \text{K} \le T \le 647.096\ \text{K}.$$

To assist the user in computer-program verification of Eq. (28), Table A12 contains corresponding test values.

5.5.4.1 Development of Eq. (27). In the course of the development of the basic and backward equation for the saturation curve three alternatives were pursued, namely a "fast" polynomial equation pair with integer exponents, a pair of so-called short polynomial equations with fractional exponents, and implicit equations which are directly solvable with regard to both $p_s(T)$ and $T_s(p)$, for details of these developments see Kretzschmar et al. [22]. After checking these equations and considering carefully their pros and cons, an implicit saturation equation, which provides complete numerical consistency between the $p_s(T)$ form and $T_s(p)$ form, was finally chosen as saturation equation for region 4 of IAPWS-IF97; this equation corresponds to Eq. (27).

Equation (27) was fitted to p_s values calculated from IAPWS-95 [7, 8] and was constrained to the p-T values at the triple point, normal boiling point and critical point given by Eqs. (7) to (9), (4), and (5). In addition, Eq. (27) was also fitted to the p_s values from the Helmholtz free energy equation of region 3, Eq. (25), so that Eq. (28) yields vapor pressures which are, even very close to the critical temperature, between the pressures of the vapor and liquid spinodals of Eq. (25); the reasoning of this special fitting process is given by the corresponding statement in connection with Eq. (28). The entire fitting procedure is based on the approximation algorithm developed by Willkommen et al. [23] which includes the simultaneous steady approximation of Zschunke et al. [24].

5.5.4.2 Accuracy of Eq. (28). Figure 19 shows that the saturation-pressure equation, Eq. (28), represents the saturation pressures calculated from IAPWS-95 for the entire range from the triple-point temperature T_t to the critical temperature T_c to within the IST-85 tolerances [9]. Even for temperatures below the temperature T_b of the normal boiling point, the p_s values from Eq. (28) remain within the IST-85 tolerances which are, in this region, clearly smaller than the permissible deviations of ± 0.025 percent (see Section 4.2). It can also be seen that Eq. (28) meets the p_s values at the triple point according to Eqs. (7) and (8), at the normal boiling point according to Eq. (9), and at the critical point according to Eqs. (4) and (5). For comparison, the figure also

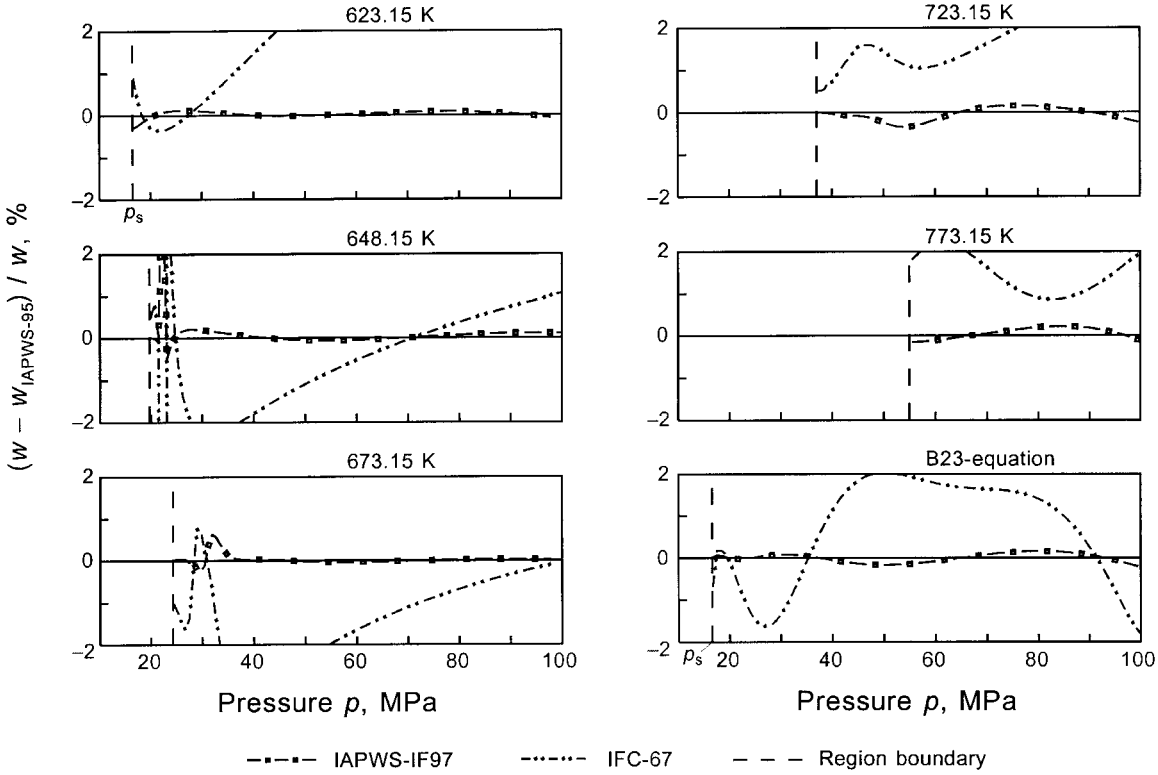

Fig. 17 Percentage deviations of the speeds of sound w calculated from Eq. (25) and IFC-67, respectively, from values $w_{IAPWS-95}$ calculated from IAPWS-95 [7, 8]

contains the corresponding Δp_s line generated from IFC-67; the maximum deviation of the IFC-67 values amounts to 0.12 percent.

5.5.5 The Gibbs Free Energy Equation for Region 5. The basic equation for this high-temperature region is a fundamental equation for the specific Gibbs free energy g in its dimensionless form, $\gamma = g/(RT)$, which is again separated into an ideal-gas part γ^o and a residual part γ^r, so that

$$\frac{g(p, T)}{RT} = \gamma(\pi, \tau) = \gamma^o(\pi, \tau) + \gamma^r(\pi, \tau), \tag{29}$$

where $\pi = p/p^*$ and $\tau = T^*/T$ with R given by Eq. (1).

The equation for the ideal-gas part γ^o of the dimensionless Gibbs free energy reads

$$\gamma^o = \ln \pi + \sum_{i=1}^{6} n_i^o \tau^{J_i^o}, \tag{30}$$

where $\pi = p/p^*$ and $\tau = T^*/T$ with $p^* = 1$ MPa and $T^* = 1000$ K. The coefficients n_1^o and n_2^o were adjusted in such a way that for

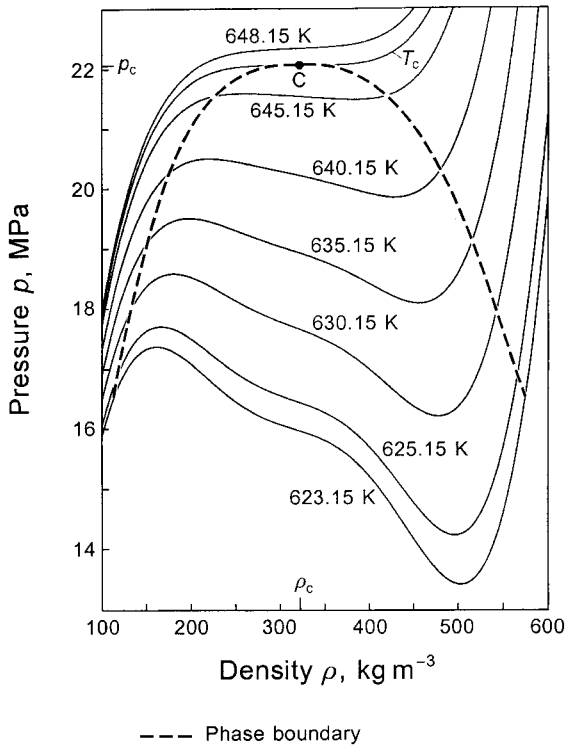

Fig. 18 Behavior of Eq. (25) in the vapor-liquid two-phase region of region 3

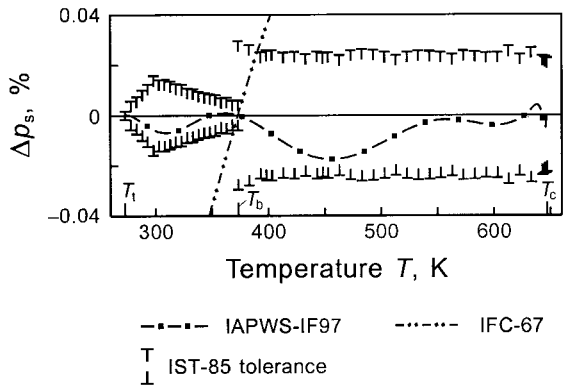

Fig. 19 Percentage deviations of the saturation pressure p_s calculated from Eq. (28) and IFC-67, respectively, from values $p_{s,IAPWS-95}$ calculated from IAPWS-95 [7, 8]

$T = 1073.15$ K the values for the specific internal energy and specific entropy, calculated from Eq. (29), relate to the corresponding values calculated from Eq. (19). Table A13 contains the coefficients n_i^o and exponents J_i^o of Eq. (30).

The form of the residual part γ^r of the dimensionless Gibbs free energy is as follows:

$$\gamma^r = \sum_{i=1}^{5} n_i \pi^{I_i} \tau^{J_i}, \tag{31}$$

where $\pi = p/p^*$ and $\tau = T^*/T$ with $p^* = 1$ MPa and $T^* = 1000$ K. The coefficients n_i and exponents I_i and J_i of Eq. (31) are listed in Table A14.

All thermodynamic properties can be derived from Eq. (29) by using the appropriate combinations of the ideal-gas part γ^o, Eq. (30), and the residual part γ^r, Eq. (31), of the dimensionless Gibbs free energy and their derivatives. Relations between the relevant thermodynamic properties and γ^o and γ^r and their derivatives are summarized in Table 4. All required derivatives of the ideal-gas part and of the residual part of the dimensionless Gibbs free energy are explicitly given in Table 11 and Table 12, respectively.

Equation (29) covers region 5 of IAPWS-IF97 defined by the following temperature and pressure range, see Fig. 2:

$$1073.15 \text{ K} \le T \le 2273.15 \text{ K} \quad 0 < p \le 10 \text{ MPa}.$$

In this range Eq. (29) is only valid for pure undissociated water, dissociation has not been considered.

To assist the user in computer-program verification of Eq. (29), Table A15 contains test values of the most relevant properties.

Development and Accuracy of Eq. (29). For high-temperature applications of the thermodynamic properties of steam such as in gas turbines it was requested to have a simple equation of state for temperatures above 1073.15 K and pressures up to 10 MPa. According to this demand a fundamental equation for the specific Gibbs free energy in its absolute form was developed by Mareš and Šifner [25]. Equation (29) is a simplified version (shortened in residual part) of this equation.

The coefficients n_3^o to n_6^o of Eq. (30) were fitted to values of the dimensionless isobaric heat capacity in the ideal-gas state, (c_p^o/R), calculated from the ideal-gas part ϕ^o of IAPWS-95 [7, 8]. Since this ϕ^o equation of IAPWS-95 is based on the (c_p^o/R) equation of Cooper [26] which was fitted to data in the temperature range from 130 K to 2000 K, the calculation of (c_p^o/R) values from IAPWS-95 for temperatures from 1073.15 K to 2273.15 K corresponds only to a marginal extrapolation. The values of the coefficients n_1^o and n_2^o of Eq. (30) were determined as described in connection with Eq. (30). The coefficients n_i of Eq. (31) were determined by fitting Eq. (29) to values of the specific volume v calculated from IAPWS-95 [7, 8] for given values of p and T at selected grid points distributed over region 5 for $1073.15 \text{ K} < T \le 2273.15$ K and from Eq. (19) for $T = 1073.15$ K. For $T > 1273.15$ K the corresponding IAPWS-95 values were obtained by extrapolating this formulation.

Table 11 The ideal-gas part γ^o of the dimensionless Gibbs free energy, Eq. (30), and its derivatives

$\gamma^o = \ln \pi + \sum_{i=1}^{6} n_i^o \tau^{J_i^o}$	$\gamma_\tau^o = \sum_{i=1}^{6} n_i^o J_i^o \tau^{J_i^o - 1}$
$\gamma_\pi^o = \pi^{-1}$	$\gamma_{\tau\tau}^o = \sum_{i=1}^{6} n_i^o J_i^o (J_i^o - 1) \tau^{J_i^o - 2}$
$\gamma_{\pi\pi}^o = -\pi^{-2}$	$\gamma_{\pi\tau}^o = 0$

$$\gamma_\pi^o = \left(\frac{\partial \gamma^o}{\partial \pi}\right)_\tau, \ \gamma_{\pi\pi}^o = \left(\frac{\partial^2 \gamma^o}{\partial \pi^2}\right)_\tau, \ \gamma_\tau^o = \left(\frac{\partial \gamma^o}{\partial \tau}\right)_\pi, \ \gamma_{\tau\tau}^o = \left(\frac{\partial^2 \gamma^o}{\partial \tau^2}\right)_\pi, \ \gamma_{\pi\tau}^o = \left(\frac{\partial^2 \gamma^o}{\partial \pi \partial \tau}\right)$$

Table 12 The residual part γ^r of the dimensionless Gibbs free energy, Eq. (31), and its derivatives

$\gamma^r = \sum_{i=1}^{5} n_i \pi^{I_i} \tau^{J_i}$	$\gamma_\tau^r = \sum_{i=1}^{5} n_i \pi^{I_i} J_i \tau^{J_i - 1}$
$\gamma_\pi^r = \sum_{i=1}^{5} n_i I_i \pi^{I_i - 1} \tau^{J_i}$	$\gamma_{\tau\tau}^r = \sum_{i=1}^{5} n_i \pi^{I_i} J_i (J_i - 1) \tau^{J_i - 2}$
$\gamma_{\pi\pi}^r = \sum_{i=1}^{5} n_i I_i (I_i - 1) \pi^{I_i - 2} \tau^{J_i}$	$\gamma_{\pi\tau}^r = \sum_{i=1}^{5} n_i I_i \pi^{I_i - 1} J_i \tau^{J_i - 1}$

$$\gamma_\pi^r = \left(\frac{\partial \gamma^r}{\partial \pi}\right)_\tau, \ \gamma_{\pi\pi}^r = \left(\frac{\partial^2 \gamma^r}{\partial \pi^2}\right)_\tau, \ \gamma_\tau^r = \left(\frac{\partial \gamma^r}{\partial \tau}\right)_\pi, \ \gamma_{\tau\tau}^r = \left(\frac{\partial^2 \gamma^r}{\partial \tau^2}\right)_\pi, \ \gamma_{\pi\tau}^r = \left(\frac{\partial^2 \gamma^r}{\partial \pi \partial \tau}\right)$$

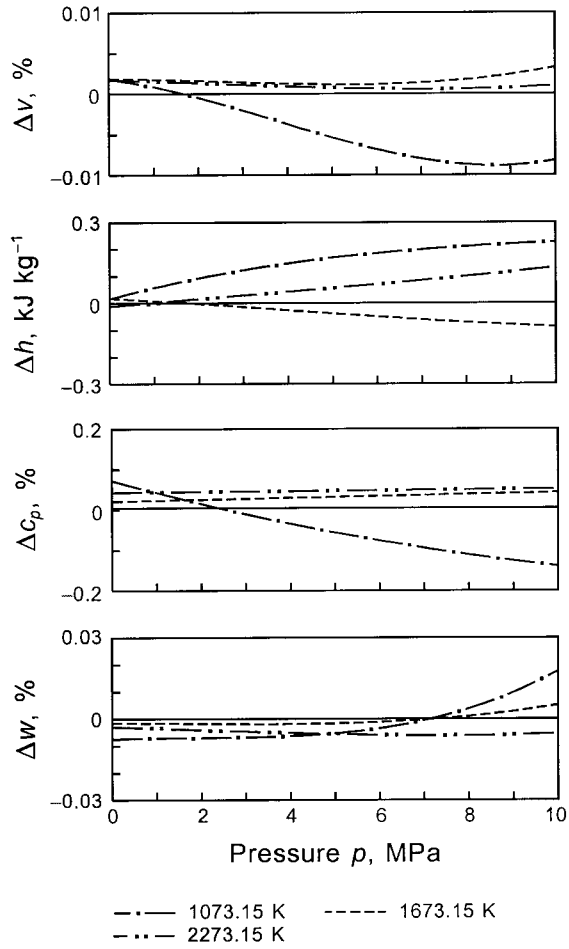

Fig. 20 Percentage deviations of the values of v, c_p, and w and absolute deviations of h values calculated from Eq. (29) from the corresponding values calculated from IAPWS-95 [7, 8]: $\Delta v = (v - v_{\text{IAPWS-95}})/v$; $\Delta c_p = (c_p - c_{p,\text{IAPWS-95}})/c_p$; $\Delta h = h - h_{\text{IAPWS-95}}$; $\Delta w = (w - w_{\text{IAPWS-95}})/w$.

Figure 20 illustrates for three characteristic isotherms that Eq. (29) represents the values of the properties v, h, c_p, and w from IAPWS-95 to within very small deviations. In the entire region, the maximum deviations occur at 10 MPa and amount to 0.009 percent in v at about 1073.15 K, 0.34 kJ kg^{-1} in h near 1373 K, 0.14 percent in c_p at 1073.15 K, and 0.023 percent in w near 1173 K.

5.5.6 Consistency at Region Boundaries. For any calculation of thermodynamic properties of water and steam across the region boundaries of IAPWS-IF97, the basic equations have to be sufficiently consistent at the corresponding boundary, see Section 4.3. For the properties considered in this respect, this section presents the achieved consistencies in comparison with the permitted inconsistencies according to the so-called Prague values [10].

5.5.6.1 Consistency at Boundaries Between Single-Phase Regions. For the boundaries between single-phase regions the consistency investigations were performed for the following basic equations and region boundaries; see Fig. 2:

Table 13 Inconsistencies between basic equations for single-phase regions at the corresponding region boundaries given as maximum and root-mean square (RMS) values

Inconsistency	Prague value [10]	Regions 1/3 Eqs. (15)/(25) Maximum value[a]	RMS value	Regions 2/3 Eqs. (19)/(25) Maximum value[a]	RMS value	Regions 2/5 Eqs. (19)/(29) Maximum value[a]	RMS value
Δv, %	0.05	0.004	0.002	0.018	0.007	0.002	0.001
Δh, kJ kg^{-1}	0.2	0.031	0.014	0.134	0.073	0.020	0.012
Δc_p, %	1	0.195	0.058	0.353	0.169	0.081	0.048
Δs, J kg^{-1}K^{-1}	0.2	0.042	0.022	0.177	0.094	0.042	0.025
Δg, kJ kg^{-1}	0.2	0.005	0.005	0.005	0.003	0.026	0.021
Δw, %	1[b]	0.299	0.087	0.403	0.073	0.021	0.009

[a] Absolute value

[b] The permitted inconsistency value for w is not included in the Prague values

- Equations (15) and (25) along the 623.15 K isotherm for pressures from 16.53 MPa (p_s from Eq. (28) for 623.15 K) to 100 MPa corresponding to the boundary between regions 1 and 3.
- Equations (19) and (25) with respect to the boundary between regions 2 and 3 defined by the B23-equation, Eq. (10), for temperatures between 623.15 K and 863.15 K.
- Equations (19) and (29) with respect to the 1073.15 K isotherm for $p \leq 10$ MPa corresponding to the boundary between regions 2 and 5.

The results of the consistency investigations for these three region boundaries are summarized in Table 13. In addition to the permitted inconsistencies corresponding to the Prague values [10], the actual inconsistencies characterized by their maximum and root-mean-square values at the three boundaries are given for the properties v, h, c_p, s, g, and w. It can be seen that the inconsistencies between the basic equations at the corresponding region boundaries are very small and the consistency requirements given in Section 4.3 are clearly exceeded.

Figure 21 presents the results of these consistency investigations in form of percentage deviations for v, c_p, and w and in form of absolute deviations for s, h, and g for IAPWS-IF97 and for IFC-67 as well; for the permitted inconsistencies according to the Prague values [10] see Table 13.

The diagrams on the left-hand side of Fig. 21 show the results for the 623.15 K isotherm that is the boundary between regions 1 and 3 of IAPWS-IF97 and between regions 1 and 4 of IFC-67, see Figs. 1 and 2. For IAPWS-IF97 the deviations correspond to the inconsistencies between Eq. (15) and Eq. (25), and for IFC-67 between its corresponding g and f equation. The diagrams show how small the inconsistencies between the basic equations of IAPWS-IF97 are along this region boundary. When comparing these inconsistencies with the permitted values it can be seen that the consistency requirement regarding this boundary was exceeded by a large margin. In contrast to this, the corresponding IFC-67 inconsistencies are clearly larger. With regard to v, c_p, and s there are ranges where IFC-67 is slightly outside the permitted inconsistencies; with respect to g IFC-67 is outside the permitted inconsistency value ($\Delta g = 0.2$ kJ kg^{-1}) along the entire boundary.

The diagrams on the right-hand side of Fig. 21 present the result for the boundary between regions 2 and 3 defined by the B23-equation for IAPWS-IF97 and by the so-called L-function for IFC-67, see Figs. 1 and 2. For IAPWS-IF97 the deviations correspond to the inconsistencies between Eqs. (19) and (25) and for IFC-67 between its corresponding g and f equation. In comparison with the diagrams on the left of Fig. 21, here the inconsistencies are on average larger which is a sign of the problems along this boundary. Particularly, for v, h, and s there are greater inconsistencies which are, however, still well within the Prague values. It is very positive that the inconsistencies in c_p remain within 0.35 percent along the entire boundary whereas the corresponding IFC-67 inconsistencies increase up to ± 6 percent. The fulfillment of the consistency requirements regarding c_p along the B23-equation was one of the decisive points during the development of the basic equations for regions 2 and 3 and influenced substantially the structure of these equations. The consistency in w is similarly good as for c_p. For IFC-67 the following consistency statements along this boundary can be made: for g the requirement was completely met, for c_p it was not met at all (see above) and for the other properties considered the inconsistencies are slightly outside the permitted values in a few places.

5.5.6.2 Consistency at the Saturation Curve. The vapor-liquid saturation curve forms the boundary between the following regions of IAPWS-IF97, see Fig. 2: For 273.15 K $\leq T \leq$ 623.15 K it is the boundary between region 4 and regions 1 and 2, respectively, and for 623.15 K $\leq T \leq T_c$ between region 3 and region 4. Thus, the calculations concern the basic equations and ranges of the saturation curve listed below. According to the Prague values the consistency investigations at the saturation curve are performed for the properties p_s, T_s, and g; the way of calculating the inconsistencies Δp_s, ΔT_s, and Δg is given in the following:

- Equations (15), (19) and (28) on the saturation curve for temperatures from 273.15 K to 623.15 K:

$$\Delta p_s = p_{s,\mathrm{Eq.(15)},\mathrm{Eq.(19)}} - p_{s,\mathrm{Eq.(28)}} \tag{32a}$$

$$\Delta T_s = T_{s,\mathrm{Eq.(15)},\mathrm{Eq.(19)}} - T_{s,\mathrm{Eq.(55)}} \tag{32b}$$

$$\Delta g = g_{\mathrm{Eq.(15)}} - g_{\mathrm{Eq.(19)}} \tag{32c}$$

  The calculation of p_s and of T_s from Eqs. (15) and (19) was made via the Maxwell criterion (phase-equilibrium condition) for given values of T or p. The g values are determined for given T values and corresponding p_s values from Eq. (28).
- Equations (25) and (28) on the saturation curve for temperatures from 623.15 K to $T_c = 647.096$ K:

$$\Delta p_s = p_{s,\mathrm{Eq.(25)}} - p_{s,\mathrm{Eq.(28)}} \tag{33a}$$

$$\Delta T_s = T_{s,\mathrm{Eq.(25)}} - T_{s,\mathrm{Eq.(55)}} \tag{33b}$$

$$\Delta g = g'_{\mathrm{Eq.(25)},\mathrm{Eq.(28)}} - g''_{\mathrm{Eq.(25)},\mathrm{Eq.(28)}} \tag{33c}$$

  The calculation of p_s and T_s from Eq. (25) was made via the Maxwell criterion for given temperatures or pressures, respectively. The inconsistency Δg corresponds to the difference $g'(\rho', T) - g''(\rho'', T)$ which was calculated from Eq. (25) after ρ' and ρ'' had been determined from Eq. (25) by iteration for given T values and corresponding p_s values from Eq. (28).
- Equations (15), (19) and (25) on the saturation curve at 623.15 K. This is the only point on the saturation curve where the validity ranges of the fundamental equations of regions 1 to 3 meet each other:

$$\Delta p_s = p_{s,\mathrm{Eq.(15)},\mathrm{Eq.(19)}} - p_{s,\mathrm{Eq.(25)}} \tag{34a}$$

$$\Delta T_s = T_{s,\mathrm{Eq.(15)},\mathrm{Eq.(19)}} - T_{s,\mathrm{Eq.(25)}} \tag{34b}$$

$$\Delta g = g_{\mathrm{Eq.(15)},\mathrm{Eq.(19)}} - g_{\mathrm{Eq.(25)}} \tag{34c}$$

  All three properties p_s, T_s, and g were calculated via the Maxwell criterion from the corresponding equations.

The results of these consistency investigations along the saturation curve are summarized in Table 14. In addition to the permitted inconsistencies corresponding to the Prague values [10], the actual inconsistencies characterized by their maximum and root-mean-square values are given for the two sections of the saturation curve and for the special point at 623.15 K. It can be seen that the inconsistencies between the basic equations for the corresponding single-phase regions and the saturation-pressure equation are very small; except for the Δp_s values for $T \leq 623$ K they are less than one tenth of the permitted value. This statement also holds for the fundamental equations in relation to each other and not just in relation to the saturation-pressure equation, Eq. (28), see Eqs. (34*a*) to (34*c*) and the last column in Table 14.

Along the entire saturation curve, Fig. 22 shows the inconsistencies with regard to the saturation pressure p_s, which is the most important and most sensitive property in this respect. The maxi-

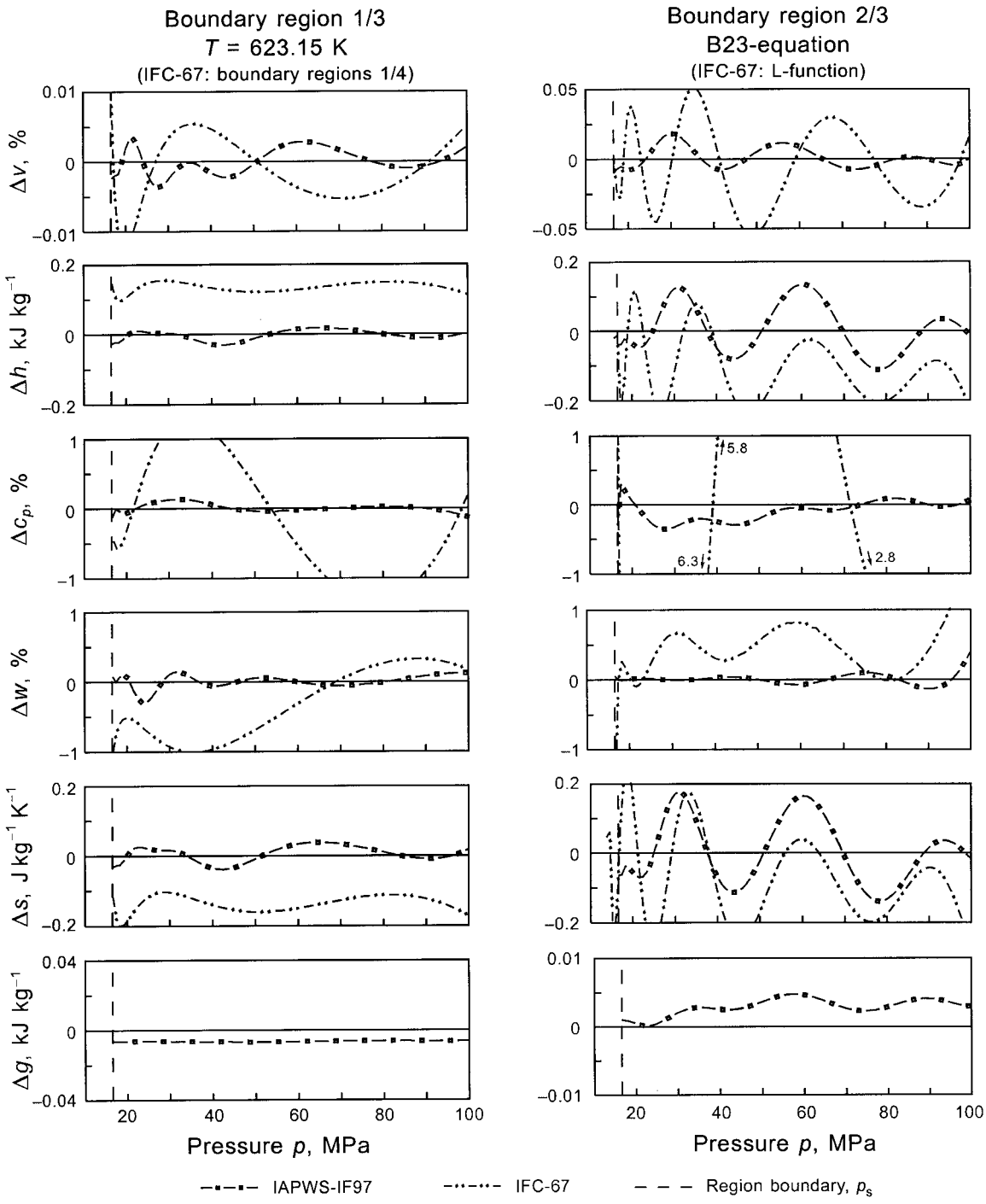

Fig. 21 Inconsistencies Δv, Δh, Δc_p, Δw, Δs, and Δg along the boundary between regions 1 and 3 (left column) and the boundary between regions 2 and 3 (right column) when calculating the properties without an index from the corresponding g equation (Eq. (15) for region 1 and Eq. (19) for region 2) and the properties with the index f from the f equation for region 3, Eq. (25). For the calculations with IFC-67 its corresponding g and f equations were used, see text: $\Delta v = (v - v_f)/v$; $\Delta c_p = (c_p - c_{p,f})/c_p$; $\Delta s = s - s_f$; $\Delta h = h - h_f$; $\Delta w = (w - w_f)/w$; $\Delta g = g - g_f$.

mum difference Δp_s when p_s is calculated once from the basic equations for regions 1 to 3 and the other time from the saturation-pressure equation remains less than 0.007 percent and the (unavoidable) step at 623.15 K when switching from the g equations to the f equation amounts only to 0.005 percent. For IFC-67 the corresponding inconsistency in p_s is on average more than one order of magnitude larger; the maximum inconsistency amounts to 0.12 percent and the step at 623.15 K when switching to the f equations for regions 3 and 4 of IFC-67 (see Fig. 1) is even 0.22 percent.

Table 14 Inconsistencies between the basic equations valid at the saturation curve given as maximum and root-mean square (RMS) values

Inconsistency	Prague value [10]	$T_t \le T \le 623.15$ K Eqs. (15),(19)/(28) Maximum value[a]	$T_t \le T \le 623.15$ K Eqs. (15),(19)/(28) RMS value	623.15 K $\le T \le T_c$ Eqs. (25)/(28) Maximum value[a]	623.15 K $\le T \le T_c$ Eqs. (25)/(28) RMS value	$T = 623.15$ K Eqs. (15),(19)/(25)
Δp_s, %	0.05	0.0069	0.0033	0.0026	0.0015	0.0041
ΔT_s, %	0.02	0.0006	0.0003	0.0003	0.0002	0.0006
Δg, kJ kg^{-1}	0.2	0.012	0.006	0.002	0.001	0.005

[a] Absolute value

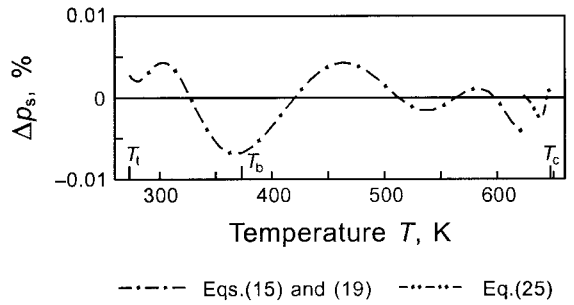

Fig. 22 Inconsistencies Δp_s along region 4 (saturation curve) when calculating the saturation pressures as p_s values from Eq. (15) together with Eq. (19) and from Eq. (25), respectively, and as values $p_{s,\mathrm{Eq.(28)}}$ directly from the saturation-pressure equation, Eq. (28): $\Delta p_s = (p_s - p_{s,\mathrm{Eq.(28)}})/p_s$.

In addition to the inconsistencies in Δp_s shown in Fig. 22, it might be helpful for practical calculations to have an idea of the differences in v, h, s, c_p, and w along the saturated vapor and saturated liquid line when, for given temperatures, these values were calculated one time directly from the corresponding g and f equations by applying the phase-equilibrium condition and the other time from the basic equations after p_s had been calculated from Eq. (28). The second method for these calculations is clearly easier to carry out but the results would not be in full consistency with the results from the fundamental equations. Figure 23 illustrates the corresponding inconsistencies along the saturated vapor line for v'', s'', and c_p''. It can be seen that the inconsistencies $\Delta v''$, $\Delta s''$, and $\Delta c_p''$ are very small (smaller than the Prague values for the region boundaries between single-phases) and increase only when approaching the critical point; however, for temperatures up to (T_c − 2 K) the inconsistencies remain within the corresponding Prague values [10] listed in Table 13. Compared with these three properties the corresponding inconsistencies in h'', w'', v', h', s', c_p', and w' are clearly smaller and thus negligible except for the range 1 K to 2 K below T_c. When approaching the critical point it is not surprising that the inconsistency in c_p' and c_p'' increases to 60 percent and to 75 percent, respectively, at 1 mK below T_c, see also the discussion of Fig. 16(*b*) in Section 5.5.3.2 regarding the c_p behavior in region 3.

5.6 The Backward Equations for Regions 1, 2, and 4. In order to meet the computation-speed requirement for IAPWS-IF97 "three times faster than IFC-67" (see Section 4.4) the concept of so-called backward equations $T(p, h)$ and $T(p, s)$ for regions 1 and 2 and $T_s(p)$ for region 4 has been developed, see Section 5.1 and Fig. 2.

Proceeding from Eq. (13) with $z = T/T^*$, $x = p$, $a = p^*$, $y = h$, and $c = h^*$ or $y = s$ and $c = s^*$ the following general form of a combined polynomial for the $T(p, h)$ and $T(p, s)$ equations is obtained [18, 29]:

$$\frac{T(p,\,h)}{T^*} = \sum_i n_i \left(\frac{p}{p^*} + b\right)^{I_i} \left(\frac{h}{h^*} + d\right)^{J_i}, \tag{35}$$

$$\frac{T(p,\,s)}{T^*} = \sum_i n_i \left(\frac{p}{p^*} + b\right)^{I_i} \left(\frac{s}{s^*} + d\right)^{J_i}, \tag{36}$$

where T^*, p^*, h^*, and s^* are again reducing parameters. These two equations form the basis of the backward equations for regions 1 and 2.

In the following sections first the final form of the corresponding backward equation is given including all numerical information for its use, then details of its development are summarized and finally its numerical consistency with the corresponding basic equation is discussed; all table numbers starting with an "A" are listed in the appendix.

5.6.1 The Backward Equations for Region 1. According to the considerations in section 5.1 (item 2*a*, *b*) the two backward equations $T(p, h)$ and $T(p, s)$ have to be numerically consistent with the basic equation of this region, Eq. (15), within $\Delta T = \pm 25$ mK for the same p-h values and p-s values, respectively.

5.6.1.1 The Backward Equation T(p, h). The backward equation $T(p, h)$ for region 1 has the following dimensionless form:

$$\frac{T(p,\,h)}{T^*} = \theta(\pi,\,\eta) = \sum_{i=1}^{20} n_i \pi^{I_i} (\eta + 1)^{J_i}, \tag{37}$$

where $\theta = T/T^*$, $\pi = p/p^*$, and $\eta = h/h^*$ with $T^* = 1$ K, $p^* = 1$ MPa, and $h^* = 2500$ kJ kg^{-1}. The coefficients n_i and exponents I_i and J_i of Eq. (37) are listed in Table A16.

Equation (37) covers the same range of validity as the basic equation, Eq. (15), except for the metastable superheated-liquid region, where Eq. (37) is not valid. For the actual numerical inconsistencies between Eqs. (37) and (15) see below.

To assist the user in computer-program verification of Eq. (37), Table A17 contains the corresponding test values.

Development of Eq. (37). Based on test calculations with Eq. (35) for the maximum ranges of the exponents I_i and J_i, the values of the reducing parameters T^*, p^*, and h^* and the shifting parameters b and d, the following dimensionless comprehensive expression of 233 terms (bank of terms) was used as starting point for the development of the backward equation $T(p, h)$ for region 1:

$$\theta = \sum_{i=0}^{6} \sum_{j=0}^{32} n_{ij} \pi^i (\eta + 1)^j, \tag{38}$$

where $\theta = T/T^*$, $\pi = p/p^*$, and $\eta = h/h^*$ with $T^* = 1$ K, $p^* = 1$ MPa, and $h^* = 2500$ kJ kg^{-1}.

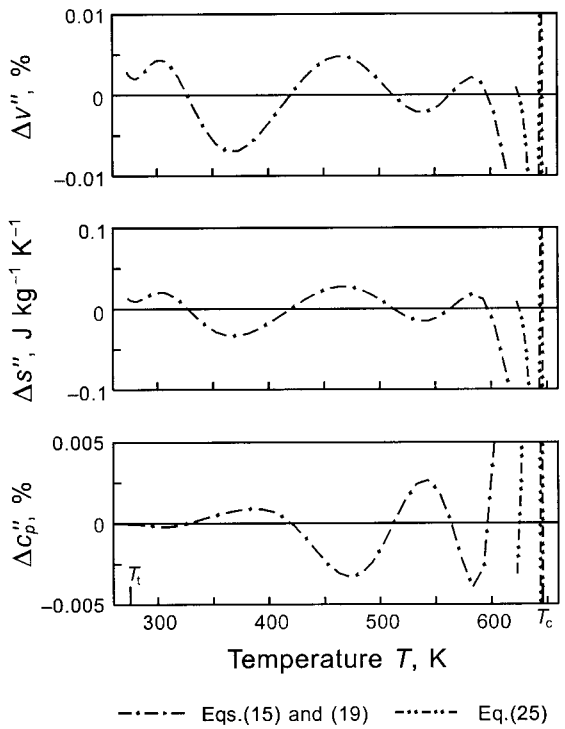

Fig. 23 Inconsistencies $\Delta v''$, $\Delta s''$, and $\Delta c_p''$ caused by two different ways of determining the needed saturation pressures p_s. For $v''_{\mathrm{Eq.(28)}}$, $s''_{\mathrm{Eq.(28)}}$, and $c''_{p,\mathrm{Eq.(28)}}$ the p_s values were directly calculated from Eq. (28) and for v'', s'', and c_p'' the p_s values were determined from Eqs. (15) and (19) and from Eq. (19), respectively, via the phase-equilibrium condition: $\Delta v'' = (v''_{\mathrm{Eq.(28)}} - v'')/v''$, $\Delta s'' = s''_{\mathrm{Eq.(28)}} - s''$, $\Delta c_p'' = (c''_{p,\mathrm{Eq.(28)}} - c_p'')/c_p''$.

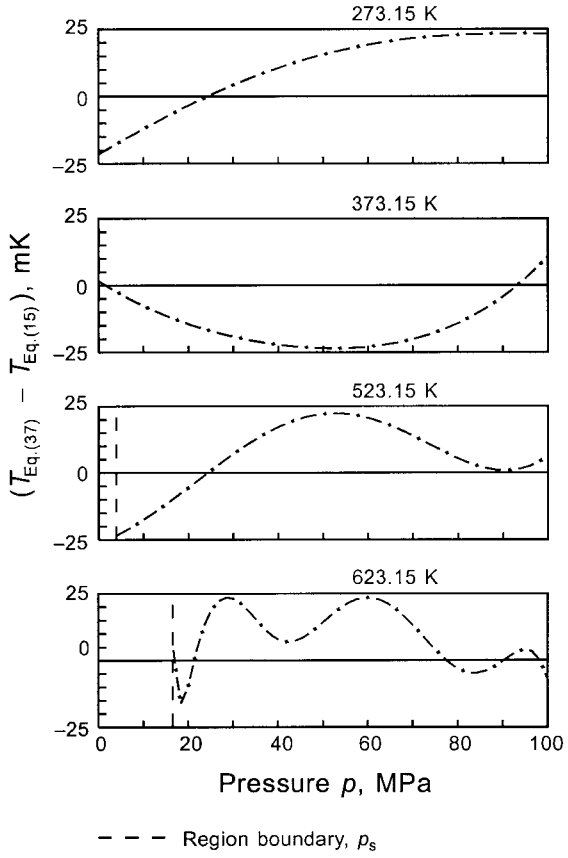

Fig. 24 Absolute deviations of temperatures $T_{Eq.(37)}$ calculated from Eq. (37) from values $T_{Eq.(15)}$ calculated from Eq. (15) for given values of *p* and *h*

The structure of the final $T(p, h)$ equation, Eq. (37), was found from Eq. (38) by using the approximation algorithm of Willkommen et al. [23, 27] which combines a special modification of the structure-optimization method of Wagner [19] with the elements automatic data weighting and data-grid condensation. In this entire optimization process Eq. (37) was fitted to *T-p-h* values, where *h* had been calculated from the basic equation for region 1, Eq. (15), for given values of *p* and *T* distributed as selected grid points over region 1; the final coefficients were determined with the simultaneous steady approximation of Zschunke et al. [24]. Details of such fitting processes are given by Willkommen [27].

Numerical Consistency Between Eqs. (37) and (15). Figure 24 illustrates the numerical consistency achieved between the $T(p, h)$ equation for region 1, Eq. (37), and the corresponding basic equation, Eq. (15), along four isotherms considered to be characteristic for the behavior of Eq. (37). Over the entire region the numerical inconsistency between Eqs. (37) and (15) has a maximum of 23.6 mK and a root-mean-square average of 13.4 mK.

5.6.1.2 The Backward Equation T(p, s). The backward equation $T(p, s)$ for region 1 has the following dimensionless form:

$$\frac{T(p, s)}{T^*} = \theta(\pi, \sigma) = \sum_{i=1}^{20} n_i \pi^{I_i} (\sigma + 2)^{J_i}, \tag{39}$$

where $\theta = T/T^*$, $\pi = p/p^*$, and $\sigma = s/s^*$ with $T^* = 1$ K, $p^* = 1$ MPa, and $s^* = 1$ kJ kg^{-1} K^{-1}. The coefficients n_i and exponents I_i and J_i of Eq. (39) are listed in Table A18.

Equation (39) covers the same range of validity as the basic equation, Eq. (15), except for the metastable superheated-liquid region, where Eq. (39) is not valid.

To assist the user in computer-program verification of Eq. (39), Table A19 contains the corresponding test values.

Development of Eq. (39). Based on test calculations with Eq. (36) for the maximum ranges of the exponents I_i and J_i, the values of the reducing parameters T^*, p^*, and s^* and the shifting parameters b and d, the following dimensionless comprehensive expression of 165 terms (bank of terms) was used as starting point for the development of the backward equation $T(p, s)$ for region 1 [18]:

$$\theta = \sum_{i=0}^{4} \sum_{j=0}^{32} n_{ij} \pi^i (\sigma + 2)^j, \tag{40}$$

where $\theta = T/T^*$, $\pi = p/p^*$, and $\sigma = s/s^*$ with $T^* = 1$ K, $p^* = 1$ MPa, and $s^* = 1$ kJ kg^{-1} K^{-1}.

The structure of the final $T(p, s)$ equation, Eq. (39), was found from Eq. (40) with the structure-optimization method of Setzmann and Wagner [5]. When using this method alone it can happen (as for all procedures based on the least square method) that in relatively small ranges the deviations from the input data are significantly larger than in the rest of the fitting range. Thus, in order to reduce these larger deviations in small ranges at the expense of smaller deviations over larger ranges, a special fitting procedure was tandem-arranged to the application of the structure-optimization method [5]. This special fitting procedure [18, 28] performs a recursive fitting process in which an amplification function increases the weighting factors of such data having the largest deviations in the preceding fitting step. When applying these two methods Eq. (39) was fitted to *T-p-s* values, where *s* had been calculated from the basic equation for region 1, Eq. (15), for given values of *p* and *T* distributed as selected grid points over region 1. Details of this entire fitting process are given by Kruse and Wagner [18].

Numerical Consistency Between Eqs. (39) and (15). Figure 25 illustrates the numerical consistency achieved between the $T(p, s)$ equation for region 1, Eq. (39), and the corresponding basic equation, Eq. (15), along four isotherms considered to be characteristic for the behavior of Eq. (39). Over the entire region the numerical inconsistency between Eqs. (39) and (15) has a maximum of 21.8 mK and a root-mean-square average of 5.8 mK. It can be seen that the maximum inconsistencies occur only in a small part of region 1, namely at higher temperatures around 600 K.

5.6.2 The Backward Equations for Region 2. According to the considerations in Section 5.1 (item 2*a*,*b*) the two backward equations $T(p, h)$ and $T(p, s)$ have to be numerically consistent with the basic equation of this region, Eq. (19), within $\Delta T = \pm 25$ mK for $s \leq 5.85$ kJ kg^{-1} K^{-1} and within $\Delta T = \pm 10$ mK for $s > 5.85$ kJ kg^{-1} K^{-1}, for the same *p-h* values and *p-s* values, respectively.

Due to this very high consistency demand region 2 is covered by three $T(p, h)$ and three $T(p, s)$ equations. Figure 26 shows how region 2 is divided into the three subregions for the backward equations. The boundary between subregions 2(*a*) and 2(*b*) is the isobar $p = 4$ MPa; the boundary between subregions 2(*b*) and 2(*c*) corresponds to the entropy line $s = 5.85$ kJ kg^{-1} K^{-1}.

In order to know whether the $T(p, h)$ equation for subregion 2(*b*) or for subregion 2(*c*) has to be used for given values of *p* and *h*, a special correlation equation for the boundary between subregions 2(*b*) and 2(*c*) (which approximates $s = 5.85$ kJ kg^{-1} K^{-1}) is needed, see Fig. 26. This boundary equation, called B2bc-equation, is a simple quadratic pressure-enthalpy relation which reads

$$\pi = n_1 + n_2 \eta + n_3 \eta^2, \tag{41}$$

where $\pi = p/p^*$ and $\eta = h/h^*$ with $p^* = 1$ MPa and $h^* = 1$ kJ kg^{-1}. The coefficients n_1 to n_3 of Eq. (41) are listed in Table A20. Based on its simple form, Eq. (41) does not describe exactly

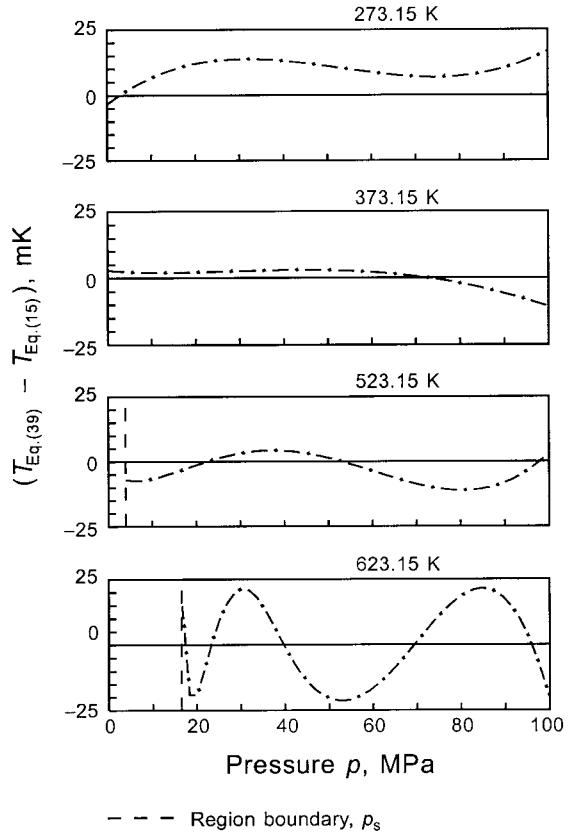

Fig. 25 Absolute deviations of temperatures $T_{Eq.(39)}$ calculated from Eq. (39) from values $T_{Eq.(15)}$ calculated from Eq. (15) for given values of p and s

the isentropic line $s = 5.85$ kJ kg^{-1} K^{-1}; the entropy values corresponding to this p-h relation are between $s = 5.81$ kJ kg^{-1} K^{-1} and $s = 5.85$ kJ kg^{-1} K^{-1}. The enthalpy-explicit form of Eq. (41) is as follows:

$$\eta = n_4 + [(\pi - n_5)/n_3]^{0.5} \tag{42}$$

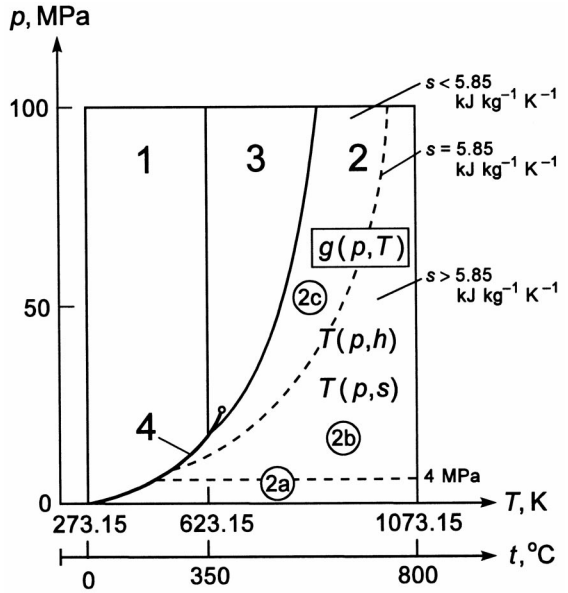

Fig. 26 Division of region 2 of IAPWS-IF97 into the three subregions 2(a), 2(b), and 2(c) for the backward equations $T(p, h)$ and $T(p, s)$

with η and π according to Eq. (41) and the coefficients n_3 to n_5 listed in Table A20. Equations (41) and (42) define the boundary line between subregions 2(b) and 2(c) from the saturation state at $p_s = 6.546\ 669\ 967\ 8$ MPa (corresponding to about $T = 554.5$ K) up to $p = 100$ MPa (corresponding to about $T = 1019.3$ K).

For the backward equations $T(p, s)$ the boundary between subregions 2(b) and 2(c) corresponds directly to the isentropic line $s = 5.85$ kJ kg^{-1} K^{-1} and is therefore automatically defined for given values of p and s.

5.6.2.1 The Backward Equations T(p, h) for Subregions 2(a), 2(b), and 2(c). The backward equation $T(p, h)$ for subregion 2(a) in its dimensionless form reads

$$\frac{T_{2a}(p, h)}{T^*} = \theta_{2a}(\pi, \eta) = \sum_{i=1}^{34} n_i \pi^{I_i} (\eta - 2.1)^{J_i}, \tag{43}$$

where $\theta = T/T^*$, $\pi = p/p^*$, and $\eta = h/h^*$ with $T^* = 1$ K, $p^* = 1$ MPa, and $h^* = 2000$ kJ kg^{-1}. The coefficients n_i and exponents I_i and J_i of Eq. (43) are listed in Table A21.

The backward equation $T(p, h)$ for subregion 2(b) in its dimensionless form reads

$$\frac{T_{2b}(p, h)}{T^*} = \theta_{2b}(\pi, \eta) = \sum_{i=1}^{38} n_i (\pi - 2)^{I_i} (\eta - 2.6)^{J_i}, \tag{44}$$

where $\theta = T/T^*$, $\pi = p/p^*$, and $\eta = h/h^*$ with $T^* = 1$ K, $p^* = 1$ MPa, and $h^* = 2000$ kJ kg^{-1}. The coefficients n_i and exponents I_i and J_i of Eq. (44) are listed in Table A22.

The backward equation $T(p, h)$ for subregion 2(c) in its dimensionless form reads

$$\frac{T_{2c}(p, h)}{T^*} = \theta_{2c}(\pi, \eta) = \sum_{i=1}^{23} n_i (\pi + 25)^{I_i} (\eta - 1.8)^{J_i}, \tag{45}$$

where $\theta = T/T^*$, $\pi = p/p^*$, and $\eta = h/h^*$ with $T^* = 1$ K, $p^* = 1$ MPa, and $h^* = 2000$ kJ kg^{-1}. The coefficients n_i and exponents I_i and J_i of Eq. (45) are listed in Table A23.

Equations (43), (44), and (45) are only valid in the respective subregion 2(a), 2(b), and 2(c) that do not include the metastable-vapor region. The boundaries between these subregions are defined at the beginning of Section 5.6.2; the lowest pressure for which Eq. (43) is valid amounts to 611.153 Pa corresponding to the sublimation pressure [20] at 273.15 K.

To assist the user in computer-program verification of Eqs. (43) to (45), Table A24 contains the corresponding test values.

Development of Eqs. (43) to (45). Based on test calculations with Eq. (35) for the maximum ranges of the exponents I_i and J_i, the values of the reducing parameters T^*, p^*, and h^* and the shifting parameters b and d, the following dimensionless comprehensive expressions (bank of terms)[12] were formulated as starting points for the development of the backward equations $T(p, h)$ for subregions 2(a), 2(b), and 2(c):

$$\theta_{2a} = \sum_{i=1}^{10} \sum_{j=1}^{20} n_{ij} \pi^{I_i} (\eta - 2.1)^{J_j} \tag{46}$$

$$\text{with} \quad I_i = 0 \ldots (1) \ldots 9,$$

$$J_j = 0 \ldots (1) \ldots 6, 8 \ldots (2) \ldots 20, 24 \ldots (4) \ldots 44,$$

where $\theta = T/T^*$, $\pi = p/p^*$, and $\eta = h/h^*$ with $T^* = 1$ K, $p^* = 1$ MPa, and $h^* = 2000$ kJ kg^{-1},

[12] The figures given in brackets in the series of the exponents I_i and J_j in Eqs. (46) to (48) correspond to the step size.

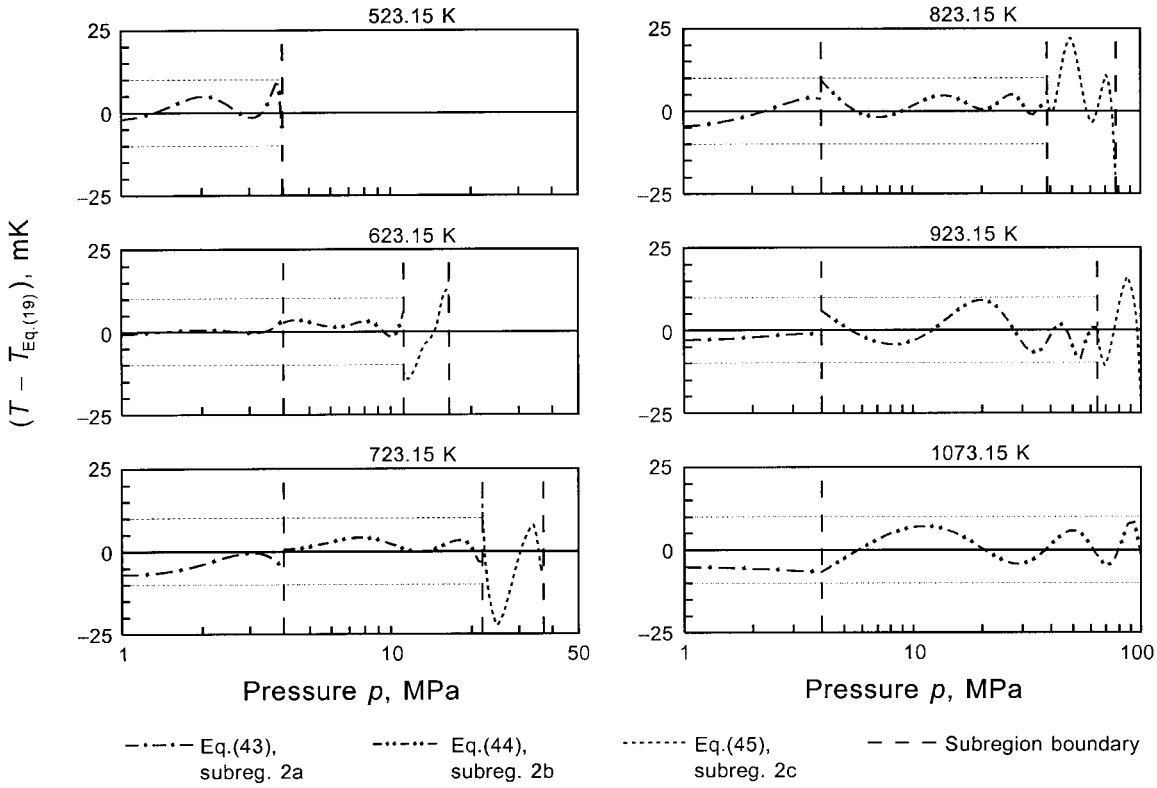

Fig. 27 Absolute deviations of temperatures *T* calculated from Eq. (43) for subregion 2(*a*), Eq. (44) for subregion 2(*b*), and Eq. (45) for subregion 2(*c*) from values $T_{Eq.(19)}$ calculated from Eq. (19) for given values of *p* and *h*

$$\theta_{2b} = \sum_{i=1}^{10} \sum_{j=1}^{30} n_{ij} (\pi - 2)^{I_i} (\eta - 2.6)^{J_j} \tag{47}$$

$$\text{with} \quad I_i = 0 \ldots (1) \ldots 9,$$

$$J_j = 0 \ldots (1) \ldots 17,\ 18 \ldots (2) \ldots 40,$$

where $\theta = T/T^*$, $\pi = p/p^*$, and $\eta = h/h^*$ with $T^* = 1$ K, $p^* = 1$ MPa, and $h^* = 2000$ kJ kg^{-1},

$$\theta_{2c} = \sum_{i=1}^{15} \sum_{j=1}^{20} n_{ij} (\pi + 25)^{I_i} (\eta - 1.8)^{J_j} \tag{48}$$

$$\text{with} \quad I_i = -7 \ldots (1) \ldots 7,$$

$$J_j = 0 \ldots (1) \ldots 6,\ 8 \ldots (2) \ldots 32,$$

where $\theta = T/T^*$, $\pi = p/p^*$, and $\eta = h/h^*$ with $T^* = 1$ K, $p^* = 1$ MPa, and $h^* = 2000$ kJ kg^{-1}.

Equations (43), (44), and (45) were determined from the respective Eqs. (46), (47), and (48) by using the approximation algorithm of Willkommen et al. [23, 27] in which a modified form of the structure-optimization method of Wagner [19] is incorporated. In addition, the algorithm of Trübenbach [29] for setting up equations optimized regarding their computing-time consumption was used. In this entire optimization process Eqs. (43) to (45) were fitted to *T*-*p*-*h* values, where *h* had been calculated from the basic equation for region 1, Eq. (19), for given values of *p* and *T* distributed as selected grid points over subregions 2(*a*), 2(*b*), and 2(*c*). Details of such fitting processes are given by Trübenbach [29].

Numerical Consistency Between Eqs. (43) to (45) and Eq. (19). Figure 27 illustrates the achieved numerical consistency between the three $T(p, h)$ equations for region 2, Eqs. (43) to (45), and the corresponding basic equation, Eq. (19), along six isotherms considered to be characteristic for the behavior of these backward equations. In the diagrams the smaller tolerated inconsistency of ±10 mK for subregions 2(*a*) and 2(*b*) is marked whereas the tolerated inconsistency value of ±25 mK for subregion 2(*c*) corresponds to the maximum value of the deviation scale.

It can be seen that the ΔT values between the two backward equations of adjacent subregions are smaller than the tolerated ΔT values between the backward and basic equation. At the boundaries between subregions 2(*a*) and 2(*b*) and between subregions 2(*b*) and 2(*c*) the maximum temperature differences between the corresponding backward equations amount to 8.7 mK and 21.6 mK, respectively. The tolerated and actual numerical inconsistencies between Eqs. (43) to (45) and Eq. (19), given as maximum and root-mean-square (RMS) temperature differences over the entire region 2, are listed in Table 15.

5.6.2.2 The Backward Equations T(p, s) for Subregions 2(a), 2(b), and 2(c). The backward equation $T(p, s)$ for subregion 2(*a*) in its dimensionless form reads

$$\frac{T_{2a}(p, s)}{T^*} = \theta_{2a}(\pi, \sigma) = \sum_{i=1}^{46} n_i \pi^{I_i} (\sigma - 2)^{J_i}, \tag{49}$$

where $\theta = T/T^*$, $\pi = p/p^*$, and $\sigma = s/s^*$ with $T^* = 1$ K, $p^* = 1$ MPa, and $s^* = 2$ kJ kg^{-1} K^{-1}. The coefficients n_i and exponents I_i and J_i of Eq. (49) are listed in Table A25.

Table 15 Tolerated and actual temperature differences between Eqs. (43) to (45) and Eq. (19)

Subregion	Equation	Temperature differences ΔT, mK		
		Tolerated	Maximum	RMS
2a	43	10	9.3	2.9
2b	44	10	9.6	3.9
2c	45	25	23.7	10.4

The backward equation $T(p, s)$ for subregion 2(b) in its dimensionless form reads

$$\frac{T_{2b}(p, s)}{T^*} = \theta_{2b}(\pi, \sigma) = \sum_{i=1}^{44} n_i \pi^{I_i} (10 - \sigma)^{J_i}, \qquad (50)$$

where $\theta = T/T^*$, $\pi = p/p^*$, and $\sigma = s/s^*$ with $T^* = 1$ K, $p^* = 1$ MPa, and $s^* = 0.7853$ kJ kg^{-1} K^{-1}. The coefficients n_i and exponents I_i and J_i of Eq. (50) are listed in Table A26.

The backward equation $T(p, s)$ for subregion 2(c) in its dimensionless form reads

$$\frac{T_{2c}(p, s)}{T^*} = \theta_{2c}(\pi, \sigma) = \sum_{i=1}^{30} n_i \pi^{I_i} (2 - \sigma)^{J_i}, \qquad (51)$$

where $\theta = T/T^*$, $\pi = p/p^*$, and $\sigma = s/s^*$ with $T^* = 1$ K, $p^* = 1$ MPa, and $s^* = 2.9251$ kJ kg^{-1} K^{-1}. The coefficients n_i and exponents I_i and J_i of Eq. (51) are listed in Table A27.

Equations (49), (50), and (51) are only valid in the respective subregion 2(a), 2(b), and 2(c) which do not include the metastable-vapor region. The boundaries between these subregions are defined at the beginning of Section 5.6.2; the lowest pressure for which Eq. (49) is valid amounts to 611.153 Pa corresponding to the sublimation pressure [20] at 273.15 K.

To assist the user in computer-program verification of Eqs. (49) to (51), Table A28 contains the corresponding test values.

Development of Eqs. (49) to (51). Based on test calculations with Eq. (36) for the maximum ranges of the exponents I_i and J_i, the values of the reducing parameters T^*, p^*, and s^* and the shifting parameters b and d, comprehensive expressions (bank of terms) were formulated as starting points for the development of the backward equations $T(p, s)$ for regions 2(a), 2(b), and 2(c).

For subregion 2(a) this expression in its dimensionless form, consisting of 315 terms [18], was used:

$$\theta_{2a} = \sum_{i=-6}^{-1} \sum_{j=-27}^{0} n_{ij} \pi^{i/4} (\sigma - 2)^j + \sum_{i=0}^{6} \sum_{j=0}^{20} n_{ij} \pi^{i/4} (\sigma - 2)^j, \qquad (52)$$

where $\theta = T/T^*$, $\pi = p/p^*$, and $\sigma = s/s^*$ with $T^* = 1$ K, $p^* = 1$ MPa, and $s^* = 2$ kJ kg^{-1} K^{-1}.

Except for the saturation equation, Eq. (27), this is the only expression which needs noninteger exponents. This fact takes into account that region 2(a) is, when an equation is considered with entropy and pressure as independent variables, a "difficult" region because for $p \to 0$ (ideal-gas behavior) the relation between entropy and pressure is given by $s - s_0 \approx R \ln (p/p_0)$. This means that an logarithmic function in pressure would normally have been necessary. However, due to the long computing times for such functions, as a compromise a power function with noninteger exponents and step sizes of $\frac{1}{4}$ was used.

For subregion 2(b) the bank of terms consisted of 156 terms and had the form [18]:

$$\theta_{2b} = \sum_{i=-6}^{5} \sum_{j=0}^{12} n_{ij} \pi^i (10 - \sigma)^j, \qquad (53)$$

where $\theta = T/T^*$, $\pi = p/p^*$, and $\sigma = s/s^*$ with $T^* = 1$ K, $p^* = 1$ MPa, and $s^* = 0.7853$ kJ kg^{-1} K^{-1}.

For subregion 2(c) the bank of 72 terms read [18]:

$$\theta_{2c} = \sum_{i=-4}^{7} \sum_{j=0}^{5} n_{ij} \pi^i (2 - \sigma)^j, \qquad (54)$$

where $\theta = T/T^*$, $\pi = p/p^*$, and $\sigma = s/s^*$ with $T^* = 1$ K, $p^* = 1$ MPa, and $s^* = 2.9251$ kJ kg^{-1} K^{-1}.

Based on the bank of terms, Eqs. (52) to (54), for the corresponding subregion, the structure of the final $T(p, s)$ equations was determined with the structure-optimization procedure of Setzmann and Wagner [5] supplemented by the recursive fitting procedure [18, 28] to distribute the deviations from the input data more proportionated over the entire region, see the corresponding description in Section 5.6.1.2. When applying these methods Eqs. (49) to (51) were fitted to T-p-s values, where s had been calculated from the basic equation for region 2, Eq. (19), for given values of p and T distributed as selected grid points over regions 2(a), 2(b), and 2(c). Details of these comprehensive fitting processes are given by Kruse and Wagner [18].

Numerical Consistency Between Eqs. (49) to (51) and Eq. (19). Figure 28 illustrates the achieved numerical consistencies between the three $T(p, s)$ equations for region 2, Eqs. (49) to (51), and the corresponding basic equation, Eq. (19), along six isotherms considered to be typical for the behavior of these backward equations. In the diagrams the smaller tolerated inconsistency of ± 10 mK for subregions 2(a) and 2(b) is marked whereas the tolerated inconsistency value of ± 25 mK for subregion 2(c) corresponds to the maximum value of the deviation scale.

It can be seen that the ΔT values between the two backward equations of adjacent subregions are smaller than the tolerated ΔT values between the backward and basic equation. At the boundaries between subregions 2(a) and 2(b) and between subregions 2(b) and 2(c) the maximum temperature differences between the corresponding backward equations amount to 4.1 mK and 9.1 mK, respectively. The tolerated and actual numerical inconsistencies between Eqs. (49) to (51) and Eq. (19), given as maximum and root-mean-square (RMS) temperature differences over the entire region 2, are listed in Table 16.

5.6.3 Typical Effects When Using the Backward Equations for Regions 1 and 2. As described in section 5.1, IAPWS-IF97 is essentially based on the concept of combining the basic equations $g(p, T)$ of regions 1 and 2 with the two types of backward equations $T(p, h)$ and $T(p, s)$. With these three types of equations, properties as function of (p, h) and (p, s) can be calculated without any iteration and for properties as function of (h, s) it is only necessary to perform one-dimensional iterations (instead of two-dimensional iterations when using only $g(p, T)$ equations). This special concept is the basis for achieving high computation speeds with IAPWS-IF97 even for rather complex property functions. However, as the most important precondition for a successful realization of this concept the basic and backward equations had to be numerically extremely consistent with each other. Based on test calculations with characteristic power cycles via iterations with IFC-67, the permitted inconsistencies were set by IAPWS to 10 mK and 25 mK, respectively, depending on the range of state (for details see Section 5.1).

Although all the backward equations $T(p, h)$ and $T(p, s)$ presented in Sections 5.6.1 and 5.6.2 clearly meet these numerical consistency requirements, the inconsistencies are, as a matter of course, not zero. This fact has several consequences of which the user should be aware, for example:

- When calculating a property as function of (p, h) and (p, s), respectively, two different results can be obtained depending on using the $T(p, h)$ and $T(p, s)$ equations or calculating the property directly from the $g(p, T)$ equation by iteration.
- When calculating a property as function of (h, s) three different results can be obtained depending on whether the $T(p, h)$ or the $T(p, s)$ equation is used for a one-dimensional iteration in combination with the basic equation $g(p, T)$ or whether the property is determined directly from the $g(p, T)$ equation by a two-dimensional iteration.
- When calculating properties extremely close to the region boundaries and particularly to the vapor-liquid phase boundary, the user should be aware of the small inconsistencies between the backward and basic equations. For example, in region 2 very close to the saturated vapor line ($|T - T_s| < 25$ mK for

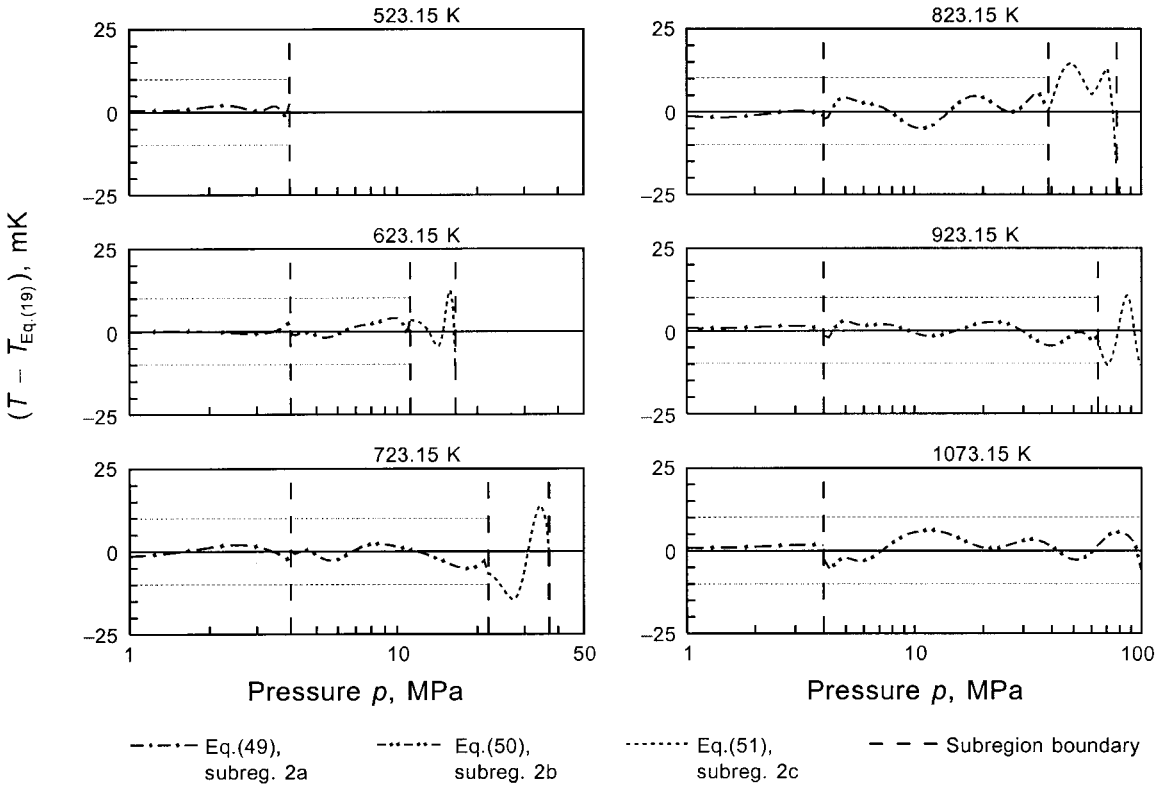

Fig. 28 Absolute deviations of temperatures *T* calculated from Eq. (49) for subregion 2(*a*), Eq. (50) for subregion 2(*b*), and Eq. (51) for subregion 2(*c*) from values $T_{Eq.(19)}$ calculated from Eq. (19) for given values of *p* and *s*

region 1 and subregion 2(*c*) and $|T - T_s| < 10$ mK for subregions 2(*a*) and 2(*b*)), the $T(p, h)$ and the $T(p, s)$ equation, respectively, might yield temperatures $T(p, h) < T_s(p)$ and $T(p, s) < T_s(p)$. Such results would indicate a state in region 1 instead of the correct region 2. The opposite case can occur when the calculations are carried out in region 1 correspondingly close to the saturated liquid line. The user should be aware of such effects in order to avoid possible problems by taking suitable measures in the program code.

The described inconsistencies are unavoidable when using backward equations and are therefore an agreed upon feature of IAPWS-IF97. Due to the insignificance of these inconsistencies they do not have any practical relevance for nearly all technical applications. Thus, because of the great advantage with regard to short computing times, the backward equations should be used whenever possible. For such applications, however, where these small inconsistencies are indeed not acceptable, the calculations must be performed with the basic equations $g(p, T)$ only by iterations. Even in this case the inconsistency is not zero, but depends on the selected convergence criterion of the iteration. The convergence criterion has to be less than 10^{-4} to 10^{-5} in $\Delta T/T$ (depending on region) to achieve a smaller inconsistency than with the backward equations.

5.6.4 The Backward Equation for Region 4. According to the concept of IAPWS-IF97 there is also a backward equation for region 4, the saturation curve, see Section 5.1 and Fig. 2. This backward equation is the saturation-temperature equation, which follows directly from the implicit saturation equation, Eq. (27), by solving it with respect to the saturation temperature T_s.

The saturation-temperature equation reads

$$\frac{T_s}{T^*} = \frac{n_{10} + D - [(n_{10} + D)^2 - 4(n_9 + n_{10}D)]^{0.5}}{2}, \quad (55)$$

where $T^* = 1$ K and

$$D = \frac{2G}{-F - (F^2 - 4EG)^{0.5}}$$

with

$$E = \beta^2 + n_3\beta + n_6$$

$$F = n_1\beta^2 + n_4\beta + n_7$$

$$G = n_2\beta^2 + n_5\beta + n_8$$

$$\text{and} \quad \beta = (p_s/p^*)^{0.25} \quad (55a)$$

with $p^* = 1$ MPa; Eq. (55*a*) is identical with Eq. (27*a*). The coefficients n_i of Eq. (55) are listed in Table A11.

Equation (55) has the same range of validity as the saturation-pressure equation, Eq. (28), which means that it covers the vapor-liquid saturation curve according to the pressure range

$$611.213 \text{ Pa} \le p \le 22.064 \text{ MPa}.$$

The value of 611.213 Pa corresponds to the pressure when Eq. (55) is extrapolated to 273.15 K. Since the saturation-pressure equation, Eq. (28), and the saturation-temperature equation, Eq. (55), have been derived from the same implicit equation, Eq. (27), for de-

Table 16 Tolerated and actual temperature differences between Eqs. (49) to (51) and Eq. (19)

Subregion	Equation	Temperature differences ΔT, mK		
		Tolerated	Maximum	RMS
2a	49	10	8.8	1.2
2b	50	10	6.5	2.8
2c	51	25	19.0	8.3

Table 17 Results of the computing-time investigations of IAPWS-IF97 in relation to IFC-67 for regions 1, 2, and 4

Region[a]	Function	Frequency of use %	Computing-time ratio (CTR value) IFC-67/IAPWS-IF97
1	$v(p,T)$	2.9	2.7
	$h(p,T)$	9.7	2.9
	$T(p,h)$	3.5	24.8
	$h(p,s)$	1.2	10.0
		Σ region 1:	5.6[b]
2	$v(p,T)$	6.1	2.1
	$h(p,T)$	12.1	2.9
	$s(p,T)$	1.4	1.4
	$T(p,h)$	8.5	12.4
	$v(p,h)$	3.1	6.4
	$s(p,h)$	1.7	4.2
	$T(p,s)$	1.7	8.1
	$h(p,s)$	4.9	5.6
		Σ region 2:	5.0[b]
4	$p_s(T)$	8.0	1.7
	$T_s(p)$	30.7	5.6
	$h'(p)$	2.25	4.4
	$h''(p)$	2.25	4.2
		Σ region 4:	4.9[b]
		Σ regions 1, 2 and 4:	**5.1**[b]

[a] For the definition of the regions see Fig. 2

[b] This CTR value is based on the computing times for the single functions weighted by the frequency-of-use values, see text

Table 18 Results of the computing-time investigations of IAPWS-IF97 in relation to IFC-67 for regions 3 and 5

Region[a]	Function	Computing-time ratio (CTR value) IFC-67/IAPWS-IF97
3	$p(v,T)$	3.8
	$h(v,T)$	4.3
	$c_p(v,T)$	2.9
	$s(v,T)$	3.2
5	$v(p,T)$	8.9[b]
	$h(p,T)$	11.9[b]
	$c_p(p,T)$	15.8[b]

[a] For the definition of the regions see Fig. 2

[b] Determined for the 1073.15 K isotherm for which IFC-67 was valid

scribing the saturation curve both Eq. (28) and Eq. (55) are completely consistent with each other. Thus, the basic and backward equation for region 4 meet the numerical consistency requirements, see Section 5.1 (item 2(*c*)).

To assist the user in computer-program verification of Eq. (55), Table A29 contains corresponding test values.

5.7 Computing Time of IAPWS-IF97 in Relation to IFC-67. A very important requirement on IAPWS-IF97 was that its computation speed in relation to IFC-67 should be significantly faster, see Section 4.4. The computation-speed investigations of IAPWS-IF97 in comparison with IFC-67 were based on a special procedure agreed within IAPWS.

The computing times were measured with a benchmark program developed by IAPWS; this program calculates the corresponding functions at a large number of state points well distributed proportionately over each region. The test configuration agreed on was a PC Intel 486 DX 33 processor and the MS Fortran 5.1 compiler.[13] The relevant functions of IAPWS-IF97 were programmed with regard to short computing times. The calculations with IFC-67 were carried out with the ASME program package [30] speeded up by excluding all parts which were not needed for these special benchmark tests.

The measured computing times were used to calculate computing-time ratios IFC-67/IAPWS-IF97, called CTR values in the following. These CTR values, determined in a different way for regions 1, 2, and 4 and for regions 3 and 5 (see Section 4.4), are the characteristic quantities for the judgment of how much faster the calculations with IAPWS-IF97 are in comparison with IFC-67. Metastable states were not included in these investigations.

5.7.1 Computing-Time Investigations for Regions 1, 2, and 4. The computing-time investigations for regions 1, 2, and 4 of IAPWS-IF97, which are particularly relevant to computing time for industrial calculations, were performed for the functions listed in Table 17. Each function is associated with a frequency-of-use value. Both the selection of the functions and the values for the corresponding frequency of use are based on a worldwide survey made among the power plant companies and related industries, see also Section 4.4.

For the computing-time comparison between IAPWS-IF97 and IFC-67 for regions 1, 2, and 4, the total CTR value of these three regions together was the decisive criterion, where the frequencies of use have to be taken into account. The total CTR value was calculated as follows: As has been described before, the computing times for each function were determined for IFC-67 and for IAPWS-IF97. Then, these values were weighted by the corresponding frequencies of use and added up for the 16 functions of the three regions. The total CTR value is obtained from the sum of the weighted computing times for IFC-67 divided by the corresponding value for IAPWS-IF97. The total CTR value for regions 1, 2, and 4 amounts to

$$\mathrm{CTR}_{\mathrm{regions1,2,4}} = 5.1. \tag{56}$$

This means that for regions 1, 2, and 4 together the property calculations with IAPWS-IF97 are more than five times faster than with IFC-67.

Table 17 also contains total CTR values separately for each of regions 1, 2, and 4. In addition, CTR values for each single function are given. When using IAPWS-IF97 the functions depending on p, h and p, s for regions 1 and 2 and on p for region 4 were calculated from the backward equations alone (functions explicit in T) or from the basic equations in combination with the corresponding backward equation.

5.7.2 Computing-Time Investigations for Regions 3 and 5. For regions 3 and 5 of IAPWS-IF97 the CTR values only relate to the single functions listed in Table 18 and are given by the quotient of the computing time needed for IFC-67 calculation and the computing time when using IAPWS-IF97; there were no frequency-of-use values for functions relevant to these two regions.

For region 3 of IAPWS-IF97, corresponding to regions 3 and 4 of IFC-67, 10 percent of the test points were in region 4 of IFC-67. For region 5 of IAPWS-IF97, the CTR values were determined for 1073.15 K, the maximum temperature for which IFC-67 was valid. Table 18 lists the CTR values obtained for the relevant functions of regions 3 and 5. Roughly speaking, IAPWS-IF97 is more than three times faster than IFC-67 for region 3 and more than nine times faster for region 5 measured for the 1073.15 K isotherm where region 5 overlaps IFC-67.

5.8 Uncertainties of IAPWS-IF97. In this section uncertainties are given for the properties specific volume, specific isobaric heat capacity, speed of sound, and saturation pressure when calculated from the corresponding equations of IAPWS-IF97. Uncertainties cannot be derived for the specific enthalpy, since there is no reasonable basis for their estimation; the values of the specific enthalpy depend on the selection of the zero point. For enthalpy differences, and here only these are of interest, one can conclude that the uncertainty of isobaric enthalpy differences is always smaller than the uncertainty of the isobaric heat capacity.

[13] This test configuration was established at the IAPWS meeting in 1992. If a faster processor and/or an other compiler than specified above are used for the described benchmark tests, similar results are obtained for the computation-speed comparisons between IAPWS-IF97 and IFC-67; this statement is based on recent test calculations using more recent processors and compilers.

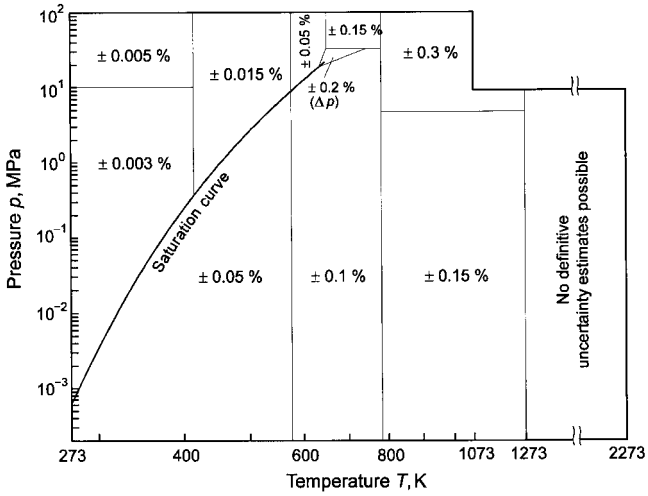

Fig. 29 Uncertainties in specific volume, Δv, estimated for the corresponding equations of IAPWS-IF97. In the enlarged critical region (triangle), the uncertainty is given as percentage uncertainty in pressure, Δp. This region is bordered by the two isochores 0.0019 m^3 kg^{-1} and 0.0069 m^3 kg^{-1} and by the 30 MPa isobar. The positions of the lines separating the uncertainty regions are approximate.

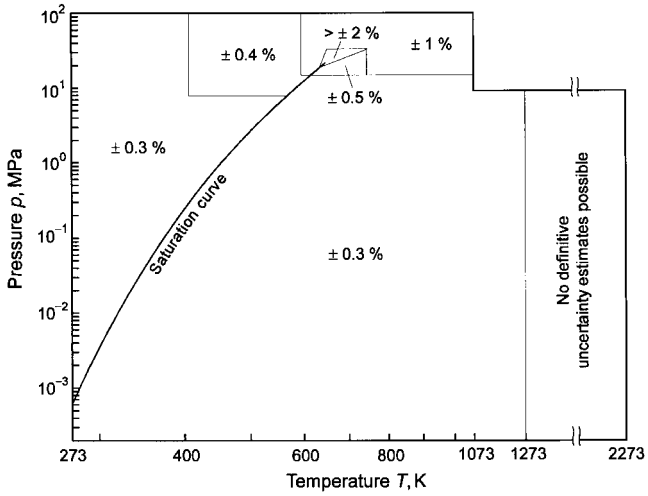

Fig. 31 Uncertainties in speed of sound, Δw, estimated for the corresponding equations of IAPWS-IF97. For the definition of the triangle around the critical point, see Fig. 29. The positions of the lines separating the uncertainty regions are approximate.

The estimated uncertainties for the above mentioned properties result from two contributions:

- Uncertainty of the scientific standard for the thermodynamic properties of water and steam, the IAPWS-95 formulation [7, 8], from which the values of the properties were calculated to fit the equations of the industrial formulation IAPWS-IF97. The uncertainty of IAPWS-95 is mainly based on the estimated uncertainties of the selected experimental data of the properties [8], which had been used for the development of the scientific standard.
- Deviations of IAPWS-IF97 from IAPWS-95 regarding the properties considered.

The uncertainties of the properties v, c_p, and w calculated from IAPWS-IF97 for the single-phase region are indicated in Figs. 29 to 31 as tolerance values. As used here "tolerance" means the range of possible values as judged by IAPWS, and no statistical significance can be attached to it. With regard to the uncertainty for the specific isobaric heat capacity and the speed of sound, see Figs. 30 and 31, it should be noted that the uncertainties for these properties increase drastically when approaching the critical point. The statement "no definitive uncertainty estimates possible" for temperatures above 1273 K is based on the fact that this range is beyond the range of validity of IAPWS-95 and the corresponding input values for IAPWS-IF97 were extrapolated from IAPWS-95.

The estimated uncertainties of the saturation pressure calculated from the IAPWS-IF97 are given in Fig. 32.

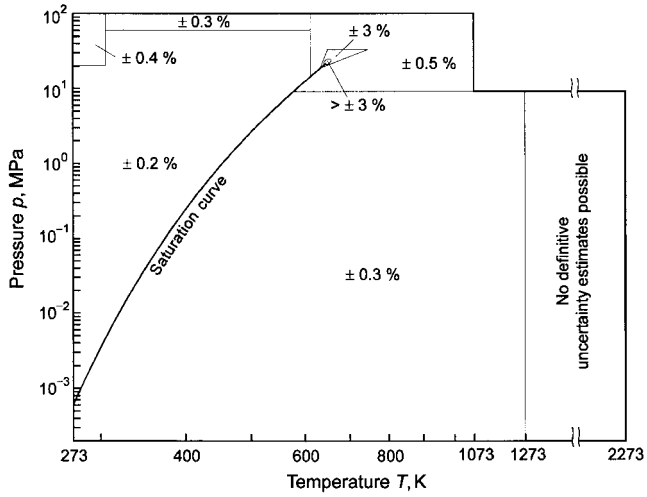

Fig. 30 Uncertainties in specific isobaric heat capacity, Δc_p, estimated for the corresponding equations of IAPWS-IF97. For the definition of the triangle around the critical point, see Fig. 29. The positions of the lines separating the uncertainty regions are approximate.

6 Concluding Remarks

The decisive factor for the development of a new industrial formulation was the explicit desire for a significant increase of the computation speed in comparison with the previous industrial standard IFC-67. For the technically most important regions of state the calculations with IAPWS-IF97 are more than five times faster than with IFC-67 and hence the new formulation clearly exceeds the requirement of a three times faster calculation of the thermodynamic properties of water and steam. Moreover, in the meantime, from many test calculations it has become evident that the enormous improvement of the consistency along region boundaries is of great advantage particularly for common use. Concerning accuracy, IAPWS-IF97 is clearly better than IFC-67, namely on average 7.5 times more accurate in the specific volume, 18 times in the specific enthalpy, 12 times in the isobaric heat capacity, 32 times in the speed of sound, and 8.5 times in the saturation pressure, where the improvement in both the isobaric heat capacity and the speed of sound is to be particularly emphasized. A further important advantage is that IAPWS-IF97 does not only yield reasonable results for the main properties v, h, s, c_p, and w but

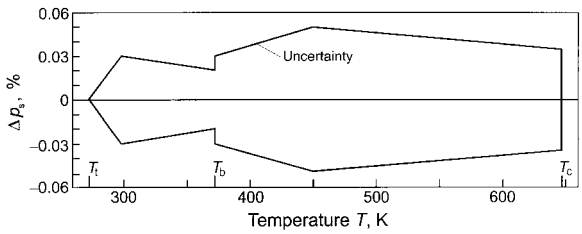

Fig. 32 Uncertainties in saturation pressure, Δp_s, estimated for the saturation-pressure equation, Eq. (28)

for any property which can be calculated from any combination of the first and second derivatives of the fundamental equations $g(p, T)$ and $f(\rho, T)$, respectively, with respect to their independent variables. All in all it can be concluded that with regard to all three items, computation speed, consistency along region boundaries, and accuracy, a new quality standard has been achieved with the IAPWS Industrial Formulation 1997.

The new formulation IAPWS-IF97 is valid for immediate general use. Thus, there is need to modify the corresponding design and application codes.

In addition to this comprehensive article, there are also new steam tables based on IAPWS-IF97, as examples see references [3, 4, 4*a*]. Moreover, computer codes based on IAPWS-IF97 are available from several institutions; information about such software can be obtained from the IAPWS national committees, see the IAPWS Web site http://www.iapws.org.

Acknowledgments

The authors are indebted to the members of the following IAPWS groups (so far as we are not members ourselves): Task Group "New Industrial Formulation," Working Group "Industrial Calculations," Working Group "Thermophysical Properties of Water and Steam," and Task Group "New Industrial Formulation-Evaluation." In particular we are grateful to the chairman and vice chairman of the Working Group "Industrial Calculations," B. Rukes and W. T. Parry, for their continuous support of this comprehensive project over the years. We are also indebted to the chairman of the Task Group "New Industrial Formulation-Evaluation," K. Miyagawa, and his colleagues R. Spencer, R. B. McClintock, and H. W. Bradly for their exceptional efforts when testing IAPWS-IF97 regarding the fulfillment of requirements and checking the influence on real power-cycle calculations. Moreover, we are grateful to all IAPWS colleagues who contributed to the entire project of the development of the new industrial formulation IAPWS-IF97. On behalf of all of them we would like to thank the presidents of IAPWS who held office during the development period of IAPWS-IF97, namely J. R. Cooper, J. M. H. Levelt Sengers, K. Watanabe, and R. Fernández-Prini.

One of us (W.W.) wishes to express his warmest thanks to Mr. C. Bonsen for his help in handling the computer programs for plotting the most part of the figures. Two of us (W.W. and A.D.) are particularly grateful to the Deutsche Forschungsgemeinschaft (German Research Association) for their financial support of that part of the development of IAPWS-IF97 which was carried out at the Ruhr-University Bochum and the Technical University Dresden.

Finally, we are very grateful to the members of the US Steam Properties subcommittee and to the US National Representative to IAPWS, J. M. H. Levelt Sengers, for their help to get published this comprehensive article in the ASME journal. Our special thank is due to the Secretary of the US subcommittee, A. H. Harvey, for his very effective help in this matter.

References

1 International Formulation Committee of the 6th International Conference on the Properties of Steam, 1967, "The 1967 IFC Formulation for Industrial Use," Verein Deutscher Ingenieure, Düsseldorf.

2 International Association for the Properties of Water and Steam, 1997, "IAPWS Industrial Formulation 1997 for the Thermodynamic Properties of Water and Steam," IAPWS Release, IAPWS Secretariat.[14]

3 Wagner, W., and Kruse, A., 1998, "Properties of Water and Steam/ Zustandsgrößen von Wasser und Wasserdampf/IAPWS-IF97," Springer-Verlag, Berlin, Heidelberg.

4 1999 JSME Steam Tables Based on IAPWS-IF97, 1999, The Japan Society of Mechanical Engineers, Tokyo.

4*a* Parry, W. T., Bellows, J. C., Gallagher, J. S., and Harvey, A. H., 2000, "ASME International Steam Tables for Industrial Use," ASME Press, New York.

5 Setzmann, U., and Wagner, W., 1989, "A New Method for Optimizing the Structure of Thermodynamic Correlation Equations," *Int. J. Thermophysics*, Vol. 10, pp. 1103–1126.

6 Preston–Thomas, H., 1990, "The International Temperature Scale of 1990 (ITS-90)," *Metrologia*, Vol. 27, pp. 3–10.

7 International Association for the Properties of Water and Steam, 1996, "IAPWS Formulation 1995 for the Thermodynamic Properties of Ordinary Water Substance for General and Scientific Use," *IAPWS Release*, IAPWS Secretariat.[14]

8 Wagner, W., and Pruß, A., 1999, "The IAPWS Formulation 1995 for the Thermodynamic Properties of Ordinary Water Substance for General and Scientific Use," to be submitted to J. Phys. Chem. Ref. Data.

9 International Association for the Properties of Water and Steam, 1994, "Skeleton Tables 1985 for the Thermodynamic Properties of Ordinary Water Substance," *IAPWS Release*, IAPWS Secretariat; also in: White, Jr., H. J., Sengers, J. V., Neumann, D. B., and Bellows, J. C., eds., 1995, "Physical Chemistry of Aqueous Systems: Meeting the Needs of Industry," Proceedings of the 12th International Conference on the Properties of Water and Steam, Begell House, New York, pp. A13–A32.

10 International Formulation Committee of ICPS, 1965, "Minutes of the Meeting of the International Formulation Committee of ICPS," Prague.

11 Cohen, E. R., and Taylor, B. N., 1986, "The 1986 Adjustment of the Fundamental Physical Constants," *CODATA Bulletin*, No. 63, Committee on Data for Science and Technology, Int. Council of Scientific Unions, Pergamon Press, Oxford.

12 Audi, G., and Wapstra, A. H., 1993, "The 1993 Atomic Mass Evaluation, (I) Atomic Mass Table," *Nuclear Physics*, Vol. A 565, pp. 1–65.

13 IUPAC, 1991, "Isotopic Compositions of the Elements 1989," Commission on Atomic Weights and Isotopic Abundances, Subcommittee for Isotopic Abundance Measurements, *Pure and Appl. Chem.*, Vol. 63, pp. 991–1002.

14 International Association for the Properties of Water and Steam, 1995, "Release on The Values of Temperature, Pressure and Density of Ordinary and Heavy Water Substances at Their Respective Critical Points," IAPWS Secretariat; also in: White, Jr., H. J., Sengers, J. V., Neumann, D. B., and Bellows, J. C., eds., 1995, "Physical Chemistry of Aqueous Systems: Meeting the Needs of Industry," Proceedings of the 12th International Conference on the Properties of Water and Steam, Begell House, New York, pp. A101–A102.

15 Guildner, L. A., Johnson, D. P., and Jones, F. E., 1976, "Vapor Pressure of Water at Its Triple Point," *J. Res. Natl. Bur. Stand.*, Vol. 80A, pp. 505–521.

16 Setzmann, U., and Wagner, W., 1991, "A New Equation of State and Tables of Thermodynamic Properties for Methane Covering the Range from the Melting Line to 625 K at Pressures up to 1000 MPa," *J. Phys. Chem. Ref. Data*, Vol. 20, pp. 1061–1155.

17 Span, R., and Wagner, W., 1996, "A New Equation of State for Carbon Dioxide Covering the Fluid Region from the Triple-Point Temperature to 1100 K at Pressures up to 800 MPa," *J. Phys. Chem. Ref. Data*, Vol. 25, pp. 1509–1596.

18 Kruse, A., and Wagner, W., 1998, "Neue Zustandsgleichungen für industrielle Anwendungen im technisch relevanten Zustandsgebiet von Wasser," *Fortschr.-Ber. VDI*, Reihe 6, Nr. 393, VDI-Verlag, Düsseldorf.

19 Wagner, W., 1974, "Eine mathematisch statistische Methode zum Aufstellen thermodynamischer Gleichungen—gezeigt am Beispiel der Dampfdruckkurve reiner fluider Stoffe," *Fortschr.-Ber. VDI-Z.*, Reihe 3, Nr. 39, VDI-Verlag, Düsseldorf.

19*a* Kretzschmar, H.-J., Stöcker, I., Klinger, J., and Dittmann, A., 2000, "Calculation of Thermodynamic Derivatives of Water and Steam Using the New Industrial Formulation IAPWS-IF97," Proceedings of the 13th International Conference on the Properties of Water and Steam, P. Tremaine, P. G. Hill, D. Irish, and P. V. Balakrishnan, eds., NRC Press, Ottawa.

20 International Association for the Properties of Water and Steam, 1994, "Release on the Pressure along the Melting and the Sublimation Curves of Ordinary Water Substance," in Wagner, W., Saul, A., and Pruß, A., 1994, *J. Phys. Chem. Ref. Data*, Vol. 23, pp. 515–527; also in White, Jr., H. J., Sengers, J. V., Neumann, D. B., and Bellows, J. C., eds., 1995, "Physical Chemistry of Aqueous Systems: Meeting the Needs of Industry," Proceedings of the 12th International Conference on the Properties of Water and Steam, Begell House, New York, pp. A9–A12.

21 Miyagawa, K., Spencer, R. C., McClintock, R. B., Bradly, H. W., Kodl, I., Perstrup, C., Parry, W. T., Rukes, B., Scala, M., and Smith, P. F., 1997, "Acceptance Test Report of Proposal of a New Industrial Formulation of IAPWS," report, IAPWS Task Group NIF Evaluation.[14]

22 Kretzschmar, H.-J., Oguchi, K., and Willkommen, Th., 2000, "Numerically Consistent Equations for Vapor Pressure $p_s(T)$ and Saturation Temperature $T_s(p)$ of Ordinary Water Substance," to be submitted to *Int. J. Thermophysics.*

23 Willkommen, Th., Kretzschmar, H.-J., and Dittmann, A., 1995, "An Algorithm for Setting Up Numerically Consistent Forward and Backward Equations for Process Modelling," in White, Jr., H. J., Sengers, J. V., Neumann, D. B., Bellows, J. C., eds., "Physical Chemistry of Aqueous Systems: Meeting the Needs of Industry," Proceedings of the 12th International Conference on the Properties of Water and Steam, Begell House, New York, pp. 194–201.

24 Zschunke, T., Kretzschmar, H.-J., and Dittmann, A., 1991, "Erstellung von konsistenten Zustandsgleichungen mit simultaner gleichmäßiger Approximation," *Brennstoff-Wärme-Kraft*, Vol. 43, pp. 567–570.

25 Mareš, R., and Šifner, O., 1996, "Equation of state for Superheated Steam in the Range from 800 to 2000°C and Pressures up to 10 MPa," *Acta Techn. CSAV*, Vol. 41, pp. 647–652.

26 Cooper, J. R., 1982, "Representation of the Ideal-Gas Thermodynamic Properties of Water," *Int. J. Thermophysics*, Vol. 3, pp. 35–43.

27 Willkommen, Th., 1996, "Ein Algorithmus zur Aufstellung numerisch kon-

[14] Mailing address: Executive Secretary of IAPWS, Dr. R. B. Dooley, EPRI, 3412 Hillview Avenue, Palo Alto, California 94304, USA

sistenter Gleichungen für die in Prozeßmodellierungen benötigten thermodynamihen Umkehrfunktionen," dissertation, Technische Universität Dresden, Fakultät Maschinenwesen, Dresden.

28 Smukala, J., 1995, "Entwicklung eines Verfahrens zur Berücksichtigung der numerischen Konsistenz bei der Aufstellung von Zustandsgleichungen in Form von Vorwärts- und Rückwärtsgleichungen," Diplomarbeit, Lehrstuhl für Thermodyamik, Ruhr-Universität Bochum, Bochum.

29 Trübenbach, J., 1999, "Ein Algorithmus zur Aufstellung rechenzeitoptimierter Gleichungen für thermodynamische Zustandsgrößen," *Fortschr.-Ber. VDI*, Reihe 6, Nr. 417, VDI-Verlag, Düsseldorf.

30 McClintock, R. B., and Silvestri, G. J., 1968, *Formulations and Iterative Procedures for the Calculation of Properties of Steam*, ASME, New York.

APPENDIX

This appendix contains Tables A1 to A29 in which the coefficients, exponents, and test values for computer-program verification are listed.

Table A1 Coefficients of Eqs. (10) and (11)[a]

i	n_i	i	n_i
1	$0.348\,051\,856\,289\,69 \times 10^{3}$	4	$0.572\,544\,598\,627\,46 \times 10^{3}$
2	$-0.116\,718\,598\,799\,75 \times 10^{1}$	5	$0.139\,188\,397\,788\,70 \times 10^{2}$
3	$0.101\,929\,700\,393\,26 \times 10^{-2}$		

[a] For computer-program verification, Eqs.(10) and (11) must meet the following T-p point: $T = 0.623\,150\,000 \times 10^{3}$ K, $p = 0.165\,291\,643 \times 10^{2}$ MPa

Table A2 Coefficients and exponents of Eq. (15)

i	I_i	J_i	n_i	i	I_i	J_i	n_i
1	0	−2	$0.146\,329\,712\,131\,67$	18	2	3	$-0.441\,418\,453\,308\,46 \times 10^{-5}$
2	0	−1	$-0.845\,481\,871\,691\,14$	19	2	17	$-0.726\,949\,962\,975\,94 \times 10^{-15}$
3	0	0	$-0.375\,636\,036\,720\,40 \times 10^{1}$	20	3	−4	$-0.316\,796\,448\,450\,54 \times 10^{-4}$
4	0	1	$0.338\,551\,691\,683\,85 \times 10^{1}$	21	3	0	$-0.282\,707\,979\,853\,12 \times 10^{-5}$
5	0	2	$-0.957\,919\,633\,878\,72$	22	3	6	$-0.852\,051\,281\,201\,03 \times 10^{-9}$
6	0	3	$0.157\,720\,385\,132\,28$	23	4	−5	$-0.224\,252\,819\,080\,00 \times 10^{-5}$
7	0	4	$-0.166\,164\,171\,995\,01 \times 10^{-1}$	24	4	−2	$-0.651\,712\,228\,956\,01 \times 10^{-6}$
8	0	5	$0.812\,146\,299\,835\,68 \times 10^{-3}$	25	4	10	$-0.143\,417\,299\,379\,24 \times 10^{-12}$
9	1	−9	$0.283\,190\,801\,238\,04 \times 10^{-3}$	26	5	−8	$-0.405\,169\,968\,601\,17 \times 10^{-6}$
10	1	−7	$-0.607\,063\,015\,658\,74 \times 10^{-3}$	27	8	−11	$-0.127\,343\,017\,416\,41 \times 10^{-8}$
11	1	−1	$-0.189\,900\,682\,184\,19 \times 10^{-1}$	28	8	−6	$-0.174\,248\,712\,306\,34 \times 10^{-9}$
12	1	0	$-0.325\,297\,487\,705\,05 \times 10^{-1}$	29	21	−29	$-0.687\,621\,312\,955\,31 \times 10^{-18}$
13	1	1	$-0.218\,417\,171\,754\,14 \times 10^{-1}$	30	23	−31	$0.144\,783\,078\,285\,21 \times 10^{-19}$
14	1	3	$-0.528\,383\,579\,699\,30 \times 10^{-4}$	31	29	−38	$0.263\,357\,816\,627\,95 \times 10^{-22}$
15	2	−3	$-0.471\,843\,210\,732\,67 \times 10^{-3}$	32	30	−39	$-0.119\,476\,226\,400\,71 \times 10^{-22}$
16	2	0	$-0.300\,017\,807\,930\,26 \times 10^{-3}$	33	31	−40	$0.182\,280\,945\,814\,04 \times 10^{-23}$
17	2	1	$0.476\,613\,939\,069\,87 \times 10^{-4}$	34	32	−41	$-0.935\,370\,872\,924\,58 \times 10^{-25}$

Table A3 Thermodynamic property values calculated from Eq. (15) for selected temperatures and pressures

Property	$T = 300$ K $p = 3$ MPa	$T = 300$ K $p = 80$ MPa	$T = 500$ K $p = 3$ MPa
v, m^3 kg^{-1}	$0.100\,215\,168 \times 10^{-2}$	$0.971\,180\,894 \times 10^{-3}$	$0.120\,241\,800 \times 10^{-2}$
h, kJ kg^{-1}	$0.115\,331\,273 \times 10^{3}$	$0.184\,142\,828 \times 10^{3}$	$0.975\,542\,239 \times 10^{3}$
u, kJ kg^{-1}	$0.112\,324\,818 \times 10^{3}$	$0.106\,448\,356 \times 10^{3}$	$0.971\,934\,985 \times 10^{3}$
s, kJ kg^{-1} K^{-1}	0.392 294 792	0.368 563 852	$0.258\,041\,912 \times 10^{1}$
c_p, kJ kg^{-1} K^{-1}	$0.417\,301\,218 \times 10^{1}$	$0.401\,008\,987 \times 10^{1}$	$0.465\,580\,682 \times 10^{1}$
w, m s^{-1}	$0.150\,773\,921 \times 10^{4}$	$0.163\,469\,054 \times 10^{4}$	$0.124\,071\,337 \times 10^{4}$

Table A4 Coefficients and exponents of Eq. (20)[a]

i	J_i^o	n_i^o	i	J_i^o	n_i^o
1[a]	0	$-0.969\,276\,865\,002\,17 \times 10^{1}$	6	−2	$0.142\,408\,191\,714\,44 \times 10^{1}$
2[a]	1	$0.100\,866\,559\,680\,18 \times 10^{2}$	7	−1	$-0.438\,395\,113\,194\,50 \times 10^{1}$
3	−5	$-0.560\,879\,112\,830\,20 \times 10^{-2}$	8	2	$-0.284\,086\,324\,607\,72$
4	−4	$0.714\,527\,380\,814\,55 \times 10^{-1}$	9	3	$0.212\,684\,637\,533\,07 \times 10^{-1}$
5	−3	$-0.407\,104\,982\,239\,28$			

[a] If Eq. (20) is incorporated into Eq. (23), instead of the values for n_1^o and n_2^o given above, the following values for these two coefficients must be used:
$n_1^o = -0.969\,372\,683\,930\,49 \times 10^{1}$, $n_2^o = 0.100\,872\,759\,700\,06 \times 10^{2}$

Table A5 Coefficients and exponents of Eq. (21)

i	I_i	J_i	n_i	i	I_i	J_i	n_i
1	1	0	$-0.177\,317\,424\,732\,13 \times 10^{-2}$	23	7	0	$-0.590\,595\,643\,242\,70 \times 10^{-17}$
2	1	1	$-0.178\,348\,622\,923\,58 \times 10^{-1}$	24	7	11	$-0.126\,218\,088\,991\,01 \times 10^{-5}$
3	1	2	$-0.459\,960\,136\,963\,65 \times 10^{-1}$	25	7	25	$-0.389\,468\,424\,357\,39 \times 10^{-1}$
4	1	3	$-0.575\,812\,590\,834\,32 \times 10^{-1}$	26	8	8	$0.112\,562\,113\,604\,59 \times 10^{-10}$
5	1	6	$-0.503\,252\,787\,279\,30 \times 10^{-1}$	27	8	36	$-0.823\,113\,408\,979\,98 \times 10^{1}$
6	2	1	$-0.330\,326\,416\,702\,03 \times 10^{-4}$	28	9	13	$0.198\,097\,128\,020\,88 \times 10^{-7}$
7	2	2	$-0.189\,489\,875\,163\,15 \times 10^{-3}$	29	10	4	$0.104\,069\,652\,101\,74 \times 10^{-18}$
8	2	4	$-0.393\,927\,772\,433\,55 \times 10^{-2}$	30	10	10	$-0.102\,347\,470\,959\,29 \times 10^{-12}$
9	2	7	$-0.437\,972\,956\,505\,73 \times 10^{-1}$	31	10	14	$-0.100\,181\,793\,795\,11 \times 10^{-8}$
10	2	36	$-0.266\,745\,479\,140\,87 \times 10^{-4}$	32	16	29	$-0.808\,829\,086\,469\,85 \times 10^{-10}$
11	3	0	$0.204\,817\,376\,923\,09 \times 10^{-7}$	33	16	50	$0.106\,930\,318\,794\,09$
12	3	1	$0.438\,706\,672\,844\,35 \times 10^{-6}$	34	18	57	$-0.336\,622\,505\,741\,71$
13	3	3	$-0.322\,776\,772\,385\,70 \times 10^{-4}$	35	20	20	$0.891\,858\,453\,554\,21 \times 10^{-24}$
14	3	6	$-0.150\,339\,245\,421\,48 \times 10^{-2}$	36	20	35	$0.306\,293\,168\,762\,32 \times 10^{-12}$
15	3	35	$-0.406\,682\,535\,626\,49 \times 10^{-1}$	37	20	48	$-0.420\,024\,676\,982\,08 \times 10^{-5}$
16	4	1	$-0.788\,473\,095\,593\,67 \times 10^{-9}$	38	21	21	$-0.590\,560\,296\,856\,39 \times 10^{-25}$
17	4	2	$0.127\,907\,178\,522\,85 \times 10^{-7}$	39	22	53	$0.378\,269\,476\,134\,57 \times 10^{-5}$
18	4	3	$0.482\,253\,727\,185\,07 \times 10^{-6}$	40	23	39	$-0.127\,686\,089\,346\,81 \times 10^{-14}$
19	5	7	$0.229\,220\,763\,376\,61 \times 10^{-5}$	41	24	26	$0.730\,876\,105\,950\,61 \times 10^{-28}$
20	6	3	$-0.167\,147\,664\,510\,61 \times 10^{-10}$	42	24	40	$0.554\,147\,153\,507\,78 \times 10^{-16}$
21	6	16	$-0.211\,714\,723\,213\,55 \times 10^{-2}$	43	24	58	$-0.943\,697\,072\,412\,10 \times 10^{-6}$
22	6	35	$-0.238\,957\,419\,341\,04 \times 10^{2}$				

Table A6 Thermodynamic property values calculated from Eq. (19) for selected temperatures and pressures

Property	$T = 300$ K $p = 0.0035$ MPa	$T = 700$ K $p = 0.0035$ MPa	$T = 700$ K $p = 30$ MPa
v, m^3 kg^{-1}	$0.394\,913\,866 \times 10^{2}$	$0.923\,015\,898 \times 10^{2}$	$0.542\,946\,619 \times 10^{-2}$
h, kJ kg^{-1}	$0.254\,991\,145 \times 10^{4}$	$0.333\,568\,375 \times 10^{4}$	$0.263\,149\,474 \times 10^{4}$
u, kJ kg^{-1}	$0.241\,169\,160 \times 10^{4}$	$0.301\,262\,819 \times 10^{4}$	$0.246\,861\,076 \times 10^{4}$
s, kJ kg^{-1} K^{-1}	$0.852\,238\,967 \times 10^{1}$	$0.101\,749\,996 \times 10^{2}$	$0.517\,540\,298 \times 10^{1}$
c_p, kJ kg^{-1} K^{-1}	$0.191\,300\,162 \times 10^{1}$	$0.208\,141\,274 \times 10^{1}$	$0.103\,505\,092 \times 10^{2}$
w, m s^{-1}	$0.427\,920\,172 \times 10^{3}$	$0.644\,289\,068 \times 10^{3}$	$0.480\,386\,523 \times 10^{3}$

Table A7 Coefficients and exponents of Eq. (24)

i	I_i	J_i	n_i	i	I_i	J_i	n_i
1	1	0	$-0.733\,622\,601\,865\,06 \times 10^{-2}$	8	3	4	$-0.634\,980\,376\,573\,13 \times 10^{-2}$
2	1	2	$-0.882\,238\,319\,431\,46 \times 10^{-1}$	9	3	16	$-0.860\,430\,930\,285\,88 \times 10^{-1}$
3	1	5	$-0.723\,345\,552\,132\,45 \times 10^{-1}$	10	4	7	$0.753\,215\,815\,227\,70 \times 10^{-2}$
4	1	11	$-0.408\,131\,785\,344\,55 \times 10^{-2}$	11	4	10	$-0.792\,383\,754\,461\,39 \times 10^{-2}$
5	2	1	$0.200\,978\,033\,802\,07 \times 10^{-2}$	12	5	9	$-0.228\,881\,607\,784\,47 \times 10^{-3}$
6	2	7	$-0.530\,459\,218\,986\,42 \times 10^{-1}$	13	5	10	$-0.264\,565\,014\,828\,10 \times 10^{-2}$
7	2	16	$-0.761\,904\,090\,869\,70 \times 10^{-2}$				

Table A8 Thermodynamic property values calculated from Eq. (23) for selected values of temperature and pressure

Property	$T = 450$ K $p = 1$ MPa	$T = 440$ K $p = 1$ MPa	$T = 450$ K $p = 1.5$ MPa
v, m^3 kg^{-1}	0.192 516 540	0.186 212 297	0.121 685 206
h, kJ kg^{-1}	$0.276\,881\,115 \times 10^{4}$	$0.274\,015\,123 \times 10^{4}$	$0.272\,134\,539 \times 10^{4}$
u, kJ kg^{-1}	$0.257\,629\,461 \times 10^{4}$	$0.255\,393\,894 \times 10^{4}$	$0.253\,881\,758 \times 10^{4}$
s, kJ kg^{-1} K^{-1}	$0.656\,660\,377 \times 10^{1}$	$0.650\,218\,759 \times 10^{1}$	$0.629\,170\,440 \times 10^{1}$
c_p, kJ kg^{-1} K^{-1}	$0.276\,349\,265 \times 10^{1}$	$0.298\,166\,443 \times 10^{1}$	$0.362\,795\,578 \times 10^{1}$
w, m s^{-1}	$0.498\,408\,101 \times 10^{3}$	$0.489\,363\,295 \times 10^{3}$	$0.481\,941\,819 \times 10^{3}$

Table A9 Coefficients and exponents of Eq. (25)

i	I_i	J_i	n_i	i	I_i	J_i	n_i
1	0	0	$0.106\,580\,700\,285\,13 \times 10^{1}$	21	3	4	$-0.201\,899\,150\,235\,70 \times 10^{1}$
2	0	0	$-0.157\,328\,452\,902\,39 \times 10^{2}$	22	3	16	$-0.821\,476\,371\,739\,63 \times 10^{-2}$
3	0	1	$0.209\,443\,969\,743\,07 \times 10^{2}$	23	3	26	$-0.475\,960\,357\,349\,23$
4	0	2	$-0.768\,677\,078\,787\,16 \times 10^{1}$	24	4	0	$0.439\,840\,744\,735\,00 \times 10^{-1}$
5	0	7	$0.261\,859\,477\,879\,54 \times 10^{1}$	25	4	2	$-0.444\,764\,354\,287\,39$
6	0	10	$-0.280\,807\,811\,486\,20 \times 10^{1}$	26	4	4	$0.905\,720\,707\,197\,33$
7	0	12	$0.120\,533\,696\,965\,17 \times 10^{1}$	27	4	26	$0.705\,224\,500\,879\,67$
8	0	23	$-0.845\,668\,128\,125\,02 \times 10^{-2}$	28	5	1	$0.107\,705\,126\,263\,32$
9	1	2	$-0.126\,543\,154\,777\,14 \times 10^{1}$	29	5	3	$-0.329\,136\,232\,589\,54$
10	1	6	$-0.115\,244\,078\,066\,81 \times 10^{1}$	30	5	26	$-0.508\,710\,620\,411\,58$
11	1	15	$0.885\,210\,439\,843\,18$	31	6	0	$-0.221\,754\,008\,730\,96 \times 10^{-1}$
12	1	17	$-0.642\,077\,651\,816\,07$	32	6	2	$0.942\,607\,516\,650\,92 \times 10^{-1}$
13	2	0	$0.384\,934\,601\,866\,71$	33	6	26	$0.164\,362\,784\,479\,61$
14	2	2	$-0.852\,147\,088\,242\,06$	34	7	2	$-0.135\,033\,722\,413\,48 \times 10^{-1}$
15	2	6	$0.489\,722\,815\,418\,77 \times 10^{1}$	35	8	26	$-0.148\,343\,453\,524\,72 \times 10^{-1}$
16	2	7	$-0.305\,026\,172\,569\,65 \times 10^{1}$	36	9	2	$0.579\,229\,536\,280\,84 \times 10^{-3}$
17	2	22	$0.394\,205\,368\,791\,54 \times 10^{-1}$	37	9	26	$0.323\,089\,047\,037\,11 \times 10^{-2}$
18	2	26	$0.125\,584\,084\,243\,08$	38	10	0	$0.809\,648\,029\,962\,15 \times 10^{-4}$
19	3	0	$-0.279\,993\,296\,987\,10$	39	10	1	$-0.165\,576\,797\,950\,37 \times 10^{-3}$
20	3	2	$0.138\,997\,995\,694\,60 \times 10^{1}$	40	11	26	$-0.449\,238\,990\,618\,15 \times 10^{-4}$

Table A10 Thermodynamic property values calculated from Eq. (25) for selected temperatures and densities

Property	$T = 650$ K $\rho = 500$ kg m^{-3}	$T = 650$ K $\rho = 200$ kg m^{-3}	$T = 750$ K $\rho = 500$ kg m^{-3}
p, MPa	$0.255\,837\,018 \times 10^{2}$	$0.222\,930\,643 \times 10^{2}$	$0.783\,095\,639 \times 10^{2}$
h, kJ kg^{-1}	$0.186\,343\,019 \times 10^{4}$	$0.237\,512\,401 \times 10^{4}$	$0.225\,868\,845 \times 10^{4}$
u, kJ kg^{-1}	$0.181\,226\,279 \times 10^{4}$	$0.226\,365\,868 \times 10^{4}$	$0.210\,206\,932 \times 10^{4}$
s, kJ kg^{-1} K^{-1}	$0.405\,427\,273 \times 10^{1}$	$0.485\,438\,792 \times 10^{1}$	$0.446\,971\,906 \times 10^{1}$
c_p, kJ kg^{-1} K^{-1}	$0.138\,935\,717 \times 10^{2}$	$0.446\,579\,342 \times 10^{2}$	$0.634\,165\,359 \times 10^{1}$
w, m s^{-1}	$0.502\,005\,554 \times 10^{3}$	$0.383\,444\,594 \times 10^{3}$	$0.760\,696\,041 \times 10^{3}$

Table A11 Coefficients of Eqs. (27), (28), and (55)

i	n_i	i	n_i
1	$0.116\,705\,214\,527\,67 \times 10^{4}$	6	$0.149\,151\,086\,135\,30 \times 10^{2}$
2	$-0.724\,213\,167\,032\,06 \times 10^{6}$	7	$-0.482\,326\,573\,615\,91 \times 10^{4}$
3	$-0.170\,738\,469\,400\,92 \times 10^{2}$	8	$0.405\,113\,405\,420\,57 \times 10^{6}$
4	$0.120\,208\,247\,024\,70 \times 10^{5}$	9	$-0.238\,555\,575\,678\,49$
5	$-0.323\,255\,503\,223\,33 \times 10^{7}$	10	$0.650\,175\,348\,447\,98 \times 10^{3}$

Table A12 Saturation-pressure values calculated from Eq. (28) for selected temperatures

T, K	p_s, MPa
300	$0.353\,658\,941 \times 10^{-2}$
500	$0.263\,889\,776 \times 10^{1}$
600	$0.123\,443\,146 \times 10^{2}$

Table A13 Coefficients and exponents of Eq. (30)

i	J_i^o	n_i^o	i	J_i^o	n_i^o
1	0	$-0.131\,799\,836\,742\,01 \times 10^{2}$	4	−2	0.369 015 349 803 33
2	1	$0.685\,408\,416\,344\,34 \times 10^{1}$	5	−1	$-0.311\,613\,182\,139\,25 \times 10^{1}$
3	−3	$-0.248\,051\,489\,334\,66 \times 10^{-1}$	6	2	−0.329 616 265 389 17

Table A14 Coefficients and exponents of Eq. (31)

i	I_i	J_i	n_i	i	I_i	J_i	n_i
1	1	0	$-0.125\,631\,835\,895\,92 \times 10^{-3}$	4	2	9	$-0.397\,248\,283\,595\,69 \times 10^{-5}$
2	1	1	$0.217\,746\,787\,145\,71 \times 10^{-2}$	5	3	3	$0.129\,192\,282\,897\,84 \times 10^{-6}$
3	1	3	$-0.459\,428\,208\,999\,10 \times 10^{-2}$				

Table A15 Thermodynamic property values calculated from Eq. (29) for selected temperatures and pressures

Property	$T = 1500$ K $p = 0.5$ MPa	$T = 1500$ K $p = 8$ MPa	$T = 2000$ K $p = 8$ MPa
v, m^3 kg^{-1}	$0.138\,455\,354 \times 10^{1}$	$0.865\,156\,616 \times 10^{-1}$	0.115 743 146
h, kJ kg^{-1}	$0.521\,976\,332 \times 10^{4}$	$0.520\,609\,634 \times 10^{4}$	$0.658\,380\,291 \times 10^{4}$
u, kJ kg^{-1}	$0.452\,748\,654 \times 10^{4}$	$0.451\,397\,105 \times 10^{4}$	$0.565\,785\,774 \times 10^{4}$
s, kJ kg^{-1} K^{-1}	$0.965\,408\,431 \times 10^{1}$	$0.836\,546\,724 \times 10^{1}$	$0.915\,671\,044 \times 10^{1}$
c_p, kJ kg^{-1} K^{-1}	$0.261\,610\,228 \times 10^{1}$	$0.264\,453\,866 \times 10^{1}$	$0.285\,306\,750 \times 10^{1}$
w, m s^{-1}	$0.917\,071\,933 \times 10^{3}$	$0.919\,708\,859 \times 10^{3}$	$0.105\,435\,806 \times 10^{4}$

Table A16 Coefficients and exponents of Eq. (37)

i	I_i	J_i	n_i	i	I_i	J_i	n_i
1	0	0	$-0.238\,724\,899\,245\,21 \times 10^{3}$	11	1	4	$-0.659\,647\,494\,236\,38 \times 10^{1}$
2	0	1	$0.404\,211\,886\,379\,45 \times 10^{3}$	12	1	10	$0.939\,654\,008\,783\,63 \times 10^{-2}$
3	0	2	$0.113\,497\,468\,817\,18 \times 10^{3}$	13	1	32	$0.115\,736\,475\,053\,40 \times 10^{-6}$
4	0	6	$-0.584\,576\,160\,480\,39 \times 10^{1}$	14	2	10	$-0.258\,586\,412\,820\,73 \times 10^{-4}$
5	0	22	$-0.152\,854\,824\,131\,40 \times 10^{-3}$	15	2	32	$-0.406\,443\,630\,847\,99 \times 10^{-8}$
6	0	32	$-0.108\,667\,076\,953\,77 \times 10^{-5}$	16	3	10	$0.664\,561\,861\,916\,35 \times 10^{-7}$
7	1	0	$-0.133\,917\,448\,726\,02 \times 10^{2}$	17	3	32	$0.806\,707\,341\,030\,27 \times 10^{-10}$
8	1	1	$0.432\,110\,391\,835\,59 \times 10^{2}$	18	4	32	$-0.934\,777\,712\,139\,47 \times 10^{-12}$
9	1	2	$-0.540\,100\,671\,705\,06 \times 10^{2}$	19	5	32	$0.582\,654\,420\,206\,01 \times 10^{-14}$
10	1	3	$0.305\,358\,922\,039\,16 \times 10^{2}$	20	6	32	$-0.150\,201\,859\,535\,03 \times 10^{-16}$

Table A17 Temperature values calculated from Eq. (37) for selected pressures and enthalpies

p, MPa	h, kJ kg^{-1}	T, K
3	500	$0.391\,798\,509 \times 10^{3}$
80	500	$0.378\,108\,626 \times 10^{3}$
80	1500	$0.611\,041\,229 \times 10^{3}$

Table A18 Coefficients and exponents of Eq. (39)

i	I_i	J_i	n_i	i	I_i	J_i	n_i
1	0	0	$0.174\,782\,680\,583\,07 \times 10^{3}$	11	1	12	$0.356\,721\,106\,073\,66 \times 10^{-9}$
2	0	1	$0.348\,069\,308\,928\,73 \times 10^{2}$	12	1	31	$0.173\,324\,969\,948\,95 \times 10^{-23}$
3	0	2	$0.652\,925\,849\,784\,55 \times 10^{1}$	13	2	0	$0.566\,089\,006\,548\,37 \times 10^{-3}$
4	0	3	0.330 399 817 754 89	14	2	1	$-0.326\,354\,831\,397\,17 \times 10^{-3}$
5	0	11	$-0.192\,813\,829\,231\,96 \times 10^{-6}$	15	2	2	$0.447\,782\,866\,906\,32 \times 10^{-4}$
6	0	31	$-0.249\,091\,972\,445\,73 \times 10^{-22}$	16	2	9	$-0.513\,221\,569\,085\,07 \times 10^{-9}$
7	1	0	$-0.261\,076\,364\,893\,32$	17	2	31	$-0.425\,226\,570\,422\,07 \times 10^{-25}$
8	1	1	0.225 929 659 815 86	18	3	10	$0.264\,004\,413\,606\,89 \times 10^{-12}$
9	1	2	$-0.642\,564\,633\,952\,26 \times 10^{-1}$	19	3	32	$0.781\,246\,004\,597\,23 \times 10^{-28}$
10	1	3	$0.788\,762\,892\,705\,26 \times 10^{-2}$	20	4	32	$-0.307\,321\,999\,036\,68 \times 10^{-30}$

Table A19 Temperature values calculated from Eq. (39) for selected pressures and entropies

p, MPa	s, kJ kg^{-1} K^{-1}	T, K
3	0.5	$0.307\,842\,258 \times 10^{3}$
80	0.5	$0.309\,979\,785 \times 10^{3}$
80	3	$0.565\,899\,909 \times 10^{3}$

Table A20 Coefficients of Eqs. (41) and (42)[a]

i	n_i	i	n_i
1	$0.905\,842\,785\,147\,23 \times 10^{3}$	4	$0.265\,265\,719\,084\,28 \times 10^{4}$
2	−0.679 557 863 992 41	5	$0.452\,575\,789\,059\,48 \times 10^{1}$
3	$0.128\,090\,027\,301\,36 \times 10^{-3}$		

[a] For computer-program verification, Eqs. (41) and (42) must meet the following p-h point: $p = 0.100\,000\,000 \times 10^{3}$ MPa, $h = 0.351\,600\,432\,3 \times 10^{4}$ kJ kg^{-1}

Table A21 Coefficients and exponents of the backward equation $T(p, h)$ for subregion 2(*a*), Eq. (43)

i	I_i	J_i	n_i	i	I_i	J_i	n_i
1	0	0	$0.108\,989\,523\,182\,88 \times 10^{4}$	18	2	7	$0.116\,708\,730\,771\,07 \times 10^{2}$
2	0	1	$0.849\,516\,544\,955\,35 \times 10^{3}$	19	2	36	$0.128\,127\,984\,040\,46 \times 10^{9}$
3	0	2	$-0.107\,817\,480\,918\,26 \times 10^{3}$	20	2	38	$-0.985\,549\,096\,232\,76 \times 10^{9}$
4	0	3	$0.331\,536\,548\,012\,63 \times 10^{2}$	21	2	40	$0.282\,245\,469\,730\,02 \times 10^{10}$
5	0	7	$-0.742\,320\,167\,902\,48 \times 10^{1}$	22	2	42	$-0.359\,489\,714\,107\,03 \times 10^{10}$
6	0	20	$0.117\,650\,487\,243\,56 \times 10^{2}$	23	2	44	$0.172\,273\,499\,131\,97 \times 10^{10}$
7	1	0	$0.184\,457\,493\,557\,90 \times 10^{1}$	24	3	24	$-0.135\,513\,342\,407\,75 \times 10^{5}$
8	1	1	$-0.417\,927\,005\,496\,24 \times 10^{1}$	25	3	44	$0.128\,487\,346\,646\,50 \times 10^{8}$
9	1	2	$0.624\,781\,969\,358\,12 \times 10^{1}$	26	4	12	$0.138\,657\,242\,832\,26 \times 10^{1}$
10	1	3	$-0.173\,445\,631\,081\,14 \times 10^{2}$	27	4	32	$0.235\,988\,325\,565\,14 \times 10^{6}$
11	1	7	$-0.200\,581\,768\,620\,96 \times 10^{3}$	28	4	44	$-0.131\,052\,365\,450\,54 \times 10^{8}$
12	1	9	$0.271\,960\,654\,737\,96 \times 10^{3}$	29	5	32	$0.739\,998\,354\,747\,66 \times 10^{4}$
13	1	11	$-0.455\,113\,182\,858\,18 \times 10^{3}$	30	5	36	$-0.551\,966\,970\,300\,60 \times 10^{6}$
14	1	18	$0.309\,196\,886\,047\,55 \times 10^{4}$	31	5	42	$0.371\,540\,859\,962\,33 \times 10^{7}$
15	1	44	$0.252\,266\,403\,578\,72 \times 10^{6}$	32	6	34	$0.191\,277\,292\,396\,60 \times 10^{5}$
16	2	0	$-0.617\,074\,228\,683\,39 \times 10^{-2}$	33	6	44	$-0.415\,351\,648\,356\,34 \times 10^{6}$
17	2	2	$-0.310\,780\,466\,295\,83$	34	7	28	$-0.624\,598\,551\,925\,07 \times 10^{2}$

Table A22 Coefficients and exponents of the backward equation $T(p, h)$ for subregion 2(*b*), Eq. (44)

i	I_i	J_i	n_i	i	I_i	J_i	n_i
1	0	0	$0.148\,950\,410\,795\,16 \times 10^{4}$	20	2	40	$0.712\,803\,519\,595\,51 \times 10^{-4}$
2	0	1	$0.743\,077\,983\,140\,34 \times 10^{3}$	21	3	1	$0.110\,328\,317\,899\,99 \times 10^{-3}$
3	0	2	$-0.977\,083\,187\,978\,37 \times 10^{2}$	22	3	2	$0.189\,552\,483\,879\,02 \times 10^{-3}$
4	0	12	$0.247\,424\,647\,056\,74 \times 10^{1}$	23	3	12	$0.308\,915\,411\,605\,37 \times 10^{-2}$
5	0	18	$-0.632\,813\,200\,160\,26$	24	3	24	$0.135\,555\,045\,549\,49 \times 10^{-2}$
6	0	24	$0.113\,859\,521\,296\,58 \times 10^{1}$	25	4	2	$0.286\,402\,374\,774\,56 \times 10^{-6}$
7	0	28	$-0.478\,118\,636\,486\,25$	26	4	12	$-0.107\,798\,573\,575\,12 \times 10^{-4}$
8	0	40	$0.852\,081\,234\,315\,44 \times 10^{-2}$	27	4	18	$-0.764\,627\,124\,548\,14 \times 10^{-4}$
9	1	0	$0.937\,471\,473\,779\,32$	28	4	24	$0.140\,523\,928\,183\,16 \times 10^{-4}$
10	1	2	$0.335\,931\,186\,049\,16 \times 10^{1}$	29	4	28	$-0.310\,838\,143\,314\,34 \times 10^{-4}$
11	1	6	$0.338\,093\,556\,014\,54 \times 10^{1}$	30	4	40	$-0.103\,027\,382\,121\,03 \times 10^{-5}$
12	1	12	$0.168\,445\,396\,719\,04$	31	5	18	$0.282\,172\,816\,350\,40 \times 10^{-6}$
13	1	18	$0.738\,757\,452\,366\,95$	32	5	24	$0.127\,049\,022\,719\,45 \times 10^{-5}$
14	1	24	$-0.471\,287\,374\,361\,86$	33	5	40	$0.738\,033\,534\,682\,92 \times 10^{-7}$
15	1	28	$0.150\,202\,731\,397\,07$	34	6	28	$-0.110\,301\,392\,389\,09 \times 10^{-7}$
16	1	40	$-0.217\,641\,142\,197\,50 \times 10^{-2}$	35	7	2	$-0.814\,563\,652\,078\,33 \times 10^{-13}$
17	2	2	$-0.218\,107\,553\,247\,61 \times 10^{-1}$	36	7	28	$-0.251\,805\,456\,829\,62 \times 10^{-10}$
18	2	8	$-0.108\,297\,844\,036\,77$	37	9	1	$-0.175\,652\,339\,694\,07 \times 10^{-17}$
19	2	18	$-0.463\,333\,246\,358\,12 \times 10^{-1}$	38	9	40	$0.869\,341\,563\,441\,63 \times 10^{-14}$

Table A23 Coefficients and exponents of the backward equation $T(p, h)$ for subregion 2(*c*), Eq. (45)

i	I_i	J_i	n_i	i	I_i	J_i	n_i
1	−7	0	$-0.323\,683\,985\,552\,42 \times 10^{13}$	13	1	4	$0.379\,660\,012\,724\,86 \times 10^{1}$
2	−7	4	$0.732\,633\,509\,021\,81 \times 10^{13}$	14	1	8	$-0.108\,429\,848\,800\,77 \times 10^{2}$
3	−6	0	$0.358\,250\,899\,454\,47 \times 10^{12}$	15	2	4	$-0.453\,641\,726\,766\,60 \times 10^{-1}$
4	−6	2	$-0.583\,401\,318\,515\,90 \times 10^{12}$	16	6	0	$0.145\,591\,156\,586\,98 \times 10^{-12}$
5	−5	0	$-0.107\,830\,682\,174\,70 \times 10^{11}$	17	6	1	$0.112\,615\,974\,072\,30 \times 10^{-11}$
6	−5	2	$0.208\,255\,445\,631\,71 \times 10^{11}$	18	6	4	$-0.178\,049\,822\,406\,86 \times 10^{-10}$
7	−2	0	$0.610\,747\,835\,645\,16 \times 10^{6}$	19	6	10	$0.123\,245\,796\,908\,32 \times 10^{-6}$
8	−2	1	$0.859\,777\,225\,355\,80 \times 10^{6}$	20	6	12	$-0.116\,069\,211\,309\,84 \times 10^{-5}$
9	−1	0	$-0.257\,457\,236\,041\,70 \times 10^{5}$	21	6	16	$0.278\,463\,670\,885\,54 \times 10^{-4}$
10	−1	2	$0.310\,810\,884\,227\,14 \times 10^{5}$	22	6	20	$-0.592\,700\,384\,741\,76 \times 10^{-3}$
11	0	0	$0.120\,823\,158\,659\,36 \times 10^{4}$	23	6	22	$0.129\,185\,829\,918\,78 \times 10^{-2}$
12	0	1	$0.482\,197\,551\,092\,55 \times 10^{3}$				

Table A24 Temperature values calculated from Eqs. (43) to (45) for selected pressures and enthalpies

Equation	p, MPa	h, kJ kg^{-1}	T, K
	0.001	3000	$0.534\,433\,241 \times 10^{3}$
43	3	3000	$0.575\,373\,370 \times 10^{3}$
	3	4000	$0.101\,077\,577 \times 10^{4}$
	5	3500	$0.801\,299\,102 \times 10^{3}$
44	5	4000	$0.101\,531\,583 \times 10^{4}$
	25	3500	$0.875\,279\,054 \times 10^{3}$
	40	2700	$0.743\,056\,411 \times 10^{3}$
45	60	2700	$0.791\,137\,067 \times 10^{3}$
	60	3200	$0.882\,756\,860 \times 10^{3}$

Table A25 Coefficients and exponents of the backward equation $T(p, s)$ for subregion 2(*a*), Eq. (49)

i	I_i	J_i	n_i	i	I_i	J_i	n_i
1	−1.5	−24	$-0.392\,359\,838\,619\,84 \times 10^{6}$	24	−0.25	−11	$-0.597\,806\,388\,727\,18 \times 10^{4}$
2	−1.5	−23	$0.515\,265\,738\,272\,70 \times 10^{6}$	25	−0.25	−6	$-0.704\,014\,639\,268\,62 \times 10^{3}$
3	−1.5	−19	$0.404\,824\,431\,610\,48 \times 10^{5}$	26	0.25	1	$0.338\,367\,841\,075\,53 \times 10^{3}$
4	−1.5	−13	$-0.321\,937\,909\,239\,02 \times 10^{3}$	27	0.25	4	$0.208\,627\,866\,351\,87 \times 10^{2}$
5	−1.5	−11	$0.969\,614\,242\,186\,94 \times 10^{2}$	28	0.25	8	$0.338\,341\,726\,561\,96 \times 10^{-1}$
6	−1.5	−10	$-0.228\,678\,463\,717\,73 \times 10^{2}$	29	0.25	11	$-0.431\,244\,284\,148\,93 \times 10^{-4}$
7	−1.25	−19	$-0.449\,429\,141\,243\,57 \times 10^{6}$	30	0.5	0	$0.166\,537\,913\,564\,12 \times 10^{3}$
8	−1.25	−15	$-0.501\,183\,360\,201\,66 \times 10^{4}$	31	0.5	1	$-0.139\,862\,920\,558\,98 \times 10^{3}$
9	−1.25	−6	0.356 844 635 600 15	32	0.5	5	−0.788 495 479 998 72
10	−1.0	−26	$0.442\,353\,358\,481\,90 \times 10^{5}$	33	0.5	6	$0.721\,324\,117\,538\,72 \times 10^{-1}$
11	−1.0	−21	$-0.136\,733\,888\,117\,08 \times 10^{5}$	34	0.5	10	$-0.597\,548\,393\,982\,83 \times 10^{-2}$
12	−1.0	−17	$0.421\,632\,602\,078\,64 \times 10^{6}$	35	0.5	14	$-0.121\,413\,589\,539\,04 \times 10^{-4}$
13	−1.0	−16	$0.225\,169\,258\,374\,75 \times 10^{5}$	36	0.5	16	$0.232\,270\,967\,338\,71 \times 10^{-6}$
14	−1.0	−9	$0.474\,421\,448\,656\,46 \times 10^{3}$	37	0.75	0	$-0.105\,384\,635\,661\,94 \times 10^{2}$
15	−1.0	−8	$-0.149\,311\,307\,976\,47 \times 10^{3}$	38	0.75	4	$0.207\,189\,254\,965\,02 \times 10^{1}$
16	−0.75	−15	$-0.197\,811\,263\,204\,52 \times 10^{6}$	39	0.75	9	$-0.721\,931\,552\,604\,27 \times 10^{-1}$
17	−0.75	−14	$-0.235\,543\,994\,707\,60 \times 10^{5}$	40	0.75	17	$0.207\,498\,870\,811\,20 \times 10^{-6}$
18	−0.5	−26	$-0.190\,706\,163\,020\,76 \times 10^{5}$	41	1.0	7	$-0.183\,406\,579\,113\,79 \times 10^{-1}$
19	−0.5	−13	$0.553\,756\,698\,831\,64 \times 10^{5}$	42	1.0	18	$0.290\,362\,723\,486\,96 \times 10^{-6}$
20	−0.5	−9	$0.382\,936\,914\,373\,63 \times 10^{4}$	43	1.25	3	0.210 375 278 936 19
21	−0.5	−7	$-0.603\,918\,605\,805\,67 \times 10^{3}$	44	1.25	15	$0.256\,812\,397\,299\,99 \times 10^{-3}$
22	−0.25	−27	$0.193\,631\,026\,203\,31 \times 10^{4}$	45	1.5	5	$-0.127\,990\,029\,337\,81 \times 10^{-1}$
23	−0.25	−25	$0.426\,606\,436\,986\,10 \times 10^{4}$	46	1.5	18	$-0.821\,981\,026\,520\,18 \times 10^{-5}$

Table A26 Coefficients and exponents of the backward equation $T(p, s)$ for subregion 2(*b*), Eq. (50)

i	I_i	J_i	n_i	i	I_i	J_i	n_i
1	−6	0	$0.316\,876\,650\,834\,97 \times 10^{6}$	23	0	2	$0.417\,273\,471\,596\,10 \times 10^{2}$
2	−6	11	$0.208\,641\,758\,818\,58 \times 10^{2}$	24	0	4	$0.219\,325\,494\,345\,32 \times 10^{1}$
3	−5	0	$-0.398\,593\,998\,035\,99 \times 10^{6}$	25	0	5	$-0.103\,200\,500\,090\,77 \times 10^{1}$
4	−5	11	$-0.218\,160\,585\,188\,77 \times 10^{2}$	26	0	6	0.358 829 435 167 03
5	−4	0	$0.223\,697\,851\,942\,42 \times 10^{6}$	27	0	9	$0.525\,114\,537\,260\,66 \times 10^{-2}$
6	−4	1	$-0.278\,417\,034\,458\,17 \times 10^{4}$	28	1	0	$0.128\,389\,164\,507\,05 \times 10^{2}$
7	−4	11	$0.992\,074\,360\,714\,80 \times 10^{1}$	29	1	1	$-0.286\,424\,372\,193\,81 \times 10^{1}$
8	−3	0	$-0.751\,975\,122\,991\,57 \times 10^{5}$	30	1	2	0.569 126 836 648 55
9	−3	1	$0.297\,086\,059\,511\,58 \times 10^{4}$	31	1	3	$-0.999\,629\,545\,849\,31 \times 10^{-1}$
10	−3	11	$-0.344\,068\,785\,485\,26 \times 10^{1}$	32	1	7	$-0.326\,320\,377\,784\,59 \times 10^{-2}$
11	−3	12	0.388 155 642 491 15	33	1	8	$0.233\,209\,225\,767\,23 \times 10^{-3}$
12	−2	0	$0.175\,112\,950\,857\,50 \times 10^{5}$	34	2	0	−0.153 348 098 574 50
13	−2	1	$-0.142\,371\,128\,544\,49 \times 10^{4}$	35	2	1	$0.290\,722\,882\,399\,02 \times 10^{-1}$
14	−2	6	$0.109\,438\,033\,641\,67 \times 10^{1}$	36	2	5	$0.375\,347\,027\,411\,67 \times 10^{-3}$
15	−2	10	0.899 716 193 084 95	37	3	0	$0.172\,966\,917\,024\,11 \times 10^{-2}$
16	−1	0	$-0.337\,597\,400\,989\,58 \times 10^{4}$	38	3	1	$-0.385\,560\,508\,445\,04 \times 10^{-3}$
17	−1	1	$0.471\,628\,858\,183\,55 \times 10^{3}$	39	3	3	$-0.350\,177\,122\,926\,08 \times 10^{-4}$
18	−1	5	$-0.191\,882\,419\,936\,79 \times 10^{1}$	40	4	0	$-0.145\,663\,936\,314\,92 \times 10^{-4}$
19	−1	8	0.410 785 804 921 96	41	4	1	$0.564\,208\,572\,672\,69 \times 10^{-5}$
20	−1	9	−0.334 653 781 720 97	42	5	0	$0.412\,861\,500\,746\,05 \times 10^{-7}$
21	0	0	$0.138\,700\,347\,775\,05 \times 10^{4}$	43	5	1	$-0.206\,846\,711\,188\,24 \times 10^{-7}$
22	0	1	$-0.406\,633\,261\,958\,38 \times 10^{3}$	44	5	2	$0.164\,093\,936\,747\,25 \times 10^{-8}$

Table A27 Coefficients and exponents of the backward equation $T(p, s)$ for subregion 2(*c*), Eq. (51)

i	I_i	J_i	n_i	i	I_i	J_i	n_i
1	−2	0	$0.909\,685\,010\,053\,65 \times 10^{3}$	16	3	1	$-0.145\,970\,082\,847\,53 \times 10^{-1}$
2	−2	1	$0.240\,456\,670\,884\,20 \times 10^{4}$	17	3	5	$0.566\,311\,756\,310\,27 \times 10^{-2}$
3	−1	0	$-0.591\,623\,263\,871\,30 \times 10^{3}$	18	4	0	$-0.761\,558\,645\,845\,77 \times 10^{-4}$
4	0	0	$0.541\,454\,041\,280\,74 \times 10^{3}$	19	4	1	$0.224\,403\,429\,193\,32 \times 10^{-3}$
5	0	1	$-0.270\,983\,084\,111\,92 \times 10^{3}$	20	4	4	$-0.125\,610\,950\,134\,13 \times 10^{-4}$
6	0	2	$0.979\,765\,250\,979\,26 \times 10^{3}$	21	5	0	$0.633\,231\,326\,609\,34 \times 10^{-6}$
7	0	3	$-0.469\,667\,729\,594\,35 \times 10^{3}$	22	5	1	$-0.205\,419\,896\,753\,75 \times 10^{-5}$
8	1	0	$0.143\,992\,746\,047\,23 \times 10^{2}$	23	5	2	$0.364\,053\,703\,900\,82 \times 10^{-7}$
9	1	1	$-0.191\,042\,042\,304\,29 \times 10^{2}$	24	6	0	$-0.297\,598\,977\,892\,15 \times 10^{-8}$
10	1	3	$0.532\,991\,671\,119\,71 \times 10^{1}$	25	6	1	$0.101\,366\,185\,297\,63 \times 10^{-7}$
11	1	4	$-0.212\,529\,753\,759\,34 \times 10^{2}$	26	7	0	$0.599\,257\,196\,923\,51 \times 10^{-11}$
12	2	0	−0.311 473 344 137 60	27	7	1	$-0.206\,778\,701\,051\,64 \times 10^{-10}$
13	2	1	0.603 348 408 946 23	28	7	3	$-0.208\,742\,781\,818\,86 \times 10^{-10}$
14	2	2	$-0.427\,648\,397\,025\,09 \times 10^{-1}$	29	7	4	$0.101\,621\,668\,250\,89 \times 10^{-9}$
15	3	0	$0.581\,855\,972\,552\,59 \times 10^{-2}$	30	7	5	$-0.164\,298\,282\,813\,47 \times 10^{-9}$

Table A28 Temperature values calculated from Eqs. (49) to (51) for selected pressures and entropies

Equation	p, MPa	s, kJ kg^{-1}K^{-1}	T, K
49	0.1	7.5	$0.399\,517\,097 \times 10^{3}$
	0.1	8	$0.514\,127\,081 \times 10^{3}$
	2.5	8	$0.103\,984\,917 \times 10^{4}$
50	8	6	$0.600\,484\,040 \times 10^{3}$
	8	7.5	$0.106\,495\,556 \times 10^{4}$
	90	6	$0.103\,801\,126 \times 10^{4}$
51	20	5.75	$0.697\,992\,849 \times 10^{3}$
	80	5.25	$0.854\,011\,484 \times 10^{3}$
	80	5.75	$0.949\,017\,998 \times 10^{3}$

Table A29 Saturation-temperature values calculated from Eq. (55) for selected pressures

p, MPa	T_s, K
0.1	$0.372\,755\,919 \times 10^{3}$
1	$0.453\,035\,632 \times 10^{3}$
10	$0.584\,149\,488 \times 10^{3}$